Electrochemical Engineering of Low-Cost and High-Power Redox Flow Batteries

by

Jarrod D. Milshtein

B.S., Mechanical Engineering
Boston University, 2013

M.S., Materials Science and Engineering
Boston University, 2013

Submitted to the Department of Materials Science and Engineering
in Partial Fulfillment of the Requirements for the Degree of

Doctor of Philosophy

at the

MASSACHUSETTS INSTITUTE OF TECHNOLOGY

June 2017

Author……
Department of Materials Science and Engineering
April 25, 2017

Certified by……....
Fikile R. Brushett
Raymond A. and Helen E. St. Laurent Career Development Professor of Chemical Engineering
Thesis Supervisor

Certified by……....
Antoine Allanore
Associate Professor of Metallurgy
Thesis Reader

Accepted by……...……....
Donald R. Sadoway
John F. Elliot Professor of Materials Chemistry
Chair, Department Committee on Graduate Students

Electrochemical Engineering of Low-Cost and High-Power Redox Flow Batteries

by

Jarrod D. Milshtein

Submitted to the Department of Materials Science and Engineering
on May 11, 2017, in Partial Fulfillment of the
Requirements for the degree of Doctor of Philosophy in
Materials Science and Engineering

ABSTRACT

Grid-scale energy storage has emerged as a key technology for improving sustainability in the electricity generation sector, and redox flow batteries (RFBs) are promising devices to serve this application. Unlike enclosed batteries, RFBs implement soluble redox active species dissolved in liquid electrolytes, which are stored in large tanks. The electrolyte is pumped through an electrochemical reactor where the active species are oxidized or reduced. The size of the reactor determines the power rating, while the tank volume determines the total energy capacity, enabling scalability unique to this architecture. Recent studies have investigated a number of strategies to reduce RFB system cost. One pathway is to lower the electrolyte cost via decreased chemical costs or increased electrolyte energy density. Low-cost active species, such as redox active organic molecules (ROMs) or abundant inorganics, have gained notoriety. Raising cell potential, by identifying active species with more extreme redox potentials or implementing non-aqueous electrolytes, is an effective approach in reducing RFB cost because higher cell potential will reduce both electrolyte and reactor costs. Engineering the electrochemical stack for lower area-specific resistance (ASR) is another strategy towards dropping reactor cost through increased cell power.

The plethora of options for reducing RFB prices can be overwhelming. As such, the present work combines techno-economic (TE) modeling, reactor optimization, and new electrolyte design as a toolbox for developing a low-cost RFB prototype. The TE model first predicts RFB system price as a function of reactor performance and electrolyte materials properties, quantifying metrics to achieve desired price targets. With respect to reactor performance, the TE model identifies a range of viable reactor ASRs, and cell performance is verified experimentally. A parallel modeling study, incorporating electrolyte conductivities, Butler-Volmer kinetics, and transport in porous media, calculates cell polarization. With respect to active material and supporting electrolyte properties, the TE model provides bounded design spaces for cost effective RFBs, guiding material development campaigns. Through collaborations with organic chemists and guided materials selection, new RFB electrolytes are generated and validated in performance prototypes. Ultimately, this thesis utilizes TE modeling to guide reactor optimization and materials development cycles, targeting cost-conscious RFB design.

Thesis Supervisor: Professor Fikile R. Brushett
Title: Raymond A. and Helen E. St. Laurent Career Development Professor of Chemical Engineering

Acknowledgements

I will begin by thanking my advisor, Professor Fikile R. Brushett, for working with me and providing guidance during my tenure at MIT. His support and flexibility has made my graduate studies an enjoyable experience. Further I would like to thank Professor Klavs Jensen, Professor Yet-Ming Chiang, and Professor Antoine Allanore for serving on my thesis committee and offering continued input on my projects and career development.

I reserve a special thank you for Dr. Robert M. Darling of United Technologies, who provided much of the foundation for the experimental and modeling efforts throughout the course of my PhD. Working alongside him for the last three years has been a pleasure. His colleague, Mr. Mike L Perry, has also provided exceptional guidance. Dr. Javit Drake was also extremely helpful with some modeling studies described in this thesis.

I would also like to thank the PI's of collaborating institutions who contributed significantly to the research projects contained in this thesis: Professor Levi T. Thompson, Professor Kyle C. Smith, and Professor Susan A. Odom. Through their participation, I have had the excellent opportunity to co-author manuscripts with several talented researchers, namely: Dr. Aman Kaur, Mrs. Sydney Fisher, and Mr. Rylan Dmello. I also enjoyed working with and Mr. Kevin Tenny, who joined my project through the MIT Summer Research Program.

I thank my colleagues in the Brushett Group at MIT for their assistance on many projects and making the lab a fun place to work every day: Dr. Kyler Carroll, Dr. Liang Su, Dr. Emily Carino, Dr. Sujat Sen, Dr. Chaerin Kim, Mr. Thomas Carney, Mr. Jeff Kowalski, Mr. John Barton, Mr. Steven Brown, Mr. Mike Orella, Mr. Vincent Dietrich, Mr. McLain Leonard, Mr. Miao Wang, Mr. Andres Badel, and Ms. Jessie Hsiao. An additional thank you goes to the JCESR Flow Chemistry and Prototyping teams, whom I collaborated with for several years: Dr. Xiaoliang Wei, Dr. Wentao Duan, Dr. Rama Vemuri, Professor Brett Helms, Dr. Miles Braten, Dr. Lin Ma, Professor Jeff Moore, Dr. Yu Cao, Dr. Kevin Gallagher, Dr. Krista Hawthorne, and Dr. Tanya Breault. Finally, I would like to thank my family and friends for their continued support.

The research presented in this thesis has been funded in part by the Joint Center for Energy Storage Research, an Energy Innovation Hub funded by the United States Department of Energy, Office of Science, Basic Energy Sciences and by the MIT Energy Initiative. I also acknowledge the MIT Energy Initiative and National Science Foundation Graduate Research Fellowship for funding me over the past four years.

Table of Contents

1. Introduction

Sections of this chapter are reprinted from *Current Opinion in Chemical Engineering*, Vol 13, J. A. Kowalski, L. Su, J. D. Milshtein, F. R. Brushett, Recent advances in molecular engineering of redox active organic molecules for non-aqueous flow batteries, 45–52, Copyright (2016), with permission from Elsevier under license number 4087110623714.

1.1 Motivation

Energy storage has emerged as a key technology for improving the sustainability of electricity generation[1] by improving the efficiency of existing fossil-fuel infrastructure through load-leveling or price arbitrage,[2] alleviating the intermittency of renewables (*i.e.*, solar, wind) to promote their broad implementation,[3] and providing high-value services such as frequency regulation, voltage support, or back-up power.[2] A broad variety of grid-scale energy storage devices have been proposed, including pumped hydroelectric, compressed air, flywheels, solar-thermal, supercapacitors, and batteries, and each of these technologies offers unique attributes for grid services varying in required power or energy.[1] The primary impediment to the adoption of a new grid-scale energy storage technology is cost; the unique combination of high power, long service life, and low cost required for ubiquitous adoption makes technical innovation in this application space exceptionally difficult.[4] Successful grid-storage technologies will rely on identification of scalable architectures, where rate of cost increase does not rise with storage capacity, and inexpensive, abundant materials that can be easily purchased in enormous quantities (i.e., kilotons).[4]

Redox flow batteries (RFBs) are promising devices for low-cost grid energy storage due to decoupled capacity and power scaling, among other benefits including long lifetime, facile manufacturing, easy thermal management, and good safety features.[2,5–9] Unlike enclosed batteries (e.g., lithium ion, nickel-metal hydride), RFBs (Figure 1) implement soluble redox active species dissolved in liquid electrolytes, which are stored in large, inexpensive tanks. The electrolyte is pumped through an electrochemical stack where the active species are oxidized or reduced to store or deliver energy. The size of the electrochemical stack determines the power rating of a RFB, while the tank volume determines the total energy capacity, enabling scalability unique to the RFB architecture. A variety of RFB chemistries have been researched in recent years[8,10–12] with many examples of successful commercial deployment, such as zinc-bromine (e.g., Redflow[13]) and

organometallics (e.g., Lockheed Martin[14]). The all-vanadium redox flow battery (VRFB) has been the most successful chemistry[15,16] and several companies (e.g., Vionx Energy,[17] Gildemeister,[18] UniEnergy Technologies[19]) are presently commercializing VRFB technology with grid installations. The success of the VRFB has hinged on its facile engineering, given that all accessible redox couples lie just within the electrochemical window of the sulfuric acid-based electrolyte, enabling high cell potential without electrochemically dissociating water. Additionally, both the positive and negative electrolytes utilize the same parent species (vanadium sulfate), such that crossover does not irreversibly degrade cell performance.[16]

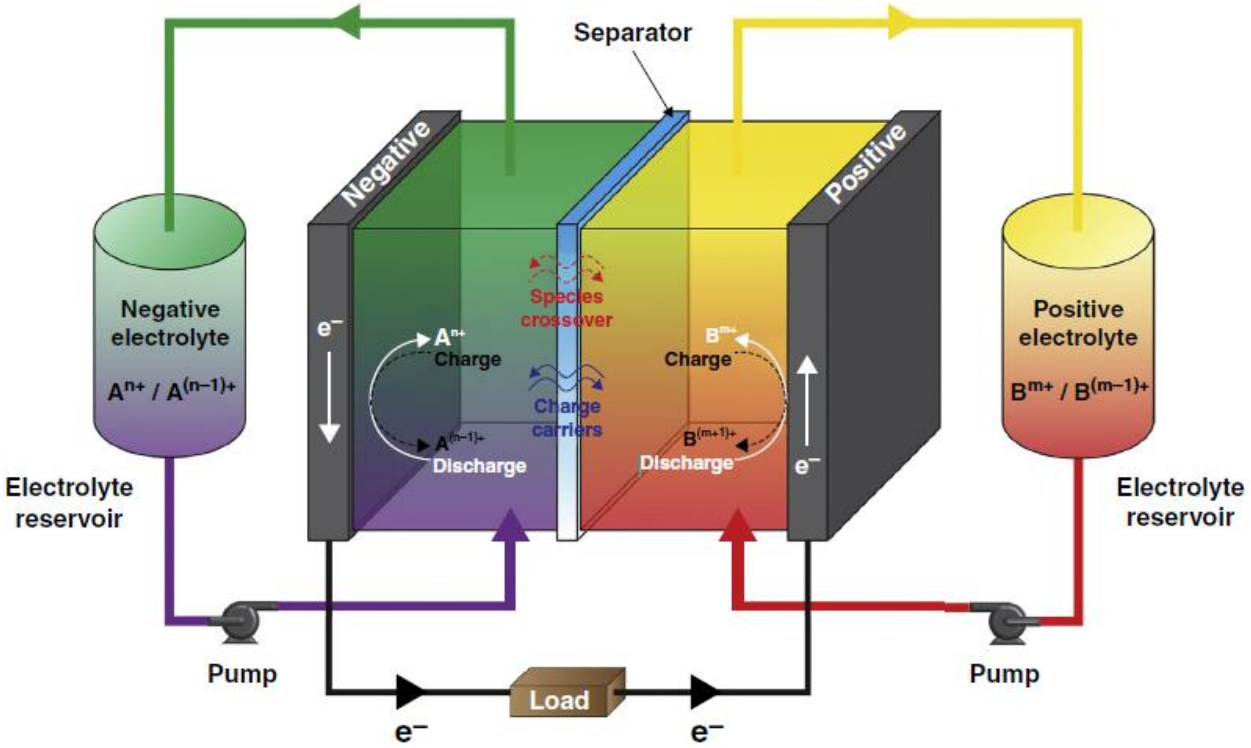

Figure 1: Schematic of a RFB. The system includes an electrochemical reactor, storage tanks, pumps, a heat exchanger, and power conditioning equipment (e.g., inverter). In operation, the two electrolyte streams are pumped into the electrochemical reactor. During charging, the active species in the positive electrolyte stream are oxidized, while the active species in the negative electrolyte stream are reduced. The opposite redox reactions take place during discharge. In this schematic, the RFB is in discharge mode. Inside the reactor, the electrolytes are separated by a membrane or porous separator that enables transport of charge-balancing ions, while blocking active species crossover.

Despite the technological success of the VRFB and other aqueous redox flow battery (AqRFB) chemistries, their capital costs are too high to enable widespread adoption. RFB prices in 2014 exceeded \$500 kWh^{-1},[20–22] well above the Department of Energy recommended target (\$150 kWh^{-1}) for an installed energy storage system with 4 h discharge.[2] Hence, recent literature

reports have investigated a variety of technological strategies to reduce RFB costs, ranging from new electrolyte materials that offer higher performance or lower cost, to improved reactor design for higher power density. As will be demonstrated quantitatively in Chapter 2, RFB costs are especially sensitive to cell potential (V) and active material cost ($\$ kg^{-1}$),[20,23] and both of these reduce the electrolyte (energy) cost contribution to the total RFB cost. Raising cell potential, by identifying active species with more extreme redox potentials or implementing non-aqueous electrolytes with wide electrochemical windows (3 – 4 V), is a particularly effective approach in reducing RFB prices because increasing cell potential will decrease both the electrolyte and reactor (power) cost contributions. Finally, engineering the electrochemical stack for lower area-specific resistance (ASR), reducing ohmic, charge transfer, or mass transport losses, is an additional strategy towards dropping reactor cost through increased cell power.

1.2 Advent of Non-aqueous Electrolytes

To date, the overwhelming majority of RFB literature reports have focused on aqueous electrolytes, arguably due to the success and optimization of the VRFB. Water is generally an easy solvent to engineer around, due to its incredibly low cost, abundance, absent toxicity, and inflammability. Aqueous-based electrolytes also will typically exhibit much higher ionic conductivies than non-aqueous options, which is a desirable feature in galvanic cells for mitigating overpotential losses. The drawback of aqueous electrolytes, however, is the relatively small electrochemical window. The thermodynamic dissociation potential for water, under standard conditions, is 1.229 V, at which water can split into hydrogen and oxygen gas.[24] These gas-evolving side reactions can negatively impact battery performance; both reactions will act as a parasitic Faradaic process, reducing the system's energy efficiency when transitioning from charge to discharge mode. The hydrogen evolution reaction (HER) produces explosive and flammable hydrogen gas, which presents safety concerns on the negative side of an aqueous battery. The oxygen evolution reaction (OER) produces oxygen gas, which can spontaneously oxidize active species in the electrolyte solutions. In the specific case of the VRFB, oxygen gas dissolved in the electrolyte can lead to imminent self-discharge due to spontaneous oxidation of V^{2+} ions to V^{3+}. In some instances, the supporting electrolyte and electrode material selection can suppress the HER and OER through slow reaction kinetics (Figure 2), permitting battery cell potentials as high as 2.0 V in some lead-acid or Zn-Br systems.[20,25]

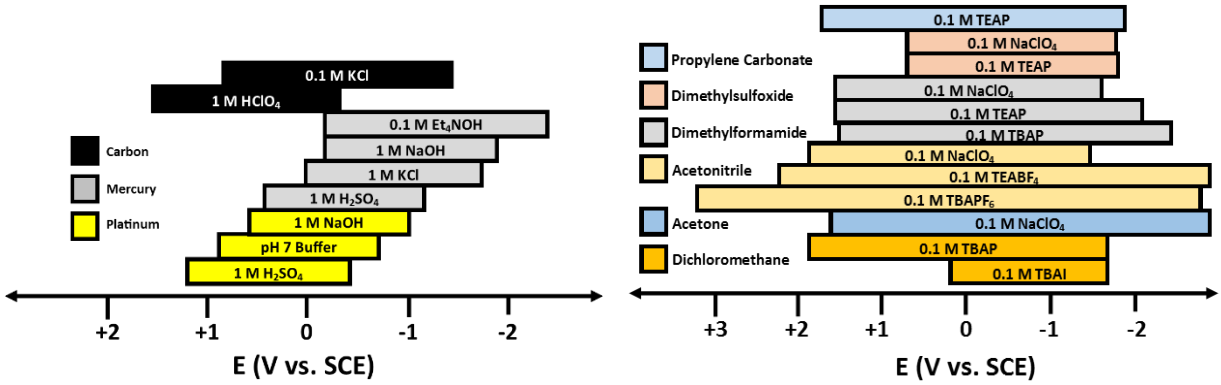

Figure 2: Electrochemical windows of water and organic solvents with different electrodes or supporting salts. (adapted from Ref. 23)[26]

Identifying electrolytes with larger electrochemical windows can enable galvanic cells with higher potentials, and higher cell potential will directly improve energy density and reduce battery costs.[20,23] Non-aqueous electrolytes have been employed in a variety of electrochemical devices, such as lithium ion batteries or electrochemical capacitors, enabling electrochemical stability windows as large as 5 V.[27] Non-aqueous electrolytes for implementation in RFBs were first proposed in the 1980s,[28] but these early reports were limited both in number and technical scope. A flurry of recent reports (post-2012) have revisited non-aqueous RFBs (NAqRFBs) as a viable pathway towards increasing the cell potential, and thereby the energy density, of RFBs.[9,11,12,29] These newer reports have considered a variety of non-aqueous solvents and supporting salt s typically employed in lithium-ion batteries or electrochemical capacitors,[30] that typically exhibit electrochemical windows in the range of 3 – 4 V (Figure 2).[26] A number of laboratory-scale NAqRFB prototypes have also surfaced, employing a range of active materials that will be described later.

Despite the technological growth of NAqRFBs, there have been two major drawbacks impeding the further adoption of non-aqueous electrolytes. First, although non-aqueous electrolytes can exhibit large electrochemical windows, laboratory prototypes have rarely exceeded the cell potentials of the best performing AqRFBs; for example, the highest cell potential reported in a functional NAqRFB prototype was 2.6 V. Second, the relatively low ionic conductivity of non-aqueous electrolytes, in comparison to their aqueous counterparts, is cited as a major impediment to NAqRFBs ever achieving power densities that are relevant for economically feasible grid operation. The low ionic conductivity of the non-aqueous electrolytes

is exacerbated when considering the even lower ionic conductivities of non-aqueous compatible ion-exchange membranes, which further limit cell performance.[31] Beyond the performance limitations of cell potential and low power density, NAqRFBs also present safety and cost concerns due to the increased flammability and cost of organic solvents.

1.3 New Active Materials: Organic Molecules, Organometallics, and Abundant Inorganics

One strategy to reduce RFB price has been to investigate new chemistries that could lower the electrolyte (energy) cost contribution to the total system price via decreased chemical costs or increased electrolyte energy density.[20,23] Key active species characteristics in determining the RFB electrolyte cost are the material cost ($\$ kg^{-1}$), molar mass ($kg mol^{-1}$), number of electrons stored per molecule, and redox potential (V).[20,23] Recently, organic redox active molecules (ROMs) have gained notoriety in possibly supplanting incumbent RFB chemistries.[10,11] ROMs are comprised of earth abundant elements (i.e., hydrogen, carbon, oxygen, nitrogen, sulfur), and their cost is not determined by production rates of raw materials or material reserves.[11] Additionally, ROMs exhibit a broad design space that can be accessed via molecular modification to tailor physicochemical characteristics, such as solubility or redox potential, for optimal behavior in a RFB.[10,11,32]

Several families of ROMs have been investigated to exploit various attractive attributes. The first literature report of a ROM for implementation in a RFB came in 2012, where 2,2,6,6-tetramethyl-1-piperidinyloxy (TEMPO) and N-methylphthalimide (NMP) served as the positive and negative active materials, respectively. Some of these chemistry combinations are highlighted in Figure 2, illustrating the active species pair and supporting salt. Many of the high potential compounds, such as TEMPO,[33] 4-Oxo-TEMPO (O-TEMPO),[34] 2,5-di-tert-butyl-1,4-bis(2-methoxyethoxy)benzene (DBBB),[35] 2,5-di-tertbutyl-1-methoxy-4-[2'-methoxyethoxy]benzene (DBMMB),[36] and 3,7-bis(trifluoromethyl)-N-ethylphenothiazine (BCF3EPT),[37] are either proven overcharge protection materials for lithium-ion batteries, or derivatives of such materials. Low potential active materials have been more difficult to identify,[38] leading to the exploration of new redox active organic molecules such as 2,3,6-trimethylquinoxaline (TMQ),[35,37] 9-fluorenone (FL),[36] and (1S)-(+)-camphoroquinone (CPQ).[34] Various other families of small redox active organic molecules have been proposed or studied for use in NAqRFBs, but have yet to be

demonstrated in a prototype cell of any kind. Some notable compounds in this category include rubrene,[39] cyanoazacarbons,[40] biphenyl,[30] and octafluoronapthalene.[30]

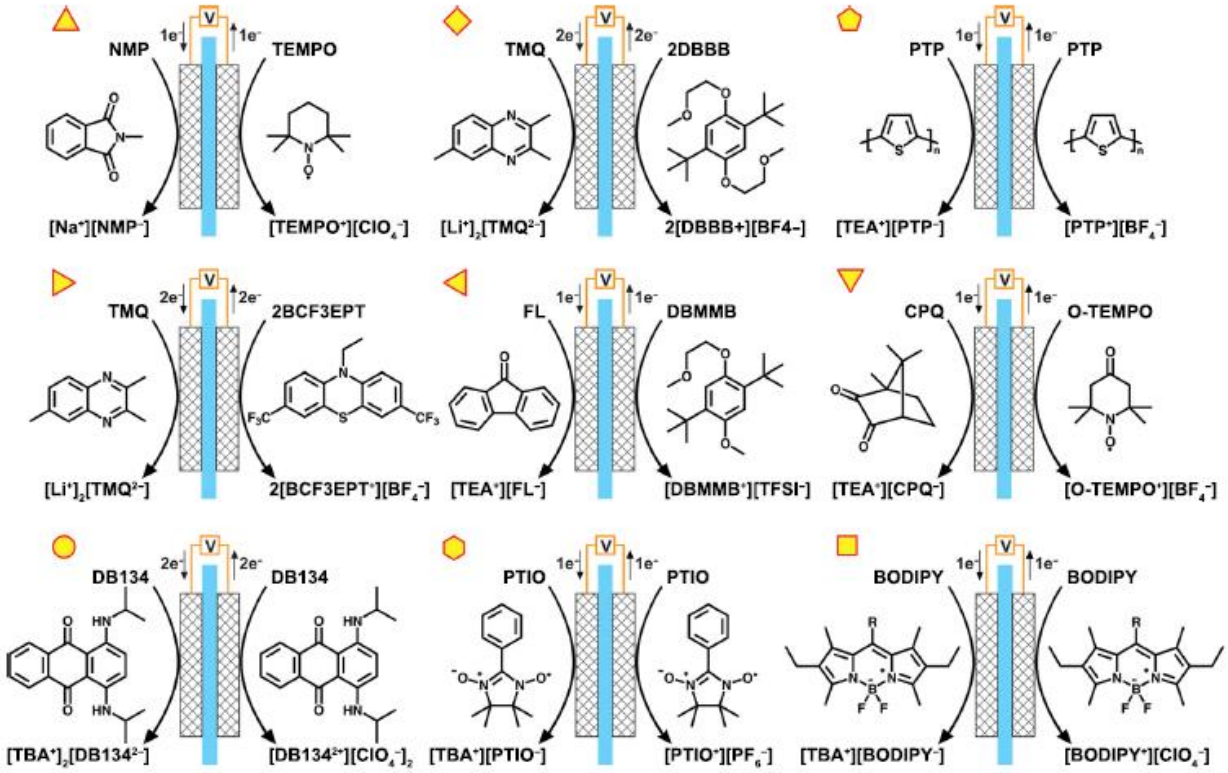

Figure 3: Summary of organic, NAqRFB chemistries employed in prototype cells.

In two specific instances, symmetric organic NAqRFBs prototypes employed the same parent molecule on both sides of the battery. These demonstration chemistries are 2-phenyl-4,4,5,5-tetramethylimidazoline-1-oxyl-3-oxide (PTIO)[41] and 1,4-bis(isopropylamino)anthraquinone (Disperse Blue 134, DB134).[42] Such symmetric organic chemistries are especially convenient because the fully discharged cell contains the same parent molecule on both sides, unlike other symmetric flow batteries (i.e. all-vanadium) that access different redox states.[42] Discharging to a single parent species can help alleviate deleterious RFB cycling effects such as irreversible crossover and electrolyte imbalance.[42,43] Of the published set of symmetric demonstration chemistries, DB134 is particularly notable because this molecule has five accessible redox states and can engage in multi-electron transfer on both sides of the battery.[42] Additionally, recent efforts have considered polymers as redox active organic charge storing species, beginning with an insoluble suspension of polythiophene (PTP).[44] This concept not only illustrated polymers as active materials for flow batteries, but also suggests that the organic species

does not necessarily have to be soluble in the electrolyte. The first soluble organic redox active polymer (RAP) proposed for use in a RFB was poly(vinylbenzyl ethyl viologens) in 2014,[45] but the first implementation of a soluble organic polymer in a NAqRFB arrived two years later in the form of poly(boron-dipyrromethane) (BODIPY). Soluble RAPs show promise for enabling low-cost size exclusion separators, in place of more expensive charge-selective membranes, but currently suffer from high solution viscosities leading to pumping challenges.[45]

Materials development campaigns for ROMs in AqRFBs have been more limited than those for non-aqueous electrolyte implementation. This discrepancy could be due to a smaller number of electrochemically active or stability redox centers in aqueous media. Nonetheless, the quinone family of molecules has been most broadly investigated for application in AqRFBs. Anthraquinone derivatives have served as promising two-electron transfer species on the negative side of the battery,[46–48] whereas benzoquinone derivatives have been targeted for the positive electrolyte.[48,49] Several TEMPO derivatives have also been investigated for use in the positive electrolyte of AqRFBs,[50–53] but the rapid decay of the charged oxoammonium cation has prevented further development beyond these initial demonstrations.[51] Three other negative electrolyte active species include viologens,[50,53,54] alloxazine,[55] and flavin.[56] A few examples of ROMs for implementation in symmetric AqRFBs have also been synthesized and tested.[57] Although a smaller number of ROMs have been investigated for AqRFBs, as compared to the non-aqueous design space, prototype demonstrations have made much more rapid advancements, drastically improving cell performance when transitioning from initial prototypes[46] to performance devices.[58]

Organometallic active species, typically comprised of a redox active metal center with innocent or non-innocent ligands, makeup another class of active material to possibly replace vanadium. These species combine the stability of a metal redox active material with the ability for molecular modification exhibited by ROMs. Some organometallic compounds are already being introduced in commercial devices, but their identities are largely unknown to the public.[14] In a similar trend to ROMs, organometallic active species for implementation in NAqRFBs have been much more heavily investigated. Metal centers have included chrome, iron, cobalt ruthenium, vanadium, nickel, manganese, and uranium, while the three ligands that have been most heavily investigated are acytelacetonate, bipyridine, and bis(acetylacetone)ethylenediamine.[29] While the organometallic active species offer fascinating fundamental electrochemistry, typically the metal selection in the active center makes many of these options cost-prohibitive before even

implementing in a flow cell. Additionally, recent literature has investigated inherently abundant inorganic species,[23] such as metal polysulfides[59–61] or iodide.[60,61] Bromine is another abundant active species, which has already gained commercial success,[13] but its toxicity and corrosive nature present safety and system durability concerns.[21]

1.4 Advances in Reactor Engineering

Resistive losses in the electrochemical reactor of an RFB can broadly be categorized as: 1) ohmic losses, 2) charge transfer losses, and 3) mass transport losses. Ohmic losses can originate from the current collector, porous electrodes, or, most significantly, the membrane. Charge transfer losses are a result of slow heterogeneous reaction kinetics (i.e., slow electron transfer between the active species and the electrode). Mass transport losses arise due to slow rates of active species delivery to the electrode surface. Figure 2 depicts how ohmic, charge transfer, and mass transfer losses contribute to the total voltage loss as a function of current density applied through the cell for a typical VRFB.[62] Engineering the electrochemical reactor can serve to reduce losses and improve performance by mitigating losses due to any of the aforementioned sources. For example, current collector and porous electrode ohmic losses can be mitigated through improved cell engineering (i.e., zero-gap architecture).[63,64] Charge transfer losses can be mitigated by enhancing reaction rates through the addition of a catalyst or electrode pretreatments, or by increasing the available reaction surface area. Mass transport rates can be mitigated by improving the rate of convective mass transfer through varied flow field design or adapting the electrode morphology.[65–67]

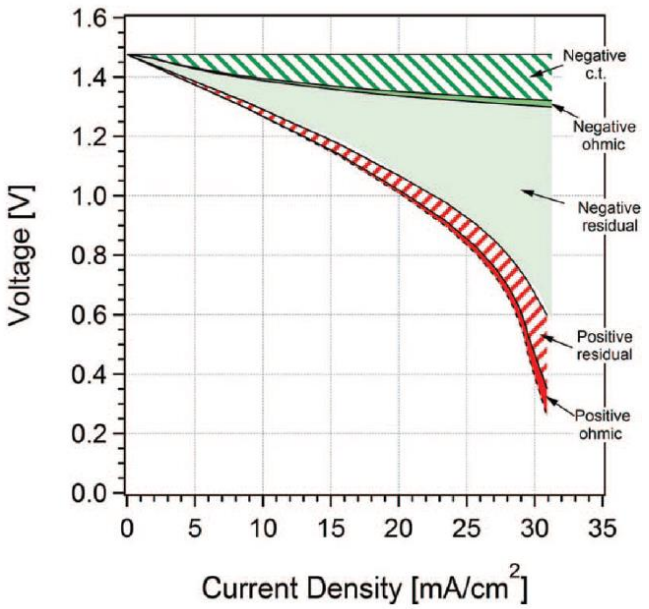

Figure 4: Polarization curve depicting the various sources of voltaic losses in a VRFB as a function of current density. Charge transfer is abbreviated as c.t., and the residual losses are due to mass transfer. Reproduced from Ref. 60 with permission of the Electrochemical Society under license number 4087190051267.

Electrochemical reactor design for the first RFBs was crude; planar electrodes with low surface area were separated from the membrane by thick layers of liquid electrolyte. The low electrolyte ionic conductivity, as compared to the electronic conductivity of the current collectors or electrodes, in combination with the low electrode surface area and slow mass transfer rates led to low device power density. The shortcomings of the initial RFB reactor designs was initially alleviated by adapting designs from fuel cells, which included flow-through porous electrodes, a structured flow field, and zero-gap architecture.[64] Porous electrodes increase the available area for heterogeneous electrochemical reactions to take place, as well as reduce the path length over which active species transport occurs. The flow field provides a structured format for distributed electrolyte delivery into the porous electrode, while also dictating the pressure drop through the reactor. Finally, the zero-gap architecture directly contacts the porous electrode to the membrane, such that electron conduction is the primary mechanism of charge transport through the thickness of the device, vastly improving the ohmic performance of a RFB.

The adoption of fuel cell-like flow fields and the zero-gap architecture enabled dramatic improvements in RFB power density,[63] and, arguably, the VRFB reactor has been engineered to a point where only marginal gains can be made. Reactor design improvements for RFBs, however,

are far from complete. In the present literature, for each newly proposed RFB chemistry, new reactor optimization studies are required to select the best flow field, electrode thickness, and electrode morphology (e.g., anthraquinone disulfonic acid / bromine[58]). NAqRFBs in particular have seen few advances in adopting AqRFB reactor design for non-aqueous electrolytes; the drastically different materials properties associated with non-aqueous electrolytes yields new design challenges and considerations. The next step in RFB reactor design is to develop chemistry-agnostic design rules so that a reactor can rapidly be optimized for an emerging chemistry.

1.5 Cost-Based Engineering Approach to RFB Design

Cost is the primary impediment to the adoption of energy storage devices, and, as such, cost must be embedded as a design criteria for RFBs during early stages of development.[4] The conventional research approach typically engages cost-agnostic design to improve performance or durability of a device, with the hope that the refined technology can achieve low costs through manufacturing innovation.[4] Cost-based materials selection and performance specification could enable discoveries[4] that push flow batteries through the low cost threshold required for broad implementation. The RFB field is aching for cost-based development guidelines, as only a few studies report cost estimates for established RFB chemistries (e.g., the VRFB),[21,68] but cost estimations merely indicate that RFBs are presently too expensive.

A recent techno-economic (TE) mode by Darling and Gallagher et al. took a critical step towards defining cost-based criteria for RFBs, by comparing the price performance of several established energy storage technologies with hypothetical, future state aqueous and non-aqueous RFBs.[20] That study specified two sets of metrics, one for each aqueous or non-aqueous, to roughly describe what the materials set and performance must look like for future RFBs to compete with other energy storage technologies. Figure 5 shows a key figure from Darling and Gallagher's analysis, indicating the available design space for aqueous and non-aqueous RFBs; the design map in Figure 5 is a powerful tool in beginning to target chemistries and performance that can achieve an aggressive cost target of \$120 kWh^{-1} for a 5 h discharge application, excluding installation costs.[20] A subsequent study recommended a range of transport characteristics for cost-effective RFB membranes,[43] and one additional study by Crawford et al. estimated NAqRFB price for various performance input parameters.[69] Given the complexity of the RFB, an investigation to

define acceptable cost and performance ranges for all components, on the level of detail of the membrane specifications outlined in Ref. 43, is warranted.

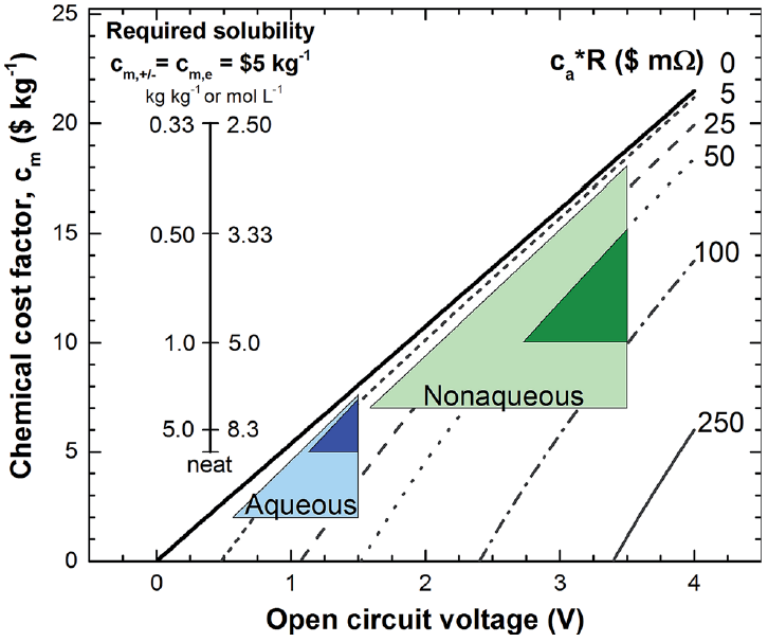

Figure 5: Available design spaces for aqueous and non-aqueous redox flow batteries, showing chemical cost factor vs. open circuit voltage (V) for various reactor costs ($c_a \cdot R$, \$ mΩ). The darkened regions of the triangles denote regions of greater likelihood for entrance to the design space. The leftmost inset vertical axis denotes required active species concentration. Reproduced from Ref. 20 under the Creative Commons Attribution 3.0 Unported License.

The plethora of engineering options for reducing RFB prices, from materials selection to reactor optimization, can be overwhelming. As such, the present work combines techno-economic (TE) modeling, reactor optimization, and new active material synthesis as a toolbox in developing design principles for an economically viable RFB prototype. The TE model first predicts RFB system price as a function of reactor performance and electrolyte materials properties, quantifying metrics to achieve the DOE-established target price. With respect to reactor performance, the TE model identifies a range of viable reactor ASRs. In the particular case of non-aqueous RFBs, experimental polarization and impedance studies quantify the relative magnitudes of ohmic, activation, and mass transfer contributions to the total ASR of a high-performance non-aqueous flow cell, originally designed for VRFB chemistry and modified for non-aqueous compatibility. While experimental efforts can quantify reactor ASR, examining the entire RFB design space experimentally would be costly and time intensive. A parallel modeling study, incorporating electrolyte / electrode conductivities, Butler-Volmer kinetics, and transport in porous media,

calculates variations in ASR contributions as functions of electrolyte and electrode properties (i.e., viscosity, conductivity, porosity). With respect to active materials properties (i.e., redox potential, solubility), the TE model provides bounded design spaces for cost effective RFBs, guiding material development campaigns. Through collaborations with organic chemists, new ROMs are synthesized and validated in performance prototypes. Ultimately, this research utilizes TE modeling to guide electrochemical reactor optimization and materials development cycles, targeting cost-conscious RFB prototypes.

1.6 Thesis Scope

This thesis aims to identify and quantify key technical hurdles impeding cost reductions for RFBs and then engages a series of experimental and modeling studies to explore several underdressed areas for improvement. To begin quantifying technical challenges, Chapter 2 develops a techno-economic model to describe the price performance of a RFB considering cost contributions from the electrolyte, reactor, balance-of-plant, and addition-to-price. In brief, the techno-economic model computes RFB price as a function of the properties and costs of materials employed in the RFB, as well as the electrochemical performance of the RFB. Once in place, the DOE cost target for grid-scale energy storage is used a guide to specify desired RFB price performance, and the techno-economic model is used to back-compute the available materials and reactor design space for economically feasible RFBs. By analyzing the available design space, quantitative performance metrics and materials selection criteria are established, and these benchmarks are placed in context of the contemporary literature. The largest discrepancies between the established literature and the techno-economic model specifications serve as launching points for the experimental studies in later chapters.

Chapter 3 is the first in a series of studies experimentally addressing cost-reducing materials for RFB electrolytes. In particular, this chapter investigates the fundamental electrochemical behavior of a new ROM, quinoxaline, for implementation in AqRFBs. Quinoxaline is an attractive molecular candidate for use in an AqRFB due it high solubility and two-electron transfer capability. A series of voltammetric studies, including cyclic or rotating disk voltammetry, considers the stability, reaction rates, and transport properties of this new molecule on small time scales. Through rapid voltammetric screening, this study identifies optimal

supporting salts and pH to enable the highest energy density and best stability, while also revealing the intriguing thermodynamic properties of this material.

Chapter 4 continues on the theme of electrolyte cost reduction, but moves into the non-aqueous electrolyte space, examining a full cell that engages two-electron transfer events in a manner that also reduces the amount of supporting salt required for cell operation. A systematic pipeline of solubility, voltammetry, bulk electrolysis, H-cell, and flow cell experiments demonstrates challenges associated with accessing multiple electron transfers in a RFB. The chapter ends with a brief quantification of how reducing the amount of supporting salt can decrease RFB price.

Chapter 5 extends the low supporting salt requirement to the limit of no supporting salt. This study demonstrates experimentally the first supporting salt free NAqRFB, offering similar electrochemical performance as the state-of-the-art laboratory prototypes. The successful of this unique configuration hinges on properly selecting active species that remain as ions throughout all states-of-charge (SOC), such that the active species provides charge storage capability, introduces high electrolyte conductivity, and affords bulk electroneutrality. Again, a brief techno-economic calculation indicates the drastic cost reductions that operating a NAqRFB can offer.

Chapter 6 transitions from electrolyte design to a broader viewpoint, investigating the relationship between non-aqueous electrolyte properties and reactor performance. A model, commercially-available ROM is employed so that electrolyte properties (e.g., conductivity, viscosity) can be measured as a function of SOC. The electrolyte is then employed in a diagnostic flow cell experiment to begin exploring how cell performance is affected by the electrolyte properties. From these experimental investigations of materials properties and cell performance, performance limitations for NAqRFBs are uncovered.

Chapter 7 builds on the knowledge of performance limitations in NAqRFBs to simultaneously engineer a new active species and flow cell architecture, evincing the lowest ASR and highest current densities achieving in a non-aqueous flow cell to date. In terms of molecular engineering, a highly soluble phenothiazine derivative is synthesized and taken through a similar electrochemical validation pipeline as outlined in Chapter 3. To validate molecular performance even more rigorously, the phenothiazine derivative is chemically oxidized so that its solubility and stability in the charged state can be evaluated. For flow cell design, a state-of-the-art vanadium flow cell architecture is modified for chemical compatibility with non-aqueous solvents. The

supporting electrolyte is selected to minimize ohmic and mass transport losses, as the final puzzle piece in delivering unprecedented non-aqueous flow cell performance.

Chapter 8 considers the excellent electrochemical performance described in Chapter 7 and engages a series of diagnostic flow cell experiments to enable a deeper understanding of key performance limitations in non-aqueous flow cell design. In a similar fashion to Chapter 6, a model active material is employed as a probe to investigate cell performance as a function of separator type, supporting electrolyte composition, electrode thickness, flow rate, and active material concentration. Through this systematic study, general guidelines for reducing non-aqueous flow cell ASR are highlighted, and performance trends are contrasted to typical observations for AqRFBs.

Chapter 9 continues reactor engineering efforts by quantifying mass transfer coefficients as a function of flow field design and flow rate. Through literature surveys surrounding the experimental studies in prior chapters, the RFB field has a lack of quantitative information linking mass transfer rates to electrode and flow field design. As such, this chapter develops a simplistic polarization model that describes the I-V characteristic of a flow cell, considering resistive losses from the electrolyte, Butler-Volmer kinetics, and convective mass transfer. The model is deliberately simple so that its mathematical form can be reduced to two dimensionless fitting parameters. This enables facile fitting of the polarization model to experimental data and subsequent extraction of quantitative mass transfer rates. A new set of systematic, diagnostic flow cell experiments are performed, where the cell polarization of a model aqueous system is measured for four different flow field design, five different flow rates, and three active species concentrations. By combing the model and experimental data, relationships among mass transfer rate, flow field design, and flow rate are discovered. This information can be used to guide future decision-making for RFB reactor design.

Chapter 10 revisits the initial techno-economic model, combining that cost description will the cell polarization model in Chapter 9. This cross-functional modeling enables refined materials selection criteria, incorporating a performance-based model; RFB price is directly linked to variations in cell performance with changes in the electrolyte properties. This refined version of the techno-economic model is applied to a case study in AqRFB membrane and supporting electrolyte selection, explicitly illustrating how changes in ionic conductivity, electrolyte viscosity, and materials costs impact RFB price.

Finally, Chapter 11 explores the implications of the results and methodology throughout from this thesis. Particular attention is given to advancing materials selection strategies and the most promising pathways for reducing RFB price.

1.7 References

1. B. Dunn, H. Kamath, and J.-M. Tarascon, *Science*, **334**, 928–935 (2011).
2. I. Gyuk et al., *Grid Energy Storage*, US Department of Energy, Washington DC, (2013) http://energy.gov/sites/prod/files/2013/12/f5/Grid%20Energy%20Storage%20December%202013.pdf.
3. P. Denholm, E. Ela, B. Kirby, and M. Milligan, *The Role of Energy Storage with Renewable Electricity Generation. NREL/TP-6A2-47187*, (2010).
4. B. L. Spatocco and D. R. Sadoway, *Electrochem. Eng. Scales Vol. 15 Mol. Process.*, **7**, 1 (2015).
5. C. Ponce de León, A. Frías-Ferrer, J. González-García, D. A. Szánto, and F. C. Walsh, *J. Power Sources*, **160**, 716–732 (2006).
6. P. Leung et al., *RSC Adv.*, **2**, 10125–10156 (2012).
7. M. Skyllas-Kazacos, M. H. Chakrabarti, S. A. Hajimolana, F. S. Mjalli, and M. Saleem, *J. Electrochem. Soc.*, **158**, R55–R79 (2011).
8. A. Z. Weber et al., *J. Appl. Electrochem.*, **41**, 1137–1164 (2011).
9. W. Wang et al., *Adv. Funct. Mater.*, **23**, 970–986 (2013).
10. M. L. Perry and A. Z. Weber, *J. Electrochem. Soc.*, **163**, A5064–A5067 (2016).
11. J. Winsberg, T. Hagemann, T. Janoschka, M. D. Hager, and U. S. Schubert, *Angew. Chem. Int. Ed.*, **56**, 686–711 (2016).
12. W. Wang and V. Sprenkle, *Nat. Chem.*, **8**, 204–206 (2016).
13. Online: Redflow, "Redflow-Field-Application-Experience-of-Zinc-Bromine-Flow-Batteries-in-a-Smart-Grid," http://redflow.com/wp-content/uploads/2015/06/Redflow-Field-Application-Experience-of-Zinc-Bromide-Flow-Batteries-in-a-Smart-Grid.pdf; cited May 9, 2017.
14. J. Goeltz et al., "Aqueous redox flow batteries comprising metal ligand coordination compounds," US Pat. US 20160276693 A1, Filed May 27, 2016.
15. G. Kear, A. A. Shah, and F. C. Walsh, *Int. J. Energy Res.*, **36**, 1105–1120 (2012).
16. M. Skyllas-Kazacos, L. Cao, M. Kazacos, N. Kausar, and A. Mousa, *ChemSusChem*, **9**, 1521–1543 (2016).
17. B. Gellerman, "A novel liquid battery could hold potential for unlimited energy storage," *BostonomiX Ser*, (2017) http://www.wbur.org/bostonomix/2017/01/09/vanadium-liquid-energy-storage; cited May 9, 2017.
18. Online: Gildemeister, "brochure-cellcube-download-data.pdf," http://energy.gildemeister.com/blob/260408/75b561f2922f864bf42cc372612c93b9/brochure-cellcube-download-data.pdf; cited May 9, 2017.
19. Online: UniEnergy Technologies, "UET_UniSystem_Product_Sheet_reduced," http://www.uetechnologies.com/images/product/UET_UniSystem_Product_Sheet_reduced.pdf; cited May 9, 2017.
20. R. M. Darling, K. G. Gallagher, J. A. Kowalski, S. Ha, and F. R. Brushett, *Energy Environ. Sci.*, **7**, 3459–3477 (2014).
21. V. Viswanathan et al., *J. Power Sources*, **247**, 1040–1051 (2014).
22. S. Ha and K. G. Gallagher, *J. Power Sources*, **296**, 122–132 (2015).

23. R. Dmello, J. D. Milshtein, F. R. Brushett, and K. C. Smith, *J. Power Sources*, **330**, 261–272 (2016).
24. P. Vanysek, *CRC Handb. Chem. Phys.*, **87** (1998)
25. A. Hazza, D. Pletcher, and R. Wills, *Phys. Chem. Chem. Phys.*, **6**, 1773–1778 (2004).
26. P. Zanello, *Inorganic Electrochemistry: Theory, Practice and Applications*, 1st ed., p. 59, Royal Society of Chemistry, Cambridge, UK, (2003).
27. L. Hu, Z. Xue, K. Amine, and Z. Zhang, *J. Electrochem. Soc.*, **161**, A1777–A1781 (2014).
28. Y. Matsuda et al., *J. Appl. Electrochem.*, **18**, 909–914 (1988).
29. Y. Huang, S. Gu, Y. Yan, and S. F. Y. Li, *Curr. Opin. Chem. Eng.*, **8**, 105–113 (2015).
30. K. Gong, Q. Fang, S. Gu, S. F. Y. Li, and Y. Yan, *Energy Env. Sci*, **8**, 3515–3530 (2015).
31. S.-H. Shin, S.-H. Yun, and S.-H. Moon, *RSC Adv.*, **3**, 9095–9116 (2013).
32. J. A. Kowalski, L. Su, J. D. Milshtein, and F. R. Brushett, *Curr. Opin. Chem. Eng.*, **13**, 45–52 (2016).
33. Z. Li et al., *Electrochem. Solid-State Lett.*, **14**, A171–A173 (2011).
34. S.-K. Park et al., *Electrochem. Commun.*, **59**, 68–71 (2015).
35. F. R. Brushett, J. T. Vaughey, and A. N. Jansen, *Adv. Energy Mater.*, **2**, 1390–1396 (2012).
36. X. Wei et al., *Angew. Chem. Int. Ed.*, **54**, 8684–8687 (2015).
37. A. P. Kaur, N. E. Holubowitch, S. Ergun, C. F. Elliott, and S. A. Odom, *Energy Technol.*, **3**, 476–480 (2015).
38. C. S. Sevov et al., *J. Am. Chem. Soc.*, **137**, 14465–14472 (2015).
39. M. H. Chakrabarti, R. A. W. Dryfe, and E. P. L. Roberts, *Electrochimica Acta*, **52**, 2189–2195 (2007).
40. P. G. Rasmussen, "Electical storage device utilizing pyrazine-based cyanoazacarbons and polymers deviced therefrom," US Pat. US 8080327 B1, Filed June 27, 2011.
41. W. Duan et al., *J Mater Chem A*, **4**, 5448–5456 (2016).
42. R. A. Potash, J. R. McKone, S. Conte, and H. D. Abruna, *J. Electrochem. Soc.*, **163**, A338–A344 (2016).
43. R. Darling, K. Gallagher, W. Xie, L. Su, and F. Brushett, *J. Electrochem. Soc.*, **163**, A5029–A5040 (2016).
44. S. H. Oh et al., *J Mater Chem A*, **2**, 19994–19998 (2014).
45. G. Nagarjuna et al., *J. Am. Chem. Soc.*, **136**, 16309–16316 (2014).
46. B. Huskinson et al., *Nature*, **505**, 195–198 (2014).
47. K. Lin et al., *Science*, **349**, 1529–1532 (2015).
48. B. Yang, L. Hoober-Burkhardt, F. Wang, G. S. Prakash, and S. R. Narayanan, *J. Electrochem. Soc.*, **161**, A1371–A1380 (2014).
49. L. Hoober-Burkhardt et al., *J. Electrochem. Soc.*, **164**, A600–A607 (2017).
50. T. Liu, X. Wei, Z. Nie, V. Sprenkle, and W. Wang, *Adv. Energy Mater.*, **6**, 1501449 (2015).
51. A. Orita, M. G. Verde, M. Sakai, and Y. S. Meng, *J. Power Sources*, **321**, 126–134 (2016).
52. J. Winsberg et al., *ACS Energy Lett.*, **1**, 976–980 (2017).
53. T. Janoschka, N. Martin, M. D. Hager, and U. S. Schubert, *Angew. Chem. Int. Ed.*, **382**, 14427–14430 (2016).
54. E. S. Beh et al., *ACS Energy Lett.*, **2**, 639–644 (2017).
55. K. Lin et al., *Nat. Energy*, **1**, 16102 (2016).
56. A. Orita, M. G. Verde, M. Sakai, and Y. S. Meng, *Nat. Commun.*, **7**, 13230 (2016).
57. T. Janoschka, C. Friebe, M. D. Hager, N. Martin, and U. S. Schubert, *ChemistryOpen*, **6**, 216–220 (2017).

58. Q. Chen, M. R. Gerhardt, L. Hartle, and M. J. Aziz, *J. Electrochem. Soc.*, **163**, A5010–A5013 (2016).
59. X. Wei et al., *J. Electrochem. Soc.*, **163**, A5150–A5153 (2016).
60. Z. Li, G. Weng, Q. Zou, G. Cong, and Y.-C. Lu, *Nano Energy*, **30**, 283–292 (2016).
61. G.-M. Weng, Z. Li, G. Cong, Y. Zhou, and Y.-C. Lu, *Energy Environ. Sci.*, **10**, 735–741 (2017).
62. C.-N. Sun et al., *ECS Electrochem. Lett.*, **2**, A43–A45 (2013).
63. D. S. Aaron et al., *J. Power Sources*, **206**, 450–453 (2012).
64. Q. H. Liu et al., *J. Electrochem. Soc.*, **159**, A1246–A1252 (2012).
65. R. M. Darling and M. L. Perry, *J. Electrochem. Soc.*, **161**, A1381–A1387 (2014).
66. C. R. Dennison, E. Agar, B. Akuzum, and E. C. Kumbur, *J. Electrochem. Soc.*, **163**, A5163–A5169 (2016).
67. X. L. Zhou, T. S. Zhao, L. An, Y. K. Zeng, and L. Wei, *J. Power Sources*, **339**, 1–12 (2017).
68. M. Zhang, M. Moore, J. S. Watson, T. A. Zawodzinski, and R. M. Counce, *J. Electrochem. Soc.*, **159**, A1183–A1188 (2012).
69. A. Crawford et al., *Int. J. Energy Res*, **40**, 16111–1623 (2016).

2. Materials selection criteria for redox flow battery electrolytes

This chapter is reprinted from *Journal of Power Sources*, Vol 330, R. Dmello, J. D. Milshtein, F. R. Brushett, K. C. Smith, Cost-driven materials selection criteria for redox flow battery electrolytes, 261–272, Copyright (2016), with permission from Elsevier under license number 4087101452926.

2.1 Introduction

Current redox flow battery (RFB) prices are too high for broad market penetration.[1–3] According to the Department of Energy (DOE) Office of Electricity Delivery and Energy Reliability, decreasing RFB system price to \$120 kWh^{-1} in the near-term will enable widespread adoption for 4 hour discharge grid-scale energy storage applications.[1,4] In comparison, the DOE's Advanced Research Projects Agency - Energy (ARPA-E) suggests a long-term energy storage battery price target of \$100 kWh^{-1} for 1 hour of discharge.[5] In 2014, RFB prices exceeded \$500 kWh^{-1}.[1,2] Despite the existing high prices, recent work has established that both aqueous and nonaqueous RFBs can meet the desired \$100 kWh^{-1} battery price target by appropriately decreasing RFB reactor and materials costs contributions.[1] To achieve the price target, the price-to-energy ratios of aqueous and nonaqueous RFBs can drop by following different cost reduction pathways that optimize their fundamentally different reactor and materials characteristics.[1] Aqueous RFBs (AqRFBs) leverage inexpensive electrolytes, utilizing water as the solvent and typically a low cost inorganic salt (e.g., H_2SO_4, KOH, and NaCl), while exhibiting high power density due to low cell resistance. The typical electrochemical stability window of water (less than 1.5 V), however, limits the maximum achievable AqRFB electrolyte energy density. In contrast, nonaqueous RFBs (NAqRFBs) employ nonaqueous solvents with wide electrochemical stability windows (3 – 4 V) and can thus enable electrolytes with greater energy density as compared to aqueous systems. Despite attractive voltage capabilities, NAqRFBs suffer from relatively expensive nonaqueous solvents (e.g., nitriles, glymes, and carbonates) and fluorinated salts (e.g., tetrafluoroborates, hexafluorophosphates, and bis(trifluoromethylsulfonyl)imides), as well as low power density due to low membrane conductivities. Considering the advantages and drawbacks of each system, AqRFB cost cutting efforts should maximize cell voltage, while NAqRFB design should decrease electrolyte cost and improve power density.

Redox-active materials for both families of RFBs require continued research and development for widespread adoption. Inorganic non-metallic (e.g., polysulfide-bromine) and transition metal (e.g., all-vanadium) redox-active materials have traditionally been at the forefront of AqRFB development, although metal coordination complexes have also been explored.[6–8] AqRFBs utilizing certain inorganic non-metallic redox-active materials, such as bromine, have failed to penetrate the market due to their corrosive and toxic nature, making the practical design of flow fields, pumps, storage tanks, and pipes difficult.[9] Additionally, transition metal based AqRFBs have struggled to achieve the battery price targets due to the high cost and limited abundance of the redox-active material.[10] Early investigations into NAqRFBs employed metal coordination complexes as redox-active materials that suffer from low solubility, poor stability, or expensive precursors.[11–14] A significant portion of recent RFB progress beyond vanadium RFBs, arguably the current state-of-the-art systems, has aimed at identifying low cost redox-active materials such as abundant inorganic species[15,16] and tailored organic molecules.[17–29] Organic redox-active molecules are particularly attractive for use in both aqueous and nonaqueous RFBs since organic molecules are comprised of earth abundant elements (e.g., hydrogen, carbon, oxygen, sulfur) and offer a broad design space, allowing for rational control of molecular weight, solubility, and redox potential, by molecular functionalization.[30]

RFB price relates to experimentally measurable chemical properties, electrochemical performance, and cost parameters, which serve as critical inputs towards developing RFB cost projections via a techno-economic (TE) model. TE models have quantified the price performance of transportation[31,32] and grid-scale[1–3,33–35] energy storage devices. In 2014, Darling, Gallagher, and co-workers developed a comprehensive TE model (hereafter referred to as the DG model) to compare the price performance of aqueous and nonaqueous RFBs.[1] The DG model defined benchmark values for redox-active material concentration, molecular weight, cell voltage, and area-specific resistance (ASR), for both families of RFBs, to reduce battery price to \$100 kWh^{-1}. Although instrumental in elucidating future RFB prices, the DG model focused on a single set of benchmarks but did not explore alternative design iterations. A recent investigation into separator performance characteristics for RFBs considered the tradeoffs among cell voltage, ASR, and reactor cost,[36] but no such sensitivity analysis has accounted for the relative cost contributions from the electrolyte constituent materials: solvent, salt, and redox-active compounds.

The present work addresses the lack of RFB design strategies by exploring the materials space mapped by an electrolyte-centric TE model, which identifies new RFB price reduction strategies. A detailed electrolyte cost model, explicitly accounting for redox-active species, salt, and solvent cost contributions, combined with the existing DG model, enables a sensitivity study of aqueous and nonaqueous RFB prices to various material and cost parameters. We explore the available RFB design space and investigate the sensitivity of both aqueous and nonaqueous RFBs to pertinent electrolyte constituent cost variables, cell voltage, and ASR. Further, maps of the available design space translate abstract price targets into quantitative performance targets, bridging the TE model to prototype guidelines. As such, this paper demonstrates tradeoffs in RFB constituent costs and performance to achieve a \$100 kWh^{-1} battery price. While previous modeling efforts have highlighted cost performance challenges with specific RFB chemistries (e.g. all-vanadium, zinc-bromine)[1–3,35], our analysis culminates in a set of design maps to aid in selecting materials for new RFB electrolytes. We also suggest research pathways to most easily achieve the near-term target battery price (\$100 kWh^{-1}) and even decrease RFB price to \$80 kWh^{-1}. This electrolyte-centric analysis can guide future research efforts in the development and selection of new, promising materials for use in economically viable RFB prototypes.

2.2 Methodology

Model Definitions. Redox flow battery price is defined as the RFB's future-state battery price P_0 (excluding power conditioning systems) per unit discharge energy E_d, delivered over a time t_d. The present TE model (which builds on the DG model[1]) separates RFB price into four major cost contributions from the reactor $C_{Reactor}$, electrolyte $C_{Electrolyte}$, additional $C_{Additional}$, and balance-of-plant (BOP) C_{BOP}:

$$\frac{P_0}{E_d} = C_{Reactor} + C_{Electrolyte} + C_{Additional} + C_{BOP} \quad (1)$$

Table 1 provides variable definitions for all cost equations, as well as benchmark values and units. Here, a series of design maps are presented in which certain model parameters vary. The parameters that do not vary in the design maps assume benchmark values (Table 1), unless otherwise explicitly stated. In these design maps, thin dotted black lines denote benchmark values from the original DG model.

Table 1: Parameters utilized in the present techno-economic model. Benchmark values were obtained from the DG model.[1] These material-specific targets were set in Ref. [9] as guidelines to achieve \$100 kWh^{-1} battery price, based on the values of the other parameters listed here.

Modeling Parameter	**Benchmark Values**	
	Nonaqueous	*Aqueous*
Reactor Parameters		
Cost per unit area, c_a	\$107.5 m^{-2}	\$122.5 m^{-2}
Area-specific resistance, R	5.0 Ω cm^{-2}	0.5 Ω cm^{-2}
Open-Circuit Cell Voltage, U	3 V	1.5 V
Discharge time, t_d	5 h	5 h
System discharge efficiency, $\varepsilon_{sys,d}$	0.94	0.94
Voltage discharge efficiency, $\varepsilon_{v,d}$	0.916	0.916
Electrolyte Parameters		
Round-trip coulombic efficiency, $\varepsilon_{q,rt}$	0.97	0.97
Stoichiometric coefficient, $s_{+/-}$	1	1
Allowable state-of-charge range, $\chi_{+/-}$	0.80	0.80
Actives molecular weight,* $M_{+/-}$	100 g mol^{-1}	100 g mol^{-1}
Actives cost per unit mass, $c_{m,+/-}$	\$5 kg^{-1}	\$5 kg^{-1}
Electrolyte cost per unit mass, $c_{me,+/-}$	\$5 kg^{-1}	\$0.1 kg^{-1}
Actives solubility,* $S_{+/-}$	1.0 kg kg^{-1}	0.2 kg kg^{-1}
Additional Parameters		
Addition to price, c_{add}	\$112.5 kW^{-1}	\$87.5 kW^{-1}
Balance-of-plant cost, c_{bop}	\$102.5 kW^{-1}	\$102.5 kW^{-1}
DG Model Parameters		
Salt cost per unit mass, c_{salt}	\$20 kg^{-1}	-
Solvent cost per unit mass, $c_{solvent}$	\$2 kg^{-1}	\$0.1 kg^{-1}
Salt solubility,* $S_{salt,+/-}$	0.16 kg kg^{-1}	-
Mean molar salt ratio,* r_{avg}	0.20 mol mol^{-1}	-
Salt molecular weight, M_{salt}	100 g mol^{-1}	-
Mean actives molality,* b_{avg}	9.6 mol kg^{-1}	1.6 mol kg^{-1}

This work builds on the reactor, additional, and BOP cost descriptions from the DG model. In the DG model [1], the reactor cost (in \$ kWh^{-1}) depends on the reactor cost per unit area c_a, which incorporates the costs associated with bi-polar plates, membranes, and seals; the cost of each reactor hardware component is detailed in Ref. [9]. Additionally, the reactor cost varies with area-specific resistance R (including resistance contributions from the membrane, porous electrode, reaction kinetics, mass transfer, and electrical contacts), open-circuit cell voltage U, discharge voltage efficiency $\varepsilon_{v,d}$, system efficiency during discharge $\varepsilon_{sys,d}$ (including losses due to auxiliary equipment and pumping), and discharge time t_d:

$$C_{Reactor} = \frac{c_a R}{\varepsilon_{sys,d} U^2 \varepsilon_{v,d} \left(1-\varepsilon_{v,d}\right) t_d} \tag{2}$$

The balance-of-plant cost accounts for the ancillary equipment (such as pumps, controls, sensors, and pipes) required to build a working system, while the additional cost accounts for economic factors like depreciation, overhead, labor, and profit margin. A full discussion of these costs is provided in Ref. [9]. Importantly, this work considers a battery price, which excludes power conditioning systems (i.e., inverters) and installation costs.[1] The battery price is not to be confused with the system price, which does include power conditioning systems costs, as the system price may be the focus of other techno-economic modeling literature. The \$120 kWh^{-1} system price target used in the DG model is thus converted to a \$100 kWh^{-1} battery price target by excluding a power conditioning system that costs \$100 kW^{-1} for 5 hours of discharge.[37]

A new model is used for the electrolyte cost $C_{Electrolyte}$, in \$ kWh^{-1}, that incorporates cost contributions from individual materials in the electrolyte. Specifically, the costs from redox-active materials (used in the positive and negative electrolytes), supporting salt, and solvent are included explicitly. This electrolyte cost model captures the state of RFB materials as purchased from a chemical supplier. Further, the model normalizes the electrolyte materials costs by the total system energy, accounting for discharge efficiencies (as included in the reactor cost), round-trip coulombic efficiency $\varepsilon_{q,rt}$ (accounting for crossover and shunt current effects), open-circuit cell voltage, and depth-of-dischargeχ (the fraction of theoretical capacity accessed):

$$C_{Electrolyte} = \frac{1}{\varepsilon_{sys,d}\varepsilon_{q,rt}F\varepsilon_{v,d}U}\left(\frac{s_+M_+}{\chi_+ n_{e+}}c_{m,+} + \frac{s_-M_-}{\chi_- n_{e-}}c_{m,-} + 2r_{avg}M_{salt}c_{salt} + \frac{2}{b_{avg}}c_{solvent}\right) \quad (3)$$

The redox-active materials used in either the positive or negative electrolytes (denoted with '+' or '-' subscripts, respectively) store n_e electrons per s formula units of the particular redox-active species (also called the stoichiometric coefficient) that has molecular weight M with a cost per unit mass c_m. Equation (3) also accounts for the benefits of employing a cheaper salt or solvent in the RFB. Several variables specify the type and amount of salt employed, including the molar ratio of salt to redox-active species r (in moles of salt per mole of electrons stored), salt molecular weight M_{salt}, and the salt cost per unit mass c_{salt}. Solvent costs depend on the redox-active species concentration b (molality in units of moles of electrons transferred per kilogram of solvent) and the cost per unit mass of the solvent $c_{solvent}$.

Note here that the molar ratio of salt to redox-active species and the redox-active species concentration appear as average values of the positive and negative electrolytes, assuming the symbols r_{avg} and b_{avg}, respectively [r_{avg} is an arithmetic mean with $r_{avg} = \left(r_+ + r_-\right)/2$, while b_{avg} is

a harmonic mean with $b_{avg} = 2b_+b_- / \left(b_+ + b_-\right)$]. The DG model accounts for salt and solvent cost using an electrolyte cost per unit mass ($c_{m,e+/-}$ in units of \$ kg^{-1}). By lumping salt and solvent costs together in this manner, the DG model did not capture the sensitivity of battery price to salt concentration and molecular weight. Additionally, the DG model does not allow comparison between rocking-chair and salt-splitting ion transfer configurations that are discussed in detail later. Thus, the present detailed electrolyte model expands the electrolyte cost per unit mass in terms of the mass ratio of salt to total mass of salt and solvent S_{salt}, as well as the costs per unit mass of the salt and solvent (c_{salt} and $c_{solvent}$, respectively):

$$c_{m,e} = S_{salt}c_{salt} + \left(1 - S_{salt}\right)c_{solvent} \tag{4}$$

To capture salt and solvent costs explicitly, the electrolyte cost per unit mass for each electrolyte ($c_{m,e+}$ and $c_{m,e-}$) was substituted into the battery price expression from Ref. [9]. The resulting expression for battery price expressed in terms of the average molar salt ratio r_{avg} and the average redox-active species concentration b_{avg}. In terms of parameters from the DG model, r_{avg} and b_{avg} are expressed as shown in Equations (5) and (6), where the redox-active species concentration S is expressed in units of kilograms per kilogram of solvent.

$$r_{avg} = \frac{1}{2}\left(\frac{s_+ M_+ S_{salt+}}{\chi_+ n_{e+} M_{salt+} S_+} + \frac{s_- M_- S_{salt-}}{\chi_- n_{e-} M_{salt-} S_-} \right) \tag{5}$$

$$\frac{1}{b_{avg}} = \frac{1}{2}\left[\frac{s_+ M_+ \left(1 - S_{salt+}\right)}{\chi_+ n_{e+} S_+} + \frac{s_- M_- \left(1 - S_{salt-}\right)}{\chi_- n_{e-} S_-} \right] \tag{6}$$

Material Cost Assumptions. The costs-per-unit-mass (\$ kg^{-1}) of redox-active materials, salts, and solvents in Table 1 assume future commodity-scale production and can vary depending on the choice of material. While these costs may appear optimistic, certain materials could achieve these values today; for example, the 2006 bulk price of acetonitrile, a typical NAqRFB solvent, was ~\$1.50 kg^{-1}.[38] Additionally, the two-fold decrease in lithium-ion battery electrolyte (1 mol L^{-1} salt + solvent) costs from \$40 kg^{-1} to \$18 kg^{-1} between 1999 and 2011,[32,39] suggests that other solvent and salt costs could realistically fall to the values listed in Table 1 over the next decade. Redox-active materials have an estimated future-state cost of \$5 kg^{-1}, however, tailored molecules can cost more if complicated synthetics procedures are required for manufacture.[1] Anthraquinone, a precursor to several other redox-active materials,[17,18,40,41] has an estimated price of ~\$4.40 kg^{-}

[1].[18,42] Alternatively, inherently low cost materials, such as those containing sulfur[43] or bromine[18] (the 2006 prices of S_8 and Br_2 were \$0.20 kg^{-1} and \$1.41 kg^{-1}, respectively [38]), can decrease future-state costs compared to tailored redox-active molecules. Furthermore, this study considers RFBs implementing a fluorinated ion-exchange membrane (i.e., Nafion) with an estimated future-state price of \$50 m^{-2}.[1] Our study does not consider how variations in membrane cost affects the available RFB design space because an excellent prior study (Ref. [40]) offers a comprehensive analysis of tradeoffs in membrane cost and performance.

2.3 Mapping the RFB Materials Design Space

We map the available materials design space for aqueous and nonaqueous RFBs, within physical reason, to achieve a \$100 kWh^{-1} battery price. The analysis presented here remains within a design space commonly accessible by laboratory and industrial scale RFBs, even though extreme RFB electrolyte systems may be possible. To begin, this work explores the tradeoffs among cell voltage, redox-active material molecular weight, and redox-active material concentration for both aqueous and nonaqueous RFBs. Contours of constant concentration in Figure 1a represent possible RFB designs with a \$100 kWh^{-1} price. Note that design maps throughout this work present molecular weight in units of "grams per mole of electrons" to accommodate active species that undergo multiple electron transfer events.

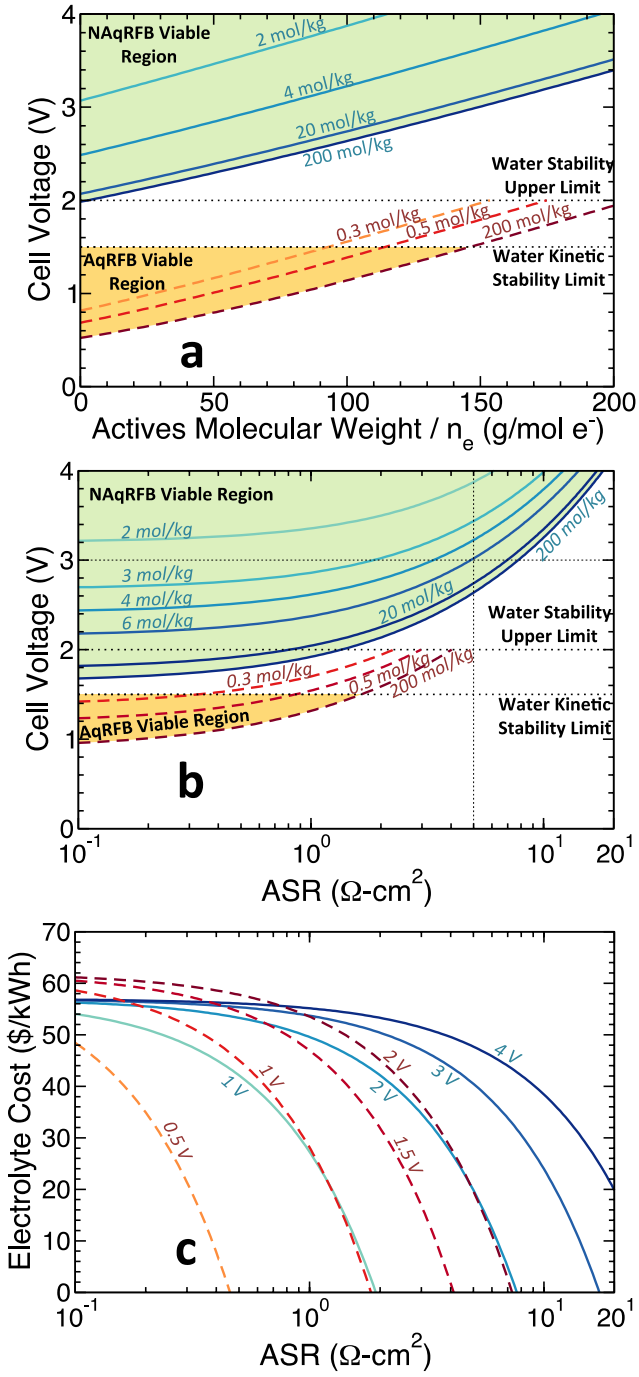

Figure 1: Contours of constant redox-active species concentration for aqueous and nonaqueous RFBs as a function of cell voltage and **(a)** redox-active species molecular weight or **(b)** reactor ASR. Each contour achieves a battery price of \$100 kWh^{-1}. Contours above 2 V represent the NAqRFB feasible design space, while the shaded region below 1.5 V represents the AqRFB design space. Horizontal dotted lines at 1.5 V and 2 V denote the typical electrochemical stability window and upper stability limit of aqueous electrolytes, respectively. **(c)** Contours of constant cell voltage as a function of electrolyte cost ($C_{Electrolyte}$) and reactor ASR, where each contour achieves a battery price of \$100 kWh^{-1}. For all sub-figures, NAqRFB and AqRFB contours are represented as solid and dashed lines, respectively.

The thermodynamic dissociation potential of water is 1.23 V, but due to the sluggish kinetics of the hydrogen and oxygen evolution reactions on porous carbon electrodes, AqRFB cell voltages can typically reach 1.5 V (Figure 1a, horizontal dashed line). [44] In some exceptional battery systems, such as lead-acid and zinc-bromine, the water stability limit has exceeded 1.7 V.[6,45] RFBs with cell voltages greater than 2 V, however, will require the use of an aprotic nonaqueous solvent,[1] which can easily exhibit electrochemical windows from 3 – 4 V.[46] Each concentration contour in Figure 1a, for both aqueous and nonaqueous RFBs, demonstrates that as the molecular weight of the redox-active species increases, the required cell voltage to achieve \$100 kWh^{-1} also increases. Increasing molecular weight subsequently increases RFB price (in \$), so to offset higher redox-active material costs, the cell voltage must also rise, increasing the available system energy and decreasing reactor and electrolyte costs (in \$ kWh^{-1}).

Notably for NAqRFBs, as the redox-active species molality decreases, either the cell voltage must increase or the molecular weight must decrease significantly to attain the target battery price, and this sensitivity results from higher solvent costs (\$2 kg^{-1}) than water. Redox-active species molality is directly proportional to electrolyte energy density, which subsequently defines the total available energy of the RFB. As redox-active material concentration decreases, the volume of electrolyte required to achieve a fixed system energy increases, and subsequently the amount and total cost of solvent also increases. Therefore, to achieve the target price, the battery energy must increase via a voltage increase, or the electrolyte cost must reduce by utilizing redox-active compounds with lower molecular weight. As a quantitative nonaqueous example, a 100 g mol^{-1} redox-active material at 20 mol kg^{-1} concentration requires a 2.8 V cell, but the same redox-active material requires a 4 V cell if the operating concentration drops to 2 mol kg^{-1}. Further, the NAqRFB design space is insensitive to molality changes at high redox-active material concentrations (greater than 20 mol kg^{-1}) because, in this regime, the solvent cost contribution approaches zero. Ultra-high NAqRFB concentrations (greater than 200 mol kg^{-1}) correspond to redox-active materials in near-neat form with minimal solvent content, and only liquid redox-active species can achieve such high concentrations. Liquid redox-active species are a new concept for NAqRFBs, demonstrated in Ref. [32]. Due to the decreasing solvent cost contribution at ultra-high redox-active material molality, the concentration contours for such redox-active liquids will closely match the 200 mol kg^{-1} contour, and thus, the NAqRFB feasible region in Figure 1a,

highlighted in green, exists above the 200 mol kg^{-1} contour. Additionally, Figure 1a shows that a NAqRFB with a cell voltage less than 2 V will be financially infeasible.

In contrast to nonaqueous systems, AqRFB designs demonstrate negligible sensitivity across order of magnitude changes in redox-active species concentration (0.5 – 200 mol kg^{-1}). For AqRFBs, the supporting electrolyte cost contribution (\$0.1 kg^{-1}) is extremely low, and thereby, only the redox-active material molecular weight or cell voltage can substantially affect the design space. At extremely low concentrations (less than 0.5 mol kg^{-1}), however, AqRFBs require cell voltages greater than the electrochemical stability window of water to meet the cost targets. This voltage requirement suggests a minimum concentration requirement of 0.5 mol kg^{-1} to maintain electrolyte stability and eliminate redox-active material molality as a cost constraint. The maximum stable cell voltage in aqueous solution and the minimum cell voltage required to recover electrolyte costs bound the AqRFB feasible design space (highlighted in yellow in Figure 1a). In the regime of ultra-low redox-active species concentration (less than 0.5 mol kg^{-1}), AqRFBs may become sensitive to variations in other cost parameters such as pumping losses, cycle efficiencies, or tank sizes, which the design maps in Figure 1a do no capture.

RFB design is also sensitive to reactor ASR. A recent study has shown that reactor ASR can drastically impact the required cell voltage for economically feasible RFBs,[36] but changes in ASR can also affect the required redox-active material concentrations for NAqRFBs. Figure 1b plots contours of constant concentration as a function of cell voltage and reactor ASR for both aqueous and nonaqueous RFBs. First, this analysis establishes that an upper bound on a maximum plausible ASR is approximately 20 Ω cm^2; at this ASR value all NAqRFB designs would require cell voltages above 4.5 V, which would be difficult due to electrolyte breakdown.[46] Similarly, a maximum plausible ASR for AqRFBs is approximately 1.5 Ω cm^2, beyond which an AqRFB would require a cell voltage exceeding 1.5 V, leading to imminent water dissociation. Considering the nonaqueous contours, Figure 1b demonstrates a rapid decrease in required cell voltage or redox-active species concentration as ASR decreases in the range of 20 to 1 Ω cm^2. The DG model recommended employing 3 V NAqRFB reactors with 5 Ω cm^2 ASR and redox-active species concentration of 9.6 mol kg^{-1},[1] but a later study recommended decreasing the ASR of NAqRFBs down to 2.3 Ω cm^2,[36] which could reduce the required redox-active species concentration to 4 mol kg^{-1}. For ASR values below 1 Ω cm^2, NAqRFB cell voltage targets become relatively insensitive to further decreases in ASR. Again, due to low solvent costs, for concentrations greater than 0.5

mol kg^{-1} AqRFB cell voltage and ASR requirements are less sensitive to redox-active species concentration, even over order of magnitude changes. AqRFBs with concentrations less than 0.5 mol kg^{-1} are infeasible at \$100 kWh^{-1} due to high cell voltage requirements that extend beyond the stability window of aqueous electrolytes. Figure 1b, however, also demonstrates that decreasing ASR for aqueous systems below 1 Ω cm^2 could decrease cell voltage requirements down to under 1.2 V, broadening the number of viable redox-active materials for use in AqRFBs. Due to the inherent constraint of the narrow AqRFB electrochemical window, small improvements in ASR could lead to a critical decrease in required AqRFB cell voltage.

We directly illustrate the relationship among reactor ASR and electrolyte cost ($C_{Electrolyte}$) with a series of concave-down cell voltage contours in Figure 1c. Generally, as ASR decreases, electrolytes that are more expensive enter the available design space, but as ASR increases, electrolyte cost must decrease to compensate for the associated rise in reactor cost. In addition, higher cell voltage permits both higher electrolyte cost and ASR, as the cell voltage is a critical parameter in determining both the reactor and electrolyte costs. For example, the higher cell voltages possible in NAqRFBs can offset the higher costs and ASR values associated with nonaqueous electrolytes. Given the electrochemical stability windows of typical aqueous and nonaqueous electrolytes, Figure 1c reaffirms our suggested bounds on reactor ASR for both RFB families. While Figure 1c demonstrates interesting tradeoffs in reactor and electrolyte cost contributions, the total electrolyte cost is difficult to decompose into price optimization pathways for individual electrolyte components.

Considering only cell voltage, ASR, redox-active material molecular weight, and redox-active material concentration as design parameters, the variability of battery price is evident for both aqueous and nonaqueous RFBs. The difference in design sensitivity between the two systems leads to fundamentally different challenges in materials selection at fixed battery price. Recent reports have already demonstrated NAqRFBs with cell voltages greater than 2 V,[47,48] and low molecular weights less than 200 g mol^{-1}.[23,28,49] These early advances suggest that the cell voltage and molecular weight benchmarks of 3 V and 100 g mol^{-1} may be possible in the future. The corresponding redox-active material concentration target of 9.6 mol kg^{-1} (~ 4 – 5 mol L^{-1}, assuming specific electrolyte volume of 1 L kg^{-1} and solvent mass fraction of ~ 0.4 – 0.5) for NAqRFBs, however, would be difficult to achieve experimentally. State-of-the-art tailored organic redox-active materials developed by Sevov et al. and Huang et al. had solubility limits less than 2 mol L^{-}

[1].[28,49] Decreasing the required redox-active material concentration becomes a critical design optimization pathway for economically viable NAqRFBs. Since AqRFB design is relatively insensitive to solvent costs, AqRFBs can operate in a cost effective manner even at low redox-active material concentrations, but viable AqRFBs will require cell voltages in the range of 1.2 – 1.5 V and ASR values below 1.5 Ω cm^2. While many AqRFBs, including vanadium systems, demonstrate cell voltages exceeding 1 V, low cost redox-active species that maximize use of aqueous electrochemical stability windows are essential to achieve a low battery price.

2.4 Nonaqueous RFB Design Optimization

To enable NAqRFBs with sufficiently high cell voltages, positive electrolyte materials must have relatively high redox potentials, while negative electrolyte materials must have relatively low redox potentials. The difference between the redox potentials of the positive and negative redox-active materials will define the total NAqRFB cell voltage, and thus, the positive and negative electrolytes each require unique materials selection criteria. Figure 2 quantifies required changes in individual electrolyte material redox potential as a function of molecular weight for various redox-active material concentrations.

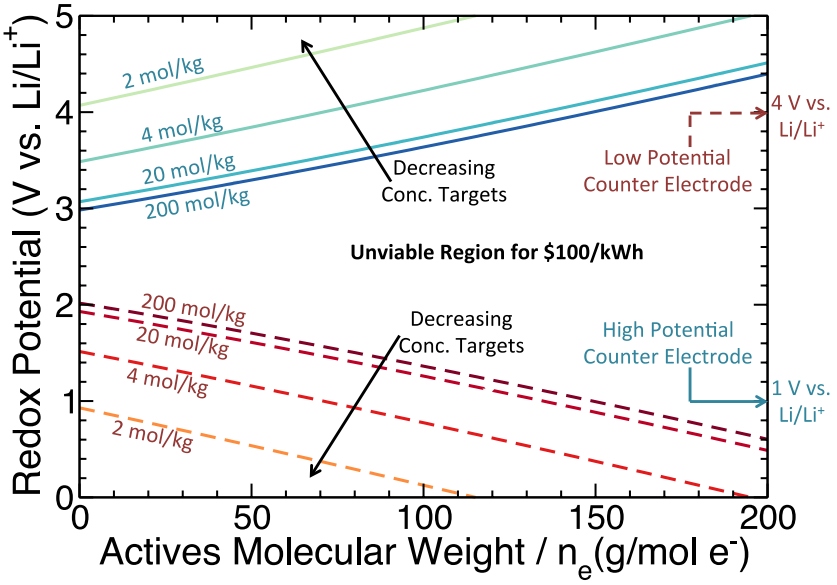

Figure 2: Contours of constant of redox-active species concentration, as a function of redox-active species molecular weight and redox potential, for NAqRFBs, that achieve a battery price of $100 kWh^{-1}. Solid contours correspond to positive redox-active materials, and dashed contours correspond to negative redox-active materials. The right hand *y*-axis displays the benchmark counter-electrode potentials.

To allow such an analysis, Figure 2 pairs positive electrolyte materials with a benchmark negative electrolyte material that has the same molecular weight per electron transferred as the positive active material of interest, but with a redox potential of 1 V vs. Li/Li^+. Conversely, the analysis pairs negative electrolyte materials with a benchmark positive electrolyte material, again, with the same molecular weight per electron transferred as the negative active material of interest, but exhibiting a redox potential of 4 V vs. Li/Li^+. In Figure 2 contours with $E^\circ > 3$ V vs. Li/Li^+ (solid) correspond to positive electrolyte materials, while contours with $E^\circ < 2$ V vs. Li/Li^+ (dashed) correspond to negative electrolyte materials. The positive and negative electrolyte contours exhibit complementary trends to the cell voltage contours in Figure 1a; specifically, increasing redox-active material molecular weight requires a more extreme redox potential to achieve \$100 kWh^{-1}. In addition, as redox-active material concentration decreases for a fixed molecular weight, the target system design requires more extreme redox potentials. The region between the positive and negative electrolyte contours represents an infeasible region for redox-active material use in a NAqRFB. Redox potentials in this region are too moderate to enable high enough cell voltages to offset the associated reactor and electrolyte costs. Figure 2 ultimately demonstrates that by identifying redox-active materials with more extreme redox potentials, or by decreasing redox-active material molecular weight, nonaqueous electrolytes with lower concentrations of redox-active materials become cost effective.

Until now, the TE analysis has only considered the redox-active material and solvent cost contributions to NAqRFB electrolytes, but salt costs (\$20 kg^{-1}) will be higher than either redox-active materials (\$5 kg^{-1}) or solvent costs (\$2 kg^{-1}) due to the high cost associated with fluorinated anions. Figure 3a demonstrates the relationship among salt cost, salt molecular weight, and redox-active species concentration. For each contour of constant concentration, as salt cost increases, the salt molecular weight must decrease, and vice versa. This simple trend arises to maintain the same overall cost of salt (in \$) for a fixed redox-active material concentration. The DG model estimated a salt cost of \$20 kg^{-1}, but the variation in cost among lithium salts,[50] suggests that cheaper materials, below \$20 kg^{-1}, could be used for NAqRFBs. Salt candidate searches should consider new lithium-ion battery salts, such as chelated phosphates, borates, imides, and heterocyclic amines,[51] as a possible pathway to decrease materials cost. Identifying cheaper or lower molecular weight salts can minimize redox-active species concentration requirements for NAqRFBs.

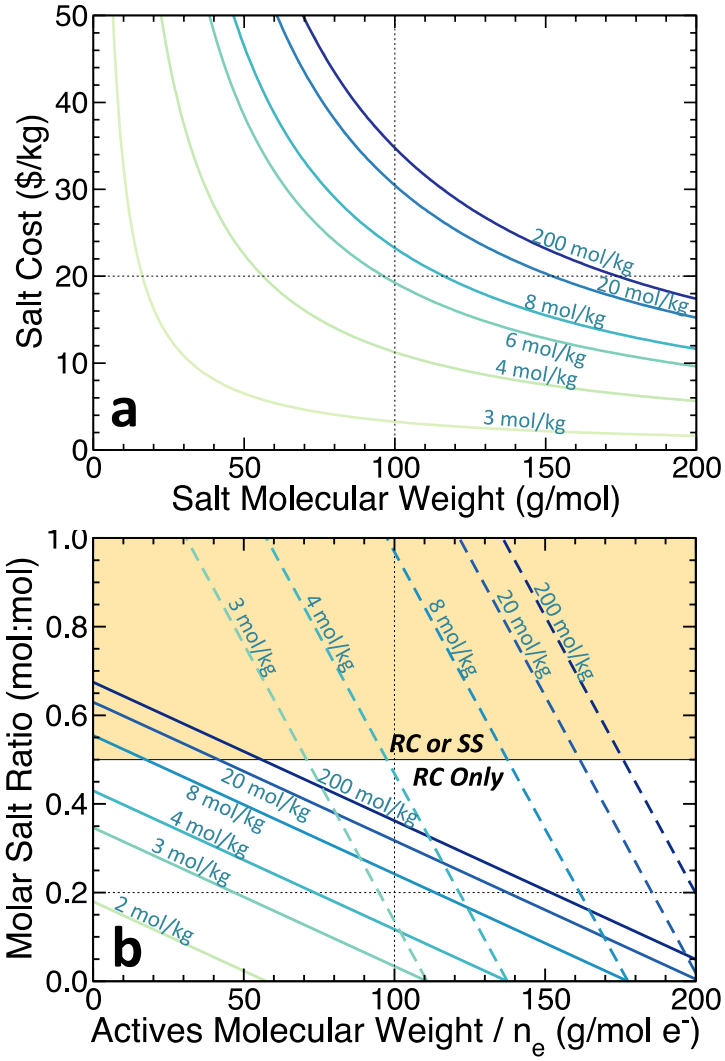

Figure 3: **(a)** Contours of constant redox-active species concentration as a function of salt cost and salt molecular weight for NAqRFBs. Each contour achieves the target \$100 kWh^{-1} battery price. **(b)** Contours of constant redox-active species concentration for NAqRFBs, as a function of average molar salt ratio and redox-active species molecular weight, which satisfy the \$100 kWh^{-1} battery price target. The bottom half of the design space ($r_{avg} < 0.5$) is only accessible by rocking-chair (RC) configuration RFBs, while the upper half ($r_{avg} \geq 0.5$) is available to either rocking-chair or salt-splitting (SS) cells. The shaded upper half region represents the viable design space for salt-splitting cells. Solid contours correspond to a salt cost of \$20 kg^{-1}, and dashed contours correspond to a salt cost of \$5 kg^{-1}. Dotted black lines denote benchmark values.

Aside from identifying overall cheaper salts, carefully selecting NAqRFB redox reactions can minimize the total salt cost contribution to the electrolyte cost. Consider that the salt plays three roles in a NAqRFB electrolyte. First, dissolved salt imparts conductivity on an otherwise insulating nonaqueous solvent, allowing for ionic conduction through the pore phase of a porous electrode. Second, the salt ions act as ionic charge carriers through the membrane of the RFB,

which is a key attribute of any electrochemical cell. Third, the salt will serve to maintain electroneutrality in the bulk electrolyte throughout the entire RFB while redox-active materials undergo reduction or oxidation. Importantly, the requirement of bulk electroneutrality can lead to unnecessarily high concentrations of salt and subsequently unnecessarily high salt costs if the charges on the redox-active materials are dissimilar.[52]

Equations (7), (8), and (9) show three distinct reaction schemes for RFBs (assuming one electron stored for each redox-active species), where A is the positive electrolyte redox-active material and B is the negative electrolyte redox-active material:

$$\mathrm{A} + \mathrm{B} \leftrightarrow \mathrm{A}^{+} + \mathrm{B}^{-} \tag{7}$$

$$\mathrm{A}^{(n+1)-} + \mathrm{B}^{n-} \leftrightarrow \mathrm{A}^{n-} + \mathrm{B}^{(n+1)-} \tag{8}$$

$$\mathrm{A}^{n+} + \mathrm{B}^{(n+1)+} \leftrightarrow \mathrm{A}^{(n+1)+} + \mathrm{B}^{n+} \tag{9}$$

The first reaction (Equation (7)) represents a salt-splitting configuration, where both redox-active materials begin as neutral species at 0 % state of charge (SOC), but then A oxidizes to a cation and B reduces to an anion at 100 % SOC. The use of dissimilar charged species at 100 % SOC will drive salt cations to the negative electrolyte, while salt anions migrate to the positive electrolyte. Thus, the salt-splitting configuration requires a minimum of one salt molecule for every two redox-active molecules (i.e., including redox-active molecules in both the positive and negative electrolytes) to maintain electroneutrality across all SOCs. This condition restricts the molar salt ratio r_{avg} to values in excess of 50 % for salt-splitting configurations. Many NAqRFBs presented in literature exhibit a salt-splitting configuration due to the wider availability of stable redox-active materials in neutral state.[19–21,29,48] In contrast, Equations (8) and (9) (where n is an integer greater than or equal to zero) represent a special case of rocking-chair configuration RFBs, also sometimes referred to as common-ion exchange RFBs.[52] In these systems, either a single cation (Equation (8)) or a single anion (Equation (9)) transfers across the membrane to maintain electroneutrality,[52] resembling ion transfer in a traditional lithium-ion battery.[53] By utilizing a single ion to facilitate charge transfer across the membrane and redox-active materials that maintain the same sign of charge (cation or anion) across all SOCs, rocking-chair RFBs do not require any salt to charge balance (i.e., $r_{avg} \geq 0$); the salt in a rocking-chair cell merely imparts ionic conductivity to the electrolyte and membrane. Rocking-chair RFBs require that at least one of the redox-active materials be ionic at 0 % SOC, and this ionic redox-active material must pair

with an associating counter ion.[52] While uncommon in recent literature, some reports demonstrate rocking-chair NAqRFBs.[11,12,54–57]

Switching NAqRFB configuration towards rocking-chair systems will allow for decreasing salt concentrations, which can dramatically widen the NAqRFB design space by eliminating costly salt from the system. Figure 3b relates the required redox-active species concentration to molar salt ratio and redox-active species molecular weight for various NAqRFB designs, assuming two different salt costs of \$5 kg^{-1} (dashed lines) and \$20 kg^{-1} (solid lines). Each iso-concentration contour exhibits a near linear decrease of molar salt ratio with increasing redox-active species molecular weight; to offset higher total redox-active material costs, the total salt cost, and thereby salt concentration, must decrease. When constructing a RFB in rocking-chair configuration, redox-active species in at least one of the electrolytes must be in an ion. Such a material would be purchased with an associated counter ion that increases the molecular weight of the redox-active material (relative to its molecular weight as a neutral species). Thus, Figure 3b can assist in balancing molecular weight with the amount of dissolved salt in the NAqRFB. Further, as the redox-active species concentration decreases, either the molar salt ratio or redox-active species molecular weight must decrease to offset higher solvent costs. In Figure 3b, values of $r_{avg} < 0.5$ represent a design space that is only accessible by employing a rocking-chair NAqRFB design. The DG model assumed 1 mol L^{-1} salt concentration for NAqRFB electrolytes,[1] which, through our analysis, corresponds to $r_{avg} = 0.20$. As we show here, this salt ratio is only compatible with a rocking-chair configuration NAqRFB, where fewer moles of salt are present in the electrolyte than moles of redox-active material. For a salt cost of \$20 kg^{-1}, salt-splitting cells are financially infeasible, unless the redox-active materials exhibit unrealistically low molecular weights (< 50 g mol^{-1}) and high concentrations (> 8 mol kg^{-1}). The salt-splitting design space, however, does become accessible for a salt cost of \$5 kg^{-1}. As such, NAqRFB design is sensitive to salt cost and salt concentration due to the anticipated high costs of NAqRFB salts relative to redox-active material and solvent costs, and, by carefully minimizing salt cost and concentration, lower redox-active species concentrations, under 4 mol kg^{-1}, become feasible.

2.5 AqRFB Design Optimization

While NAqRFB price is sensitive to all constituent electrolyte material costs, cell voltage, and ASR, the cost contributions of salt and solvent in AqRFBs are small. Consequently, the battery

price of AqRFBs is sensitive neither to redox-active species concentration nor cell configuration (i.e., either rocking-chair or salt-splitting). These insensitivities stem from the extremely low-cost supporting electrolytes afforded in aqueous systems. Therefore, AqRFB design optimization focuses on varying cell voltage, ASR, redox-active material molecular weight, and redox-active material cost per unit mass to achieve \$100 kWh^{-1}.

Aqueous redox-active materials require sufficiently extreme redox potentials (high potential for positive redox-active materials, low potential for negative redox-active materials) to construct cells with voltages that are high enough to achieve the target battery price, but the redox potentials of the redox-active species are also constrained by the electrochemical stability window of aqueous electrolytes. Figure 4 demonstrates the difficulty in identifying viable redox-active species for AqRFBs, by plotting contours of constant redox-active material concentration in the space of redox potential (vs. the Reversible Hydrogen Electrode (RHE)) and molecular weight. Here, the respective benchmark counter-electrodes at -0.1 V and 1.4 V vs. RHE are paired with positive and negative electrolyte materials of interest for AqRFBs in a manner similar to NAqRFBs in Figure 2. As a quantitative example, a positive electrolyte material with a molecular weight of 100 g mol^{-1} must have a redox potential in the range 1.1 V < E^o < 1.4 V vs. RHE; this is a narrow 300 mV design space to investigate, eliminating many possible redox-active material candidates. If the redox-active species molecular weight increases beyond 100 g mol^{-1}, the available design space shrinks even further. Selecting redox-active materials that enable AqRFBs with cell voltages > 1.1 V is of paramount importance.

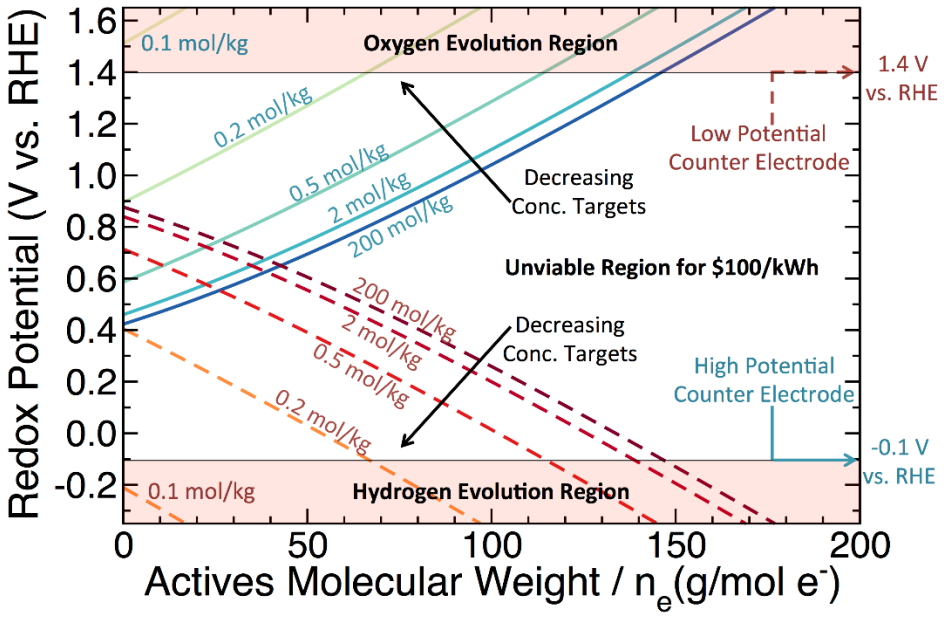

Figure 4: Contours of constant redox-active species concentration for AqRFBs, as a function of redox-active species molecular weight and redox potential, which achieve a battery price of \$100 kWh^{-1}. Solid contours correspond to positive electrode materials, and dashed contours correspond to negative electrode materials. The right hand *y*-axis displays the benchmark counter-electrode potentials.

Beyond individual redox-active species selection, tradeoffs between reactor and electrolyte cost contributions can broaden the available design space. Figure 5a shows the relationship among required cell voltage, ASR, and redox-active material molecular weight to achieve a battery price of \$100 kWh^{-1}. As previously shown in Figure 1b, the ASR must be under 1.5 Ω cm^2 if the redox-active material exhibits a reasonable molecular weight (~100 g mol^{-1}), and any molecular weight greater than 150 g mol^{-1} would require unrealistically high cell voltages for aqueous systems. If extremely low molecular weight redox-active materials (< 50 g mol^{-1}) were available, the maximum allowable ASR could increase to 4 Ω cm^2, but such low weights would require molecular simplicity similar to that of an ethanol molecule (46 g mol^{-1}). Such simple species are likely to undergo only chemically irreversible redox events. Additionally, drastically decreasing cell ASR to an ultra-low value of 0.1 Ω cm^2 affords only a 20 % decrease in cell voltage target. The practical difficulties in decreasing molecular weight and ASR suggest that these are unviable design pathways towards decreasing AqRFB cell voltage requirements. Thus, we conclude that the most viable pathways towards achieving the desired battery price for AqRFBs are either by minimizing redox-active material cost (\$ kg^{-1}) or by maximizing cell voltage.

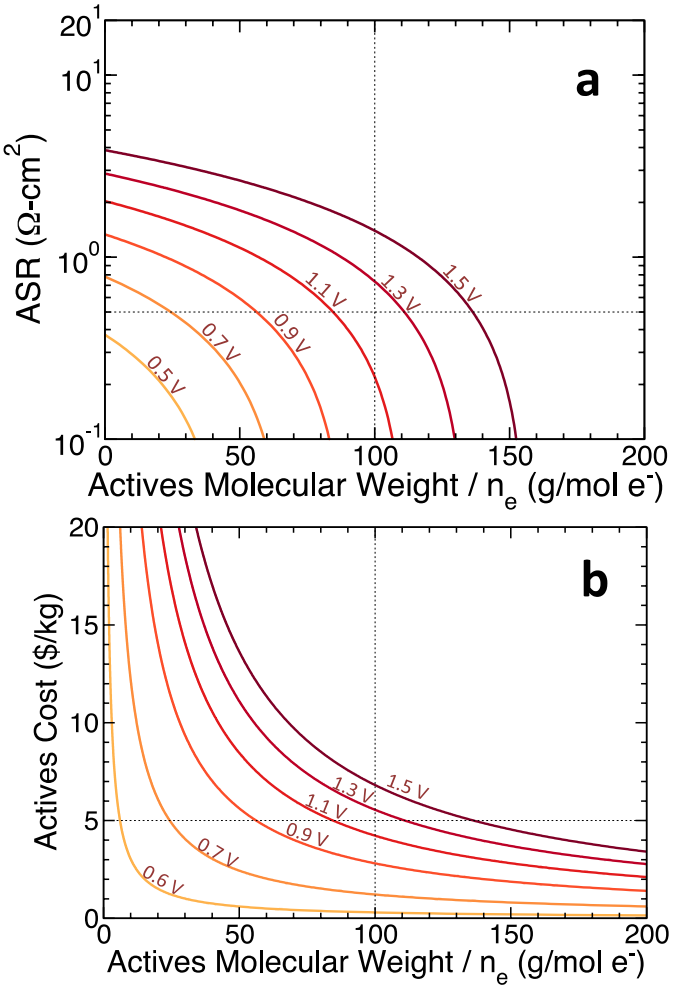

Figure 5: **(a)** Contours of constant cell voltage for AqRFBs, as a function of ASR and redox-active species molecular weight, which achieve a battery price of \$100 kWh^{-1}. **(b)** Contours of constant cell voltage for AqRFBs, as a function of redox-active species cost and molecular weight, which achieve a \$100 kWh^{-1} battery price. Dotted lines illustrate the benchmark values for an AqRFB.

As an illustration, Figure 5b reveals how decreasing redox-active material cost balances variations in cell voltage to achieve \$100 kWh^{-1}. The benchmark value for redox-active material cost of \$5 kg^{-1} corresponds to a required cell voltage of 1.2 V, but employing a redox-active material cost of \$1 kg^{-1} reduces the cell voltage requirement as low as 0.7 V. We can thus identify redox-active material cost and cell voltage as the two most critical parameters in building economically viable AqRFBs.

2.6 Recommended RFB Design Pathways

The RFB materials selection maps presented in this work are powerful tools for quantifying the tradeoffs among various electrolyte material costs, cell voltage, and ASR, but extracting design

rules from them can be overwhelming due to the large number of variables and wide range of values each variable may assume. To this end, we propose generalized RFB design guidelines aimed at assisting in electrolyte materials selection. The DG model began such a design process by suggesting single iterations of aqueous and nonaqueous RFB designs,[1] but the plethora of available iterations outlined in this work hints that even more realistic and cost effective pathways may exist.

2.7 NAqRFB Design Pathways

As NAqRFB price is sensitive to electrolyte components, cell voltage, and ASR, many possible NAqRFB design iterations become available, and Figure 6a outlines new design pathways, showing NAqRFB price as a function of redox-active species concentration for various design improvements over the DG model baseline. As observed in Figure 6a, the DG model suggestions achieve the target \$100 kWh^{-1} battery price at challenging redox-active material concentrations (greater than 6 mol kg^{-1}).[1] As a first possible design improvement, decreasing cell ASR down to 2.5 Ω cm^2, a value recommended by a study of RFB area-specific resistance,[36] affords a small decrease in battery price. Experimental studies of membrane performance demonstrate significant variability in preventing crossover and facilitating ion transfer.[48,54,58,59] Finding a membrane (or separator) for NAqRFBs with high selectivity and that performs at high currents is one major materials challenge to overcome.[36] Beyond the ohmic contribution to NAqRFB resistance, the transport capabilities of nonaqueous solvents in porous electrodes present a challenge. Due to the high viscosity of some NAqRFB electrolytes,[60,61] resistance due to pore-scale mass transfer of redox-active species and ionic conduction through the electrode thickness could possibly be similar in magnitude to the separator / membrane resistance.

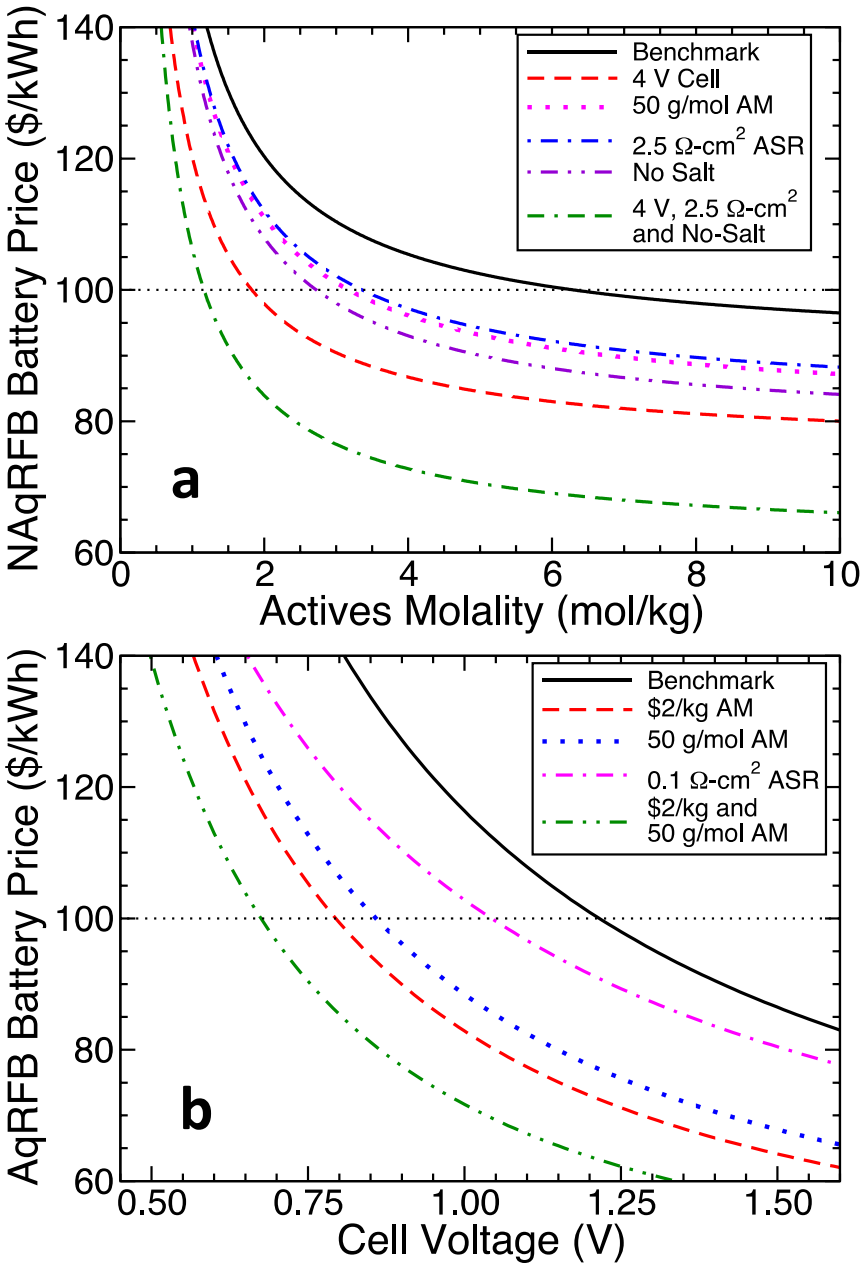

Figure 6: Suggested design pathways that minimize cost and expand the design space for critical design constraints for **(a)** NAqRFBs and **(b)** AqRFBs. "Active Material" is abbreviated as AM in the legend. The horizontal dashed line represents the \$100 kWh^{-1} battery price target.

Employing extremely cheap or lightweight redox-active materials (~ 50 g mol^{-1}) could afford similar cost savings as the decrease in ASR described above (Figure 6a), but, as previously mentioned, such light species are unlikely to be electrochemically reversible compounds. Identifying redox-active materials with molecular weights between 100 – 200 g mol^{-1}, which participate in multiple electron transfer events, such as those developed by Sevov et al.,[49] may

present a viable cost-cutting pathway. Recent reports demonstrate metal coordination complexes exhibiting up to six redox events,[55] but these compounds have very high molecular weights and offer only moderate redox potentials. Two electron (or more) transfer materials could decrease the equivalent weight (molecular weight normalized by number of electrons transferred) into the range of 50 – 100 g mol^{-1}.

Salt cost contributions have a particularly large effect on NAqRFB system design options. In particular, Figure 6a shows that the battery price of a NAqRFB with no salt is lower than the benchmark value by approximately \$10 kWh^{-1} for moderately high redox-active species concentration. Removing salt from NAqRFBs may actually be a practical option in decreasing battery price by employing ionic liquid solvents, deep eutectic melts,[62,63] or all ionic redox-active materials. First, ionic liquid solvents can cost 5 – 20 times more than molecular solvents,[64] but the cost decrease afforded by removing salt from the electrolyte could make certain ionic liquid solvents viable. Additionally, we recommend investigation into RFBs utilizing protic ionic liquids (e.g., methanesulfonic acid, triethylammonium hydrogen sulfate), which can exhibit costs[65] and electrochemical windows[66] in between those of water and molecular nonaqueous solvents. Second, deep eutectic melts employing a redox-active material (e.g., $FeCl_3$[62]) and a miscible host (e.g., choline chloride[62,63]) may offer an attractive pathway to no-salt NAqRFBs with moderate redox-active species concentrations (approximately 3.6 mol kg^{-1}).[62] Third, redox-active materials that maintain ionic nature throughout all SOCs (e.g., metal center bypiridines[11–13,57]) could serve as redox-active charge carriers, also eliminating the need for a supporting salt. Identifying any such multi-function materials that assume two or more roles in the electrolyte (i.e., redox-active, charge carrier, solvation) could enable large cost savings for NAqRFBs.

One final recommendation towards decreasing NAqRFB price is simply to increase cell voltage to approximately 4 V, which yields the most drastic decrease in NAqRFB price considered. Nonaqueous electrolytes offering a 4 V electrochemical window could easily enable low concentration batteries with a low price. Cell voltage affects the total battery price so dramatically because increased voltage decreases both the electrolyte (Eq. 3) *and* reactor (Eq. 2) cost contributions simultaneously. Molecular nonaqueous solvents, such as propylene carbonate, exhibit large electrochemical windows allowing for 4 V electrochemical cells,[46] and some work has demonstrated fluorinated organic solvents designed for use in 5 V lithium-ion batteries.[67] Additionally, soluble redox-active compounds have proven redox potentials as high as 4.6 V vs.

Li/Li^+,[68] but stable, soluble redox-active compounds with potentials less than 1.5 V vs. Li/Li^+ are not available. Identifying redox-active species with low redox potentials for use in the negative electrolyte of a NAqRFB remains a major materials design challenge.[30,49]

To complement the price minimization trends offered in Figure 6a, Table 2 presents quantitative design iterations for NAqRFBs to achieve a \$100 kWh^{-1} battery price, providing tangible performance guidelines for materials selection. By pushing NAqRFB design to incorporate any one of the proposed cost cutting pathways (high voltage, low ASR, low salt concentration, or low redox-active material weight), redox-active material concentration requirements shrink by more than 50 % of the DG model benchmark (9.6 mol kg^{-1}). Driving redox-active material concentration below 1 mol kg^{-1} is unlikely, as demonstrated by the divergence to infinity of every price curve in Figure 6a at low values of redox-active species molality. If a NAqRFB can leverage all of the cost cutting pathways presented here, the battery price could easily drop below \$100 kWh^{-1} for redox-active species concentrations greater than 2 mol kg^{-1}.

Table 2: Alternative NAqRFB and AqRFB design iterations that decrease redox-active material molality targets and cell voltage targets by changing other parameters (bolded). All cells shown achieve the \$100 kWh^{-1} price target.

Nonaqueous RFB					
Cell Type	*Cell Voltage (V)*	*Actives Mol. Weigh ($g\ mol^{-1}$)*	*ASR ($\Omega\ cm^2$)*	*Salt Ratio*	*Actives Molality ($mol\ kg^{-1}$)*
1. Benchmark	3	100	5	0.20	6.3
2. High Cell Voltage	**4**	100	5	0.20	1.8
3. Low Actives Molecular Weight	3	**50**	5	0.20	3.1
4. Low ASR	3	100	**2.5**	0.20	3.3
5. Low Salt	3	100	5	**0**	2.7
6. High Cell Voltage, Low ASR, and Low Salt	**4**	100	**2.5**	**0**	1.1

Aqueous RFB				
Cell Type	*Actives Cost ($\$\ kg^{-1}$)*	*Actives Mol. Weight ($g\ mol^{-1}$)*	*ASR ($\Omega\ cm^2$)*	*Cell Voltage (V)*
1. Benchmark	5	100	0.5	1.21
2. Low Actives Cost	**2**	100	0.5	0.79
3. Low Actives Molecular Weight	5	**50**	0.5	0.85
4. Low ASR	5	100	**0.1**	1.04
5. Low Actives Cost and Low Actives Molecular Weight	**2**	**50**	0.5	0.67

2.8 AqRFB Design Pathways

While this work presents many pathways towards low price NAqRFBs, design optimization pathways for AqRFBs are substantially more limited since AqRFBs are only sensitive to variations in cell voltage, ASR, and redox-active species cost. Figure 6b displays AqRFB prices as a function of cell voltage for a limited number of possible cell improvement pathways. In addition, Table 2 also presents quantitative iterations of AqRFB designs that achieve \$100 kWh^{-1}. Much like the NAqRFB, employing redox-active materials with low molecular weights only affords a small

decrease in battery price, and, as previously described, synthesizing redox-active species with molecular weight much below 100 g mol^{-1} is unlikely. Decreasing redox-active species cost, however, can provide the most drastic savings, alleviating cell voltage requirements or driving battery prices down below \$100 kWh^{-1}; low cost tailored organic[17,18,24,25,40,69] or abundant inorganic[15] materials could offer redox-active species costs under \$5 kg^{-1}. If an AqRFB exploits both low redox-active material cost and high cell voltage (approaching the stability limit of 1.5 V), AqRFB price could drop below \$100 kWh^{-1} and even approach \$70 kWh^{-1}.

2.9 Conclusions

In this work, we present a detailed electrolyte cost model, which explicitly accounts for redox-active material, salt, and solvent contributions to RFB price, as an adaptation to and an extension of prior work by Darling, Gallagher, and co-workers.[1] This techno-economic model explores the available design space for both aqueous and nonaqueous RFBs by considering variations in electrolyte cost parameters, cell voltage, and reactor ASR, as well as identifying critical cost constraining variables for RFBs. In a broad sense, this analysis first defines lower bounds on cell voltage requirements of 1.1 V and 2.0 V for aqueous and nonaqueous RFBs, respectively, to obtain a \$100 kWh^{-1} battery price. Additionally, upper bounds on reactor ASR for aqueous and nonaqueous RFBs are 1.5 Ω cm^2 and 20 Ω cm^2, respectively.

NAqRFBs are sensitive to every cost parameter considered in this analysis due to comparable cost contributions from the electrolyte components and reactor, but the largest potential cost savings for NAqRFBs come from either increasing cell voltage above 3 V or minimizing the amount of supporting salt. We propose identifying materials that provide two or more functions in the electrolyte (i.e., charge balancing, electroactivity, solubilization, and ionic conductivity), which remove the need for a true salt or solvent and could enable drastically more cost effective nonaqueous electrolytes. In comparison, NAqRFB cost cutting by decreasing cell ASR below 5 Ω cm^2 or reducing redox-active material molecular weight below 100 g mol^{-1} only affords small gains. These same techniques can also reduce the required NAqRFB redox-active species concentration to reasonably low values of 2 – 4 mol kg^{-1}, which are near experimental realization. Unlike nonaqueous systems, AqRFBs only exhibited large cost sensitivities to cell voltage and redox-active material cost. Identifying low cost (less than \$5 kg^{-1}) redox-active

materials that enable a cell voltage in the range of 1.1 – 1.5 V is the most promising pathway towards economically viable AqRFBs.

Another application of the present cost-driven materials selection approach is to curate databases of redox-active molecules compiled either experimentally[70–73] or computationally.[74] By comparing the performance of a real, new RFB electrolyte material with these design maps, experimentalists can quickly determine if the new electrolyte chemistry could achieve the \$100 kWh^{-1} price target. Further, computational data sieving is already underway, in conjunction with the Materials Project, which stores electrochemical data for thousands of *ab initio* predicted redox-active molecules as candidates for RFB electrolytes.[74] Accordingly, the present model has been implemented as an interactive online tool within the Materials Project, called the RFB Dashboard.[75] The RFB Dashboard filters redox-active molecules with suitable redox potentials and molecular weights to build a \$100 kWh^{-1} aqueous or nonaqueous RFB by using the design maps presented here (see Figs. 2 and 3). This online tool also allows users to adjust model input parameters to assess impact on materials selection, as well as accommodate future changes to material cost factors and RFB performance parameters.

Beyond the immediate application to RFB materials selection, this analysis presents a framework for cost-conscious research efforts. The design maps translate system-level price and performance metrics to quantitative guidelines for materials properties and performance. Bridging the gap between abstract cost models and focused experimental research will enable rapid transition of new materials into economically viable prototypes. Design maps also highlight promising regions of design space that may be underexplored in the contemporary literature. We hope that this methodology will apply to other systems where cost is a major inhibitor to success by creating tangible experimental targets from detailed techno-economic modeling.

2.10 List of Symbols

$b_{+/-}$	individual electrolyte active species molality	mol kg^{-1}
b_{avg}	mean active species molality	mol kg^{-1}
c_a	reactor cost per unit area	\$ m^{-2}
c_{add}	addition to price	\$ kW^{-1}
c_{bop}	balance-of-plant cost	\$ kW^{-1}
$c_{m,+/-}$	active material cost per unit mass	\$ kg^{-1}
$c_{me,+/-}$	electrolyte cost per unit mass	\$ kg^{-1}
c_{salt}	salt cost per unit mass	\$ kg^{-1}
$c_{solvent}$	solvent cost per unit mass	\$ kg^{-1}
$C_{Additional}$	additional cost	\$ kWh^{-1}
C_{BOP}	balance-of-plant cost	\$ kWh^{-1}
$C_{Electrolyte}$	electrolyte cost	\$ kWh^{-1}
$C_{Reactor}$	reactor cost	\$ kWh^{-1}
E_d	battery discharge energy	kWh
F	Faraday constant	kAh mol^{-1}
$M_{+/-}$	active species molecular weight	g mol^{-1}
M_{salt}	salt molecular weight	g mol^{-1}
$n_{e+/-}$	number of electrons stored per active molecule	mol_{e-} mol^{-1}
P_0	battery future-state price	\$
$r_{+/-}$	individual electrolyte molar salt ratio	mol mol^{-1}
r_{avg}	mean molar salt ratio	mol mol^{-1}
R	area-specific resistance	Ω cm^2
$s_{+/-}$	stoichiometric coefficient	mol mol^{-1}
$S_{+/-}$	active species solubility	kg kg^{-1}
$S_{salt,+/-}$	salt solubility	kg kg^{-1}
t_d	battery discharge time	h
U	open-circuit cell voltage	V
$\varepsilon_{q,rt}$	round-trip coulombic efficiency	-
$\varepsilon_{sys,d}$	system discharge efficiency	-
$\varepsilon_{v,d}$	voltage discharge efficiency	-
$\chi_{+/-}$	depth-of-discharge	-

2.11 References

1. R. M. Darling, K. G. Gallagher, J. A. Kowalski, S. Ha, and F. R. Brushett, *Energy Environ. Sci.*, **7**, 3459–3477 (2014).
2. V. Viswanathan et al., *J. Power Sources*, **247**, 1040–1051 (2014).
3. S. Ha and K. G. Gallagher, *J. Power Sources*, **296**, 122–132 (2015).
4. U.S. Department of Energy: Office of Electricity Delivery and Energy Reliability, *Energy Storage: Program Planning Document*, (2011).
5. U . S . Department of Energy - Headquarters Advanced Research Projects Agency – Energy (ARPA-E), *Grid-Scale Rampable Intermittent Dispatchable Storage Funding Opportunity Announcement*, p. 10, (2010).
6. A. Z. Weber et al., *J. Appl. Electrochem.*, **41**, 1137–1164 (2011).
7. P. Alotto, M. Guarnieri, and F. Moro, *Renew. Sustain. Energy Rev.*, **29**, 325–335 (2014).
8. J. Goeltz et al., "Aqueous redox flow batteries comprising metal ligand coordination compounds," US Pat. US 20160276693 A1, Filed May 27, 2016.
9. Z. Yang et al., *Chem. Rev.*, **111**, 3577–3613 (2011).
10. M. Skyllas-Kazacos, M. H. Chakrabarti, S. A. Hajimolana, F. S. Mjalli, and M. Saleem, *J. Electrochem. Soc.*, **158**, R55 (2011).
11. Y. Matsuda, K. Tanaka, M. Okada, U. Takasu, and M. Morita, *J. Appl. Electrochem.*, **18**, 909–914 (1988).
12. M. H. Chakrabarti, R. A. W. Dryfe, and E. P. L. Roberts, *Electrochimica Acta*, **52**, 2189–2195 (2007).
13. M. H. Chakrabarti, E. P. Lindfield Roberts, and M. Saleem, *Int. J. Green Energy*, **7**, 445–460 (2010).
14. A. A. Shinkle, T. J. Pomaville, A. E. S. Sleightholme, L. T. Thompson, and C. W. Monroe, *J. Power Sources*, **248**, 1299–1305 (2014).
15. X. Wei et al., *J. Electrochem. Soc.*, **163**, A5150–A5153 (2016).
16. H. Pan et al., *Adv. Energy Mater.*, **5**, 150113 (2015).
17. K. Lin et al., *Science*, **349**, 1529–1532 (2015).
18. B. Huskinson et al., *Nature*, **505**, 195–198 (2014).
19. F. R. Brushett, J. T. Vaughey, and A. N. Jansen, *Adv. Energy Mater.*, **2**, 1390–1396 (2012).
20. S. H. Oh et al., *J Mater Chem A*, **2**, 19994–19998 (2014).
21. S. K. Park et al., *Electrochem. Commun.*, **59**, 68–71 (2015).
22. X. Wei et al., *Angew. Chem. Int. Ed.*, **54**, 8684–8687 (2015).
23. X. Wei et al., *Adv. Mater.*, **26**, 7649–7653 (2014).
24. J. D. Milshtein, L. Su, C. Liou, A. F. Badel, and F. R. Brushett, *Electrochimica Acta*, **180**, 695–704 (2015).
25. Y. Xu, Y. H. Wen, J. Cheng, G. P. Cao, and Y. S. Yang, *Electrochimica Acta*, **55**, 715–720 (2010).
26. A. P. Kaur, N. E. Holubowitch, S. Ergun, C. F. Elliott, and S. A. Odom, *Energy Technol.*, **3**, 476–480 (2015).
27. J. Huang et al., *Adv. Energy Mater.*, **5**, 1401782 (2015).
28. J. Huang et al., *J Mater Chem A*, **3**, 14971–14976 (2015).
29. T. Liu, X. Wei, Z. Nie, V. Sprenkle, and W. Wang, *Adv. Energy Mater.*, **6**, 1501449 (2016).
30. J. A. Kowalski, L. Su, J. D. Milshtein, and F. R. Brushett, *Curr. Opin. Chem. Eng.*, **13**, 45–52 (2016).
31. K. G. Gallagher et al., *Energy Environ. Sci.*, **7**, 1555–1563 (2014).

32. P. A. Nelson, K. G. Gallagher, I. Bloom, and D. W. Dees, *Modeling the Performance and Cost of Lithium-Ion Batteries for Electric-Drive Vehicles*, p. 1-102, (2012).
33. C. Zhou, K. Qian, M. Allan, and W. Zhou, *IEEE Trans. Energy Convers.*, **26**, 1041–1050 (2011).
34. G. Kear, A. A. Shah, and F. C. Walsh, *Int. J. Energy Res.*, **36**, 1105–1120 (2012).
35. M. Zhang, M. Moore, J. S. Watson, T. A. Zawodzinski, and R. M. Counce, *J. Electrochem. Soc.*, **159**, A1183–A1188 (2012).
36. R. Darling, K. Gallagher, W. Xie, L. Su, and F. Brushett, *J. Electrochem. Soc.*, **163**, A5029–A5040 (2016).
37. D. Rastler, *Market Driven Distributed Energy Storage System Requirements for Load Management Applications*, Energy and Power Research Institute (2007).
38. ICIS Indicative Chemical Prices A-Z, (2006) http://www.icis.com/chemicals/channel-info-chemicals-a-z/.
39. L. Gaines and R. Cuenca, *Costs of Lithium-Ion Batteries for Vehicles: ANL/ESD-42*, p. 31, (2000).
40. B. Yang, L. Hoober-Burkhardt, F. Wang, G. K. Surya Prakash, and S. R. Narayanan, *J. Electrochem. Soc.*, **161**, A1371–A1380 (2014).
41. R. A. Potash, J. R. McKone, S. Conte, and H. D. Abruña, *J. Electrochem. Soc.*, **163**, A338–A344 (2016).
42. A. J. Cofrancesco, in *Kirk-Othmer Encyclopedia of Chemical Technology: Anthraquinone*, p. 1–13, John Wiley & Sons, Inc., New York (2001).
43. F. Y. Fan et al., *Nano Lett.*, **14**, 2210–2218 (2014).
44. S. H. Shin, S. H. Yun, and S. H. Moon, *RSC Adv.*, **3**, 9095–9116 (2013).
45. D. Pletcher and R. Wills, *Phys. Chem. Chem. Phys.*, **6**, 1779–1785 (2004).
46. D. Aurbach et al., *Electrochimica Acta*, **50**, 247–254 (2004).
47. J. Mun et al., *Electrochem. Solid-State Lett.*, **15**, A80–A82 (2012).
48. I. L. Escalante-García, J. S. Wainright, L. T. Thompson, and R. F. Savinell, *J. Electrochem. Soc.*, **162**, A363–A372 (2015).
49. C. S. Sevov et al., *J. Am. Chem. Soc.*, **137**, 14465–14472 (2015).
50. R. Younesi, G. M. Veith, P. Johansson, K. Edstrom, and T. Vegge, *Energy Environ. Sci.*, **8**, 1905–1922 (2015).
51. K. Xu, *Chem. Rev.*, **114**, 11503–11618 (2014).
52. S. M. Laramie, J. D. Milshtein, T. M. Breault, F. R. Brushett, and L. T. Thompson, *J. Power Sources*, **327**, 681–692 (2016).
53. B. Scrosati, *J. Electrochem. Soc.*, **139**, 2776–2781 (1992).
54. N. S. Hudak, L. J. Small, H. D. Pratt, and T. M. Anderson, *J. Electrochem. Soc.*, **162**, A2188–A2194 (2015).
55. P. J. Cabrera et al., *J. Phys. Chem. C*, **119**, 15882–15889 (2015).
56. J. H. Kim et al., *Electrochem. Commun.*, **13**, 997–1000 (2011).
57. J. Mun et al., *Electrochem. Solid-State Lett.*, **15**, A80–A82 (2012).
58. L. Su et al., *J. Electrochem. Soc.*, **163**, A5253–A5262 (2016).
59. S. H. Shin, Y. Kim, S. H. Yun, S. Maurya, and S. H. Moon, *J. Power Sources*, **296**, 245–254 (2015).
60. L. Su, M. Ferrandon, J. A. Kowalski, J. T. Vaughey, and F. R. Brushett, *J. Electrochem. Soc.*, **161**, A1905–A1914 (2014).

61. J. D. Milshtein, J. L. Barton, R. M. Darling, and F. R. Brushett, *J. Power Sources*, **327**, 151–159 (2016).
62. M. A. Miller, J. S. Wainright, and R. F. Savinell, *J. Electrochem. Soc.*, **163**, A578–A579 (2016).
63. L. Bahadori et al., *J. Electrochem. Soc.*, **163**, A632–A638 (2016).
64. N. V Plechkova and K. R. Seddon, *Chem. Soc. Rev.*, **37**, 123–150 (2008).
65. L. Chen et al., *Green Chem.*, **16**, 3098–3106 (2014).
66. J. Luo et al., *J. Mater. Chem.*, **21**, 10426–10436 (2011).
67. L. Hu, Z. Xue, K. Amine, and Z. Zhang, *J. Electrochem. Soc.*, **161**, A1777–A1781 (2014).
68. Z. Chen et al., *Electrochem. Solid-State Lett.*, **13**, A39–A42 (2010).
69. T. Janoschka et al., *Nature*, **527**, 78–81 (2015).
70. N. G. Connelly and W. E. Geiger, *Chem. Rev.*, **96**, 877–910 (1996).
71. Y. Liang, Z. Tao, and J. Chen, *Adv. Energy Mater.*, **2**, 742–769 (2012).
72. Z. Song and H. Zhou, *Energy Environ. Sci.*, **6**, 2280–2301 (2013).
73. R. T. Boeré and T. L. Roemmele, *Coord. Chem. Rev.*, **210**, 369–445 (2000).
74. A. Jain et al., *APL Mater.*, **1**, 011002 (2013).
75. *Mater. Proj.* (2016) https://materialsproject.org/#apps/RFBDashboard.

3. Voltammetry study of quinoxaline: a potential aqueous redox flow battery active species

This chapter is reprinted from *Electrochimica Acta*, Vol 180, J. D. Milshtein, L. Su, C. Liou, A. F. Badel, F. R. Brushett, Voltammetry study of quinoxaline in aqueous electrolytes, 695–704, Copyright (2015), with permission from Elsevier under license number 4087101329285.

3.1 Introduction

Electrochemical behavior of redox active organic compounds in aqueous solutions has been studied for nearly a century, with research efforts dating back to the 1920s.[1,2] During this long period, the family of organic compounds termed quinones showed good electrochemical reversibility, leading to further investigation.[3–5] Quinones are a class of aromatic-derived compounds in which an even number of –CH= groups are converted into ketone (R–C(=O)–R') groups, yielding a fully conjugated and cyclic dione structure.[6] Recent research efforts on quinone electrochemistry have focused on identifying compounds with electrochemical characteristics that are well-suited for RFB applications. One such compound is 4,5-dibenzoquinone-1,3-benzedisulfonate (BQBDS), which has been proven as a two-electron transfer, high potential redox active material (E° = 0.72 V vs. SHE) and demonstrated in a flow cell with a lead (Pb) low potential electrode.[7] Additionally, Huskinson et al. studied the electrochemical behavior of 9,10-anthraquinone-2,7-disulphonic acid as a two-electron transfer, low potential redox active material (E° = 0.23 V vs. SHE), and demonstrated its cycling performance in a flow cell with the Br_2/Br^- redox couple on the high potential side.[8] Engineering developments have also coupled BQBDS with anthraquinone-2-sulfonic acid (E° = 0.09 V vs. SHE) to create an all-organic aqueous RFB.[9] Beyond quinones, some efforts have also focused on identifying organic redox couple replacements for the I^{3-}/I^- couple, which acts as a mediator in dye sensitized solar cells, in order to minimize the corrosive effects of I^{3-}/I^-. One successful organic redox couple has been the 5-mercapto-1-methyltetrazole ion (E° = 0.5 V vs. SHE).[10]

This study aims to explore the electrochemical behavior of quinoxaline as a low-potential redox active compound in different aqueous electrolytes, extending the knowledge base of organic redox active compounds beyond the quinone family. The quinoxaline structure is characterized by a benzene ring and a –C–N=C– containing pyrazine ring, as depicted in Figure 1. A variety of quinoxaline derivatives have been studied as component materials in organic sensitizers for dye-

sensitized solar cells, and as lower band gap materials in organic photovoltaics.[11,12] Triquinoxalinylene specifically was used in a lithium-ion (Li-ion) battery application, acting as an organic cathode material.[13] A quinoxaline derivative has also been studied as a low potential redox active compound in an all-organic, non-aqueous Li-ion flow battery.[14] Also, a number of studies reported on quinoxaline electrochemistry in non-aqueous solvents.[15–19] Aqueous quinoxaline was recently applied as a redox active compound in a solar-rechargeable RFB device, however, exploration of quinoxaline electrochemical behavior was not the focus of that study.[20] Finally, several studies have investigated quinoxaline electrochemical behavior in acidic and near-neutral electrolytes with a focus on determining kinetic rate parameters and related organic chemistry.[21–25]

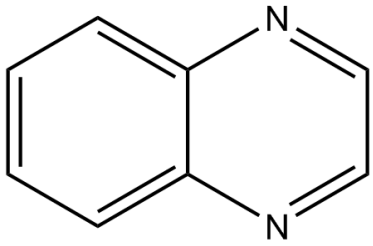

Figure 1: The molecular structure of quinoxaline.

In this work, the electrochemical behavior of quinoxaline is investigated using voltammetric techniques in over 30 aqueous electrolytes, comprised of 12 different supporting salts across the pH range of ca. 4 to 14. Specifically, cyclic and hydrodynamic voltammetry are used to qualitatively and quantitatively assess the electrochemical performance and stability of quinoxaline as a function of supporting salt choice and solution pH. Our studies reveal quinoxaline to be a promising redox active material for aqueous RFBs due to its high solubility in water (~4.5 M) and attractive theoretical energy density of 410 mAh g^{-1}, which is attributed to its low molecular weight (130.15 g mol^{-1}) and ability to store two electrons. The redox potential was found to be $E^{\circ} \approx$ -0.02 V vs. RHE, which is lower than the reported redox potentials of quinones in aqueous solution.

3.2 Experimental

Materials. In this work, quinoxaline electrochemical behavior was characterized in a number of aqueous electrolytes, resulting in the use of a large number of chemical compounds. Quinoxaline

was purchased from Sigma-Aldrich and had a purity of 99.9%. The suppliers and purities of all salt compounds used are presented in Table 1. Additionally, a table of all electrolyte compositions tested is available in Section 3.1. Deionized water (DI H_2O, 18.2 MΩ) for all solutions was purified in the laboratory using a Milli-Q system. In the specific case of $NaHCO_3$ solution preparation, first a stock Na_2CO_3 solution was prepared, and then gaseous CO_2 was bubbled into the solution for 45 min to create $NaHCO_3$ solution. In all experiments, the quinoxaline concentration was 5 mM, and the supporting salt cation concentration was 1 M.

Table 1: Suppliers and purities of salts used in electrochemical experiments.

Salt	**Supplier**	**Assay (%)**
KCl	Sigma-Aldrich	99.0 – 100.5
KNO_3	Sigma-Aldrich	99.0
KOH	Sigma-Aldrich	99.99
K_2SO_4	Sigma-Aldrich	99.0
LiCl	Fluka	99.0
$LiNO_3$	Sigma-Aldrich	99.99
LiOH	Sigma-Aldrich	98
Li_2SO_4	Sigma-Aldrich	99.0
$NaC_2H_3O_2$	Sigma-Aldrich	99.0
Na_2CO_3	Sigma-Aldrich	99.0
$NaNO_3$	Sigma-Aldrich	99.0
NaOH	Macron	98.0

Voltammetry. Cyclic voltammetry (CV) and rotating disk voltammetry (RDV) techniques were employed to probe the electrochemical behavior of quinoxaline. Two separate procedures were used in CV experiments. The first procedure was designed for rapid screening of electrochemical behavior of quinoxaline in many different electrolyte compositions. The second CV procedure was designed for calculating the number of electrons transferred, diffusion coefficients, and transfer coefficients in only the electrolytes with promising electrochemical characteristics. All electrochemical measurements presented in this paper were performed using a Biologic VSP-300 potentiostat. Glassy carbon working electrodes were used in voltammetry

experiments and polished with 0.05 μm alumina suspension before performing a new set of measurements. The initial CV scan direction was always cathodic (reductive).

Cell resistances were measured prior to electrochemical experiments to be ~5 Ω. Due to small peak currents during CV (≤ 1 mA), the maximum estimated iR drop was ~5 mV. During rapid screening CV, an 85% cell resistance compensation (iR correction) was applied during the experiment to ensure high quality data with new electrolyte compositions. In promising electrolyte systems where quantitative CV techniques were applied, no iR correction was initiated as the small potential offset was unlikely to affect experimental results. Additionally, no iR correction was applied during RDV experiments because analyses only considered the limiting RDV current, which is unaffected by ohmic losses in the absence of gas evolving side reactions. All potentials in this paper are reported versus either the reversible hydrogen electrode (RHE) or the standard hydrogen electrode (SHE). The RHE scale was used to compare voltammetric behavior of quinoxaline over a wide range of pH. The SHE scale was used to evaluate the relationship between solution pH and quinoxaline redox potential. In practice, data was collected using a Ag/AgCl reference electrode, calibrated using methods described in the following sections, and, post-experiment, solution pH was measured using a pH meter (Thermo-Scientific, Orion Star A215). Potentials were then adjusted to the SHE or RHE scale via the Nernst equation. For every CV data set presented in this study, a number of quantitative characteristics were used to determine the electrochemical performance of quinoxaline in a given electrolyte, including redox potential, peak separation, peak currents (anodic and cathodic), and approximate linear slopes before peaks (anodic and cathodic). All experimental currents used in these calculations were background corrected. The background current was comprised of non-faradaic, hydrogen evolution reaction (HER), and oxygen reduction reaction currents.

Qualitative CV (for Rapid Screening). The rapid screening CV experiments were carried out in a three-electrode cell with a 0.3 cm diameter glassy carbon electrode (GCE, 0.071 cm^2, CH Instruments), a platinum (Pt) wire counter electrode (CH Instruments) and a Ag/AgCl (3 M NaCl, BASi Inc.) reference electrode. These reference electrodes were calibrated prior to experiments by measuring the open circuit voltage (OCV) between the reference and a Pt wire in 0.5 M H_2SO_4 while bubbling hydrogen. Three-electrode cells were filled with 10 mL of solution, and the solution was bubbled with argon for 10 min prior to experiments. The argon bubbling tube was then adjusted such that it provided a blanket of argon gas over the surface of the solution. Then,

ten cycles of CV were recorded at a scan rate of 100 mV s^{-1}. For rapid screening CV experiments, only one experimental trial was performed per electrolyte composition due to the large number of electrolytes tested.

Quantitative Voltammetry. A set of quantitative experiments were designed to calculate the number of electrons transferred and diffusion coefficients using the Randles-Sevcik equation for irreversible CVs (Equation (1)[26]) and the Levich equation (Equation (2)). In Equation (1), i_p is the peak current, n is the total number of electrons transferred, n' ($< n$) is the number of electrons transferred prior to the rate limiting kinetic step, $\alpha_{n'+1}$ is the transfer coefficient of the rate limiting step, A is the electrode surface area, F is Faraday's constant, C is the reactant concentration, s is the scan rate, R is the universal gas constant, T is temperature, and D is the diffusion coefficient.[26] Additionally, in Equation (2), i_L is the RDV limiting current, ω is the electrode rotation rate, and ν is the kinematic viscosity.[27] Kinematic viscosities were determined from dynamic viscosities, which were interpolated from tables by Zaytsev and Aseyev,[28] and electrolyte densities, which were measured using a balance (Metler-Toledo, XP105) and known solution volume. All remaining variables are constants or were determined by the experimental design.

$$i_p = 0.496\sqrt{n' + \alpha_{n'+1}}\, nAFC\sqrt{\frac{FsD}{RT}} \tag{1}$$

$$i_L = 0.62nFAD^{\frac{2}{3}}\omega^{\frac{1}{2}}\nu^{\frac{-1}{6}}C \tag{2}$$

Quantitative CV and RDV experiments were carried out in a water-jacketed three-electrode cell. Chilled water at a temperature of 295 K (22 °C) was continuously passed through the water jacket in order to maintain a constant temperature throughout the experiment. A rotating disk electrode with a 0.5 cm diameter glassy carbon electrode (0.196 cm^2) was used as a working electrode. A coiled Pt wire counter electrode was housed in a glass compartment separated from the main chamber by a porous frit. Both chambers were filled with the same bulk electrolyte. The reference electrode was a double junction Ag/AgCl (10% KNO_3), which was calibrated against a commercially available reversible hydrogen electrode (BAS Inc.) in 1 M $NaHCO_3$ solution by measuring OCV between the two electrodes. As a consistency check, redox potentials measured via different reference electrodes and calibration processes were compared, and the results were found to be identical. All cell components were purchased from Pine Instruments Co., including the rotator and motor used in RDV experiments.

Cells were filled with 80 mL of solution, and the solution was bubbled with argon using a porous glass frit for 1 h before taking any electrochemical measurements. After 1 h, the argon gas bubbling stream was switched to an argon gas blanket above the solution. Three CV cycles, with a stationary electrode, were recorded at each of the following scan rates: 5, 10, 20, 50, and 100 mV s^{-1}. Between CV and RDV experiments, the glassy carbon electrode was re-polished. Then, two CV scans were performed at a 10 mV s^{-1} scan rate for each of the following RDV rotation speeds: 100, 400, 900, 1600, and 2500 rpm. Experiments were performed in triplicate using freshly prepared solution and freshly polished glassy carbon electrodes for each trial.

Solubility. For five promising electrolytes, the solubility limit (at room temperature) of quinoxaline in each electrolyte of interest and DI H_2O was estimated using the following method. Scintillation vials were filled with a known volume of electrolyte, and quinoxaline was added in ~0.13 g increments. The vials were then vortex sonicated for ~5 min between quinoxaline additions. Once no more quinoxaline could be dissolved into the vial, the solubility limit was recorded. Volume changes due to the addition of quinoxaline were accounted for by measuring solution densities just before the solubility limit was reached. This method was accurate to the nearest 0.5 M concentration.

3.3 Electrolyte Screening

More than 30 electrolyte compositions were screened in order to identify the effects of pH, cation, and anion on the electrochemical behavior of quinoxaline during CV experiments. Due to the large number of electrolytes screened during this study, only a few select figures exhibiting representative trends have been included in this paper. A quantitative analysis of all CV data sets can be found in Table 2.

First, an estimate of the redox potential, $E^{\circ} = (E_{p,a} + E_{p,c})/2$, for the 2nd cycle is provided in each electrolyte. As such, the ratio of peak separations between the 10th and 2nd cycles ($\Delta E_{pp,10}/\Delta E_{pp,2}$) was calculated as a measure of the increase in peak separation as a function of cycle number. Note that compounds which were stable for 10 CV scans demonstrated stability out to 100 cycles (at which point the experiment was stopped). In the ideal electrolyte system, this ratio remains at unity, but if the ratio exceeds a value of one, the peak separation increases with cycle number, indicating that quinoxaline becomes less electrochemically reversible. Minimizing $\Delta E_{pp,10}/\Delta E_{pp,2}$ across electrolytes is one indicator of good (electro)chemical stability. The ratios of

peak currents between the 10^{th} and 2^{nd} cycles for the cathodic ($i_{pc,10}/i_{pc,2}$) and anodic ($i_{pa,10}/i_{pa,2}$) scans were calculated as an indicator of the chemical reversibility of quinoxaline. If the peak current ratios fall below one, reactant is consumed during either the forward or backward electrochemical reactions by a competing chemical reaction. This decay in peak current suggests poor quinoxaline stability in a particular electrolyte. Although a non-traditional CV descriptor, approximating a linear slope to the front of an anodic peak (m_a) or a cathodic peak (m_c) provides a simple indicator of the overall reaction rate of either the forward or backward reaction, combining effects of both reaction kinetics and mass-transport. Achieving a slope ratio (m_a/m_c) of one, indicates an equally fast forward and backward overall reaction rate.

Table 2: Quantitative analysis of cyclic voltammograms of quinoxaline in various aqueous electrolytes.

Electrolyte	**pH**	**E° vs. RHE (V)**	**$\Delta E_{pp,10}/\Delta E_{pp,2}$**	**$i_{pc,10}/i_{pc,2}$**	**$i_{pa,10}/i_{pa,2}$**	**m_a/m_c**
1 M KCl	5.4	-0.80	1.85	0.56	0.57	0.75
0.99 M KCl / 0.01 M KOH	11.8	-0.48	1.02	0.97	1.00	0.59
0.9 M KCl / 0.1 M KOH	12.8	-0.45	1.05	0.96	0.99	0.46
1 M KNO_3†	7.2	-0.76†	1.04†	1.01†	0.91†	1.51†
0.99 M KNO_3 / 0.01 M KOH	11.7	-0.52	1.01	0.97	1.00	0.64
0.9 M KNO_3 / 0.1 M KOH	12.8	-0.50	1.03	0.98	0.99	0.53
1 M KOH	13.7	-0.48	1.04	0.97	0.98	0.42
0.5 M K_2SO_4‡	8.9	-0.90‡	2.16‡	0.45‡	‡	0.91‡
0.495 M K_2SO_4 / 0.01 M KOH	11.8	-0.51	1.08	0.95	0.98	0.64
0.45 M K_2SO_4 / 0.1 M KOH	12.8	-0.50	1.05	0.97	0.99	0.51
1 M LiCl	3.8	-0.94‡	2.95‡	0.08‡	‡	0.96‡
0.99 M LiCl / 0.01 M LiOH	11.4	-0.52	1.05	0.96	0.99	0.63
0.9 M LiCl / 0.1 M LiOH	12.1	-0.53	1.04	0.99	1.00	0.51
1 M $LiNO_3$†	6.0	-0.75†	1.11†	0.91†	0.80†	1.94†
0.99 M $LiNO_3$ / 0.01 M LiOH	11.3	-0.47	1.08	0.95	0.98	0.67
0.9 M $LiNO_3$ / 0.1 M LiOH	12.1	-0.48	1.10	0.95	0.99	0.51
1 M LiOH	12.7	-0.55	1.00	0.96	0.98	0.45
0.5 M Li_2SO_4‡	6.6	-0.81‡	‡	‡	‡	‡
0.495 M Li_2SO_4 / 0.01 M LiOH	12.0	-0.52	1.06	0.95	0.96	0.55
0.45 M Li_2SO_4 / 0.1 M LiOH	12.2	-0.52	1.02	0.99	1.00	0.46
1 M $NaC_2H_3O_2$*	8.6	-0.68*	*	*	*	*
0.99 M $NaC_2H_3O_2$ / 0.01 M NaOH	11.8	-0.52	1.06	0.97	1.01	0.58
0.9 M $NaC_2H_3O_2$ / 0.1 M NaOH	12.7	-0.51	1.04	0.97	1.00	0.46
1 M $NaHCO_3$‡	8.7	-0.53‡	‡	‡	‡	1.51‡
0.99 M $NaHCO_3$ / 0.01 M NaOH	8.7	-0.53	2.90	0.50	0.06	1.61
0.9 M $NaHCO_3$ / 0.1 M NaOH	9.1	-0.53	1.56	0.78	0.82	1.63
1 M $NaNO_3$	6.8	-0.77	1.78	0.46	0.12	0.82
0.99 M $NaNO_3$ / 0.01 M NaOH	11.6	-0.52	1.04	0.96	1.00	0.61
0.9 M $NaNO_3$ / 0.1 M NaOH	12.5	-0.52	1.07	0.98	0.98	0.50
1 M NaOH	13.8	-0.48	1.01	0.98	0.99	0.46

†Data set showed significant HER current.

‡Data set showed considerable degradation.

*CV exhibited two distinct reduction and oxidation peaks.

Redox potentials shifted linearly with pH in alkaline environments (Table 2). By comparison, in acidic and neutral electrolytes, the redox potential exhibited only a weak dependence on pH. When considering the slope ratios between the anodic and cathodic peaks, the ratios for chemically reversible CV data sets varied between 0.45 and 0.65, indicating that the backward overall reaction rate was noticeably more sluggish than the forward overall reaction rate.

Visually, this difference manifests as CVs asymmetric about the redox potential, likely caused by different diffusion coefficients and rate constants for the forward and backward reactions. Although not provided in Table 2, the amount of charge transferred during the cathodic and anodic scans was calculated by integrating the area underneath peaks (first subtracting background current) for every CV cycle to ensure that quinoxaline was chemically reversible. In all electrolytes with pH ≥ 11.4, the ratio of charge transferred between the cathodic and anodic scans, within a particular CV cycle, always exceeded 0.9, indicating that quinoxaline was chemically stable.

Figure 2 shows cycles 2 and 10 for six different KCl or LiCl based solutions with varying hydroxide (OH^-) concentrations, and subsequently varying pH. First, consider the effect of cation size on the electrochemical behavior of quinoxaline. The CV characteristics for a fixed OH^- concentration between the LiCl and the KCl data do not vary greatly, suggesting that cation size does not significantly affect quinoxaline behavior. Note that the electrochemical stability of quinoxaline with respect to differing cations enables flexibility in RFB design as varying cation size can have beneficial effects on the performance of ion-selective membranes (e.g., lower resistance).[29,30]

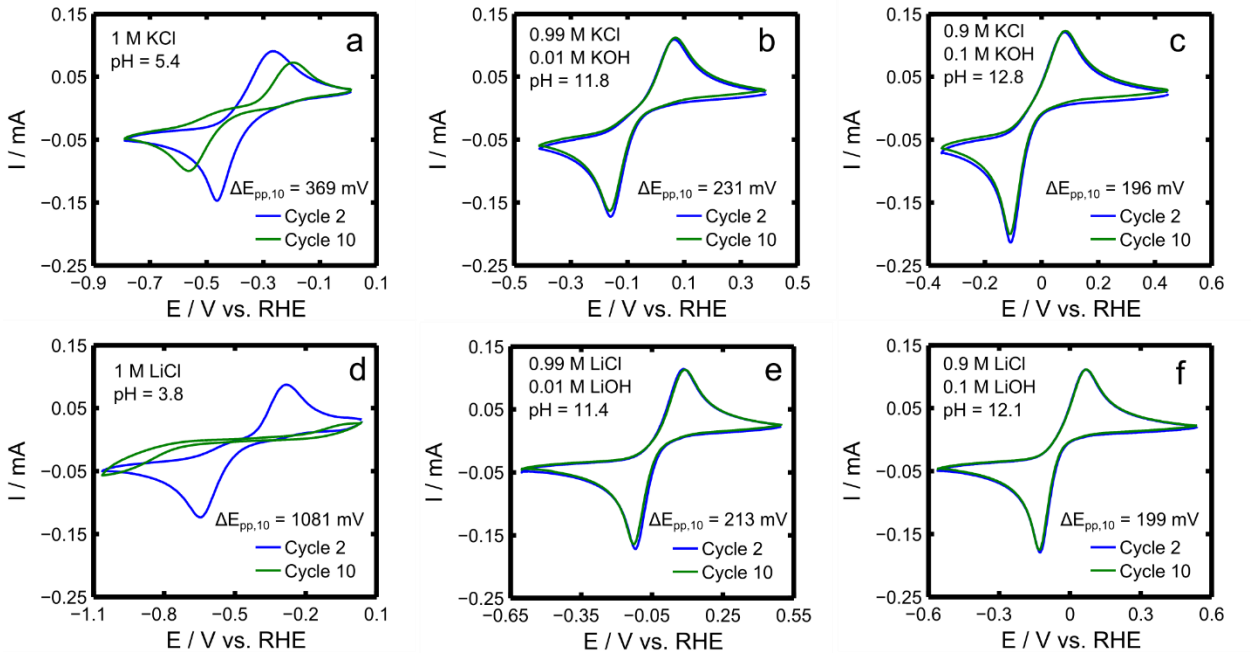

Figure 2: CVs of quinoxaline in six KCl or LiCl based solutions of different pHs, showing cycles 2 and 10: **a)** 1 M KCl, pH = 5.4; **b)** 0.99 M KCl / 0.01 M KOH, pH = 11.8; **c)** 0.9 M KCl / 0.1 M KOH, pH = 12.8; **d)** 1 M LiCl, pH = 8.1; **e)** 0.99 M LiCl / 0.01 M LiOH, pH = 11.4; **f)** 0.9 M LiCl / 0.1 M LiOH, pH = 12.1.

Figure 2 demonstrates that the electrochemical reversibility, chemical reversibility, and overall reaction rates all improve as the pH increases. When the electrolyte was comprised of only 1 M KCl or 1 M LiCl, significant decay in the peak current over 10 cycles suggests that an electrochemical-chemical (EC) process may have occurred. As OH^- was added to the electrolytes, the peak currents remained constant over 10 CV cycles ($i_{pa,10}/i_{pa,2}$ and $i_{pc,10}/i_{pc,2}$ near unity), suggesting improved chemical reversibility over cases with no added OH^-. Additionally, the peak separation decreases as pH increases, indicating improved electrochemical reversibility (faster reaction kinetics). For example, between the KCl electrolytes with 0.01 and 0.1 M KOH, the peak separation in cycle 10 decreases from 231 to 196 mV. The same general trends apply to all electrolytes as shown in Table 2.

Due to the promising trend of improved quinoxaline performance with increasing pH, CV studies were performed on quinoxaline in electrolytes containing only 1 M KOH, 1 M NaOH, or 1 M LiOH. Cyclic voltammograms collected in these electrolytes are shown in Figure 3. Across each of these electrolytes, the peak separation (~150 mV) and peak slope ratios (0.41 to 0.45) are approximately the same, and the anodic and cathodic peak currents do not change as a function of cycle number. The CV studies presented in Figure 3 exhibit the best overall quinoxaline CV performance in any of the electrolytes screened. Also, only minor differences exist between quantitated CV characteristics in each electrolyte (see Table 2), providing further evidence that the electrochemical behavior of quinoxaline appears independent of monovalent cation size (ranging across Li^+, Na^+, and K^+).

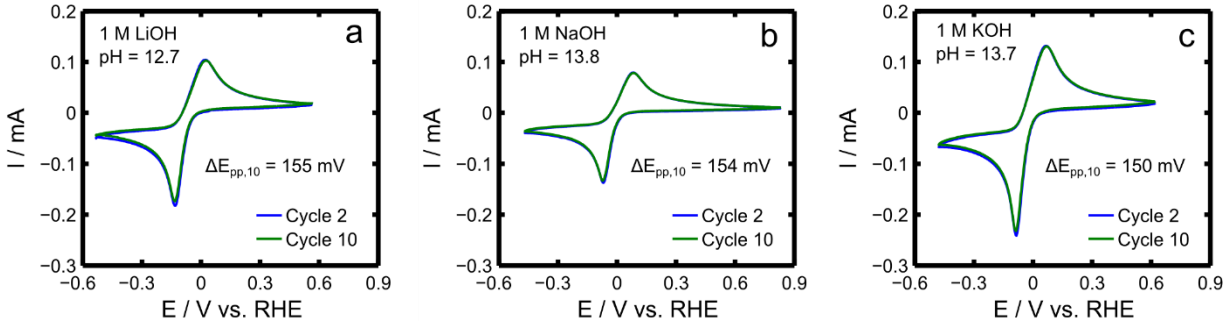

Figure 3: CVs of quinoxaline in three alkaline solutions with different cations, showing cycles 2 and 10: **a)** 1 M LiOH, pH = 12.7; **b)** 1 M NaOH, pH = 13.8; **c)** 1 M KOH, pH = 13.7.

Finally, the electrolyte screening process considered the effects of different anions (Cl^-, SO_4^-, NO_3^-, $C_2H_3O_2^-$, and HCO_3^-) on quinoxaline electrochemical performance. Figure 4 shows CV data for quinoxaline in 0.99 M KNO_3 / 0.01 M KOH, 0.99 M $NaC_2H_3O_2$ / 0.01 M NaOH, 0.99

M $NaHCO_3$ / 0.01 M NaOH, and 0.495 M K_2SO_4 / 0.01 M KOH, fixing the complementary alkaline salt concentrations. The poor electrochemical performance in $NaHCO_3$-based solution can be reconciled by recalling the buffering capability of the bicarbonate ions. Indeed, the pH of the $NaHCO_3$-based solution remained relatively low, leading to quinoxaline instability.

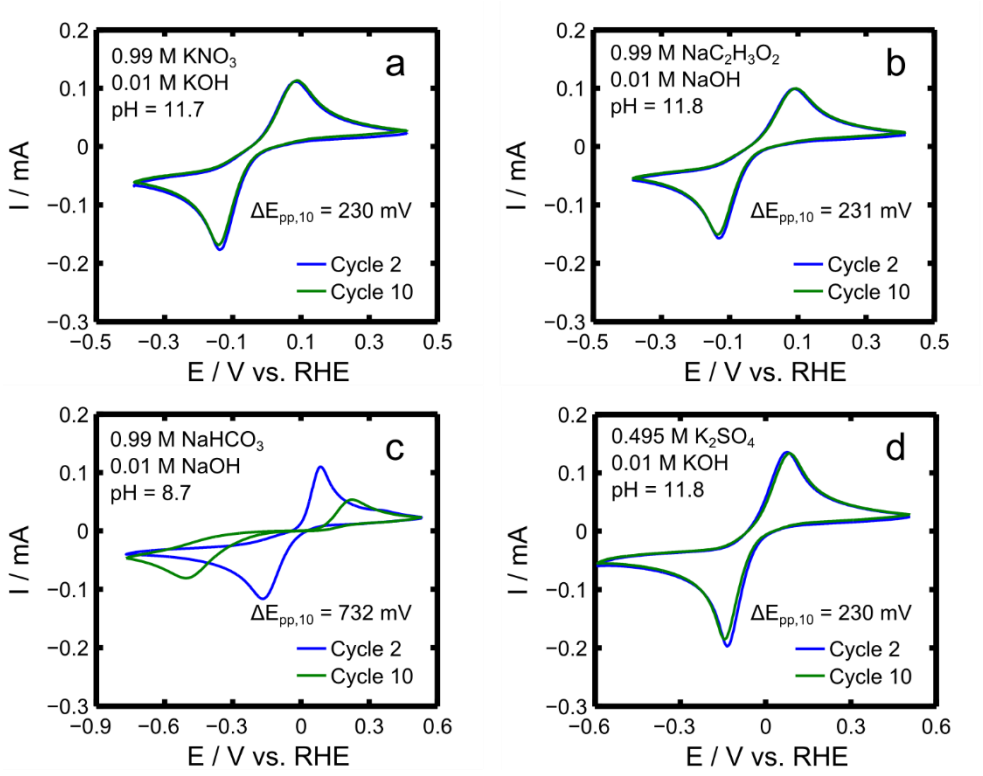

Figure 4: CVs of quinoxaline in electrolytes with four different anions (SO_4^-, NO_3^-, $C_2H_3O_2^-$, and HCO_3^-), showing cycles 2 and 10: **a)** 0.99 M KNO_3 / 0.01 M KOH, pH = 11.7; **b)** 0.99 M $NaC_2H_3O_2$ / 0.01 M NaOH, pH = 11.8; **c)** 0.99 M $NaHCO_3$ / 0.01 M NaOH, pH = 8.7; **d)** 0.495 M K_2SO_4 / 0.01 M KOH, pH = 11.8.

As shown in Figure 2, Figure 3, and Figure 4, as well as in Table 2, varying the non-buffering anion type does not affect the electrochemical response. The electrolytes containing only the alkaline salts (LiOH, NaOH, and KOH) demonstrated the best electrochemical performance in the CV screening experiments. However, for the practical design of electrochemical systems utilizing quinoxaline, performance in less caustic electrolytes (lower pH) than the alkaline salts should also be considered. Additional work presented in this paper is concerned with further characterizing quinoxaline electrochemical behavior in solutions comprised of K_2SO_4, KCl, and / or KOH, which, through the screening process, have been identified as promising salts. Five electrolytes were identified as candidates to optimize quinoxaline performance: **a)** 0.495 M K_2SO_4 / 0.01 M KOH (pH = 11.8); **b)** 0.45 M K_2SO_4 / 0.1 M KOH (pH = 12.9); **c)** 0.99 M KCl / 0.01 M

KOH (pH = 11.8); **d)** 0.9 M KCl / 0.1 M KOH (pH = 12.9); **e)** 1 M KOH (pH = 13.7). These labels (**a - f**), hold for all following figures in this chapter.

3.4 CV and RDV Analysis

To further elucidate the electrochemical behavior of quinoxaline in select electrolytes, CV experiments were performed at five different scan rates, and RDV experiments were performed at five different rotation speeds for each electrolyte of interest. The aim of these experiments was to determine the number of electrons transferred during a quinoxaline redox reaction as well as the diffusion coefficients of quinoxaline and its reduced species. Figure 5 and Figure 6 display the third cycle of typical CV data at different scan rates and the second cathodic scan of typical RDV data at different rotation speeds, respectively.

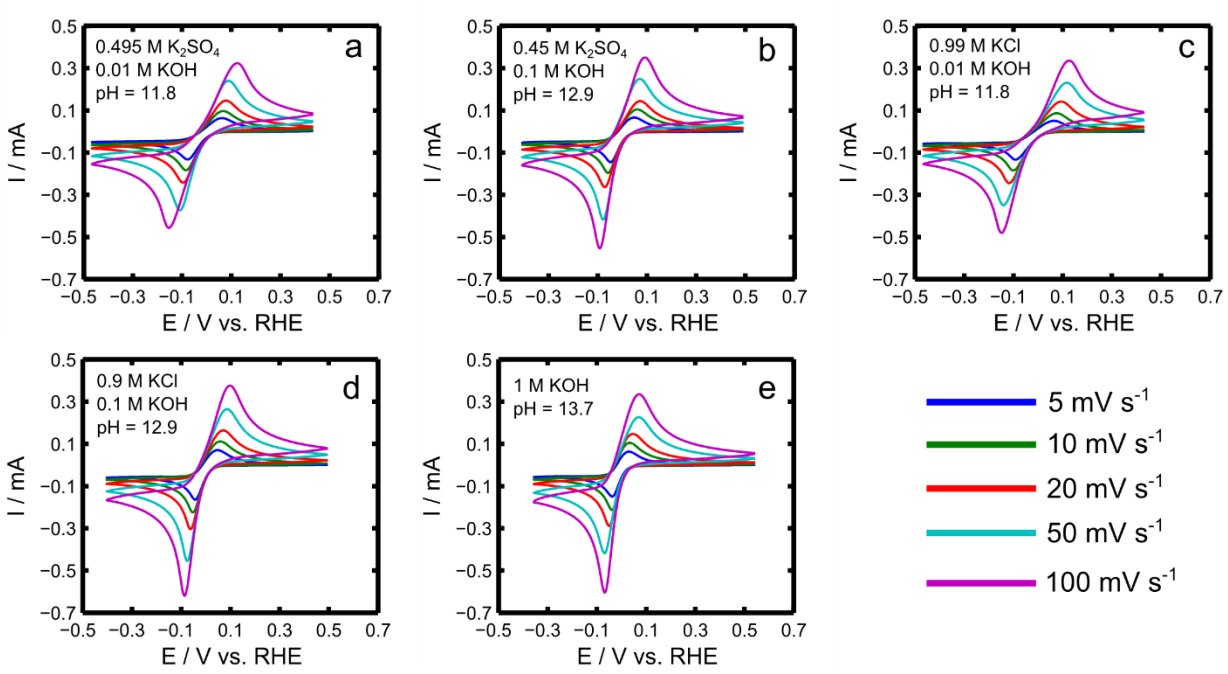

Figure 5: Third cycles of CVs of quinoxaline in five promising electrolytes for five different CV scan rates (5, 10, 20, 50, and 100 mV s^{-1}). Only the third CV cycle is shown. The electrolytes tested were: **a)** 0.495 M K_2SO_4 / 0.01 M KOH, pH = 11.8; **b)** 0.45 M K_2SO_4 / 0.1 M KOH, pH = 12.9; **c)** 0.99 M KCl / 0.01 M KOH, pH = 11.8; **d)** 0.9 M KCl / 0.1 M KOH, pH = 12.9; **e)** 1 M KOH, pH = 13.7.

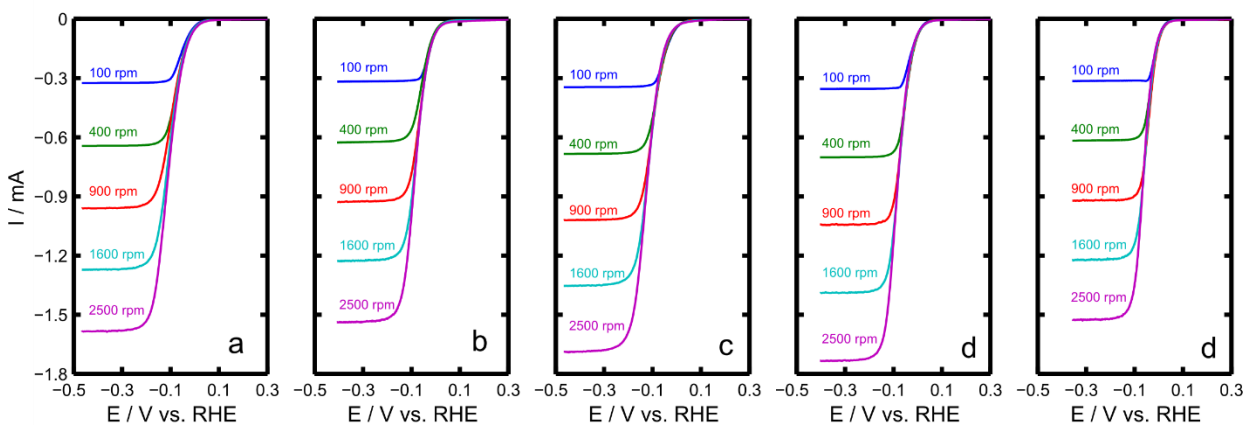

Figure 6: Second cathodic scans of RDV data for quinoxaline reduction in five promising electrolytes for five different rotation speeds (100, 400, 900, 1600, and 2500 rpm). Only the cathodic scan of the second cycle is shown. The electrolytes tested were: **a)** 0.495 M K_2SO_4 / 0.01 M KOH, pH = 11.8; **b)** 0.45 M K_2SO_4 / 0.1 M KOH, pH = 12.9; **c)** 0.99 M KCl / 0.01 M KOH, pH = 11.8; **d)** 0.9 M KCl / 0.1 M KOH, pH = 12.9; **e)** 1 M KOH, pH = 13.7.

Since quinoxaline has not yet been closely studied as an electrochemically active material in aqueous solution, it was appropriate to make no assumptions regarding the number of electrons transferred during quinoxaline reduction or oxidation. In order to quantitatively determine the number of electrons transferred, a numerical fitting technique was employed. Among the irreversible Randles-Sevcik (Equation (1)) and Levich (Equation (2)) equations, there are seven unknown variables: the number of electrons transferred, n, two diffusion coefficients, D_O / D_R, the transfer coefficients, α_O / α_R, and the number of electrons transferred prior to rate limiting kinetic steps n'_O / n'_R. Thus, each variable was used as a parameter to numerically fit three analytical equations (Levich, Randles-Sevcik cathodic, Randles-Sevcik anodic) to the experimental data. While expressions for peak currents of irreversible, multi-electron transfer CVs (i.e. Equation (1)) are limited in their ability to accurately describe wave peak currents,[26,27] variations of Equation (1) have been previously been employed for similar analyses with success.[31,32]

To simplify the computational procedure, n' and α were combined to define a fitting parameter, $\chi = (n' + \alpha)$. For every electrolyte tested, one fit was performed for each combined trial of CV (a total of five scan rates) and RDV (a total of five rotation speeds), coupling the data from both experimental methods. In brief, MATLAB generated values of n, χ, D_O, and D_R, from which simulated peak currents (for CV) and simulated limiting currents (for RDV) were calculated. Numerical fitting was performed using a constrained optimization function, which aimed to minimize a sum of least squares objective function (Z) shown in Equation (3). Specifically an

interior-point optimization algorithm was employed to minimize the objective function and find best fit values of n, χ, D_O, and D_R. In Equation (3), variables $i_{a,exp}$, $i_{c,exp}$, and $i_{a,exp}$, are the experimentally measured anodic CV peak current, cathodic CV peak current, and RDV limiting current, respectively. The variables $i_{a,sim}$, $i_{c,sim}$, and $i_{L,sim}$ are the simulated current analogues of the experimental data, which were computed from the numerically determined parameter values. The objective function aims to minimize the difference between the experimentally measured currents and the simulated currents. Constraints on parameters for the optimization function were selected using typically accepted ranges of values for the physical constants of interest.

$$Z = \frac{\left(i_{a,\text{exp}} - i_{a,\text{sim}}\right)^2}{\left|i_{a,\text{exp}}\right|} + \frac{\left(i_{c,\text{exp}} - i_{c,\text{sim}}\right)^2}{\left|i_{c,\text{exp}}\right|} + \frac{\left(i_{L,\text{exp}} - i_{L,\text{sim}}\right)^2}{\left|i_{L,\text{exp}}\right|} \tag{3}$$

Table 3 shows the results of the numerical fitting analysis, where n, χ_O, χ_R, D_O, and D_R were fitted to the Levich and the irreversible Randles-Sevcik equations. Each entry in Table 3 also shows the 95% confidence interval calculated from the precision uncertainty of the three numerical fits. Since the first aim of the fitting analysis was to determine a number of electrons transferred during an electrochemical reaction, an integer value for number of electrons must be identified, and, as shown in Table 3, the numerical analysis yielded non-integer values. Note that the numerical fitting method only identifies a value for n that best fits the data, and the scatter in the numerically determined values of n is reasonable given the limitations of the technique. Although not shown, three more variations of irreversible Randles-Sevcik analyses found in literature[27,31,32] were compared to check the robustness of our numerical technique. Each of the four attempted methods led to the same conclusions as discussed below. To make physical sense of the numerical data, a nearest integer value can be distinguished. By rounding each entry for n in Table 3, the nearest integer value is *always* $n = 2$, providing strong evidence that the quinoxaline redox processes incorporate two electron transfers. This result is in agreement with previous literature which report two electron transfer behavior in aqueous electrolytes,[21–25] although only recent work by Aleksić et al. quantitates the process.[24] Thus, on this basis, we conclude that quinoxaline exhibits a two-electron transfer process during redox reactions, leading to a theoretical capacity of 410 mAh g^{-1}.

Table 3: Diffusion coefficients for quinoxaline (D_O) and for the reduced species (D_R) in the five promising electrolytes. Transfer coefficients (α) for the reduction (forward) reaction, are also given.

Electrolyte	pH	n	D_O (10^{-6} cm^2 s^{-1})	D_R (10^{-6} cm^2 s^{-1})	χ_O	χ_R
0.495 M K_2SO_4 / 0.01 M KOH	11.8	2.01 ± 0.12	5.7 ± 0.6	3.3 ± 0.1	1.35 ± .014	1.50 ± 0.12
0.45 M K_2SO_4 / 0.1 M KOH	12.9	2.14 ± 0.25	4.9 ± 1.3	2.7 ± 0.6	1.73 ± 0.30	1.72 ± 0.31
0.99 M KCl / 0.01 M KOH	11.8	1.93 ± 0.11	6.3 ± 0.7	3.1 ± 0.4	1.21 ± 0.48	1.32 ± 0.33
0.9 M KCl / 0.1 M KOH	12.9	2.21 ± 0.07	5.0 ± 0.2	2.9 ± 0.4	2.07 ± 0.05	1.83 ± 0.13
1 M KOH	13.7	2.05 ± 0.26	5.1 ± 1.4	2.4 ± 0.2	1.71 ± 0.83	1.58 ± 0.55

In each electrolyte, the diffusion coefficient of the oxidized species was greater (~1.7 – 2.1×) than the diffusion coefficient of the reduced species, in line with CV observations, where the oxidation peak is always wider and shorter than the reduction peak. The diffusion coefficient was also estimated using the Stokes-Einstein relationship and assuming the hydrodynamic radius (r_h) of quinoxaline was equivalent to the mean of its minor and major axes (r_h = 0.382 nm). This calculated diffusion coefficient (5.7×10^{-6} cm^2 s^{-1}) is in good agreement with the values in Table 3. As the generally accepted range of transfer coefficients is 0.3 to 0.7, the rate limiting kinetic step cannot be unambiguously identified from the obtained values of χ, thus further analysis is required to experimentally evaluate n' and α.

3.5 Estimated Solubility Limits

The estimated solubility limits of quinoxaline in each of these above electrolytes and DI H_2O are listed in Table 4. Electrolytes containing K_2SO_4 or only KOH were able to dissolve up to 0.5 M quinoxaline. In contrast, solutions containing KCl were able to dissolve up to 4.0 M quinoxaline, and DI H_2O was able to dissolve 4.5 M quinoxaline. The high solubility of quinoxaline in KCl-based electrolytes offers a pathway to redox electrolytes with high volumetric and gravimetric capacity which, in turn, may lead to energy dense RFBs.

Table 4: Diffusion coefficients for quinoxaline (D_O) and for the reduced species (D_R) in the five promising electrolytes. Transfer coefficients (α) for the reduction (forward) reaction, are also given.

Electrolyte	**pH**	**Solubility Limit (M)**
0.495 M K_2SO_4 / 0.01 M KOH	11.8	0.5†
0.45 M K_2SO_4 / 0.1 M KOH	12.9	0.5†
0.99 M KCl / 0.01 M KOH	11.8	4.0‡
0.9 M KCl / 0.1 M KOH	12.9	4.0‡
1 M KOH	13.7	0.5*
DI H_2O	6.4	4.5‡

†Three phase separation; ‡Bed of small crystals; *Dendritic precipitation of crystals.

The wide range of quinoxaline solubilities couples with three distinct quinoxaline precipitation behaviors upon solution saturation. Figure 7 shows photographs of electrolytes containing quinoxaline immediately before and after reaching the solubility limit. In 1 M KOH, only solid dendritic crystals were observed after solution saturation at the bottom of the vial. In electrolytes containing K_2SO_4, a three phase system consisting of solid dendritic crystals (bottom), an aqueous phase (middle), and an organic phase (top) were observed. Finally, in DI H_2O and electrolytes containing KCl, a bed of small dendritic crystal precipitates was observed throughout the liquid. These observations raise intriguing questions about the quinoxaline – supporting electrolyte interactions within the aqueous electrolytes and motivate further studies in the thermodynamics and solution equilibria of quinoxaline electrolytes; such topics will be addressed in a future publication. When comparing results in K_2SO_4 and KCl electrolytes, the pH and ionic strengths remained constant, but the solubility was 8× higher in KCl electrolytes. Thus we postulate that the dramatic solubility changes are caused by interactions between quinoxaline and the chloride anion, but the detailed mechanism is unclear

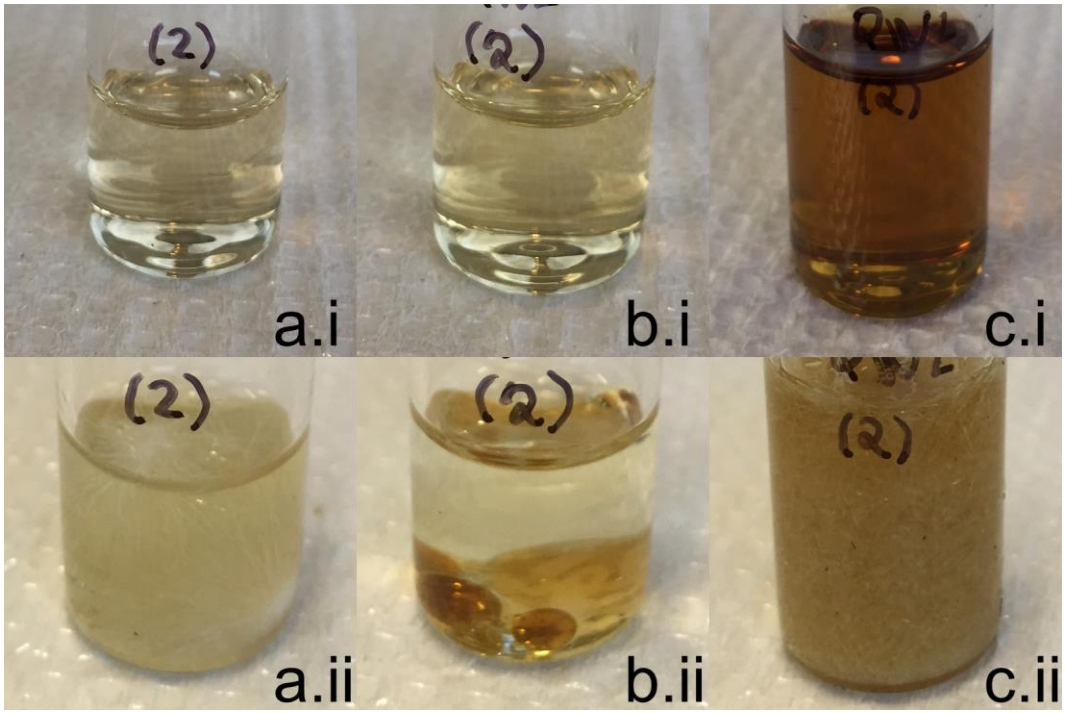

Figure 7: Representative photographs of quinoxaline solutions near the quinoxaline solubility limit. Row **i)** shows solutions just before the solubility limit. Row **ii)** shows solutions just after saturation. The solution compositions are: **a)** 1 M KOH, pH = 13.7; **b)** 0.45 M K_2SO_4 / 0.01 M KOH, pH = 11.8; **c)** 0.9 M KCl / 0.1 M KOH, pH = 12.9.

3.6 Discussion

Quinoxaline has been demonstrated in this study to undergo a single wave, two-electron redox process, where redox potential, stability, and reaction rates depend heavily on pH. This response contrasts reported quinoxaline behavior in non-aqueous electrolytes where quinoxaline reduction to a divalent anion occurs through two separate, one-electron reduction waves.[14,15,18,19,33] Further, the potentials at which these reactions occur differ significantly. Similar observations have been made for other electroactive aromatic hydrocarbons (i.e., quinones[34]) and the differences between electrochemical behavior in aqueous and non-aqueous electrolytes can broadly be attributed to changes in thermodynamics and redox mechanisms.

A recent DFT study calculated quinoxaline reduction potentials of $E_{red,1}$ = -1.49 V vs. SHE and $E_{red,2}$ = -2.04 V vs. SHE, for the first and second reduction waves, respectively.[35] These computed potentials are in good agreement with reported experimental values measured in non-aqueous electrolytes containing non-coordinating salts (e.g., acetonitrile with tetrabutylammonium hexafluorophosphate).[15,18,19] In contrast, the quinoxaline single wave redox potential in aqueous

electrolytes was found to be much higher and to depend on pH, where the redox potential ranges from E° = -0.78 V vs. SHE (in 1 M NaOH) to E° = -0.55 V vs. SHE (in 1 M $NaHCO_3$). We hypothesize that both the positive shift in redox potential and the merging of the two reduction waves can be attributed to hydrogen bonding effects within the aqueous electrolyte.[34]

The variation in redox potentials and improvement in (electro)chemical reversibility of quinoxaline with increasing pH in aqueous electrolytes indicates that reaction mechanisms are pH dependent. In lower pH electrolytes (pH ≤ 8.6), the measured redox potentials were $E^{\circ} \leq$ -0.19 V vs. RHE. These values (in acid and buffer) are in good agreement with literature.[24,25] In alkaline electrolytes, the redox potential was $E^{\circ} \approx$ -0.02 V vs. RHE, with slight variation depending on the electrolyte. First consider the unstable redox behavior in acidic electrolytes. Prior studies hypothesize that under acidic conditions, quinoxaline undergoes a coupled 2 e^- / 2 H^+ electrochemical reaction where quinoxaline reduces to 1,4-dihydroquinoxaline.[21–24] Prior work also notes that 1,4-dihydroquinoxaline can undergo a H^+ catalyzed chemical reaction to produce 1,4-dihydroquinalin-1-ium, followed by an additional electrochemical reaction to an disagreed upon quinoxaline derivative.[22–24] Furthermore, spontaneous chemically-driven protonation events have been observed when quinoxaline is dissolved in acidic solutions.[36] These degradation processes may explain the poor cycle stability observed in acidic electrolytes.

To further investigate quinoxaline redox mechanisms in alkaline electrolytes, a representative system was selected to demonstrate the CV dependence on pH. Figure 8 considers the K_2SO_4 / KOH electrolyte system, where the cation concentration was maintained at 1 M and the OH^- concentration was varied from 0 M to 1 M. Although only data for the K_2SO_4 / KOH electrolyte system is presented, similar trends were observed in all electrolyte systems except for buffering solutions. Figure 8a shows voltammograms of quinoxaline in 8 different K_2SO_4-based electrolytes, with varying pH, against the SHE. As detailed in the Results section, the increasing pH leads to a negative shift in the redox potential as well as improvements in electrochemical reversibility (reduced peak separation). Figure 8b plots the anodic peak potential ($E_{p,a}$), the cathodic peak potential ($E_{p,c}$) and the redox potential (E°) as a function of pH. These potentials show a weak dependence on pH from 5 < pH < 11 at which there is an inflection point and a transition to a linear decrease in potential as a function of pH for pH ≥ 11, which implies that the quinoxaline redox mechanism involves H^+. Similar results of pH dependent redox potentials for

quinoxaline derivatives were observed in buffered aqueous experiments[21,24,25] and in a study of quinoxaline voltammetry in DMF / water-mixed acidic media.[37]

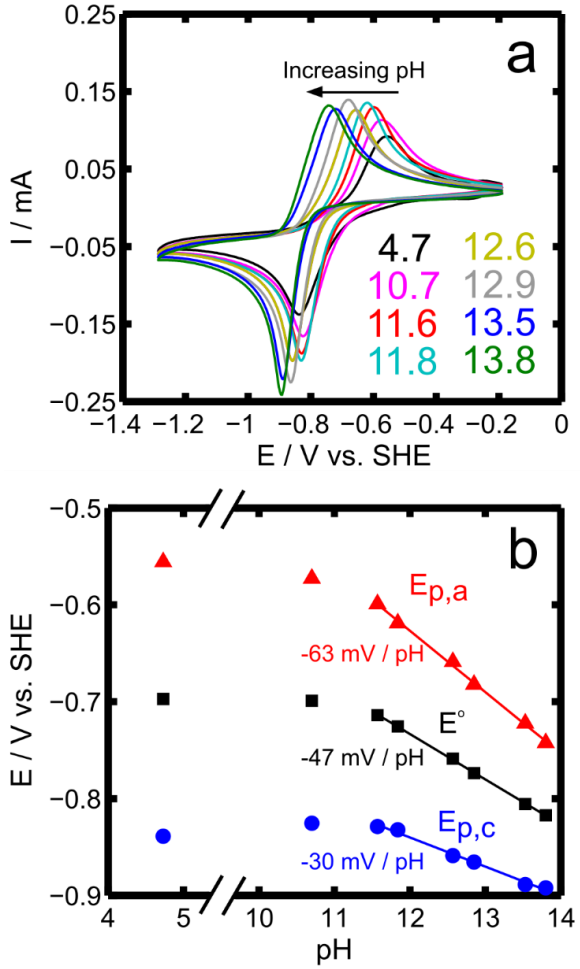

Figure 8: Some pH dependent CV characteristics (from cycle 2) for electrolytes containing K_2SO_4 and / or KOH: **a)** Quinoxaline CVs plotted against the SHE; **b)** cathodic peak potentials (● $E_{p,a}$), anodic peak potentials (▲ $E_{p,c}$), and redox potentials (■ E°).

Notably the cathodic peak potentials shift at a rate of -63 mV / pH, whereas the anodic peak potentials shift at a rate -30 mV / pH; the redox potential shifts as the mean (-47 mV / pH). Although the near-neutral regime (5 < pH < 10) was not directly probed in K_2SO_4-based electrolytes, the redox potential appears to be only weakly dependent on pH in this range suggesting a different redox mechanism. It has previously been described that for electrochemically irreversible cyclic voltammograms ($\Delta E_{pp} >> 59/n$) the peak potentials will shift according to Equation (4), where ΔE_p is the peak potential shift, K is the equilibrium constant, and m is the number of H^+ involved in the reaction.[26] Equation (4) holds in the limit of $[H^+] << K$,

while in the limit of $[H^+] >> K$, ΔE_p is approximately zero.[26] The transition between the plateau region ($\Delta E_p \sim 0$), and the linearly decreasing region occurs at the pKa of the molecule of interest.[26,34,38] Thus, the pH-dependent peak potential shifts can be reconciled, and a pKa of quinoxaline is estimated to be near 11.

$$\Delta E_p = -\frac{2.303RTm}{(n'+\alpha)F}\text{pH} + \frac{2.303RTm}{(n'+\alpha)F}\log_{10} K \quad (4)$$

The asymmetric potential shifts of the anodic and cathodic peaks indicate either a different rate limiting kinetic step between the reduction and oxidation reactions (different n'), asymmetric transfer coefficients (different α), or a combination of both. Prior studies have successfully correlated asymmetric pH-dependent potential shifts of anthraquinone to varying molecular structures of the reduced species.[38,39] While such results are desirable here, predicting reduced species structures from only the electrochemical data is difficult and spectroelectrochemical analysis is required. These studies are ongoing and will be reported in due course. However, at this point, we hypothesize that in alkaline electrolytes, quinoxaline will reduce to an equilibrium combination of protonated neutral species, monovalent anions, and divalent anions.[34]

3.7 Conclusions

The electrochemical behavior of quinoxaline in electrolytes spanning a wide range of cations (Li^+, Na^+, K^+), anions (Cl^-, NO_3^-, OH^-, SO_4^{2-}, HCO_3^-, $C_2H_3O_2^-$), and pH were investigated to determine the best conditions for the (electro)chemical reversibility. Quantitative analysis indicated that quinoxaline redox involved a single wave two-electron transfer process, resulting in a theoretical capacity of 410 mAh g^{-1}. More than 30 electrolytes were screened and several key trends were observed. First, solution pH has the strongest impact on quinoxaline electrochemical performance, lowering redox potentials, decreasing peak separation, and improving cycle stability. Quinoxaline was found to be stable on the CV time scale in nearly every electrolyte with at least 10 mM OH^- ($pH \geq 11.4$) by eliminating H^+ induced chemical degradation reactions. When stable the redox potential shifts linearly with pH ($E^\circ \approx -0.02$ V vs. RHE) due to low H^+ concentration relative to the reaction equilibrium constant (Equation (4)). Second, although non-buffering anions did not affect electrochemical performance, quinoxaline solubilities were found to vary by nearly an order of magnitude when switching from the SO_4^{2-} to the Cl^- anion. Quinoxaline solubility in KCl-based electrolytes were found to be as high as 4 M. Third, cations were found to have a negligible effect

on CV behavior. The combination of high gravimetric capacity, high solubility, and low redox potential makes quinoxaline a promising material for application in an aqueous RFB.

3.8 References

1. J. B. Conant, H. M. Kahn, L. F. Fieser, and S. S. Kurtz Jr, *J. Am. Chem. Soc.*, **44**, 1382–1396 (1922).
2. L. F. Fieser, *J. Am. Chem. Soc.*, **50**, 439–465 (1928).
3. P. S. Guin, S. Das, and P. C. Mandal, *Int. J. Electrochem.*, **2011**, 1–22 (2011).
4. J. Q. Chambers, in *Quinonoid Compounds (1974)*, S. Patai, Editor, p. 737–791, John Wiley & Sons, Ltd. (1974).
5. S. I. Bailey and I. M. Ritchie, *Electrochimica Acta*, **30**, 3–12 (1985).
6. G. P. Moss, P. A. S. Smith, and D. Tavernier, *Pure Appl. Chem.*, **67**, 1307–1375 (1995).
7. Y. Xu, Y.-H. Wen, J. Cheng, G.-P. Cao, and Y.-S. Yang, *Electrochimica Acta*, **55**, 715–720 (2010).
8. B. Huskinson et al., *Nature*, **505**, 195–198 (2014).
9. B. Yang, L. Hoober-Burkhardt, F. Wang, G. S. Prakash, and S. R. Narayanan, *J. Electrochem. Soc.*, **161**, A1371–A1380 (2014).
10. M. Wang et al., *Nat. Chem.*, **2**, 385–9 (2010).
11. D. W. Chang et al., *Org. Lett.*, **13**, 3880–3883 (2011).
12. J.-Y. Lee, W.-S. Shin, J.-R. Haw, and D.-K. Moon, *J. Mater. Chem.*, **19**, 4938–4945 (2009).
13. T. Matsunaga, T. Kubota, T. Sugimoto, and M. Satoh, *Chem. Lett.*, **40**, 750–752 (2011).
14. F. R. Brushett, J. T. Vaughey, and A. N. Jansen, *Adv. Energy Mater.*, **2**, 1390–1396 (2012).
15. D. van der Meer and D. Feil, *Recl. Trav. Chim. Pays-Bas*, **87**, 746–754 (1968).
16. D. van der Meer, *Recl. Trav. Chim. Pays-Bas*, **88**, 1361–1372 (1969).
17. D. van der Meer, *Recl. Trav. Chim. Pays-Bas*, **89**, 51–67 (1970).
18. K. R. Barqawi and M. A. Atfah, *Electrochimica Acta*, **32**, 597–599 (1987).
19. J. R. Ames, M. A. Houghtaling, and D. L. Terrain, *Electrochimica Acta*, **37**, 1433–1436 (1992).
20. N. F. Yan, G. R. Li, and X. P. Gao, *J. Electrochem. Soc.*, **161**, A736–A741 (2014).
21. M. P. Strier and J. C. Cavagnol, *J. Am. Chem. Soc.*, **79**, 4331–4335 (1957).
22. O. Fischer and T. H. Thuy, *Collect. Czechoslov. Chem. Commun.*, **41**, 1853–1859 (1976).
23. G. W. H. Cheeseman and R. F. Cookson, *The Chemistry of Heterocyclic Compounds*, p. 7-16, John Wiley & Sons, New York, (1979).
24. M. Aleksic, J. Pantic, and V. Kapetanovic, *Facta Univ. - Ser. Phys. Chem. Technol.*, **12**, 55–63 (2014).
25. M. Takagi and S. Ono, *Bull. Univ. Osaka Prefect. Ser. B Agric. Biol.*, **21**, 77–122 (1969).
26. R. G. Compton and C. E. Banks, *Understanding Voltammetry*, 2nd ed., p. 119-126, Imperial College Press, London, (2011).
27. A. J. Bard and L. R. Faulkner, *Eletrochemical Methods: Fundamentals and Applications*, John Wiley & Sons, Inc., Danvers, (2001).
28. I. D. Zaytsev and G. G. Aseyev, *Properties of Aqueous Solutions of Electrolytes*, 1st ed., p. 7-299, CRC Press, Inc., Boca Raton, (1992).
29. M. Doyle, M. E. Lewittes, M. G. Roelofs, S. A. Perusich, and R. E. Lowrey, *J. Membr. Sci.*, **184**, 257–273 (2001).
30. S. Koter, P. Piotrowski, and J. Kerres, *J. Membr. Sci.*, **153**, 83–90 (1999).

31. H. Matsuda and Y. Ayabe, *Z. Für Elektrochem. Berichte Bunsenges. Für Phys. Chem.*, **6**, 494–503 (1955).
32. R. Zahn, G. Coullerez, J. Vörös, and T. Zambelli, *J. Mater. Chem.*, **22**, 11073–11078 (2012).
33. E. V. Carino et al., *RSC Adv*, **5**, 18822–18831 (2015).
34. M. Quan, D. Sanchez, M. F. Wasylkiw, and D. K. Smith, *J. Am. Chem. Soc.*, **129**, 12847–12856 (2007).
35. R. S. Assary, F. R. Brushett, and L. A. Curtiss, *RSC Adv*, **4**, 57442–57451 (2014).
36. S. M. Beck and L. E. Brus, *J. Chem. Phys.*, **75**, 4934–4940 (1981).
37. R. Wang et al., *J. Electroanal. Chem.*, **567**, 85–94 (2004).
38. C. Batchelor-McAuley, Q. Li, S. M. Dapin, and R. G. Compton, *J. Phys. Chem. B*, **114**, 4094–4100 (2010).
39. P. He, R. M. Crooks, and L. R. Faulkner, *J. Phys. Chem.*, **94**, 1135–1141 (1990).

4. Experimental investigation of multi-electron transfer, common ion exchange non-aqueous redox flow batteries

This chapter is reprinted from *Journal of Power Sources*, Vol 327, S. M. Laramie, J. D. Milshtein, T. M. Breault, F. R. Brushett, L. T. Thompson, Performance and cost characteristics of multi-electron transfer, common ion exchange non-aqueous redox flow batteries, 681–692, Copyright (2016), with permission from Elsevier under license number 4087101511322.

4.1 Introduction

Recent efforts to increase the energy density and decrease the cost of NAqRFBs have focused on improving active species solubility via molecular modifications[1–3] and developing active species with low molecular weights.[4,5] The development of common ion exchange systems is an additional consideration that will aid in designing economically viable NAqRFBs. In a common ion exchange NAqRFB, both active species have charges of the same sign, either positive or negative, and as a result, only a single ion of the supporting salt migrates across the separator as a charge carrier. Equations (1) and (2) show the full cell reactions for cation and anion exchange systems, respectively.

$$A^{n+} + B^{(n+1)+} \leftrightarrow A^{(n+1)+} + B^{n+} \quad (1)$$

$$A^{(n+1)-} + B^{n-} \leftrightarrow A^{n-} + B^{(n+1)-} \quad (2)$$

In both cases, A is the positive redox active compound, B is the negative redox active compound, and *n* is an integer greater than or equal to zero. Utilizing active species with similar charges eliminates the salt splitting that occurs in non-common ion exchange systems. Figure 1a schematically illustrates salt splitting RFB redox reactions. Note that to maintain bulk electroneutrality, supporting salt anions migrate to the positive electrolyte (posolyte), and supporting salt cations migrate to the negative electrolyte (negolyte). In this configuration, the supporting salt ions are critical reactants in the redox processes and could limit RFB capacity.

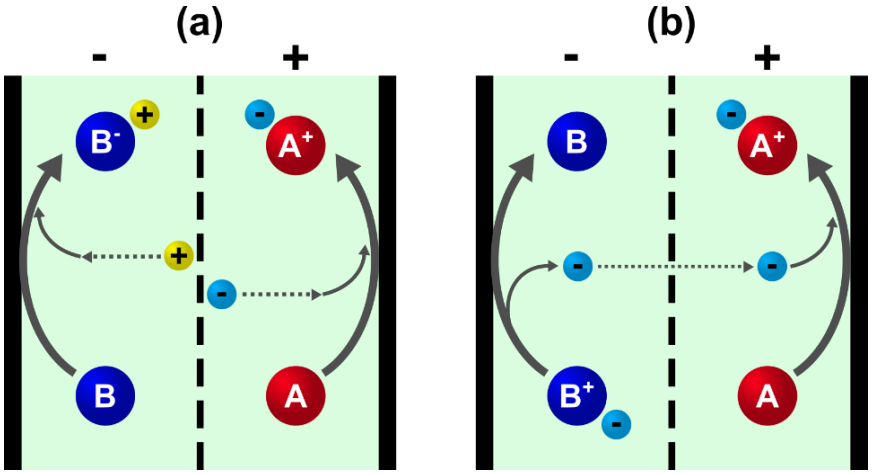

Figure 1: Schematic comparison of charging processes in (a) a salt splitting RFB and (b) a common anion exchange RFB. A is the posolyte active material (red), and B is the negolyte active material (dark blue). Supporting salt cations are denoted by "+" (yellow), and supporting salt anions are denoted by "-" (light blue).

Figure 1b illustrates common anion exchange redox events, where only supporting salt anions carry charge across the membrane or separator. This configuration resembles a "rocking chair" lithium ion battery.[6] From an economic perspective, common ion exchange systems are advantageous as they reduce the required amount of expensive supporting salt ($\geq$ \$20 kg^{-1} for NAqRFBs[7–9]). For a salt splitting configuration, the electrolyte must dissolve enough supporting salt to maintain bulk electroneutrality in the presence of the charged active species (Figure 1a). In contrast, for the common ion exchange configuration, the salt only serves to enhance electrolyte conductivity. High concentrations of salt can limit the solubility of the active species in the electrolyte solution[10,11] and suppress the conductivity of ion selective membranes, subsequently increasing the area specific resistance (ASR).[12] Overall, common ion exchange enables higher active species concentrations, increasing electrolyte energy density, and minimizing the use of expensive NAq solvents.

To date, many reported NAqRFBs employ a salt splitting configuration.[13–16] A notable example is the vanadium acetylacetonate ($V(acac)_3$) NAqRFB, where, upon charging, an anion is formed in the negolyte ($V(acac)_3^-$), while a cation is generated in the posolyte ($V(acac)_3^+$).[10] Some studies report the use of common ion exchange for NAqRFBs, but do not contemplate the cost and performance benefits of employing this configuration. The majority of these prior reports describe symmetric common anion exchange systems utilizing tris-bipyridine metal coordination complexes, including chromium, iron, and ruthenium tris-bipyridines.[17–19] A few asymmetric

anion exchange systems utilized two tris-bipyridine complexes with different metal centers.[20–22] A vanadium dithiolate complex was the focus of the only symmetric common cation exchange system.[23] Of these, only one report demonstrated a $2e^-$ transfer system, which utilized a $Cr(bpy)_3$ derivative in a symmetric, $2e^-$ H-cell, but that study did not cycle the active species in a full flow cell.[19]

This paper is the first to purposefully design and demonstrate the benefits of common ion exchange NAqRFBs. Iron (II) tris(2,2'-bypridine) tetrafluoroborate ($Fe(bpy)_3(BF_4)_2$) and ferrocenylmethyl dimethyl ethyl ammonium tetrafluoroborate ($Fc1N112\text{-}BF_4$) serve as model active species (Figure 2), and are examined via a progression of electrochemical techniques. First, cyclic voltammetry (CV) and bulk electrolysis of both the individual species and the mixture highlight the compatibility and stability of each redox event. Small volume H-type cells with reference electrodes evaluate cell performance while confirming that the cell accesses the desired redox events. As a final analysis, flow cell studies demonstrate the practicality of common ion exchange RFBs, as well as the complexity of multi-electron transfer systems. Flow cell cycling experiments characterize both the one electron ($1e^-$) and, for the first time, two electron ($2e^-$) variations of the $Fe(bpy)_3(BF_4)_2$/$Fc1N112\text{-}BF_4$ system. A techno-economic model quantifies the financial benefits of common ion exchange systems. Taken as a whole, this work develops an extensive compatibility analysis of asymmetric NAqRFB chemistries. The systematic approach and suite of electrochemical techniques utilized here can apply to other promising active species, including organics, metal coordination complexes (MCCs), and mixed MCC/organic systems, enabling asymmetric NAqRFBs that approach the DOE price target.

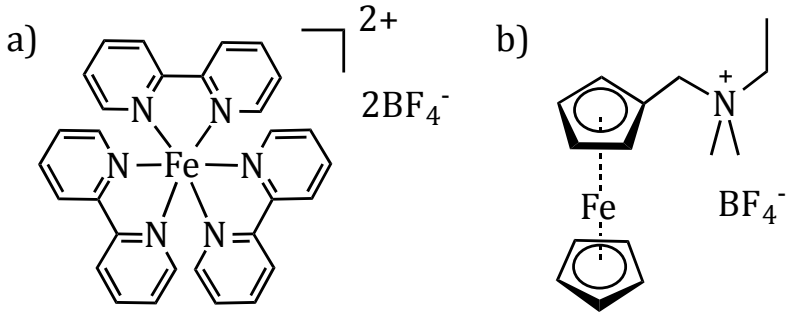

Figure 2: Structures of **(a)** $Fe(bpy)_3(BF_4)_2$ and **(b)** $Fc1N112\text{-}BF_4$.

4.2 Experimental

Synthesis and Materials. All reagents and starting materials (iron(II) tetrafluoroborate hexahydrate (97%), (dimethylaminomethyl)ferrocene (96%), bromoethane (98%), sodium tetrafluoroborate

(98%)) for active species synthesis were purchased from Sigma-Aldrich, with the exception of 2,2'-bipyridine (98%, Alfa Aesar). All synthesis materials were used as received. $Fe(bpy)_3(BF_4)_2$ was prepared according to a literature procedure.[24] Fc1N112-BF_4 was synthesized through a bromide salt intermediate also as reported in literature.[25] Ion exchange of Br^- with BF_4^- was performed in deionized water to afford the final product. All electrochemical experiments were performed in acetonitrile (MeCN, 99.9%, Acros Organics), which was stored over molecular sieves to remove any residual water. Electrochemical grade tetrabutylammonium tetrafluoroborate ($TBABF_4$, 99%, Sigma Aldrich) was dried under vacuum at 80°C overnight before use. Fritted Ag/Ag^+ quasi-reference electrodes (BASi) filled with 0.01 M silver tetrafluoroborate (98%, Sigma Aldrich) in MeCN were used. All solution preparation and electrochemical measurements were performed inside argon filled glove boxes (O_2 < 5 ppm, H_2O < 1 ppm). Daramic 175 microporous separator, with a thickness of 175 µm, porosity of 58%, and average pore size of 100 nm, was employed as received during battery cycling experiments.

Solubility Measurements. Active material solubility measurements were performed using a UV-Vis method[1] in both pure solvent and in the presence of supporting salt. First, stock solutions of $Fe(bpy)_3(BF_4)_2$ or Fc1N112-BF_4 were prepared at known concentrations in MeCN. Five-point calibration curves of characteristic absorbance peaks as a function of active species concentration were established. The individual active species were added in excess to pure MeCN or 0.5 M $TBABF_4$/MeCN to generate solutions saturated with the active material. The saturated solutions were centrifuged at 6000 rpm for 5 min. The supernatant was diluted with MeCN or 0.5 M $TBABF_4$/MeCN to within the range of the absorption calibration curve, and the absorption of the diluted solution was measured using UV-Vis (Figure 3). Given the difficulty of measuring solubility in ternary electrolytes, it was assumed that $TBABF_4$ did not precipitate out of solution due to the high solubility limit of $TBABF_4$ in MeCN (> 3 M).[26]

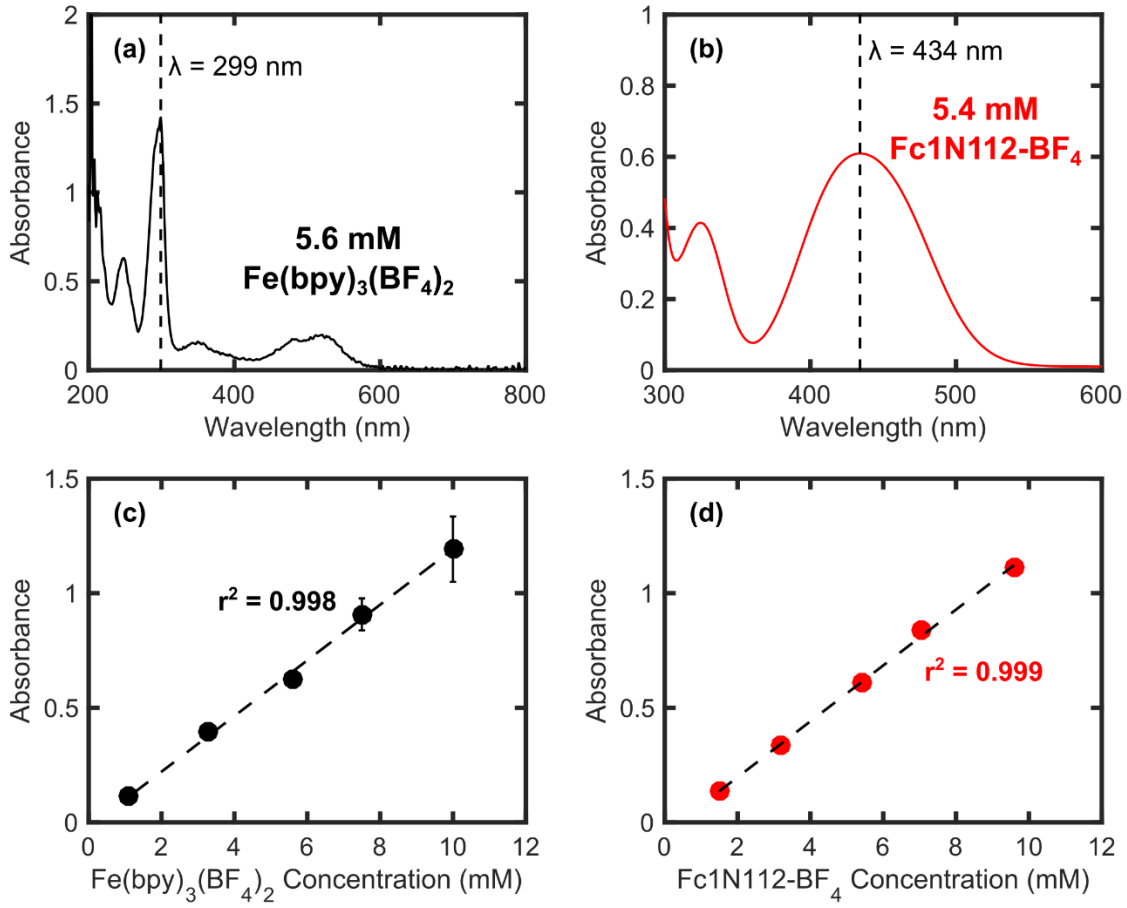

Figure 3: Example UV-Vis spectra at ~5.5 mM active species for **(a)** $Fe(bpy)_3(BF_4)_2$ and **(b)** Fc1N112-BF_4, as well as calibration curves utilized in solubility measurements for **(c)** $Fe(bpy)_3(BF_4)_2$ and **(d)** Fc1N112-BF_4. Characteristic wavelengths (λ) to build the calibration curves were 299 nm and 434 nm for $Fe(bpy)_3(BF_4)_2$ and Fc1N112-BF_4, respectively. Most error bars on calibration curves are too small to see given the y-axis scales, and error bars were calculated from the standard deviation of three data points.

Cyclic Voltammetry. Cyclic voltammetry was performed using an Autolab PGSTAT100 potentiostat. CVs were recorded at a scan rate of 100 mV s^{-1} in a custom 10 mL three electrode electrochemical cell with a 3 mm diameter glassy carbon (GC) working electrode (BASi), a coiled platinum (Pt) wire counter, and Ag/Ag^+ quasi-reference electrode. All solutions contained 0.5 M $TBABF_4$/MeCN with either 5 mM of the individual active species or an equi-molar mixture containing 5 mM of both $Fe(bpy)_3(BF_4)_2$ and Fc1N112-BF_4 (10 mM total). A background CV of the supporting electrolyte without any active species is available in Figure 4.

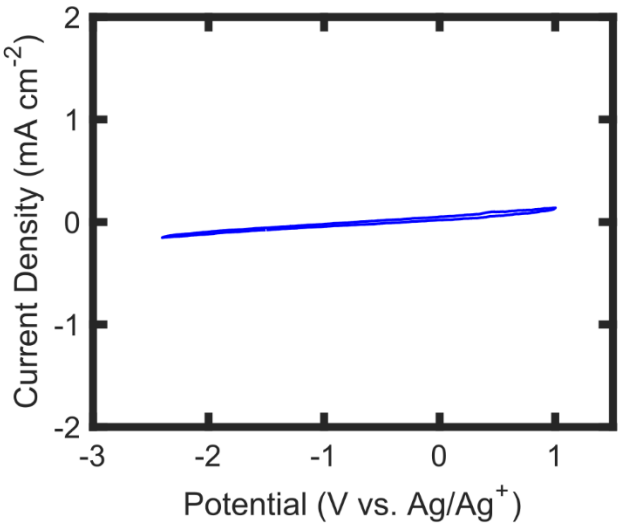

Figure 4: Background CV scan of the blank electrolyte containing no active species. The solution composition was 0.5 M $TBABF_4$ / MeCN. The current density (j) magnitude across the potential range of interest is $|j| \leq 0.154$ mA cm^{-2}.

Bulk Electrolysis. Bulk electrolysis experiments were performed in a custom glass H-type cell (Figure 5) comprised of two 5 mL chambers separated with an ultra-fine glass frit (P5, Adams and Chittenden) to minimize crossover. Both chambers were stirred continuously during cycling. Reticulated vitreous carbon (100 PPI, Duocell) was used as the working electrode with a Pt coil counter electrode and Ag/Ag^+ quasi-reference electrode. An Autolab PGSTAT100 potentiostat was used to apply a constant current, 1.32 mA, which is equivalent to a C-rate of 2C. Potential cutoffs and a 100% SOC coulombic cut-off were used during cycling. A 3 mm diameter GC working electrode (BASi) was used to record CVs before and during cycling. Solutions of 5 mM active species in 0.5 M $TBABF_4$/MeCN were used for the single species experiments and for the mixed species tests; 5 mM of both active species (10 mM total) were dissolved in 0.5 M $TBABF_4$/MeCN.

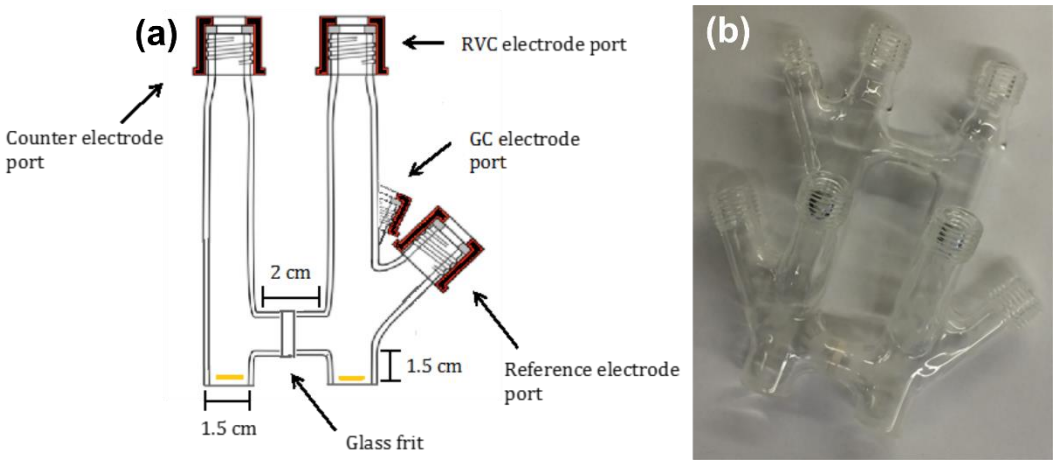

Figure 5: **(a)** Schematic of the custom bulk electrolysis cell including relevant ports and dimensions. **(b)** Photograph of the bulk electrolysis cell.

H-Cell Cycling. Glass H-type cells (Adams and Chittenden) requiring 5 mL of solution in each chamber, with an inter-electrode distance of 5 cm, were used for the H-cell experiments. Graphite electrodes (3.6 cm^2, iso-molded, ground finish, Graphite Store) were heat treated at 500°C for 5 h under argon before use. Quasi-reference electrodes were inserted into the posolyte and negolyte chambers to monitor the potential of each half-cell during cycling. Daramic 175 (1.3 cm^2) was employed as the separator. To reduce crossover, two layers were stacked together in the cell. Cycling experiments were performed using a Maccor 4000 Series Battery Tester at a constant C-rate of C/2 (0.95 mA cm^{-2}) to 100% SOC, with negolyte and posolyte cutoffs based on CV potentials. All cells used a solution of 0.5 M $TBABF_4$/MeCN with 50 mM of both $Fe(bpy)_3(BF_4)_2$ and Fc1N112-BF_4 as the negolyte and posolyte.

Flow Cell Cycling. Custom cells with flow through electrodes (Figure 6), similar to those employed by Wei et al.[3,27], were used for flow cell cycling experiments. The flow channels and current collectors were machined from type 316 stainless steel. Electrodes were cut from 6 mm thick carbon felt (GFA6, SGL Group) and compressed by 12.4% in the assembled flow cell, providing a geometric active area of 4.63 cm^2. Two layers of Daramic 175 separator were stacked together to serve as the battery separator. Teflon gaskets sealed the separator into the cell. All flow cells were initially assembled outside the glove box, and were then dried under vacuum (-91 kPa_g) at room temperature for at least 1 h before beginning flow cell experiments.

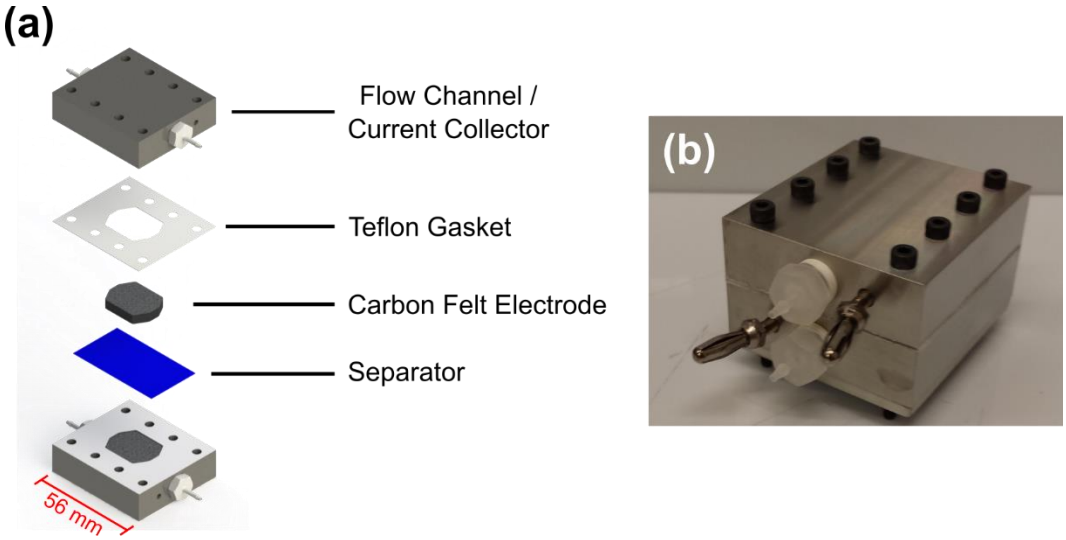

Figure 6: **(a)** Exploded view schematic of the flow cell employed in this study. Hardware (i.e. nuts, bolts, washers, banana plugs) is not included in the schematic. **(b)** Photograph of the flow cell employed in this study.

Glass scintillation vials were filled with electrolyte, which was carried into the flow cell at 20 mL min^{-1} using a peristaltic pump (Masterflex L/S series) with Tygon tubing (Saint-Gobain, 1.6 mm inner diameter). Galvanostatic cycling experiments were performed using a Biologic-VMP3 potentiostat at a constant current density of 5 mA cm^{-2} (23.2 mA). Electrolytes were comprised of 0.1 M $Fe(bpy)_3(BF_4)_2$/0.1 M Fc1N112-BF_4/0.5 M $TBABF_4$/MeCN. 10 mL of electrolyte was added to each of the two flow cell reservoirs. During the cycling experiments, cell potential cutoffs were 1.0 – 2.01 V and 1.0 – 2.45 V for the 1e- and $2e^-$ cells, respectively. Upper voltage cutoffs were selected to eliminate accessing undesired electrochemical reactions, while lower voltage cutoffs were selected to ensure complete discharge of the cells.

4.3 Active Species and Separator Selection

Several criteria aid the selection of electrochemical couples for the common ion exchange NAqRFB. The first, and most important, criterion is to exhibit multiple electron transfers, which should result in significant energy density gains. Second, the active species have to be soluble and stable in the same solvent at all relevant oxidation states. Third, the active species need to be commercially available or easy to synthesize in large quantities, facilitating use in a lab-scale flow cell. Based on these considerations, $Fe(bpy)_3(BF_4)_2$ was selected as the low potential active material and Fc1N112-BF_4 as the high potential active material. $Fe(bpy)_3(BF_4)_2$ exhibits four redox events[28] and has moderate solubility in MeCN. Although $Fe(bpy)_3(BF_4)_2$ undergoes relatively

quick capacity fade, this active material is one of only a few rigorously characterized cationic negolyte NAqRFB species,[18] and thus is suitable for the demonstration of a common ion cell over relatively short cycling experiments. The redox active $Fc1N112^+$ cation is an attractive posolyte material due to its electrochemical stability and high solubility.[3,25] This study pairs the $Fc1N112^+$ cation with a BF_4^- anion to achieve common ion exchange.[25] Designing an asymmetric system enables independent selection of the negolyte and posolyte materials to achieve desirable properties for both sides. Due to the limited selectivity of available NAqRFB membranes and separators[12,29], active species mixing in an asymmetric NAqRFB is presently unavoidable. Imminent active species crossover motivated our active species compatibility studies. Further, anion exchange membranes exhibit limited stability in non-aqueous solvents.[20,29] Thus, full cells (H-cell and flow) in this study employ a stable Daramic separator to minimize interactions between the separator and the active species and eliminate separator degradation as a performance decay mechanism.

4.4 Solubility

As previously mentioned, a key advantage associated with common ion exchange NAqRFBs is the ability to minimize the quantity of supporting salt required for RFB operation. Minimizing the salt content enables reduced solvent costs (Section 3.5) and higher active materials concentrations, which can subsequently decrease concentration (mass transport) and activation (kinetic) polarization losses.[30] Shinkle et al. reported that the solubility of V(acac)3 in MeCN decreased monotonically with increased concentration of tetraethylammonium tetrafluoroborate in the ternary electrolyte.[10] To quantify the dual-solute effects for the Fe(bpy)3(BF4)2/Fc1N112-BF4 chemistries, a UV-Vis absorbance study demonstrates the effect of supporting salt concentration on active material solubilities. This methodology does not map the entire chemical space, but does demonstrate the utility of minimizing supporting salt content to maximize active species solubility. Fc1N112-BF4/TBABF4/MeCN and Fe(bpy)3(BF4)2/TBABF4/MeCN are the ternary electrolytes of interest. Table 1 displays the solubilities of Fe(bpy)3(BF4)2 and Fc1N112-BF4 in MeCN with either 0 M or ~0.5 M supporting salt. The solubilities of both active materials decrease significantly (50% for Fe(bpy)3(BF4)2 and 27% for Fc1N112-BF4) with ~0.5 M TBABF4 in solution. For application in a commercial asymmetric RFB system, identifying the active material solubilities in the quaternary $Fe(bpy)_3(BF_4)_2$/Fc1N112-BF_4/$TBABF_4$/MeCN mixed electrolyte system would

be crucial to avoid active material precipitation. Nonetheless, this preliminary solubility study demonstrates that by implementing a common ion exchange NAqRFB configuration, the concentration of supporting salt can vary independently from the active material concentration to optimize active material solubility and electrolyte conductivity.

Table 1: Active species solubilities with and without supporting salt in MeCN.

Active Material	**$TBABF_4$ Concentration (M)**	**Active Species Solubility (M)**
$Fe(bpy)_3(BF_4)_2$	0	0.6
$Fe(bpy)_3(BF_4)_2$	~0.5	0.3
Fc1N112-BF_4	0	1.9
Fc1N112-BF_4	~0.5	1.4

To enable cost-effective NAqRFBs, electrolytes must exhibit sufficiently high energy density to offset additional system costs (e.g. chemicals, balance of plant). Increasing the solubility per accessed electron or cell potential can deliver higher energy densities, and as illustrated in Table 1, common ion cell configurations facilitate the former approach. Darling et al. suggested that for NAqRFBs to achieve a \$150 kWh^{-1} system price, including installation and invertor costs, the solubility per accessed electron must be 4 – 5 M.[7] For a $1e^-$ transfer NAqRFB, this requirement implies a minimum solubility of 4 – 5 M. Since the electrolyte would require an additional 4 – 5 M supporting salt, the total concentration of active species and supporting salt would be 8 – 10 M. Most nonaqueous solvents (e.g. MeCN, propylene carbonate, dimethoxyethane) cannot achieve such high solute concentrations without significantly increasing temperature or employing ionic liquid solvents. Ionic liquids would afford charge balance, but can cost 5 – 20 times more than molecular solvents.[31] A high concentration salt splitting NAqRFB employing molten organic redox active compounds with dissolved salt[32,33] or deep eutectic electroactive melts[34,35] may be possible but, with limited reports, the feasibility of these systems remains relatively unexplored. For near term NAqRFB prototypes, a common ion configuration will enable low cost electrolytes and energy dense batteries.

4.5 Cyclic Voltammetry

Cyclic voltammetry (CV) provides an initial assessment of the electrochemical compatibility of the various active species and supporting electrolyte on a short time scale. Figure 7 shows CVs of

both the individual species and an equi-molar mixture. $Fe(bpy)_3(BF_4)_2$ demonstrates four quasi-reversible redox couples (-2.08, -1.85, -1.65, and 0.74 V vs. Ag/Ag^+) with the single positive redox event (V) associated with the Fe^{II}/Fe^{III} transition and the three negative couples (I, II, III) corresponding to ligand-based processes.[36] Fc1N112-BF_4 exhibits a single redox couple (IV) at 0.28 V vs. Ag/Ag^+, with no other redox activity within the potential window where $Fe(bpy)_3(BF_4)_2$ is active. The redox potentials of the five electron transfer events agree with previous literature reports.[3,22,25] The CV of the mixture is essentially a combination of those for the individual species, indicating that these materials are chemically and electrochemically compatible, at least for the time scales of this CV experiment.

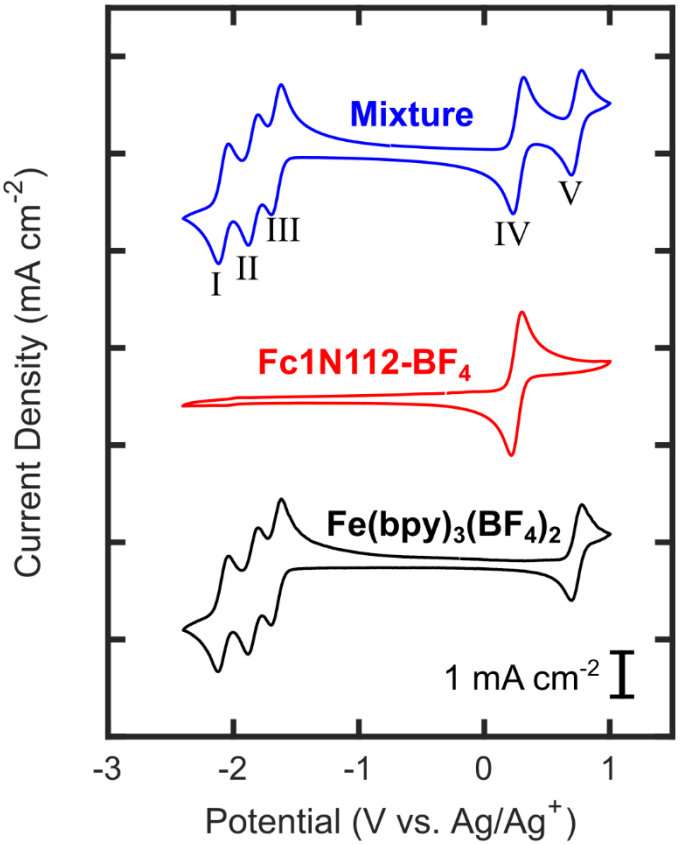

Figure 7: CV of $Fe(bpy)_3(BF_4)_2$ (black), Fc1N112-BF_4 (red), and an equi-molar mixture of both (blue).

Pairing couple III of $Fe(bpy)_3(BF_4)_2$ with Fc1N112-BF_4 (IV) produces a $1e^-$, 1.92 V cell. This cell offers an increased cell potential over several aqueous systems, but NAqRFBs will require even higher voltages ($\geq$ 3 V) for economic feasibility.[7] One of the most promising strategies to increase the energy density of NAqRFBs is to utilize multiple electron transfers. For this system,

pairing two of the negative couples of $Fe(bpy)_3(BF_4)_2$ (II and III) with the positive couples of both Fc1N112-BF_4 and $Fe(bpy)_3(BF_4)_2$ (IV and V) results in a $2e^-$ transfer cell. The use of Fc1N112-BF_4 provides the additional capacity required on the posolyte side to afford a multi-electron transfer cell. This eliminates the need to double the concentration of the posolyte material, which would be necessary if employing only a single positive couple.[20,22] Additionally, the positive redox couples are easily distinguishable, aiding in visualization of charge/discharge events. The average cell potential for this $2e^-$ system is 2.25 V, which when coupled with the use of multiple redox events, provides a cell with more than twice the theoretical energy density of the analogous single electron system.

4.6 Bulk Electrolysis

Bulk electrolysis experiments were used to further characterize the electrochemical compatibility of $Fe(bpy)_3(BF_4)_2$ and Fc1N112-BF_4, and to assess the feasibility of employing these species in an asymmetric flow cell. Cycling experiments on each individual component first establish the baseline stability and then cycling a mixture of the two species helps identify any interactions between $Fe(bpy)_3(BF_4)_2$ and Fc1N112-BF_4.

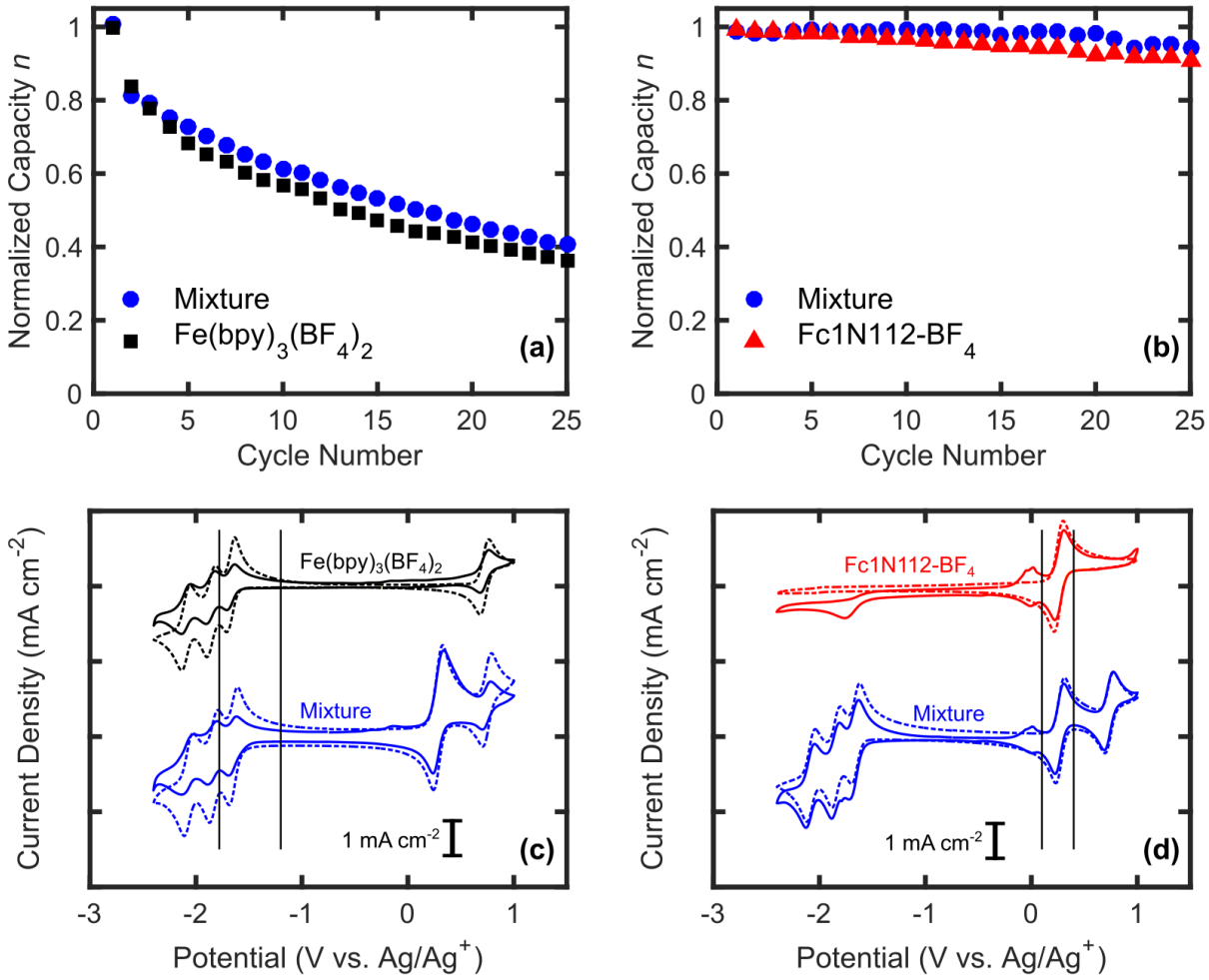

Figure 8: Capacity retention measured by bulk electrolysis for $Fe(bpy)_3(BF_4)_2$ (black), $Fc1N112\text{-}BF_4$ (red), and an equi-molar mixture of $Fe(bpy)_3(BF_4)_2$/$Fc1N112\text{-}BF_4$ (blue) through (a) a single negative e^- and (b) a single positive e^-. (c, d) CVs before (dashed) and after cycling (solid) are shown for each case, with the black vertical lines denoting the potential cutoffs used during cycling.

Figure 8 displays capacity retention plots and CVs for the $1e^-$ system (III and IV). Through a single negative electron transfer (III), $Fe(bpy)_3(BF_4)_2$ shows significant capacity fade (Figure 8a), in agreement with previous reports.[18] Examination of the CV after cycling (Figure 8c) reveals a decrease in peak heights for all couples associated with $Fe(bpy)_3(BF_4)_2$, supporting the observed capacity fade. No new redox processes arise, suggesting that the reaction byproducts are either electrochemically inactive within the potential window of interest or insoluble in the electrolyte solution. A comparison with the mixture, cycled under identical conditions, reveals near identical capacity fade and similar degradation (indicated by CV), suggesting minimal interactions between the active species; the majority of the capacity fade arises from $Fe(bpy)_3(BF_4)_2$ instability. The $Fc1N112\text{-}BF_4$ couple does lose some peak intensity, indicating minor interactions with the

$Fe(bpy)_3(BF_4)_2$, however, this couple does not play a role in the negolyte cell chemistry and should have minimal effect on cell performance. Analysis of the single positive couple of Fc1N112-BF_4 (IV) reveals highly stable cycling behavior (Figure 8b), as expected based on previous reports. [3] CVs after cycling (Figure 8d) show a minimal decrease in peak height for the Fc1N112-BF_4, which correlates with the observed capacity fade. For both the single species and the mixture, electrochemically active degradation products are observed at 0 and -1.7 V vs. Ag/Ag^+. These peaks could be due to detachment of the pendant ionic group from Fc1N112-BF_4 as the peak at 0 V vs. Ag/Ag^+ matches the redox potential of ferrocene.[37] No substantial changes are observed for the peaks associated with $Fe(bpy)_3(BF_4)_2$. In all cases, the potential curves (Figure 9) match the potentials expected based on the initial CV. Taken as a whole, the near identical capacity fade and degradation products observed after cycling for both the single active species and the mixture establish that Fc1N112-BF_4 and $Fe(bpy)_3(BF_4)_2$ are compatible chemistries for use in a $1e^-$ asymmetric NAqRFB.

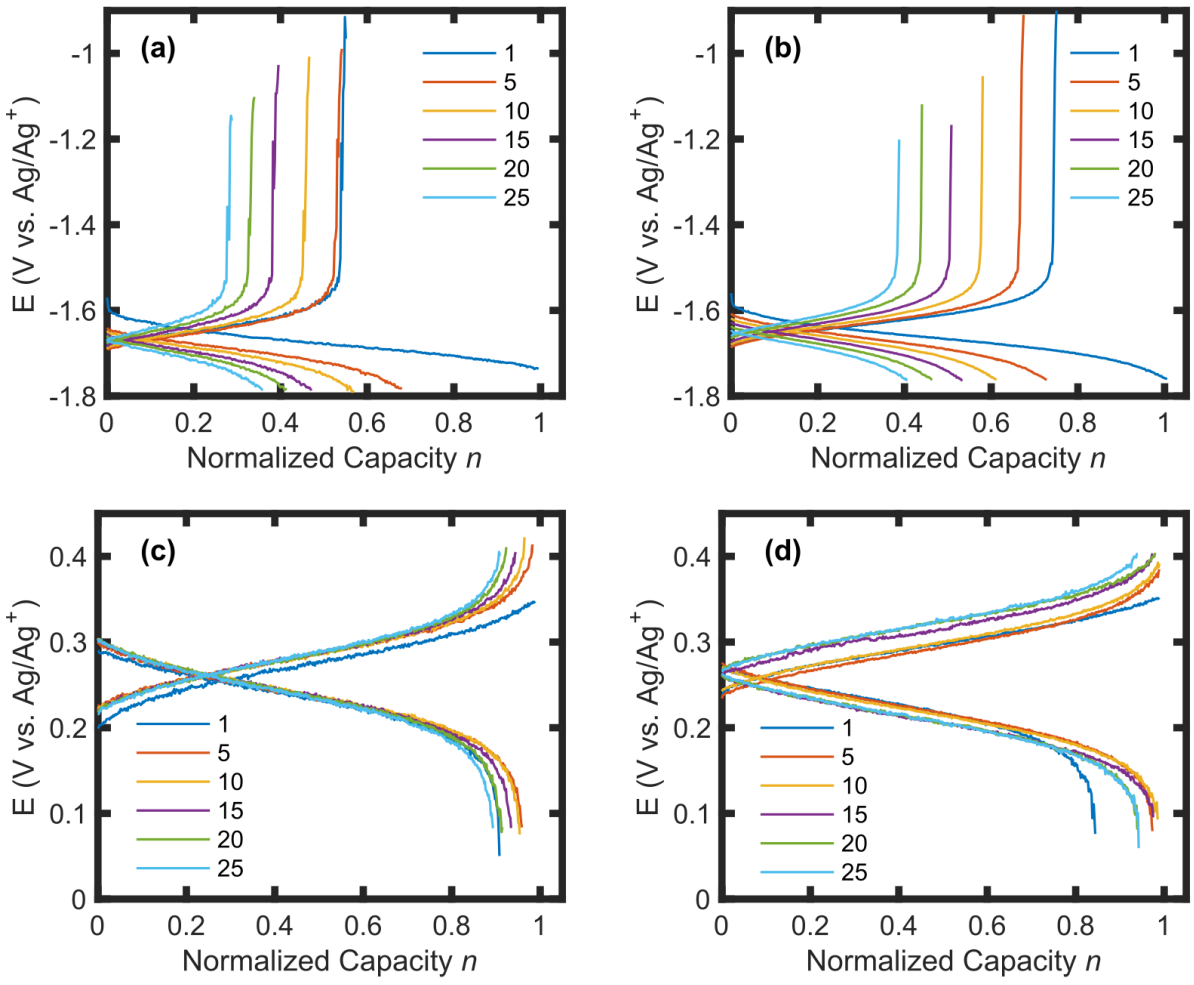

Figure 9: Bulk electrolysis potential curves for the $1e^-$ system: **(a)** $Fe(bpy)_3(BF_4)_2$ accessing couple III, **(b)** $Fe(bpy)_3(BF_4)_2$/Fc1N112-BF_4 accessing couple III. In both cases, the plateau potential is in agreement with the -1.65 V expected from CV. **(c)** Fc1N112-BF_4 accessing couple IV, **(d)** $Fe(bpy)_3(BF_4)_2$/Fc1N112-BF_4 accessing couple IV. The plateau potential corresponds to the 0.28 V expected based on CV. Capacity (x-axis) is normalized as total charge (number of electrons) per molecule and the legends denote cycle numbers.

The $2e^-$ system utilizes two negative couples (II and III) from $Fe(bpy)_3(BF_4)_2$ and the positive couples (IV and V) of both Fc1N112-BF_4 and $Fe(bpy)_3(BF_4)_2$. Figure 10 presents capacity retention data and CVs for the $2e^-$ bulk electrolysis experiments, while potential curves are plotted in Figure 11. Cycling through the two negative couples (II and III) reveals minimal interactions between the active species (Figure 10a/c). For both $Fe(bpy)_3(BF_4)_2$ and a mixture of the two species, the capacity fade profile is very similar (Figure 10a). In both cases, cycling never reaches the theoretical capacity due to the close proximity of couple I; a voltage cutoff ensured that the cell cycled only through couples II and III, subsequently limiting charge capacity. Examination of the CV after cycling (Figure 10c) shows a decrease in the peak height of the $Fe(bpy)_3(BF_4)_2$ couples, similar to that observed for the $1e^-$ transfer. In the case of the mixture, evidence of minor degradation products appear in the CV at the same potentials as for Fc1N112-BF_4 (Figure 8d), suggesting that the active species interact to an extent. Despite the development of these new irreversible electrochemical processes, the cycling behavior confirms that these two redox couples are compatible for use on the negative side of a multi-electron transfer cell.

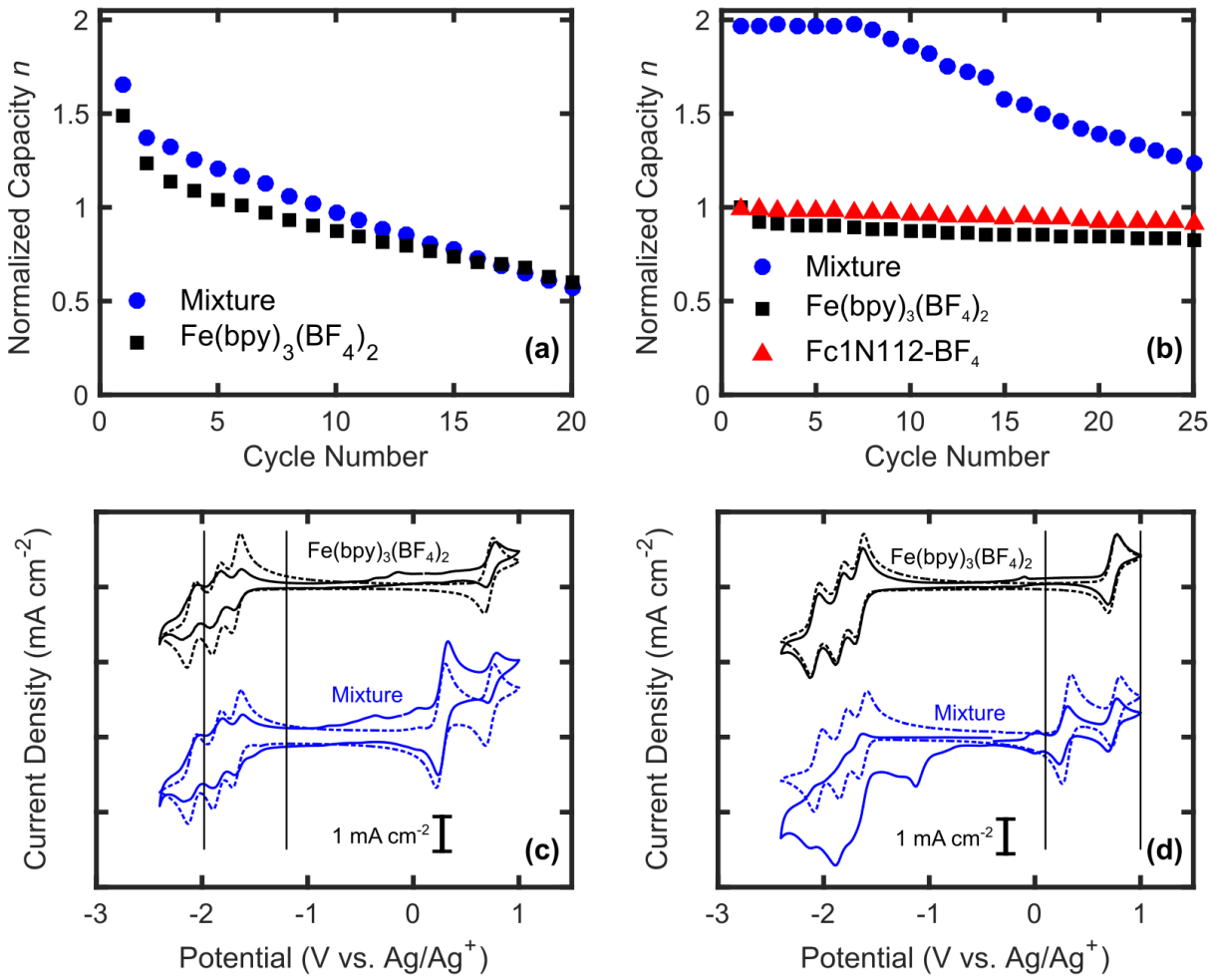

Figure 10: Capacity retention measured by bulk electrolysis for $Fe(bpy)_3(BF_4)_2$ (black), Fc1N112-BF_4 (red) and an equi-molar mixture of $Fe(bpy)_3$/Fc1N112-BF_4 (blue) through (a) two negative e^- and (b) both one and two positive e^-. (c, d) CVs before (dashed) and after cycling (solid) are shown for each case, with the black vertical lines denoting the potential cutoffs used during cycling.

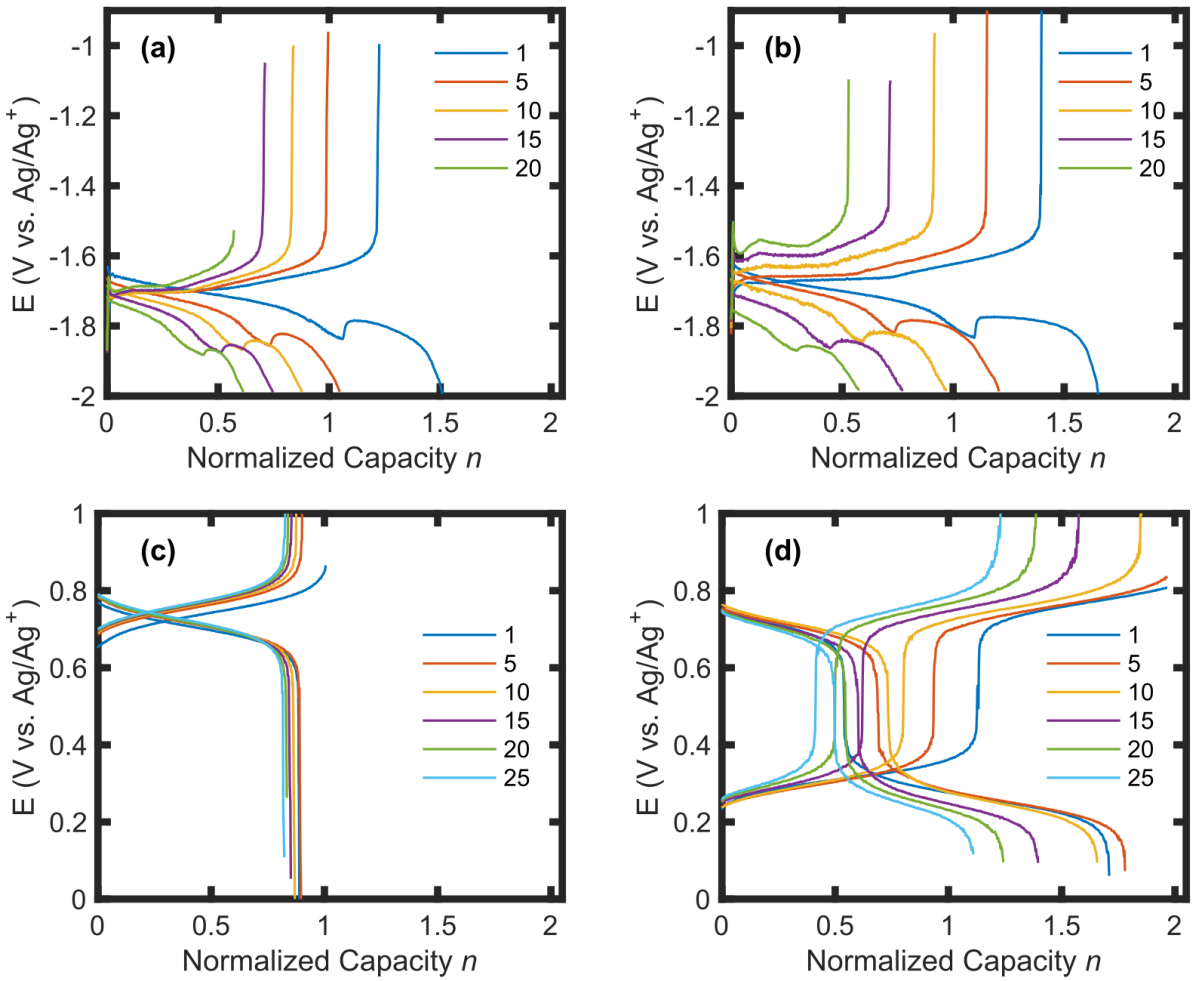

Figure 11: Bulk electrolysis cycling curves for the 2e- system: **(a)** $Fe(bpy)_3(BF_4)_2$ accessing couples II and III, **(b)** $Fe(bpy)_3(BF_4)_2$/Fc1N112-BF_4 accessing couples III and III, **(c)** $Fe(bpy)_3(BF_4)_2$ accessing couple V, **(d)** $Fe(bpy)_3(BF_4)_2$/Fc1N112-BF_4 accessing couples IV and V. In all cases, the plateau potentials correspond to those expected based on CV (Table S1). Capacity (x-axis) is normalized as total charge (number of electrons) per molecule and legends denote cycle numbers.

Cycling data through the two positive redox couples shows the highest degree of interactions observed for these two chemistries. Bulk electrolysis through the single positive couple of each individual species reveals stable cycling behavior (Figure 10b), and CVs after cycling show minimal degradation for both Fc1N112-BF_4 (Figure 8d) and $Fe(bpy)_3(BF_4)_2$ (Figure 10d). The mixed positive couples, however, exhibit significant capacity fade after the first 8 cycles (Figure 10b). Analysis of the CV after cycling shows clear evidence of degradation (Figure 10d). Peak heights for both positive couples decrease while those for the negative couples of $Fe(bpy)_3(BF_4)_2$ degrade completely. Despite the significant capacity fade and interactions

observed over time for the mixture at positive potentials, the cell maintains a constant capacity for at least the first 8 cycles, and therefore, affords a cell to demonstrate a multi-electron system.

4.7 H-Cell Cycling

H-type cell experiments demonstrate cycling of the $1e^-$ and $2e^-$ $Fe(bpy)_3(BF_4)_2$/Fc1N112-BF_4 systems at non-dilute concentrations in the absence of flow. These H-cell experiments utilize quasi-reference electrodes in each chamber to monitor electrode potentials and confirm the accessed redox couples during cycling. Both sides of the cell contained an identical mixture of $Fe(bpy)_3(BF_4)_2$/Fc1N112-BF_4 to ensure any capacity fade is due primarily to degradation of the active species, not irreversible crossover. Crossover will occur due to the formation of concentration gradients during cycling, but should only lead to decreased coulombic efficiency, not capacity fade. Figure 12a/b show potential curves for the $1e^-$ and $2e^-$ H-cell cycling experiments, respectively. Figure 12c/d display electrode potentials for the $1e^-$ and $2e^-$ cells, respectively.

For the $1e^-$ system, the negative electrode potential matches the potential of couple III, while the positive electrode potential matches that for couple IV. These results confirm that the $Fe(bpy)_3(BF_4)_2$/Fc1N112-BF_4 cell accesses only the desired couples, while reaching 100% of the theoretical capacity (1.34 Ah L^{-1}) on the first cycle, further establishing the compatibility of the selected active species. Figure 12a does reveal a large cell overpotential (~0.45 V) during cycling, comparable to other H-cell cycling reports.[19] Ohmic losses constitute a majority (~0.4 V) of the observed overpotential, due to the wide inter-electrode separation, and the remaining overpotential is due to activation and concentration polarization losses. Because of these significant overpotentials, the average voltaic efficiency is only 60%. The coulombic efficiency is also relatively low (73%) due to the high permeability of the Daramic separator.

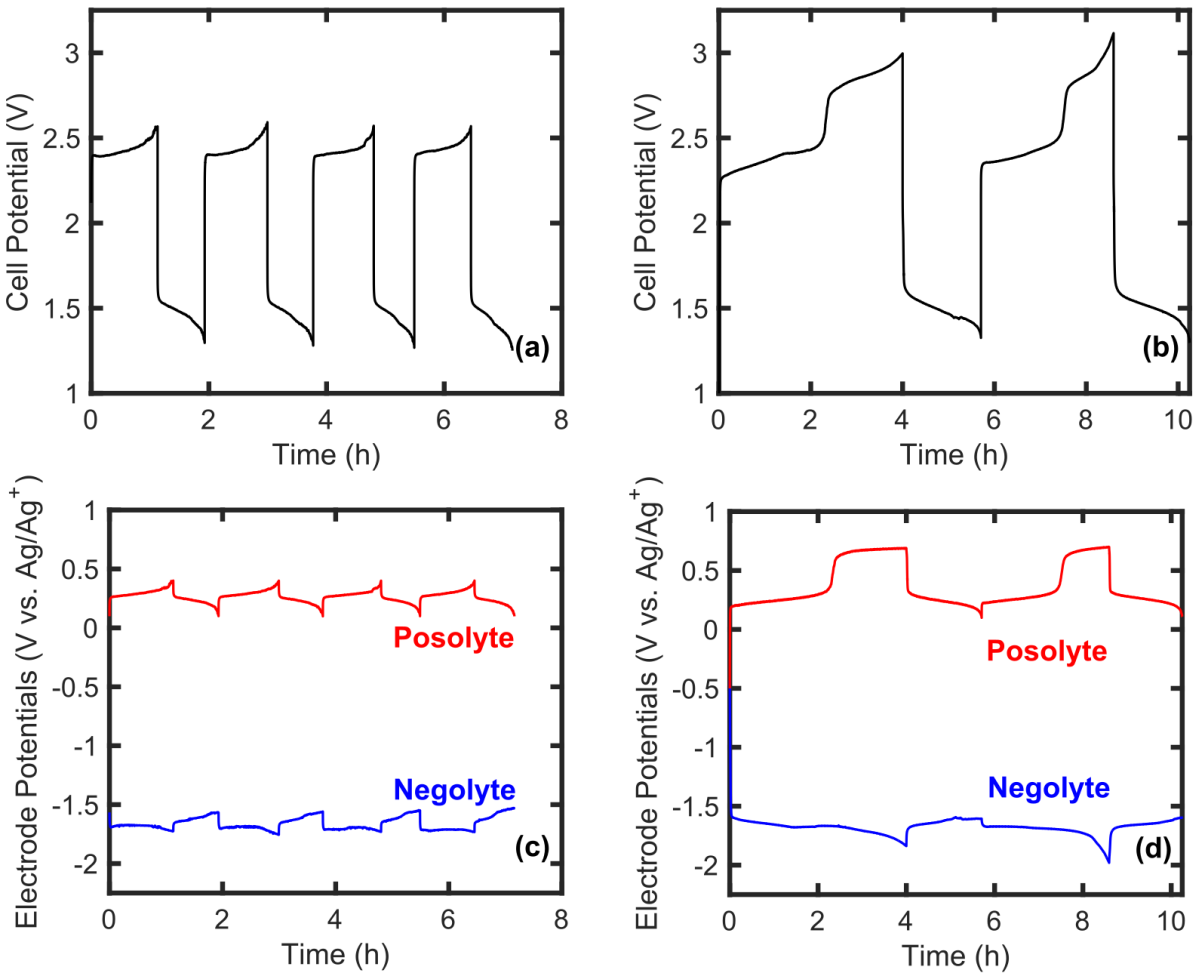

Figure 12: H-cell cycling data for the $Fe(bpy)_3(BF)_4$/Fc1N112-BF_4 system showing the total cell potential for the (a) $1e^-$ and (b) $2e^-$ experiments, and the posolyte (red) and negolyte (blue) potentials for the (c) $1e^-$ and (d) $2e^-$ H-cells, measured using Ag/Ag^+ quasi-reference electrodes in each chamber. The theoretical cell capacities are 1.34 Ah L^{-1} and 2.68 Ah L^{-1} for the $1e^-$ and $2e^-$ cells, respectively.

Quasi-reference electrodes in the $2e^-$ H-cell experiment confirm that the cell accesses all of the desired couples (II, III, IV, and V) upon charging. Considering Figure 12d, the posolyte first charges through the positive couple IV of Fc1N112-BF_4 at 0.28 V vs. Ag/Ag^+, and once couple IV is exhausted, the cell activates couple V of $Fe(bpy)_3(BF_4)_2$ at 0.75 V vs. Ag/Ag^+. Both plateaus are visible in the charging profile and match the potentials expected based on CV. For the negative side, the switch from couples III to II of $Fe(bpy)_3(BF_4)_2$ is less pronounced due to the close proximity of these couples, but a change in the slope of the charging curve after ~2 h indicates that the cell accesses both of these redox couples. On the first charge, the cell reaches 100% of the theoretical capacity (2.68 Ah L^{-1}), however, on discharge the cell only accesses the positive couple IV of Fc1N112-BF_4. The separator allows significant self-discharge, and a high rate of crossover

caused the charged $Fe(bpy)_3(BF_4)_3$ to fully self-discharge before partaking in an electrode reaction. The average coulombic efficiency for the $2e^-$ cell is 50%, due to the high rate of crossover, and the voltaic efficiency is 58%. Similar to the $1e^-$ cell, this is primarily due to a large cell overpotential. For the $2e^-$ cell, however, the inability to discharge through both couples results in an even lower voltaic efficiency. In this case, the voltaic efficiency is higher than the coulombic efficiency due to the significant contribution of active species degradation. Despite the inability of this cell to fully discharge, these results demonstrate that the system can access the desired electrons from each of the active species.

4.8 Flow Cell Studies

Our electrochemical studies culminate in flow cell cycling experiments, transitioning the vetted active materials to a laboratory prototype. Flow cells achieve higher current densities than H-cells, due to a significantly lower ASR, overcoming crossover limitations and offering higher voltaic efficiencies. The ASR of the flow cell is ~36 Ω cm^2, measured via electrochemical impedance spectroscopy (Figure 13) prior to beginning cycling experiments. From the measured solubilities (Table 1), in the presence of salt, the solubility of $Fe(bpy)_3(BF_4)$ limits the maximum theoretical energy density of the electrolyte to 15.3 Wh L^{-1} for the $1e^-$ transfer system and 36.2 Wh L^{-1} for the $2e^-$ system. Since flow cell experiments in this study employ only 0.1 M active material, the achievable energy densities in this experimental work are 5.1 Wh L^{-1} and 12.1 Wh L^{-1} for the $1e^-$ and $2e^-$ transfer systems, respectively.

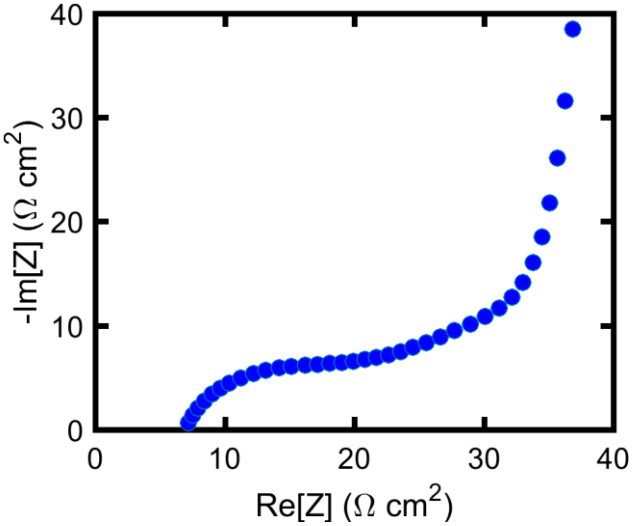

Figure 13: Nyquist plot of the $Fe(bpy)_3(BF_4)_2$/Fc1N112-BF_4 prior to beginning a cycling experiment. The total direct current (DC) contribution to the area specific resistance is $R_{DC} \sim 36\ \Omega\ cm^2$. Data was collected using the Biologic VMP3 potentiostat over the frequency range of 200 kHz to 1 Hz.

A small-scale flow cell demonstrates $1e^-$ cycling for a battery employing redox couples III and IV. Charge/discharge profiles in Figure 14a exhibit a single potential plateau that corresponds to the expected $1e^-$ process. The theoretical capacity of the $1e^-$ transfer cell was 2.68 Ah L^{-1}, and the flow cell accesses 66% of this capacity during the first cycle. This relatively low depth-of-charge is a result of the upper cell potential cutoff of 2.01 V, selected to avoid accessing additional redox couples (II or V). Figure 14b illustrates the charge and discharge capacities as a function of cycle number. Over the first 5 cycles, the charge capacity is significantly greater than the discharge capacity, resulting in coulombic efficiencies < 80%, as depicted in Figure 15c. Active species crossover and subsequent self-discharge through the Daramic separator, combined with active species degradation, led to the low coulombic efficiencies. The coulombic efficiency improves from 70% to 90% over 20 cycles, with a mean value of 81%, due to decreasing depths-of-charge as the experiment progresses. A prior NAqRFB study employing a Daramic separator with similar active species concentrations and current densities reported comparable coulombic efficiencies.[14] The voltaic efficiency is nearly constant as a function of cycle number, with a mean value of 91 ± 0.2%. The voltaic efficiency is relatively high due to two factors. First, the Daramic separator exhibits a lower ASR compared to other NAqRFB separators[3,13,15,21,27,38] as a result of its high porosity and the high conductivity of the electrolyte phase. Second, the voltaic efficiency is high in comparison to many AqRFBs due to lower current densities and a higher cell voltage; overpotential losses constitute a smaller fraction of the total cell potential. As with the $2e^-$ H-cell experiment, the voltaic efficiency is higher than the coulombic efficiency due to the significant contribution of active species degradation to the low coulombic efficiency. The range of coulombic efficiencies observed during cycling further supports this result. As the cell capacity stabilizes, indicating that active species degradation has slowed, the coulombic efficiency approaches the voltaic efficiency, as would be expected for a stable system.

Capacity fade for the flow cell experiment is in agreement with the limited stability of $Fe(bpy)_3(BF_4)_2$ observed during bulk electrolysis experiments. For couple III of $Fe(bpy)_3(BF_4)_2$, the capacity fades to 47% of its initial charge capacity after 20 bulk electrolysis cycles. Since the flow cell never reaches the theoretical capacity, flow cell cycling demonstrates slightly slower fade to only 62% of its initial charge capacity over 20 cycles.

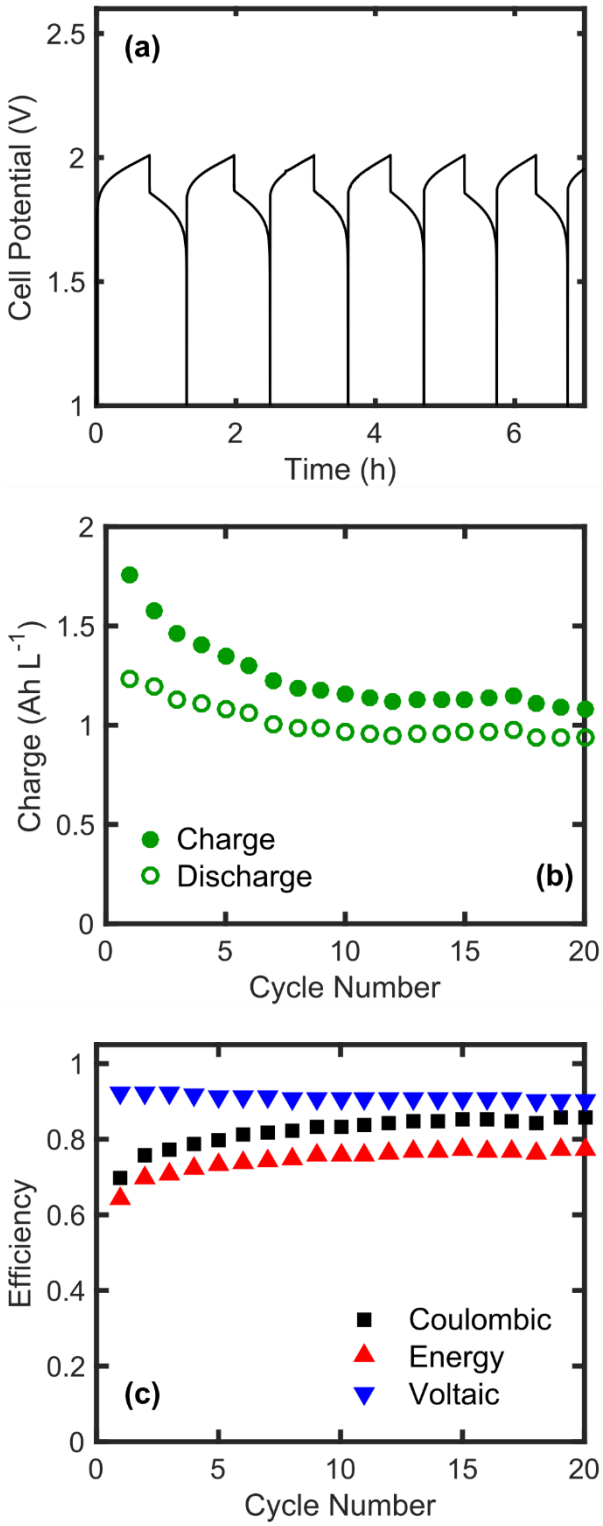

Figure 14: $Fe(bpy)_3(BF)_4$/Fc1N112-BF_4 1e- transfer flow cell cycling performance: (a) charge and discharge potential curves as a function of time, (b) charge (●) and discharge (○) capacities as a function of cycle number, and (c) coulombic (■), energy (▲), and voltaic (▼) efficiencies as a function of cycle number. The theoretical cell capacity is 2.68 Ah L^{-1}.

A $2e^-$ flow cell study completes the electrochemical analysis of the $Fe(bpy)_3(BF_4)_2$/Fc1N112-BF_4 system . As shown in Figure 15a, the $2e^-$ flow cell accesses all available redox processes during both charge and discharge, and cycle 1 displays a unique charging profile due to the 4 accessible redox couples in the $Fe(bpy)_3(BF_4)_2$/Fc1N112-BF_4 $2e^-$ system. Consider Figure 15b, which plots cell potential as a function of capacity for only the first charging process. The initial charging plateau accesses redox couples III and IV. This behavior is consistent with observations during charging of the $1e^-$ transfer flow cell. As the cell continues to charge, however, a second plateau appears; a non-differentiable decrease in cell potential characterizes the start of the second plateau. As the electrodes continue to polarize, redox couples II, III, and IV become thermodynamically accessible, but *not* couple V. Eventually, couple IV is exhausted, and a sharp increase in cell potential marks the start of a third plateau. The third plateau then accesses couples II, III, and V. Finally, for a fourth plateau, only couples II and IV participate in charge transfer reactions because all other couples have been completely exhausted. Upon cell discharge, two major plateaus appear (Figure 15a), corresponding to the reduction of couple V, followed by the reduction of couple IV, but detailed processes are indistinguishable.

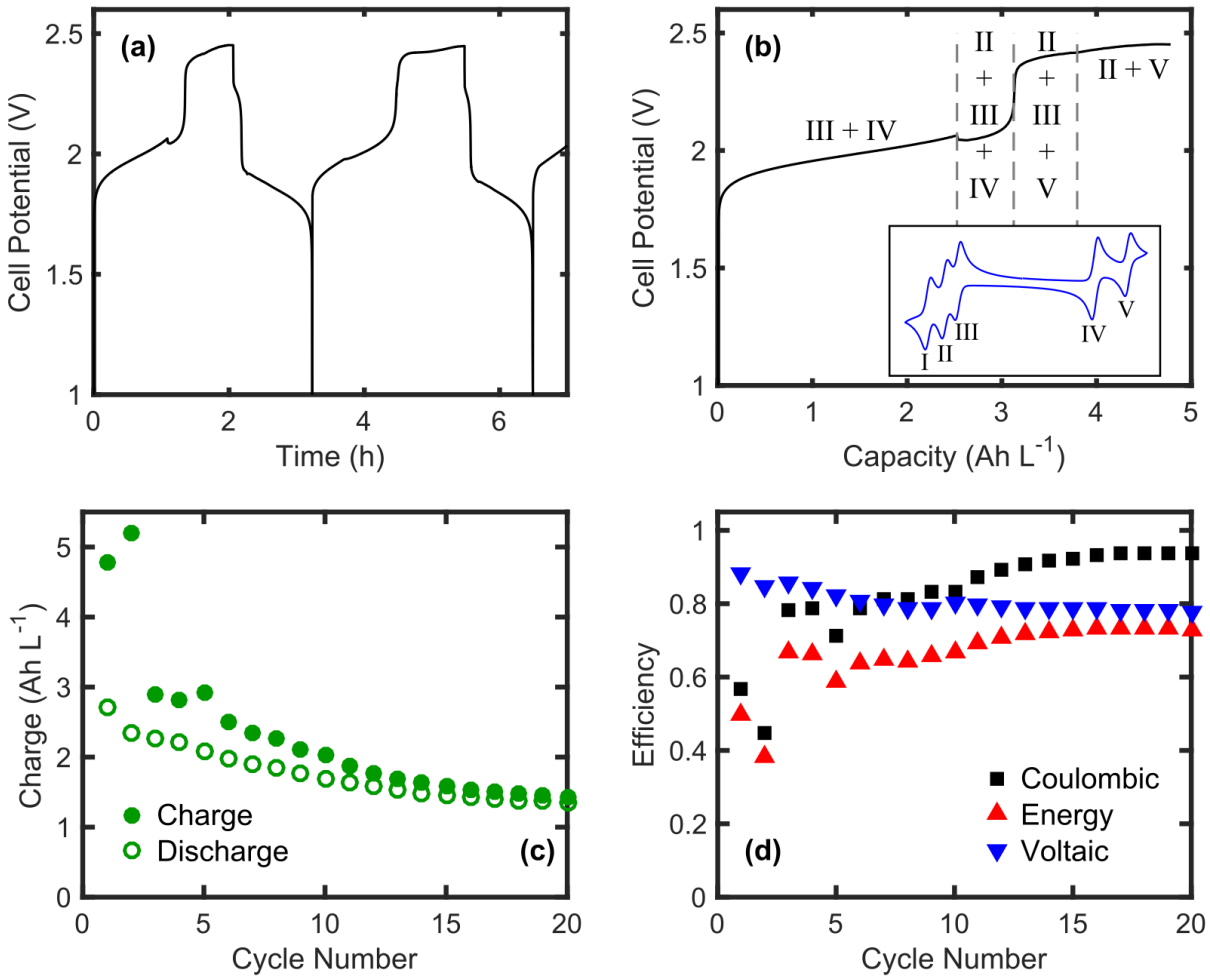

Figure 15: $Fe(bpy)_3(BF_4)_2$/Fc1N112-BF_4 $2e^-$ transfer flow cell cycling performance: (a) Charge and discharge curves as a function of time, (b) Charging voltage profile as a function of capacity for the 1st cycle, (c) Charge (●) and discharge (○) capacities as a function of cycle number, and (d) Coulombic (■), energy (▲), and voltaic (▼) efficiencies as a function of cycle number. The theoretical cell capacity is 5.36 Ah L^{-1}.

The unconventional $2e^-$ charge behavior results from the presence of two pairs of unequally separated redox couples. The decrease in cell potential at ~2.5 Ah L^{-1} during cycle 1 charging (see Figure 15b) is unusual, but an associated decrease in concentration overpotential reconciles the behavior. During the first charge plateau, the negative electrode continuously consumes reactant for couple III, and the negative electrode overpotential increases to maintain constant current, subsequently increasing the total cell potential. Unique to this multi-electron transfer system, at a significantly large overpotential on the negative electrode, couple II becomes nearly instantaneously accessible. During the second plateau, the negative electrode could reduce *either* couple II *or* III, increasing reactant concentration as compared to the end of the first plateau. With

an increase in available reactant, the negative electrode concentration overpotential decreases, subsequently decreasing the overall cell potential instantaneously at ~2.5 Ah L^{-1}. Bulk electrolysis (Figure 11) and H-cell (Figure 12, negolyte) cycling curves confirm this behavior. Additionally, replicate flow cell experiments displayed the same potential dip phenomena during charging.

The theoretical capacity of the $2e^-$ flow cell is 5.36 Ah L^{-1}. The upper cell potential cutoff of 2.45 V prohibits accessing the unstable couple I, but also prohibits the cell from accessing 100% of its theoretical capacity. Figure 15b indicates that the first two charge cycles accessed 89% and 97% of the theoretical cell capacity, respectively. Despite the high depth-of-charge during the first two cycles, the coulombic efficiencies for these cycles are 57% and 45% (Figure 15c). The low coulombic efficiencies are a result of crossover through the Daramic separator and rapid active species degradation. The short discharge plateau for cycle 1 (Figure 15a), demonstrates that discharge processes incorporating redox couple V are short-lived. During cycling, a large volume (~2 mL) of electrolyte migrates from the posolyte to the negolyte, suggesting that active material migration plays a significant role in crossover. The higher cell potential of the $2e^-$ system, relative to the $1e^-$ system, provides a large driving force for active species migration during cycling. Mitigating migration of like-charged active species is a challenge to overcome for common ion exchange NAqRFBs. Diffusive crossover of active material also likely plays a significant role in the low coulombic efficiency during cycles 1 and 2.

Beyond cycle 2, charge capacities decrease significantly, likely caused by active material degradation and low depths-of-charge. Bulk electrolysis experiments over 20 cycles exhibit rapid capacity degradation down to 71% and 36% for the $2e^-$ posolyte and negolyte redox couples, respectively. Further, the distinct charge plateaus identified in cycle 1 merge in subsequent cycles, convoluting specific redox processes in late cycle charge plateaus. This $2e^-$ transfer system suffers from poor active material stability and high crossover rates, but, nonetheless, demonstrates for the first time the unique charging characteristics associated with multi-electron RFBs.

4.9 Chemical Cost ($ kWh^{-1}) Benefit of Common Ion Exchange NAqRFBs

The techno-economic model defined in Equation (3) compares the cost for a common ion configuration to that of a salt splitting cell. Equation (3) defines the chemical cost per total energy stored (C/E) in $ kWh^{-1} based on contributions from the active species, solvent, and salt. Table 2 details all variable definitions. Due to uncertainties in active material cost $\left(c_m^{\$}\right)$, calculations

considered a low ($5 kg^{-1}) and high ($20 kg^{-1}) value to illustrate changes in the model as a function of active material cost. A prior study suggested that tailored molecules could achieve an optimistic cost of $5 kg^{-1},[7] defining the lower bound for this analysis. In the particular case of the $Fe(bpy)_3(BF_4)_2$/Fc1N112-BF_4 chemistry, the active species resemble other tetrafluoroborate salts employed in lithium-ion batteries, so the upper bound active material cost for this analysis is $20 kg^{-1}, a projected future state price of salts for lithium-ion batteries.[7] Our description varies from a previous model by Darling et al.[7] in that the electrolyte cost is divided into its constituent salt and solvent costs. For simplicity, efficiencies, depth-of-discharge, and reaction stoichiometry equal unity.

$$\frac{C}{E} = \frac{1}{nFU}\left[M_m c_m^{\$} + r_{sol} M_{sol} c_{sol}^{\$} + r_{salt} M_{salt} c_{salt}^{\$} \right] \quad (3)$$

Table 2: Equation (3) variable definitions and units. Values of each variable used in the common ion versus salt splitting cost analysis are also provided.

Variable	Description	Unit	Common Ion	Salt Splitting
n	Number of Electrons	-	1	
F	Faraday Constant	kA·h mol^{-1}	0.026801	
U	Cell Potential	V	1.9	
M_m	Active Material Molecular Weight	kg mol^{-1}	0.359	
M_{sol}	Solvent Molecular Weight	kg mol^{-1}	0.041	
M_{salt}	Salt Molecular Weight	kg mol^{-1}	0.329	
r_{sol}	Solvent-to-Actives Molar Ratio	-	-	
r_{salt}	Salt-to-Actives Molar Ratio	-	0.5	1.5
$c_m^{\$}$	Active Material Cost	$ kg^{-1}	5 [7] or 20	
$c_{sol}^{\$}$	Solvent Cost	$ kg^{-1}	2 [7]	
$c_{salt}^{\$}$	Salt Cost	$ kg^{-1}	20 [7]	

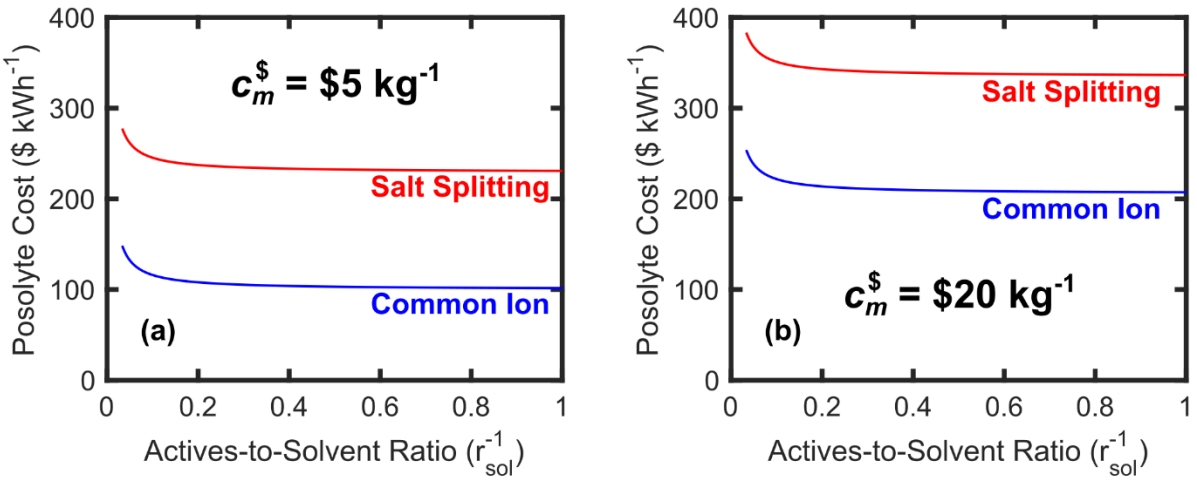

Figure 16: Posolyte costs for salt splitting and common ion exchange asymmetric NAqRFBs as a function of molar actives-to-solvent ratio $\left(r_{sol}^{-1}\right)$, where the active material cost $\left(c_m^{\$}\right)$ is (a) \$5 kg^{-1} or (b) \$20 kg^{-1}. Fc1N112-BF_4 is the sole active material in an unmixed posolyte, and the negolyte active material has a redox potential of -1.65 V vs Ag/Ag$^+$ with 1e$^-$ transfer. The common ion configuration is cheaper across all values of r_{sol}^{-1} due to the decreased salt cost.

Figure 16 plots the costs of posolytes in salt splitting and common ion configurations as a function of molar actives-to-solvent ratio $\left(r_{sol}^{-1}\right)$, clearly demonstrating the economic advantage of common ion exchange. Table 2 lists quantitative details for each variable in the cost analysis, where Fc1N112-BF_4 (M_m = 0.359 kg mol^{-1}) is the sole posolyte redox active material (unmixed, asymmetric configuration), MeCN is the solvent (M_{sol} = 0.041 kg mol^{-1}), and $TBABF_4$ is the supporting salt (M_{salt} = 0.329 kg mol^{-1}). The negolyte active material has a redox potential of -1.65 V vs Ag/Ag$^+$, defining the cell potential, but the asymmetric posolyte cost does not account for the cost of the negolyte active material. As illustrated by Figure 16, the cost of both cell configurations decreases as a function of active species concentration, but the common ion cell is less expensive across *all* concentrations. These chemical cost savings are a result of the decreased salt requirement for common ion exchange NAqRFBs. While varying the active material cost linearly shifts the cost curves to higher and lower values, the cost difference in moving from a salt splitting to common ion configuration remains the same due to an identical savings (\$129 kWh^{-1} for this particular example) in total salt cost. As previously described, salt-splitting RFBs require a minimum n:1 molar ratio of salt-to-actives ($r_{salt} \geq n$) to maintain charge neutrality, while common ion exchange cells can charge balance at any supporting salt concentration ($r_{salt} \geq 0$). The techno-economic analysis uses r_{salt} values of 0.5 and 1.5 for the salt splitting and common ion NAqRFBs,

respectively, representing a salt concentration 0.5 M above the minimum charge balancing salt requirement for each type of cell. In addition to increasing costs, the prior experimental results show that increasing salt concentration in the electrolyte suppresses active species solubility. Active species with lower solubilities require a higher molar ratio of solvent-to-actives (r_{sol}) to dissolve completely all active species and salt in the electrolyte. Since NAqRFBs can have solvent costs $\left(c_{sol}^{\$}\right)$ on the same order of magnitude as the active species $\left(c_{m}^{\$}\right)$ costs, minimizing r_{sol} can significantly decrease chemical costs. The posolyte cost as a function of r_{sol} asymptotically approaches a value where the solvent cost contribution is zero ($r_{sol} = 0$). Ultimately, common ion exchange cells decrease chemical costs by minimizing both r_{salt} and r_{sol}.

Note, however, that selecting a common ion exchange chemistry often requires active species with high(er) molecular weights. Common ion exchange RFBs must contain ionic active species at 0 % SOC. Functionalization of neutral redox active species can produce redox active ions[3,25], which necessarily will increase the molecular weight of the active species and could also increase active material cost (higher $c_{m}^{\$}$) due to additional synthesis steps. Equation (4) defines a dimensionless cost ratio, γ, to determine whether to employ heavier, ionic active materials considering only the chemical cost. In Equation (4), the subscript *CI* denotes the heavier, common ion compatible active material and the subscript *SS* denotes the lighter, salt splitting active material. The cost ratio γ compares the cost increase (numerator) of employing a heavier active material to the cost savings (denominator) associated with the low salt concentration requirement and higher solubility of the common ion compatible active material. If $\gamma < 1$, the common ion exchange RFB is cheaper, whereas if $\gamma > 1$, the salt splitting RFB is more cost effective. Notably, as the number of electron transfers per molecule increases (higher n) the salt cost contribution increases linearly for the salt splitting configuration, making common ion exchange RFBs increasingly favorable for multi-electron transfer systems. In most practical examples, the common ion exchange system is cheaper, despite a higher active species molecular weight or cost. This cost analysis does not consider other advantages of ionic modification that can further decrease cost, such as increased redox potential (higher U).[3,37]

$$\gamma = \frac{\left(M_{m,\mathrm{CI}} c_{m,\mathrm{CI}}^{\$} - M_{m,\mathrm{SS}} c_{m,\mathrm{SS}}^{\$}\right)}{M_{sol} c_{sol}^{\$} \left(r_{sol,\mathrm{CI}} - r_{sol,\mathrm{SS}}\right) + n M_{salt} c_{salt}^{\$}} \tag{4}$$

4.10 Conclusions

Common ion exchange systems could enable low cost, high energy density NAqRFBs by enhancing active species solubilities and decreasing salt concentration requirements as compared to their salt splitting alternatives. In this work, a multi-electron, common ion NAqRFB was designed employing $Fe(bpy)_3(BF_4)_2$ and Fc1N112-BF_4 as the active species. A systematic electrolyte compatibility study investigated possible interactions between the selected species by examining the stability of both active materials, across all relevant oxidation states, both individually and as mixtures. CV, bulk electrolysis, and H-cell experiments confirmed the feasibility of $1e^-$ and $2e^-$ transfer cycling prior to engaging a flow cell study. The $1e^-$ flow cell cycled as predicted from the bulk electrolysis and H-cell experiments. The $2e^-$ NAqRFB successfully accessed all desired redox couples, revealing a unique progression of charge plateaus. Results from the systematic electrochemical studies explained the complex charging phenomena, and each plateau during the charging process corresponded to specific redox processes observed by CV. A techno-economic analysis highlighted the cost savings afforded by a common ion configuration NAqRFB. Overall, this research establishes the cost and performance benefits of common ion exchange NAqRFBs and demonstrates the first $2e^-$ full flow NAqRFB. Although the stability, efficiency, energy density, and cost of the demonstration chemistry and performance of the flow cell selected for this study are insufficient for grid implementation, the developed methodologies can extend to other promising redox chemistries, including all-organic, all-MCC, and mixed MCC/organic systems. Coupling tailored posolyte and negolyte active species with the concept of common ion exchange, multi-electron transfer, and asymmetric compatibility, will lead to the development of NAqRFBs that approach the DOE price target.

4.11 References

1. P. J. Cabrera et al., *Inorg. Chem.*, **54**, 10214–10223 (2015).
2. J. A. Suttil et al., *J Mater Chem A*, **3**, 7929–7938 (2015).
3. X. Wei et al., *Adv. Energy Mater.*, **5**, 1400678 (2014).
4. J. Huang et al., *J Mater Chem A*, **3**, 14971–14976 (2015).
5. C. S. Sevov et al., *J. Am. Chem. Soc.*, **137**, 14465–14472 (2015).
6. B. Scrosati, *J. Electrochem. Soc.*, **139**, 2776 (1992).
7. R. M. Darling, K. G. Gallagher, J. A. Kowalski, S. Ha, and F. R. Brushett, *Energy Environ. Sci.*, **7**, 3459–3477 (2014).
8. L. Gaines and R. Cuenca, *Costs of Lithium-Ion Batteries for Vehicles: ANL/ESD-42*, p. 31, (2000).
9. P. A. Nelson, K. G. Gallagher, I. Bloom, and D. W. Dees, *Modeling the Performance and Cost of Lithium-Ion Batteries for Electric-Drive Vehicles: ANL-12/55*, p. 55, (2011).

10. A. A. Shinkle, T. J. Pomaville, A. E. S. Sleightholme, L. T. Thompson, and C. W. Monroe, *J. Power Sources*, **248**, 1299–1305 (2014).
11. J. R. Dahn et al., *J. Electrochem. Soc.*, **152**, A1283–A1289 (2005).
12. L. Su et al., *J. Electrochem. Soc.*, **163**, A5253–A5262 (2016).
13. F. R. Brushett, J. T. Vaughey, and A. N. Jansen, *Adv. Energy Mater.*, **2**, 1390–1396 (2012).
14. I. L. Escalante-García, J. S. Wainright, L. T. Thompson, and R. F. Savinell, *J. Electrochem. Soc.*, **162**, A363–A372 (2015).
15. S. H. Oh et al., *J Mater Chem A*, **2**, 19994–19998 (2014).
16. S. Park et al., *Electrochem. Commun.*, **59**, 68–71 (2015).
17. Y. Matsuda, K. Tanaka, M. Okada, U. Takasu, and M. Morita, *J. Appl. Electrochem.*, **18**, 909–914 (1988).
18. M. H. Chakrabarti, R. A. W. Dryfe, and E. P. L. Roberts, *Electrochimica Acta*, **52**, 2189–2195 (2007).
19. P. J. Cabrera et al., *J. Phys. Chem. C*, **119**, 15882–15889 (2015).
20. N. S. Hudak, L. J. Small, H. D. Pratt, and T. M. Anderson, *J. Electrochem. Soc.*, **162**, A2188–A2194 (2015).
21. M. Park et al., *ACS Appl. Mater. Interfaces*, **6**, 10729–10735 (2014).
22. J. Mun et al., *Electrochem. Solid-State Lett.*, **15**, A80–A82 (2012).
23. P. J. Cappillino et al., *Adv. Energy Mater.*, **4**, 1300566 (2014).
24. J. Park, M. Lee, S. Hwang, D. Lee, and D. Oh, "Redox flow battery," US Pat. US 20120171541 A1, Filed October 6, 2012.
25. L. Cosimbescu et al., *Sci. Rep.*, **5**, 14117 (2015).
26. J. A. Riddick and W. B. Bunger, *Organic Solvents*, Wiley-Interscience, (1971).
27. X. Wei et al., *Adv. Mater.*, **26**, 7649–7653 (2014).
28. M. Morita, Y. Tanaka, K. Tanaka, Y. Matsuda, and T. Matsumura-Inoue, *Chem. Soc. Jpn.*, **61**, 2711–2714 (1988).
29. S. H. Shin, S. H. Yun, and S. H. Moon, *RSC Adv.*, **3**, 9095–9116 (2013).
30. P. Alotto, M. Guarnieri, and F. Moro, *Renew. Sustain. Energy Rev.*, **29**, 325–335 (2014).
31. N. V Plechkova and K. R. Seddon, *Chem. Soc. Rev.*, **37**, 123–150 (2008).
32. J. Huang et al., *Adv. Energy Mater.*, **5**, 1401782 (2015).
33. K. Takechi, Y. Kato, and Y. Hase, *Adv. Mater.*, **27**, 2501–2506 (2015).
34. M. A. Miller, J. S. Wainright, and R. F. Savinell, *J. Electrochem. Soc.*, **163**, A578–A579 (2016).
35. L. Bahadori et al., *J. Electrochem. Soc.*, **163**, A632–A638 (2016).
36. J. England, C. C. Scarborough, T. Weyhermüller, S. Sproules, and K. Wieghardt, *Eur. J. Inorg. Chem.*, **2012**, 4605–4621 (2012).
37. B. Hwang, M. S. Park, and K. Kim, *ChemSusChem*, **8**, 310–314 (2015).
38. X. Wei et al., *Angew. Chem. Int. Ed.*, **54**, 8684–8687 (2015).

5. Feasibility of a supporting salt free non-aqueous redox flow battery

This chapter is reprinted from *ChemSusChem*, J. D. Milshtein, S. M. Fisher, T. M. Breault, L. T. Thompson, F. R. Brushett, Feasibility of a supporting salt free non-aqueous redox flow battery, doi: 10.1002cssc.201700028, Copyright (2017), with permission from John Wiley & Sons, Inc. under license number 4087110194418.

5.1 Introduction

Future-state prices for non-aqueous (NAq) supporting electrolytes (solvent + 1 M salt) are anticipated to be relatively high (~\$5 kg^{-1}), as compared to their aqueous counterparts (~\$0.10 kg^{-1}),[1] so decreasing the costs and / or quantities of both the solvent and supporting salt will be critical.[2] A number of studies have focused on enhancing active species solubility,[3–8] which serves to decrease the total amount of solvent required.[2] The supporting salt, however, especially the fluorinated derivatives typically employed in NAq batteries (e.g., lithium hexafluorophosphate, tetrabutylammonium tetrafluoroborate), will constitute a majority of the future-state supporting electrolyte cost (~\$20 kg^{-1} vs. ~\$2 kg^{-1} for the salt and solvent, respectively).[1] Despite the opportunity for substantial cost savings,[2,9] few studies have focused on minimizing supporting salt content. In a prior report, we described a common-ion exchange NAqRFB design that reduced the required amount of supporting salt by employing similarly charged active species that share a common, counter-ion.[9] Additional cost savings are possible through the use of multi-functional materials, which serve two or more critical roles in the electrolyte (i.e., solvation, charge carrier, redox active).[2] Herein, we combine multi-functional active species with the common-ion exchange configuration to demonstrate a NAqRFB proof-of-concept prototype operating in the limit of no supporting salt.

NAqRFBs utilize supporting salts to enhance electrolyte conductivity and maintain electroneutrality during charge and discharge.[10,11] High salt concentrations, however, can limit the solubility of the active species in the electrolyte solution[9,12,13] and suppress the conductivity of ion-selective membranes, increasing area-specific resistance (ASR).[14] The need for supporting salt can be eliminated entirely by using similarly charged active species (positive or negative) that remain as ions across all accessible states-of-charge (SOCs). In this scheme, counter-ions that are associated with the redox-active ion provide charge balance, and both the active species and counter-ions contribute to the ionic conductivity of the electrolyte. Figure 1 highlights the charging

process for a NAqRFB utilizing cationic active species with no supporting salt, where counter-anions transport from the negative electrolyte (negolyte) to the positive electrolyte (posolyte), maintaining electroneutrality. The same concept can be extended to redox-active anions with counter-cations.

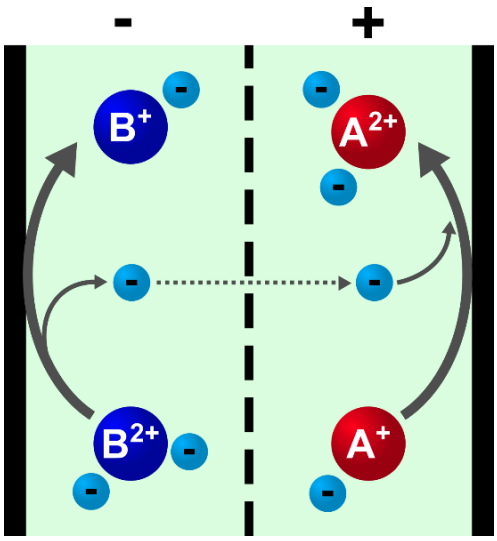

Figure 1: Schematic of the charging process in a supporting salt free RFB employing cationic redox-active species. "A" is the posolyte active material (red), and "B" is the negolyte active material (dark blue). Associating counter-anions are denoted by "-" (light blue).

For this study, we selected iron(II) tris(2,2'-bipyridine) tetrafluoroborate ($Fe(bpy)_3(BF_4)_2$, Figure 2a)[15] and ferrocenylmethyl dimethyl ethyl ammonium tetrafluoroborate ($Fc1N112\text{-}BF_4$, Figure 2b)[4,5] as model ionic redox active species to demonstrate the salt free cell concept. The lack of viable NAqRFB chemistries, especially those with the characteristics necessary for the demonstration of a salt free device, drove our selections. $Fc1N112\text{-}BF_4$ is known to be a highly soluble and stable posolyte active material,[4,5,9] however, it is too expensive for implementation in a low cost grid-scale device.[2] $Fe(bpy)_3(BF_4)_2$ is one of the only well-characterized NAqRFB negolyte active materials that remains as a cation across all relevant SOCs, but suffers from relatively poor stability.[9,15] Both species have been investigated extensively in prior literature, have well-characterized properties, and are therefore excellent model compounds.

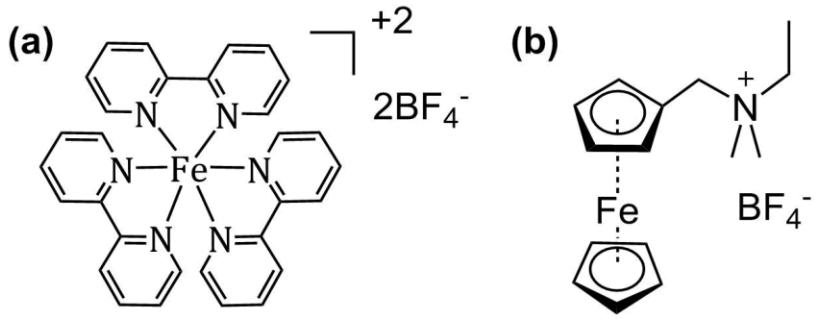

Figure 2: Structures of **(a)** iron(II) tris(2,2'-bipyridine) tetrafluoroborate ($Fe(bpy)_3(BF_4)_2$) and **(b)** ferrocenylmethyl dimethyl ethyl ammonium tetrafluoroborate ($Fc1N112\text{-}BF_4$).

In this system, $Fe(bpy)_3^{2+}$ and $Fc1N112^+$ act as the redox-active cations (at 0% SOC), while BF_4^- serves as the common, charge balancing, counter-anion. The posolyte and negolyte half-cell reactions are provided in Equations (1) and (2), respectively, while Equation (3) shows the full-cell reaction:

$$\left[Fc1N112^{2+}\right]\left[BF_4^-\right]_2 + e^- \leftrightarrow \left[Fc1N112^+\right]\left[BF_4^-\right] + BF_4^- \quad (1)$$

$$\left[Fe(bpy)_3^{2+}\right]\left[BF_4^-\right]_2 + e^- \leftrightarrow \left[Fe(bpy)_3^+\right]\left[BF_4^-\right] + BF_4^- \quad (2)$$

$$\left[Fe(bpy)_3^{2+}\right]\left[BF_4^-\right]_2 + \left[Fc1N112^+\right]\left[BF_4^-\right] \leftrightarrow \left[Fe(bpy)_3^+\right]\left[BF_4^-\right] + \left[Fc1N112^{2+}\right]\left[BF_4^-\right]_2 \quad (3)$$

Importantly, these active species are positively charged at all relevant oxidation states, enabling the salt free cell configuration outlined in Figure 1. Additionally, these compounds exhibit minimal inter-species reactions in the singly charged state, are soluble in acetonitrile (MeCN), and are easily synthesized in large quantities, facilitating a proof-of-concept flow cell enlisting the no supporting salt framework.[9]

This study demonstrates a NAqRFB configured to operate in the absence of any supporting salt, utilizing well-studied model active species. First, conductivity measurements demonstrate the high conductivities of the model ionic active species in MeCN. Second, cyclic voltammetry (CV) and bulk electrolysis experiments show that the ionic active species maintain redox activity in the absence of supporting salt. Third, proof-of-concept flow cell experiments demonstrate the feasibility of a supporting salt free NAqRFB, exhibiting resistances and efficiencies similar to those of other recently reported NAqRFBs.[16,17] Finally, a chemistry-agnostic techno-economic analysis highlights the significant cost savings afforded by minimizing or eliminating the amount of salt in NAqRFBs with varying active species costs, salt costs, and cell potentials. Overall, this paper highlights the design of a NAqRFB operating without supporting salt. Further, the design

and configuration principles of NAqRFBs employing similarly charged, all-ionic active species outlined in this work can extend beyond the model compounds to other active species, including organic molecules, providing a viable route to minimizing the price of promising future NAqRFBs.

5.2 Experimental

Materials. All solution preparation and electrochemical experiments were performed inside argon filled glove boxes (O_2 < 5 ppm, H_2O < 1 ppm). MeCN (Extra Dry, 99.9%) was purchased from Acros Organics. Tetraethylammonium tetrafluoroborate (99.9%) and lithium tetrafluoroborate (99.9%) were purchased from BASF and used as received.

Active Species Synthesis. All reagents and starting materials (iron(II) tetrafluoroborate hexahydrate (97%), (dimethylaminomethyl)ferrocene (96%), bromoethane (98%), sodium tetrafluoroborate (98%)) were purchased from Sigma-Aldrich, with the exception of 2,2'-bipyridine (98%, Alfa Aesar), and used as received. $Fe(bpy)_3(BF_4)_2$ was prepared according to a literature procedure.[9] Fc1N112-BF_4 was synthesized through a bromide salt intermediate also as reported in literature.[4,5,9] Ion exchange of Br^- with BF_4^- was performed in deionized water to afford the final product.[9]

Conductivity Measurements. Electrolyte conductivity measurements were collected using a two electrode, Swagelok style conductivity cell that has been described previously in literature.[18] The conductivity cell was filled with electrolyte (600 µL) and then sealed. The impedance of the conductivity cell was measured over a small frequency range (1 MHz to 100 Hz) about the OCV with a potential amplitude of 10 mV. The high frequency intercept of the Nyquist plot was used as the cell resistance value for subsequent calculations of electrolyte conductivity. Cell resistances were measured 10 times for 3 aliquots of each electrolyte composition. In between measurements, the conductivity cell was rinsed with pure MeCN. The conductivity cell was calibrated in an ice water bath (0 °C), outside of the glove box, to build a 4-point calibration curve (Figure 3), using the following aqueous sodium chloride standards (Orion™): 0.100, 1.413, 12.90, and 111.9 mS cm^{-1}. NAq electrolyte conductivities were determined from cell resistance measurements and the calibration curve. Error bars for electrolyte conductivities represent 95% confidence intervals of the standard error, accounting for the experimental uncertainties, measurement noise, repeatability, and quality of the calibration fit.

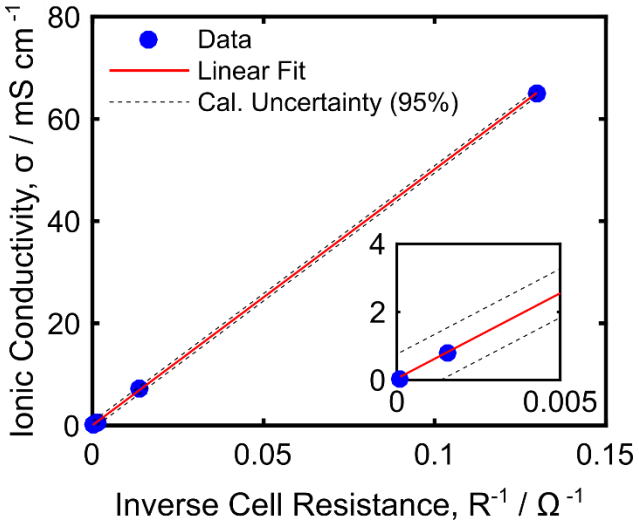

Figure 3: Conductivity cell 4-point calibration curve showing the raw cell resistance data (blue ●), the linear calibration curve (red solid line), and the range of uncertainty in the calibration curve (black dashed line), calculated from 95% confidence intervals. Inset: Expansion in the ionic conductivity range of 0 – 4 mS cm^{-1}.

Cyclic Voltammetry. CVs were performed using a BioLogic VSP potentiostat in a custom 10 mL three-electrode electrochemical cell. A 3 mm diameter glassy carbon disk was used as the working electrode (BASi), a coiled platinum wire as the counter electrode, and a fritted Ag/Ag^+ quasi-reference electrode (BASi) filled with silver tetrafluoroborate (0.01 M, 98%, Sigma Aldrich) in MeCN. CVs were recorded at a scan rate of 100 mV s^{-1} in MeCN solutions containing the individual active species (5 mM) or an equimolar mixture containing both $Fe(bpy)_3(BF_4)_2$ and Fc1N112-BF_4 (10 mM total). Impedance measurements were recorded about OCV over a frequency range of 1 MHz to 1 Hz, with a potential amplitude of 10 mV.

Bulk Electrolysis. Bulk electrolysis experiments were performed in a custom glass H-type cell comprised of two electrolyte chambers (5 mL), separated with an ultra-fine glass frit (P5, Adams and Chittenden) to minimize crossover, as described in prior literature.[9] Both chambers were stirred continuously during cycling. Reticulated vitreous carbon (100 PPI, Duocell) was used as the working and counter electrode, with a fritted Ag/Ag^+ quasi-reference electrode. A BioLogic VSP potentiostat was used to apply a constant current equivalent to a C-rate of 1C (0.67 mA). Potential cutoffs (0.55 to 0 V and -1.7 to -1.2 V for the positive and negative experiments, respectively) and a 100% SOC coulombic cutoff were used during cycling. A 3 mm diameter glassy carbon working electrode (BASi) was used to record CVs before and after cycling. For each test, both active species (10 mM total) were dissolved in MeCN.

Flow Cell. The flow cell used in this study is similar to previous literature reports (Figure 4),[8,18] with interdigitated flow fields (IDFFs) and a geometric active area of 2.55 cm^2. Flow cells were assembled outside of the glove box and then dried under vacuum (-91 kPa_g) for at least 1 h before beginning experiments; all electrochemical measurements were performed inside the glovebox. Backing plates were machined from polypropylene, and flow fields were machined from 3.18 mm thick impregnated graphite (G347B graphite, MWI, Inc.). Electrodes were cut (16.1 mm × 14.1 mm) from 190 ± 30 µm thick carbon paper (25 AA, SGL Group) and used as received, without any pre-treatment. Carbon paper electrodes were layered two pieces thick and compressed by 20 ± 2% in the assembled flow cell, yielding a final total compressed electrode thickness of 304 ± 49 µm. A single layer of Daramic 175 was used as received as the cell separator. Teflon gaskets sealed the separator and electrodes inside the cell. Sealed jars (10 mL, Savillex), made from perfluoroalkoxy alkane (PFA), served as the electrolyte reservoirs. A peristaltic pump (Masterflex L/S Series) was used to drive electrolyte through the flow cell and reservoirs. Norprene tubing (Masterflex) was used inside the peristaltic pump head. PFA tubing (Swagelok) linked together the pump head, flow cell, and reservoirs. All tubing connections were made with pressure rated PFA (Swagelok), Teflon (Swagelok), or stainless steel (McMaster-Carr) compression fittings. Further, all tubing had an inner diameter of 1.6 mm (Figure 5). All flow cell materials (polypropylene, impregnated graphite, PFA, Teflon, stainless steel, and Daramic) were selected in part due to their chemical compatibility with MeCN.

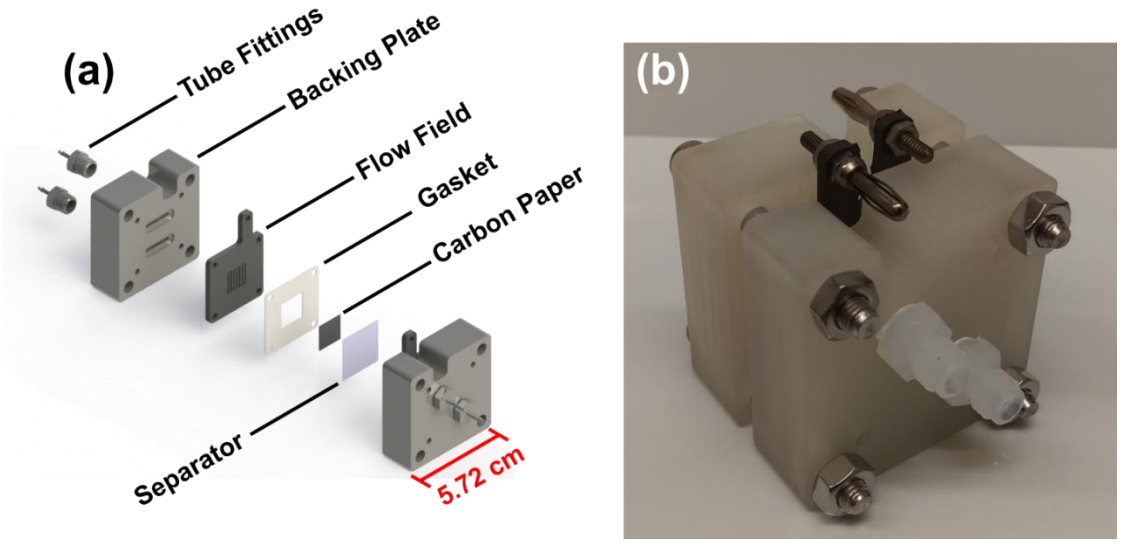

Figure 4: **(a)** Exploded view schematic of the flow cell and **(b)** photograph of the assembled flow cell.

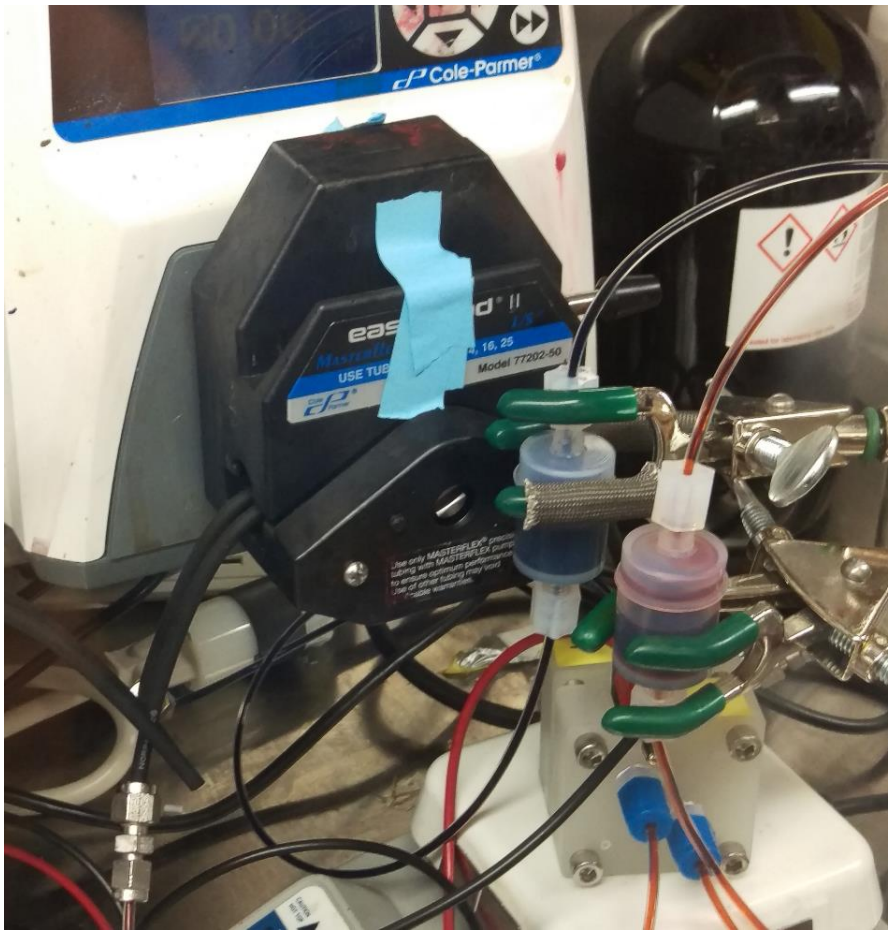

Figure 5: Photograph of the assembled and connected flow cell inside the glove box. In this photograph, the cell is charging, where the negolyte stream is red, and the posolyte stream is dark blue.

Pre-mixed electrolyte (10 mL), containing $Fe(bpy)_3(BF4)_2$ (0.2 M) / Fc1N112-BF_4 (0.2 M) / MeCN, was pumped into each flow cell reservoir. For the redox couples accessed, the theoretical capacity of the electrolyte was 5.36 Ah L^{-1} (53.6 mAh). During the first flow cell cycling experiment, a constant current density of 20 mA cm^{-2} (51 mA) was applied, and cell potential cutoffs of 1.00 – 1.97 V were imposed. The upper voltage cutoff was selected to avoid accessing additional, unstable redox couples of $Fe(bpy)_3(BF_4)_2$, and the lower voltage cutoff ensured complete discharge of the cell. The cell was cycled 10 times over ~5.3 h. Flow cell impedance measurements before and after the first flow cell experiment were recorded about OCV over a frequency range of 100 kHz to 5 mHz, with a potential amplitude of 10 mV. A second flow cell cycling experiment was performed in which constant current cycling (20 mA cm^{-2}) was paused at each half cycle to measure flow cell impedance in a higher frequency regime (100 kHz to 20 Hz).

5.3 Active Species Conductivity

To demonstrate the feasibility of performing electrochemical experiments in solutions of MeCN with no supporting salt, the conductivities of the active species are measured and compared to those of supporting salts typically employed in NAqRFBs. Figure 2 illustrates the high conductivities afforded by 0.2 M of the ionic active species in MeCN, especially in comparison to 0.2 M lithium tetrafluoroborate ($LiBF_4$) and tetraethylammonium tetrafluoroborate ($TEABF_4$) in the same solvent. Not shown in this figure is the conductivity of an equimolar solution containing 0.2 M Fc1N112-BF_4 / 0.2 M $Fe(bpy)_3(BF_4)_2$ / MeCN (0.4 M total active species), the electrolyte composition employed later in flow cell experiments, which is 22.5 mS cm^{-1}.

The conductivities of the ionic species increase in the following order: $LiBF_4$ < Fc1N112-BF_4 < $TEABF_4$ < $Fe(bpy)_3(BF_4)_2$. $LiBF_4$ likely exhibits the lowest conductivity because Li^+ is a hard acid and will strongly interact with BF_4^-, a hard base. This interaction leads to a low degree of dissociation and subsequently lower ionic strength in solution for the Li^+ cation salt as compared to the larger and more polarizable TEA^+, $Fc1N112^+$, and $Fe(bpy)_3^{2+}$ cations.[19] $Fe(bpy)_3(BF_4)_2$ exhibits an enhanced conductivity relative to the other salts considered because $Fe(bpy)_3^{2+}$ is a divalent cation, leading to a higher ionic strength of the $Fe(bpy)_3(BF_4)_2$ solution as compared to the monovalent cation salts. Since the conductivities of the model ionic active species (Fc1N112-BF_4 and $Fe(bpy)_3(BF_4)_2$) are on the same order of magnitude as $TEABF_4$, a typical supporting salt for NAqRFBs,[8,10,16] they lend themselves for implementation in electrochemical systems without supporting salt.

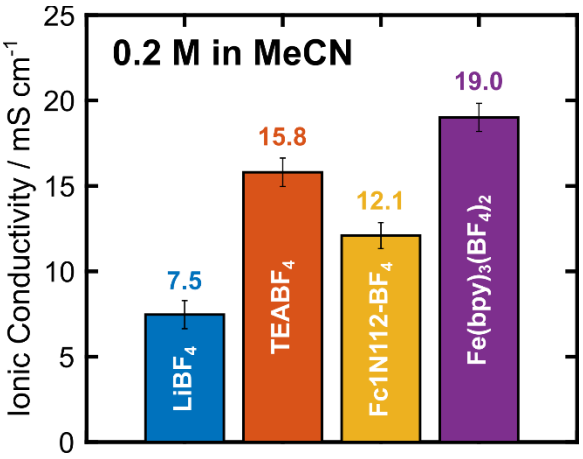

Figure 6: Comparison of electrolyte ionic conductivities for solutions containing 0.2 M of $LiBF_4$, $TEABF_4$, Fc1N112-BF_4, or $Fe(bpy)_3(BF_4)_2$ in MeCN. Error bars represent 95% confidence intervals of the standard error.

5.4 Cyclic Voltammetry

Cyclic voltammetry is used to determine if the active species maintain their redox activity in the absence of supporting salt, while further validating that the electrolytes exhibit sufficient ionic conductivity to perform electrochemical measurements. Figure 3 (solid lines) displays CVs of solutions containing the individual active species and an equimolar mixture of each in MeCN, all without supporting salt. The redox potentials and peak height ratios are similar to those of solutions at the same concentration in the presence of supporting salt (Table 1).[4,5,9,15] Notably, the redox potential of Fc1N112-BF_4 is ~70 mV greater than previously reported in a supporting electrolyte of 0.5 M $TBABF_4$ / MeCN. This discrepancy is reconciled when considering that BF_4^- appears in the Nernst equation, resulting in an increase in the equilibrium potential as the supporting salt is removed.

Further analysis of the peak potentials reveals large peak-to-peak separations (Table 1) in the absence of supporting salt, as is anticipated due to the lower solution conductivity with only 5 mM active species in MeCN.[20] To confirm that this large peak-to-peak separation is primarily a result of low solution conductivity and not sluggish reaction kinetics, the CVs are *i*R-corrected (see dashed lines in Figure 3). The uncompensated solution resistance is measured via electrochemical impedance spectroscopy (Figure 6). The *i*R-corrected CVs exhibit significantly smaller peak-to-peak separation values, but are still larger than those for a solution containing 0.5 M tetrabutylammonium tetrafluoroborate[9] ($TBABF_4$) (Table 1). This indicates that the electrokinetics are slightly slower in the regime of low ion concentration, perhaps due to the limited availability of anions. This interpretation is further supported by the decreased peak separation observed with the addition of more active species (i.e., single species vs. the equimolar mixture). These slight differences are expected to have negligible impact during bulk cycling, especially at the high concentrations used in the flow cell experiments. Overall, these results demonstrate that a supporting salt free, one-electron flow cell utilizing Fc1N112-BF_4 and $Fe(bpy)_3(BF_4)_2$ is feasible and should exhibit similar electrochemical behavior to that of a cell containing a high concentration ($\geq$ 0.5 M) of supporting salt.[9]

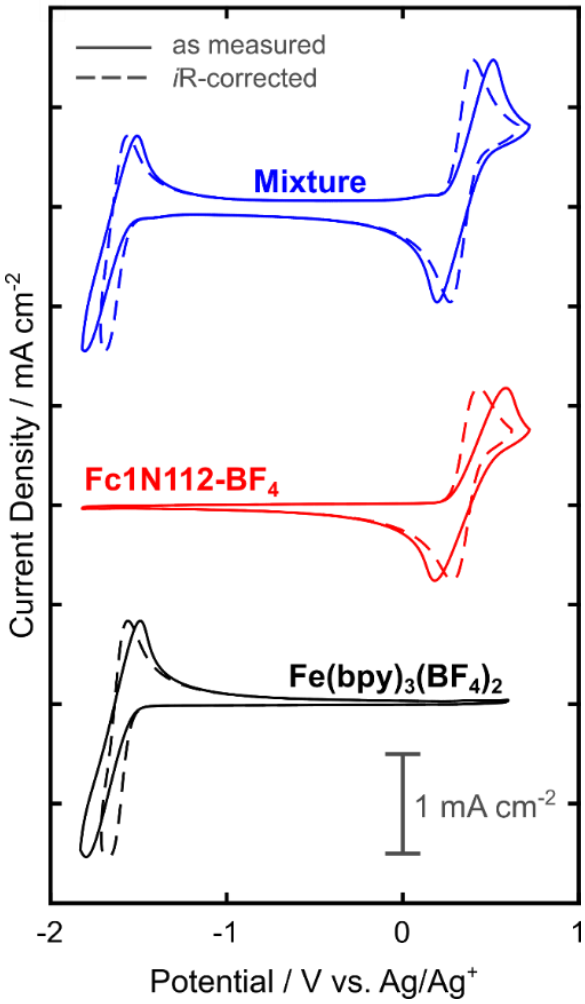

Figure 7: Cyclic voltammograms of 5 mM $Fe(bpy)_3(BF_4)_2$, Fc1N112-BF_4, and an equimolar mixture of each (10 mM total) in MeCN with no supporting salt. For each solution, the solid lines show the data as measured, and the dashed lines represent *i*R-compensated CVs.

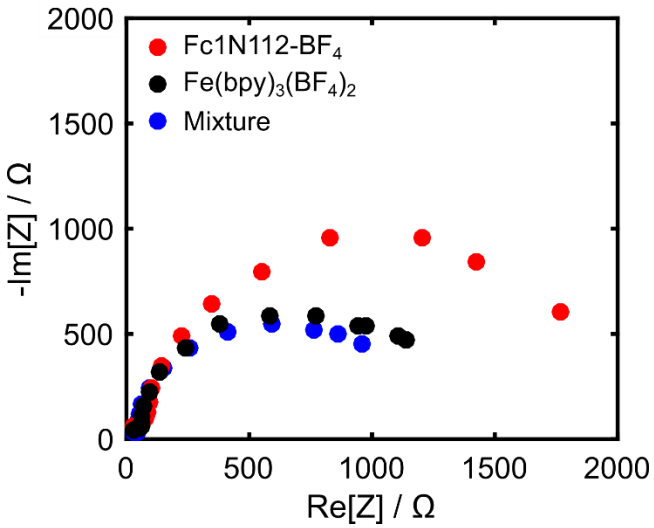

Figure 8: Nyquist plots for CV cells containing 5 mM $Fe(bpy)_3(BF_4)_2$, 5 mM Fc1N112-BF_4, and an equimolar mixture (10 mM total) in MeCN with no supporting salt.

Table 1: Comparative CV analysis of electrolytes containing no supporting salt as measured and with *i*R correction, and electrolytes with a supporting salt concentration of 0.5 M $TBABF_4$.[9] In all cases, the active species concentration is 5 mM.

	5 mM Fc1N112-BF_4			**5 mM $Fe(bpy)_3(BF_4)$**		
	Potential (V vs. Ag/Ag+)	*Peak Height Ratio*	*Peak Separation (mV)*	*Potential (V vs. Ag/Ag+)*	*Peak Height Ratio*	*Peak Separation (mV)*
No Salt (as measured)	0.35	1.0	405	-1.65	0.9	310
No Salt (*i*R-corrected)	0.36	1.0	147	-1.62	0.9	96
0.5 M $TBABF_4$[9]	0.28	1.0	81	-1.65	0.9	66

5.5 Bulk Electrolysis

Bulk electrolysis experiments are used to determine if a cell containing a mixture of $Fe(bpy)_3(BF_4)_2$ and Fc1N112-BF_4 in MeCN (without supporting salt) will access the desired redox couples during cycling. Figure 4 displays capacity retention plots and potential curves for cells cycling through either a single positive or a single negative electron transfer event. In both cases, the plateaus observed during cycling occur at the expected potentials based on CV (Figure 3) and

demonstrate that fonly the desired redox couples are accessed. Furthermore, the results are consistent with those reported in the literature.[4,9] Fc1N112-BF_4 exhibits no detectable capacity fade over the 10 cycles (Figure 4a), which is in agreement with prior reports.[5,9] Not unexpectedly, CVs before and after the bulk electrolysis experiment (Figure 8) show little to no evidence of degradation. Conversely, $Fe(bpy)_3(BF_4)_2$ exhibits capacity decay over the course of the experiment due to the irreversibility of the negative couple.[9] CVs indicate that peak heights associated with the $Fe(bpy)_3^{2+}$ / $Fe(bpy)_3^{+}$ couple decrease after cycling, confirming active species degradation (Figure 8). Despite the suboptimal capacity retention of $Fe(bpy)_3(BF_4)_2$, in both cases the bulk electrolysis cells access the redox couples of interest, confirming the feasibility of using these model active species in a proof-of-concept flow cell without supporting salt.

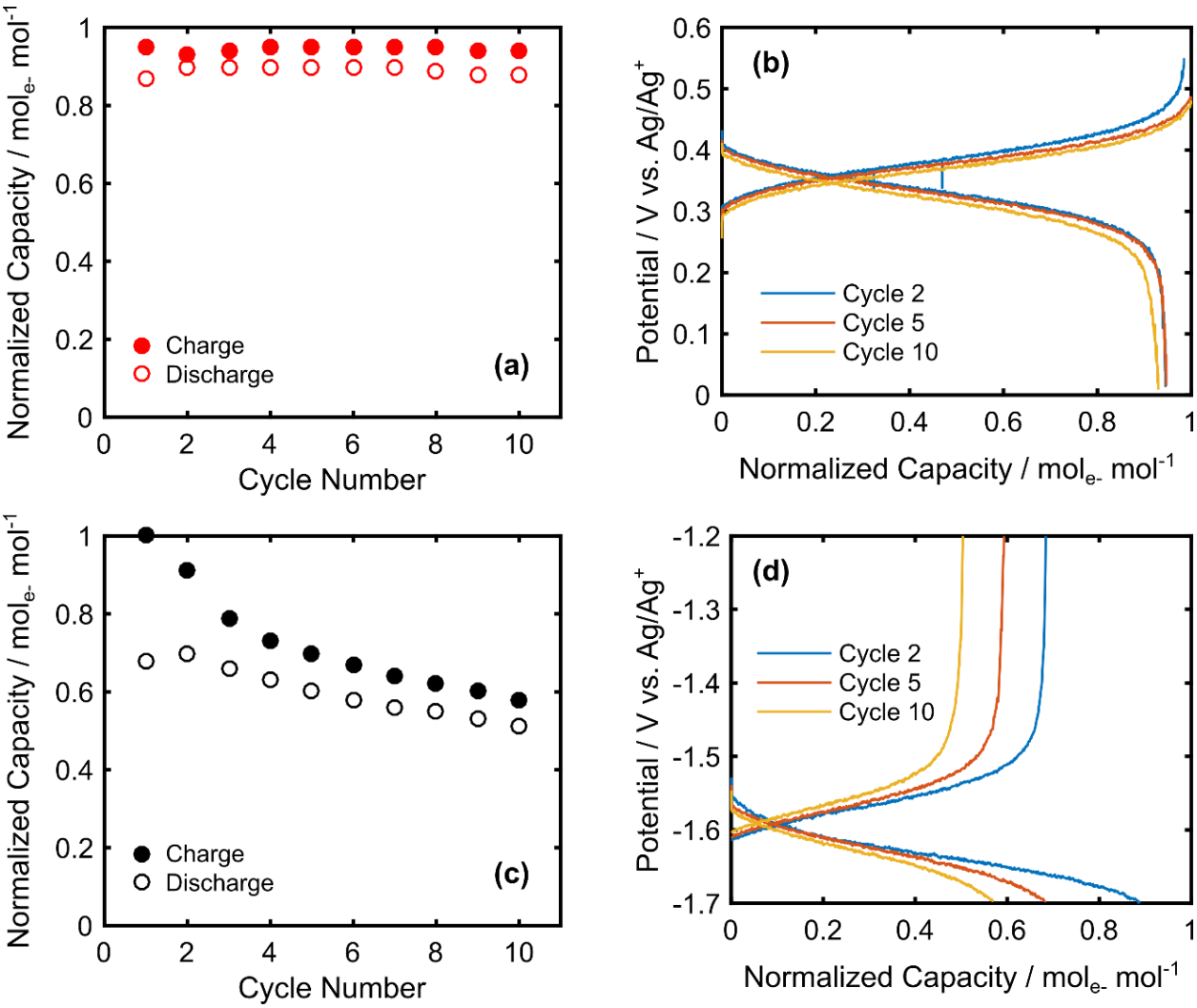

Figure 9: Bulk electrolysis of equimolar mixtures (5 mM each) of $Fe(bpy)_3(BF_4)_2$ and Fc1N112-BF_4 in MeCN, without supporting salt. **(a)** Capacity retention of the mixture, normalized to the theoretical capacity and **(b)** representative charge / discharge curves through a single positive electron transfer. **(c)** Capacity retention, normalized to the theoretical capacity and **(d)** representative charge / discharge curves through a single negative electron transfer.

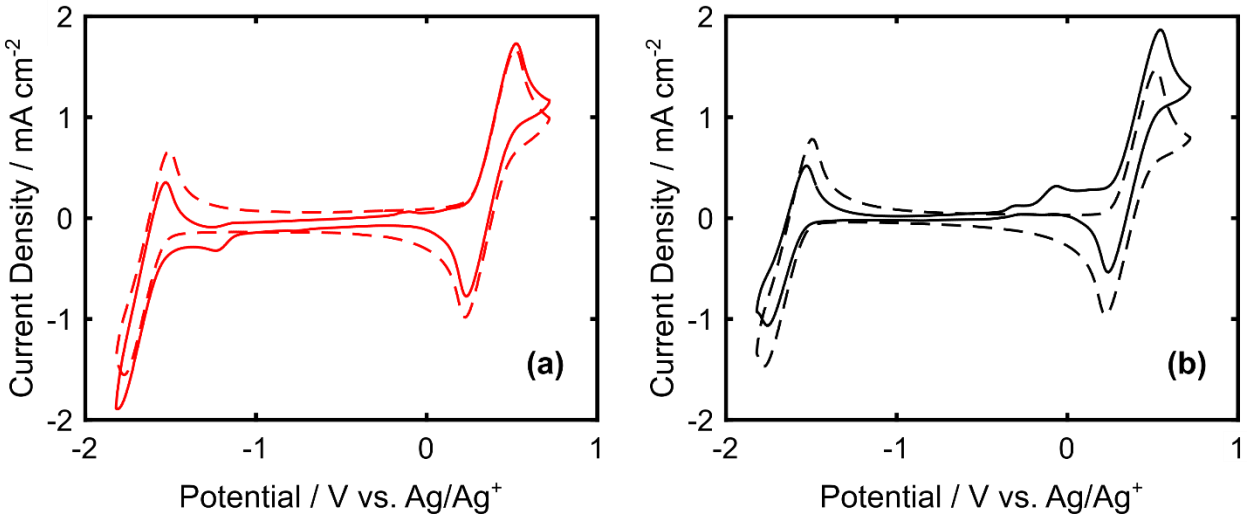

Figure 10: CVs before (dashed) and after (solid) 10 cycles in a bulk electrolysis cell for an equimolar mixture (10 mM total) of $Fe(bpy)_3(BF_4)_2$ and Fc1N112-BF_4, through a single **(a)** positive and **(b)** negative electron transfer. CVs are not *i*R-corrected.

5.6 Proof-of-Concept Flow Cell

The conductivities and fundamental electrochemical properties of the model ionic active species, $Fe(bpy)_3(BF_4)_2$ and Fc1N112-BF_4, are attractive for incorporation into a proof-of-concept, supporting salt free NAqRFB,. The flow cell has a similar architecture to a high performance all-vanadium flow cell,[21] modified for chemical compatibility with NAq electrolytes.[8,18] Since anion-exchange membranes exhibit limited stability in MeCN,[22,23] Daramic is selected for use as the separator due to its chemical stability in the electrolyte of interest, ensuring that separator degradation would not be a confounding factor in evaluating flow cell performance. Due to the high porosity (58%) and large characteristic pore sizes (~100 nm) for this separator, crossover is expected in these experiments, so both reservoirs are filled with an equimolar mixture of 0.2 M $Fe(bpy)_3(BF_4)_2$ / 0.2 M Fc1N112-BF_4 / MeCN. Prior demonstration studies on RFBs have utilized pre-mixed electrolytes to mitigate effects of rapid crossover in the first few cycles,[9,17,24] although mixed active species electrolytes will be too expensive to implement in grid-scale devices.[1,2] One additional drawback of this configuration is the limited operating concentration of each active species. Adding supporting salt can limit the solubility of active species,[9,12,13] and similar decreases are observed with the addition of other ionic active species. As a result, an active species concentration of 0.2 M ensures that the species remain soluble at all relevant SOCs.

The flow cell also employs interdigitated flow fields (IDFFs) with carbon paper electrodes. Prior literature has suggested that IDFFs will offer the best performance for large-scale RFBs by

balancing cell ASR and pressure drop.[21,25] Additionally, thin carbon paper electrodes offer a balance of high surface area, low ohmic losses, and facile mass transport.[8,26] Despite the relatively thick Daramic separator (175 μm), the cell exhibits an ohmic contribution (R_Ω, Ω cm^2) to the ASR of just 3.95 Ω cm^2 (Figure 5a) before cycling, a value similar to those reported in a prior flow cell study employing a Daramic separator and MeCN solvent.[16] Combining the IDFF with carbon paper electrodes alleviates mass transfer resistances at each electrode,[8] leading to a flow cell with a total ASR of 7.52 Ω cm^2, determined from an impedance measurement after cycling (Figure 5a, after). Increasing the active species concentration could further reduce mass transfer limitations, as well as improve ionic conductivity, subsequently decreasing the ohmic contribution to the ASR as well.

Further analysis of the impedance spectra reveals that, prior to cycling, the cell exhibits an unbounded, high overall impedance (Figure 5a, before). Since only the fully discharged active species ($Fe(bpy)_3^{2+}$ and $Fc1N112^+$) are present before cycling, the discharge reaction is heavily mass transfer limited and cannot proceed. After cycling, however, residual charged ($Fe(bpy)_3^+$ and $Fc1N112^{2+}$) and discharged species allow for the electrochemical reactions to proceed in either the forward or reverse directions, significantly improving the mass transfer characteristics of the cell at open-circuit voltage (OCV). The bounded semicircle observed after cycling (Figure 5a, after), represents a diffusive mass transfer limitation through a boundary layer of finite thickness.[27] The low-frequency intercept, on the Nyquist plot exhibiting a bounded mass transfer element (Figure 5a, after), represents the total direct current (DC) cell resistance, at a particular SOC, and is typically a good measure of the flow cell ASR.[8,16,18,28]

The relatively low ASR in this study, as compared to those reported for other NAqRFBs,[16,17,29] allows for constant current cycling at a current density of 20 mA cm^{-2}, which is among the highest reported for NAqRFBs.[30,31] Figure 9b illustrates cycling curves of the proof-of-concept supporting salt free NAqRFB, with single charge and discharge plateaus corresponding to the desired one-electron transfer processes and a nominal cell potential of ~1.9 V. To avoid accessing the additional, less stable redox couples of $Fe(bpy)_3(BF_4)_2$ (Figure 9),[9,15] an upper cell potential cutoff of 1.97 V is employed. This cutoff limited the available capacity (Figure 5c) of the first cycle to 32.8% (1.76 Ah L^{-1}) of the theoretical capacity (5.36 Ah L^{-1}). We also limit cycling experiments to 10 cycles due to the known long term instability of $Fe(bpy)_3(BF_4)_2$.[9,15] After the

first cycle, the coulombic, voltaic, and energy efficiencies are constant for the remaining 9 cycles, with mean values of 87.3 ± 0.1%, 87.5 ± 0.1%, 76.4 ± 0.1%, respectively (Figure 5d).

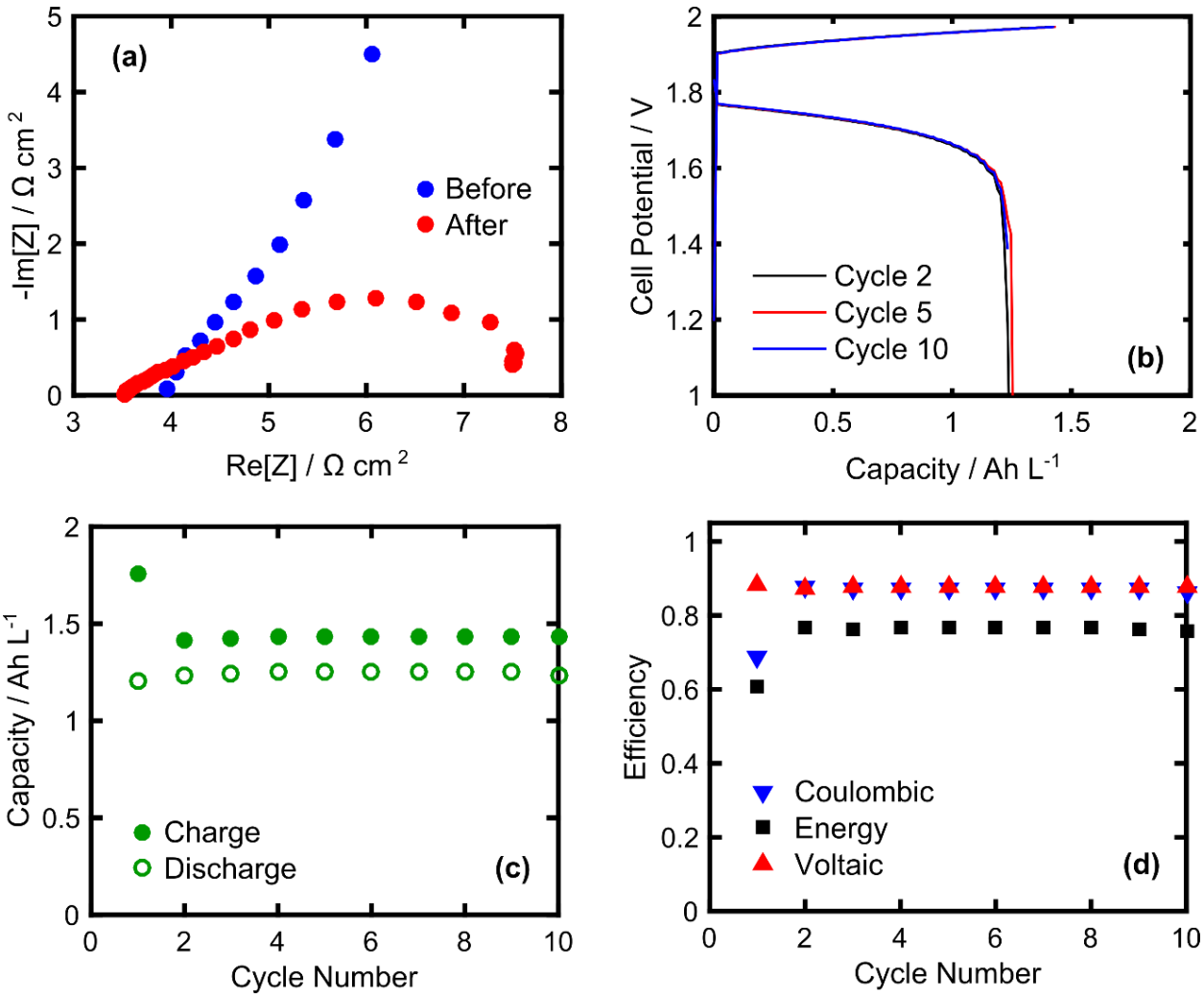

Figure 11: Cycling performance of a supporting salt free NAqRFB employing 0.2 M $Fe(bpy)_3(BF_4)_2$ / 0.2 M Fc1N112-BF_4 / sMeCN: **(a)** Nyquist plots before and after 10 cycles, **(b)** representative charge / discharge curves, **(c)** capacities, and **(d)** efficiencies. The theoretical capacity is 5.36 Ah L^{-1} (53.6 mAh), and 10 full cycles completed in ~5.3 h.

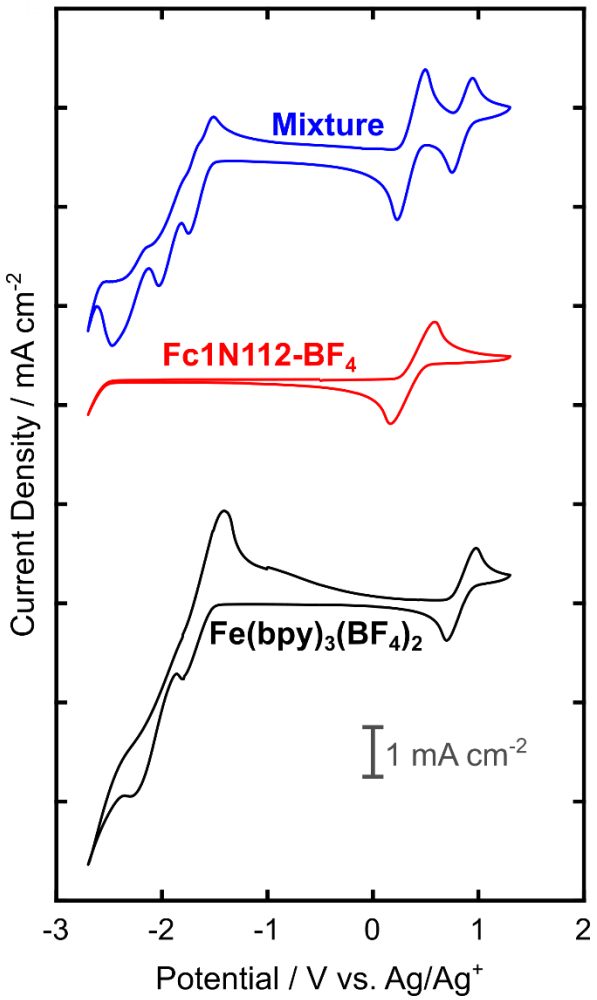

Figure 12: CVs of 5 mM $Fe(bpy)_3(BF_4)_2$, 5 mM Fc1N112-BF_4, and an equimolar mixture (10 mM total) of each active species in MeCN without supporting salt, across the entire redox active window of $Fe(bpy)_3(BF_4)_2$. CVs are not *i*R-corrected.

Notably, the capacity retention during flow cell cycling is higher than that observed during bulk electrolysis cycling for $Fe(bpy)_3(BF_4)_2$. This result is counterintuitive given the higher concentration of active species employed in the flow cell experiment (0.2 M) as compared to the bulk electrolysis experiment (5 mM) but can be reconciled when considering differences in the accessed capacity. The bulk electrolysis experiments access nearly 100% of the theoretical capacities, as compared to < 33% for the flow cell experiment. Since a smaller fraction of the theoretical capacity is accessed in the flow cell experiment, deleterious side reactions associated with the less stable, reduced $Fe(bpy)_3(BF_4)_2$ species do not degrade the observed capacity as rapidly as in the bulk electrolysis experiment. This phenomena has been reported in prior literature

for battery systems with low accessed capacities.[32,33] While the low accessed capacity in this demonstration flow cell is not useful for a grid scale device, the cycling results sufficiently illustrate a proof-of-concept flow cell operating with redox active ions to completely remove the supporting salt.

This proof-of-concept flow cell displays cycling efficiencies similar to state-of-the-art NAqRFBs described in the literature,[16,17] even without any supporting salt. Moderate current density and voltaic efficiencies are achieved because of the high separator conductivity and favorable mass transfer characteristics. The high separator conductivity is achieved by using a microporous separator, in which case the electrolyte conductivity defines the conductivity through the separator pores. Since Daramic is a passive separator, the migration of BF_4^- anions through the separator is sufficiently rapid to afford simultaneously charge balance and moderate currents across the range of accessed SOCs. Critically, the BF_4^- anions act as both charge carriers and charge balancing species in the relevant electrochemical reactions.

To highlight further the dual functionality of the BF_4^- anions, which are associated with the ionic redox active species, we perform a second flow cell cycling experiment where R_Ω is recorded at every half cycle. Figure 6 shows that R_Ω remains nearly constant, oscillating by ± 4.0% about a mean value of 3.48 Ω cm^2. The small oscillations in R_Ω between half cycles (inset Figure 6), are likely caused by variations in ion-pair association constants as a function of SOC,[18,34] subsequently changing the effective conductivity of the separator and porous electrodes. Oscillations in electrolyte conductivity as a function of SOC are common during RFB cycling, as demonstrated for the all-vanadium RFB[34] and quantified in one NAqRFB electrolyte study.[18] Ultimately, the data in Figure 6 points to a cell devoid of supporting salt that maintains R_Ω values comparable to the contemporary literature.[16]

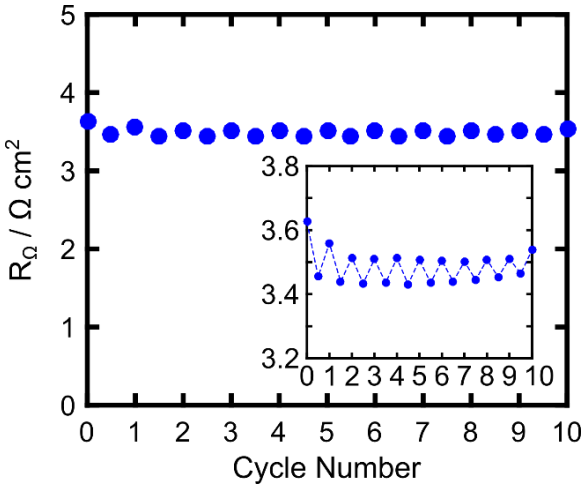

Figure 13: Ohmic contribution to cell ASR measured every half cycle for a supporting salt free NAqRFB. The electrolyte composition is 0.2 M $Fe(bpy)_3(BF_4)_2$ / 0.2 M Fc1N112-BF_4 / MeCN. Inset: Expansion in the R_Ω range of 3.2 – 3.8 Ω cm^2, where the dashed line serves as a visual guide. R_Ω is smaller in the cell's charged state.

5.7 Chemistry-Agnostic Techno-Economic Analysis of Salt Free NAqRFBs

To investigate the financial benefits of removing, or minimizing, the supporting salt requirement in NAqRFB electrolytes, we perform a chemistry-agnostic techno-economic analysis to quantify how salt cost and concentration affect battery price. Techno-economic analysis is a powerful tool for evaluating the price performance of an energy storage system by relating the total battery price to material properties, electrochemical performance, and component cost parameters. Given that the proof-of-concept flow cell does not have sufficiently stable or low cost active materials, as well as an insufficient cell potential, we develop a chemistry-agnostic representation that illustrates the cost savings afforded by minimizing supporting salt concentration for a variety of active species costs, salt costs, and cell potentials.

This work employs a prior model developed by Dmello and Milshtein *et al.*,[2] which considers the reactor cost (C_r), electrolyte cost (C_{el}), additional cost (C_{add}), and balance-of-plant (BOP) cost (C_{BOP}) contributions to the battery price per unit energy (P_0 / E_d (\$ kWh^{-1})), as shown in Equation (4). The reactor cost incorporates the costs of bipolar plates, membranes, and seals, as well as the reactor ASR and battery discharge time. The BOP costs account for auxiliary equipment such as pumps, sensors, tanks, pipes, and heat exchangers, while the additional costs account for overhead, labor, profit margin, and depreciation. Detailed assumptions and calculations of the reactor, additional, and BOP costs are available elsewhere.[1,2] Note that this work considers a

future-state battery price, with a 5 h discharge time,[1,2,35,36] which does not include the cost of installation or power conditioning systems (e.g., inverter), as opposed to a system price that does incorporate such costs.[2] A prior RFB cost modeling study has estimated that installation and power conditioning systems would contribute future-state costs of \$30 kWh^{-1} and \$20 kWh^{-1} (\$100 kW^{-1} over 5 h discharge), respectively, to the RFB system price.[1] Hence, to achieve the DOE system price target of \$150 kWh^{-1},[35,36] we can afford a \$100 kWh^{-1} battery price.[2]

$$\frac{P_0}{E_d} = C_r + C_{el} + C_{add} + C_{BOP} \tag{4}$$

To calculate the electrolyte cost, a detailed model (Equation (5)) explicitly accounts for the costs associated with the electrolyte materials, namely the active species, solvent, and salt.[2] The electrolyte material costs are comprised of the following parameters: M (kg mol^{-1}) is the molar mass of the active species, s is the stoichiometric coefficient of the discharge reaction, χ is the depth-of-discharge, n_e is the number of electrons stored per mole of active material, c_m (\$ kg^{-1}) is the active species cost per unit mass, b (mol kg^{-1}) is the harmonic mean molality of the active species across both electrodes, c_{sol} (\$ kg^{-1}) is the solvent cost per unit mass, M_{salt} (kg mol^{-1}) is the molar mass of the salt, c_{salt} (\$ kg^{-1}) is the salt cost per unit mass, and r_{salt} is the arithmetic mean ratio of moles of salt per mole of active species across both electrodes. The +/– subscripts denote the posolyte and negolyte active materials, respectively. The electrolyte materials costs are normalized by the total discharge energy of the battery, encompassed by the following additional parameters: F (kAh mol^{-1}) is the Faraday constant, and U (V) is the cell potential, while ε_e, ε_q, and ε_v are the energy, coulombic, and voltaic efficiencies, respectively. Here we assume an active species molality of 3 mol kg^{-1}. Assumptions for the values of all other parameters not outlined in this work, are described in detail by Dmello and Milshtein *et al.*[2]

$$C_{el} = \frac{1}{\varepsilon_e \varepsilon_q \varepsilon_v F U}\left(\frac{s_+ M_+}{\chi_+ n_{e+}} + \frac{s_- M_-}{\chi_- n_{e-}} + \frac{2}{b} c_{sol} + 2 r_{salt} M_{salt} c_{salt}\right) \tag{5}$$

To illustrate the benefits of reducing salt cost contributions, we define the salt cost factor $\left(C_{salt}^{\$}\right)$ and the active material cost factor $\left(C_m^{\$}\right)$ in Equations (6) and (7), respectively, both of which have units of dollars per mole of electrons $\left(\$\ mol_{e^-}^{-1}\right)$:

$$C_{salt}^{\$} = 2 r_{salt} M_{salt} c_{salt} \tag{6}$$

$$C_m^{\$} = \frac{sM}{\chi n_e} c_m \tag{7}$$

Figure 7 shows the relationship between battery price and the salt cost factor for various cell potentials and active material cost factors. In general, as cell potential decreases, the battery price reduces more rapidly with decreasing $\left(C_{salt}^{\$}\right)$, showing that RFB price becomes more sensitive to variations in $\left(C_{salt}^{\$}\right)$, at lower cell potentials. Furthermore, battery price rises with increasing $\left(C_{salt}^{\$}\right)$, but variations in $\left(C_m^{\$}\right)$ do not affect the slopes of the price curves in Figure 7. Critically, to achieve the recommended battery price of \$100 kWh^{-1},[2] NAqRFBs will require high cell potentials near ~3 V and values of $\left(C_{salt}^{\$}\right)$ near zero,[1,2] the combination of which has yet to be experimentally realized. Decreasing the salt molecular weight (small M_{salt}) or identifying low cost salts (small c_{salt}) are two strategies to decrease $\left(C_{salt}^{\$}\right)$, but considering the prevalence of salts with fluorinated anions in NAqRFB literature, identifying salts with molecular weights lower than that of $LiBF_4$ (93.75 g mol^{-1}) or costs under \$20 kg^{-1} [1] seems unlikely in the near term. In this work, we pursue a third option of minimizing r_{salt}, by removing the salt altogether and setting $r_{salt} = 0$, which Figure 7 and Equation (5) illustrate is a powerful pathway towards economically viable NAqRFBs.

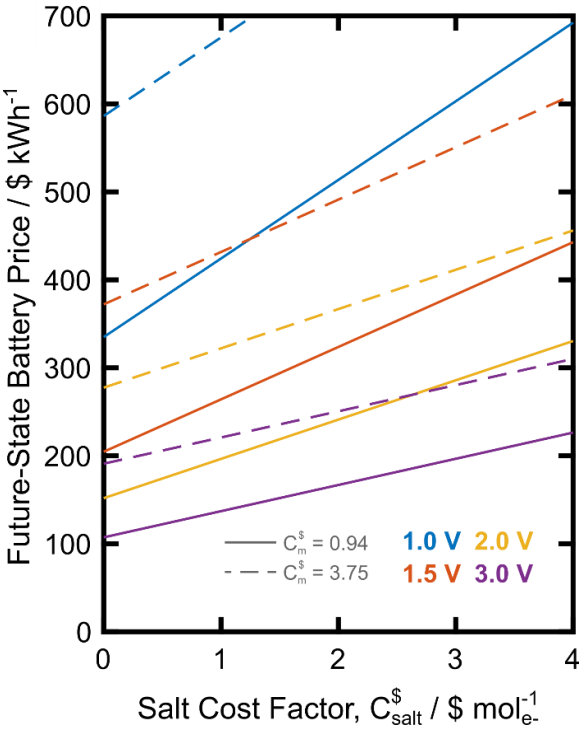

Figure 14: Future-state battery price as a function of salt cost factor $\left(C_{salt}^{\$}\right)$ for various cell potentials (U). Solid lines denote active material cost factors of $C_m^{\$} = 0.94$ while dashed lines denote $C_m^{\$} = 3.75$. As practical examples, consider a cell with a depth-of-discharge (χ) of 80%, stoichiometric coefficients (s) equal to 1, and active material molecular weight (M) of 150 g mol^{-1}. Then, $C_m^{\$} = 0.94$ would represent an active material with a cost (c_m) of \$5 kg^{-1}, and $C_m^{\$} = 3.75$ would represent an active material with a cost of \$20 kg^{-1}. Further, $C_{salt}^{\$} = 2$ could represent a salt with molecular weight (M_{salt}) of 100 g mol^{-1} and cost (c_{salt}) of \$20 kg^{-1} dissolved in a ratio of 0.5 moles of salt per mole of active species (r_{salt} = 0.5).

5.8 Conclusions

We present a proof-of-concept NAqRFB operating in the absence of supporting salt, utilizing Fc1N112-BF_4 and $Fe(bpy)_3(BF_4)_2$ as model ionic active materials. Efficiencies comparable to state-of-the-art NAqRFBs that employ high concentrations of supporting salt are observed over 10 cycles at a moderate current density (20 mA cm^{-2}). This operation is possible due to the high conductivities of the active species in MeCN, which remain as ions across all relevant SOCs. Solutions of 0.2 M Fc1N112-BF_4 and $Fe(bpy)_3(BF_4)_2$ in MeCN display conductivities of 12.1 and 19.0 mS cm^{-1}, respectively, which is ~2 times higher than the conductivity of 0.2 M $LiBF_4$ and comparable to 0.2 M $TEABF_4$ in the same solvent. Furthermore, a chemistry-agnostic techno-economic analysis highlights the potential cost savings of minimizing salt content in NAqRFBs of varying active material cost, salt cost, and cell potential. Overall, this paper offers proof-of-concept

of a NAqRFB operating without supporting salt, opening a pathway for exceptional performance and cost savings.

While the model active species employed in this work are too expensive or unstable for practical grid implementation,[1,2,9,15] our investigation highlights the promise of utilizing ionic redox-active species to enable cost effective NAqRFBs without sacrificing performance. Designing lower-cost counter-anions to replace the existing, expensive fluorinated options (e.g., tetrafluoroborate, hexafluorophosphate) could lead to additional cost savings. Further, ionic modification of otherwise neutral redox active compounds,[4,5] or implementation of deep eutectic, redox active melts[37–39] could be powerful approaches in realizing electrolytes with low salt content. Redox active ionic liquids,[40,41] adapted for flow battery applications, represent an extreme realization of the supporting salt free concept by enabling ultra-high concentration or even solvent free electrolytes. Tailoring ionic active species to display desirable physicochemical (i.e., high solubility[30], low viscosity) and electrochemical properties (i.e., extreme redox potentials[2], stability[30]) will enable the extension of the supporting salt free concept to more practical NAqRFB prototypes.

5.9 References

1. R. M. Darling, K. G. Gallagher, J. A. Kowalski, S. Ha, and F. R. Brushett, *Energy Environ. Sci.*, **7**, 3459–3477 (2014).
2. R. D. Dmello, J. D. Milshtein, F. R. Brushett, and K. C. Smith, *J. Power Sources*, **330**, 261–272 (2016).
3. J. Huang et al., *Adv. Energy Mater.*, **5**, 1401782 (2015).
4. L. Cosimbescu et al., *Sci. Rep.*, **5**, 14117 (2015).
5. X. Wei et al., *Adv. Energy Mater.*, **5**, 1400678 (2014).
6. P. J. Cabrera et al., *J. Phys. Chem. C*, **119**, 15882–15889 (2015).
7. P. J. Cabrera et al., *Inorg. Chem.*, **54**, 10214–10223 (2015).
8. J. D. Milshtein et al., *Energy Env. Sci*, **9**, 3531–3543 (2016).
9. S. M. Laramie, J. D. Milshtein, T. M. Breault, F. R. Brushett, and L. T. Thompson, *J. Power Sources*, **327**, 681–692 (2016).
10. W. Wang et al., *Adv. Funct. Mater.*, **23**, 970–986 (2013).
11. A. Z. Weber et al., *J. Appl. Electrochem.*, **41**, 1137–1164 (2011).
12. A. A. Shinkle, T. J. Pomaville, A. E. S. Sleightholme, L. T. Thompson, and C. W. Monroe, *J. Power Sources*, **248**, 1299–1305 (2014).
13. J. R. Dahn et al., *J. Electrochem. Soc.*, **152**, A1283–A1289 (2005).
14. L. Su et al., *J. Electrochem. Soc.*, **163**, A5253–A5262 (2016).
15. M. H. Chakrabarti, R. A. W. Dryfe, and E. P. L. Roberts, *Electrochimica Acta*, **52**, 2189–2195 (2007).
16. I. Escalante-Garcia, J. S. Wainright, L. T. Thompson, and R. F. Savinell, *J. Electrochem. Soc.*, **162**, A363–A372 (2015).

17. X. Wei et al., *Angew. Chem. Int. Ed.*, **54**, 8684–8687 (2015).
18. J. D. Milshtein, J. L. Barton, R. M. Darling, and F. R. Brushett, *J. Power Sources*, **327**, 151–159 (2016).
19. M. Ue, *J. Electrochem. Soc.*, **141**, 2989–2996 (1994).
20. S. R. Belding and R. G. Compton, *J. Electroanal. Chem.*, **683**, 1–13 (2012).
21. R. M. Darling and M. L. Perry, *J. Electrochem. Soc.*, **161**, A1381–A1387 (2014).
22. S. H. Shin, S. H. Yun, and S. H. Moon, *RSC Adv.*, **3**, 9095–9116 (2013).
23. N. S. Hudak, L. J. Small, H. D. Pratt, and T. M. Anderson, *J. Electrochem. Soc.*, **162**, A2188–A2194 (2015).
24. Y. K. Zeng, X. L. Zhou, L. An, L. Wei, and T. S. Zhao, *J. Power Sources*, **324**, 738–744 (2016).
25. C. R. Dennison, E. Agar, B. Akuzum, and E. C. Kumbur, *J. Electrochem. Soc.*, **163**, A5163–A5169 (2015).
26. Q. H. Liu et al., *J. Electrochem. Soc.*, **159**, A1246–A1252 (2012).
27. X.-Z. Yuan, C. Song, H. Wang, and J. Zhang, *Fundam. Appl.-Verl. Lond.* (2010).
28. C.-N. Sun et al., *J. Electrochem. Soc.*, **161**, A981–A988 (2014).
29. M. Park et al., *ACS Appl. Mater. Interfaces*, **6**, 10729–10735 (2014).
30. J. A. Kowalski, L. Su, J. D. Milshtein, and F. R. Brushett, *Curr. Opin. Chem. Eng.*, **13**, 45–52 (2016).
31. W. Duan et al., *J Mater Chem A*, **4**, 5448–5456 (2016).
32. A. J. Smith, J. C. Burns, D. Xiong, and J. R. Dahn, *J. Electrochem. Soc.*, **158**, A1136–A1142 (2011).
33. A. Orita, M. G. Verde, M. Sakai, and Y. S. Meng, *J. Power Sources*, **321**, 126–134 (2016).
34. M. Skyllas-Kazacos and M. Kazacos, *J. Power Sources*, **196**, 8822–8827 (2011).
35. D. Rastler, *Market Driven Distributed Energy Storage System Requirements for Load Management Applications*, Energy and Power Research Institute (2007).
36. U.S. Department of Energy: Office of Electricity Delivery and Energy Reliability, *Energy Storage: Program Planning Document*, (2011).
37. M. A. Miller, J. S. Wainright, and R. F. Savinell, *J. Electrochem. Soc.*, **163**, A578–A579 (2016).
38. L. Bahadori et al., *J. Electrochem. Soc.*, **163**, A632–A638 (2016).
39. M. H. Chakrabarti et al., *Renew. Sustain. Energy Rev.*, **30**, 254–270 (2014).
40. E. Mourad et al., *Electrochimica Acta*, **206**, 3–8 (2016).
41. J. Park, M. Lee, S. Hwang, D. Lee, and D. Oh, "Redox flow battery," US Pat. US 20120171541 A1, Filed October 6, 2012.

6. Relating non-aqueous redox flow battery electrolyte properties with cell performance

This chapter is reprinted from *Journal of Power Sources*, Vol 327, J. D. Milshtein, J. L. Barton, R. M. Darling, F. R. Brushett, 4-acetamido-2,2,6,6-tetramethylpiperidine-1-oxyl as a model organic redox active compound for non-aqueous redox flow batteries, 151–159, Copyright (2016), with permission from Elsevier under license number 4087110125694.

6.1 Introduction

Recent research efforts on RFBs have focused on identifying new organic active materials[1–7] and non-aqueous solvents, which enable high cell voltages[8–10] and high cell energy densities, as a pathway towards low cost batteries. While organic active materials in non-aqueous electrolytes appear to offer a viable route toward next generation RFBs, the field is nascent and many critical system properties remain unexplored. To date, most research activities have focused on molecular discovery and electrochemical characterization under dilute conditions.[1,2,4] Such studies provide valuable information relating to fundamental electrochemical properties (e.g., redox potential, rate constant), but they do not offer much insight on the solution properties (e.g., viscosity, conductivity) of redox electrolytes (solutions comprised of active species, salt, and solvent) containing moderate-to-high concentrations of active materials. The knowledge gap in redox electrolyte properties, at moderate-to-high concentrations, leads to uncertainty in how to effectively design flow cells for non-aqueous RFBs (NAqRFBs); in particular, the increased viscosities and decreased conductivities associated with non-aqueous redox electrolytes, in comparison to aqueous systems, pose a new set of obstacles. Reported NAqRFBs show poor performance and durability, but identifying performance-limiting factors is challenging as cell failure may relate to either active species degradation (e.g., instability, insolubility, incompatibility) or shortcomings in flow cell design (e.g., crossover, membrane degradation, high resistance). Disentangling the effects of a new active species and cell design in NAqRFB studies can be difficult, and, as such, advancing cell engineering for NAqRFBs requires systematic investigations employing redox electrolytes containing near practical active species concentration with well-understood electrochemical and physicochemical properties.

Platform redox chemistries are needed for controlled studies of non-aqueous redox electrolyte properties and associated flow cell performance characteristics. For example, aqueous RFB studies have exploited the VO^{2+} / VO_2^+ redox couple to study cell performance as a function

of cell configuration[11,12] and spatial variation of solution properties in the reactor.[13] To be considered for such applications, a redox active species must be stable over multiple cycles, soluble in the electrolyte of interest (≥ 0.5 M in organic electrolytes), and readily available in the reduced and oxidized states. Ideally, such a redox couple would be commercially available in both oxidation states, considering that chemical or electrochemical redox syntheses can be time and materials intensive, and may introduce impurities. Several candidate materials for NAqRFB studies are viologens, ferrocene, or 2,2,6,6-tetramethyl-1-piperidinyloxy (TEMPO). Viologens offer multi-electron transfer behavior with fast kinetics,[14] but exhibit low, state-of-charge (SOC) dependent solubility and are not readily available in the reduced state. Ferrocene also has stable electrochemical performance[15] and is commercially available (Sigma Aldrich) as both ferrocene and ferrocenium, but ferrocene still suffers from low solubility (< 0.2 M).[16] Finally, TEMPO is a stable, soluble active species with facile kinetics,[3] but is not commercially available in its oxidized form.

A TEMPO analogue, the 4-acetamido-2,2,6,6-tetramethylpiperidine-1-oxyl cation (AcNH-TEMPO$^+$), which is typically paired with a tetrafluoroborate anion ('Bobbitt's Salt'), is an oxoammonium ion commonly used as a chemical oxidant.[17–26] The simpler TEMPO molecule also has a variety of oxidant applications, but the synthesis procedures of and precursors to AcNH-TEMPO$^+$ are cheaper, leading to the commercial availability of AcNH-TEMPO$^+$.[26] The neutral 4-acetamido-2,2,6,6-tetramethylpiperidine-1-oxyl (AcNH-TEMPO) radical molecule is relatively easy to synthesize[26] and is also commercially available as an electron spin resonance spectroscopy standard.[27] TEMPO, and many of its derivatives, have been explored for their electrochemical properties,[28–32] with applications in overcharge protection,[33–35] solid electrodes for stationary batteries,[36,37] and flowing redox electrolytes.[3,38–41] While, in general, the electrochemical behavior of TEMPO-derived molecules appears extensively studied, the properties of AcNH-TEMPO have only been evaluated in aqueous conditions, for dye-sensitized solar cells,[42] and remain unreported in non-aqueous conditions.

We propose the AcNH-TEMPO / AcNH-TEMPO$^+$ redox pair (Figure 1) as a platform chemistry for systematic NAqRFB studies. First, the viscosity, conductivity, density, and spectral properties of redox electrolytes containing AcNH-TEMPO are measured as a function of SOC. Second, the electrochemical properties of the redox pair are investigated. Cyclic voltammetry (CV) provides an initial electrochemical investigation of both AcNH-TEMPO and AcNH-TEMPO$^+$ to

identify its redox potential and reversibility. Third, symmetric flow cell cycling determines the capacity retention of both AcNH-TEMPO species. Finally, we embark on single electrolyte flow cell studies[11,12], with higher concentrations of the AcNH-TEMPO redox pair, to demonstrate NAqRFB reactor performance and quantify performance-limiting factors. Ultimately, these investigations present AcNH-TEMPO as a viable model redox chemistry, which can be used as a tool for NAqRFBs performance diagnostics.

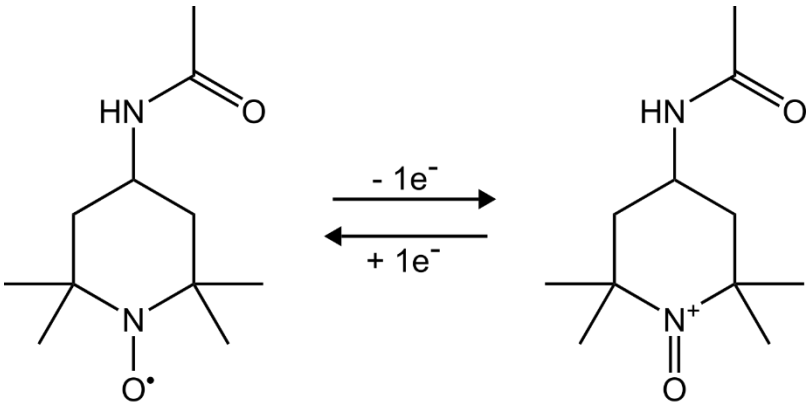

Figure 1: Schema of the redox reaction between AcNH-TEMPO and AcNH-TEMPO$^+$. The counter ion in this work is BF_4^-.

6.2 Experimental

Materials, Equipment, and Uncertainty Analysis. 4-acetamido-2,2,6,6-tetramethylpiperidine-1-oxyl (AcNH-TEMPO, 97 %) and 4-acetylamino-2,2,6,6-tetramethyl-1-oxo-piperidinium tetrafluoroborate (AcNH-TEMPO$^+$, 97 %) were purchased from Sigma-Aldrich and used as received. For electrochemical experiments, lithium tetrafluoroborate ($LiBF_4$, 99.9 %), and propylene carbonate (PC, 99.99 %) were purchased from BASF and used as received. For spectroscopy experiments, $LiBF_4$ (99.99 %) and PC (99.7 %) were purchased from Sigma-Aldrich; PC was dried and stored over molecular sieve beads (Sigma Aldrich, 3A) for at least 12 h before use. Lithium metal foil (99 %) was purchased from Alfa Aesar. All solution preparation and electrochemical experiments were performed in argon-filled glove boxes (O_2 < 1 ppm, H_2O < 0.5 ppm) from Inert Technology, maintained near 25 °C. In flow cell studies, Daramic 175 microporous separator (thickness = 175 μm, porosity = 58 %, mean pore size = 100 nm) was employed as the separator material. All electrochemical measurements were performed using a Biologic-VMP3 potentiostat. All quantitative results reported in figures and tables are mean values

of three independent measurements, unless otherwise explicitly stated. Error bars and uncertainties represent 95 % confidence intervals of the standard error, accounting for experimental uncertainties, measurement noise, and repeatability.

Electrolyte Conductivity Measurements. Conductivity measurements were performed by using a two-electrode Swagelok conductivity cell, similar to those employed previously in literature.[43] A schematic of the conductivity cell employed in this work is provided in Figure 2. The conductivity cell was filled with 700 μL of electrolyte and sealed shut. An impedance measurement was made about the cell open circuit voltage (OCV), with a RMS amplitude of 10 mV, over a frequency range of 1 MHz to 100 Hz. The high frequency intercept of the impedance curve was identified and used as the cell resistance value in subsequent calculations. Ten impedance measurements were performed for each electrolyte aliquot, and these measurements were repeated three times using a fresh electrolyte aliquot. In between measurements, the conductivity cell was rinsed with pure PC. The conductivity cell was calibrated using aqueous conductivity standards, and non-aqueous electrolyte conductivities were determined from total cell resistance measurements and the calibration curve. The following aqueous conductivity standards (Orion^{TM}) were used to build a four-point calibration curve in an ice-water bath (0 $^{\circ}$C): 100 μS cm^{-1}, 1.413 mS cm^{-1}, 12.90 mS cm^{-1}, and 111.9 mS cm^{-1}.

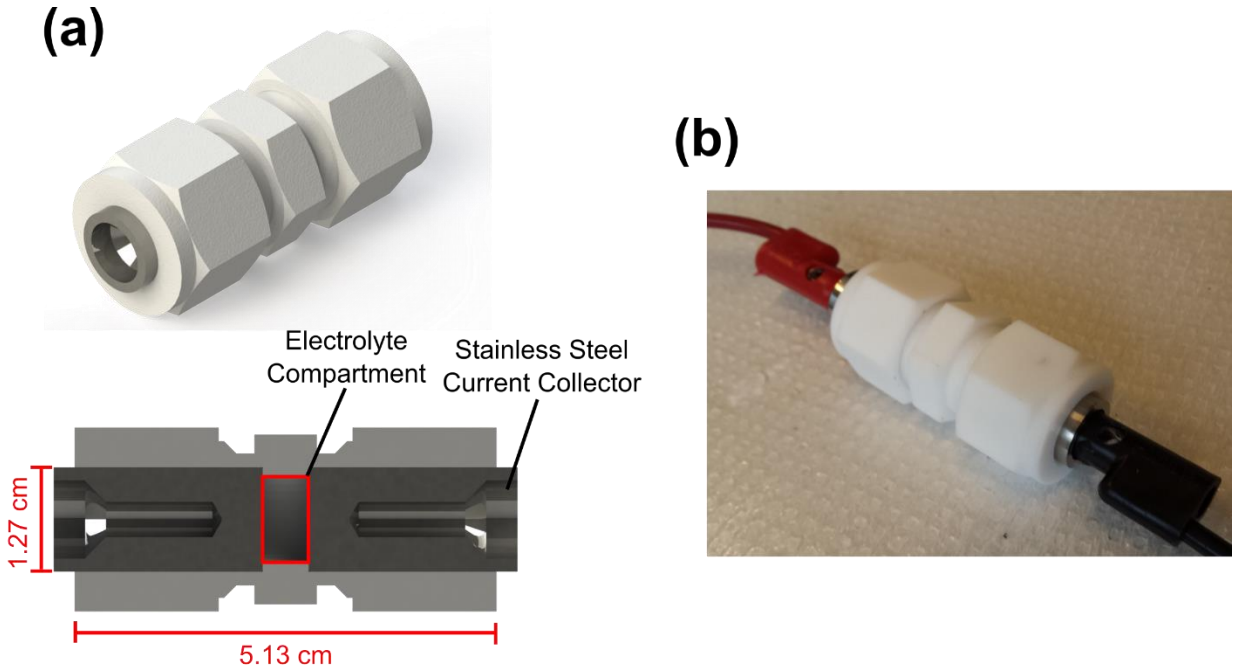

Figure 2: **(a)** Schematic of the Swagelok conductivity cell. **(b)** Digital photograph of the Swagelok conductivity cell. The electrolyte compartment is a cylinder with a height of 5.58 mm and a diameter of 10.67 mm.

Viscosity, Density, and UV-vis Measurements. A vibrational viscometer probe (Viscolite V-700) was used to measure the viscosity of 15 mL electrolyte samples held in glass scintillation vials. Three viscosity measurements were made for each electrolyte composition for one vial of fresh electrolyte. Electrolyte density measurements were performed in triplicate using a balance (Metler-Toledo XP105) and known electrolyte volume. Electrolyte densities were required for viscosity measurements. UV-vis measurements were performed once using a SEC2000 spectrometer (ALS Co., Ltd) with 50 mM total active species in 0.5 M $LiBF_4$ / PC.

Cyclic Voltammetry. CV experiments were performed in three electrode cells consisting of a 3 mm diameter glassy carbon working electrode (CH Instruments), a gold coil counter electrode (CH Instruments), and an un-fritted lithium foil pseudo-reference electrode. The three-electrode cell contained 2 – 5 mL of redox electrolyte, which was comprised of 5 mM active material in 0.5 M $LiBF_4$ / PC. Prior to beginning electrochemical measurements, the glassy carbon electrode was polished using 0.05 μm alumina suspension, sonicated in a water bath, dried in air, and then rinsed with supporting electrolyte (0.5 M $LiBF_4$ / PC) in the glove box. A 100 % resistance compensation (*i*R correction) was applied by the potentiostat during CV experiments. Three CV cycles were performed for each of the following scan rates: 5, 10, 20, 50, and 100 mV s^{-1}. For CV experiments where scan rate was varied, three independent experiments were performed with a freshly polished glassy carbon electrode and freshly prepared redox electrolyte. In the first set of CV experiments, following the scan-rate dependence study, 100 CV cycles were performed at a scan rate of 100 mV s^{-1}; this long duration cycling experiment was performed only once.

$$i_p = 0.4463nFAC\left(\frac{nFsD}{RT}\right)^{\frac{1}{2}} \quad (1)$$

The Randles-Sevcik equation (Equation (1)) was used to calculate the diffusion coefficients of the active species. In Equation (1), i_p is the peak current, n is the number of electrons transferred, A is the electrode surface area, C is the reactant concentration, s is the scan rate, R is the universal gas constant, T is temperature, and D is the diffusion coefficient.[44] For quantitative CV analysis, only the second cycle was considered. Peak currents (i_p) were background corrected using a technique previously employed in literature.[1,45] Redox (half-wave) potentials (E°) were calculated as the mean potential between CV peaks.

Symmetric Flow Cell Cycling. Symmetric flow cell cycling was carried out using a flow cell with flow-through carbon felt electrodes (GFA6, SGL Group), which was previously described by Laramie and Milshtein et al.[46] The separator material was two layers of Daramic 175. The flow cell was assembled outside the glove box and then dried under vacuum (-91 kPa_g) at room temperature for at least 1 h before beginning electrochemical experiments. Glass scintillation vials served as the reservoirs, each filled with 10 mL of redox electrolyte. A peristaltic pump (Masterflex L/S Series) with Norprene tubing (Masterflex, 1.6 mm inner diameter) drove redox electrolyte through the flow cell at 5 mL min^{-1}. The positive reservoir contained a redox electrolyte of 50 mM AcNH-TEMPO / 0.5 M $LiBF_4$ / PC, while the negative reservoir contained 50 mM $AcNH\text{-}TEMPO^+$ / 0.5 M $LiBF_4$ / PC. A constant current density of 2 mA cm^{-2} (9.270 mA), calculated from the geometric electrode area (4.635 cm^2), was applied during cycling, and cell potential cutoffs of -0.4 V to 0.4 V were imposed. Individual charge (or discharge) half-cycles required ~1.25 h to complete, and 20 full cycles completed in 51 h.

Single Electrolyte Flow Cell Experiments. A small volume, custom flow cell (Figure 3) employing an interdigitated flow field was used in single electrolyte diagnostic experiments. The flow field was machined from 3.18 mm thick impregnated graphite (G347B graphite, MWI, Inc.). The end plates were machined from polypropylene, selected due to its chemical compatibility with PC. Electrodes were cut from 300 μm thick carbon paper (35 AA, SGL Group), and compressed by 15.3 % in the assembled flow cell, providing a geometric active area of 2.25 cm^2. A single layer of Daramic 175 served as the separator. Teflon gaskets sealed the separator and electrodes into the cells. Flow cells were initially assembled outside the glove box, and were then dried for at least 1 h under vacuum (-91 kPa_g) before beginning electrochemical testing.

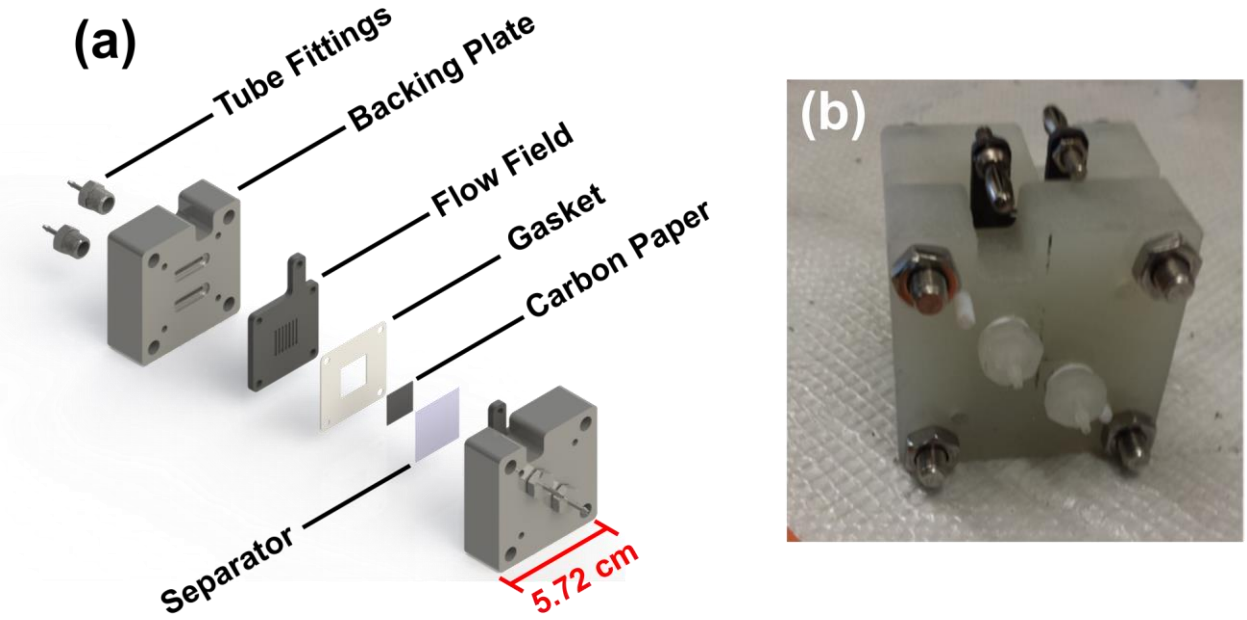

Figure 3: **(a)** Exploded view schematic and **(b)** digital photograph of the flow cell employed in the single electrolyte study. Hardware (i.e., nuts, bolts, O-rings, banana plugs) is not included in the schematic.

A single 10 mL sealed jar (Savillex), made from perfluoroalkoxy alkane (PFA), was filled with redox electrolyte, which was carried into the flow cell at a variable flow rate. A peristaltic pump (Masterflex L/S Series) with a high performance pump head (Masterflex) was used to drive redox electrolyte from the reservoir to the flow cell. PharMed BPT tubing (Masterflex) was used inside the peristaltic pump head, while PFA tubing (Swagelok) connected the pump head, reservoir, and flow cell together. All tubing had an inner diameter of 1.6 mm, and all tubing connections were coupled together with pressure rated PFA or stainless steel compression fittings.

Redox electrolytes were comprised of 0.25 M AcNH-TEMPO / 0.25 M AcNH-TEMPO$^+$ / 1 M $LiBF_4$ / PC. 10 mL of redox electrolyte was pumped into the flow cell system. Impedance measurements were recorded about the OCV, with a RMS amplitude of 10 mV, over a frequency range of 200 kHz to 5 mHz. Polarization measurements were performed by initiating potentiostatic holds for 2 min in 50 mV steps from 0 – 0.5 V. Data points were recorded every 1 s, and the mean current and potential values of the final 75 % of data points were used in the final I-V curves. Impedance and polarization measurements were performed at redox electrolyte flow rates of 2 and 10 mL min^{-1}.

6.3 State of Charge Dependent Solution Properties

Stock redox electrolytes consisting of 0.5 M total active species in 1 M $LiBF_4$ / PC at 5 different SOCs demonstrate variations in redox electrolyte properties as a function of SOC. Although we did not measure solubility limits of AcNH-TEMPO or AcNH-$TEMPO^+$, we found both species to be soluble to at least 0.5 M in our supporting electrolyte of interest (1 M $LiBF_4$ / PC), which is a comparable concentration to state-of-the-art literature engaging in non-aqueous flow cell studies.[3,7,16,47] A digital photograph of these redox electrolytes (Figure 4) shows a marked change in solution color as a function of SOC. To quantify this color change, dilute solutions containing 50 mM active species in 0.5 M $LiBF_4$ / PC undergo a UV-vis study. Figure 5a shows UV-vis spectra in the wavelength (λ) range of interest for AcNH-TEMPO solutions as a function of SOC; note the characteristic spectral peaks at λ = 460 and 479 nm. The absolute absorbance in the range of interest increases in magnitude across all wavelengths as SOC increases, and the peak at 479 nm grows slightly faster (8 %) than the peak at 460 nm. The presence of two distinct spectral features allows for construction of calibration curves (Figure 5b), at two different wavelengths, to correlate absorbance with SOC. Best-fit lines achieve *r*-squared values > 0.999, suggesting that UV-vis could monitor SOC of AcNH-TEMPO-based redox electrolytes during electrochemical experiments.

Figure 4: 0.5 M AcNH-TEMPO solutions in 1 M $LiBF_4$ / PC at 5 SOCs (0 %, 25 %, 50 %, 75 %, and 100 %).

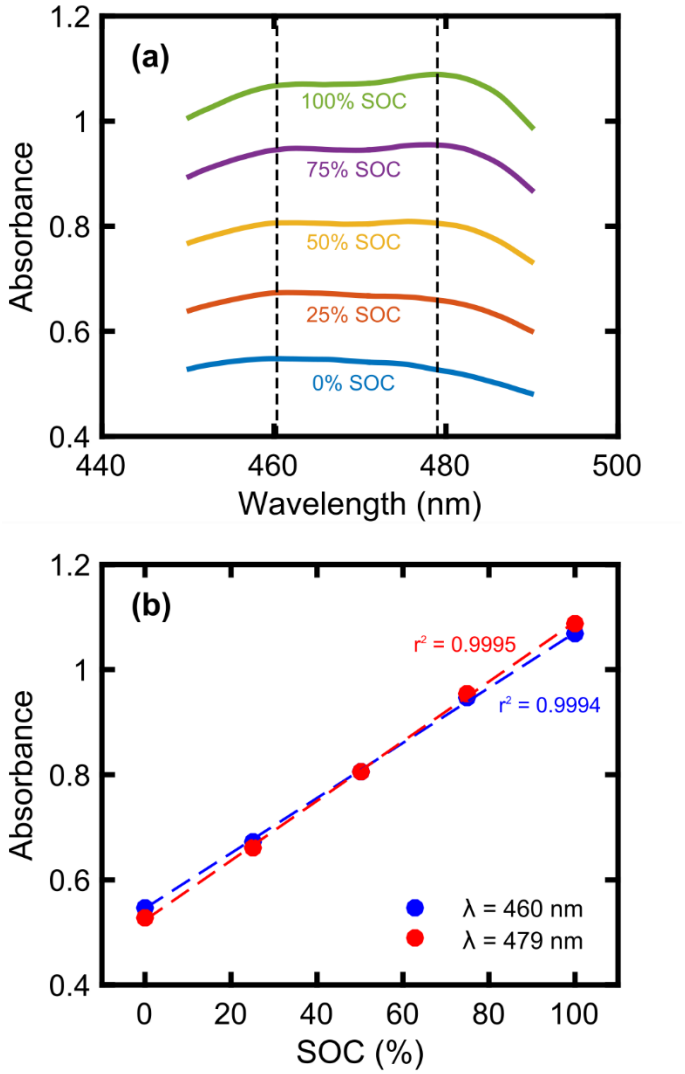

Figure 5: UV-vis absorbance spectra of **(a)** AcNH-TEMPO redox electrolytes at 5 SOCs (0 %, 25 %, 50 %, 75 %, and 100 %), and **(b)** absorbance spectra as a function of SOC at wavelengths of 460 and 479 nm. Redox electrolytes for UV-vis spectra measurements are comprised of 50 mM total active species in 0.5 M $LiBF_4$ / PC.

After investigating the spectral properties of AcNH-TEMPO solutions, the redox electrolytes depicted in Figure 4 are utilized to perform further measurements of other physicochemical solution properties, namely ionic conductivity (Figure 6a) and viscosity (Figure 6b). Table 1 tabulates the conductivities, viscosities, and densities of all electrolytes considered, as well as the pure solvent (PC) and the supporting electrolyte (1 M $LiBF_4$ / PC). As a check to the experimental methods employed in this work, the conductivity and viscosity values of the 1 M $LiBF_4$ / PC supporting electrolyte agree with prior literature.[48]

Table 1: Conductivities (σ), dynamic viscosities (μ), kinematic viscosities (κ), and densities (ρ) of 0.5 M total active species in 1 M $LiBF_4$ / PC ternary electrolytes for various SOCs. Property values are also provided for the pure solvent (PC) and supporting electrolyte (1 M $LiBF_4$ / PC). 95 % confidence intervals are also included.

	PC	**1 M $LiBF_4$ / PC**	**0.5 M AcNH-TEMPO / 1 M $LiBF_4$ / PC**				
SOC	-	-	0 %	25 %	50 %	75 %	100%
$\boldsymbol{\sigma}$ (mS cm^{-1})	-	3.03 ± 0.08	2.23 ± 0.03	2.33 ± 0.07	2.41 ± 0.02	2.47 ± 0.01	2.52 ± 0.02
$\boldsymbol{\mu}$ (mPa · s)	2.4 ± 0.1	6.7 ± 0.1	9.9 ± 0.1	10.9 ± 0.1	11.7 ± 0.1	12.7 ± 0.1	14.4 ± 0.1
$\boldsymbol{\kappa}$ (10^{-6} m^2 s^{-1})	2.0 ± 0.1	5.4 ± 0.1	8.1 ± 0.1	9.1 ± 0.1	9.4 ± 0.1	10.3 ± 0.1	11.5 ± 0.1
$\boldsymbol{\rho}$ (g mL^{-1})	1.208 ± 0.002	1.240 ± 0.002	1.228 ± 0.002	1.205 ± 0.018	1.237 ± 0.003	1.231 ± 0.007	1.252 ± 0.002

Both the conductivity and viscosity of AcNH-TEMPO redox electrolytes increase monotonically as a function of SOC. Typically, increases in viscosity correlate with decreases in ionic conductivity due to lower mobility of the charge carrying species. In the case of AcNH-TEMPO redox electrolytes, the ionic strength increases as a function of SOC; the active species oxidizes from a neutral molecule to a cation, bringing an associated BF_4^- counter-ion. Increasing ionic strength with increasing SOC yields a subsequent increase in conductivity, despite a corresponding increase in solution viscosity. As compared to the supporting electrolyte, solutions containing AcNH-TEMPO exhibited lower conductivities. Additional inter-molecular forces (higher ionic strength) and solute (higher BF_4^- concentration) likely cause solution viscosity to increase with SOC. Viscosities of the redox electrolytes are also higher than the viscosities of the supporting electrolyte or the pure solvent. While redox electrolyte conductivity only varies by 13 % across all SOCs, the viscosity swings by 45 % from 0 – 100 % SOC. Thus, the AcNH-TEMPO redox pair offers a tool for experimentally studying how changes in viscosity may affect mass transport and pumping losses in a flow cell during cell cycling.

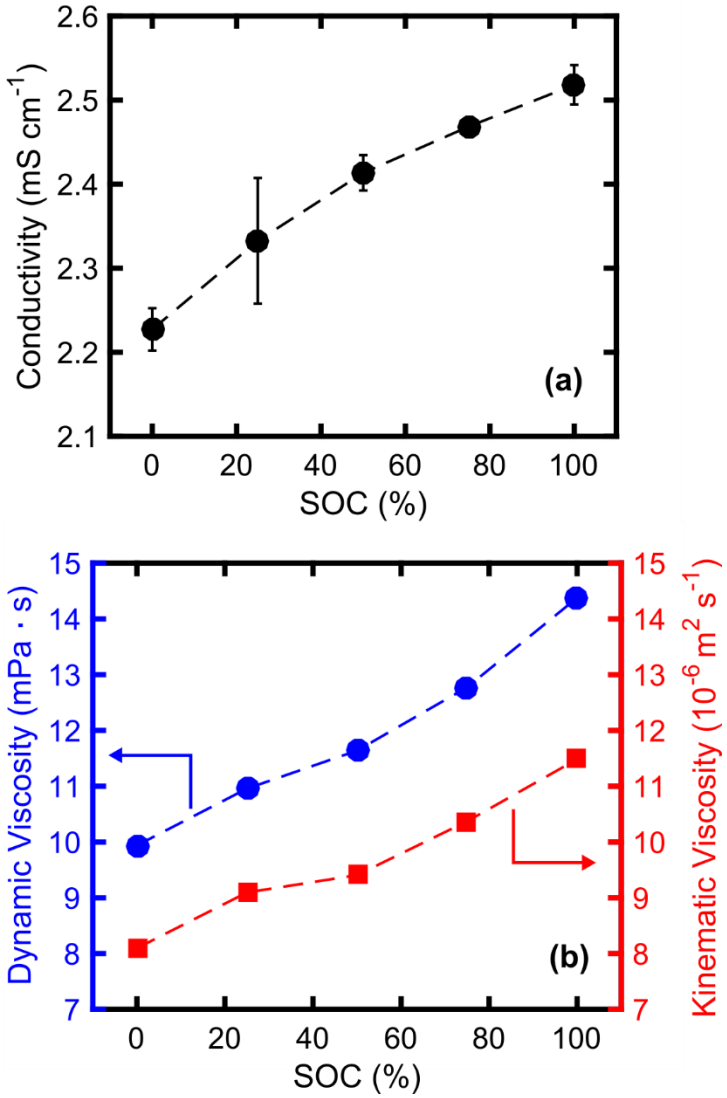

Figure 6: **(a)** Conductivities, and **(b)** dynamic and kinematic viscosities of 0.5 M total active species in 1 M $LiBF_4$ / PC as functions of SOC (0 %, 25 %, 50 %, 75 %, and 100 %). 95 % confidence intervals represent the experimental uncertainty calculated from 3 independent measurements. Confidence intervals for viscosity measurements are too small to see on either y-scale of the plot.

6.4 Cyclic Voltammetry

CV provides a method of investigating the redox potential, kinetics, and diffusion coefficients associated with the AcNH-TEMPO couple. Figure 8a and Figure 8b show CVs of AcNH-TEMPO and AcNH-TEMPO$^+$, respectively, at varying scan rates. Ideally, for a model compound, the redox potential would be well within the electrochemical window of common organic electrolytes,[8,9] allowing for studies that are not convoluted by electrolyte decomposition. The redox potential is E° = 3.63 V vs. Li/Li$^+$, which is within the bounds of the electrochemical stability window of this

electrolyte system (Figure 7). Across three repeat experiments of five CV scan rates, the cathodic peak potential of AcNH-TEMPO is 3.664 ± 0.002 V vs. Li/Li^+, and the anodic peak potential is 3.602 ± 0.002 V vs. Li/Li^+. Similarly, the cathodic peak potential of AcNH-$TEMPO^+$ is 3.664 ± 0.002 V vs. Li/Li^+, and the anodic peak potential is 3.602 ± 0.001 V vs. Li/Li^+. Additionally, the peak current ratios for AcNH-TEMPO and AcNH-$TEMPO^+$ are identical and equal to 1.01 ± 0.14 across all scan rates and replicate experiments. The lack of change in peak potential and peak current ratios as a function of scan rate for both the neutral radical and cation salt indicates that the AcNH-TEMPO redox pair is electrochemically reversible under the CV experimental conditions. Furthermore, Figure 8c and Figure 8d show CVs of AcNH-TEMPO and AcNH-$TEMPO^+$, respectively, for the 2^{nd} and 100^{th} cycles, at a scan rate of 100 mV s^{-1}. The CV behavior is identical over 100 cycles, indicating that AcNH-TEMPO is stable on the experimental time scale.

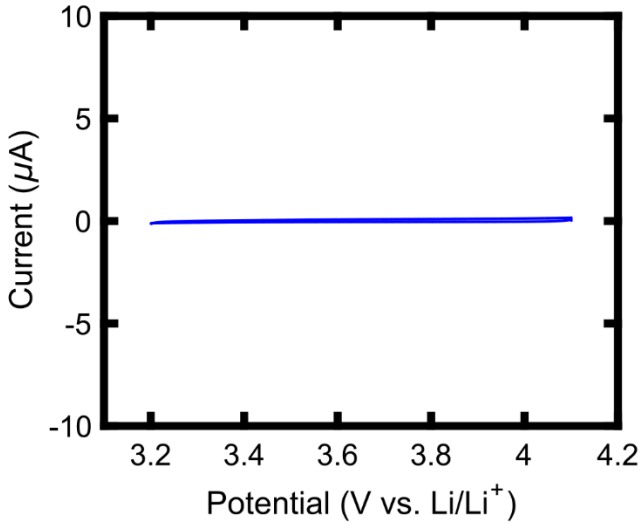

Figure 7: Background CV scan of the supporting electrolyte containing no active species. The solution composition was 0.5 M $LiBF_4$ / PC. The current (i) magnitude across the potential range of interest is $|i| \leq 0.16\ \mu A$.

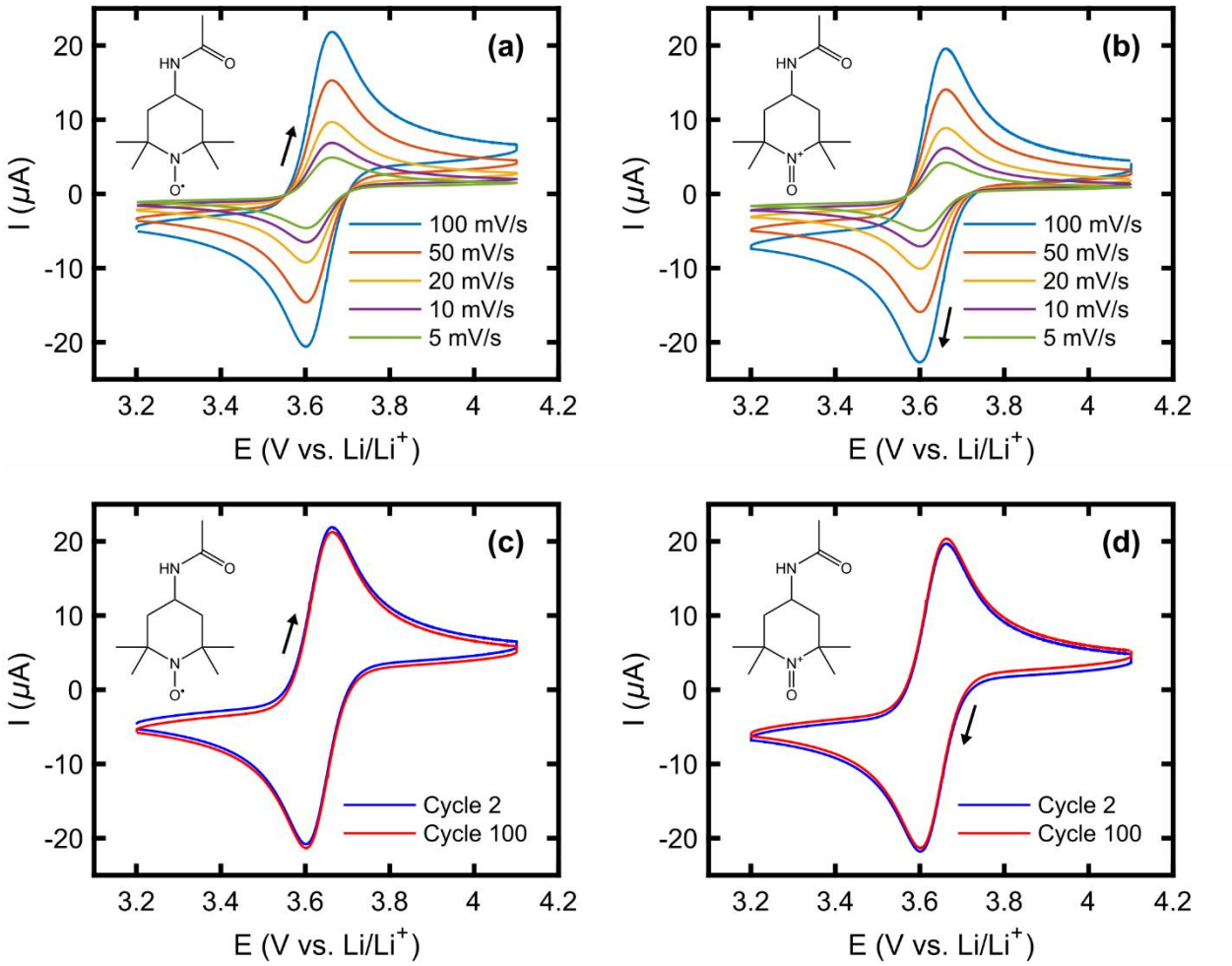

Figure 8: CVs (cycle 2) at various scan rates (5, 10, 20, 50, and 100 mV s^{-1}) for **(a)** AcNH-TEMPO and **(b)** AcNH-TEMPO$^+$, and extended CV cycling over 100 cycles (at 100 mV s^{-1}) for **(c)** AcNH-TEMPO and **(d)** AcNH-TEMPO$^+$. Active species concentration was 5 mM and the supporting electrolyte composition was 0.5 M $LiBF_4$ / PC. Arrows indicate the initial scan direction.

From the scan-rate dependence CV study, we calculated the diffusion coefficients of dilute AcNH-TEMPO and AcNH-TEMPO$^+$ using Randles-Sevcik analysis (Equation (1)). The diffusion coefficients of both the reduced (D_R) and oxidized (D_O) species are identical within experimental uncertainty ($D_R = D_O = 4.3 \times 10^{-7}$ cm^2 s^{-1}). The analysis in Figure 9 demonstrates a linear dependence of peak current as a function of square root of scan rate, leading to facile determination of diffusion coefficients at low active species concentrations.

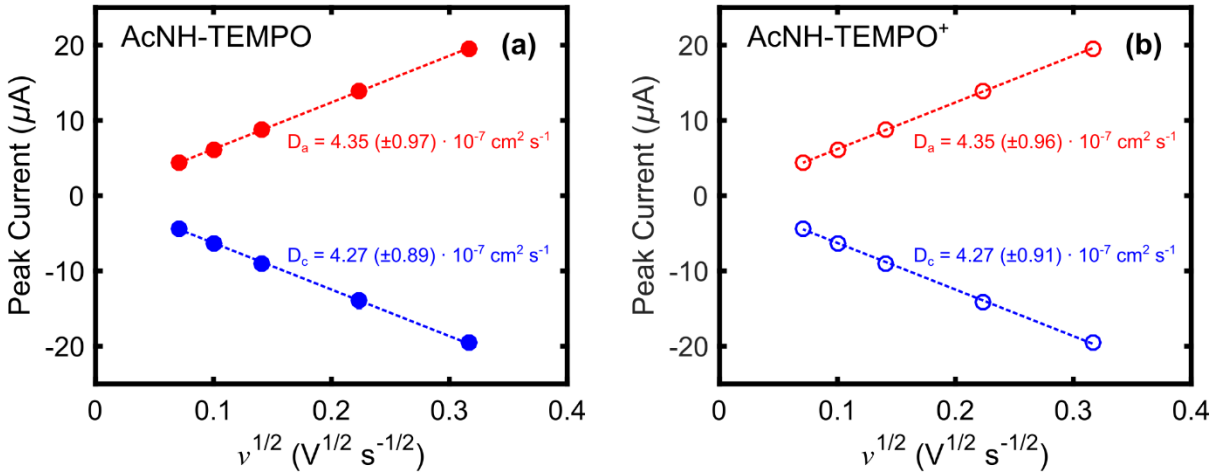

Figure 9: Randles-Sevcik analysis of anodic (red) and cathodic (blue) waves for **(a)** AcNH-TEMPO (closed circles, ●) and **(b)** AcNH-TEMPO$^+$ (open circles, ○). Redox electrolyte compositions were 5 mM active species in 0.5 M $LiBF_4$ / PC. Each data point is the mean of three independent measurements, and 95 % confidence intervals for each data point are too small to see on the y-axis scale.

6.5 Symmetric Flow Cell Cycling

A symmetric flow cell experiment allows for cycling of both the reduced and oxidized species in the AcNH-TEMPO redox pair to determine the active species stability without the presence of additional compounds. Some recent investigations into active material stability for NAqRFBs used bulk electrolysis cycling containing ≤ 5 mM active species and a sacrificial counter electrode isolated from the reaction of interest by a porous glass frit.[1,46] The symmetric flow cell technique offers a more controlled electrolyte environment by removing the need for a counter electrode of dissimilar material, eliminating the possibility of side-product species crossing over from the counter electrode chamber and contaminating the working electrode. The flowing electrolyte also improves mass transfer, enabling higher concentration cycling studies, and investigates active material stability on porous carbon electrodes relevant to flow battery applications instead of reticulated-vitreous or glassy carbon electrodes.

Figure 10a shows a schematic of the symmetric flow cell during charging, where AcNH-TEMPO serves as the starting positive redox electrolyte material and AcNH-TEMPO$^+$ is the starting negative redox electrolyte material. In this configuration, the redox active species on either side of the cell oscillates between AcNH-TEMPO and AcNH-TEMPO$^+$, shuttling BF_4^- anions across the separator to balance charge. As such, the symmetric flow cell technique offers a method of cycling only the active species of interest. Figure 10b shows representative charge and discharge

curves for the symmetric cell, which exhibit single plateaus corresponding the $1e^-$ transfer electrochemical process outlined in Figure 1. Figure 10c displays capacities and current efficiency as a function of cycle number, illustrating the stability of the AcNH-TEMPO redox pair, even after deep charging where > 81 % of the theoretical capacity is accessed during every charge cycle. The mean current efficiency is 99.4 (± 0.6) %, and, after 20 cycles, the capacity faded to just 92.6 % of its initial value. Wei et al. reported a nearly identical fade rate of ~91 % for a 0.1 M TEMPO / lithium-hybrid flow cell,[3] suggesting that AcNH-TEMPO exhibits similar stability to its parent molecule. The capacity retention of AcNH-TEMPO in $LiBF_4$ / PC lends this redox electrolyte system to diagnostic flow cell experiments, where active species decay can be ruled out as a major performance degradation mechanism.

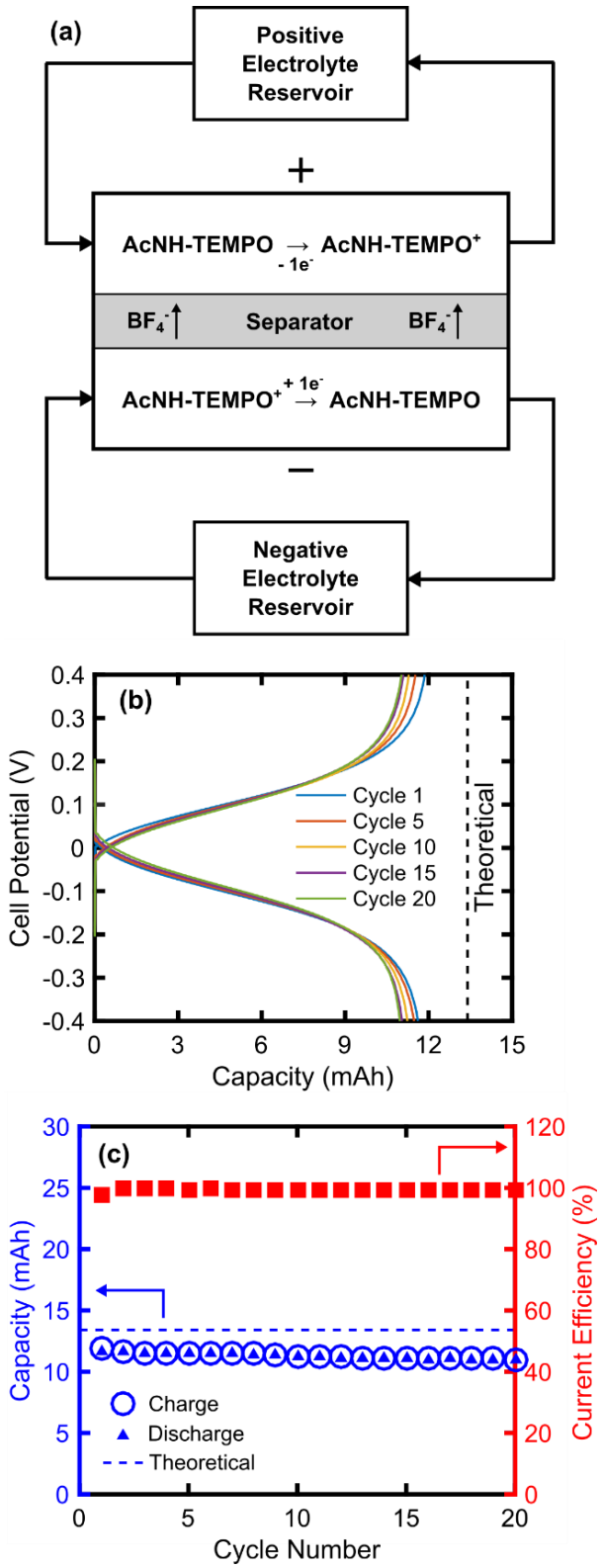

Figure 10: **(a)** Schematic of the AcNH-TEMPO symmetric flow cell during charging. **(b)** Potential curves for symmetric cell cycling of 50 mM total active species in 0.5 M $LiBF_4$ / PC including cycle numbers: 1, 5, 10, 15, and 20. **(c)** Charge (blue ○), discharge (blue ▲), and theoretical (blue dashed line) capacities, as well as current efficiencies (red ■), as a function of cycle number. Theoretical capacity is 13.40 mAh.

6.6 Single Electrolyte Flow Cell

To illustrate the value of a model redox active species for evaluating NAqRFBs, we employ a single electrolyte flow cell experiment to characterize cell performance. Figure 11a depicts a flow cell reactor in which one electrolyte stream circulates through both electrodes, and BF_4^- anions transfer across the separator to balance charge. The active species oxidizes at the anode and then reduces at the cathode, before returning to the reservoir. Thus, the SOC in the reservoir should not vary with time. In this configuration, the cell operates at steady state over a wide range of flow rates and current densities.[12] Furthermore, crossover effects do not degrade the performance of the single electrolyte flow cell because the same electrolyte composition is present on both sides of the cell, and this technique offers simple cell-level analysis, without reference electrodes, since nearly identical processes occur on both sides of the cell.[11] In this work, an AcNH-TEMPO model redox electrolyte enables a study of NAqRFB reactor performance.

Figure 11b shows polarization curves for the AcNH-TEMPO single electrolyte cell at two different flow rates, 2 and 10 mL min^{-1}. The slope of the polarization curves is equivalent to the reactor ASR. The polarization curves show that by increasing flow rate, the total cell ASR decreases, due to enhanced reactant transport to the porous electrode surface. The ASR values calculated from Figure 11b are higher than those of typical aqueous RFBs, but are on par with previous NAqRFBs reports. For example, a recent study demonstrated an all-organic NAqRFB using 0.5 M 9-fluorenone and 2,5-di-*tert*-butyl -1-methoxy-4-2-[2'-methoxy]benzene in 1.0 M tetraethylammonium bis(trifluoromethane)sulfonimide / acetonitrile and exhibited an ASR of 23.2 Ω cm^2.[49] By comparison, Escalante-Garcia et al. demonstrated a NAqRFB employing 0.1 M vanadium acetylacetonate in 0.5 M tetraethylammonium tetrafluoroborate / acetonitrile that achieved an ASR as low as 6.1 Ω cm^2,[50] however, the lower active species concentration employed in that study does not compare well with the present work. Impedance data will illustrate that the AcNH-TEMPO single electrolyte cell confirms an assumption of previous modeling reports,[10,51] that separator resistivity dominates non-aqueous flow cell ASR.

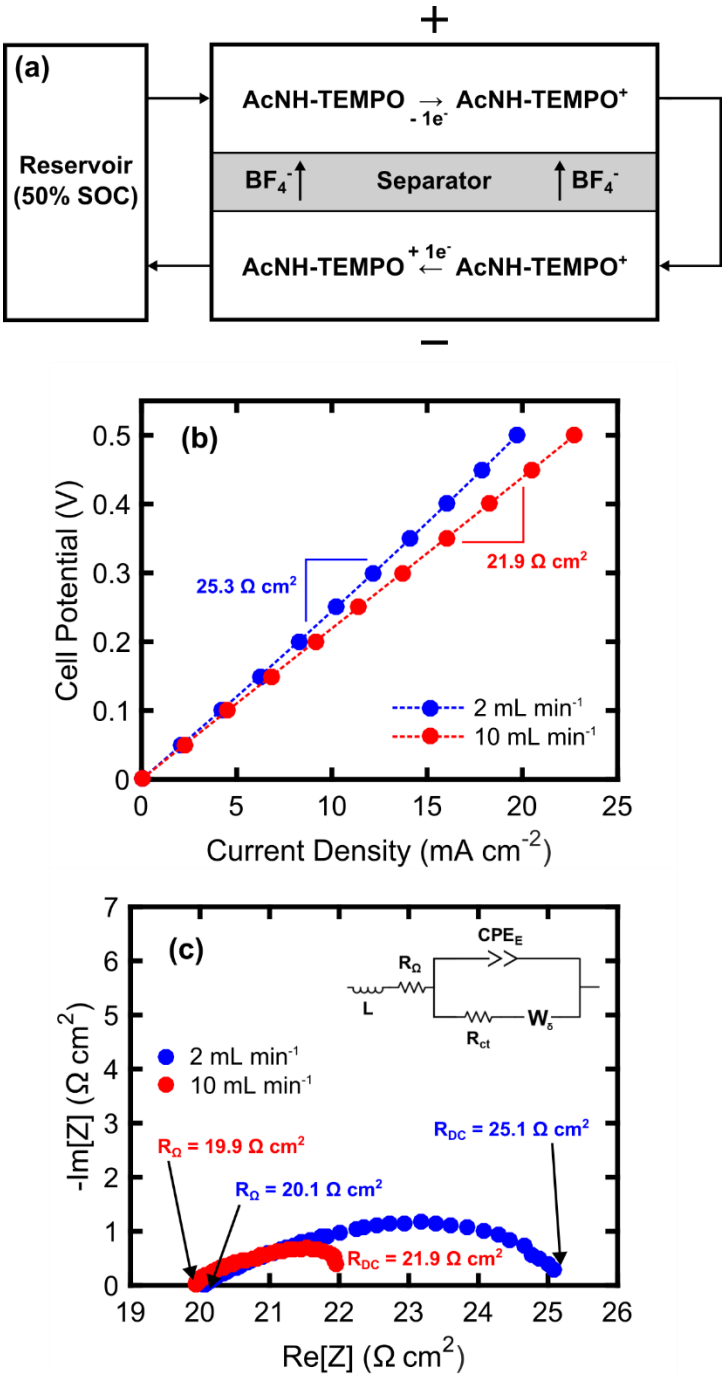

Figure 11: **(a)** Single electrolyte flow cell configuration for the AcNH-TEMPO / AcNH-TEMPO$^+$ couple at 50% SOC. **(b)** Polarization curves and **(c)** Nyquist plots of the flow cell at 2 and 10 mL min^{-1}. Redox electrolyte composition was 0.25 M AcNH-TEMPO / 0.25 M AcNH-TEMPO$^+$ / 1 M $LiBF_4$ / PC.

While successfully demonstrating overall flow cell performance, the linear polarization curve is difficult to break down into performance limiting processes. Electrochemical impedance spectroscopy adds detail to the description of reactor performance. Figure 11c presents Nyquist plots of the AcNH-TEMPO single electrolyte flow cell. For both flow rates, the Nyquist plot

displays depressed semicircles caused by the capacitive effects of the porous electrode, often described by a constant phase element (CPE_E).[52] The low frequency intercept denotes the total direct current (DC) resistance contribution (R_{DC}) to the impedance, and almost exactly matches the ASR values calculated from the slopes of the polarization curves in Figure 11b. Thus, for this system, the low frequency intercept on the Nyquist plot is a good measure of the cell ASR. Since the ASR determined from the low frequency intercept, measured about OCV, is in excellent agreement with the ASR determined from the slope of the linear polarization curve, similar processes must dominate the ASR for all cell potentials considered in the experiment. The high frequency intercept (R_Ω) denotes the ohmic contribution to the impedance, considering the resistance of the separator, electrodes, and current collectors. Both curves on the Nyquist plot are for the same cell under different flow conditions, so R_Ω should be the same. Indeed, R_Ω is 20.0 ± 0.1 Ω cm^2 for both flow conditions. The ohmic impedance contribution accounts for 80.0 % and 90.1 % of the total ASR for the experiments at 2 and 10 mL min^{-1}, respectively. This finding indicates that the major contribution to cell impedance is the ohmic portion, likely due to the relatively thick Daramic separator (175 μm) employed in this demonstration study. For future NAqRFB prototypes, the effective ASR contribution from the separator or membrane must decrease to improve flow cell performance and lower reactor cost contributions to NAqRFB prices.[10,43,51,53]

Even though separator resistance dominates the ASR, the Nyquist plots (Figure 11c) indicate critical behavior as a function of flow rate as the low frequency semicircle shrinks in magnitude with increasing flow rate. A bounded Warburg element (W_δ), which describes a linear diffusion transport limitation through a homogenous boundary layer of finite thickness, can represent the semicircular mass transport impedance exhibited in Figure 11c.[52] Other impedance studies on flow batteries describe mass transport resistance in this manner.[50,54] The decrease in the diameter of the impedance semicircle with increasing flow rate, combined with the facile reaction kinetics of AcNH-TEMPO, suggests that mass transport losses constitute a significant portion of the remaining contribution to the ASR. Note that charge transfer resistance, R_{ct}, is negligible in this system due to the extremely fast reaction kinetics ($1.0 \times 10^{-1} \geq k_0 \geq 2.3 \times 10^{-2}$ cm s^{-1}) for TEMPO and its derivatives in non-aqueous electrolytes.[31,42] Figure 11c also presents a proposed equivalent circuit for this system, which considers all of the impedance elements discussed, and

an inductor, *L*, to capture the impedance of the potentiostat leads.[52] A recent literature report on NAqRFBs suggested a similar equivalent circuit.[50]

6.7 Conclusions

This work presents AcNH-TEMPO and its oxoammonium cation AcNH-TEMPO$^+$ as a stable, reversible and soluble active species for probing redox electrolyte properties and cell performance for NAqRFBs. First, a physicochemical study investigates the conductivity, viscosity, and density as a function of SOC for redox electrolytes containing 0.5 M total active material in 1 M $LiBF_4$ / PC; both conductivity and viscosity of the redox electrolyte increase with SOC. Also, a UV-vis study of 50 mM total active material in 0.5 M $LiBF_4$ / PC exhibits two characteristic peaks, clearly demonstrating spectral changes as a function of SOC. Second, CV analysis demonstrates that the AcNH-TEMPO redox pair undergoes an electrochemically reversible one-electron transfer process at 3.63 V vs. Li/Li$^+$ and is stable on the CV time scale. A symmetric flow cell configuration further assesses the stability of the redox pair to demonstrate capacity retention over multiple cycles and hours. Third and finally, a single electrolyte flow cell studies steady state cell performance, via polarization and impedance measurements, to quantify overall cell ASR and to identify performance-limiting factors. In summary, the AcNH-TEMPO redox pair offers a practical tool for systematic investigation of redox electrolyte properties and cell geometry on the performance of NAqRFBs. Future studies will exploit AcNH-TEMPO to evaluate cell-level performance as a function of NAqRFB reactor design.

6.8 References

1. J. Huang et al., *J Mater Chem A*, **3**, 14971–14976 (2015).
2. J. Huang et al., *Adv. Energy Mater.*, **5**, 1401782 (2015).
3. X. Wei et al., *Adv. Mater.*, **26**, 7649–7653 (2014).
4. C. S. Sevov et al., *J. Am. Chem. Soc.*, **137**, 14465–14472 (2015).
5. F. R. Brushett, J. T. Vaughey, and A. N. Jansen, *Adv. Energy Mater.*, **2**, 1390–1396 (2012).
6. A. P. Kaur, N. E. Holubowitch, S. Ergun, C. F. Elliott, and S. A. Odom, *Energy Technol.*, **3**, 476–480 (2015).
7. W. Duan et al., *J Mater Chem A*, **4**, 5448–5456 (2016).
8. D. Aurbach et al., *Electrochimica Acta*, **50**, 247–254 (2004).
9. D. Aurbach, Ed., *Non-aqueous Electrochemistry*, p. 602, Marcel Dekker, New York, (1999).
10. R. M. Darling, K. G. Gallagher, J. A. Kowalski, S. Ha, and F. R. Brushett, *Energy Environ. Sci.*, **7**, 3459–3477 (2014).
11. R. M. Darling and M. L. Perry, *J. Electrochem. Soc.*, **161**, A1381–A1387 (2014).
12. R. M. Darling and M. L. Perry, *ECS Trans.*, **53**, 31–38 (2013).
13. Q. Xu, T. S. Zhao, and C. Zhang, *Appl. Energy*, **130**, 139–147 (2014).
14. C. L. Bird and A. T. Kuhn, *Chem Soc Rev*, **10**, 49–82 (1981).

15. R. R. Gagne, C. A. Koval, and G. C. Lisensky, *Inorg. Chem.*, **19**, 2854–2855 (1980).
16. X. Wei et al., *Adv. Energy Mater.*, **5**, 1400678 (2015).
17. L. J. Tilley, J. M. Bobbitt, S. A. Murray, C. E. Camire, and N. A. Eddy, *Synthesis*, **45**, 0326–0329 (2013).
18. J. M. Bobbitt and M. C. L. Flores, *Heterocycles*, **27**, 509–533 (1998).
19. J. Zakrzewski, J. Grodner, J. M. Bobbitt, and M. Karpinska, *Synthesis*, **16**, 2491–2494 (2007).
20. M. Shibuya, M. Tomizawa, and Y. Iwabuchi, *J. Org. Chem.*, **73**, 4750–4752 (2008).
21. J. M. Bobbitt, *J. Org. Chem.*, **63**, 9367–9374 (1998).
22. J. M. Bobbitt and N. Merbouh, *Org. Synth.*, **82**, 80–86 (2005).
23. W. F. Bailey, J. M. Bobbitt, and K. B. Wiberg, *J. Org. Chem.*, **72**, 4504–4509 (2007).
24. N. Merbouh, J. M. Bobbitt, and C. Brückner, *J. Org. Chem.*, **69**, 5116–5119 (2004).
25. C. B. Kelly, M. A. Mercadante, T. A. Hamlin, M. H. Fletcher, and N. E. Leadbeater, *J. Org. Chem.*, **77**, 8131–8141 (2012).
26. M. A. Mercadante, C. B. Kelly, J. M. Bobbitt, L. J. Tilley, and N. E. Leadbeater, *Nat. Protoc.*, **8**, 666–676 (2013).
27. J. M. Bobbitt, C. Brückner, and N. Merbouh, *Org. React.*, **74**, 103–424 (2009).
28. R. Barhdadi et al., *J. Appl. Electrochem.*, **37**, 723–728 (2007).
29. J. R. Fish, S. G. Swarts, M. D. Sevilla, and T. Malinski, *J. Phys. Chem.*, **92**, 3745–3751 (1988).
30. J. E. Baur, S. Wang, and M. C. Brandt, *Anal. Chem.*, **68**, 3815–3821 (1996).
31. T. Suga, Y.-J. Pu, K. Oyaizu, and H. Nishide, *Bull. Chem. Soc. Jpn.*, **77**, 2203–2204 (2004).
32. R. G. Evans, A. J. Wain, C. Hardacre, and R. G. Compton, *ChemPhysChem*, **6**, 1035–1039 (2005).
33. L. M. Moshurchak, C. Buhrmester, R. L. Wang, and J. R. Dahn, *Electrochimica Acta*, **52**, 3779–3784 (2007).
34. Z. Chen, Y. Qin, and K. Amine, *Electrochimica Acta*, **54**, 5605–5613 (2009).
35. C. Buhrmester, L. M. Moshurchak, R. L. Wang, and J. R. Dahn, *J. Electrochem. Soc.*, **153**, A1800–A1804 (2006).
36. H. Nishide et al., *Electrochimica Acta*, **50**, 827–831 (2004).
37. M. Suguro, S. Iwasa, Y. Kusachi, Y. Morioka, and K. Nakahara, *Macromol. Rapid Commun.*, **28**, 1929–1933 (2007).
38. T. Janoschka et al., *Nature*, **527**, 78–81 (2015).
39. U. S. Schubert et al., *Polym Chem*, **7**, 1711–1718 (2016).
40. J. Winsberg et al., *Adv. Mater.*, **28**, 2238–2243 (2016).
41. T. Liu, X. Wei, Z. Nie, V. Sprenkle, and W. Wang, *Adv. Energy Mater.*, **6**, 1501449 (2015).
42. F. Kato et al., *Chem. Lett.*, **39**, 464–465 (2010).
43. N. S. Hudak, L. J. Small, H. D. Pratt, and T. M. Anderson, *J. Electrochem. Soc.*, **162**, A2188–A2194 (2015).
44. H. Matsuda and Y. Ayabe, *Z. Für Elektrochem. Berichte Bunsenges. Für Phys. Chem.*, **6**, 494–503 (1955).
45. J. D. Milshtein, L. Su, C. Liou, A. F. Badel, and F. R. Brushett, *Electrochimica Acta*, **180**, 695–704 (2015).
46. S. M. Laramie, J. D. Milshtein, T. M. Breault, F. R. Brushett, and L. T. Thompson, *J. Power Sources*, **327**, 681–692 (2016).
47. J. Mun et al., *Electrochem. Solid-State Lett.*, **15**, A80–A82 (2012).
48. M. S. Ding, *J. Electrochem. Soc.*, **151**, A40–A47 (2004).
49. X. Wei et al., *Angew. Chem. Int. Ed.*, **54**, 8684–8687 (2015).

50. I. L. Escalante-García, J. S. Wainright, L. T. Thompson, and R. F. Savinell, *J. Electrochem. Soc.*, **162**, A363–A372 (2015).
51. R. Darling, K. Gallagher, W. Xie, L. Su, and F. Brushett, *J. Electrochem. Soc.*, **163**, A5029–A5040 (2016).
52. X.-Z. Yuan, C. Song, H. Wang, and J. Zhang, *Fundam. Appl.-Verl. Lond.* (2010).
53. L. Su et al., *J. Electrochem. Soc.*, **163**, A5253–A5262 (2016).
54. C.-N. Sun et al., *J. Electrochem. Soc.*, **161**, A981–A988 (2014).

7. Demonstrating high current density, long duration cycling of a soluble organic active material for non-aqueous redox flow batteries

This chapter is adapted with permission from: J. D. Milshtein, A. P. Kaur, M. D. Casselman, J. A. Kowalski, S. Modekrutti, P. L. Zhang, N. H. Attanayake, C. F. Elliott, S. R. Parkin, C. Risko, F. R. Brushett, S. A. Odom, High current density, long duration cycling of soluble organic active species for non-aqueous redox flow batteries, *Energy and Environmental Science*, **9**, 3531–3543 (2016). Reproduced by permission of The Royal Society of Chemistry.

7.1 Introduction

Many classes of redox-active organic molecules have been proposed for use in NAqRFBs, such as anthraquinones[2] and dialkoxybenzenes.[3–6] Of the proposed redox-active organic molecules, nearly all, with the exception of *N*-oxidanyl amines (e.g., TEMPO),[7–9] suffer from rapid capacity fade or poor solubility.[4,10] *N*-Ethylphenothiazine (EPT, Figure 1a) is a commercially available and stable electron-donating organic molecule that oxidizes at ~0.3 V vs. ferrocene/ferrocenium (Fc/Fc^+) in carbonate electrolytes. The long lifetime of this molecule as an overcharge-protection material in lithium-ion batteries highlights its remarkable stability.[11–14] Our studies have further demonstrated the stability of EPT in aprotic, organic solvents, both in the neutral and singly oxidized (radical-cation) states.[15] This stability suggests that EPT could serve as a one-electron-donating material in NAqRFB electrolytes, but the solubility of EPT in carbonate- or nitrile-based solvents (~0.1 M) is too low for practical implementation.[16] By comparison, we reported previously that 3,7-bis(trifluoromethyl)-*N*-ethylphenothiazine (BCF3EPT),[14,17] an EPT derivative, dissolves at concentrations up to 2 M in non-aqueous electrolytes and is even more stable than EPT.[14] The synthesis of BCF3EPT, however, requires multiple steps, the last of which entails a low-yielding trifluoromethylation reaction. [14] Ideally, organic active materials for NAqRFBs will be easily synthesized from cheap precursors, leading to active-material costs ≤ \$5 kg^{-1}. Additionally, active materials should be highly soluble (> 1 M) to ensure that electrolytes are sufficiently energy-dense and low-cost to be economically viable.[16]

Furthermore, NAqRFB design has failed to incorporate advanced flow-cell architectures developed for aqueous RFBs over the past few years.[18,19] Organic-based aqueous RFBs have demonstrated vast reductions in area-specific resistance (ASR) by transitioning from initial prototypes[20] to advanced cell designs[21,22] inspired by all-vanadium RFB literature. Many

NAqRFBs implement thick (> 1 mm) flow through electrodes, leading to large ohmic and mass-transfer resistances, subsequently forcing cell operation at low current densities only.[23,24] Prior work on vanadium RFBs suggests that zero-gap,[18,19] interdigitated flow fields (IDFFs) with thin (< 500 µm) carbon-paper electrodes will offer the best balance of ASR and pressure drop for at-scale RFBs.[25,26] The IDFF requires that all electrolyte flows through a short path of porous electrode, enabling high current densities, but not developing an unacceptably large pressure drop.[25,26] Thin carbon-paper electrodes offer a balance of high surface area, good mass transport, and low ohmic resistance.[19] We previously reported a flow cell with IDFFs and carbon-paper electrodes designed for compatibility with non-aqueous electrolytes,[27] but no demonstration of cycling of an organic active species in such a flow cell has been reported.

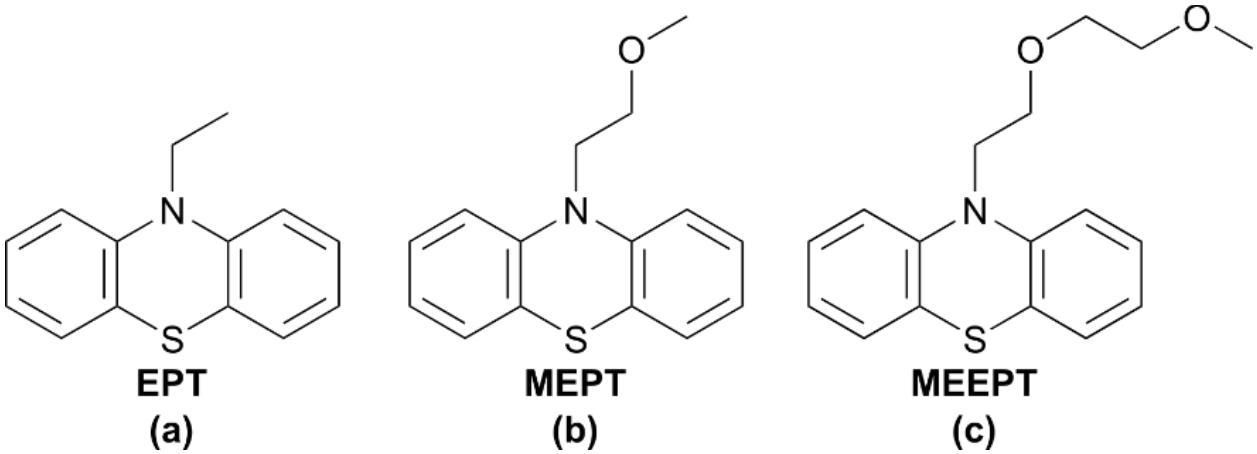

Figure 1: Chemical structures of **(a)** *N*-ethylphenothiazine (EPT), **(b)** *N*-(2-methoxyethyl)phenothiazine (MEPT), and **(c)** *N*-(2-(2-methoxyethoxy)ethyl)phenothiazine (MEEPT).

In this work, we engage in molecular and cell-level engineering to afford high-rate, long-duration cycling of soluble EPT derivatives. We first describe the synthesis and solubility of two new phenothiazine derivatives, *N*-(2-methoxyethyl)phenothiazine (MEPT, Figure 1b) and *N*-[2-(2-methyoxyethoxy)ethyl]phenothiazine (MEEPT, Figure 1c), as well as the stability of their tetrafluoroborate radical-cation salts. These compounds are synthesized in a single step from an inexpensive, commercially available precursor. Both neutral species have significantly lower melting points and higher solubilities in non-aqueous electrolytes than EPT. MEEPT, in fact, is a liquid at room temperature. We investigate the fundamental electrochemical properties of these new phenothiazine derivatives using cyclic voltammetry (CV) to determine redox potentials, reversibility, and diffusion coefficients, and use bulk electrolysis to examine cycling behavior under dilute conditions. Next, we employ the most soluble derivative (MEEPT) at a moderate

concentration (0.5 M active species) in a high-performance flow cell (Figure 2) incorporating IDFFs and carbon-paper electrodes. This flow cell exhibits the lowest reported cell ASR for NAqRFBs (3.2 – 3.3 Ω cm^2), allowing the stable MEEPT molecule to cycle at an aggressive current density of 100 mA cm^{-2} with negligible capacity fade over 100 cycles. The molecular and cell-engineering principles outlined in this paper, aimed at high concentration, high stability, and high current densities, apply to other emerging redox chemistries and provide a framework for advancing NAqRFBs towards a technology-readiness level competitive with aqueous RFBs.

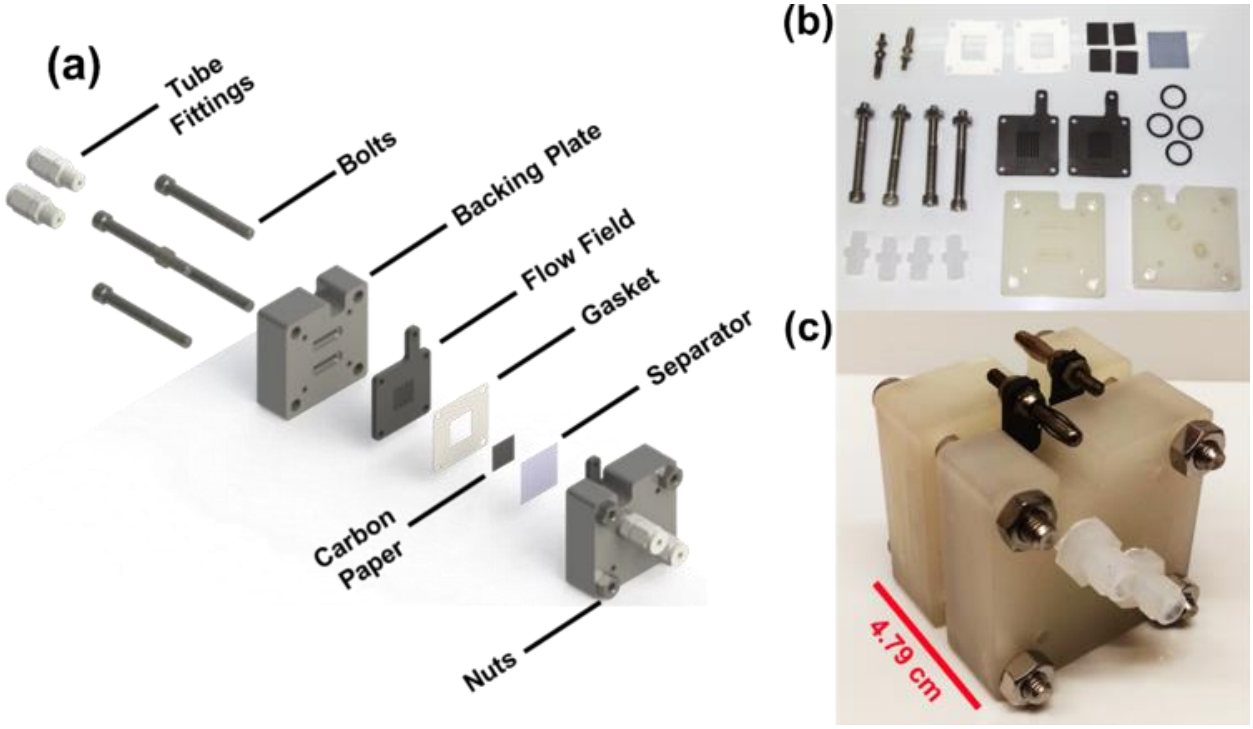

Figure 2: **(a)** Schematic of the non-aqueous-compatible flow cell employed in this work, exhibiting IDFFs and carbon paper electrodes. **(b)** Photograph of the flow cell components. **(c)** Photograph of the assembled flow cell.

7.2 Experimental

General. Phenothiazine (99%), 1-bromo-2-(2-methoxyethoxy)ethane (90%), and sodium hydride (60% dispersion in mineral oil) were purchased from Acros Organics. 2-Chloroethyl methyl ether (98%) and $NOBF_4$ (98%) were purchased from Alfa Aesar. $NOBF_4$ was stored and weighed in an argon-filled glovebox (MBraun, O_2 < 0.1 ppm, H_2O < 0.6 ppm), and removed in a capped vial only immediately prior to use. Other reagents and chromatography solvents were purchased from VWR. Silica gel (65 x 250 mesh) was purchased from Sorbent Technologies.

All electrochemical measurements were performed in argon-filled gloveboxes (O_2 < 0.7 ppm, H_2O < 0.6 ppm) from MBraun or Innovative Technologies. Propylene carbonate (PC, 99.99%) and tetraethylammonium tetrafluoroborate ($TEABF_4$, 99.9%) were purchased from BASF and used as received, while anhydrous ACN (99.9%) was purchased from Acros Organics. Kryptofix® 222 (cryptand, 4,7,13,16,21,24-hexaoxa-1,10-diazabicyclo[8.8.8]-hexacosane, Acros Organics, 98%) and silver tetrafluoroborate ($AgBF_4$, Sigma Aldrich, 98%) were used as received. Silver wire was purchased from Alfa Aesar. Silver-silver chloride (Ag/AgCl) reference electrodes were purchased from CH Instruments, removed from their glass housing, and freshly anodized before use. Daramic 175 separator (thickness = 175 μm, porosity = 58%, mean pore size = 100 nm) was used as received and employed as the separator material in flow-cell experiments.

^1H and ^{13}C nuclear magnetic resonance (NMR) spectra were obtained on Varian spectrometers in deuterated chloroform from Cambridge Isotope Laboratories. *J* values are reported in Hz. Mass spectra were obtained on an Agilent 5973 Network mass selective detector attached to Agilent 6890N Network GC system. Elemental analyses were performed by Atlantic Microlab Inc. Electron paramagnetic resonance (EPR) spectra were acquired on a Bruker EMXplus spectrometer with a PremiumX bridge containing an ER 4119HS-W1 high-sensitivity cavity. To prepare the sample, 5 mg of EPT-BF_4, MEPT-BF_4, or MEEPT-BF_4 was dissolved in 20 mL of DCM and transferred to a 4 mm Wilmad-Labglass quartz EPR tube. The spectrum was acquired immediately thereafter at room temperature.

Synthesis of Neutral Compounds. *N*-Ethylphenothiazine (EPT) was synthesized according to a prior report.[15] For small-scale synthesis of MEPT and MEEPT, phenothiazine (1.99 g, 10.0 mmol) was dissolved in anhydrous *N*,*N*-dimethylformamide (DMF, 20 mL) under nitrogen atmosphere. A 60% dispersion of sodium hydride (NaH) in mineral oil (0.48 g, 12 mmol) was added, and the reaction mixture was heated to 60 °C for 30 min. Then, 2-chloroethyl methyl ether (1.10 mL, 12 mmol, for MEPT) or 1-bromo-2-(2-methoxyethoxy)ethane (1.62 mL, 12 mmol, for MEEPT) was added, and the reaction mixture was stirred at 60 °C for 12 h. The reaction was quenched by pouring the contents into ice water, after which the organic components were extracted with ethyl acetate three times, and the combined extracts were washed with brine. The organic extracts were dried over magnesium sulfate ($MgSO_4$), filtered to remove solids, and concentrated by rotary evaporation. The crude product was purified by column chromatography

using a gradient of 0 to 10% ethyl acetate in hexanes to afford the desired products after concentration by rotary evaporation.

***N*-(2-methoxyethyl)phenothiazine (MEPT).** Yield: 2.16 g (84%). m.p. 47 ºC. ^{1}H NMR (400 MHz, $CDCl_3$) δ 1.57 (H_2O), 3.40 (s, 3H), 3.76 (t, 2H, *J* = 6.4 Hz), 4.09 (t, 2H, *J* = 6.4 Hz), 6.89-6.94 (m, 4H), 7.12-7.17 (m, 4H). ^{13}C NMR (100 MHz, $CDCl_3$) δ 47.5, 59.2, 69.9, 115.3, 122.7, 124.8, 127.5, 127.6, 145.1. EI-MS: *m/z* 257 (54%), 212 (100%), 198 (20%), 180 (61%). Anal. calcd. for $C_{15}H_{15}NOS$ C, 70.01; H, 5.88; N, 5.44. Found C, 69.99; H, 5.91; N, 5.39.

***N*-[2-(2-methoxyethoxy)ethyl]phenothiazine (MEEPT).** Yield: 2.22 g (74%). pale yellow oil. ^{1}H NMR (400 MHz, $CDCl_3$, Me_4Si) δ 1.55 (H_2O), 3.38 (s, 3H), 3.53-3.56 (m, 2H), 3.64-3.66 (m, 2H), 3.85 (t, 2H, *J* = 6.5 Hz), 4.12 (t, 2H, *J* = 6.5 Hz), 6.90-6.93 (m, 4H), 7.11-7.16 (m, 4H). ^{13}C NMR (100 MHz, $CDCl_3$, Me_4Si) δ 47.5, 59.2, 68.5, 70.8, 72.1, 115.4, 122.8, 124.8, 127.5, 127.6, 145.1, 163.2. EI-MS: *m/z* 301 (48%), 212 (100%), 198 (22%), 180 (46%). Anal. calcd. for $C_{17}H_{19}NO_2S$ C, 67.75; H, 6.35; N, 4.65. Found C, 67.48; H, 6.41; N, 4.88.

For a large-scale synthesis of MEEPT, phenothiazine (10.00 g, 50.25 mmol) was dissolved in anhydrous DMF (120 mL) under nitrogen atmosphere in an oven-dried three-neck round-bottomed flask equipped with a reflux condenser. A 60% dispersion of NaH in mineral oil (2.90 g, 72.5 mmol) was added, and the reaction mixture was stirred for 15 min. Then, 1-bromo-2-(2-methoxyethoxy)ethane (8.10 mL, 60.2 mmol) was added, and the reaction mixture was heated and stirred at 60 °C for 16 h. The reaction was quenched by pouring the reaction mixture into ice water, after which the organic components were extracted with diethyl ether, and the organic layer was washed with brine. The organic extracts were dried over $MgSO_4$, filtered to remove solids, and concentrated by rotary evaporation. The crude product was purified by column chromatography using a gradient of 0 to 10% ethyl acetate in hexanes to afford the desired products after concentration by rotary evaporation. Yield: 13.40 g (88%). ^{1}H NMR and mass spectra matched those observed for the small-scale syntheses.

Synthesis of Radical-Cation Species. General procedure: The neutral compound (1 mmol) and anhydrous DCM (10 mL) were added to an oven-dried round-bottomed flask cooled under nitrogen atmosphere. The resulting solution was purged with nitrogen for 20 min. $NOBF_4$ (0.122 g, 1.05 mmol) was added to the solution, which immediately turned dark orange. The reaction vessel was capped with a rubber septum and the reaction mixture stirred under nitrogen for 1 h, after which diethyl ether (20 mL) was added gradually with continued stirring, producing a dark

precipitate. The precipitate was filtered, then dissolved in DCM (10 mL) and re-precipitated with a second addition of diethyl ether (20 mL). This process was repeated once more to ensure removal of any unreacted starting material. The final precipitate was dried under vacuum and stored in an argon-filled glovebox.

***N*-Ethylphenothiazine tetrafluoroborate salt (EPT-BF4).** EPT (5.04 g, 22.2 mmol) and $NOBF_4$ (2.54 g, 23.3 mmol) were reacted according to the general procedure to yield EPT-BF_4 (4.53 g, 65%). Crystals for X-ray diffraction (XRD) were grown in DCM and toluene. A saturated solution of salt in DCM was placed in a NMR tube. Toluene was run down the side of the tube using a syringe to form a discrete layer. The NMR tube was capped and placed in the freezer, and crystals formed at the interface of the solvent layers.

***N*-(2-methoxyethyl)phenothiazine tetrafluoroborate salt (MEPT-BF4).** MEPT (3.00 g, 11.6 mmol) and $NOBF_4$ (1.43 g, 12.2 mmol) were reacted according to the general procedure to yield MEPT-BF_4 (2.51 g, 61%). Crystals for XRD were grown by dissolving the salt in DCM and placing this vial inside of another vial containing pentane. The outer vial was capped and was placed in a freezer, and crystals formed through vapor diffusion.

***N*-(2-(2-methoxyethoxy)ethyl)phenothiazine tetrafluoroborate salt (MEEPT-BF4).** MEEPT (16.1 g, 53.4 mmol) and $NOBF_4$ (6.55 g, 56.1 mmol) were reacted according to the general procedure to yield MEEPT-BF_4 (12.5 g, 60%). Crystals for XRD were grown in DCM and toluene. A saturated solution of salt in DCM was placed in a NMR tube. Toluene was run down the side of the tube using a syringe to form a discrete layer. The NMR tube was capped and placed in a freezer, and crystals formed at the interface of the solvent layers.

Radical-Cation Stability Studies. An Agilent diode-array spectrometer was used to collect UV-vis absorption spectra using ACN or PC as the solvent. Radical-cation salts were dissolved at 0.15 mM in the appropriate solvent and pipetted into optical glass cuvettes (Starna) with a 1 cm path length. Solutions were added to the cuvettes inside an argon-filled glovebox and then sealed with a Teflon screw cap. The sealed cuvette was then removed from the glovebox for spectral analysis. Spectra were collected at 0, 1, 3, 5, and 24 h after dissolution.

Solubility. The solubility limits of the neutral molecules (EPT, MEPT, and MEEPT) and the radical-cation salts (EPT-BF_4, MEPT-BF_4, and MEEPT-BF_4) in pure ACN and an electrolyte comprised of ~0.5 M $TEABF_4$ / ACN were estimated by a shake-flask method. Active material was added in excess to either pure ACN or the electrolyte. Then, the solution was diluted slowly,

stirring between additions, with either pure ACN or the electrolyte. The dilution process continued until the active species was dissolved, as determined by visual inspection.

Cyclic Voltammetry. CV experiments were performed using a custom three-electrode cell comprised of a 3 mm diameter glassy-carbon working electrode (CH Instruments), platinum-wire counter electrode (CH Instruments), and freshly anodized, un-fritted Ag/AgCl wire reference electrode. Electrochemical data was collected on a CH Instruments 650E potentiostat. No solution resistance compensation (*i*R correction) was applied. Electrolytes were comprised of 1 mM neutral active material (EPT, MEPT, or MEEPT), 0.1 M $TEABF_4$, and either ACN or PC as the solvent. In some experiments, ~0.7 mM ferrocene was added as an internal reference. Redox (half-wave) potentials ($E_{1/2}$) were calculated as the mean potential between CV peaks from voltammograms recorded at 100 mV s^{-1} and are reported relative to the Fc/Fc^+ internal reference (Figure 3). Diffusion coefficients of the active species were determined using Randles-Sevcik analysis (Equation (1)) and the peak currents of voltammograms, without the ferrocene internal reference, at the following scan rates: 25, 50, 75, 100, 200, 300, 400, and 500 mV s^{-1} (Figure 4). In Equation (1), i_p is the peak current (A), n is the number of electrons transferred (mol_e mol^{-1}), A is the electrode surface area (cm^2), C is the reactant concentration (mol cm^{-3}), s is the scan rate (V s^{-1}), R is the gas constant (J mol^{-1} K^{-1}), T is temperature (K), and D is the diffusion coefficient (cm^2 s^{-1}).[28]

$$i_p = 0.4463nFAC\left(\frac{nFsD}{RT}\right)^{\frac{1}{2}} \quad (1)$$

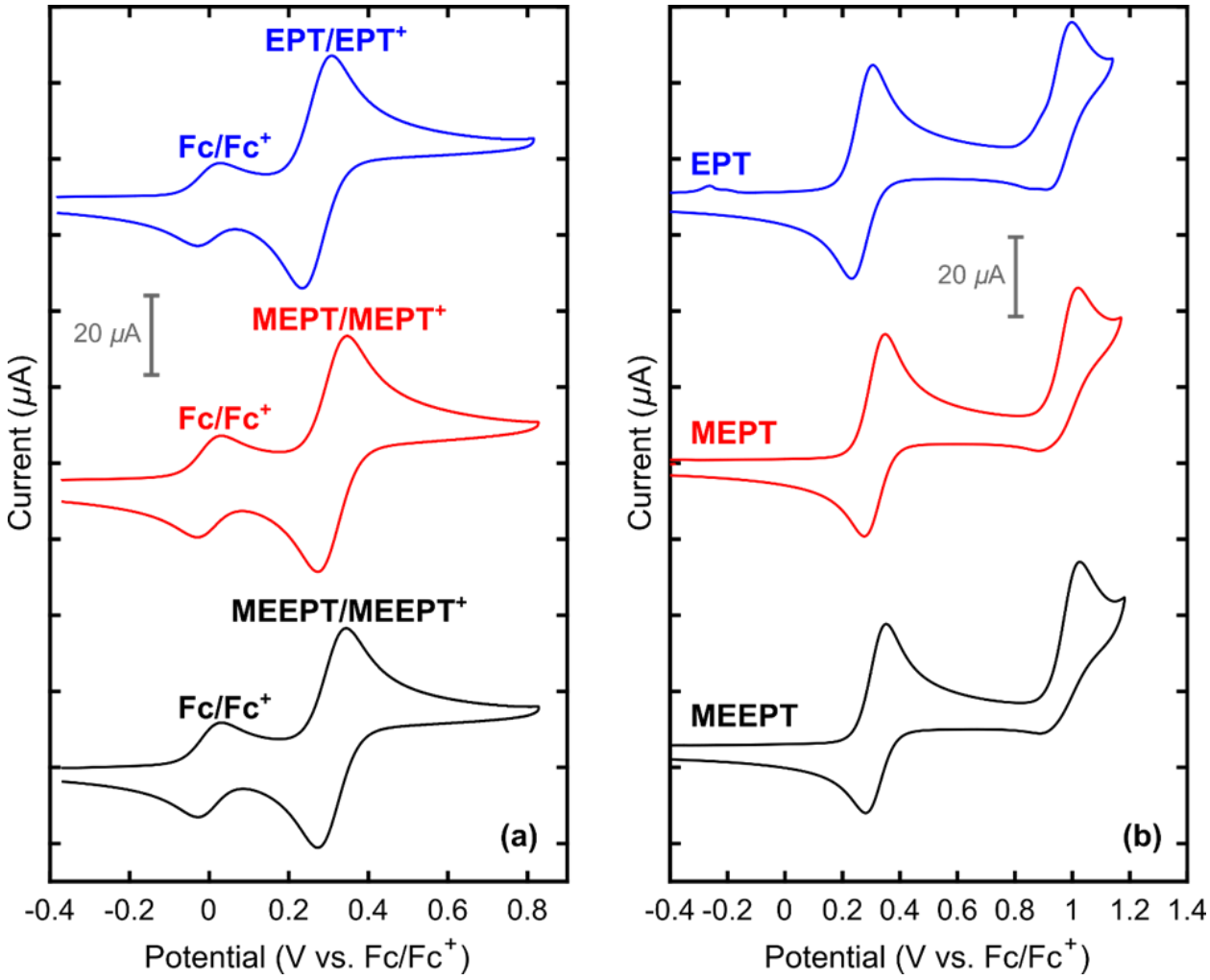

Figure 3: Cyclic voltammograms (cycle 1) of EPT (blue, top), MEPT (red, middle), and MEEPT (black, bottom) at 1 mM in 0.1 M $TEABF_4$ / ACN. **(a)** First positive couple of each active species with ~ 0.7 mM ferrocene internal reference. **(b)** Full potential window of the organic active species, indicating additional irreversible couples at 0.8 – 1.0 V vs. Fc/Fc^+.

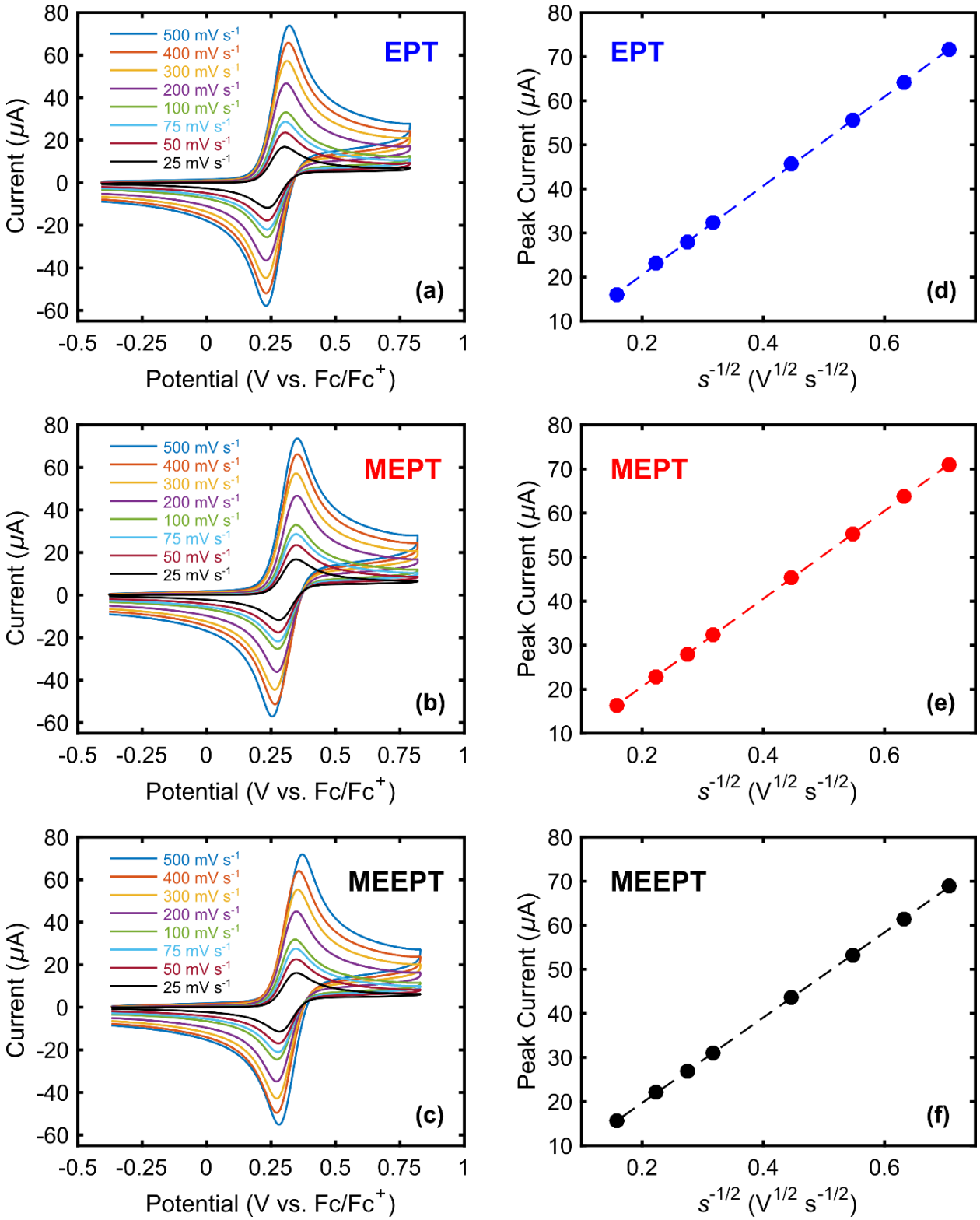

Figure 4: CV scan-rate dependence study for **(a)** EPT, **(b)** MEPT, and **(c)** MEEPT, and Randles-Sevcik construction (peak current vs. square root of scan rate) for the oxidative (anodic) waves of **(d)** EPT, **(e)** MEPT, and **(f)** MEEPT.

Bulk Electrolysis. Bulk-electrolysis experiments were performed in custom H-cells (Figure 5), similar to those reported by Laramie *et al*.,[23] which have two 3.5 mL electrolyte chambers separated by an ultra-fine porous glass frit (P5, Adams and Chittenden). The glass frit helped to minimize species crossover between the two compartments. In one chamber, a piece of reticulated vitreous carbon (45 PPI, Duocell) served as the working electrode, and a fritted Ag/Ag(cryptand)$^+$ reference electrode,[29] containing saturated cryptand, 10 mM $AgBF_4$, and 0.5 M $TEABF_4$ in PC. In the second chamber, another piece of reticulated vitreous carbon served as the counter electrode. Both the working and counter electrode chambers were continuously stirred during bulk electrolysis cycling. A Biologic VMP3 potentiostat applied a constant current of 0.469 mA, equivalent to a C-rate of 1C, for 10 cycles (7 h). Potential cut-offs of ~0.1 to 0.5 V vs. Fc/Fc^+ were imposed on the working electrode to avoid accessing undesired redox couples or electrolyte decomposition. A 3 mm glassy-carbon working electrode (CH Instruments) was used to record CVs of the electrolyte in the working-electrode chamber before and after cycling. Electrolytes comprised of 5 mM neutral active species (EPT, MEPT, or MEEPT), 1 M $TEABF_4$, and ACN were added to the working-electrode chamber, while the counter-electrode chamber contained electrolytes of 5 mM radical-cation active species (EPT-BF_4, MEPT-BF_4, or MEEPT-BF_4), 1 M $TEABF_4$, and ACN.

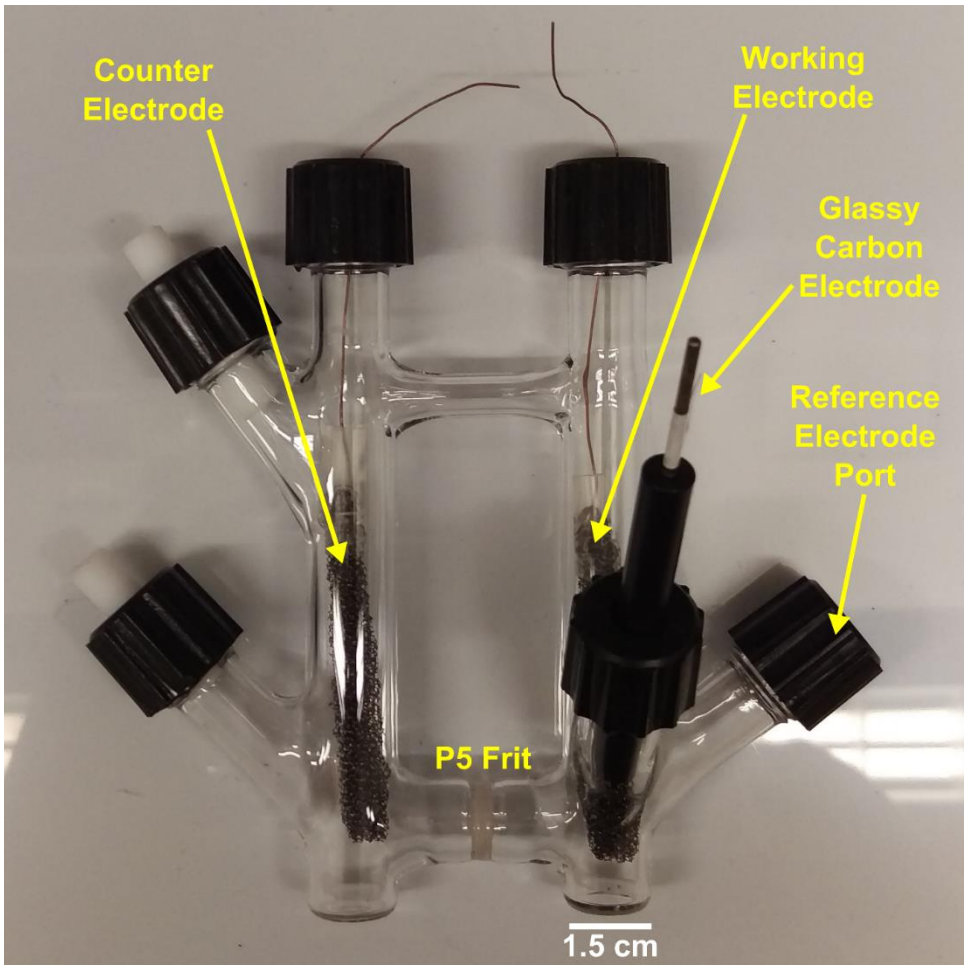

Figure 5: Photograph of the bulk-electrolysis cell, with relevant ports and electrodes labeled.

Symmetric Flow Cell Cycling. Small-volume custom flow cells with interdigitated flow fields, as previously described by Milshtein *et al*., were used in this work (Figure 2).[27] Flow-cell backing plates were machined from polypropylene, which was selected due to its chemical compatibility with ACN. Flow fields were machined from 3.18 mm thick impregnated graphite (G347B, MWI, Inc.). Electrodes were cut from 190 ± 30 µm thick carbon paper (25 AA, SGL group) and used as received without any pre-treatments. Two pieces of carbon paper were layered together to serve as electrodes for both sides of the flow cell and were compressed by ~20%. A single layer of Daramic 175 served as the battery separator material. The electrodes and separator were sealed into the cell using gaskets cut from flexible polytetrafluoroethylene gasket tape (Gore). The assembled cells had geometric active areas of 2.55 cm^2. Flow cells were assembled outside of the glovebox and then dried for at least 1 h under vacuum (-91 kPa_g) before beginning

electrochemical testing. All flow cell cycling, impedance, and polarization measurements were performed inside an argon-filled glovebox.

Sealed jars (10 mL, Savillex), made from perfluoroalkoxy alkane (PFA), housed the electrolyte. A peristaltic pump (Masterflex L/S Series) carried the electrolyte into the flow cell at 10 mL min^{-1}. Norprene tubing (Masterflex) was used inside the pump head, while PFA tubing (Swagelok) connected the pump head, reservoir, and flow cell together. All tubing had an inner diameter of 1.6 mm. All tubing connections were coupled together with PFA or stainless steel compression fittings (Swagelok). The fully assembled and filled cell is shown in Figure 6.

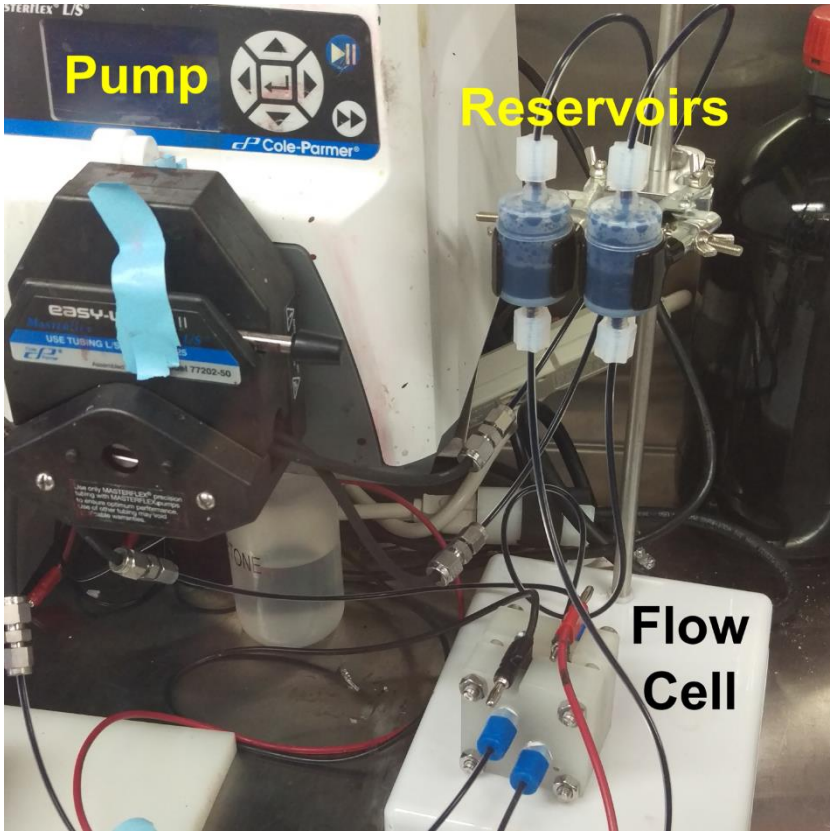

Figure 6: Photograph of the assembled flow cell, connected to the pump and reservoirs.

Starting electrolytes for flow-cell experiments were comprised of 0.25 M MEEPT / 0.25 M MEEPT-BF_4 / 0.5 M $TEABF_4$ / ACN, so that the battery was at 50% SOC. This initial configuration allowed impedance and polarization measurements to be collected at 50% SOC prior to beginning cycling experiments. Each reservoir contained 0.5 M total active species in 10 mL of electrolyte, enabling a theoretical capacity of 13.4 Ah L^{-1} (134 mAh). Impedance measurements were recorded about the cell open-circuit voltage (OCV) at 50% SOC, with an amplitude of 10 mV, over a frequency range of 200 kHz to 5 mHz. Polarization measurements were collected by

initiating potentiostatic holds for 1 min in alternating ± 50 mV steps, allowing for data collection over the range of -0.5 to 0.5 V without significantly changing electrolyte SOC. Data points were recorded every 0.1 s, and the mean current and potential values of the final 50% of data points were used in the I-V curves.

Before beginning symmetric flow-cell cycling experiments, a constant-current pre-discharge was performed to bring the cell to its fully charged state. Then, cycling experiments were performed by applying a constant current density, calculated from the geometric electrode area (2.55 cm^2). Two total flow-cell experiments were performed. In the first experiment, the current density was varied from 50 to 125 mA cm^{-2}, in increments of 25 mA cm^{-2}, for 5 cycles at each current density, and potential cut-offs of ± 0.45 V were imposed. The cell was then returned to the initial current density of 50 mA cm^{-2} for 5 additional cycles. This rate study was completed in 31.8 h. In the second experiment, the flow cell underwent constant current cycling for 100 cycles (80.6 h) at a current density of 100 mA cm^{-2}, with potential cut-offs of ± 0.45 V.

7.3 Synthesis and Stability

Deprotonation of phenothiazine and subsequent S_N2 reaction with the corresponding alkyl halide produces EPT, MEPT, or MEEPT in good yields (Figure 7). MEPT is a white, crystalline solid with a melting point (47 °C) significantly lower than that of EPT (103 – 104 °C). MEEPT is a pale yellow liquid at room temperature. NMR (Figure 8 through Figure 11), mass spectrometry, and elemental analysis confirm product structure and purity.

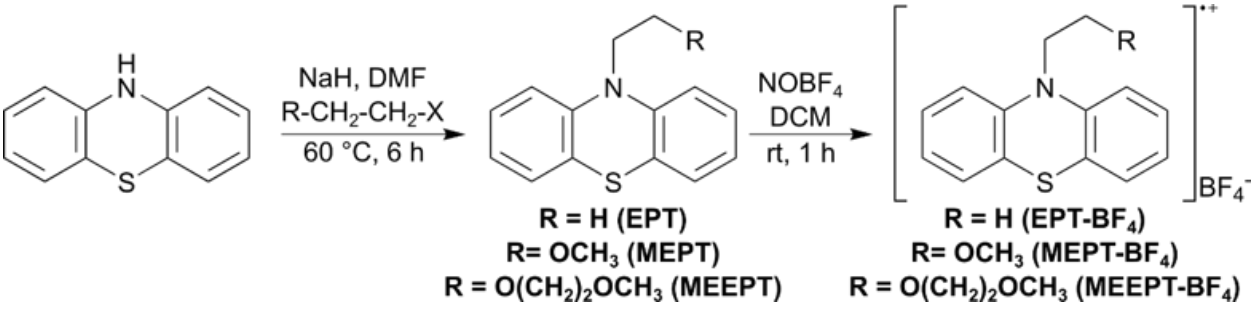

Figure 7: Synthesis of EPT, MEPT, and MEEPT via the alkylation of phenothiazine and subsequent preparation of the radical-cation salts via chemical oxidation.

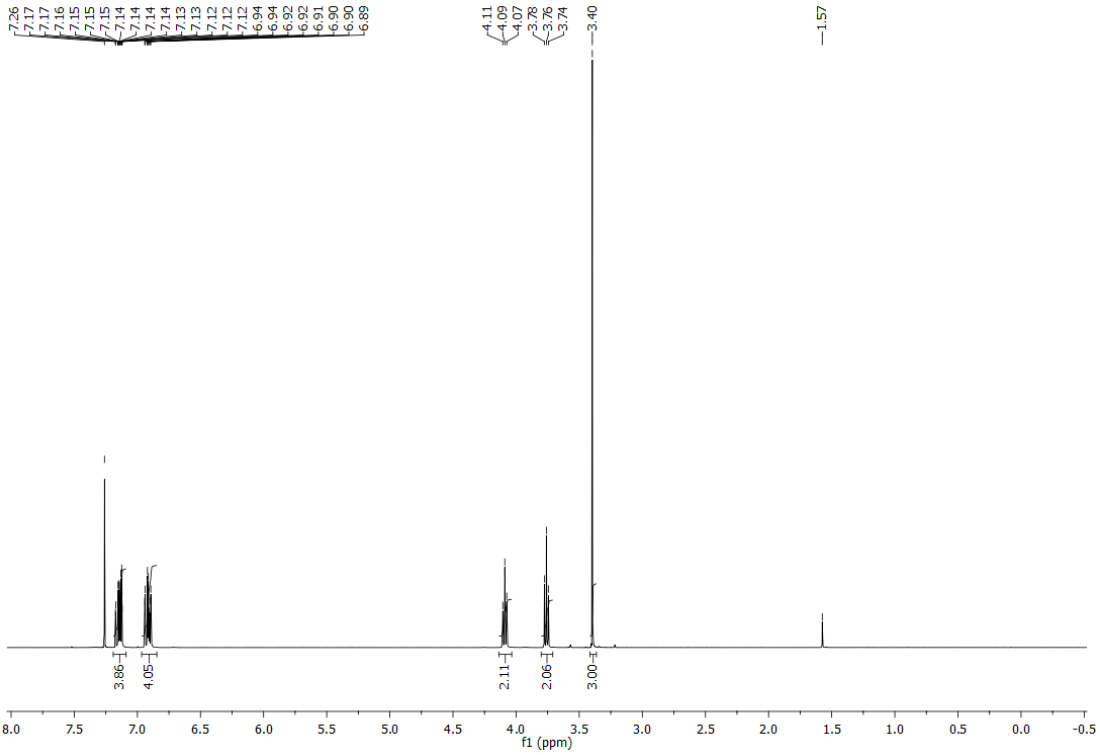

Figure 8: ^{1}H NMR spectrum of MEPT in $CDCl_3$.

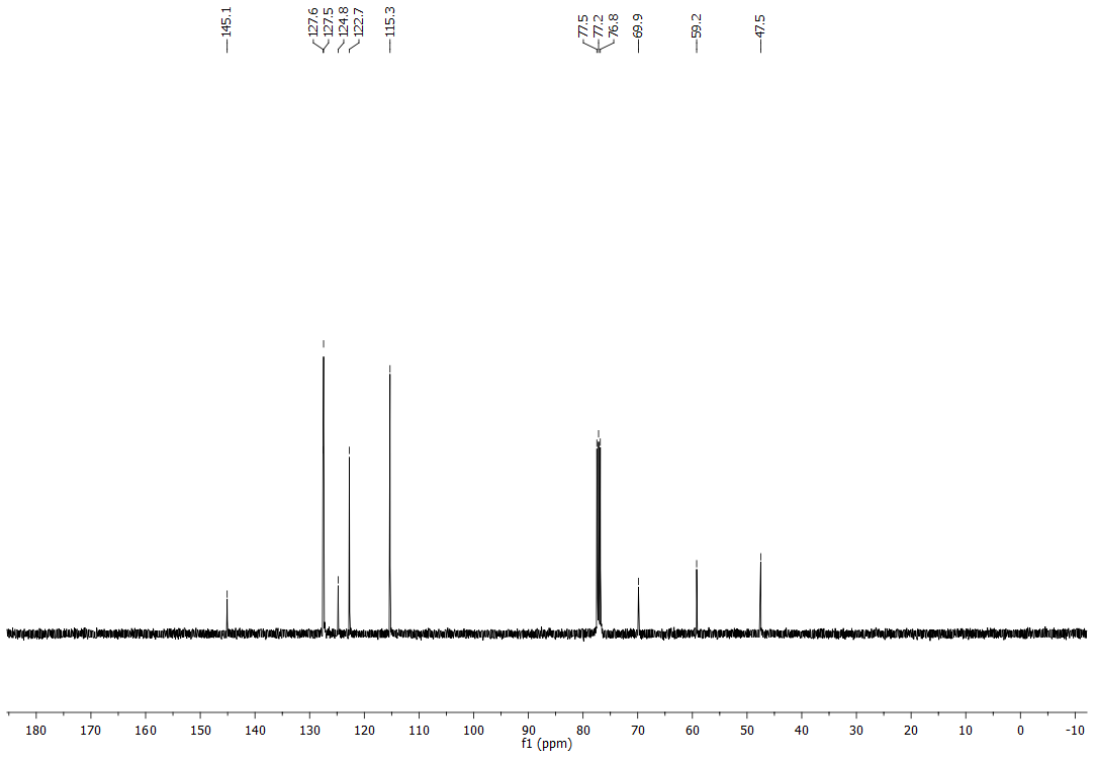

Figure 9: ^{13}C NMR spectrum of MEPT in $CDCl_3$.

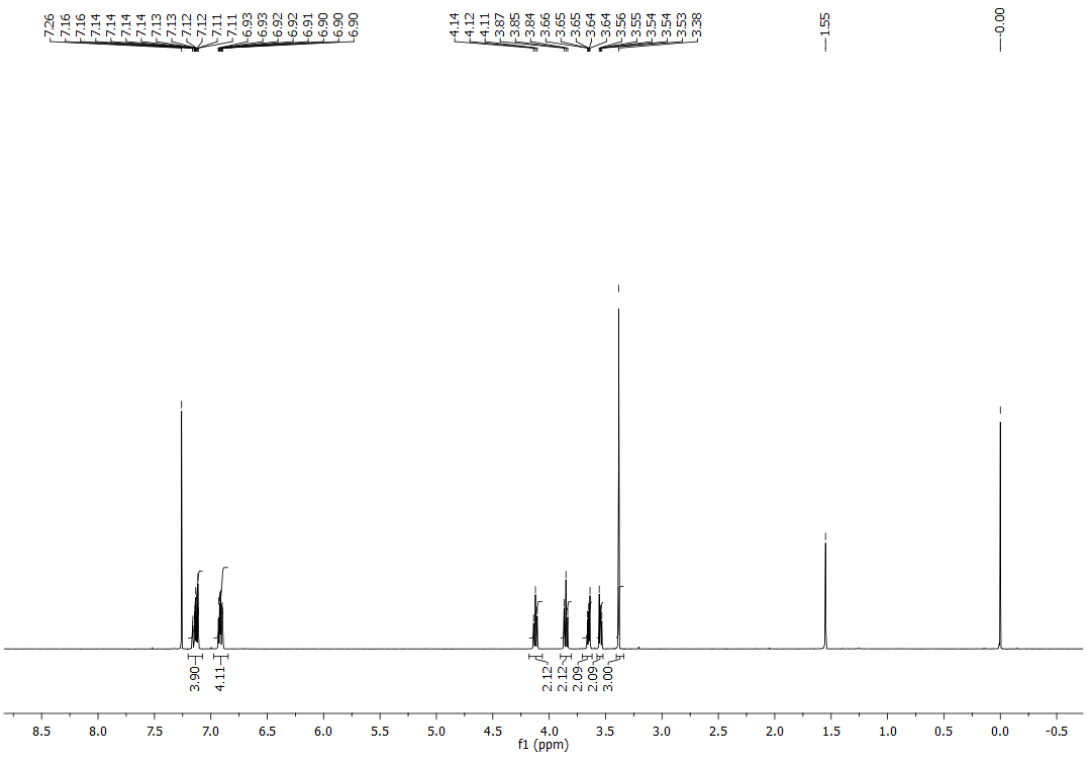

Figure 10: ^{1}H NMR spectrum of MEEPT in $CDCl_3$.

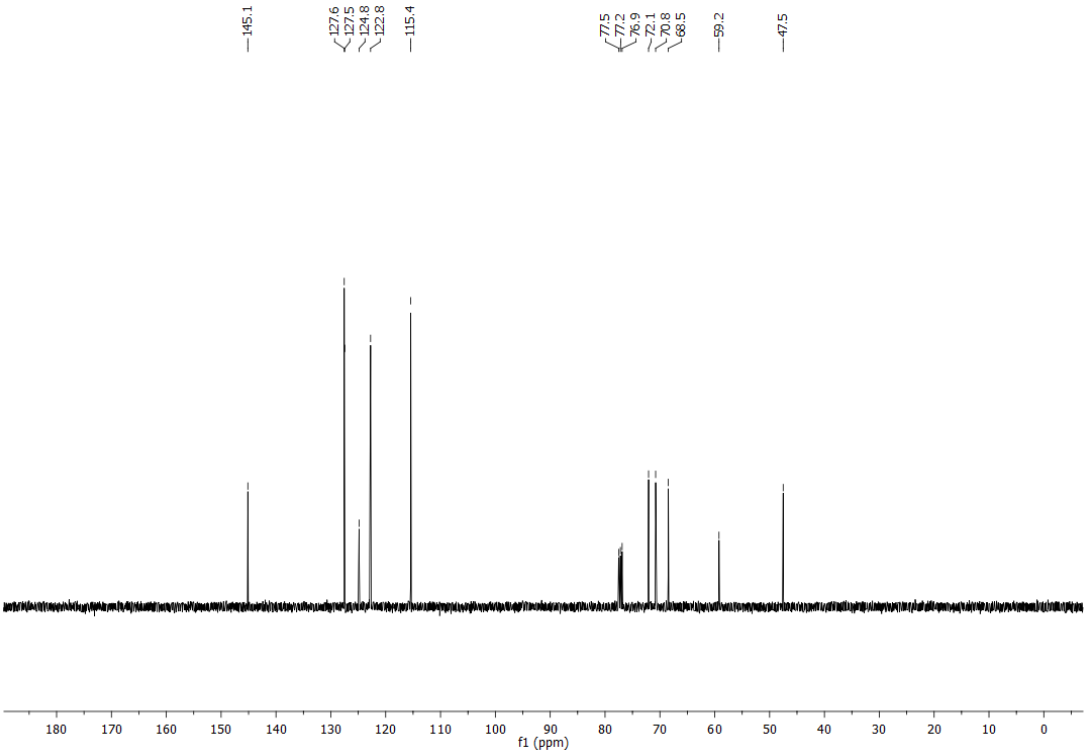

Figure 11: ^{13}C NMR spectrum of MEEPT in $CDCl_3$.

While phenothiazines have been extensively studied for applications in lithium-ion battery overcharge protection,[11–13,15] the design constraints for RFB active materials are fundamentally different than those for overcharge protection. Redox-active materials for RFBs must achieve higher concentrations and have a lower cost per unit mass. We have previously investigated a highly soluble phenothiazine derivative for RFB applications,[14] but the low-yielding, multi-step synthesis currently render the material unfeasible for low-cost NAqRFBs. Hence, the simple one-step synthesis from cheap precursors outlined in Figure 7 represents a new approach towards achieving a low-cost, soluble active species for NAqRFBs.

Isolation of a neutral redox-active molecule does not ensure the stability of the radical-cation form, which is typically the more reactive state of a redox-active organic couple. To enable stability studies of the radical cation itself, we synthesized tetrafluoroborate radical-cation salts via chemical oxidation of the neutral molecules with nitrosonium tetrafluoroborate ($NOBF_4$) (Figure 7). We employ single-crystal XRD to identify the structures of the radical-cation salts and confirm their chemical compositions (Figure 12), and electron paramagnetic resonance (EPR) (Figure 13) of solutions containing these salts in dichloromethane (DCM) to confirm the presence of a radical species. The EPR spectra are consistent with our previous reports of the hexachloroantimonate radical-cation salt of EPT,[15] an expected result due to the similar electronic structure of these *N*-alkylated phenothiazine species.

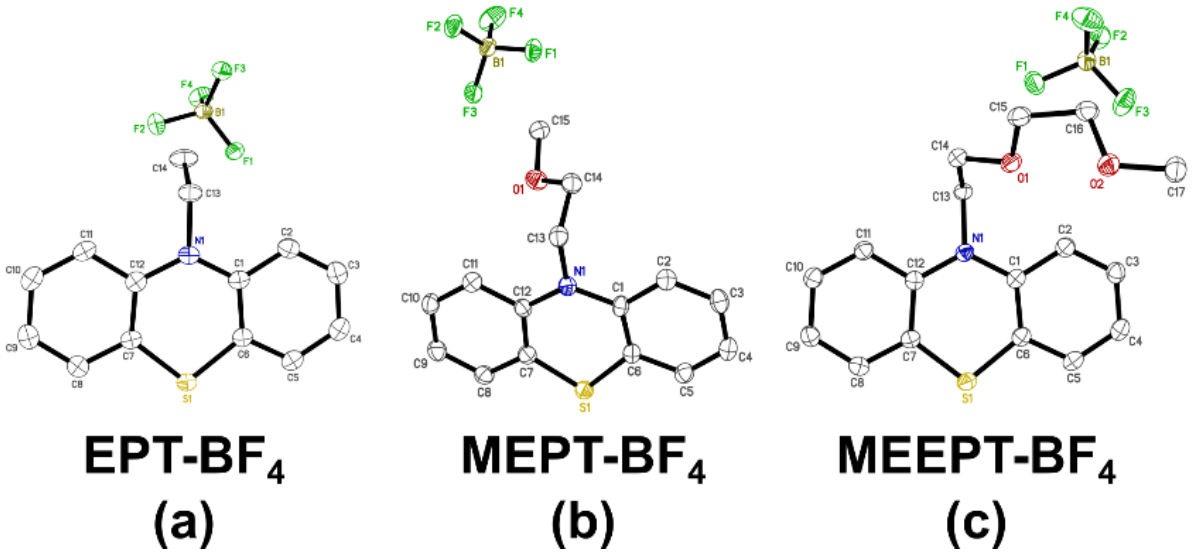

Figure 12: Thermal ellipsoid plots of the crystal structures of **(a)** *N*-ethylphenothiazine tetrafluoroborate (EPT-BF_4), **(b)** *N*-(2-methoxyethyl)phenothiazine tetrafluoroborate (MEPT-BF_4), and **(c)** *N*-(2-(2-methoxyethoxy)ethyl)phenothiazine tetrafluoroborate (MEEPT-BF_4).

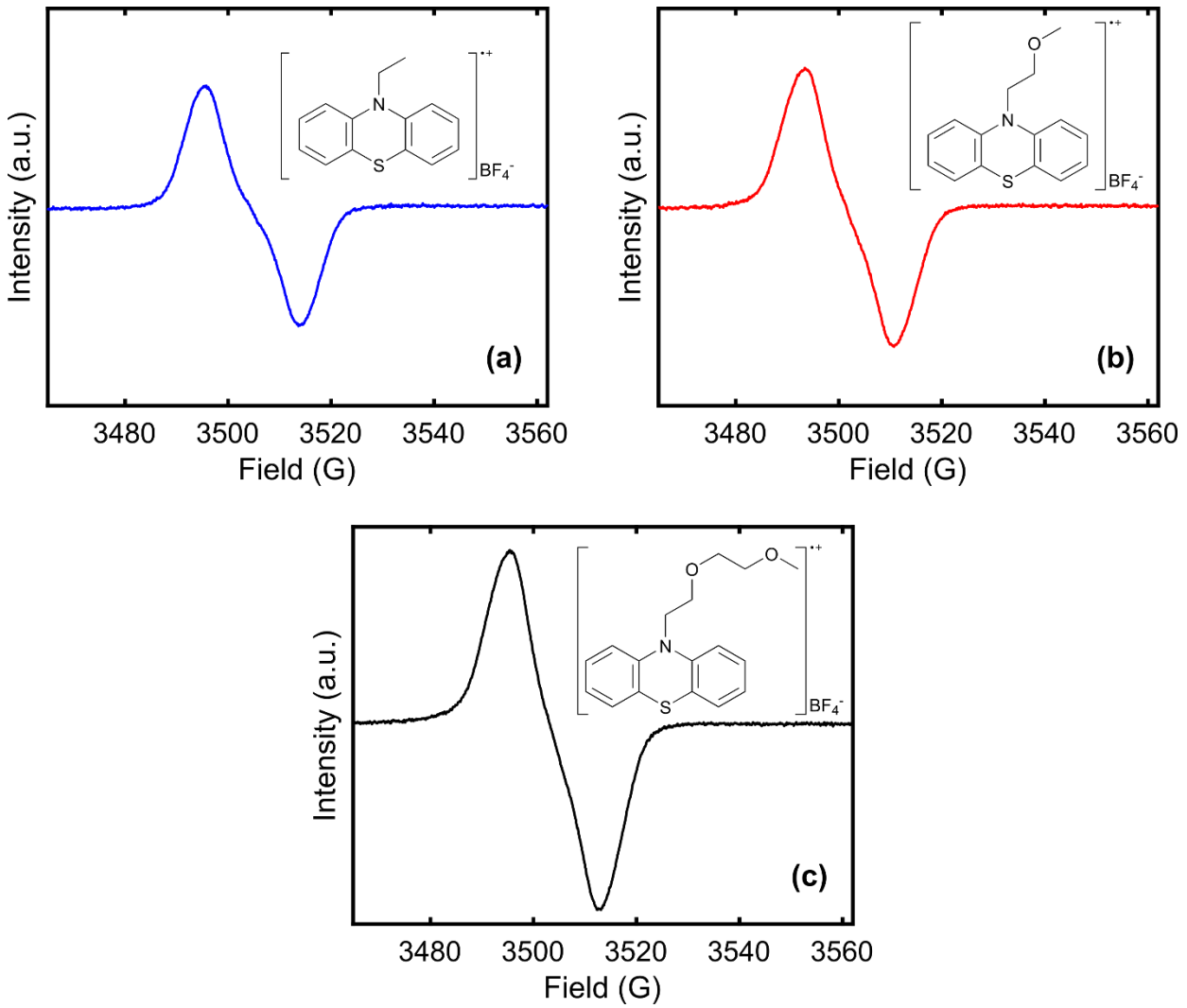

Figure 13: EPR spectra of **(a)** EPT-BF_4, **(b)** MEPT-BF_4, and **(c)** MEEPT-BF_4 salts in dichloromethane.

UV-vis absorption spectroscopy can monitor the lifetimes of radical cations that absorb visible light; this technique has been used to evaluate redox-shuttle candidates for overcharge protection of lithium-ion batteries.[12,13] Herein, we employ UV-vis to compare the stability of dilute solutions of EPT-BF_4, MEPT-BF_4, or MEEPT-BF_4 radical-cation salts in ACN and PC. Figure 14 depicts the absorption spectra of the three radical-cation salts at 0, 1, 3, 5, and 24 h after dissolution in ACN. The spectra are nearly identical for EPT-BF_4, MEPT-BF_4, and MEEPT-BF_4, exhibiting characteristic peaks at the following wavelengths: 316, 445, 514, 760, and 847 nm. Also, the major peak for all species at 514 nm decays by less than 5% over 24 h in ACN (Figure 15). We also performed the same analysis using PC as the solvent, and all of the radical-cation salts exhibit a faster decay in PC of ~15% over 24 h (Figure 16). Due to the low concentration of the active species (0.15 mM) employed in UV-vis measurements, trace impurities

in the solvent may contribute to the observed decay, which may not manifest at higher concentrations. As such, this study moves towards investigating the solubility, stability, and performance of EPT, MEPT, and MEEPT in environments relevant to their implementation in a flow battery, employing ACN, due to the greater stability of the radical-cations salts in that solvent.

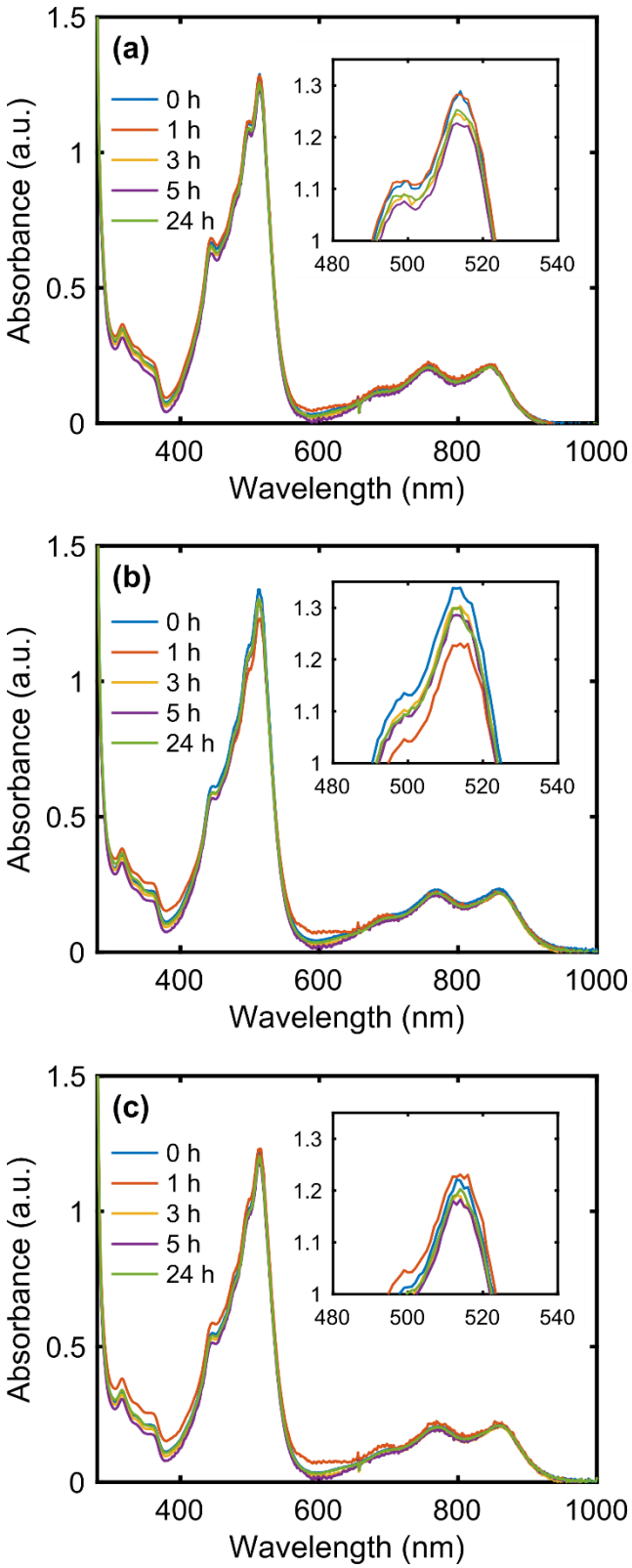

Figure 14: UV-vis spectra of **(a)** EPT-BF_4, **(b)** MEPT-BF_4, and **(c)** MEEPT-BF_4 at 0.15 mM in ACN, recorded at 0, 1, 3, 5, and 24 h after dissolution. Insets: expansion of the most intensely absorbing peak in the visible region.

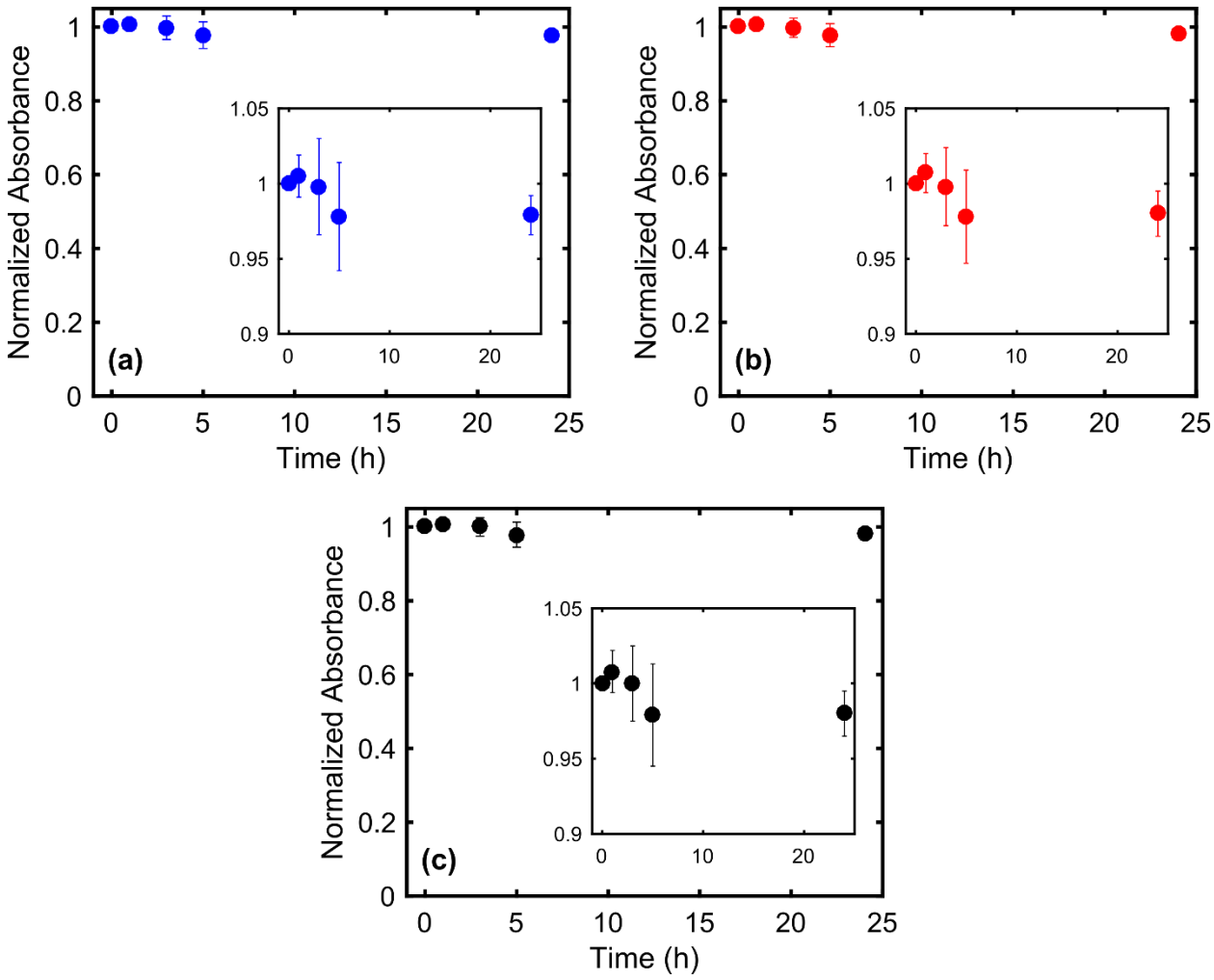

Figure 15: Normalized intensity of UV-vis absorbance at 514 nm vs. time of 0.15 mM **(a)** EPT-BF_4, **(b)** MEPT-BF_4, and **(c)** MEEPT-BF_4 in ACN. Inset: data expanded between absorbance values of 0.9-1.05, recorded at 0, 1, 3, 5, and 24 h after dissolution.

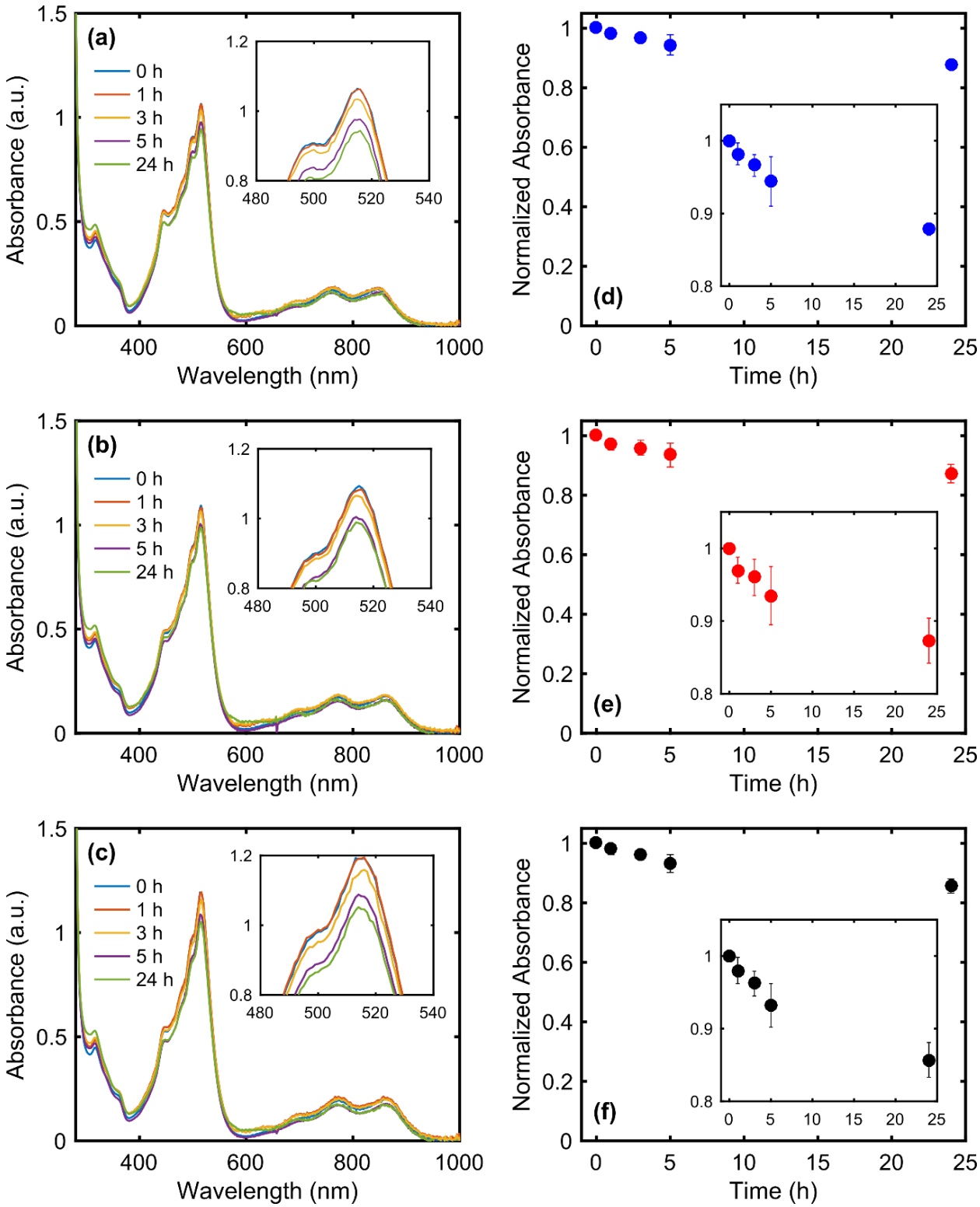

Figure 16: UV-vis spectra of **(a)** EPT-BF_4, **(b)** MEPT-BF_4, and **(c)** MEEPT-BF_4 at 0.15 mM in PC, recorded at 0, 1, 3, 5, and 24 h after dissolution. Characteristic peaks appear at 317, 446, 515, 758, and 853 nm. Normalized intensity of UV-vis absorbance at 515 nm vs. time for 0.15 mM **(d)** EPT-BF_4, **(e)** MEPT-BF_4, and **(f)** MEEPT-BF_4 in PC. Insets for a-c: expansion of most intensely absorbing peak. Insets for d-f: data expanded for absorbance values between 0.8-1.05.

7.4 Solubility

Knowledge of the active-species solubility is of paramount importance when selecting flow-battery operating conditions, because a stable battery can only support an active-species concentration as high as the solubility of the least-soluble oxidation state. The solubilities of MEPT and MEEPT are significantly higher in organic solvents compared to EPT (ca. 0.1 M), perhaps due to the greater polarity of the oligo(glycol) chains relative to the small alkyl group in EPT, as well as the increased disorder arising from the more flexible side-chains (Table 1). MEPT is soluble to > 2 M and MEEPT is miscible with both ACN and our electrolyte of interest, 0.5 M tetraethylammonium tetrafluoroborate ($TEABF_4$) / ACN. A later flow-cell experiment employs this supporting electrolyte composition.

Although MEPT and MEEPT are highly soluble in pure ACN, flow batteries require that the active species remain soluble across all states-of-charge (SOCs) in an electrolyte containing supporting salt, the presence of which can suppress the solubility of redox-active materials.[23,30,31] As such, we investigated the solubilities (Table 1) of the radical-cation salts (EPT-BF_4, MEPT-BF_4, MEEPT-BF_4) in pure ACN solvent and in 0.5 M $TEABF_4$ / ACN. We found that MEEPT-BF_4 is 3× to 5× more soluble than the smaller MEPT-BF_4, and that, unlike the neutral compounds, MEPT-BF_4 solubility does not improve over EPT-BF_4. Additionally, the solubilities of all species decrease in the presence of the supporting salt, agreeing with prior studies.[23,30,31] The MEEPT / MEEPT-BF_4 couple appears to be the best candidate for flow-cell implementation, pending validation of its electrochemical performance, because that couple maintains the highest solubility in both the neutral and oxidized states.

Table 1: Solubilities of the neutral molecules and their radical-cation salts in pure solvent (ACN) and in supporting electrolyte (0.5 M $TEABF_4$ / ACN). Solubilities are reported in molarity (M).

Solvent	**EPT, EPT-BF_4**	**MEPT, MEPT-BF_4**	**MEEPT, MEEPT-BF_4**
ACN	0.25, 0.2	> 2.0, 0.2	Miscible, 0.6
0.5 M $TEABF_4$ / ACN	0.1, 0.1	> 2.0, 0.1	Miscible, 0.5

As previously mentioned, economically viable NAqRFBs will require high active species concentrations > 1 M.[16] Several prior studies have investigated redox-active organic molecules that exhibit > 1 M solubility in pure solvent, in the fully discharged state.[5,6,8,32,33] All of these studies fail, however, to report active species solubility in an electrolyte, containing supporting

salt, or the solubility in the fully charged state. Some studies on metal-centered complexes have considered how dual-solutes impact solubility,[23,30] but still do not mention solubility of the charged species. Arguably, charged species solubilities have been ignored in recent literature due in isolating the charged states of active materials. In the present work, the drastic decreases in MEPT and MEEPT solubilities from the neutral to radical-cation states illustrate an additional molecular design challenge for redox-active organic molecules. The solubilities of the radical-cation salts thereby limit the maximum feasible operating concentrations for MEPT and MEEPT to 0.1 M and 0.5 M, respectively, in a supporting electrolyte of 0.5 M $TEABF_4$ / ACN. These values are less than required concentrations for economic viability, and addressing the challenge of improving the radical-cation salt solubility is a key step to enabling even higher feasible concentrations for future NAqRFB active materials.

7.5 Cyclic Voltammetry

CV offers a method of investigating the redox potential, chemical reversibility, kinetics, and diffusion coefficients associated with EPT, MEPT, and MEEPT. Figure 17 presents cyclic voltammograms of the active species in an electrolyte containing 0.1 M $TEABF_4$ / ACN. Like EPT, the first oxidations of MEPT and MEEPT are reversible in CV experiments, with MEPT and MEEPT exhibiting slightly higher oxidation potentials than EPT (Figure 17, Table 2). This trend in oxidation potential is consistent with increasing adiabatic ionization potentials (IPs, Table 2) from EPT to MEPT / MEEPT, determined at the B3LYP/6-311G(d,p) level of theory.[34–37] This calculation was performed with the self-consistent reaction field (SCRF) polarizable continuum method,[38] as implemented in Gaussian09 (revision A.02),[39] employed to model the acetonitrile (ε = 35.7) environment. The variations in IP arise, as expected, from the stronger electron-withdrawing character of the alkylether substituents relative to the ethyl group.

In addition, all three active species display an irreversible second oxidation event at higher potentials (0.8 – 1.0 V vs. Fc/Fc^+, Figure 3). A scan-rate-dependent CV study (Figure 4) allows for estimation of diffusion coefficients for each active species (Table 2) using Randles-Sevcik analysis (Equation (1)).[28] The diffusion coefficients decrease slightly as the size of the active species increases due to increasing solvated radii with increasing molecule size. The CV scan-rate study also indicates the electrochemical reversibility of EPT, MEPT, and MEEPT, as the peak separations (~60 mV), peak potentials, and peak current ratios (~1) are invariant with scan rate.

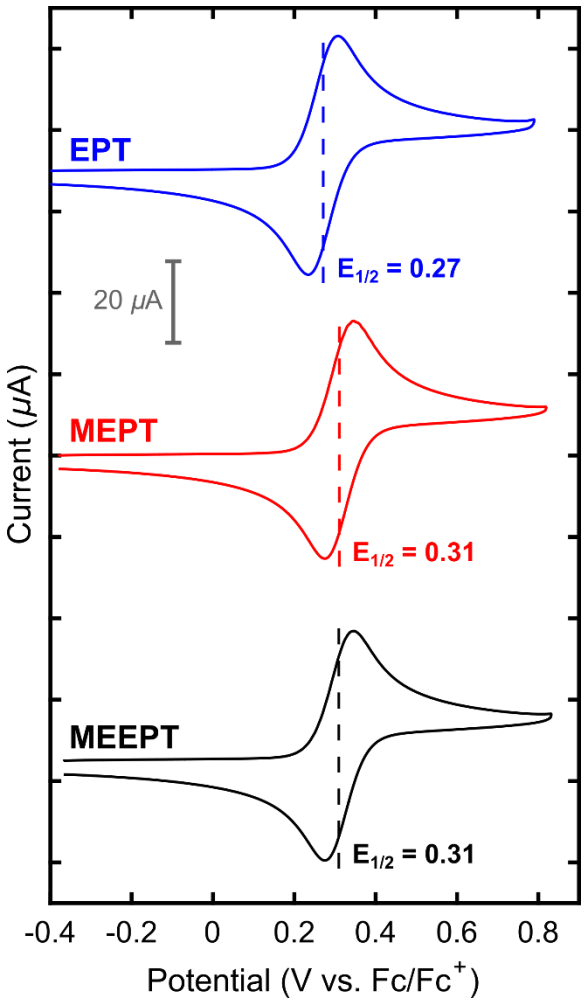

Figure 17: Cyclic voltammograms (cycle 1) of EPT (blue, top), MEPT (red, middle), and MEEPT (black, bottom) at 1 mM in 0.1 M $TEABF_4$ / ACN. Dashed lines denote the half-wave (redox) potentials ($E_{1/2}$).

Table 2: Calculated adiabatic ionization potentials (IPs), half-wave (redox) potentials ($E_{1/2}$), and diffusion coefficients for EPT, MEPT, and MEEPT. In all cases, $TEABF_4$ is dissolved at 0.1 M in ACN and the active-species concentration was 1 mM.

Compound	**Adiabatic IP (eV)**	**$E_{1/2}^{0/+}$ (V vs. Fc/Fc$^+$)**	**Diffusion Coefficient (× 10^{-5} cm^2 s^{-1})**
EPT	5.08	0.27	1.26
MEPT	5.12	0.31	1.23
MEEPT	5.13	0.31	1.16

7.6 Bulk Electrolysis

Bulk-electrolysis experiments allow for further characterization of the electrochemical performance of EPT, MEPT, and MEEPT by assessing the capacity retention of the active species while cycling under dilute conditions for hour time scales. Bulk electrolysis cannot cycle high

concentrations of active material due to mass-transfer limitations of the stirred electrolyte, and contaminant crossover from the counter electrode can poison the working-electrode environment, convoluting capacity-retention data later in the experiment. Nonetheless, bulk electrolysis (Figure 18) can confirm the ability of the active species to charge and discharge at dilute levels.

All three active species display reasonable capacity retentions of 87.7%, 82.5%, and 96.8% for EPT, MEPT, and MEEPT, respectively. The capacity fades observed in bulk electrolysis likely arise from crossover through the porous glass frit and deleterious interactions with side-product species generated in the counter electrode's chamber or on the counter electrode itself. Mean current efficiencies for EPT, MEPT, and MEEPT in bulk electrolysis were 97.6%, 96.1%, and 98.0%, respectively. Losses in current efficiency likely relate to crossover or side reactions amounting to the corresponding capacity fade. The capacity vs. potential cycling curves (Figure 19) validate charging and discharging of the anticipated one-electron process for each active species at the redox potentials measured via CV. Further, the measured charge capacities are extremely close to the theoretical capacities, indicating that all of the active material contributes one electron's worth of storage to the available capacity under dilute conditions. Finally, CVs of the active species collected before and after cycling (Figure 20, Table 3) confirm that the electrochemical behavior of all active species remains the same. Although the CV baseline signals and peak separations change before and after cycling, these effects are likely due to surface fouling of the glassy-carbon electrode. Table 3 shows that the electrochemical behavior intrinsic to the active species (e.g., redox potentials, peak heights, peak height ratios) does not change. This brief bulk-electrolysis study indicates that the active species warrant longer-duration cycling experiments in a flow cell, where the counter electrode and poor mass transfer do not confound the results.

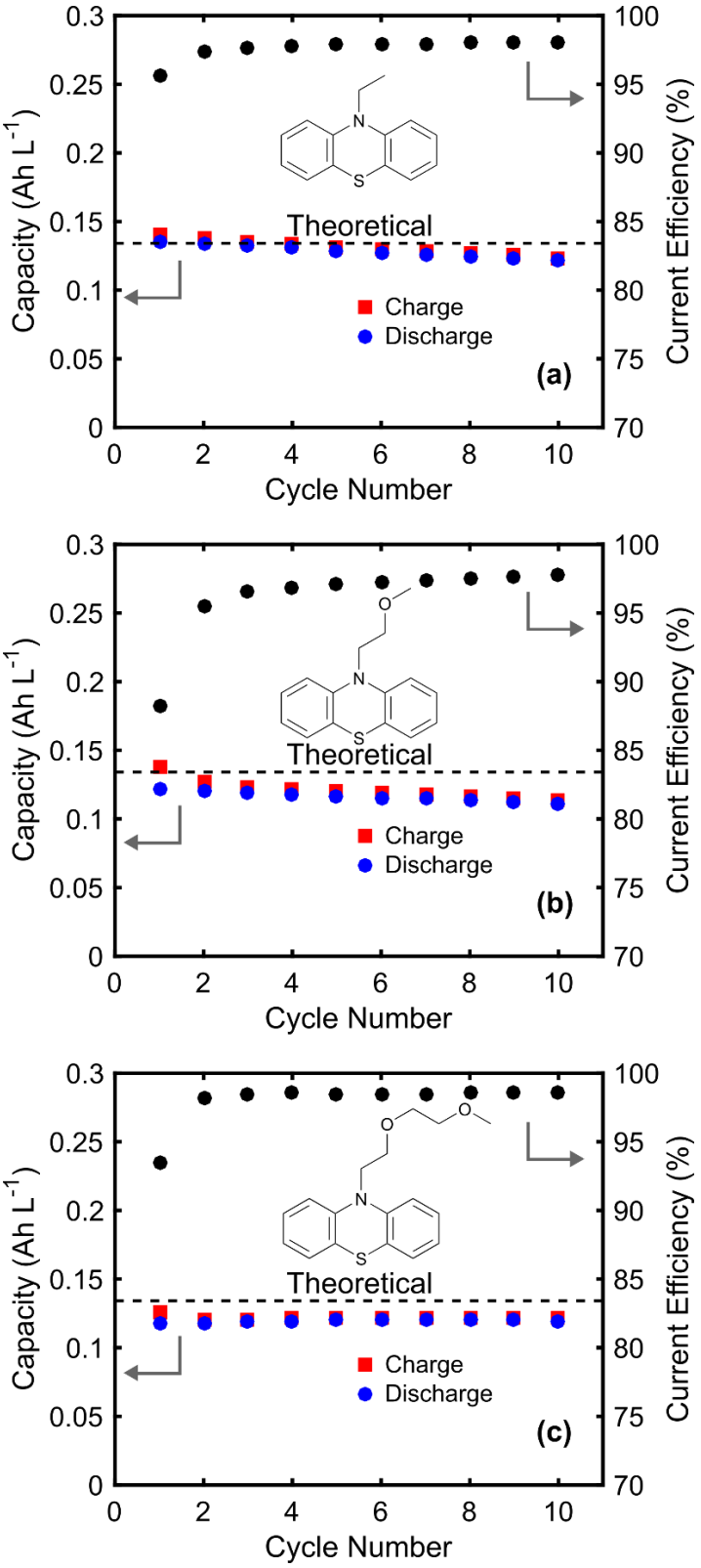

Figure 18: Capacities and current efficiencies from bulk-electrolysis cycling experiments of **(a)** EPT, **(b)** MEPT, and **(c)** MEEPT. Theoretical capacities are 0.134 Ah L^{-1} (0.469 mAh) for each experiment, and 10 cycles completed in 7 h.

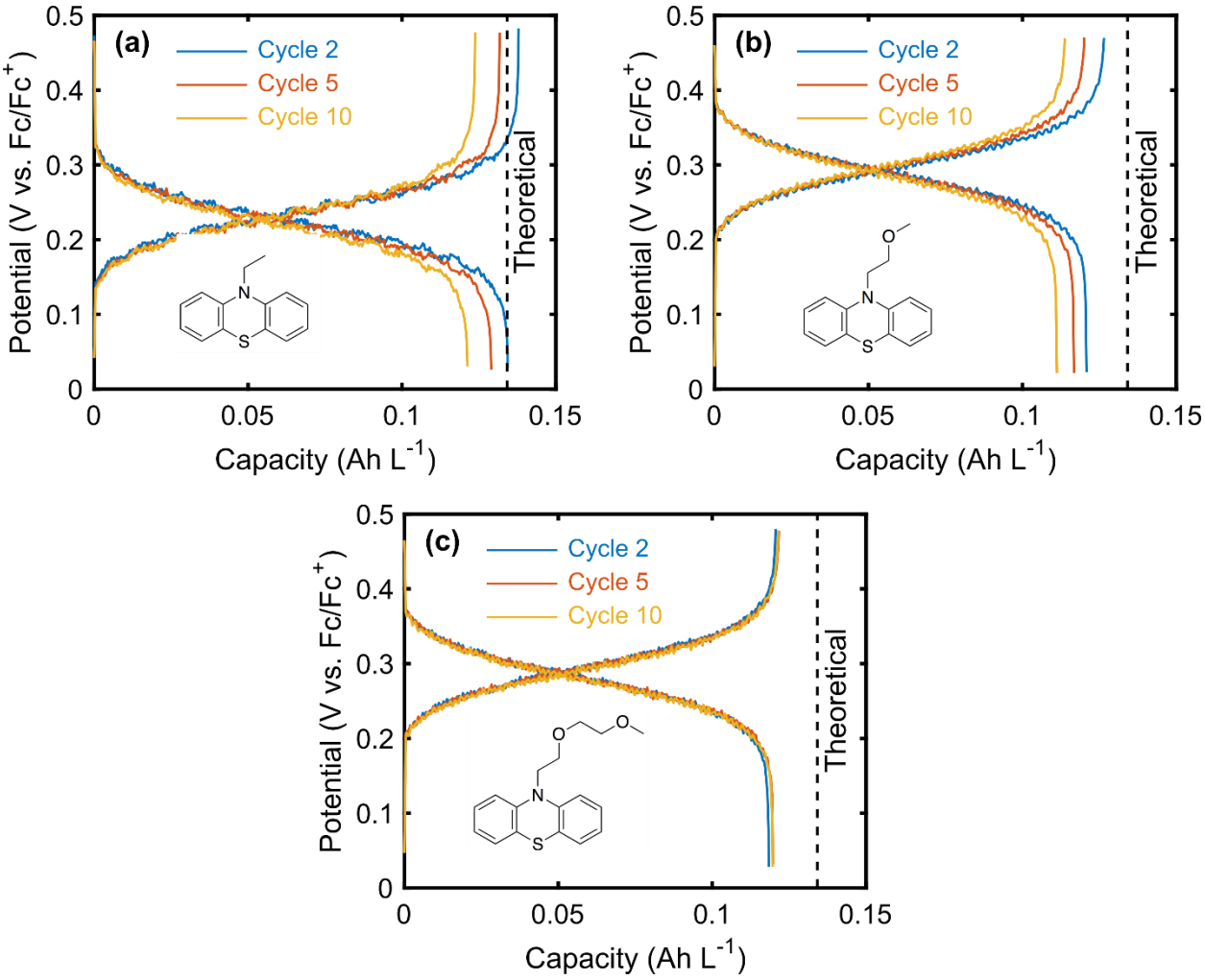

Figure 19: Potential vs. capacity curves from bulk-electrolysis experiments showing cycles 2, 5, and 10 for each of **(a)** EPT, **(b)** MEPT, and **(c)** MEEPT at 5 mM in 1 M $TEABF_4$ / ACN. Theoretical capacities are 0.134 Ah L^{-1} (0.469 mAh) for each experiment, and 10 cycles completed in 7 h.

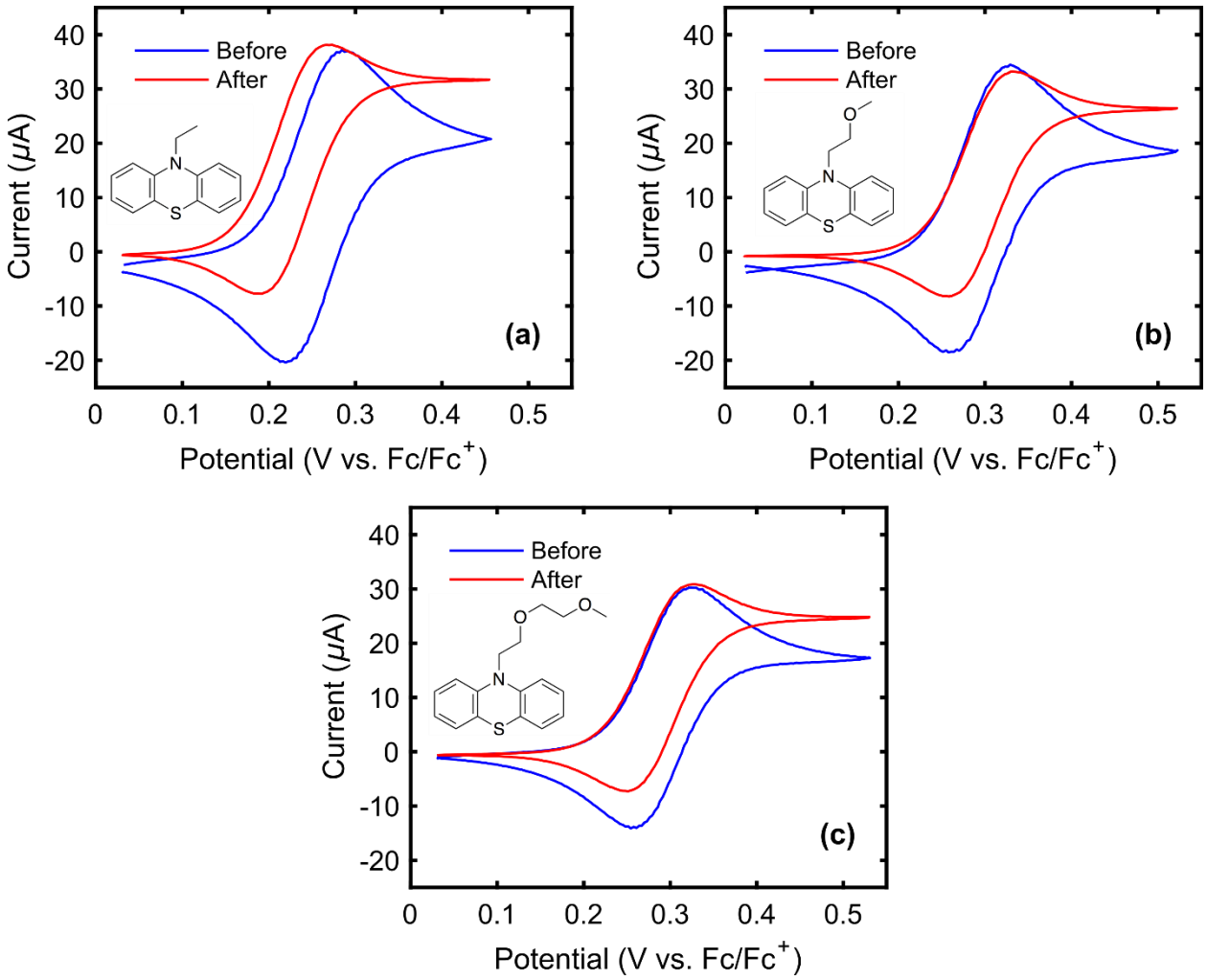

Figure 20: Cyclic voltammograms (cycle 2) before and after 10 bulk-electrolysis cycles for **(a)** EPT, **(b)** MEPT, and **(c)** MEEPT at 5 mM in 1 M $TEABF_4$ / ACN.

Table 3: Quantitative CV characteristics of EPT, MEPT, and MEEPT before and after bulk electrolysis cycling. Tabulated values are calculated from the data available in Figure 20.

	Compound	**$E_{1/2}^{0/+}$ (V vs. Fc/Fc^+)**	**Peak Separation (mV)**	**Peak Current Ratio**	**Peak Oxidative Current (μA)**
Before Bulk Electrolysis	**EPT**	0.284	65	1.050	34.7
	MEPT	0.327	63	1.072	33.9
	MEEPT	0.327	63	0.991	28.7
After Bulk Electrolysis	**EPT**	0.261	78	0.964	36.8
	MEPT	0.327	70	1.005	33.2
	MEEPT	0.324	76	1.004	30.5

7.7 MEEPT Symmetric Flow Cell Cycling

Given that EPT, MEPT, and MEEPT perform very similarly in radical-cation-stability, CV, and bulk-electrolysis experiments, we used solubility to determine which derivative to use in flow-cell cycling experiments, choosing the most-soluble active species, MEEPT. The stability and solubility of the MEEPT-BF_4 radical-cation salt allows for *symmetric* flow cell cycling, a technique we recently introduced.[27] The symmetric flow-cell technique offers several advantages when investigating the capacity retention of a single active species. First, this technique allows for simultaneous cycling of both the neutral and oxidized species in the MEEPT redox pair to determine MEEPT stability under flow-cell conditions in the absence of any other species. Second, unlike bulk electrolysis, symmetric flow-cell cycling removes the need for a counter electrode of dissimilar material, eliminating the possibility of side-products crossing from the counter-electrode chamber and contaminating the working electrode. Thus, the symmetric flow-cell technique offers a more controlled electrolyte environment as compared to bulk electrolysis. Third, the flowing electrolyte improves mass transfer of active species to the electrode surface, enabling higher-concentration and higher-current-density studies. Finally, the symmetric flow cell investigates capacity retention using porous carbon electrodes relevant to flow-battery applications (e.g., carbon paper) instead of reticulated vitreous- or glassy-carbon. [27]

Figure 21a shows a schematic of the symmetric flow cell, where MEEPT is the starting positive-electrolyte (posolyte) active species, and MEEPT-BF_4 is the initial negative-electrolyte (negolyte) active species. Accordingly, a tetrafluoroborate anion must migrate across the separator, and the active species on either side of the cell oscillates between MEEPT and MEEPT-BF_4. For all flow-cell experiments in this work, both reservoirs initially contain electrolyte pre-mixed at 50% SOC to allow for polarization (Figure 21b) and impedance measurements (Figure 21c) prior to cycling. Polarization measurements illustrate the high rate capability of the flow cell employed in this work, achieving current densities as great as ~110 mA cm^{-2} at ±0.4 V. These high current densities are possible due to a low cell ASR, as indicated by the impedance spectra in Figure 21c. The low-frequency intercept denotes the total direct current (DC) contribution (R_{DC}) to the cell impedance (3.2 Ω cm^2), and closely matches the slope of the polarization curve (3.3 Ω cm^2) for cell-potential magnitudes under 0.15 V, indicating that the Nyquist plot low-frequency intercept is a good measure of the cell ASR for small overpotentials.

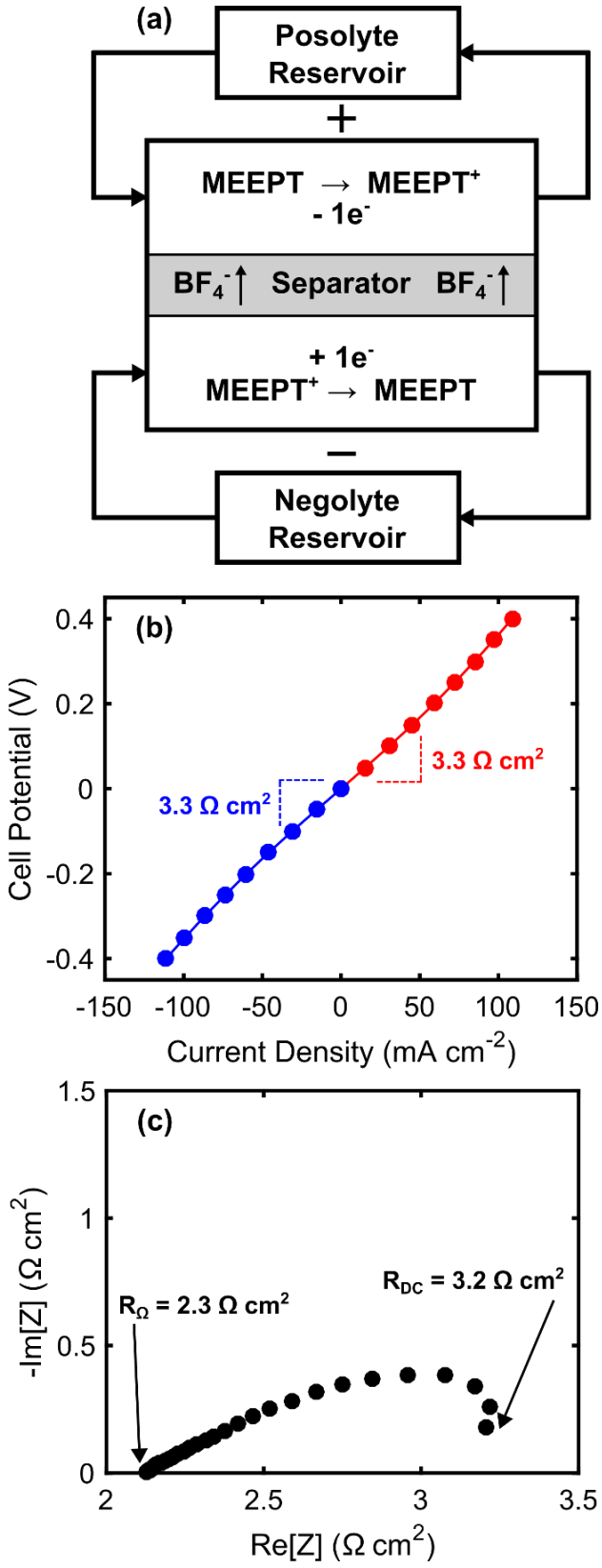

Figure 21: **(a)** Schematic of the MEEPT symmetric flow cell during charging. **(b)** Polarization curve and **(c)** Nyquist plot of the flow cell at 50% SOC before cycling.

The ohmic contribution (R_Ω = 2.3 Ω cm^2) to the cell ASR is similar to that of a prior NAqRFB study employing a Daramic separator and similar supporting electrolyte.[40] Further, the linearity of the polarization curve at low overpotentials (< 0.15 V) suggests that the charge-transfer (kinetic) resistance contribution to the total ASR is small and unchanging. Impedance analysis confirms the small charge-transfer resistance due to the absence of a distinct charge-transfer impedance feature. Redox-active organic molecules in non-aqueous electrolytes typically exhibit fast kinetic rate constants (i.e., greater than 10^{-3} cm s^{-1}),[16] as confirmed for MEEPT in the CV scan-rate study, which leads to negligibly small charge-transfer losses.[27] At higher cell potentials (> 0.15 V), the polarization curve begins a slight deviation from linearity due to increasing mass-transfer limitation; at even higher overpotentials, the cell would approach limiting current. Overall, the cell ASR in this work is low in comparison to recent NAqRFB cycling literature,[4,33,41] outperforming the lowest reported ASR to date by a factor of two.[40] The ASR reported here is on par with recommended values for enabling cost-competitive NAqRFBs (2.3 – 5.0 Ω cm^2).[16,42]

The low cell ASR facilitates high-rate cycling of MEEPT at high current densities not previously achieved by non-aqueous flow cells. The first flow-cell cycling experiment engages a rate study to understand variations in accessed capacity with increasing current density and to select optimized parameters for a long-duration cycling experiment. Figure 22 shows capacity vs. potential curves, as well as the accessed charge and discharge capacities. For constant-current cycling at 50, 75, 100, and 125 mA cm^{-2}, the accessed capacities are 97.3%, 86.3%, 66.7%, and 35.0% of the theoretical (13.4 Ah L^{-1}), respectively. As anticipated, the accessed capacity decreases with increasing current density due to larger cell polarization. The rate study also demonstrates the stability of MEEPT and the resiliency of this system's capacity after undergoing high-rate cycling; the capacity in cycle 25 rebounded to 99.8% of the accessed capacity in cycle 5.

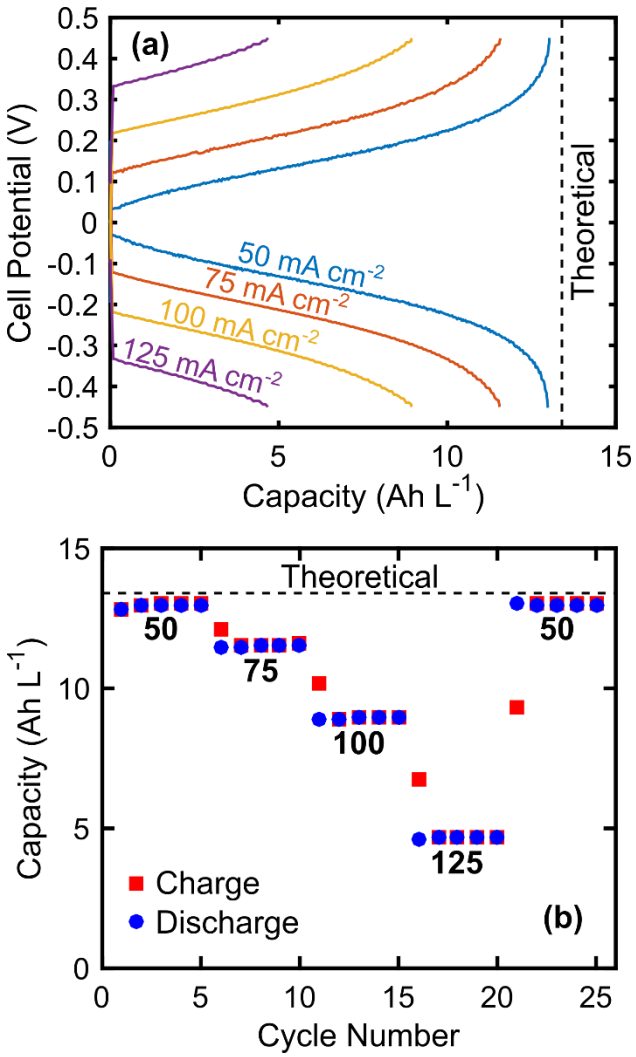

Figure 22: Rate study of MEEPT cycling in a symmetric flow cell, showing **(a)** capacity vs. potential for various current densities. Potential curves are from the 5th cycle at each current density. **(b)** Cycle number vs. capacity for various current densities. Numbers underneath each capacity segment represent current densities with units of mA cm^{-2}. Potential cut-offs imposed during the flow-cell experiment were ± 0.45 V. The theoretical capacity (dashed line) is 13.4 Ah L^{-1} (134 mAh), and the experiment runtime was 31.8 h.

From the rate study, we chose a current density of 100 mA cm^{-2} to demonstrate long-duration cycling of MEEPT. Figure 23a shows select capacity vs. potential curves over 100 cycles; each curve is nearly identical, indicating that no new electrochemical processes arise during cycling and highlighting again the robust stability of MEEPT. Also, Figure 23b displays the charge and discharge capacities as a function of cycle number, as well as the current efficiencies. The capacity rises slightly in the first ca. 15 cycles because the cell is assembled at 50% SOC, after which the capacity and current efficiencies stabilize. The mean capacity accessed is 76.9% (10.3 Ah L^{-1}) of the theoretical value (13.4 Ah L^{-1}), and after cycle 1, and all cycles access between 74.8

and 77.6% of the theoretical capacity. These charge depths are close to a recommended value of 80% for economically viable cycling of RFBs.[16] Capacity fade is undetectable over the 100 cycles of the symmetric flow cell experiment, solidifying MEEPT as a highly stable redox-active molecule, especially considering the total runtime (80.6 h) of the experiment. The mean current efficiency for this cell is 99.5%, and given the high capacity retention, current inefficiencies are most likely due to crossover through the porous Daramic separator. After the cycling experiment completed, the flow cell did not show signs of degradation to any of the components, including the Daramic separator, Gore gaskets, carbon paper electrodes, graphite flow fields, tube fittings, tubing, reservoirs, or polypropylene backing plates. As a whole, the long-duration flow-cell cycling experiment combines a robust active material with an advanced cell design, permitting stable, deep charge, and high-rate cycling of a NAqRFB active material in an unprecedented manner.

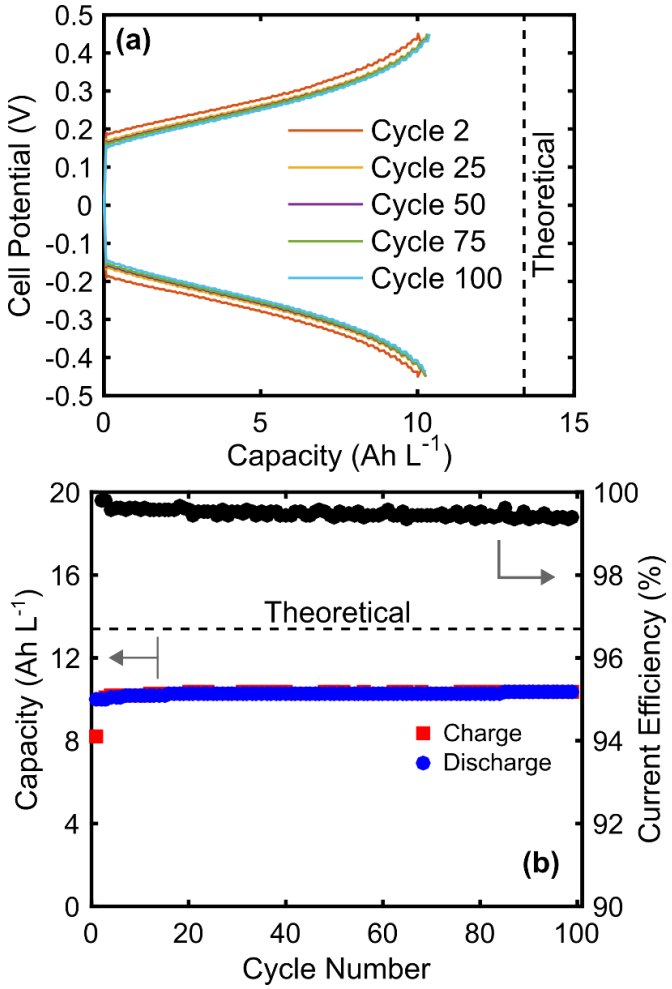

Figure 23. Constant current cycling of MEEPT in a symmetric flow cell at 100 mA cm^{-2}: **(a)** capacity vs. potential; **(b)** charge (red ■) and discharge capacities (blue ●), as well as current efficiencies (black ●), as a function of cycle number. Potential cut-offs imposed during the flow cell experiment were ± 0.45 V. The theoretical capacity (dashed line) is 13.4 Ah L^{-1} (134 mAh), and the experiment runtime was 80.6 h.

7.8 Conclusions

In this work, we demonstrated stable, soluble redox-active organic molecules and a low-ASR flow cell for NAqRFBs. By molecular modification of a stable but low-solubility parent molecule (EPT), we synthesized two new molecules, MEPT and MEEPT, in a single step each. The inexpensive phenothiazine precursor and straightforward synthesis may enable low-cost scale-up of the new derivatives, which are miscible in ACN and an electrolyte comprised of 0.5 M $TEABF_4$ / ACN. Although both the neutral MEPT and MEEPT exhibit high solubility limits, the MEEPT-BF_4 radical-cation salt exhibited superior solubility over MEPT-BF_4. The solubility of both radical-cation salts needs to be improved for practical application, presenting a new challenge for rational molecular design. A decay study of the EPT-BF_4, MEPT-BF_4, and MEEPT-BF_4 radical-cation salts under dilute conditions indicates that all three radical species exhibit essentially identical stability. CV shows that all of the molecules considered exhibit electrochemically reversible behavior. The functionalized derivatives (MEPT and MEEPT) have a redox potential of 0.31 V vs. Fc/Fc^+, a value slightly higher than that of EPT and in agreement with the calculated IPs. Bulk electrolysis illustrates that all three active species cycle similarly under dilute conditions. Further, we designed a high-performance flow cell, with IDFFs and thin carbon-paper electrodes, that demonstrates the lowest ASR for a NAqRFB to date (3.2 – 3.3 Ω cm^2), permitting current densities > 100 mA cm^{-2}. Combining the most soluble compound investigated, MEEPT, with the high-performance flow cell, we first engaged a rate study, illustrating the durability of MEEPT and the flow cell's achievable high current densities. Finally, extended cycling of MEEPT at a constant current density of 100 mA cm^{-2}, with undetectable capacity fade after 100 cycles of deep charging, highlights the unprecedented performance realized through the combination of a robust active material and high-performance flow cell.

The molecular and cell-engineering principles outlined in this work can be extended to other electrolyte systems proposed for NAqRFBs. Molecular modification of EPT represents a logical pathway towards stable and soluble molecules via facile synthesis, and thence towards low-cost NAqRFBs with long cycle lifetimes, inexpensive electrolytes, and small mass-transfer losses.

The flow cell implements prior advances in aqueous RFB architecture to improve the ohmic and mass-transfer resistances over prior non-aqueous flow-cell designs. Future molecular engineering will aim to enhance the solubility of the radical-cation species by introducing asymmetry to the active species and varying the counter-anion type.[43] Future cell engineering will focus on scale-up and further ASR reduction by minimizing separator thickness, increasing operating concentration, and lowering contact resistances.

7.9 References

1. W. Wang et al., *Chem. Commun.*, **48**, 6669–6671 (2012).
2. F. R. Brushett, J. T. Vaughey, and A. N. Jansen, *Adv. Energy Mater.*, **2**, 1390–1396 (2012).
3. X. Wei et al., *Angew. Chem. Int. Ed.*, **54**, 8684–8687 (2015).
4. J. Huang et al., *J Mater Chem A*, **3**, 14971–14976 (2015).
5. J. Huang et al., *Adv. Energy Mater.*, **5**, 1401782 (2015).
6. Z. Li et al., *Electrochem. Solid-State Lett.*, **14**, A171–A173 (2011).
7. X. Wei et al., *Adv. Mater.*, **26**, 7649–7653 (2014).
8. K. Takechi, Y. Kato, and Y. Hase, *Adv. Mater.*, 2501–2506 (2015).
9. X. Wei et al., *Adv. Energy Mater.*, **5**, 1400678 (2015).
10. S. Ergun, C. F. Elliott, A. P. Kaur, S. R. Parkin, and S. A. Odom, *Chem Commun*, **50**, 5339–5341 (2014).
11. S. Ergun, C. F. Elliott, A. P. Kaur, S. R. Parkin, and S. A. Odom, *J. Phys. Chem. C*, **118**, 14824–14832 (2014).
12. K. A. Narayana et al., *ChemPhysChem*, **16**, 1179–1189 (2015).
13. A. P. Kaur, S. Ergun, C. F. Elliott, and S. A. Odom, *J Mater Chem A*, **2**, 18190–18193 (2014).
14. S. A. Odom, S. Ergun, P. P. Poudel, and S. R. Parkin, *Energy Env. Sci*, **7**, 760–767 (2014).
15. R. M. Darling, K. G. Gallagher, J. A. Kowalski, S. Ha, and F. R. Brushett, *Energy Environ. Sci.*, **7**, 3459–3477 (2014).
16. A. P. Kaur, N. E. Holubowitch, S. Ergun, C. F. Elliott, and S. A. Odom, *Energy Technol.*, **3**, 476–480 (2015).
17. D. S. Aaron et al., *J. Power Sources*, **206**, 450–453 (2012).
18. Q. H. Liu et al., *J. Electrochem. Soc.*, **159**, A1246–A1252 (2012).
19. B. Huskinson et al., *Nature*, **505**, 195–198 (2014).
20. Q. Chen, M. R. Gerhardt, L. Hartle, and M. J. Aziz, *J. Electrochem. Soc.*, **163**, A5010–A5013 (2016).
21. Q. Chen, L. Eisenach, and M. J. Aziz, *J. Electrochem. Soc.*, **163**, A5057–A5063 (2016).
22. S. M. Laramie, J. D. Milshtein, T. M. Breault, F. R. Brushett, and L. T. Thompson, *J. Power Sources*, **327**, 681–692 (2016).
23. M.-S. Park et al., *ACS Appl. Mater. Interfaces*, **6**, 10729–10735 (2014).
24. R. M. Darling and M. L. Perry, *J. Electrochem. Soc.*, **161**, A1381–A1387 (2014).
25. C. R. Dennison, E. Agar, B. Akuzum, and E. C. Kumbur, *J. Electrochem. Soc.*, **163**, A5163–A5169 (2016).
26. J. D. Milshtein, J. L. Barton, R. M. Darling, and F. R. Brushett, *J. Power Sources*, **327**, 151–159 (2016).

27. R. G. Compton and C. E. Banks, *Understanding Voltammetry*, 2nd ed., p. 119-126, Imperial College Press, London, (2011).
28. A. Lewandowski, M. Osińska, A. Swiderska-Mocek, and M. Galinski, *Electroanalysis*, **20**, 1903–1908 (2008).
29. A. A. Shinkle, T. J. Pomaville, A. E. S. Sleightholme, L. T. Thompson, and C. W. Monroe, *J. Power Sources*, **248**, 1299–1305 (2014).
30. J. R. Dahn et al., *J. Electrochem. Soc.*, **152**, A1283–A1289 (2005).
31. C. S. Sevov et al., *J. Am. Chem. Soc.*, **137**, 14465–14472 (2015).
32. W. Duan et al., *J Mater Chem A*, **4**, 5448–5456 (2016).
33. C. Lee, W. Yang, and R. G. Parr, *Phys. Rev. B*, **37**, 785–789 (1988).
34. A. D. Becke, *Phys. Rev. A*, **38**, 3098–3100 (1988).
35. A. D. Becke, *J. Chem. Phys.*, **98**, 5648–5652 (1993).
36. R. Krishnan, J. S. Binkley, R. Seeger, and J. A. Pople, *J. Chem. Phys.*, **72**, 650–654 (1980).
37. J. Tomasi, B. Mennucci, and R. Cammi, *Chem. Rev.*, **105**, 2999–3094 (2005).
38. M. J. Frisch et al., *Gaussian 09 Revision E.01*.
39. I. L. Escalante-García, J. S. Wainright, L. T. Thompson, and R. F. Savinell, *J. Electrochem. Soc.*, **162**, A363–A372 (2015).
40. J.-H. Kim et al., *Electrochem. Commun.*, **13**, 997–1000 (2011).
41. R. Darling, K. Gallagher, W. Xie, L. Su, and F. Brushett, *J. Electrochem. Soc.*, **163**, A5029–A5040 (2016).
42. L. Cosimbescu et al., *Sci. Rep.*, **5**, 14117 (2015).

8. Towards low resistance non-aqueous flow batteries

This chapter is adapted from a manuscript in-submission: J. D. Milshtein, J. L. Barton, T. J. Carney, J. A. Kowalski, R. M. Darling, F. R. Brushett, Towards low resistance non-aqueous redox flow batteries, *Journal of the Electrochemical Society*, submitted.

8.1 Introduction

Advancing NAqRFBs to a technology-readiness level competitive with aqueous redox flow batteries (AqRFBs) will require systematic studies of the performance limitations facing NAqRFBs, in concert with the ongoing, and more serendipitous, molecular discovery activities. AqRFB development has recently benefited from a series of studies implementing a single electrolyte diagnostic flow cell technique[31] to systematically evaluate cell designs[32] and to better elucidate cell-level performance limitations relating to ohmic, charge transfer, and mass transfer losses.[27,33,34] A schematic of this single electrolyte technique is provided in Figure 1a, where a flow cell is connected to a single electrolyte reservoir at 50% state-of-charge (SOC). The electrolyte passes through the positive side of the cell, where the active species are oxidized, and then loops back through the negative side of the cell, where the charged species are reduced. Since the same active species are present on both sides of the cell, crossover will not adversely impact cell lifetime or convolute data analysis. Additionally, the reservoir SOC is constant and effectively permits cell-level polarization and electrochemical impedance spectroscopy measurements at a steady-state. This technique most accurately mimics a RFB at 50% SOC when the conversion (f) through one side of the single electrolyte cell is low.[34] The single pass conversion is described in Equation (1), where I is the total current (A), C_{red} is the concentration of reduced species in the reservoir (mol m^{-3}), n is the number of electrons transferred (-), F is the Faraday constant (C mol^{-1}), and Q is the electrolyte volumetric flow rate (m^3 s^{-1}). Figure 1b illustrates how the electrolyte SOC will vary inside the flow cell as a function of normalized path length for various conversions. For all experiments performed in this work, the single pass conversion ranges from 0 to 0.122.

$$f = \frac{I}{C_{red} nFQ} \tag{1}$$

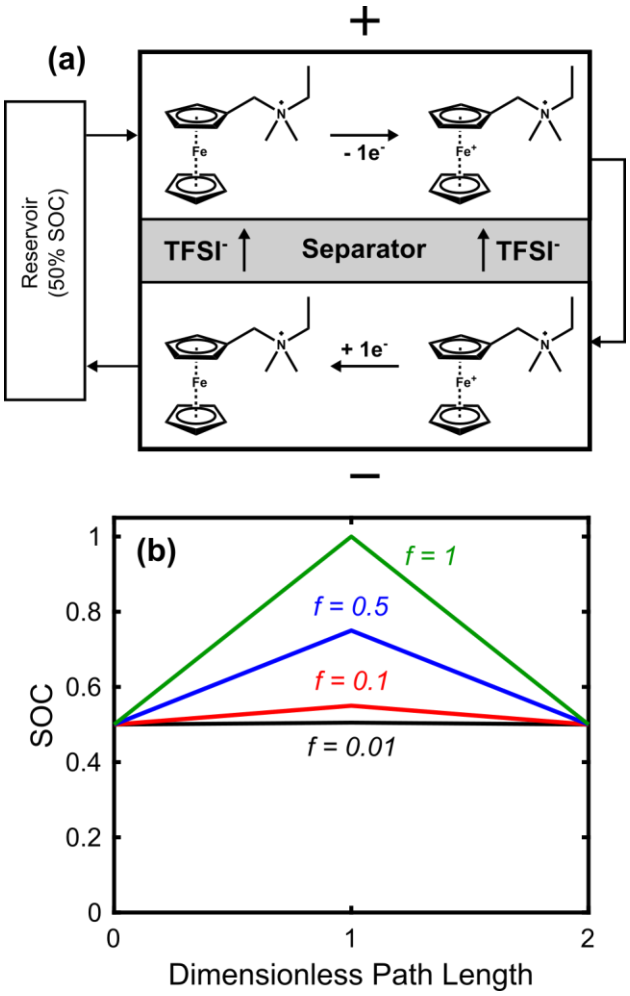

Figure 1: **(a)** Single electrolyte flow cell configuration employing the Fc1N112$^{+/2+}$ redox couple. **(b)** Schematic plot illustrating the electrolyte SOC as a function of path length for various reactant conversions.

Single electrolyte studies rely on a stable active material; for example, prior AqRFB studies with this technique have exploited the VO^{2+}/VO_2^{+} or V^{2+}/V^{3+} redox couples.[31–34] We previously reported 4-acetamido-2,2,6,6-tetramethylpiperdine-1-oxyl and its oxoammonium cation as a stable, model redox couple for studying NAqRFB electrolyte properties and cell performance.[27] In that same report, we also postulated that the ferrocene / ferrocenium redox couple could be a viable candidate for diagnostic flow cell experiments if the solubility of both species could be increased.[27] Here, that challenge is overcome through the use of a highly soluble ferrocene derivative, N-(ferrocenylmethyl)-N,N-dimethyl-N-ethylammonium bis(trifluoromethane)sulfonamide (**[Fc1N112^{+}][TFSI^{-}]**),[22,35,36] and its oxidized form (**[Fc1N112^{2+}][TFSI^{-}]$_2$**), which enables high concentration studies in a non-aqueous single electrolyte diagnostic flow cell (Figure 1a).

This study utilizes the $Fc1N112^{+/2+}$ redox couple, in conjunction with the single electrolyte technique, to demonstrate non-aqueous flow cells with low ASR and to highlight typical performance limitations in NAqRFBs. In particular, this study engages a series of polarization and impedance measurements to quantify cell performance as a function of active species concentration, supporting electrolyte composition, flow rate, separator type, and electrode thickness. Polarization measurements enable direct determination of the overall cell performance, while electrochemical impedance spectroscopy measurements enable assessment of component-level contributions to the total cell ASR. Ultimately this study demonstrates cell ASR values well below recommended specifications (2.3 – 5 Ω cm^2)[7,12,30] and highlights general approaches for reducing the ASR of NAqRFBs. Further, we demonstrate non-aqueous flow cell scalability by extending our analysis from a smaller cell (2.55 cm^2) to a larger cell (25 cm^2), without deviation of electrochemical performance. While the present study does not address all challenges associated with full RFBs, such as active species crossover or open circuit potential, these systematic experiments can guide future NAqRFB development and benchmark electrochemical performance.

8.2 Experimental

Solution Preparation. All solution preparation and electrochemical experiments were performed inside an argon (Airgas, AR UHP300, 99.999%) filled glove box (Inert Technologies, 4GB 2500, O_2 < 5 ppm, H_2O < 1 ppm) under ambient temperature (≈ 25 ºC). Propylene carbonate (PC, 99.99%) and acetonitrile (MeCN, 99.98%) solvents for electrochemical experiments were purchased from BASF and used as received. Lithium bis(trifluoromethane)sulfonamide (LiTFSI, 99.99%, BASF) and tetraethylammonium bis(trifluoromethane)sulfonamide (TEATFSI, 99%, Iolitech) were used as received.

Active Species Synthesis. N-(ferrocenylmethyl)-N,N-dimethyl-N-ethylammonium bromide (**$[Fc1N112^+][Br^-]$**) was synthesized, in the glove box, according to the following literature procedure (Figure 2).[22,35] (Dimethylaminomethyl)ferrocene (19.4 g, 79.8 mmol, 96%, Sigma Aldrich) was added to 150 mL of MeCN (Extra Dry 99.9%, Acros Organics). The flask was sealed with a rubber stopper, and the solution was stirred for 15 min. Bromoethane (6.2 mL, 83.0 mmol, 98%, Sigma Aldrich) was added dropwise at ≈ 0.5 mL min^{-1}. The solution was stirred overnight.

The precipitate was filtered and washed with ≈ 25 mL of diethyl ether (99%, Alfa Aesar). Yield: 20.20 g (71.9%).

[Fc1N112$^+$][TFSI$^-$] was generated through an ion exchange in water (Figure 2).[22,35] **[Fc1N112$^+$][Br$^-$]** (12.3235 g, 35 mmol) was added to 130 mL of deionized water (DI H_2O). LiTFSI (13.36 g, 47 mmol) was dissolved in a separate flask with 50 mL of DI H_2O. The LiTFSI solution was added dropwise into the **[Fc1N112$^+$][Br$^-$]** solution in the round bottom flask and stirred for 1 h. The yellow **[Fc1N112$^+$][TFSI$^-$]** product (Figure 2, bottom left) was filtered and dried under vacuum for 24 h at room temperature. Yield: 24.72 g (97.9%).

[Fc1N112^{2+}][TFSI$^-$]$_2$ was synthesized via a chemical oxidation[37] and subsequent ion exchange (Figure 2). **[Fc1N112$^+$][Br$^-$]** (12.3235 g, 35 mmol) was added to a 130 mL of DI H_2O. Iron(III) chloride hexahydrate (18.921 g, 70 mmol, 98%, Sigma Aldrich) was added to the solution and stirred for 1 h. LiTFSI (26.72 g, 93 mmol) was dissolved in a separate flask with 100 mL of DI H_2O. The LiTFSI solution was added dropwise and stirred for 1 h. The blue **[Fc1N112^{2+}][TFSI$^-$]$_2$** product (Figure 2, bottom left) was filtered and dried under vacuum for 24 h at room temperature. Yield: 24.76 g (85.0%).

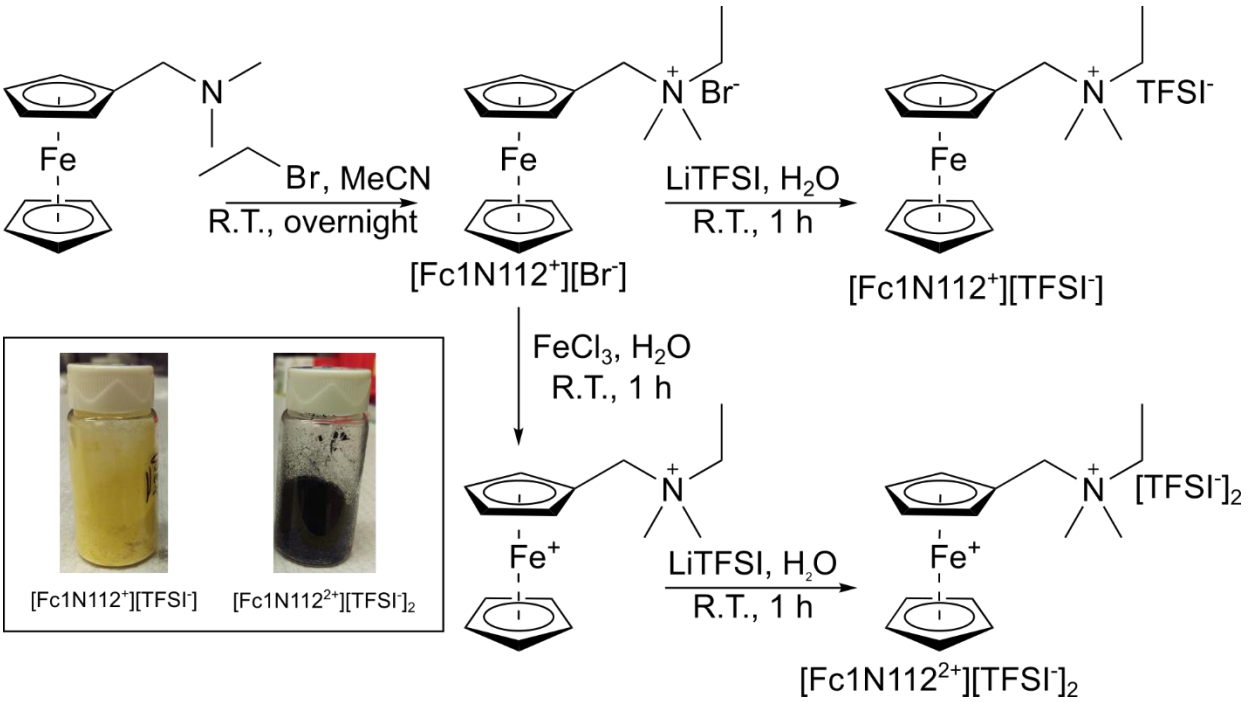

Figure 2: Synthesis scheme for **[Fc1N112$^+$][TFSI$^-$]** and **[Fc1N112^{2+}][TFSI$^-$]$_2$**.

Nuclear Magnetic Resonance Spectroscopy (NMR). ^{1}H NMR and ^{13}C NMR spectra were acquired using a Bruker Avance 400. Deuterated chloroform (D, 99.96%) was used as received

from Cambridge Isotope Laboratories. NMR spectra were aligned using the residual solvent peak and reported versus tetramethylsilane (TMS).[38] NMR spectra were obtained for only **[Fc1N112][TFSI]**, as the oxidized form contains an unpaired electron spin from Fe^{3+}.

[Fc1N112][TFSI]. ^{1}H NMR (500 MHz, $CDCl_3$) δ (ppm): 4.43-4.30 (m, 6H), 4.23 (s, 5H), 3.32 (m, 2H), 2.94 (s, 6H), 1.41 (m, 3H). ^{13}C NMR (100 MHz, $CDCl_3$) δ (ppm): 119.9 (q, J_{C-F} = 321.6 Hz), 71.9, 71.6, 70.9, 69.6, 65.9, 59.0, 48.7, 8.1.

Cyclic Voltammetry and Ultramicroelectrode. For both cyclic voltammetry (CV) and ultramicroelectrode (UME) measurements, three-electrode cells containing a 5 mL solution comprised of active species / 0.5 M TEATFSI / MeCN were used. The active species concentrations were 5 mM and 10 mM for CV and UME experiments, respectively. A coiled platinum wire (BASi) served as the counter electrode, and a fritted Ag/Ag^+ quasi-reference electrode (BASi) filled with silver tetrafluoroborate (0.1 M, 98%, Sigma Aldrich) in MeCN. The quasi-reference electrode was calibrated against the ferrocene / ferrocenium (Fc/Fc^+) redox couple, in the supporting electrolyte of interest, and all voltammogram potentials are reported against the Fc/Fc^+ reference calibration, in accordance with a prior literature procedure.[28] CV measurements utilized a 3 mm diameter glassy carbon working electrode (BASi) and were collected using a Biologic VMP3 potentiostat with 100% solution resistance compensation (iR-correction). The 3 mm glassy carbon electrode was prepared by rinsing with DI H_2O, polishing with 5 μm alumina suspension, sonicating for 1 min, and then rinsing with DI H_2O a second time. The electrode was then dried before taking CV measurements. UME measurements implemented an 11 ± 2 μm carbon fiber working electrode (BASi) and were collected using a CH Instruments 630 potentiostat. The UME was prepared in an identical fashion as the 3 mm electrode, expect without the sonication step.

Conductivity and Viscosity Measurements. Electrolyte conductivity measurements were collected using a two-electrode, Swagelok style conductivity cell and calibration method that have been previously described in literature.[27,39] All electrolyte conductivity measurements were performed in triplicate. Separator conductivity measurements were also performed using a two-electrode, spring-loaded conductivity cell as reported in literature.[40] After soaking overnight in the electrolyte of interest, one, two, three, or four separator layers (12.5 mm diameter circles) were stacked in the conductivity cell, and separator conductivities were determined from the high frequency intercept in impedance measurements, collected at each effective thickness.[40] Finally,

electrolyte viscosity measurements were collected using a vibrational viscometer probe (Viscolite V-700) as reported in literature.[27] Electrolyte densities were also measured via pipetting and massing 1.0 mL of solution at ambient glovebox conditions, as electrolyte densities were required for the viscosity measurement.

Single Electrolyte Flow Cell Experiments. Two flow cell designs of 2.55 cm^2 and 25 cm^2 active area were employed in this work, both of which are reported in previous literature.[27,28,32,39] The larger 25 cm^2 is a state-of-the-art flow cell designed for all-vanadium RFBs,[32] and the smaller 2.55 cm^2 is a miniaturized version of the state-of-the-art cell.[27,28,39] Interdigitated flow fields (IDFF) were machined from impermeable graphite (G347B, MWI, Inc.). Two layers of pristine 190 ± 30 μm carbon paper electrodes (25AA, SGL Group) were placed on each of the flow fields. Single layers of Daramic 175, Celgard 2500, or Celgard 3501 were used, without pretreatment, as separator materials in flow cell experiments. Teflon gaskets sealed the separators and electrodes into the cell; electrodes were compressed by 20 ± 2 %, affording a final thickness of 304 ± 49 μm. By comparing the elastic moduli of the separators (≈ 400 MPa)[41] and the carbon paper (≈ 4.4 MPa),[42] we assume that due to their significantly higher elastic moduli, the separators do not compress by any appreciable amount within the active area of the cell. Flow cells were assembled outside of the glove box and purged under vacuum (-91 kPa_g) three times before entering the inert atmosphere.

A sealed perfluoroalkoxy alkane (PFA) jar (10 mL, Savillex) served as the electrolyte reservoir. 10 or 30 mL of electrolyte was employed in the single electrolyte flow cell experiments for the 2.55 cm^2 and 25 cm^2 cells, respectively. A peristaltic pump (Masterflex L/S series) was used to drive electrolyte through the flow cell and reservoir. For the 2.55 cm^2 cell, PharMed BPT tubing (Masterflex L/S 14HP) was used inside a high-performance pump head and coupled to PFA tubing (1.6 mm inner diameter, Swagelok) that connected to the flow cell. For the 25 cm^2 cell, Norprene tubing (3.18 mm inner diameter, Masterflex L/S 16) was used inside an easy-load II pump head and connected directly to the flow cell.

Prior to polarization or impedance measurements, all cells were preconditioned by applying a constant potential of 0.4 V for 30 min using an Arbin battery tester (BTS-200), similar to prior single electrolyte studies.[27,32,34] Impedance measurements were collected with a 0.010 V sine wave about the open circuit potential across a frequency range of 1 MHz to 5 mHz using the Biologic VMP3 potentiostat. Potentiostatic measurements were performed to acquire polarization

data from 0 to 0.6 V in 0.050 V increments using the Arbin battery tester. Potentiostatic holds were applied for 3 min, recording data every second, and the final polarization curves were computed as the mean of the last 30% of data points.

Due to the electronic resistance associated with the hermetically sealed cable connections through the glove box, the ohmic resistance contribution from the test leads was subtracted from all polarization and impedance measurements. To quantify the resistance contribution of the test leads for impedance data, the Biologic test leads were short circuited together, and an impedance measurement was collected to directly obtain the lead resistance of the impedance channel, which was ≈ 0.05 Ω. This value was subtracted from the real contributions of all Nyquist plots. For polarization measurements, the Arbin test leads were short circuited together and their current-voltage characteristic was measured by applying galvanostatic holds in the range of 0 – 4 A. From the slope of the current-potential curve, the Arbin test leads through the glove box yielded a resistance of ≈ 0.12 Ω. This resistance value was used to calculate an effective potential drop across the test leads during flow cell experiments by multiplying the lead resistance and the experimentally measured current. The computed test lead potential drop was subtracted from cell potential measurements.

8.3 Active Species Voltammetry

Voltammetric analysis is used to confirm both the facile redox kinetics associated with the $Fc1N112^{+/2+}$ couple and the effectiveness of the chemical oxidation step. Figure 3a and Figure 3b illustrate that the CV (cycle 2) peak separation is unchanging with scan rate for $Fc1N112^{+/2+}$ in both oxidation states. The peak-to-peak separation across all CV scans, for both compounds, is 0.067 ± 0.001 V, which is slightly larger than the idealized separation (0.059 V), likely due to incomplete iR-correction. The peak-height ratio is 1.04 ± 0.009 across all scans, for both compounds. Further, CV confirms that $Fc1N112^{2+}$ maintains redox activity after the chemical oxidation. Figure 3c and Figure 3d show UME scans for $Fc1N112^{+}$ and $Fc1N112^{2+}$, respectively. Note that for $Fc1N112^{+}$, only an anodic (oxidizing) current is present, whereas for $Fc1N112^{2+}$, only a cathodic (reducing) current is present. Hence, the UME results indicate that the $Fc1N112^{+}$ sample contains only the reduced active species and the $Fc1N112^{2+}$ sample contains only the oxidized active species, at least to the detection limit of the UME method. Confirming that the

reduced and oxidized species are isolated lends confidence to the SOC (50%) of the solutions prepared for full cell measurements.

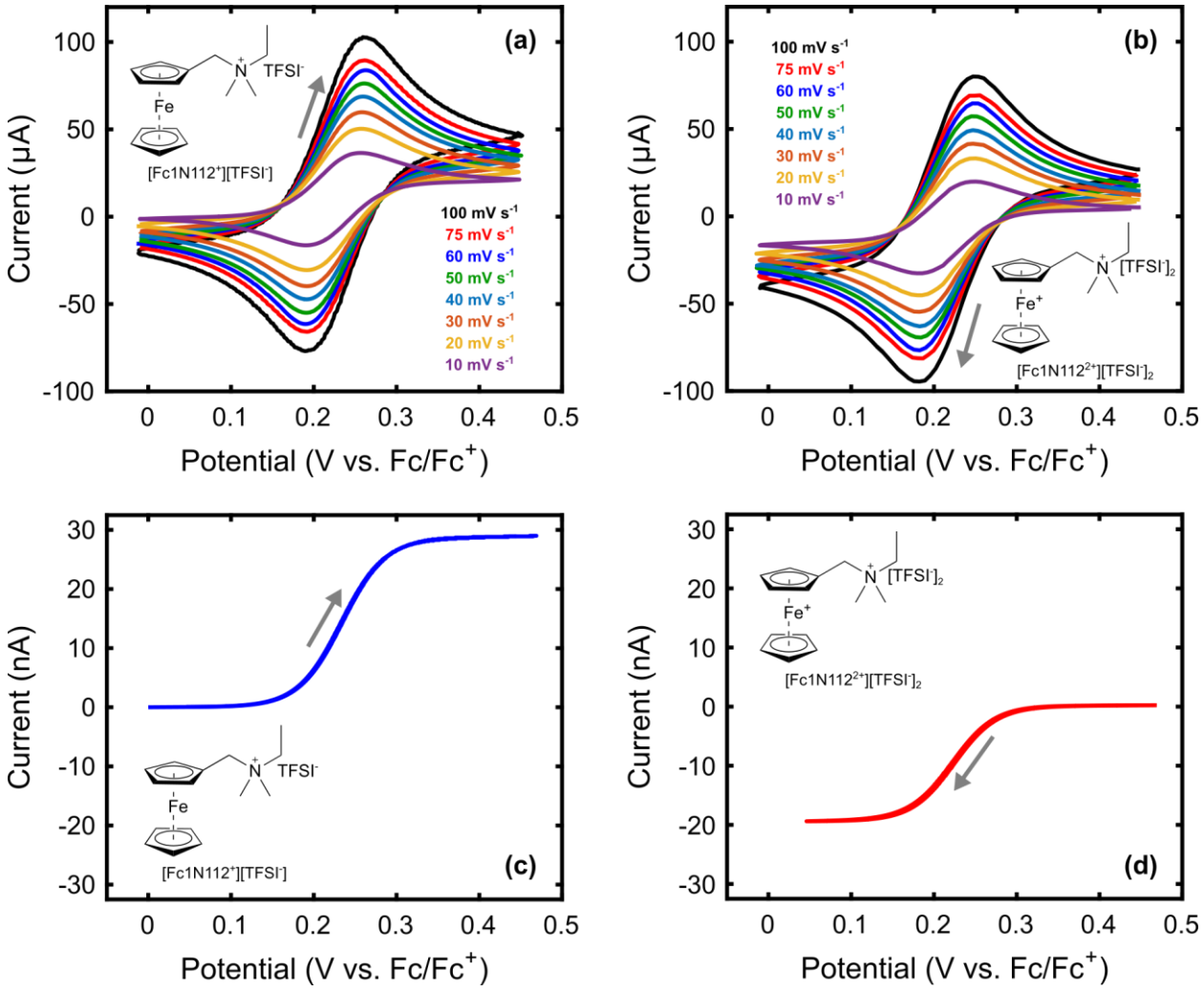

Figure 3: CVs (cycle 2) of 5 mM (a) Fc1N112+ and (b) Fc1N1122+ at various scan rates (10, 20, 30, 40, 50, 60, 75, 100 mV s^{-1}), and UME scans (cycle 1) of 10 mM (c) $Fc1N112^{+}$ and (d) $Fc1N112^{2+}$. The supporting electrolyte is 0.5 M TEATFSI / MeCN. Gray arrows denote the initial scan direction.

8.4 Separator & Electrolyte Properties

Non-aqueous electrolytes encompass a broad spectrum of materials and properties, where electrolyte conductivities and viscosities can easily vary by an order of magnitude.[10] While such a range of materials and properties provides exciting design possibilities for full NAqRFBs,[8] generalizing performance limitations becomes difficult. As such, we identify two commonly studied supporting electrolyte compositions with a roughly ten-fold variation in conductivity and

viscosity. Table 1 quantifies the conductivities and viscosities of the 4 different redox active electrolyte compositions investigated, where 0.5 M TEATFSI in MeCN serves as a low viscosity and high conductivity supporting electrolyte and 0.5 M LiTFSI in PC serves as a high viscosity and low conductivity supporting electrolyte. Additionally, the conductivity of dry SGL 25AA carbon paper was measured in a prior study to be 2200 – 2700 mS cm^{-1}, under 20% compression.[32] For this work, the supporting salt concentration is 0.5 M, and we vary the total active species concentration at a fixed 50% SOC. Notably, the conductivities and viscosities of the MeCN- and PC-based electrolytes vary by ≈ 10× with 1 M active species in solution. As active species concentration increases for the MeCN-based electrolytes, conductivity decreases and viscosity increases likely due to increasing molecular interactions and solute volume fraction,[27] and more viscous electrolytes will incur lower mass transport rates.

Table 1: Conductivities and viscosities of electrolytes employed in diagnostic flow cell experiments.

$Fc1N112^{+/2+}$ conc. (M)	**Salt (0.5 M)**	**Solvent**	**κ (mS cm^{-1})**	**μ (mPa·s)**
0.25	TEATFSI	MeCN	30.8 ± 0.5	0.7 ± 0.1
0.5	TEATFSI	MeCN	27.8 ± 0.9	1.1 ± 0.1
1.0	TEATFSI	MeCN	16.9 ± 1.1	3.7 ± 0.1
1.0	LiTFSI	PC	2.8 ± 0.4	33.2 ± 0.1

To date, no reports have identified a separator or membrane for NAqRFBs that exhibits sufficiently low ASR, high selectivity, and electrochemical / chemical stability necessary for practical operation.[8,9,30] Recent research has examined Nafion[43–45] and anion exchange[29,40,46–49] membranes. The use of size selective separators in conjunction with oligomeric or polymeric active species, is an emerging concept that has shown promise but remains relatively unexplored.[50–53] As such, the present diagnostic study uses proxy microporous separators, which are chemically stable in non-aqueous electrolytes and electrochemically stable under an applied potential, of varying thickness to mimic the ASR observed for more advanced NAqRFB membranes. Daramic 175 is a 175 µm thick separator that easily wets in both MeCN and PC. Celgard 2500 and Celgard 3501 are both 25 µm thick, with identical morphological and mechanical properties,[54] which wet in MeCN and PC, respectively.

Since the Celgard and Daramic separators are passive, their porosity, tortuosity, and thickness, as well as electrolyte conductivity, dictate the observed separator resistances (Table 2). In the case of perfect separator wetting, Equation (2) describes the separator ASR (R_{mem}), where l

is the separator thickness (m), τ is the separator tortuosity (-), ε is the separator porosity (-), and κ is the electrolyte conductivity (S m^{-1}). The l/κ ratio (Table 2) describes the effect of electrolyte conductivity on R_{mem} and can be calculated from the experimentally measured separator thickness and electrolyte conductivity. If the separators exhibit perfect wetting, the computed values of ε/τ should be constant for a given membrane type, regardless of the electrolyte composition. Table 2 indicates that the computed values of ε/τ change for different electrolytes, even when the separator morphology is the same. This discrepancy is especially large when comparing Celgard 2500 and 3501, which have the same mechanical properties, but different surface coatings.[54] The disagreement in ε/τ indicates that separator wetting plays a significant role in determining R_{mem}. We also present the experimentally determined ratio of electrolyte-to-separator conductivity (κ/κ_{eff}, MacMullin number),[55] which is ≈ 2× higher for Celgard as compared to Daramic, and offers another descriptor of the effect of electrolyte conductivity on separator conductivity. The MacMullin numbers for Celgard are in good agreement with a prior report.[55]

$$R_{\text{mem}} = \frac{\tau l}{\varepsilon \kappa} \tag{2}$$

Table 2: Conductivities of separators employed in single electrolyte flow cell experiments.

Separator	**Fc1N112$^{+/2+}$ Conc. (M)**	**Salt (0.5 M)**	**Solvent**	**R_{mem} (Ω cm^2)**	**l/κ (Ω cm^2)**	**ε/τ**	**κ/κ_{eff}**
Daramic	0.25	TEATFSI	MeCN	1.24 ± 2.72	0.568 ± 0.009	0.458 ± 1.00	2.18 ± 4.79
Daramic	0.5	TEATFSI	MeCN	1.27 ± 0.60	0.629 ± 0.020	0.496 ± 0.235	2.02 ± 0.96
Daramic	1.0	TEATFSI	MeCN	2.56 ± 0.13	1.04 ± 0.067	0.404 ± 0.033	2.47 ± 0.20
Daramic	1.0	LiTFSI	PC	17.0 ± 0.03	6.25 ± 0.89	0.368 ± 0.053	2.72 ± 0.39
Celgard 2500	1.0	TEATFSI	MeCN	0.86 ± 0.03	0.148 ± 0.004	0.172 ± 0.007	5.81 ± 0.27
Celgard 3501	1.0	LiTFSI	PC	3.87 ± 0.04	0.893 ± 0.128	0.231 ± 0.033	4.33 ± 0.62

Celgard and Daramic microporous separators do not exhibit sufficiently high selectivity for practical NAqRFB applications,[20,21,23,28] but the single electrolyte configuration (Figure 1a) permits flow cell studies without concerns of crossover degrading performance.[32] Generally, as the separator thickness increases (i.e., Celgard to Daramic) or the electrolyte conductivity

decreases, R_{mem} will increase. For example, when switching from Daramic 175 to Celgard 3501, with the PC-based electrolyte and 1 M actives, the R_{mem} drops by ≈ 4.4×. Similarly, switching from the PC- to MeCN-based electrolyte, with Daramic 175 and 1 M actives, the R_{mem} reduces by ≈ 6.6×. Further, consider the MeCN-based electrolytes where the separator ASR rises with increasing active species concentration, mirroring the decrease in electrolyte conductivity quantified in Table 1. Thus, the matrix of available separators and electrolyte compositions allows us to study flow cell performance with a variety of effective separator ASR values (Table 2).

8.5 Separator and Supporting Electrolyte Comparison

Increasing separator conductivity is arguably the most direct method for improving RFB reactor performance because a decrease in separator resistance will lead to an equivalent reduction in total cell ASR. Figure 4a illustrates this effect by comparing polarization of cells using either Celgard or Daramic separators with 1 M $Fc1N112^{+/2+}$. For both the PC and MeCN-based electrolytes, the Celgard separators yield improved cell performance over their Daramic counterparts due to lower separator resistance. The Nyquist plots in Figure 4b and Figure 4c illustrate that, for a fixed electrolyte composition, the separator choice drastically affects the high frequency intercept (R_Ω), with no other major changes to the Nyquist plots. These results indicate that varying the separator type directly affects the ohmic contribution to the total cell ASR, and the impedance reductions observed in Figure 4b and Figure 4c are equivalent to the separator ASR reductions in Table 2, when switching from Daramic to Celgard. Additionally, the high frequency intercepts are only slightly larger than the corresponding values of R_{mem}, indicating that the R_{mem} dominates the total ohmic contribution to the cell resistance; for example, the cell with a Daramic separator and 1.0 M $Fc1N112^{+/2+}$ / 0.5 M TEATFSI / MeCN electrolyte has R_Ω = 1.41 Ω cm^2 and R_{mem} = 1.27 Ω cm^2.

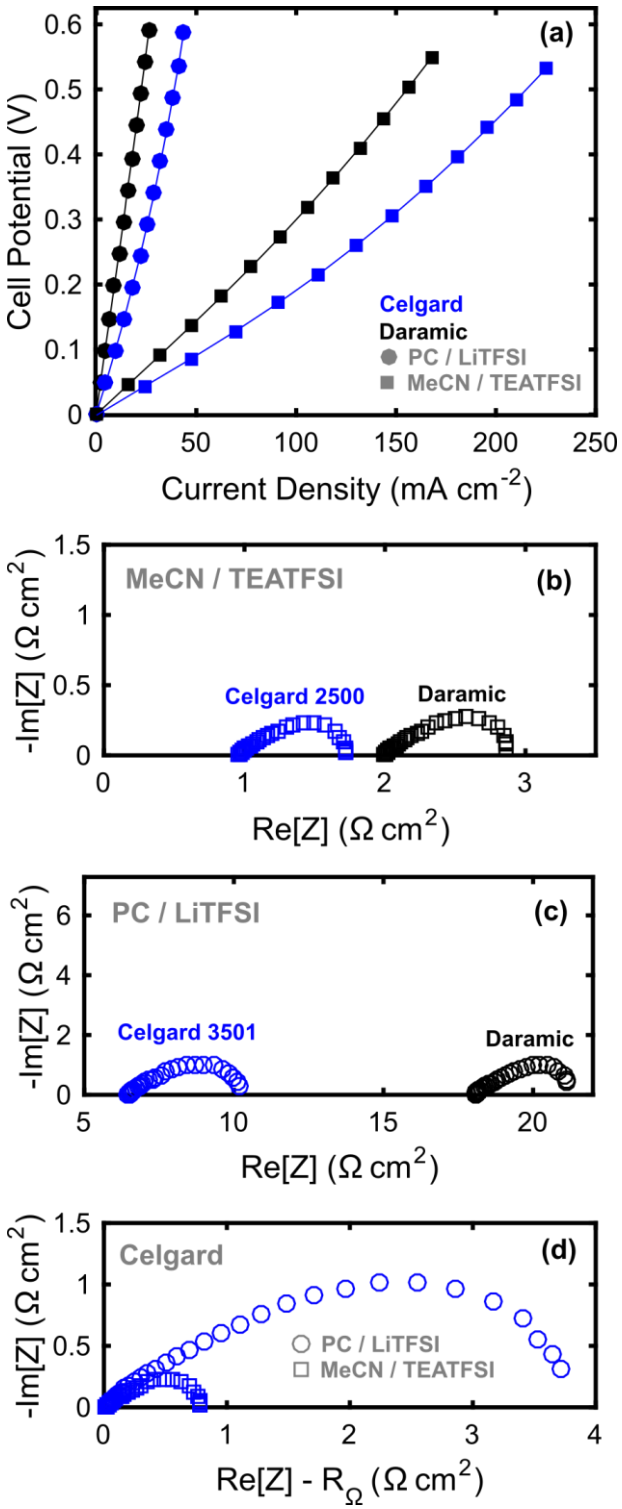

Figure 4: Cell performance of 1 M Fc1N112$^{+/2+}$ (50% SOC) with various separators and supporting electrolytes. **(a)** Polarization of Daramic / 0.5 M LiTFSI / PC, Celgard 3501 / 0.5 M LiTFSI / PC, Daramic / 0.5 M TEATFSI / MeCN, and Celgard 2500 / 0.5 M TEATFSI / MeCN. **(b)** Nyquist plots of Daramic and Celgard 2500 with 0.5 M TEATFSI / MeCN. **(c)** Nyquist plots of Daramic and Celgard 3501 with 0.5 M LiTFSI / PC. **(d)** Nyquist plots (shifted by R_Ω) of 0.5 M LiTFSI / PC and 0.5 M TEATFSI / MeCN with Celgard 3501 or 2500 separators, respectively.

Beyond the separator effect, Figure 4a also indicates that the MeCN-based electrolyte always outperforms the PC-based electrolyte, regardless of the separator thickness or identity. First, this performance enhancement is partially due to improved separator conductivity with the MeCN-based electrolyte (Table 2). Comparing the Nyquist plots in Figure 4b and Figure 4c for a fixed separator type (Celgard or Daramic), R_Ω for the MeCN-based electrolyte is always lower than that of the PC-based electrolyte, confirming that the enhanced conductivity manifests at the cell level. Further, R_Ω for the MeCN-based electrolyte reduces from 2.00 to 0.956 Ω cm^2 when transitioning from Daramic to Celgard 2500 (Figure 4b). The PC-based electrolyte cell is much more sensitive to variations in separator thickness due to the lower conductivity of that electrolyte, resulting in a decrease in R_Ω of 18.1 to 6.47 Ω cm^2 when switching from Daramic to Celgard 3501 (Figure 4c).

Variations in electrolyte conductivity only account for a portion of the improved performance observed when transitioning from the PC- to MeCN-based electrolyte system. Consider Figure 4d, which shows Nyquist plots, shifted by R_Ω, for cells with the PC- and MeCN-based electrolytes and a Celgard separator. By subtracting R_Ω from both plots (Figure 4d), the variation in the diameters of the two Nyquist plots becomes apparent. The Nyquist plot for the cell with MeCN-based electrolyte exhibits a semicircle with $\approx 4\times$ smaller diameter than the PC-based electrolyte, which is due to the decreased mass transfer resistance associated with the active species transport to the electrode surface, as will be elucidated in a following flow rate dependence study. The MeCN-based electrolyte exhibits improved mass transfer rates due to its lower viscosity as compared to the PC-based electrolyte (Table 1). Consideration of electrolyte viscosity as an electrochemical performance parameter, independent of conductivity, is a critical design concern for RFBs, though of lesser concern for non-flowing electrochemical cells (e.g., lithium ion batteries). Since RFBs rely on convection as the primary form of active species mass transfer, the electrolyte viscosity will directly affect reactant delivery rates within the porous electrode. Thus, electrolyte design for NAqRFBs must consider viscosity as a key materials optimization parameter, and, in the case of this work, MeCN vastly outperforms PC as a base solvent for a low viscosity and high conductivity electrolyte.

8.6 Flow Rate Effects

The impedance variations from Figure 4d hint that mass transfer rates are critical in determining the total ASR for RFBs, but only a handful of prior reports have systematically studied mass transfer effects in AqRFBs,[32,34,56–58] with no reports directly relating to NAqRFBs. To begin addressing this knowledge gap, Figure 5 highlights non-aqueous flow cell performance for the PC- and MeCN-based electrolytes, with a Daramic separator, at 4 flow rates spanning greater than an order of magnitude. As anticipated, for both electrolytes, increasing the electrolyte flow rate improves overall cell performance: higher current densities are achieved at a fixed cell potential (Figure 5a and Figure 3b). Considering the Nyquist plots in Figure 5c and Figure 5d, the low frequency intercept (R_{DC}) decreases with increasing flow rate, and no other major changes are observed in the overall shape or R_{Ω}. Note in Figure 5c that the variations in R_{Ω} (approximately ± 1 Ω cm^2) are small in comparison to the total cell ASR (> 21 Ω cm^2). Thus, the Nyquist plots validate that modifying flow rate affects only the mass transfer resistance. For both electrolyte systems, the electrochemical performance of the flow cell exhibits a diminishing rate of return with increasing electrolyte flow rate. For example, consider Figure 5b, where the improvement in performance from 1 – 5 mL min^{-1} is much larger than the improvement gained from 5 – 10 mL min^{-1}. We hypothesize that, as the flow rate increases, the cell approaches the limit of infinitely fast mass transfer; typically, mass transfer coefficients in porous media increase with flow velocity to a power ≤ 1.[56,59] Thus, in the limit of high electrolyte velocity, the ohmic and charge transfer losses dominate the cell's resistive characteristics. As such, selecting an optimal flow rate will require balancing the cell ASR with pumping losses; beyond a certain critical flow rate, the ASR reduction will be smaller than the magnitude of pumping loss required to boost the flow rate. One study has attempted this optimization for NAqRFBs,[60] with several other examples for AqRFBs.[57]

While both electrolyte systems exhibit a flow rate dependence, the cell with a PC-based electrolyte exhibits performance that is less sensitive to flow rate variations than the cell with MeCN. Figure 5c highlights that R_{Ω} is much larger for the PC-based electrolyte cell than all other real impedance contributions (i.e., the diameter of the Nyquist plots), and therefore, changes in the mass transfer resistance due to changes in electrolyte flow rate only account for a small fraction of the total cell ASR. By contrast, the MeCN-based electrolyte cell has a R_{Ω} that is on the same order of magnitude as all other resistance contributions ($R_{\Omega} \approx (R_{DC} - R_{\Omega})$), so variations in mass transfer resistance account for a larger fraction of the total cell ASR. Thus, we can now describe a general

trend for RFBs that as the separator conductivity decreases, cell performance will become more sensitive to variations in electrolyte flow rate.

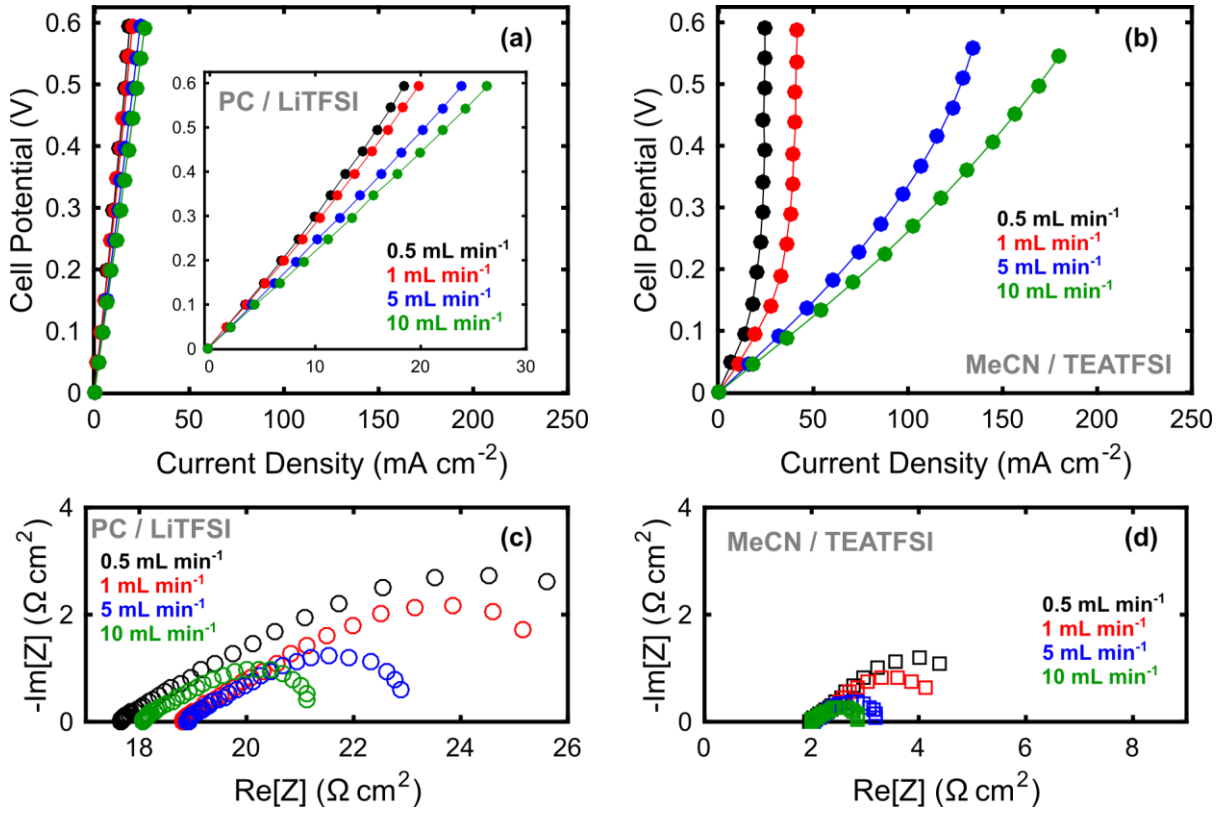

Figure 5: Cell performance with varying electrolyte flow rates, containing 1 M $Fc1N112^{+/2+}$ (50% SOC) and Daramic separators. **(a)** Polarization of 0.5 M LiTFSI / PC. Inset: Expanded dataset in current density range of 0 – 30 mA cm^{-2}. **(b)** Polarization of 0.5 M TEATFSI / MeCN. **(c)** Nyquist plots of 0.5 M LiTFSI / PC. **(d)** Nyquist plots of 0.5 M TEATFSI / MeCN.

8.7 Active Species Concentration

Continuing to investigate mass transfer effects, Figure 6 shows polarization curves at varying active species concentrations and flow rates for the MeCN-based electrolyte. At the lowest flow rate (0.5 mL min^{-1}, Figure 6a), the cell achieves limiting current density, which increases with increasing active species concentration. In fact, all current densities, at a fixed cell potential, increase with active species concentration. These two trends are anticipated as the cell with the highest active species concentration should exhibit the smallest mass transfer resistances, assuming all other cell parameters are held constant. As the flow rate increases, however, this trend no longer holds true; the 1.0 M electrolyte (highest active species concentration) performs worse than the lower concentration electrolytes (Figure 6c and Figure 6d).

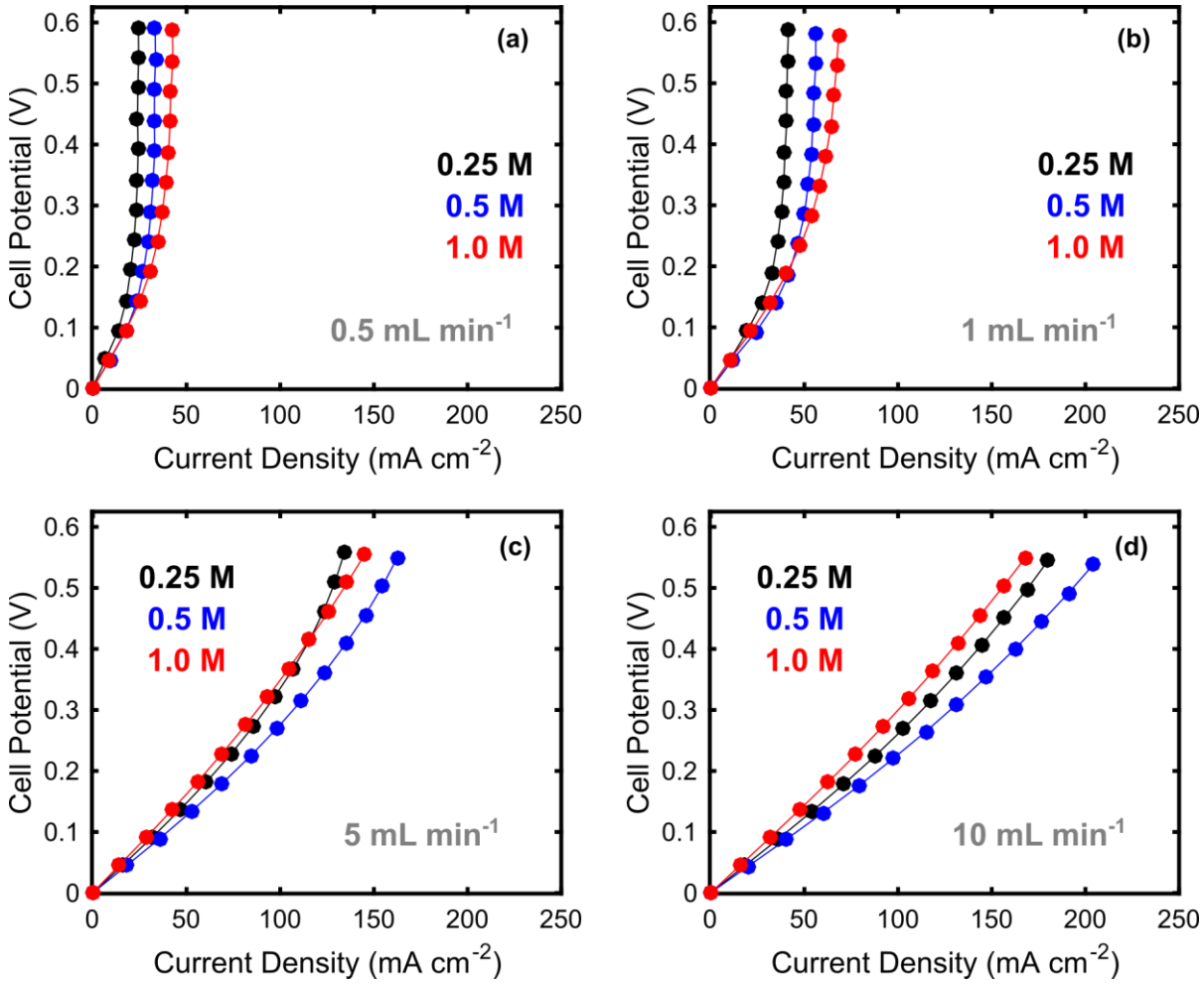

Figure 6: Cell polarization with varying active species concentrations, implementing the Daramic / 0.5 M TEATFSI / MeCN configuration, for 4 different flow rates: **(a)** 0.5, **(b)** 1.0, **(c)** 5.0, and **(d)** 10 mL min^{-1}.

To begin deconvoluting the unexpected cell performance trends at high active species concentrations, consider the Nyquist plots in Figure 7. Column i in Figure 7 shows Nyquist plots shifted by R_Ω at various active species concentrations for the 4 flow rates depicted in Figure 6. At lower flow rates (e.g., 0.5 mL min^{-1}, Figure 7a.i), the diameters of the Nyquist plots decrease with increasing active species concentration. This anticipated trend is again due to decreasing mass transfer resistance with increasing active species concentration. However, as the flow rate becomes large (e.g., 10 mL min^{-1}, Figure 7d.i), the semicircles converge, regardless of the active species concentration, indicating that at sufficiently high flow rates the mass transfer resistance becomes insensitive to variations in actives concentration.

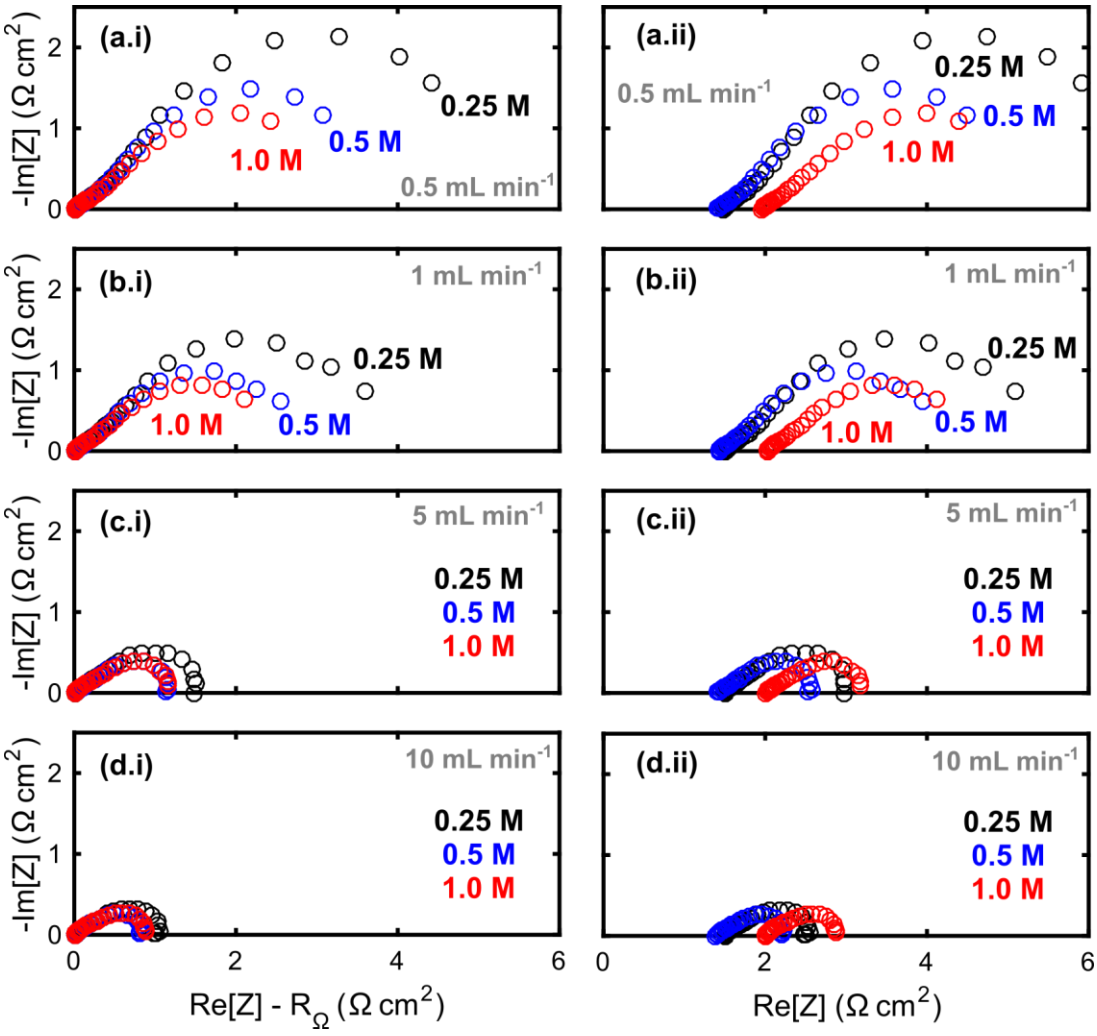

Figure 7: Nyquist plots of cells with varying Fc1N112$^{+/2+}$ (50% SOC) concentrations, implementing the Daramic / 0.5 M TEATFSI / MeCN configuration, for 4 different flow rates: **(a)** 0.5, **(b)** 1.0, **(c)** 5.0, and **(d)** 10 mL min^{-1}. Column **(i)** presents the real axis shifted by R_Ω, whereas column **(ii)** presents the total real resistance.

The lack of sensitivity to actives concentration in the Nyquist plots at high flow rates is an interesting result, but does not reconcile the behavior observed in Figure 6. Consider now the Nyquist plots in Column ii of Figure 7, which contain the entire impedance spectra. Note first that R_Ω is different for all active species concentrations, with the 1.0 M electrolyte exhibiting the highest value of R_Ω. The experimentally measured electrolyte and separator conductivities (Table 2) indicate that the 1.0 M electrolyte cell should exhibit the highest value of R_Ω due to the higher resistance associated with that electrolyte system. At low flow rates, where mass transfer is the dominant resistive feature, R_{DC} decreases with increasing active species concentration, despite differences in R_Ω (e.g., Figure 7a.ii). As flow rate increases and mass transfer rates improve, ohmic

losses become the major resistance contribution and dominate the overall cell performance. Hence, variations in R_Ω control R_{DC} under conditions with facile mass transfer. This result illustrates the importance of considering all resistance contributions to R_{DC} so that the dominant resistive features can be identified and addressed appropriately.

An optimal active species exists that will balance the electrolyte conductivity, viscosity, and concentration to deliver the best overall electrochemical performance (lowest ASR) and does not necessarily correspond to the highest active species concentration possible. The cell ASR, however, is only one performance metric in a complex energy storage system, and while the ASR plays a significant role in determining the electrochemical stack cost,[12,32] the active species concentration directly affects the electrolyte cost contribution to the total RFB cost.[7,12,60] In brief, higher energy density electrolytes suppress solvent and tank costs, yielding lower chemical costs per unit energy stored, which is especially true for NAqRFBs where the solvent cost is expected to be an order of magnitude greater than that of a typical aqueous electrolyte.[7,12] The decrease in electrolyte cost contribution competes with an increase in the reactor cost contribution associated with higher ASR.[7,12] These two cost components must be balanced when selecting an optimal operating concentration.

8.8 Electrode Thickness

Several prior studies on AqRFBs have included electrode thickness optimization to deliver the best electrochemical performance for a particular electrolyte system.[61–64] Increasing the electrode thickness increases ohmic losses through the porous electrode due to longer electron and ion path lengths to the current collector.[65–67] However, increasing the electrode thickness also increases the available surface area for electrochemical reactions, which permits a larger exchange current and reduces charge transfer losses.[65,67] Balancing these two effects, to optimize the total electrode resistance, becomes particularly important for RFBs with slow reaction kinetics.[61] Finally, increasing the electrode thickness will reduce pressure drop for a fixed flow rate or lower intra-electrode velocity for a fixed pressure drop. In the latter case, mass transport resistances will increase with increasing electrode thickness.

To evaluate the sensitivity of NAqRFB performance to electrode thickness, polarization and impedance analyses are performed on cells with thick (6×) and thin (2×) stacked carbon paper electrodes (Figure 8). For both a fixed intra-electrode velocity over the IDFF rib (Figure 8a) and fixed electrolyte flow rate (Figure 8b), the thinner electrode yields better overall electrochemical

performance, but the difference is much smaller for the fixed intra-electrode velocity case (Figure 8a). When considering a flow-through porous electrode with fixed intra-electrode velocity, the electrochemical performance should be identical. Differences in the polarization curves in Figure 8a are likely due to differences in the specific velocity field created by the IDFF, which will vary nonlinearly with increasing thickness.[68] Figure 8c supports this claim, as the different electrode thicknesses yield similarly shaped Nyquist plots. For a fixed electrolyte flow rate, the intra-electrode velocity decreases with increasing electrode thickness, yielding lower overall performance (Figure 8b) and much larger mass transfer losses, as indicated by a larger diameter Nyquist plot (Figure 8c).

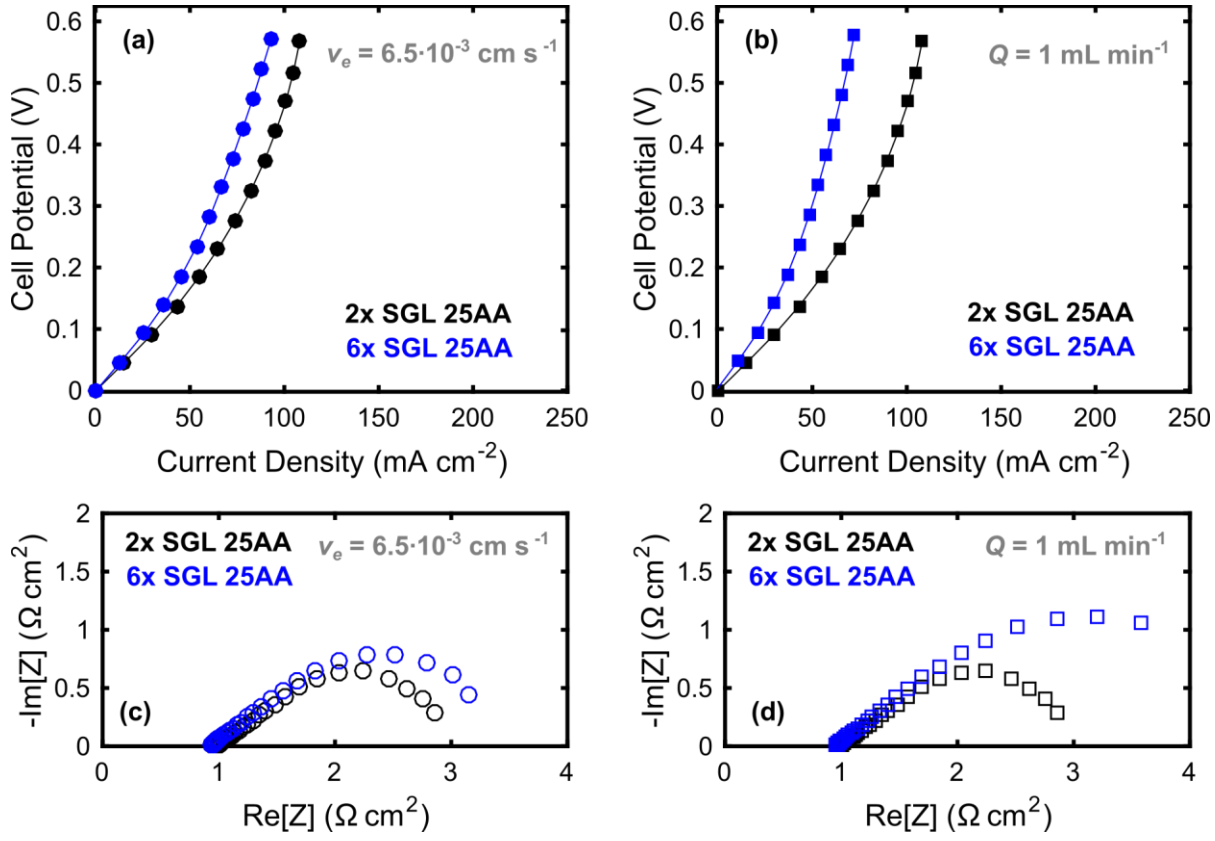

Figure 8: Cell performance with varying electrode thicknesses, containing 1 M Fc1N112$^{+/2+}$ (50% SOC), Celgard 2500, and 0.5 M TEATFSI / MeCN. **(a)** Polarization at fixed internal electrode velocity. **(b)** Polarization at fixed electrolyte flow rate. **(c)** Nyquist plots at fixed internal electrode velocity. **(d)** Nyquist plots at fixed electrolyte flow rate.

While the mass transfer effects vary significantly for the fixed velocity and flow rate cases, the shape and location of the high-frequency intercept is unchanging, regardless of the electrode or flow condition. We hypothesize that for non-aqueous flow cells, the ohmic and charge transfer

properties of the cell are insensitive to variations in electrode thickness, as compared to aqueous systems, for two reasons. First, the separator resistance for a NAqRFB is much greater than that of an AqRFB and dominates R_Ω. As such, variations in R_Ω with increasing electrode thickness are small by comparison and negligibly affect the overall cell performance. Second, most active species for NAqRFBs, including $Fc1N112^{+/2+}$, exhibit rapid reaction kinetics[8] and thereby large exchange current densities. For example, ferrocene in non-aqueous electrolyte has been reported to have a kinetic rate constant (k_0) $\approx 10^{-3}$ cm s^{-1},[69] which is two orders of magnitude greater than that of aqueous all-vanadium ($k_0 \approx 10^{-5}$ cm s^{-1}).[34] As an additional comparison, 2,2,6,6-tetramethyl-1-piperidinyloxyl (TEMPO), an organic redox active species considered for NAqRFBs,[24,27,70] exhibits even faster rate constants: $1.0 \times 10^{-1} \geq k_0 \geq 2.3 \times 10^{-2}$ cm s^{-1}.[71,72] Subsequently, NAqRFBs will exhibit negligible reductions in charge transfer resistance with increasing electrode thickness; Darling and Gallagher et al. indicated that for a typical carbon paper electrode, flow cell ASR becomes sensitive to charge transfer losses for $k_0 \lesssim 10^{-5}$ cm s^{-1}.[7] Due to a lack of sensitivity to the ohmic and kinetic effects, within the practical range of thicknesses studied, the electrode thickness for NAqRFBs should be used as a parameter to balance mass transport rates with pressure drop.

8.9 Reactor Scaling

As previously mentioned, to date, most NAqRFB studies have not leveraged advanced aqueous flow cell designs, and, to the best of our knowledge, the largest non-aqueous flow cell reported had an active area of only 10 cm^2.[20] While RFBs are scalable devices, the scaling relationships are not necessarily straightforward (e.g., matching pressure drop) and scale-dependent factors exist (e.g., edge effects) that can impact performance. The 2.55 cm^2 cell design, used to collect all the data shown to this point, has practical value as only relatively small quantities of active materials are required for cell testing. Experiments with the 2.55 cm^2 cell illustrate a range of performance tradeoffs, but, to ensure experimental validity, we must demonstrate performance scalability, at least to the size of more typical aqueous RFB studies. To this end, we constructed a 25 cm^2 cell to specifically validate observations in our small reactor and to generally evaluate performance scalability.

The 2.55 cm^2 and 25 cm^2 cells are designed to yield the same pressure drop and electrochemical performance for a fixed area specific flow rate. Darling and Perry described an analytical framework for calculating the pressure drop through an IDFF for flow batteries.[32] The

original derivation by Owejan et al. was targeted towards to polymer-electrolyte fuel cells and is available in Ref. 73.[73] The pressure drop through the IDFF (ΔP) can be computed as shown in Equation (3), where ΔP_{ch} (Pa) is the pressure drop through the rectangular flow field channels, and ζ is a dimensionless geometric factor (-).

$$\Delta P = \Delta P_{ch}\left(1+\frac{2+2\cosh\zeta}{\zeta\sinh\zeta}\right) \tag{3}$$

The pressure drop through the rectangular channel of the IDFF is calculated from the analytical expression in Equation (4), where μ is the electrolyte viscosity (Pa·s), L_{ch} is the channel length (m), d_h the hydraulic diameter of the channel (m), and v_{ch} is the electrolyte velocity in the channel (m s^{-1}).

$$\Delta P_{ch} = \frac{32\mu v_{ch}L_{ch}}{d_h^2} \tag{4}$$

The channel velocity is defined in Equation (5), where Q is the volumetric electrolyte flow rate (m^3 s^{-1}), N is the number of channels (-), w is the channel width (m), and h is the channel height (m).

$$v_{ch} = \frac{Q}{Nwh} \tag{5}$$

The geometric factor ζ, which appears in Equation (3), is calculated according to Equation (6), where k is the electrode permeability (m^2), L_e is the electrode thickness (m), and S is the path length of the electrolyte through the electrode and over the rib (m).

$$\zeta^2 = \frac{128L_{ch}^2kL_e}{Sd_h^2wh} \tag{6}$$

While the mean fluid path length through the IDFF electrode can be computed numerically,[68] such a calculation is beyond the scope of this work. We estimate S as the sum of the electrode thickness and width of two channels, as shown in Equation (7).

$$S \approx 2w + L_e \tag{7}$$

To match the pressure drop between two IDFFs of differing size or geometry, the equality relationship presented in Equation (8) must hold.

$$\frac{Q_1 L_{ch,1} N_2 w_2 h_2 d_{h,2}^2}{Q_2 L_{ch,2} N_1 w_1 h_1 d_{h,1}^2} = \frac{\left(1 + \frac{2 + 2\cosh\zeta_2}{\zeta_2 \sinh\zeta_2}\right)}{\left(1 + \frac{2 + 2\cosh\zeta_1}{\zeta_1 \sinh\zeta_1}\right)} \tag{8}$$

Table 3 carries out a calculation of the pressure drop through the IDFF for a fixed area specific flow rate, $Q/A = 6.5 \times 10^{-3}$ cm s^{-1}, for both the 2.55 cm^2 and 25 cm^2 cells, which develop near identical pressure drops of 20.0 kPa and 22.0 kPa, respectively. Table 3 also lists all relevant parameters for the pressure drop calculation.

Table 3: Relevant flow field geometry parameters for computing pressure drop through the 2.55 cm^2 and 25 cm^2 IDFFs. An example calculation is carried out for a fixed area specific flow rate: $Q/A = 6.5 \times 10^{-3}$ cm s^{-1}.

Parameter	Description	Units	2.55 cm^2 Value	25 cm^2 Value
d_h	Hydraulic Diameter	m	6.67×10^{-4}	6.67×10^{-4}
h	Channel Height	m	0.0005	0.0005
k	Electrode Permeability[74]	m^2	10^{-12}	10^{-12}
L_{ch}	Channel Length	m	0.016	0.050
L_e	Electrode Thickness	m	3×10^{-3}	3×10^{-3}
μ	Electrolyte Viscosity	Pa·s	0.001	0.001
N	Number of Inlet Channels	-	4	12
ΔP_{ch}	Open Channel Pressure Drop	Pa	54.9	511
Q	Flow Rate	m^3 s^{-1}	1.67×10^{-7}	1.63×10^{-6}
S	Flow Path Length	m	0.00230	0.00230
v_{ch}	Channel Velocity	m s^{-1}	0.084	0.272
w	Channel Width	m	0.001	0.001
ς	Geometric Factor	-	0.139	0.433
ΔP	IDFF Pressure Drop	Pa	2.00×10^4	2.20×10^4

Figure 9 compares the electrochemical performance of the 2.55 cm^2 and 25 cm^2 cells, at two different area specific flow rates (Q/A). Note that for cell polarization (Figure 9a), measurements on the 25 cm^2 cell do not extend to the same current densities as the 2.55 cm^2 cell due to larger ohmic loss through the Arbin battery tester cables. Similarly, the two area specific flow rates are selected to remain within the calibrated flow rate range of the peristaltic pump for both flow cell configurations. Figure 9a clearly indicates scalable electrochemical performance for the area specific flow rates and current densities selected, at both flow conditions, as the polarization curves overlay despite an ≈ 10× variation in flow cell active area. The Nyquist plots in Figure 9b and Figure 9c further support the scalability claim. For both area specific flow rates,

R_Ω is nearly identical, and the small deviation is likely due to differences in contact resistances between the two cell designs. At lower frequencies, the Nyquist plots exhibit greater deviation between the two cell sizes. In particular, the mismatch is largest at low frequencies for the smaller area specific flow rate (Figure 9b), which could be due to edge effects, such as non-uniform electrolyte velocity distributions near the boundaries of the porous electrode, imposed by the actual geometric differences of the two flow field sizes. In the higher area specific flow rate case (Figure 9c), the 2.55 cm^2 and 25 cm^2 cells display better agreement in the low frequency regime, possibly because edge effects are playing a smaller role in the overall cell performance. Despite minor inconsistencies in the low frequency impedance data, Figure 9 makes a strong argument as to the scalability of non-aqueous flow cell design, highlighting the validity of results collected with the miniaturized flow cell and that the flow cell's electrochemical performance remains the same across an order of magnitude increase in active area.

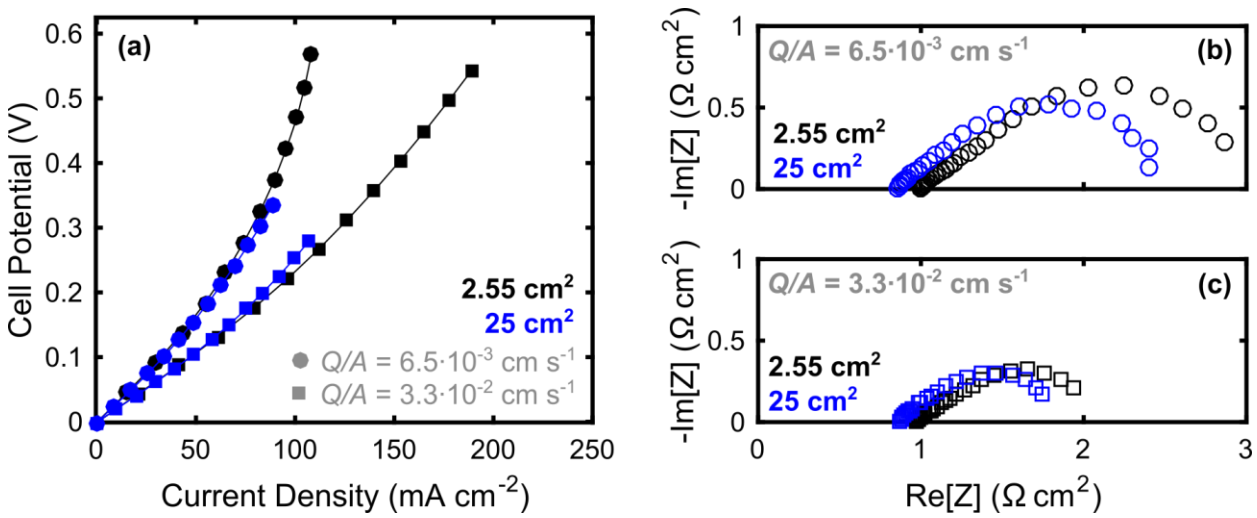

Figure 9: Comparison of cell performance with 2.55 cm^2 and 25 cm^2 active areas, containing 1 M $Fc1N112^{+/2+}$ (50% SOC), Celgard 2500, and 0.5 M TEATFSI / MeCN. **(a)** Polarization at two area specific electrolyte flow rates. **(b)** Nyquist plot for both reactor sizes when $Q/A = 6.5 \cdot 10^{-3}$ cm s^{-1}. **(c)** Nyquist plot for both reactor sizes when $Q/A = 3.3 \cdot 10^{-2}$ cm s^{-1}.

8.10 Best Performing Cell Configuration

Figure 10 displays a polarization curve and Nyquist plot of the flow cell configuration with the lowest ASR measured in this work. The electrolyte is comprised of 1 M $Fc1N112^{+/2+}$ / 0.5 M TEATFSI / MeCN, and the cell utilizes a 25 µm thick Celgard 2500 separator and 10 mL min^{-1} electrolyte flow rate. The high active species concentration, in conjunction with the high

electrolyte flow rate, yields small mass transfer resistance. Additionally, the thin nanoporous separator and MeCN-based electrolyte delivers a high separator conductivity and subsequently low value of R_Ω. This combination of preferable ohmic properties and rapid mass transport, with the already facile reaction kinetics of $Fc1N112^{+/2+}$, permits unprecedented electrochemical performance for a non-aqueous flow cell. At ≈ 0.3 V overpotential, the cell achieves a current density of ≈ 150 mA cm^{-2} (Figure 10a), which outperforms recommended values from techno-economic analysis of NAqRFBs.[7,30] Specifically, the R_Ω = 1.0 Ω cm^2 and R_{DC} = 1.7 Ω cm^2 (Figure 10b) are 26 – 34% lower than suggested targets[7,30] and approach the performance of alkaline or neutral AqRFBs.[75–78] A recent modeling study of ohmic-limited NAqRFBs, in the limit of fast mass transport at 100% SOC, suggested that the lowest possible ASR would be R_{DC} ≈ 3.4 Ω cm^2 (≈ 89 mA cm^{-2} at 0.3 V overpotential);[79] our experimental work, incorporating realistic mass transfer at 50% SOC, exceeds this predicted performance by > 40% for overpotentials < 0.3 V.

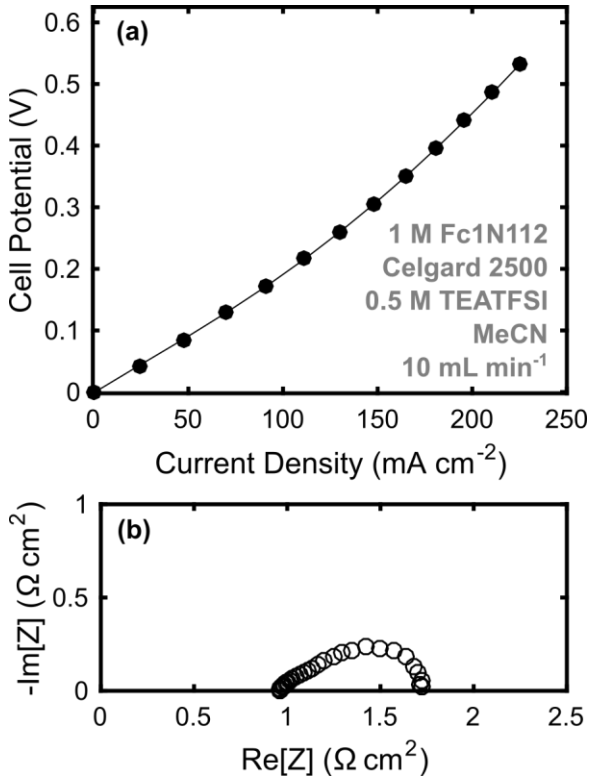

Figure 10: **(a)** Polarization and **(b)** Nyquist plot of the lowest ASR configuration tested in this work: 1 M $Fc1N112^{+/2+}$ (50% SOC), Celgard 2500, 2x SGL 25AA, 0.5 M TEATFSI / MeCN, 10 mL min^{-1}.

While the excellent electrochemical performance in Figure 10 demonstrates the potential for low ASR non-aqueous flow cells, technical hurdles remain. The implementation of the MeCN-based electrolyte and Celgard 2500 separator is critical in achieving low ASR, but the Celgard

2500 separator is impractical for a NAqRFB device since it offers no selectivity for small redox active molecules. Implementing Celgard 2500 in full flow cell would require mixed active species electrolytes,[21,23,39,80] which would be cost prohibitive,[7,12,23,39] or emerging large polymeric active species,[51–53] which may yield high viscosity electrolytes with poor mass transfer characteristics.[81] Additionally, the highly soluble $Fc1N112^{+/2+}$ model active species and low viscosity MeCN-based electrolyte facilitates small mass transfer resistances. Discovery and synthesis of stable and soluble active species for NAqRFBs is challenging,[8] and quantifying variations in mass transfer rates for electrolytes of varying viscosity has yet to be reported. Simultaneously tailoring active species radius and separator pore size offers a promising strategy to enabling NAqRFBs with sufficiently low ASR, high selectivity, and good mass transport.[50] Ultimately, the performance depicted in Figure 10 sets a benchmark for the electrochemical performance of non-aqueous flow cells, however, numerous other criteria must be simultaneously met (i.e., cell potential, stable actives) to achieve economically viable battery designs.[7,12]

8.11 Conclusions

A major criticism of NAqRFBs has been an inability to achieve power densities comparable to their aqueous counterparts.[79] Several studies have attempted to boost the cell potential of NAqRFBs through the discovery and development of new active materials,[13–19] which offer one pathway towards improving power density, reducing reactor costs, and, consequently, decreasing the overall battery cost.[7,12] The purpose of this study is to demonstrate the achievable current densities in high performance non-aqueous flow cells, which can eventually be coupled with a high voltage redox chemistry to produce a full cell with improved power density. This systematic study of resistive losses in NAqRFBs culminates in the demonstration of ASR values as low as 1.7 Ω cm^2, along with current densities near 150 mA cm^{-2} at 0.3 V overpotential (Figure 10). These metrics exceed the recommended performance for economically feasible non-aqueous flow cells.[7,12,30] This study is also the first to illustrate scalability for non-aqueous flow cell design, highlighting identical polarization performance over a 10× active area increase (Figure 9a).

The performance achieved in this study is unprecedented in the NAqRFB literature and stems from a logical analysis of the key resistive features in a non-aqueous flow cell and subsequent methodology to reduce those resistive losses. First, ohmic losses are the largest hurdle to overcome, due to the relatively low conductivities of non-aqueous electrolytes, as compared to

aqueous systems, and the subsequently low separator / membrane conductivities. Identifying thinner or more conductive separators can alleviate ohmic resistances; recent literature on size selective separators for NAqRFBs is providing a pathway towards separators that are sufficiently conductive and selective.[50–53] Interestingly, the ohmic loss through the porous electrode is negligible compared to the ohmic loss through the separator. Mass transfer losses are the second largest impediment to flow cell performance and can be alleviated by increasing electrolyte flow rate, increasing active species concentration, or decreasing electrolyte viscosity. Finally, charge transfer losses are negligible for most active species investigated for NAqRFBs because of the relatively fast reaction rate constants associated with redox active species in non-aqueous electrolytes, as compared to those in aqueous electrolytes.[8,27] Combining facile kinetics with a negligibly small ohmic resistance from the porous electrode indicates that non-aqueous flow cell performance is relatively insensitive to variations in electrode thickness, and electrode thickness should only be considered as a parameter to optimize pressure drop. This work highlights the promising performance of non-aqueous flow cells, but this performance must be coupled with a sufficiently selective separator[30] and stable, high-voltage (≈ 3 V[7,12]) chemistry. Moving forward, our work will focus on leveraging the ASR reduction principles outlined here to inform the design and development of more promising NAqRFB separators and electrolytes.

8.12 References

1. R. M. Darling and M. L. Perry, *ECS Trans.*, **53**, 31–38 (2013).
2. R. M. Darling and M. L. Perry, *J. Electrochem. Soc.*, **161**, A1381–A1387 (2014).
3. C.-N. Sun et al., *J. Electrochem. Soc.*, **161**, A981–A988 (2014).
4. A. M. Pezeshki, R. L. Sacci, F. M. Delnick, D. S. Aaron, and M. M. Mench, *Electrochimica Acta*, **229**, 261–270 (2017).
5. J. D. Milshtein, J. L. Barton, R. M. Darling, and F. R. Brushett, *J. Power Sources*, **327**, 151–159 (2016).
6. X. Wei et al., *Adv. Energy Mater.*, **5**, 1400678 (2015).
7. L. Cosimbescu et al., *Sci. Rep.*, **5**, 14117 (2015).
8. K. S. Han et al., *J. Phys. Chem. C*, **120**, 27834–27839 (2016).
9. R. M. Darling, K. G. Gallagher, J. A. Kowalski, S. Ha, and F. R. Brushett, *Energy Environ. Sci.*, **7**, 3459–3477 (2014).
10. R. Dmello, J. D. Milshtein, F. R. Brushett, and K. C. Smith, *J. Power Sources*, **330**, 261–272 (2016).
11. R. Darling, K. Gallagher, W. Xie, L. Su, and F. Brushett, *J. Electrochem. Soc.*, **163**, A5029–A5040 (2016).
12. N. G. Connelly and W. E. Geiger, *Chem. Rev.*, **96**, 877–910 (1996).
13. G. R. Fulmer et al., *Organometallics*, **29**, 2176–2179 (2010).
14. J. D. Milshtein et al., *Energy Env. Sci*, **9**, 3531–3543 (2016).

15. J. D. Milshtein, S. M. Fisher, T. M. Breault, L. T. Thompson, and F. R. Brushett, *ChemSusChem* (2016).
16. N. S. Hudak, L. J. Small, H. D. Pratt, and T. M. Anderson, *J. Electrochem. Soc.*, **162**, A2188–A2194 (2015).
17. J. Cannarella et al., *J. Electrochem. Soc.*, **161**, F3117–F3122 (2014).
18. V. Norouzifard and M. Bahrami, *J. Power Sources*, **264**, 92–99 (2014).
19. K. Gong, Q. Fang, S. Gu, S. F. Y. Li, and Y. Yan, *Energy Env. Sci*, **8**, 3515–3530 (2015).
20. J. A. Kowalski, L. Su, J. D. Milshtein, and F. R. Brushett, *Curr. Opin. Chem. Eng.*, **13**, 45–52 (2016).
21. S.-H. Shin, S.-H. Yun, and S.-H. Moon, *RSC Adv.*, **3**, 9095 (2013).
22. L. Su et al., *J. Electrochem. Soc.*, **163**, A5253–A5262 (2016).
23. M. Doyle, M. E. Lewittes, M. G. Roelofs, S. A. Perusich, and R. E. Lowrey, *J. Membr. Sci.*, **184**, 257–273 (2001).
24. H. S. Bang, D. Kim, S. S. Hwang, and J. Won, *J. Membr. Sci.*, **514**, 186–194 (2016).
25. I. L. Escalante-García, J. S. Wainright, L. T. Thompson, and R. F. Savinell, *J. Electrochem. Soc.*, **162**, A363–A372 (2015).
26. E. Cho and J. Won, *J. Power Sources*, **335**, 12–19 (2016).
27. D.-H. Kim et al., *J. Membr. Sci.*, **454**, 44–50 (2014).
28. S. Maurya, S.-H. Shin, K.-W. Sung, and S.-H. Moon, *J. Power Sources*, **255**, 325–334 (2014).
29. S.-H. Shin, Y. Kim, S.-H. Yun, S. Maurya, and S.-H. Moon, *J. Power Sources*, **296**, 245–254 (2015).
30. S. E. Doris et al., *Angew. Chem. Int. Ed.*, **55** (2016).
31. J. Winsberg et al., *Chem. Mater.*, **28**, 3401–3405 (2016).
32. G. Nagarjuna et al., *J. Am. Chem. Soc.*, **136**, 16309–16316 (2014).
33. E. C. Montoto et al., *J. Am. Chem. Soc.*, **138**, 13230–13237 (2016).
34. http://www.ldcgm.com/Celgard/CELGARD-4550.pdf.
35. J. Landesfeind, J. Hattendorff, A. Ehrl, W. A. Wall, and H. A. Gasteiger, *J. Electrochem. Soc.*, **163**, A1373–A1387 (2016).
36. S. M. Laramie, J. D. Milshtein, T. M. Breault, F. R. Brushett, and L. T. Thompson, *J. Power Sources*, **327**, 681–692 (2016).
37. W. Duan et al., *J Mater Chem A*, **4**, 5448–5456 (2016).
38. X. Wei et al., *ACS Energy Lett.*, 705–711 (2016).
39. Q. Xu and T. S. Zhao, *Phys. Chem. Chem. Phys.*, **15**, 10841 (2013).
40. X. L. Zhou, T. S. Zhao, L. An, Y. K. Zeng, and L. Wei, *J. Power Sources*, **339**, 1–12 (2017).
41. C. R. Dennison, E. Agar, B. Akuzum, and E. C. Kumbur, *J. Electrochem. Soc.*, **163**, A5163–A5169 (2016).
42. E. J. Wilson and C. J. Geankoplis, *Ind. Eng. Chem. Fundam.*, **5**, 9–14 (1966).
43. A. Crawford et al., *Int. J. Energy Res.* (2016) http://doi.wiley.com/10.1002/er.3526.
44. M. D. Kok, A. Khalifa, and J. T. Gostick, *J. Electrochem. Soc.*, **163**, A1408–A1419 (2016).
45. D. S. Aaron et al., *J. Power Sources*, **206**, 450–453 (2012).
46. Q. H. Liu et al., *J. Electrochem. Soc.*, **159**, A1246–A1252 (2012).
47. X. Li, *Electrochimica Acta*, **170**, 98–109 (2015).
48. J. S. Newman and C. W. Tobias, *J. Electrochem. Soc.*, **109**, 1183–1191 (1962).
49. W. Tiedemann and J. Newman, *J. Electrochem. Soc.*, **122**, 1482–1485 (1975).
50. J. Newman and W. Tiedemann, *AIChE J.*, **21**, 25–41 (1975).
51. A. Kazim, H. T. Liu, and P. Forges, *J. Appl. Electrochem.*, **29**, 1409–1416 (1999).

52. C. O. Laoire, E. Plichta, M. Hendrickson, S. Mukerjee, and K. M. Abraham, *Electrochimica Acta*, **54**, 6560–6564 (2009).
53. X. Wei et al., *Adv. Mater.*, **26**, 7649–7653 (2014).
54. J. Winsberg et al., *Adv. Mater.*, **28**, 2238–2243 (2016).
55. T. Suga, Y.-J. Pu, K. Oyaizu, and H. Nishide, *Bull. Chem. Soc. Jpn.*, **77**, 2203–2204 (2004).
56. F. Kato et al., *Chem. Lett.*, **39**, 464–465 (2010).
57. J. P. Owejan et al., *Int. J. Heat Mass Transf.*, **49**, 4721–4731 (2006).
58. R. Schweiss, C. Meiser, T. Damjanovic, I. Galbati, and N. Haak, *SIGRACET Gas Diffusion Layers for PEM Fuel Cells, Electrolyzers and Batteries*, SGL Group, Meitingen, p. 4 http://www.sglgroup.com/cms/_common/downloads/products/product-groups/su/fuel-cell-components/White-Paper-SIGRACET-GDL-for-Fuel-Cells.pdf.
59. K. Lin et al., *Science*, **349**, 1529–1532 (2015).
60. E. S. Beh et al., *ACS Energy Lett.*, **2**, 639–644 (2017).
61. B. Hu, C. DeBruler, Z. Rhodes, and T. L. Liu, *J. Am. Chem. Soc.*, **139**, 1207–1214 (2017).
62. X. Wei et al., *J. Electrochem. Soc.*, **163**, A5150–A5153 (2016).
63. C.-N. Sun, M. M. Mench, and T. A. Zawodzinski, *Electrochimica Acta*, **237**, 199–206 (2017).
64. X. Wei et al., *Angew. Chem. Int. Ed.*, **54**, 8684–8687 (2015).
65. V. A. Iyer et al., in *Beyond Lithium Ion Batteries II*,, Pacific Rim Meeting on Electrochemical and Solid-State Science, Honolulu (2016).
66. C. S. Sevov et al., *J. Am. Chem. Soc.*, **137**, 14465–14472 (2015).
67. C. S. Sevov, S. L. Fisher, L. T. Thompson, and M. S. Sanford, *J. Am. Chem. Soc.*, **138**, 15378–15384 (2016).
68. C. S. Sevov, S. K. Samaroo, and M. S. Sanford, *Adv. Energy Mater.*, 1602027 (2016).
69. J. Huang et al., *J Mater Chem A*, **3**, 14971–14976 (2015).
70. J. Huang et al., *Adv. Energy Mater.*, **5**, 1401782 (2015).
71. J. Huang et al., *Sci. Rep.*, **6**, 32102 (2016).
72. T. Hagemann, J. Winsberg, A. Wild, and U. S. Schubert, *Electrochimica Acta*, **228**, 494–502 (2017).

9. Quantifying mass transfer rates in redox flow batteries

This chapter is adapted from a manuscript in-submission: J. D. Milshtein, K. M. Tenny, J. L. Barton, J. Drake, R. M. Darling, F. R. Brushett, Quantifying mass transfer rates in redox flow batteries, *Journal of the Electrochemical Society*, submitted.

9.1 Introduction

Mass transport losses limit electrochemical performance due to increases in cell overpotential caused by an inability to deliver reactant to the electrode surface at a sufficient rate.[1] As overpotential losses increase due to slower mass transport rates, the energy efficiency of the battery during cycling will decrease. Further, high overpotentials can limit the accessible state-of-charge (SOC),[2] reducing the practical energy storage capacity of the battery and increasing the effective electrolyte cost.[3,4] In general, improving the convective mass transfer rate can mitigate overpotential loss. Such rates are a function of the active species concentration, state-of-charge (SOC), electrolyte velocity, active species diffusion coefficient, flow field design, and electrode structure. Increasing active species concentration is a straightforward approach, and the maximum feasible operation concentration is governed by the least soluble oxidation state of the active species,[5] as well as high viscosity or electrochemical irreversibility in concentrated electrolytes. At extreme SOCs (near 0% or 100%), active species supply for either the forward or backward reactions is limited, decreasing the thermodynamic driving force for reactant delivery. The flow field distributes the liquid electrolyte into the porous electrode, and subsequently the electrolyte must permeate through the electrode pores, where active species can react at the fiber surface. Thus, for a fixed electrolyte chemistry, the flow field and electrode are the most critical components in enhancing convective transport rates, which reduces cell resistance and expands the accessible SOC range.[2] To date, most flow field designs for RFBs have evolved from bipolar plate design from polymer electrolyte fuel cell technology.[6,7] Commonly, literature reports have investigated the parallel (PFF), serpentine (SFF), interdigitated (IDFF), and flow through (FTFF) flow fields,[1,7,8] though other niche designs exist, such as the spiral[7] or pin-type[9] flow fields. An excellent description of the benefits, shortcomings, and fluid transport mechanisms of the four common RFB flow field types can be found in Ref. 1.[1]

Several recent studies have shown that large performance gains are possible in RFBs through changes in the flow field type, as well as the electrode geometry or morphology.[2,7,8,10–14]

While such reports represent excellent engineering efforts to improve RFB power density, increases in mass transfer rates are rarely quantified, arguably due to insufficient knowledge of relevant transport processes within the specific electrode material.[1] Porous electrodes for RFBs are typically comprised of loose cylindrical fiber beds where the porosity is ~ 70 – 90%,[15] but prior electrochemical modeling efforts have described the mass transport rates in RFBs as a function of either mass transfer coefficients for packed bed reactors[8,16] or Bruggeman-corrected diffusion coefficients.[17] Additionally, recent reports have suggested that flow rate dependent reactor performance improvements vary for different flow field types.[7,8,12,18] For example, Darling and Perry observed that increasing flow rate with the IDFF yielded a diminishing rate of return on reactor performance enhancement, hinting at complicated relationships between overall cell performance and flow rate.[17] While significant efforts have quantified mass transfer rates in electrochemical reactors containing parallel plate electrodes, with and without turbulence promoters,[19,20] only a limited number of studies have investigated mass transfer rates for RFBs with porous electrodes.[13,18]

Quantifying and validating mass transfer rates in a RFB electrode requires a model of sufficient complexity to capture the underlying physics, but of sufficient simplicity to be coupled with experimental studies.[21] Specifically, in the case of extracting mass transfer coefficients, the model must be flexible enough to apply across a broad range of flow cell operating conditions and configurations, but also must not require knowledge of many experimental parameters. Several studies have engaged finite element analysis to offer a detailed description of RFB operation, but these models are computationally intensive and require significant detail.[17,21–23] Specific studies on mass transfer in flow cells with porous electrodes have utilized dimensionless correlations to quantify mass transfer in all-vanadium[18] or zinc-cerium[13] RFBs, but these models can only be applied to direct measurements of the cell's limiting current, which restricts mass transfers coefficient data collection to operating conditions with low flow rates and low active species concentrations. Prior dimensionless porous electrode models by Newman and co-workers are of interest for extracting values from experimental data due to their mathematic reduction to a small number of dimensionless parameters.[24–26] Such models are typically developed for application-specific cases, such as invoking linear or Tafel kinetic descriptions with ohmic losses.[24] RFBs require development of a new dimensionless porous electrode model of this type, as RFBs typically exhibit non-negligible contributions from electrolyte resistivity, charge transfer, and mass transfer.

In this work, we couple a one-dimensional porous electrode model with a single electrolyte flow cell diagnostic technique[8,27–29] to quantify average mass transfer rates for the PFF, SFF, IDFF, and FTFF. First, a one-dimensional, steady-state porous electrode model (Figure 1a), similar to those previously developed by Newman and co-workers,[24–26,30] calculates the overpotential drop across a RFB electrode considering ohmic losses in the electrolyte, Butler-Volmer reaction kinetics, and convective mass transfer limitations. Next, the single electrolyte method is a proven experimental technique that allows for steady-state measurement of RFB overpotential losses for one electrolyte at 50% SOC (Figure 1b),[8,27–29] without concern for performance degradation caused by crossover or need for reference electrodes.[29] Specifically using a model iron chloride electrolyte, we systematically determine cell polarization for the 4 flow fields at 5 flow rates and 3 active species concentrations. The porous electrode model is then fit to the experimental data, extracting an exchange current density and an average mass transfer coefficient for each flow field and operating condition. The aim of this work is to enable quantitative investigation of the mass transfer enhancements afforded by modifying flow field type and flow rate in RFBs and to provide guiding principles for flow field selection and operating conditions.

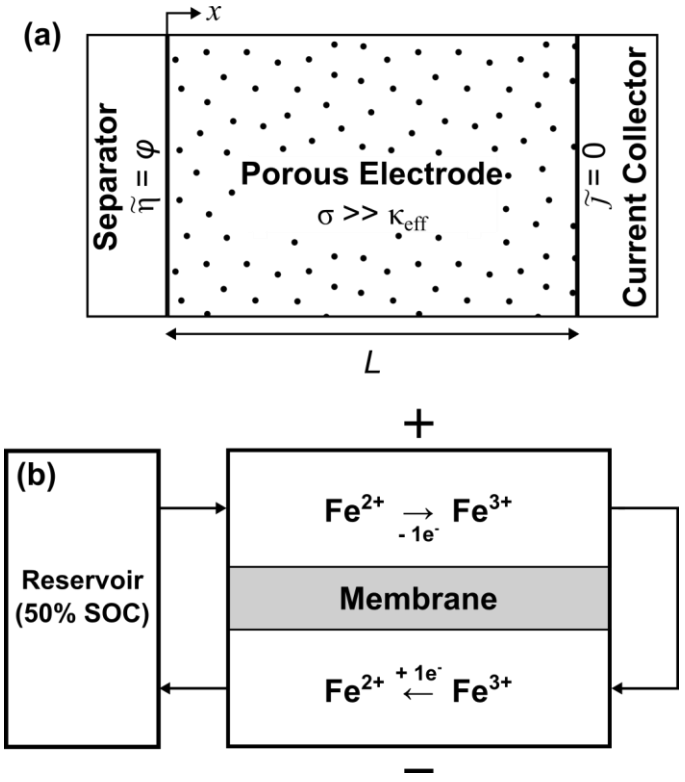

Figure 1: **(a)** Schematic of the one dimensional porous electrode model, including boundary conditions and key dimensions. **(b)** Schematic of the single electrolyte flow cell employing the $Fe^{2+/3+}$ couple.

9.2 Model Theory

Thermodynamics and Reaction Kinetics. The single electron transfer, redox reaction of interest is: $Fe^{2+} \leftrightarrow Fe^{3+} + e^-$. As such, the overall kinetic rate per unit area of electrode (mol m^{-2} s^{-1}), assuming Butler-Volmer kinetics, can be written as (1), where k is the heterogeneous reaction rate coefficient (m s^{-1}), c^s is the active species concentration at the electrode surface (mol m^{-3}), n is the number of electrons transferred, β is the cathodic transfer coefficient, F is the Faraday Constant (C mol^{-1}), R is the gas constant (J mol^{-1} K^{-1}), and T is temperature (K).[31] The a and c subscripts on the reaction rate coefficients denote the anodic and cathodic reactions, respectively.

$$r_k = k_a c^s_{Fe^{2+}} \exp\left[\frac{(1-\beta)nF(\Phi_1-\Phi_2)}{RT}\right] - k_c c^s_{Fe^{3+}} \exp\left[\frac{-\beta nF(\Phi_1-\Phi_2)}{RT}\right] \quad (1)$$

The term ($\Phi_1 - \Phi_2$) describes the potential difference (V) across the interface between the solid (electrode fiber) and liquid (electrolyte in pores) phases of the porous electrode. The potential in the solid phase is denoted as Φ_1, and the potential in the liquid phase is denoted as Φ_2. At equilibrium, the kinetic rate (1) is $r_k = 0$. Thus, the equilibrium potential $(\Phi_1 - \Phi_2)_{eq}$ is:

$$(\Phi_1-\Phi_2)_{eq} = \frac{RT}{nF}\ln\left(\frac{k_c c^s_{Fe^{3+}}}{k_a c^s_{Fe^{2+}}}\right) \quad (2)$$

We can then define the standard potential (V^θ, V) under the condition that $c_{Fe^{2+}} = c^\theta_{Fe^{2+}}$ and $c_{Fe^{3+}} = c^\theta_{Fe^{3+}}$, where $c^\theta_{Fe^{2+}}$ and $c^\theta_{Fe^{3+}}$ are the standard concentrations (1 M, 298 K) of Fe^{2+} and Fe^{3+} ions, respectively. For the $Fe^{2+} \leftrightarrow Fe^{3+} + e^-$ reaction, $V^\theta = 0.771$ V vs. SHE.[32]

$$V^\theta = (\Phi_1-\Phi_2)^\theta = \frac{RT}{nF}\ln\left(\frac{k_c}{k_a}\right) \quad (3)$$

For the simple iron redox reaction, substituting the standard potential (3) into the reaction rate (1) yields:

$$r_k = k_a c^\theta_{Fe^{2+}} \exp\left(\frac{(1-\beta)nFV^\theta}{RT}\right) \cdot \left[\frac{c^s_{Fe^{2+}}}{c^\theta_{Fe^{2+}}}\exp\left(\frac{(1-\beta)nF(\Phi_1-\Phi_2-V^\theta)}{RT}\right) - \frac{c^s_{Fe^{3+}}}{c^\theta_{Fe^{3+}}}\exp\left(\frac{\beta nF(\Phi_1-\Phi_2-V^\theta)}{RT}\right)\right] \quad (4)$$

From (4), the exchange current density (i_0, A m^{-2}) can be explicitly defined in (5). Note that in the present formulation, i_0 is invariant with concentration.

$$i_0 = Fnk_a c_{\mathrm{Fe}^{2+}}^{\theta} \exp\left(\frac{(1-\beta)nFV^{\theta}}{RT}\right) \tag{5}$$

We also define overpotential (η, V) as:

$$\eta = \Phi_1 - \Phi_2 - V^{\theta} \tag{6}$$

Subsequently, we define the kinetic current density (i_k, A m^{-2}) by substituting (5) and (6) into (4), simultaneously replacing β and (1 – β) with a cathodic (α_c) and anodic (α_a) transfer coefficient, respectively. Additionally, we substitute n = 1 for the iron redox reaction.

$$i_k = i_0\left[\frac{c_{\mathrm{Fe}^{2+}}^{s}}{c_{\mathrm{Fe}^{2+}}^{\theta}}\exp\left(\frac{\alpha_a F\eta}{RT}\right) - \frac{c_{\mathrm{Fe}^{3+}}^{s}}{c_{\mathrm{Fe}^{3+}}^{\theta}}\exp\left(\frac{-\alpha_c F\eta}{RT}\right)\right] \tag{7}$$

Mass Transfer. The current density (i_n, A m^{-2}) at the surface of the electrode is directly proportional to the total effective reaction rate (r_{eff}, mol m^{-2} s^{-1}) throughout the electrode, assuming the number of electrons transferred is equal to one (n = 1):

$$i_n = r_{\mathrm{eff}} F \tag{8}$$

Additionally, the molar fluxes of Fe^{2+} and Fe^{3+} can be written as shown in (9) and (10), respectively, where k_m is the mass transfer coefficient (m s^{-1}) of iron to or from the electrode surface. Our formulation assumes that k_m is identical for both Fe^{2+} and Fe^{3+}.

$$r_{\mathrm{Fe}^{2+}} = k_m\left(c_{\mathrm{Fe}^{2+}} - c_{\mathrm{Fe}^{2+}}^{s}\right) \rightarrow c_{\mathrm{Fe}^{2+}}^{s} = c_{\mathrm{Fe}^{2+}} - r_{eff}k_m^{-1} = c_{\mathrm{Fe}^{2+}} - i_n F^{-1}k_m^{-1} \tag{9}$$

$$r_{\mathrm{Fe}^{3+}} = k_m\left(c_{\mathrm{Fe}^{3+}}^{s} - c_{\mathrm{Fe}^{3+}}\right) \rightarrow c_{\mathrm{Fe}^{3+}}^{s} = c_{\mathrm{Fe}^{3+}} + r_{eff}k_m^{-1} = c_{\mathrm{Fe}^{3+}} + i_n F^{-1}k_m^{-1} \tag{10}$$

The total concentration of iron $\left(c_{\mathrm{Fe}^{2+}} + c_{\mathrm{Fe}^{3+}}\right)$ is constant in the diffusion layer near the surface of the electrode according to equations (9) and (10); we neglect migration in the diffusion layer due the presence of excess supporting electrolyte. Next, a combined expression for current density at the electrode surface includes reaction kinetics and mass transfer. We substitute (9) and (10) into (7) to relate current density to a mass transfer coefficient:

$$i_n = i_0\left[\frac{\left(c_{\mathrm{Fe}^{2+}} - i_n F^{-1}k_m^{-1}\right)}{c_{\mathrm{Fe}^{2+}}^{\theta}}\exp\left(\frac{\alpha_a F\eta}{RT}\right) - \frac{\left(c_{\mathrm{Fe}^{3+}} + i_n F^{-1}k_m^{-1}\right)}{c_{\mathrm{Fe}^{3+}}^{\theta}}\exp\left(\frac{-\alpha_c F\eta}{RT}\right)\right] \tag{11}$$

We then rearrange (11), solving explicitly for i_n, with the assumption that the standard state concentrations for Fe^{2+} and Fe^{3+} are identical $\left(c^\theta = c^\theta_{Fe^{2+}} = c^\theta_{Fe^{3+}}\right)$:

$$i_n = \frac{i_0\left[\frac{c_{Fe^{2+}}}{c^\theta}\exp\left(\frac{\alpha_a F\eta}{RT}\right) - \frac{c_{Fe^{3+}}}{c^\theta}\exp\left(\frac{-\alpha_c F\eta}{RT}\right)\right]}{1+\frac{i_0}{Fk_m c^\theta}\exp\left(\frac{\alpha_a F\eta}{RT}\right)+\frac{i_0}{Fk_m c^\theta}\exp\left(\frac{-\alpha_c F\eta}{RT}\right)} \tag{12}$$

For the single electrolyte flow cell employed in this work, the electrolyte remains at 50% SOC with constant iron concentration, implying that $c = c_{Fe^{2+}} = c_{Fe^{3+}}$ for all experiments. We can also define the limiting current density, $i_l = Fk_m c$ (A m^{-2}), and substitute into (12):

$$i_n = \frac{i_0\left[\frac{c}{c^\theta}\exp\left(\frac{\alpha_a F\eta}{RT}\right) - \frac{c}{c^\theta}\exp\left(\frac{-\alpha_c F\eta}{RT}\right)\right]}{1+\frac{i_0}{i_l}\left[\frac{c}{c^\theta}\exp\left(\frac{\alpha_a F\eta}{RT}\right)+\frac{c}{c^\theta}\exp\left(\frac{-\alpha_c F\eta}{RT}\right)\right]} \tag{13}$$

Additionally, we assume $\alpha_a = \alpha_c = 0.5$ for the $Fe^{2+} \leftrightarrow Fe^{3+} + e^-$ reaction, in agreement with experimental reports.[33] As such, we can simplify (13) to (14):

$$i_n = \frac{i_0\frac{c}{c^\theta}\left[\exp\left(\frac{F\eta}{2RT}\right) - \exp\left(\frac{-F\eta}{2RT}\right)\right]}{1+\frac{i_0}{i_l}\frac{c}{c^\theta}\left[\exp\left(\frac{F\eta}{2RT}\right)+\exp\left(\frac{-F\eta}{2RT}\right)\right]} \tag{14}$$

Finally, the current density for one electrode within the single electrolyte flow cell can be written in terms of hyperbolic functions. Note that in the following experimental work, with the single electrolyte cell, the open circuit potential is equivalent to V^θ in all experiments because the electrolyte is fixed at 50% SOC with low conversion per pass, indicating that η has no concentration dependence.

$$i_n = \frac{2i_0\frac{c}{c^\theta}\sinh\left(\frac{F\eta}{2RT}\right)}{1+2\frac{i_0}{i_l}\frac{c}{c^\theta}\cosh\left(\frac{F\eta}{2RT}\right)} \tag{15}$$

One-Dimensional Porous Electrode. Now that the current density has been related to the applied overpotential, we next assume that the conductivity of the electrode fibers is much greater than the effective electrolyte conductivity ($\sigma >> \kappa_{eff}$). For physical justification, the conductivity of dry carbon paper electrodes is typically $\sigma \approx 3000$ mS cm^{-1},[8] whereas the electrolyte

conductivities measured in this work are $\kappa_{eff} \leq 305$ mS cm^{-1} (Figure 9). If the electrode fiber diameter becomes very small relative to the electrode pore size, this assumption may no longer hold. Assuming $\sigma >> \kappa_{eff}$, the potential gradient in the electrode fibers is negligible in comparison to the potential gradient in the electrolyte:

$$\nabla \Phi_1 = 0 \tag{16}$$

Ohm's law holds in the electrolyte, to good approximation, due to the presence of excess supporting electrolyte, allowing us to relate the ionic current density through the electrolyte (i_2, A m^{-2}) to the potential gradient in the electrolyte phase of the porous electrode (17), where x is the position in the porous electrode ($0 < x < L$). Note that $i_2\big|_{x=0}$ represents the ionic current density passing through the separator and is equal to the total current density through the cell.

$$i_2 = -\kappa_{eff} \frac{d\Phi_2}{dx} = \kappa_{eff} \frac{d\eta}{dx} \tag{17}$$

To maintain charge balance, the divergence of the ionic current density along the electrode thickness balances the Faradaic current passing through the electrode ($a \cdot i_n$), within a plane located at x, where a is the electrode surface area per unit volume (m^2 m^{-3}):

$$\frac{di_2}{dx} = a i_n \tag{18}$$

Finally, we can combine (15), (17), and (18) to relate overpotential to current:

$$\frac{d^2\eta}{dx^2} = \frac{a}{\kappa_{eff}} i_n(\eta) = \frac{a i_0}{\kappa_{eff}} f(\eta) \tag{19}$$

Where the function, $f(\eta) = i_n/i_0$, is shown in (20). In the following experimental work, c is fixed by the electrolyte concentration and SOC, and c does not vary as a function of position in the electrode due to low conversion per pass. As such, c is a fixed parameter for each experimental set-up.

$$f(\eta) = \frac{2\frac{c}{c^\theta}\sinh\left(\frac{F\eta}{2RT}\right)}{1 + 2\frac{i_0}{i_l}\frac{c}{c^\theta}\cosh\left(\frac{F\eta}{2RT}\right)} \tag{20}$$

Dimensionless Form and Boundary Conditions. The dimensionless overpotential $(\tilde{\eta})$ is defined as the overpotential normalized by the thermal potential (RT/F, V):

$$\tilde{\eta} = \frac{F\eta}{RT} \tag{21}$$

The dimensionless position inside the electrode is defined as the position normalized by the electrode thickness (L, m):

$$\tilde{x} = \frac{x}{L} \tag{22}$$

θ is defined as the ratio of the exchange and limiting current densities:

$$\theta = \frac{i_0}{i_l} \tag{23}$$

Finally the dimensionless bulk active species concentration $\left(\tilde{c}\right)$ is defined as the bulk concentration normalized by the standard state concentration:

$$\tilde{c} = \frac{c}{c^{\theta}} \tag{24}$$

We can write (19) in dimensionless form by normalizing the total cell current density by the thermal potential, electrode thickness, and effective electrolyte conductivity, while defining a dimensionless exchange current density (ν^2):

$$\frac{d^2\tilde{\eta}}{d\tilde{x}^2} = \frac{Fai_0L^2}{\kappa_{\text{eff}}RT} f\left(\tilde{\eta}\right) = \nu^2 f\left(\tilde{\eta}\right) \tag{25}$$

As such, we must also define the dimensionless reaction rate, $f(\eta)$, as a function of the dimensionless overpotential, $f\left(\tilde{\eta}\right)$, with θ and $\tilde{c}$ as parameters:

$$f\left(\tilde{\eta}\right) = \frac{2\tilde{c}\sinh\left(\frac{\tilde{\eta}}{2}\right)}{1+2\theta\tilde{c}\cosh\left(\frac{\tilde{\eta}}{2}\right)} \tag{26}$$

The dimensionless ionic current density can then be derived from $\tilde{\eta}\left(\tilde{x}\right)$ as:

$$\tilde{j}\left(\tilde{x}\right) = -\frac{1}{2}\frac{d\tilde{\eta}}{d\tilde{x}} \tag{27}$$

At the separator-electrode interface (Figure 1a, left), we impose a constant overpotential boundary condition (φ) such that:

$$\varphi = \tilde{\eta}\big|_{\tilde{x}=0} \tag{28}$$

Ionic current cannot flow at the electrode-current collector interface (Figure 1a, right), providing the basis for a zero ionic current density boundary condition:

$$\tilde{j}\Big|_{\tilde{x}=1} = -\frac{1}{2}\frac{d\tilde{\eta}}{d\tilde{x}}\Big|_{\tilde{x}=1} = 0 \tag{29}$$

In the present analysis, we numerically solve for the dimensionless overpotential as a function of dimensionless position in the electrode, $\tilde{\eta}\left(\tilde{x}\right)$, and derive the dimensionless ionic current density, $\tilde{j}\left(\tilde{x}\right)$.

Analytical Equations for Current and Overpotential Distribution. Although the current and overpotential distribution is computed numerically in the present work, the following derivation provides an analytical relation for the ionic current density as a function of position in the electrode, assuming that the overpotential distribution in the electrode is known. We also present an integral to describe the overpotential distribution in the electrode.

As previously described, the gradient of the liquid phase electrode potential is related to the ionic current density:

$$\frac{d\Phi_2}{dx} = -\frac{i_2}{\kappa_{\text{eff}}} \tag{30}$$

Converting (30) to dimensionless form:

$$\frac{d\tilde{\eta}}{d\tilde{x}} = -2\tilde{j} \tag{31}$$

The dimensionless reaction rate expression provides the other relationship between dimensionless overpotential and ionic current density:

$$\frac{d\tilde{j}}{d\tilde{x}} = -\nu^2 \frac{\tilde{c}\sinh\left(\frac{\tilde{\eta}}{2}\right)}{1+2\theta\tilde{c}\cosh\left(\frac{\tilde{\eta}}{2}\right)} \tag{32}$$

The dimensionless ionic current density derivative, as a function of position, can be expanded as:

$$\frac{d\tilde{j}}{d\tilde{x}} = \frac{d\tilde{j}}{d\tilde{\eta}}\frac{d\tilde{\eta}}{d\tilde{x}} \tag{33}$$

We can then substitute (31) into (33):

$$\frac{d\tilde{j}}{d\tilde{x}} = -2\tilde{j}\frac{d\tilde{j}}{d\tilde{\eta}} \tag{34}$$

We then substitute (32) into (34):

$$2\tilde{j}\frac{d\tilde{j}}{d\tilde{\eta}} = \nu^2 \frac{\tilde{c}\sinh\left(\frac{\tilde{\eta}}{2}\right)}{1+2\theta\tilde{c}\cosh\left(\frac{\tilde{\eta}}{2}\right)} \tag{35}$$

We now arrange the integral to solve for ionic current density. The boundary conditions for i_2 can be easily defined. At the electrode-current collector interface, no ionic current can pass ($i_2 = 0$). At the separator-electrode interface, the ionic current density is equivalent to the geometric current density through the cell (I/A), where A is the geometric cell area (m^2). Converting to dimensionless form, the boundary conditions are $\tilde{j}\big|_{\tilde{x}=0} = \delta$, and $\tilde{j}\big|_{\tilde{x}=1} = 0$.

$$\int_{\tilde{j}(1)=0}^{\tilde{j}(0)=\delta} 2\tilde{j}\cdot d\tilde{j} = \nu^2 \int_{\tilde{\eta}(1)}^{\tilde{\eta}(0)} \frac{\tilde{c}\sinh\left(\frac{\tilde{\eta}}{2}\right)}{1+2\theta\tilde{c}\cosh\left(\frac{\tilde{\eta}}{2}\right)}\cdot d\tilde{\eta} \tag{36}$$

Integrating (36) gives us:

$$\frac{\delta^2}{\nu^2} = \frac{1}{\theta}\ln\left[1+2\theta\tilde{c}\cosh\left(\frac{\tilde{\eta}}{2}\right)\right]_{\tilde{\eta}(1)}^{\tilde{\eta}(0)} \tag{37}$$

Rearrange (37):

$$\exp\left(\theta\frac{\delta^2}{\nu^2}\right) = \frac{1+2\theta\tilde{c}\cosh\left(\frac{\tilde{\eta}(0)}{2}\right)}{1+2\theta\tilde{c}\cosh\left(\frac{\tilde{\eta}(1)}{2}\right)} \tag{38}$$

We now have a relationship between the dimensionless ionic current density and the overpotential at an electrode boundary:

$$\tilde{j}^2(\tilde{x}) = \frac{\nu^2}{\theta}\ln\left[\frac{1+2\theta\tilde{c}\cosh\left(\frac{\tilde{\eta}(\tilde{x})}{2}\right)}{1+2\theta\tilde{c}\cosh\left(\frac{\tilde{\eta}(1)}{2}\right)}\right] \tag{39}$$

The overpotential gradient is related to the ionic current density as defined in (32). Combining (32) and (39) gives:

$$\frac{d\tilde{\eta}}{d\tilde{x}} = -2\sqrt{\frac{\nu^2}{\theta}\ln\left[\frac{1+2\theta\tilde{c}\cosh\left(\frac{\tilde{\eta}(\tilde{x})}{2}\right)}{1+2\theta\tilde{c}\cosh\left(\frac{\tilde{\eta}(1)}{2}\right)}\right]} \tag{40}$$

We can then arrange an integral to describe the overpotential drop across the electrode. This integral does not have an analytical solution:

$$2\sqrt{\frac{\nu^2}{\theta}} = \int_{\tilde{\eta}(1)}^{\tilde{\eta}(0)} \left(\ln\left[\frac{1+2\theta\tilde{c}\cosh\left(\frac{\tilde{\eta}(\tilde{x})}{2}\right)}{1+2\theta\tilde{c}\cosh\left(\frac{\tilde{\eta}(1)}{2}\right)}\right]\right)^{\frac{-1}{2}} \cdot d\tilde{\eta} \tag{41}$$

Equations (38) and (41) represent an implicit solution for $\tilde{\eta}\big|_{\tilde{x}=0}$ and $\tilde{\eta}\big|_{\tilde{x}=1}$.

9.3 Experimental

Electrolyte, Electrode, and Membrane Preparation. Iron (II) chloride tetrahydrate ($FeCl_2$•$4H_2O$, > 99 %), iron (III) chloride hexahydrate ($FeCl_3$•$6H_2O$, 97 %), and hydrochloric acid (HCl, 37 wt% balance water) were all purchased from Sigma Aldrich and used as received. Appropriate amounts of the iron (II/III) chloride hydrates were combined with HCl and deionized water (18 mΩ, Millipore) to produce stock electrolytes containing 0.2, 0.5, or 0.8 M iron chloride at 50% SOC ($Fe^{2+/3+}$) in 2 M HCl. Carbon paper electrodes (25AA, SGL Group) were thermally treated at 500 ºC for 30 h to improve hydrophilicity.[34] Nafion 115 (N115, DuPont) was soaked overnight in 2 M HCl, at room temperature, before serving as the membrane in all flow cell experiments.

Electrolyte Conductivity Measurements. Electrolyte conductivity measurements were collected using a two electrode, Swagelok style conductivity cell. The conductivity cell was identical to prior literature descriptions,[28,35] except now employing graphite, instead of stainless steel, current collectors to mitigate corrosion in the presence of HCl. Conductivity standards containing 0.5, 1.5, 2.0, 3.5, and 6.0 M HCl were prepared, and a 7-point calibration curve was constructed by measuring cell impedance at 0 °C or 25 °C, according to prior literature procedures.[28,35] Known conductivity values of the standard solutions were collected from reference tables.[32]

Flow Battery Preparation and Experiment. The flow cell design, with a geometric active area of 2.55 cm^2, is reported in prior literature.[5,28,35] The interdigitated (IDFF), parallel (PFF), flow through (FTFF), and serpentine flow fields (SFF) were manufactured in-house using 3.18 mm thick impermeable graphite (G347B, MWI, Inc.). Two layers of heat treated carbon paper electrode were assembled into each side of the cell, sealed with Teflon gaskets; the gaskets compressed the electrodes by 20 ± 2%. A glass scintillation vial, sealed with a rubber stopper, served as the reservoir for 10 mL of electrolyte. The electrolyte was continuously sparged with nitrogen gas (Airgas, ≥ 99.999%). The electrolyte was pumped from the reservoir to the cell assembly using a peristaltic pump (Masterflex L/S Series) through perfluoroalkoxy alkane tubing (3.2 mm inner diameter, Swagelok), connected to the cell and pump head, with Norprene tubing (3.2 mm inner diameter, Masterflex) inside the pump head. All flow cell components and pump tubing were selected due to their chemical compatibility with the electrolytes of interest.

Prior to beginning polarization measurements, all flow cells were preconditioned by applying a constant cell potential of 100 mV for 30 min using an Arbin battery tester (BTS-200). The electrolyte flow rate was 3 mL min^{-1} during the cell preconditioning step. After preconditioning, a high-frequency impedance measurement (Biologic VMP3) was collected over the frequency range of 20 kHz to 1 Hz at open circuit potential to determine the ohmic contribution (R_Ω) to the total cell resistance. Polarization data was collected by applying potentiostatic holds for 2 min in 25 mV increments from 0 – 0.2 V, with data recording every 1 s. Polarization curves were generated by identifying the mean of the last 50% of data points from the current response. The overpotential loss associated with the ohmic contribution to the total cell resistance (contributions from the membrane, contact resistances, current collectors, and test leads) was subtracted from the overpotential measurement at each current to generate iR-corrected polarization data in accordance with literature precedence;[7] the solid conductivity of the electrodes contributes negligibly to the high-frequency impedance. Polarization measurements were collected at five flow rates (0.5, 1, 2, 3, and 10 mL min^{-1}) and 3 active species concentrations (0.2, 0.5, and 0.8 M $Fe^{2+/3+}$) for each flow field design.

In this work, polarization measurements are performed on cells with 4 flow fields, 3 iron concentrations, and 5 flow rates, resulting in 60 unique experimental conditions. The discussion section of this chapter will discuss only key representative data and trends. The polarization data,

along with model fits, for the FTFF, IDFF, PFF, and SFF are available in Figure 2, Figure 3, Figure 4, and Figure 5, respectively.

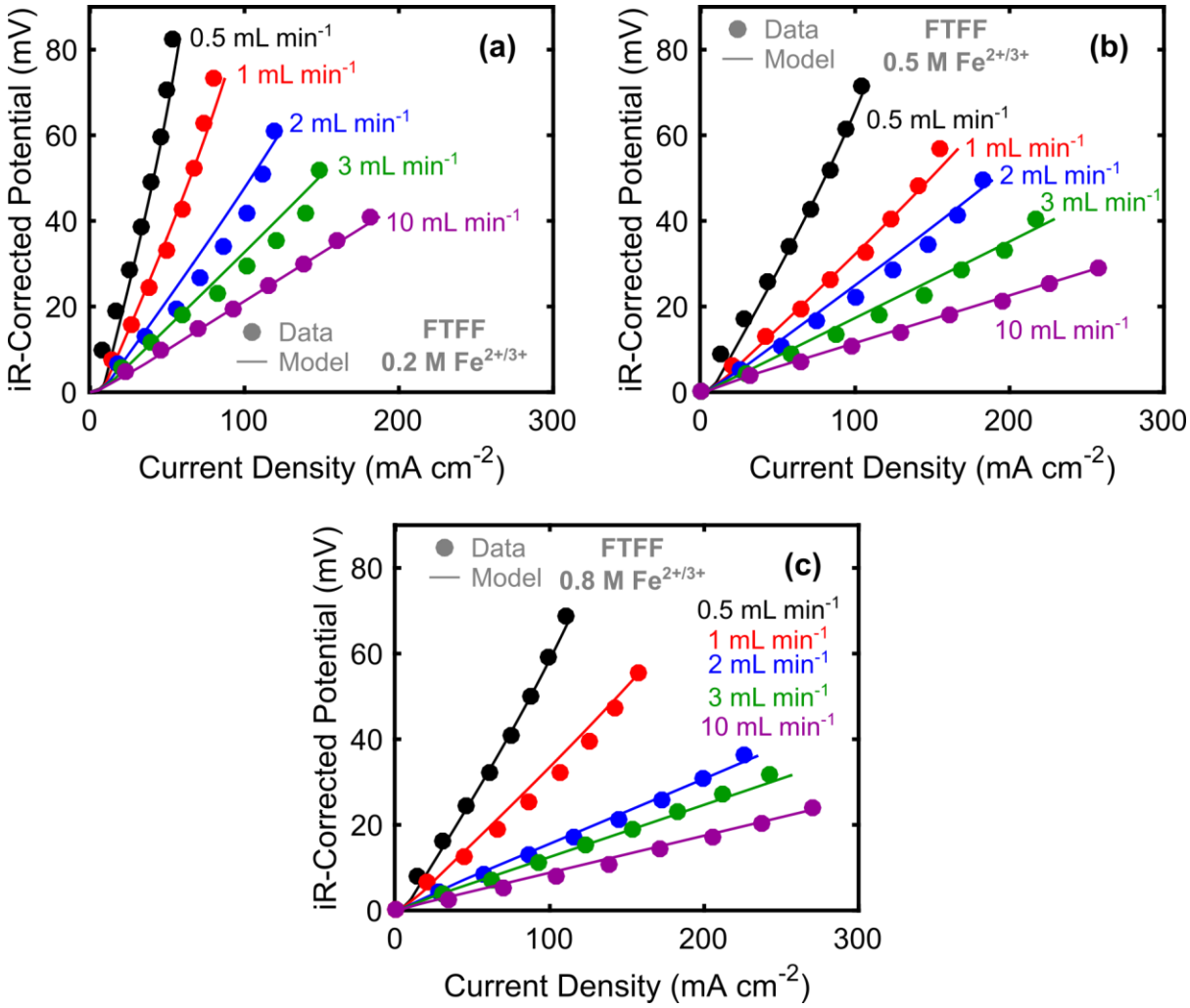

Figure 2: iR-corrected polarization curves from the single electrolyte method, employing the flow through flow field (FTFF) with 5 different flow rates. The following active species concentrations were employed: **(a)** 0.2 M $Fe^{2+/3+}$, **(b)** 0.5 M $Fe^{2+/3+}$, and **(c)** 0.8 M $Fe^{2+/3+}$. Polarization curves include the experimental data (●), as well as the porous electrode model simulation (solid lines).

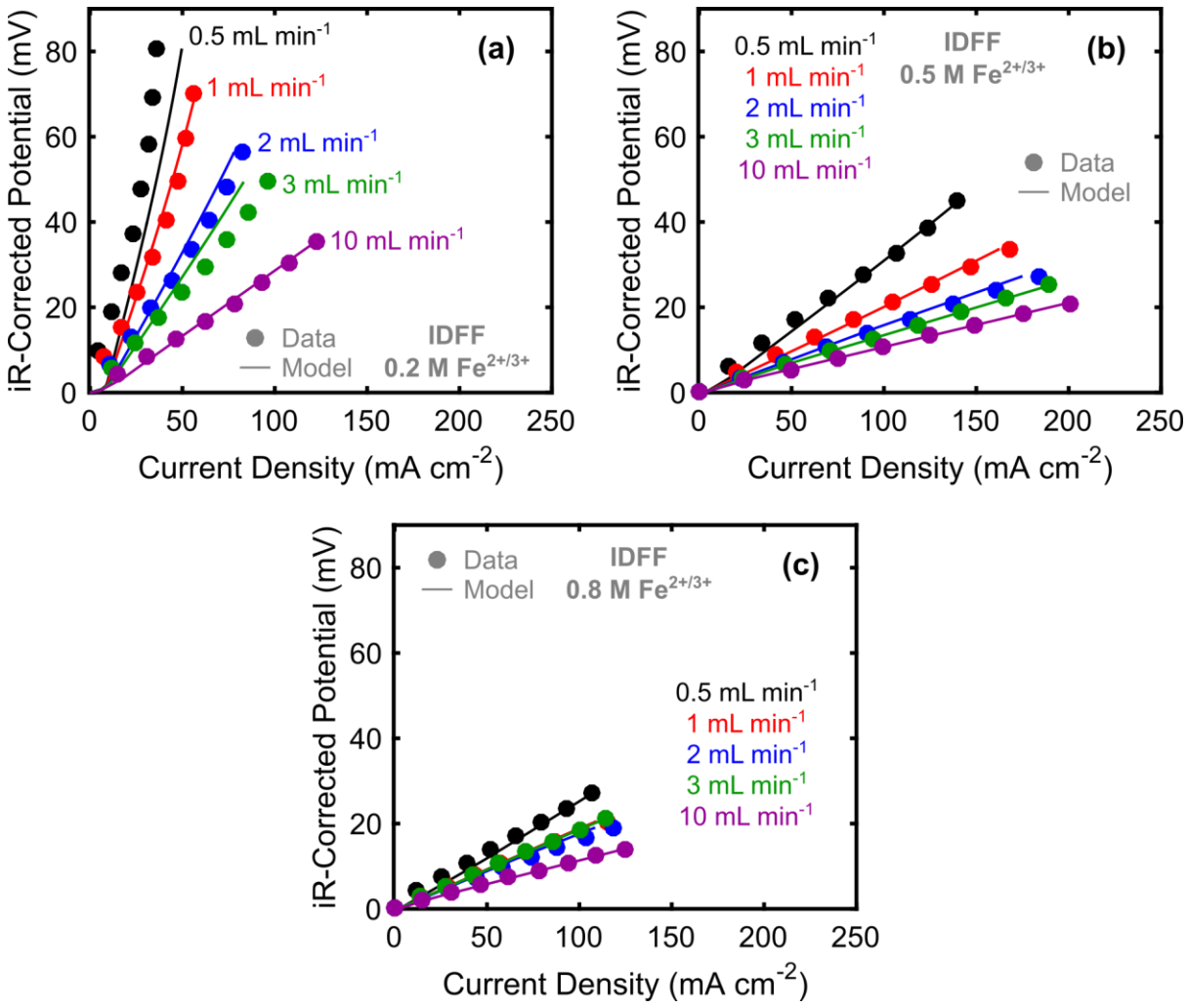

Figure 3: iR-corrected polarization curves from the single electrolyte method, employing the interdigitated flow field (IDFF) with 5 different flow rates. The following active species concentrations were employed: **(a)** 0.2 M $Fe^{2+/3+}$, **(b)** 0.5 M $Fe^{2+/3+}$, and **(c)** 0.8 M $Fe^{2+/3+}$. Polarization curves include the experimental data (●), as well as the porous electrode model simulation (solid lines).

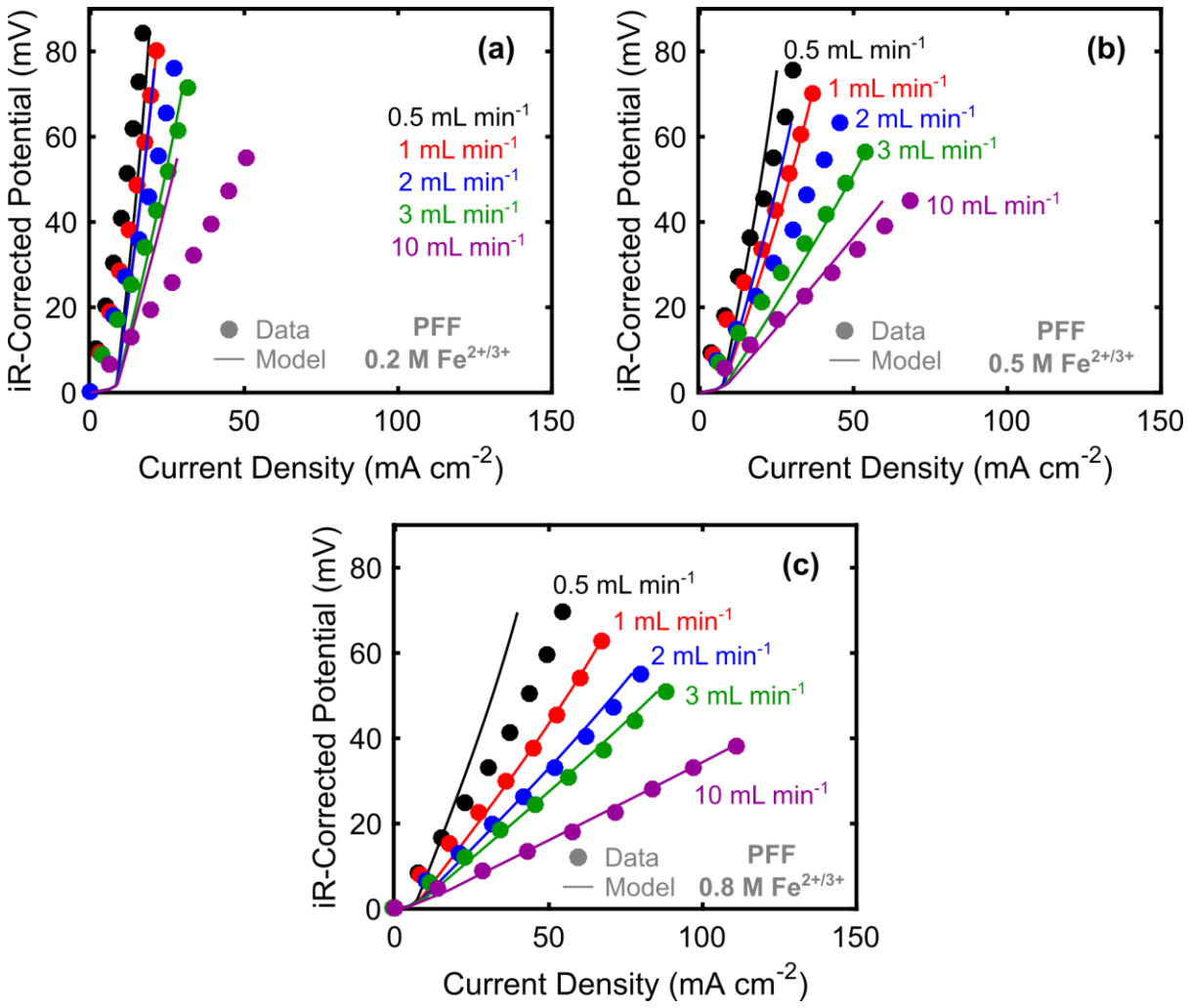

Figure 4: iR-corrected polarization curves from the single electrolyte method, employing the parallel flow field (PFF) with 5 different flow rates. The following active species concentrations were employed: **(a)** 0.2 M $Fe^{2+/3+}$, **(b)** 0.5 M $Fe^{2+/3+}$, and **(c)** 0.8 M $Fe^{2+/3+}$. Polarization curves include the experimental data (●), as well as the porous electrode model simulation (solid lines).

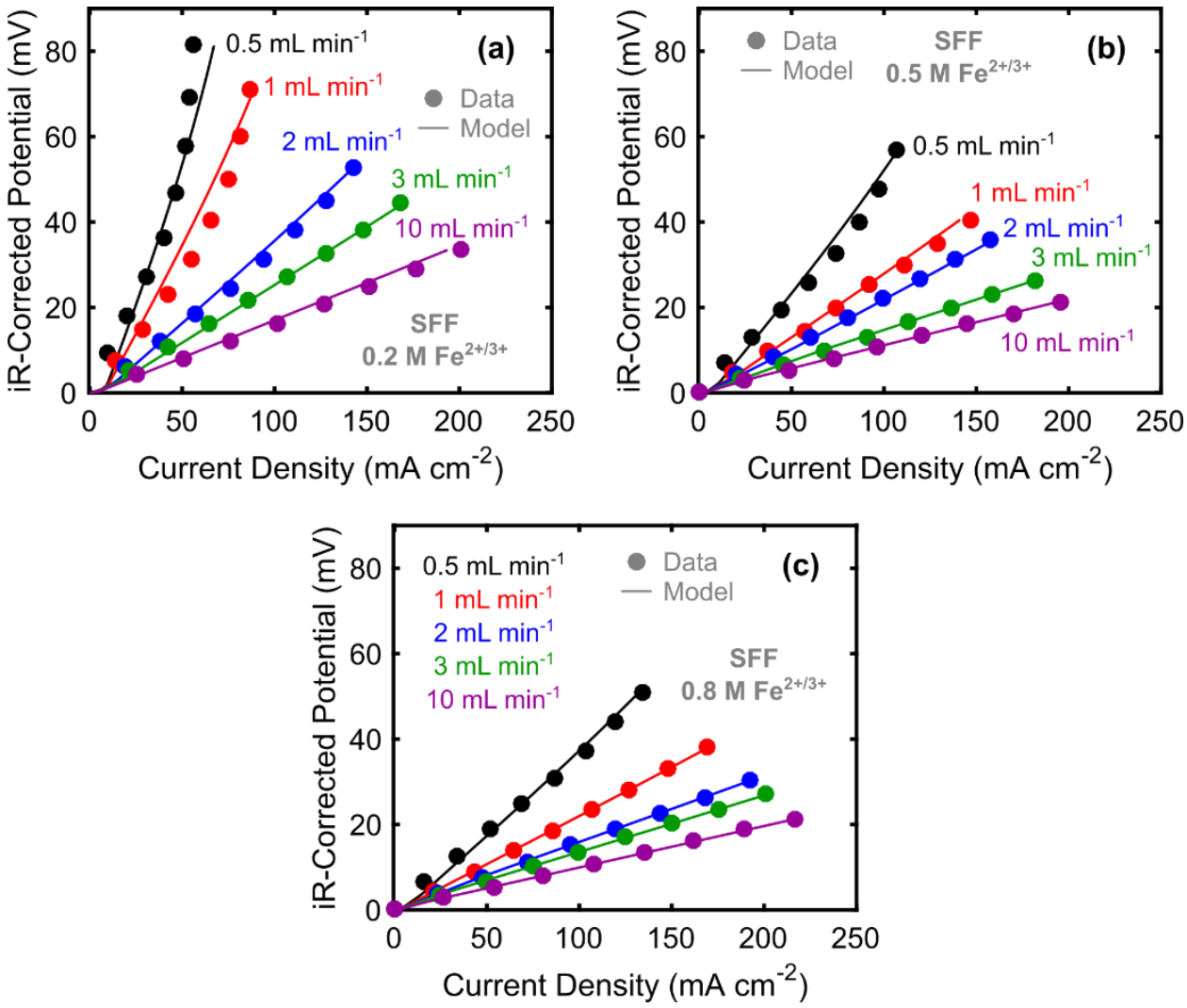

Figure 5: iR-corrected polarization curves from the single electrolyte method, employing the serpentine flow field (SFF) with 5 different flow rates. The following active species concentrations were employed: **(a)** 0.2 M $Fe^{2+/3+}$, **(b)** 0.5 M $Fe^{2+/3+}$, and **(c)** 0.8 M $Fe^{2+/3+}$. Polarization curves include the experimental data (●), as well as the porous electrode model simulation (solid lines).

9.4 Model Trends

The porous electrode model in (25) and (26) describes the dimensionless overpotential distribution as a function of position in the porous electrode. Figure 6 shows representative overpotential distributions for multiple values of v^2 and θ, at fixed concentration $\left(\tilde{c}=1\right)$. For all plots in Figure 6, the dimensionless overpotential at the separator-electrode interface is fixed at $\tilde{\eta}\big|_{\tilde{x}=0}=\varphi=3$ (Figure 1a, left), which corresponds to an electrode overpotential of η = 77 mV under the experimental conditions employed later in this work. At the electrode-current collector interface $\left(\tilde{x}=1\right)$, the overpotential achieves a plateau, as dictated by the zero ionic current boundary condition at the electrode-current collector interface (Figure 1a, right). Generally, as v^2 increases, the overpotential gradient in the electrode becomes larger. A higher value of v^2 indicates faster charge transfer kinetics and subsequently larger exchange current density. Similarly, as θ decreases, the overpotential gradient also becomes larger. Smaller values of θ imply larger limiting currents and higher mass transfer rates, and $\theta = 0$ represents the case of infinitely fast mass transfer. Interestingly, increasing the exchange (larger v^2) or limiting (smaller θ) currents achieves same effect of a steeper overpotential gradient in the electrode.

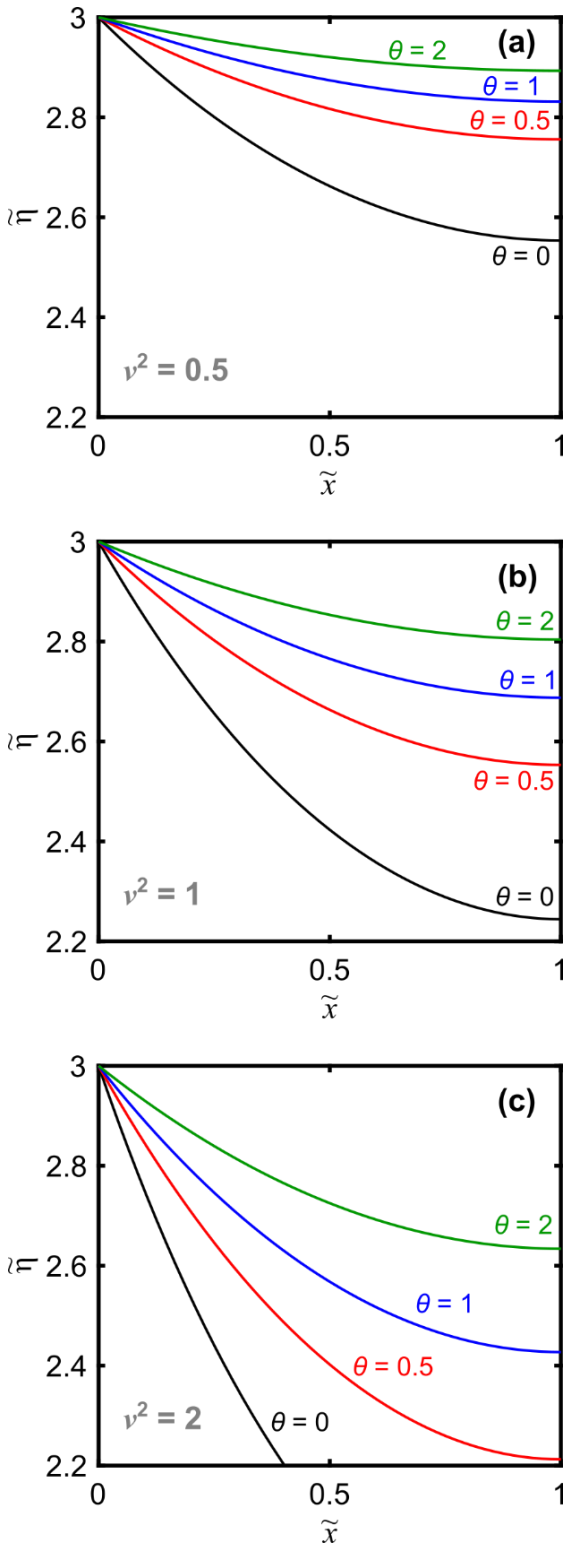

Figure 6: Dimensionless representation of overpotential $\left(\tilde{\eta}\right)$ as a function of position in the porous electrode $\left(\tilde{x}\right)$ for multiple values of ν^2 and θ. **(a)** $\nu^2 = 0.5$, **(b)** $\nu^2 = 1$, and **(c)** $\nu^2 = 2$. For all analyses, the dimensionless concentration is set equal to unity $\left(\tilde{c} = 1\right)$.

To better understand the roles of the exchange and limiting current densities in defining electrode performance, consider the dimensionless ionic current density distribution profiles in Figure 7, which are derived from the overpotential profiles in Figure 7, for multiple values of ν^2 and θ. Note that for all current density distributions in Figure 7, $\tilde{j}\big|_{\tilde{x}=1} = 0$, in accordance with the zero ionic current boundary condition at the electrode-current collector interface (Figure 1a, right). Given that the ionic current density is directly proportional to the gradient in electrode overpotential (Eq. (27)), a larger overpotential gradient yields greater current densities across the electrode, implying improved electrode performance. Thus, increasing ν^2 or decreasing θ leads to a better performing electrode because a larger current density can be achieved for the same applied potential drop across the porous electrode. Physically, this trend originates because a higher exchange current density or larger limiting current density will increase the total current density through the electrode by alleviating charge transfer or mass transfer limitations, respectively.

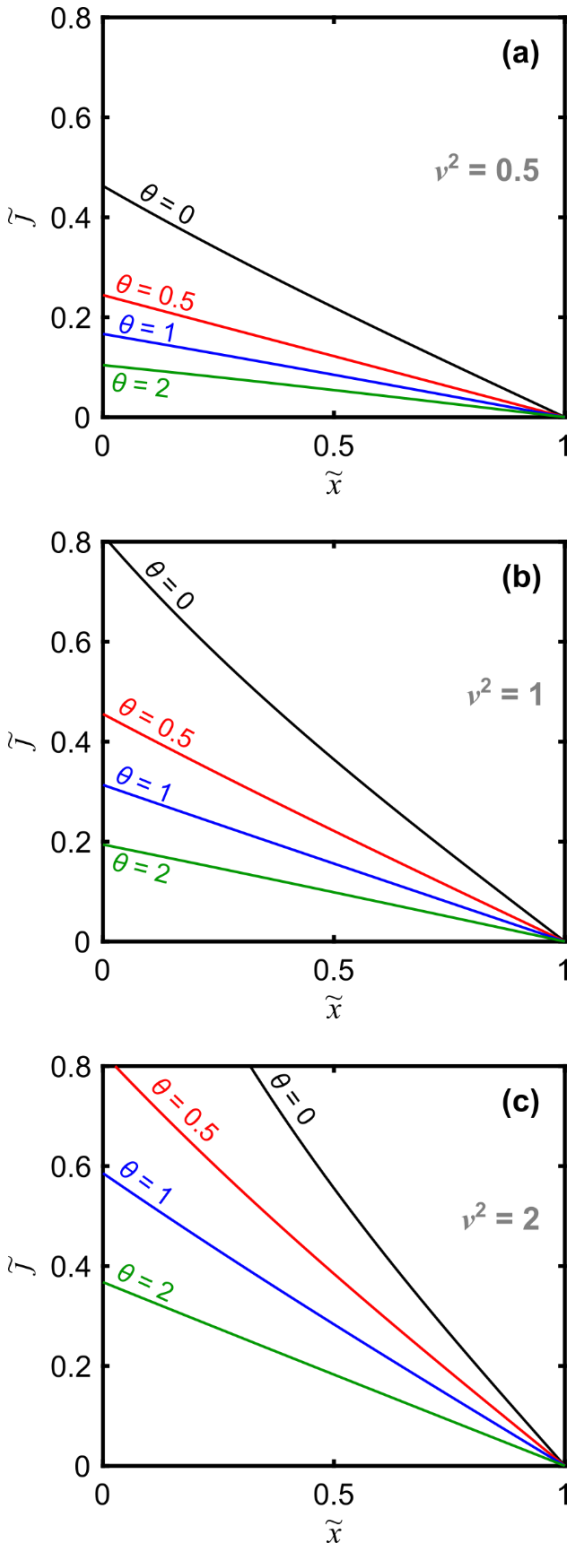

Figure 7: Dimensionless representation of ionic current $\left(\tilde{j}\right)$ as a function of position in the porous electrode $\left(\tilde{x}\right)$ for multiple values of ν^2 and θ. **(a)** $\nu^2 = 0.5$, **(b)** $\nu^2 = 1$, and **(c)** $\nu^2 = 2$. For all analyses, the dimensionless concentration is set equal to unity $\left(\tilde{c} = 1\right)$.

The earlier assumption that the electronic conductivity of the electrode fibers is much larger than the electrolyte conductivity ($\sigma >> \kappa_{\text{eff}}$) implies that the path of least resistance for charge to exit the porous electrode is through the electrode fibers. As such, the electrode prefers to push current out of the electrolyte and into the electrode fibers, which can only be achieved by invoking the electrochemical reaction to transfer charge from the active material to the electrode fibers. The electrochemical reaction, however, is limited by the reaction rate (ν^2) and mass transfer (θ). Consequently, higher reaction (larger ν^2) or mass transfer (smaller θ) rates, yield a larger gradient in the ionic current and subsequently larger gradient in the electrode overpotential. Essentially, slow mass transfer or reaction rates have the same physical effect in the porous electrode in that the electrode cannot quickly transfer the flow of charge from the electrolyte to the electrode.

From the computed overpotential and current density distributions in the porous electrode, we can develop dimensionless polarization curves that describe the current-overpotential characteristic of the electrode. Figure 8 shows dimensionless polarization curves, plotting the dimensionless overpotential at the separator-electrode interface (φ) as a function of the dimensionless current density passing through the separator (δ), which is defined in Eq. (42).

$$\delta = \frac{FL}{2\kappa_{\text{eff}} RT} \cdot \left| i_2 \right|_{x=0} \tag{42}$$

Now the electrode performance dependence on ν^2 and θ becomes even more apparent. As ν^2 increases or θ decreases, the electrode overpotential at a fixed current decreases, implying that the electrode can drive a larger current for a smaller overpotential loss. Additionally, the role of mass transfer at large overpotentials becomes apparent; slower mass transfer rates (larger θ) drive the polarization curve towards limiting current more quickly. Ultimately, this model captures the effects of charge transfer and mass transfer as they impact the overall electrode polarization.

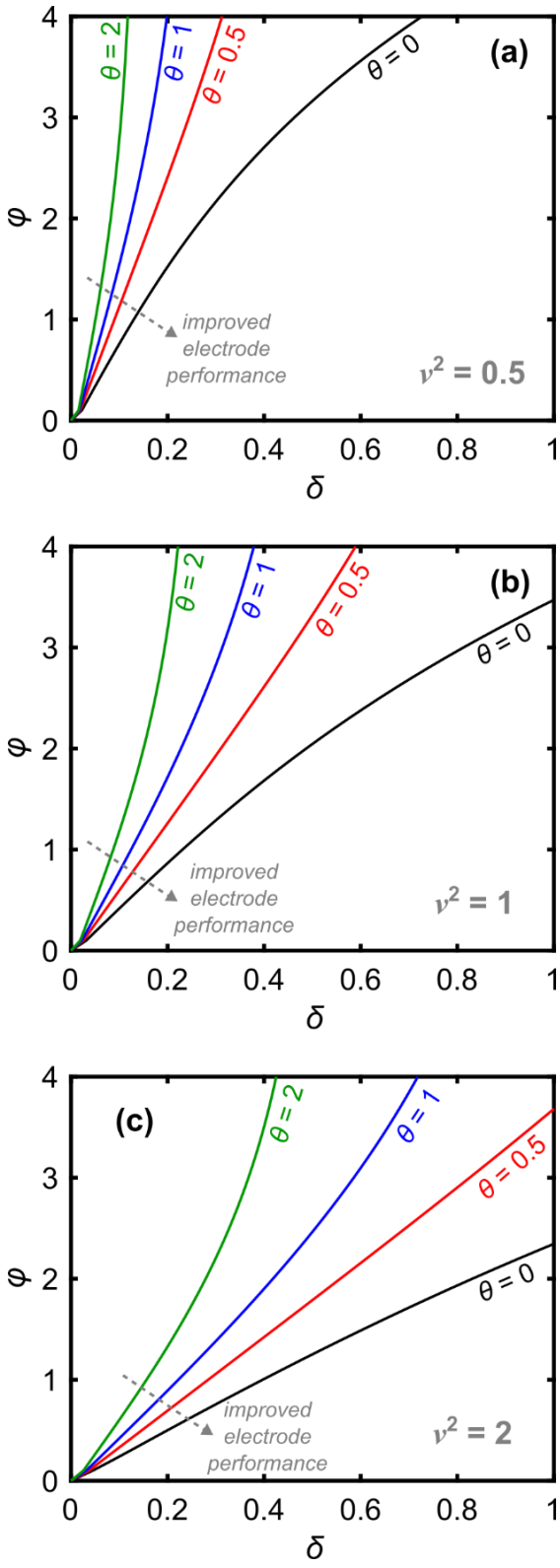

Figure 8: Dimensionless representation of computed polarization, plotting overpotential at the separator-electrode interface (φ) as a function of current density (δ) for multiple values of v^2 and θ. **(a)** $v^2 = 0.5$, **(b)** $v^2 = 1$, and **(c)** $v^2 = 2$. For all analyses, the dimensionless concentration is set equal to unity $\left(\tilde{c} = 1\right)$.

9.5 *Experimental Results and Model Fitting*

Conveniently, the dimensionless porous electrode model contains only two parameters (ν^2 and θ), enabling relatively simple curve fitting of the model to experimental data. Extracting dimensional information from these curve fits, however, requires knowledge of the electrolyte conductivity because the dimensionless exchange current is normalized by the effective electrolyte conductivity (Eq. (25)). Figure 9 shows measured and effective conductivities of the electrolytes employed in this work. All electrolytes contain a 50% SOC mix of $Fe^{2+/3+}$ with 2 M HCl, and the total iron concentration is denoted on the *x*-axis in Figure 9. Notably, the electrolyte conductivity decreases with increasing iron concentration, most likely caused by increasing electrolyte viscosity and inter-species interactions. The electrolyte conductivities (κ) are intrinsic to the electrolyte, and these conductivities are corrected using the Bruggeman relation (Eq. (43)) to compute an effective electrolyte conductivity (κ_{eff}) within the porous electrode.[25] For this work, we assume a compressed electrode porosity, $\varepsilon \approx 0.75$, as measured in a recent experimental study of SGL 25AA carbon paper morphology under compression[15] and a Bruggeman coefficient, $b = 1.5$.[25]

$$\kappa_{\text{eff}} = \kappa\varepsilon^{b} \tag{43}$$

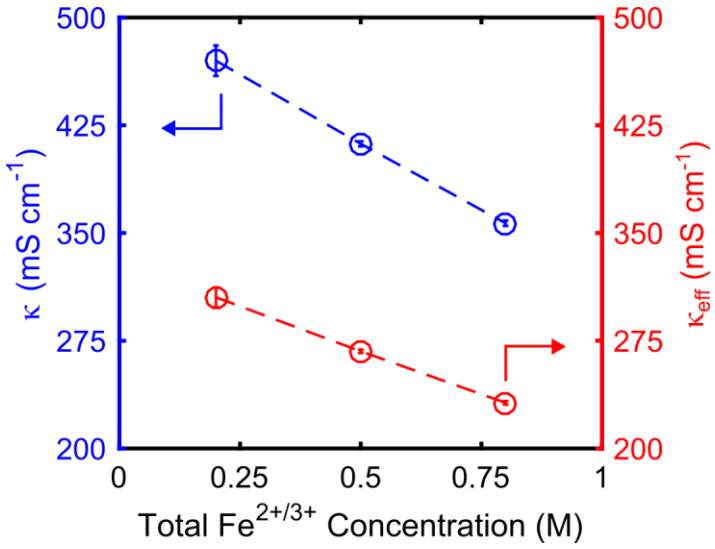

Figure 9: Electrolyte conductivity (left, blue) as a function of active species concentration at 50% SOC, with 2 M HCl supporting electrolyte. The effective electrolyte conductivity (right, red) is calculated from the Bruggeman relation, assuming $\varepsilon \approx 0.75$ and $b = 1.5$.

The single electrolyte flow cell configuration (Figure 1b) is a useful diagnostic tool for investigating flow cell performance.[8,27–29] In this configuration, a flow cell is connected to a single reservoir with one active species present at 50% SOC. The electrolyte stream circulates through the flow cell; the active material is oxidized at the positive electrode and then reduced at the

negative electrode before returning to the reservoir. As such, the reservoir SOC does not change with time, and the cell operates at steady state over a wide range of flow rates and current densities.[29] Additionally, crossover effects will not degrade the cell performance since the same electrolyte composition is present on both sides of the cell.[8] This diagnostic technique permits cell-level analysis without reference electrodes, since nearly identical electrochemical processes are taking place on either side of the cell.[8] When this technique is employed with low active species conversion per pass (i.e., small change in SOC), overpotential losses due to the electrodes can simply be divided across the two sides.[36] In the present work, the $Fe^{2+/3+}$ redox couple serves as a stable active material, with facile redox kinetics, for probing cell performance, and under all experimental conditions, the conversion per pass (f) is $f \leq 0.07$, calculated via Eq. (44), where I is the total current (A) through the cell and Q is the flow rate ($m^3\ s^{-1}$).

$$f = \frac{I}{c_{Fe^{2+}} F Q} \tag{44}$$

The small 2.55 cm^2 flow cell employed in this work offers key benefits and limitations for quantitating mass transfer in a RFB. Practically, the 2.55 cm^2 cell requires only relatively small quantities of electrolyte materials to perform the desired experiments. Additionally, shrinking the cell permits investigations of flow cell performance under a well-controlled environment, where even flow distribution is anticipated. Under such conditions, mass transfer rates within the porous electrode and flow field channels, as well as to the porous electrode from the channels, can be directly investigated. At scale (400 – 900 cm^2),[37–39] other factors arise that impact mass transfer in a RFB, such as transport losses associated with stack manifolds or uneven reactant distribution across a large electrochemical active area, cannot be probed in the small cell. For example, heterogeneous flow dispersion in filter-press reactor stacks for polysulfide-bromine RFBs have shown non-negligible effects on overall transport rates.[19,20] Finally, non-linear scaling of pressure drop with increasing geometric active area[37] and shunt currents cannot be studied with small scale cells.[40]

Figure 10 shows representative experimental polarization curves of flow cells in the single electrolyte configuration under various conditions to illustrate several key experimental trends. Note that all experimental polarization measurements have been iR-corrected to subtract the resistance contribution due to the membrane, contacts, current collectors, and test leads.

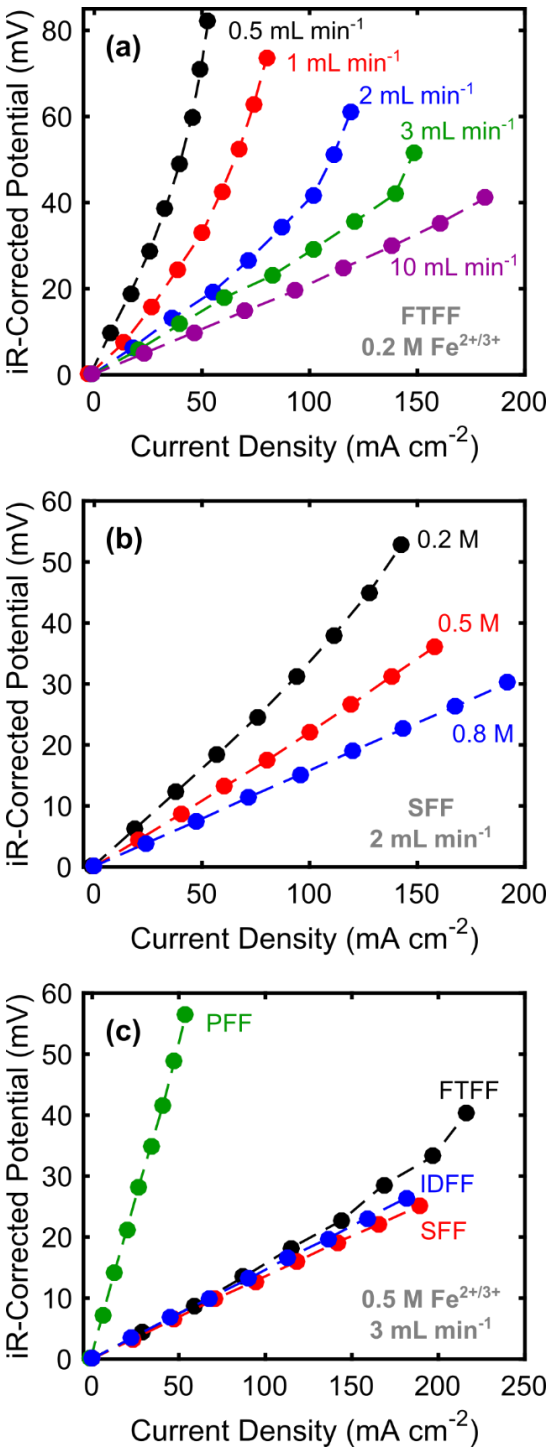

Figure 10: Representative iR-corrected polarization curves from the single electrolyte method, experimentally illustrating the effects of flow rate, active species concentration, and flow field design on cell performance. The dashed lines serve only as visual aids. **(a)** FTFF at various flow rates with fixed active species concentration (0.2 M $Fe^{2+/3+}$). **(b)** SFF at fixed flow rate (2 mL min^{-1}) with various $Fe^{2+/3+}$ concentrations. **(c)** Various flow fields at fixed flow rate (3 mL min^{-1}) and fixed active species concentration (0.5 M $Fe^{2+/3+}$).

Figure 10a demonstrates the effect of flow rate on cell polarization for the FTFF at fixed active species concentration (e.g., 0.2 M $Fe^{2+/3+}$). Increasing flow rate improves electrochemical performance by enhancing the rate of convective mass transfer inside the porous electrode, thus reducing overpotential for a fixed current density. Additionally, increasing flow rate increases the limiting current density for the cell, again due to improved mass transfer in the porous electrode. This behavior is anticipated from prior experimental reports,[7,8,13,18] as well as our model, which indicates that faster mass transfer rates (smaller θ) lead to improved electrochemical performance. Figure 10b illustrates another trend previously reported in literature,[36] where increasing the active material concentration for a one flow field (e.g., SFF) at a fixed flow rate (e.g., 2 mL min^{-1}) alleviates cell polarization despite a decrease in electrolyte conductivity (Figure 9). Increasing active material concentration increases both the kinetic (Eq. (7)) and the limiting currents, simultaneously reducing charge and mass transfer losses within the porous electrode. In the particular experimental case outlined in Figure 10b, these kinetic and mass transport gains outweigh the negative impact of decreasing electrolyte conductivity, across the concentration range investigated.

Figure 10c compares cell polarization for the 4 flow field types at fixed active species (0.5 M $Fe^{2+/3+}$) and electrolyte flow rate (3 mL min^{-1}), revealing more complicated relationships between cell performance and flow field selection. Obviously, the cell polarization for the PFF is much larger in comparison to the polarization for the 3 other flow field types, indicating that the PFF offers the worst electrochemical performance. In the PFF design, minimal convective force directly pushes electrolyte into the porous electrode, yielding small mass transfer rates.[7,8] Under the electrolyte concentration and flow rate conditions implemented in Figure 10c, the FTFF, IDFF, and SFF perform similarly and much better than the PFF. Comparing the flow field performance at fixed electrolyte flow rate, however, is not a good representation because each flow field design displays a different characteristic electrolyte velocity.

To enable a fair comparison among the mass transport characteristics of the various flow fields, we must compare mass transfer coefficients as a function of characteristic electrolyte velocity (v_c, m s^{-1}), defined in Eq. (45), where N_i is the number of inlet channels, h_c is the characteristic flow height, and L_c is the characteristic flow length (Table 1). h_c for the FTFF and IDFF is equal to the electrode thickness, whereas for the PFF and SFF, h_c is the channel height. L_c for the FTFF and IDFF are the width and length of the flow field, respectively, whereas for the

PFF and SFF, L_c is the channel width. The calculations for characteristic velocity in the FTFF, IDFF, and PFF are identical to a prior publication.[8] Since the FTFF and IDFF designs requires that all electrolyte pass through the electrode, the characteristic velocity for these flow fields describes the mean electrolyte velocity through the porous electrode. By contrast, the characteristic electrolyte velocity for the PFF represents the mean velocity through the flow field channel. The intra-electrode velocity associated with the PFF is anticipated to be near zero,[8] but could be computed numerically using the Brinkman equation. Identifying a characteristic velocity for the SFF, however, is non-trivial given that the SFF design exhibits parallel transport in the channel and porous electrode. As such, we define v_c for the SFF as the electrolyte velocity in the channel, assuming no electrolyte penetration into the porous electrode, which is similar to the calculation for the PFF; this electrolyte velocity description for the SFF represents the maximum possible pressure drop through the channel.

$$v_c = \frac{Q}{N_i h_c L_c} \tag{45}$$

Table 1: Relevant dimensions for calculating characteristic velocity (v_c) through each flow field type.

Flow Field	N_i	h_c **(mm)**	L_c **(mm)**
FTFF	1	0.228	14
PFF	7	0.5	1
IDFF	4	0.228	16
SFF	1	0.5	1

Using the porous electrode model in conjunction with the experimental polarization data, v^2 and θ can serve as fitting parameters to describe the electrode behavior for each experimental condition. For each combination of flow field and iron concentration, a single value of v^2 is fitted alongside 5 values of θ to capture the varying mass transfer rates with changing flow rate. The model is fitted to the experimental data using a sum of squares minimization, more heavily weighing data points at higher flow rates where the experiment best represents the physical assumptions of the model. Specifically, at high flow rates, the single electrolyte flow cell exhibits the lowest conversion per pass, indicating the most uniform concentration profiles and SOC as close to 50% as possible, mimicking the model assumptions. Figure 11 illustrates good fitting of the model to the experimental data for the FTFF with 0.5 M $Fe^{2+/3+}$. As mentioned, each model fit

extracts a value of v^2 and θ for each individual polarization curve, and these fitting parameters enable a quantitative analysis of mass transfer rates for all experimental conditions examined.

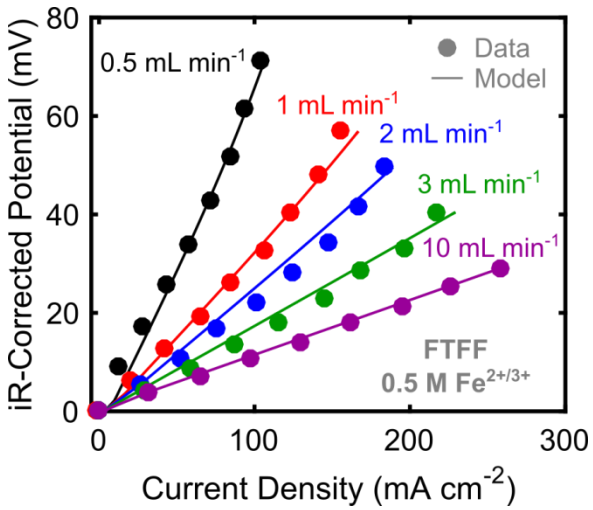

Figure 11: Example series of the porous electrode model (solid lines) fitted to the experimental data (●) for a cell with a FTFF and active species concentration of 0.5 M $Fe^{2+/3+}$.

Extracting mass transfer coefficients from fitted values of v^2 and θ begins with substituting the term $\theta \cdot i_l$ into the definition of v^2, and subsequently defining v^2 in terms of a mass transfer coefficient and active species concentration in (46). Fitted values of v^2, θ, and $a \cdot i_0 \cdot L$ (A m^{-2}) are listed in Table 2 through Table 7.

$$v^2 = \frac{Fai_0L^2}{\kappa_{\text{eff}}RT} = \frac{Fa(\theta i_l)L^2}{\kappa_{\text{eff}}RT} = \frac{Fa(\theta nFk_mc)L^2}{\kappa_{\text{eff}}RT} \tag{46}$$

Table 2: Fitted values of dimensionless exchange current density (v^2) for all flow fields and active species concentrations.

Flow Field	**Dimensionless Exchange Current Density (v^2)**		
	0.2 M $Fe^{2+/3+}$	*0.5 M $Fe^{2+/3+}$*	*0.8 M $Fe^{2+/3+}$*
FTFF	11.1	17.5	18.0
IDFF	8.44	18.4	17.6
PFF	1.88	3.82	9.13
SFF	13.1	17.8	17.9

Table 3: Fitted values of $a \cdot i_0 \cdot L$ (A m^{-2}) for all flow fields and active species concentrations. The electrode thickness (L) is 228 · 10^{-6} m.

Flow Field	**$a \cdot i_0 \cdot L$ (A m^{-2})**		
	0.2 M $Fe^{2+/3+}$	*0.5 M $Fe^{2+/3+}$*	*0.8 M $Fe^{2+/3+}$*
FTFF	0.0382	0.0526	0.0471
IDFF	0.0290	0.0554	0.0456
PFF	0.00646	0.0115	0.0234
SFF	0.0449	0.0535	0.0466

Table 4: Fitted values of θ for the flow through flow field (FTFF), at all flow rates and active species concentrations.

[$Fe^{2+/3+}$] (M)	**Ratio of Exchange to Limiting Current Densities (θ)**				
	0.5 mL min^{-1}	*1 mL min^{-1}*	*2 mL min^{-1}*	*3 mL min^{-1}*	*10 mL min^{-1}*
0.2	46.0	24.2	11.8	6.17	1.67
0.5	28.1	12.5	8.67	4.11	1.20
0.8	22.4	11.7	2.99	1.77	0.424

Table 5: Fitted values of θ for the interdigitated flow field (IDFF), at all flow rates and active species concentrations.

[$Fe^{2+/3+}$] (M)	**Ratio of Exchange to Limiting Current Densities (θ)**				
	0.5 mL min^{-1}	*1 mL min^{-1}*	*2 mL min^{-1}*	*3 mL min^{-1}*	*10 mL min^{-1}*
0.2	41.1	30.0	15.2	11.5	2.31
0.5	12.5	6.55	3.40	2.28	1.00
0.8	7.70	4.18	3.68	4.07	1.27

Table 6: Fitted values of θ for the parallel flow field (PFF), at all flow rates and active species concentrations.

[$Fe^{2+/3+}$] (M)	**Ratio of Exchange to Limiting Current Densities (θ)**				
	0.5 mL min^{-1}	*1 mL min^{-1}*	*2 mL min^{-1}*	*3 mL min^{-1}*	*10 mL min^{-1}*
0.2	36.2	28.0	28.3	13.6	11.1
0.5	38.4	21.1	25.8	10.0	6.60
0.8	39.7	19.1	14.1	11.4	5.56

Table 7: Fitted values of θ for the serpentine flow field (SFF), at all flow rates and active species concentrations.

[$Fe^{2+/3+}$] (M)	**Ratio of Exchange to Limiting Current Densities (θ)**				
	0.5 mL min^{-1}	*1 mL min^{-1}*	*2 mL min^{-1}*	*3 mL min^{-1}*	*10 mL min^{-1}*
0.2	44.8	27.7	9.41	4.69	0.804
0.5	22.6	10.4	7.17	2.73	1.11
0.8	13.3	6.22	3.08	2.16	0.793

Since the electrode area per unit volume (a) is unknown, we cannot extract independent values of k_m. The electrode area per unit volume, however, is considered a constant in this work since the same electrode type, pretreatment, and compression ratio are employed across all experiments. The expression $a \cdot k_m$ (s^{-1}), defined in Eq. (47), can provide a relative understanding of mass transfer

coefficients for each flow field type and is a common performance factor used to describe flowing electrochemical systems.[13,41]

$$a \cdot k_m = \frac{\nu^2}{\theta} \frac{\kappa_{\text{eff}} RT}{F^2 L^2 C} \tag{47}$$

Figure 12 shows values of $a \cdot k_m$ as a function of the characteristic electrolyte velocity through the various flow field designs. In the present model derivation, the mass transfer coefficient is a quantity with no dependence on active material concentration. As a confirmation of the validity of our approach, we plot $a \cdot k_m$ for each active material concentration individually (Figure 12a), which indicates only small variations in the extracted values of $a \cdot k_m$ for electrolytes with different active material concentrations, when the flow field and flow rate are fixed. Potential sources of error include slight variations in cell geometry between assemblies, drift in membrane conductivity during the experiment, and the allowable tolerance during curve fitting. Additionally, the flow fields with channels and ribs (e.g., IDFF, PFF, SFF) could lead to inhomogeneous electrode deformation under compression, causing local variations in electrode porosity, permeability, or conductivity. Furthermore, we note that the model assumptions best describe the FTFF and do not capture the more complex, multidimensional flow patterns in the IDFF, PFF, or SFF, which, in turn, yield poorer model fits than the FTFF case (Figure 3 to Figure 5). These differences between the assumed and experimental velocity distributions within the electrode are an additional source of error and likely explain the larger spread in $a \cdot k_m$ for the non-FTFF cases, however, the reasonable quantitative agreement among multiple measurements at different iron concentrations adds confidence to the overall methodology. The level of detail embedded in our polarization model balances sufficient complexity to describe the underlying physics with the flexibility to fit a large number of data sets. Figure 12b plots the mean values of $a \cdot k_m$ from the 3 iron concentrations employed for each flow field and flow rate combination, where the error bars represent the standard error from the 3 concentration measurements. Solid lines in Figure 12b are a best fit line to the experimental data, and numbers next to the legends denote the slopes of the best fit lines. The variation in v_c for the different flow fields is a result of the treatment in Eq. (45) and varying characteristic flow dimensions (Table 1); for comparison, $a \cdot k_m$ is plotted as a function of electrolyte flow rate (Figure 13).

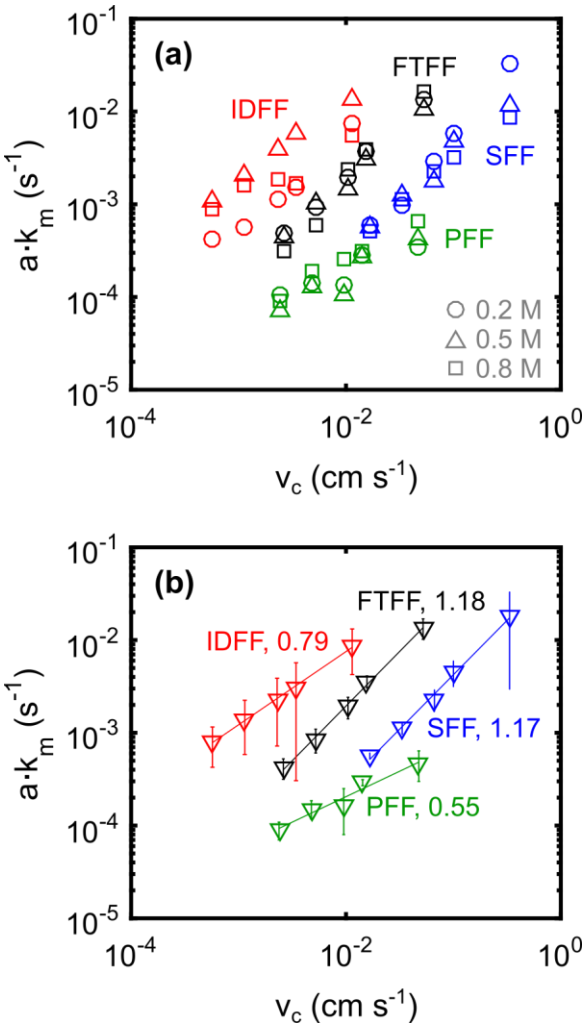

Figure 12: Computed values of the product of electrode area per unit volume and mass transfer coefficient ($a \cdot k_m$) as a function of the characteristic velocity of the electrolyte in a particular flow field design. **(a)** All computed values of $a \cdot k_m$ for each flow field and each active species concentration: 0.2 M $Fe^{2+/3+}$ (○), 0.5 M $Fe^{2+/3+}$ (△), and 0.8 M $Fe^{2+/3+}$ (□). **(b)** Mean values of $a \cdot k_m$ (▽) for each flow field and velocity condition with best fit lines (solid lines). The slopes of the best fits are denoted next to the flow field labels.

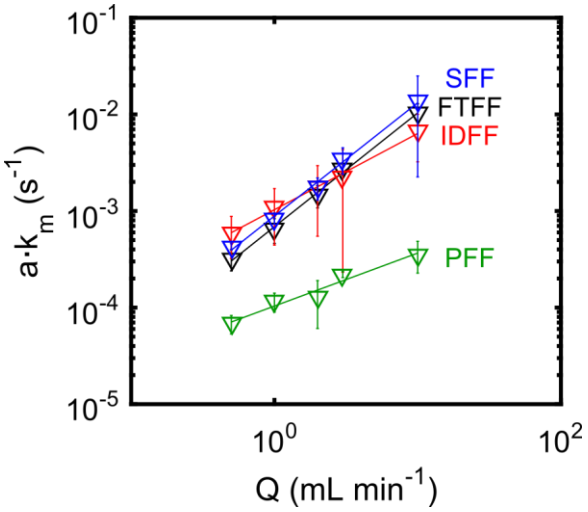

Figure 13: Computed values of the product of specific area and mass transfer coefficient ($a \cdot k_m$, ▽) as a function of electrolyte flow rate with best fit lines (solid lines).

The FTFF offers experimental conditions that best mimic the model assumptions, considering that electrolyte transport through the FTFF is one-dimensional with a uniform velocity profile as a function of position in the electrode. Since the FTFF only invokes transport within a porous electrode (i.e., no flow channels), this flow field also offers the best understanding of transport within the electrode. The FTFF may not be the best choice for implementation in full size RFBs, however, due to an unacceptably large pressure drop through the porous media in cells with large active areas.[8] The FTFF data suggests that the carbon paper employed in this work exhibits $k_m \propto v_c^{1.18}$ (Figure 12b), which is similar to a study of mass transfer coefficients in a carbon felt electrode, where $k_m \propto v_c^{0.912}$.[18] From these proportionalities, k_m and v_c appear to be nearly linearly proportional.

Few reports investigate mass transfer in electrochemical reactors with zero-gap[6] flow field designs.[1] The near-linear scaling between mass transfer coefficient and intra-electrode velocity observed in this study and by Xu and Zhao[18] contrast the quantitative investigations of mass transfer coefficients in filter-press (or flow-by) reactors, where an electrolyte gap (typically several millimeters thick) exists between the electrode and membrane.[13,16,19,20] The filter-press design, with flat plate electrodes and inert turbulence promoters, typically affords $k_m \propto v_c^b$, where $0.39 < b < 0.78$.[13,19,20] Considering transport within only porous media, Fedkiw aggregated data[42] from several studies measuring mass transfer coefficients in packed beds as a function of Peclet number (Pe), defined in Eq. (48), where d_f is the fiber or particle diameter (m) and D is the diffusion

coefficient ($m^2\ s^{-1}$) of the active species.[43] Fedkiw's analysis highlights that for Pe ≤ 20, the mass transfer coefficient is linearly proportional to fluid velocity.[44–46] Contrastingly, for Pe ≥ 20, the mass transfer coefficient is proportional to the cube root (1/3 power) of velocity,[47–51] which has been observed in some carbon fiber / felt electrodes[52–54] and utilized to estimate mass transfer in prior RFB studies.[8,16,40] Additionally, one study on platinized-titanium mesh electrodes for zinc-cerium RFBs identified this cube-root scaling behavior.[13] While prior data collected for packed powder beds indicates significant precedent for linear scaling between k_m and v_c at low Pe,[44–46] the estimated values for Pe, with the FTFF, in this work are quite high. Assuming a fiber diameter of ≈ 7 μm[15] and typical aqueous diffusion coefficient of $\approx 5 \cdot 10^{-6}\ cm^2\ s^{-1}$, we estimate 36 < Pe < 730 for the electrolyte velocities applied in the single electrolyte cell. Given the high Pe and linear dependence, we hypothesize that mass transfer within highly porous, fibrous media (e.g., SGL 25AA) resembles that of a packed particle bed with low fluid velocity, and the Pe dependence shifts due to significant morphological differences. These results motivate further study in fibrous porous media.

$$\mathrm{Pe} = \frac{v_c d_f}{D} \tag{48}$$

The low values of $a \cdot k_m$ for the PFF reiterate the poor mass transfer rates afforded by that flow field design. The PFF mass transfer coefficients also exhibit the weakest dependence on electrolyte velocity, further supporting the claim that convection does not play a significant role on mass transport in this configuration. By comparison, the FTFF, IDFF, and SFF all achieve mass transfer coefficients that can be 100× greater than those of the PFF because of forced convection through the porous electrode. In the case of the FTFF, all electrolyte is directly pushed through the porous electrode, while the IDFF requires all electrolyte to interface with the porous electrode through a shortened path length.[7,8] The SFF does offer a straight path for the electrolyte to pass through the flow field without entering the electrode, however, the pressure drop across the snaking channel of the flow field is likely so large that electrolyte permeates significantly into the porous electrode.[7]

The IDFF has been regarded in recent literature as the best flow field design to balance electrochemical performance with pressure drop,[7,8,55] although the electrode compression and electrode-to-flow-field contact area must be optimized to mitigate ohmic losses.[8] This flow field relies on dead-ended channels to force electrolyte through a short path of porous electrode, and, as

such, comprises multiple flow segments that resemble Poiseuille flow in the channels and Darcy flow in the porous electrode. While all electrolyte must interface with the porous electrode, the highest mass transfer coefficients are not as high as in the FTFF, which is likely due to the non-uniform electrolyte velocity profile within the IDFF; the local electrolyte velocity within the porous electrode is spatially dependent[56] and yields non-uniform mass transfer rates. Additionally, the IDFF exhibits an exponential dependence in between those of the PFF and FTFF designs, hinting that the IDFF behaves as a hybrid of the PFF and FTFF designs. Such hybrid mass transport properties are reasonable given that the pressure drop through the IDFF is also between those of the PFF and FTFF.[8] In fact, the pressure drop through the IDFF can be computed analytically as a product of the pressure drop through a rectangular channel and a geometric factor relating to the porous electrode.[8] For a quantitative comparison of pressure drop through the IDFF, FTFF, and PFF, Darling and Perry offer approximate analytical expressions for each as a function of flow field geometry, electrode permeability, and flow rate.[8] Ultimately, the combination of channels and porous electrode in series makes the IDFF an intriguing mass transfer case that warrants future, detailed study.

Surprisingly, the SFF and FTFF exhibit extremely similar magnitudes of $a \cdot k_m$; when plotted as a function of flow rate (Figure 13), the SFF and FTFF data points overlay almost perfectly. The similar mass transfer rates and their nearly identical velocity dependence indicate that the FTFF and SFF are promoting mass transfer in a similar fashion. The pressure drop along the SFF channel is likely so large that nearly all of the electrolyte is forced through the porous electrode, effectively converting the SFF to a FTFF. While pressure drop is not the focus of this work, we calculate that the pressure drop through just the serpentine channel, without any porous media above, evinces a pressure drop that is ≈ 2.85× higher than the FTFF, indicating that electrolyte flow through the porous electrode is more favorable than through the serpentine channel. Additionally, the single connected channel in the SFF is not a scalable flow field design; the electrolyte penetration into the electrode will depend on the total pressure drop through the single SFF channel, which increases nonlinearly with increasing cell active area. Consequently, when moving towards larger cell designs for grid scale applications (i.e., > 400 cm^2),[37] the pressure drop through the SFF will become unacceptable.[7] Exploring SFF designs with multiple, separated snaking segments, such as those commonly used in PEMFCs,[9] could be a viable option for balancing performance with pressure drop and may offer scalable behavior.

9.6 Conclusions

Mass transfer rates have a significant impact on RFB electrochemical performance, and varying active species concentration, flow rate, flow field design, or electrode morphology will all affect active species delivery rate to the electrode surface. Several recent experimental studies have investigated flow field and electrode designs that best improve performance.[7,8,36] Despite experimental interest and the key role of mass transfer in RFBs, mass transfer coefficients in these devices have seldom been reported.[1,18] As such, this study quantifies mass transfer rates in RFBs as a function of active species concentration, flow rate, and flow field design in a systematic fashion. We develop a steady-state, one-dimensional porous electrode model to describe electrode polarization, considering losses due to the electrolyte resistivity, charge transfer, and convective mass transfer. A series of dimensionless plots illustrate how the RFB electrode behaves across a range of exchange and limiting current values, considering variations in overpotential and current distribution throughout the electrode, as well as overall cell polarization (I-V characteristic). The dimensionless nature of the model reduces the physical description of the RFB electrode to two parameters, enabling facile curve fitting of the model to experimental polarization curves; several key physical assumptions (i.e., $\alpha_a = \alpha_c$, $c_{Fe^{2+}} = c_{Fe^{3+}}$) lead to the concise mathematical form. In conjunction with the model, we implement a single electrolyte diagnostic flow cell technique,[8,27,29,36] with an iron chloride electrolyte, to probe the polarization performance as a function of the aforementioned experimental parameters. Quantitative mass transfer coefficients are extracted by fitting the two model parameters to experimental polarization curves, and the only additional experimental data required is the electrolyte conductivity. In this work, power-law proportionalities between mass transfer coefficient and electrolyte velocity are revealed for 4 flow field types: flow through, interdigitated, parallel, and serpentine.

Quantifying mass transfer rates for the 4 common RFB flow fields offers mechanistic insight into transport phenomena, and provides tangible parameters for future engineering optimization. The small 2.55 cm^2 cell permits controlled evaluation of transport phenomena within the porous electrode and flow field, but prohibits study of additional mass transfer effects that only manifest in large-scale cells, such as poor flow distribution. In terms of mechanistic understanding, our FTFF measurements indicate that traditional mass transfer coefficient correlations for packed particle beds are shifted relative to porous carbon paper electrodes. The small k_m values associated

with the PFF and weak flow rate dependence confirms the findings of prior studies that the PFF does not promote forced convection in the porous electrode and is thus unsuitable for implementation in RFBs.[7,8] Additionally, the surprisingly high mass transfer rates associated with the SFF and the intermediate velocity dependence of the IDFF raise interesting questions as to the role of mixed transport in flow field designs. The mass transfer coefficient data and correlations described here can serve as a basis for more advanced computational studies, for optimizing electrolyte flow rate to balance electrochemical performance and pump work, and for more detailed system-level descriptions of technical performance and cost. Moreover, this combined modeling and experimental approach is portable and can be applied to a range of porous electrode materials, electrolyte compositions, and flow field geometries for flow batteries or other flowable electrochemical systems where electrochemical reactions occur on the surface of porous media.

9.7 List of Symbols

Symbol	Description	Units
a	Electrode area per unit volume	$m^2\ m^{-3}$
α_a	Anodic transfer coefficient	-
α_c	Cathodic transfer coefficient	-
b	Bruggeman coefficient	-
β	Cathodic transfer coefficient	-
c	Concentration	$mol\ m^{-3}$
$\tilde{c}$	Dimensionless concentration	-
c^s	Surface concentration	$mol\ m^{-3}$
c^θ	Standard state concentration	$mol\ m^{-3}$
D	Diffusion coefficient	$m^2\ s^{-1}$
d_f	Fiber (or particle) diameter	m
δ	Dimensionless geometric current density	-
ε	Electrode porosity	-
η	Overpotential	V
$\tilde{\eta}$	Dimensionless overpotential	-
f	Conversion	-
F	Faraday constant	$C\ mol^{-1}$
h_c	Characteristic flow height	m
I	Total Cell Current	A
i_0	Exchange current density	$A\ m^{-2}$
i_2	Electrolyte phase current density	$A\ m^{-2}$
i_k	Kinetic current density	$A\ m^{-2}$
i_l	Limiting current density	$A\ m^{-2}$
i_n	Kinetic + mass transfer current density	$A\ m^{-2}$
$\tilde{j}$	Dimensionless ionic current density	-
k_a	Anodic heterogeneous reaction rate	$m\ s^{-1}$
k_c	Cathodic heterogeneous reaction rate	$m\ s^{-1}$
k_m	Mass transfer coefficient	$m\ s^{-1}$
κ	Electrolyte conductivity	$S\ m^{-1}$
κ_{eff}	Electrode pore phase conductivity	$S\ m^{-1}$
L	Electrode thickness	m
L_c	Characteristic flow length	m
n	Number of electrons	-
N_i	Number of inlet channels	-
ν^2	Dimensionless exchange current density	-
Pe	Peclet number	-
φ	Overpotential at separator-electrode interface	V
Φ_1	Electrode solid phase potential	V
Φ_2	Electrolyte phase potential	V
Q	Flow rate	$m^3\ s^{-1}$
r	Reaction rate	$m^3\ s^{-1}$
r_k	Kinetic reaction rate	$mol\ m^{-2}\ s^{-1}$
r_{eff}	Effective reaction rate	$mol\ m^{-2}\ s^{-1}$
R	Gas constant	$J\ mol^{-1}\ K^{-1}$
σ	Electrode solid phase conductivity	$S\ m^{-1}$
T	Temperature	K
θ	Ratio of exchange to limiting current densities	-

V^{θ}	Standard potential	V
v_c	Characteristic electrolyte velocity	m s^{-1}
x	Position	m
$\tilde{x}$	Dimensionless position	-

9.8 References

1. X. L. Zhou, T. S. Zhao, L. An, Y. K. Zeng, and L. Wei, *J. Power Sources*, **339**, 1–12 (2017).
2. J. Houser, J. Clement, A. Pezeshki, and M. M. Mench, *J. Power Sources*, **302**, 369–377 (2016).
3. R. M. Darling, K. G. Gallagher, J. A. Kowalski, S. Ha, and F. R. Brushett, *Energy Environ. Sci.*, **7**, 3459–3477 (2014).
4. R. Dmello, J. D. Milshtein, F. R. Brushett, and K. C. Smith, *J. Power Sources*, **330**, 261–272 (2016).
5. J. D. Milshtein et al., *Energy Env. Sci*, **9**, 3531–3543 (2016).
6. D. S. Aaron et al., *J. Power Sources*, **206**, 450–453 (2012).
7. C. R. Dennison, E. Agar, B. Akuzum, and E. C. Kumbur, *J. Electrochem. Soc.*, **163**, A5163–A5169 (2016).
8. R. M. Darling and M. L. Perry, *J. Electrochem. Soc.*, **161**, A1381–A1387 (2014).
9. X. Li and I. Sabir, *Int. J. Hydrog. Energy*, **30**, 359–371 (2005).
10. M. L. Perry, R. M. Darling, and R. Zaffou, *ECS Trans.*, **53**, 7–16 (2013).
11. Online: "ARPA-E | Breakthrough flow battery stack," arpa-e.energy.gov/?q=slick-sheet-project/breakthrough-flow-battery-cell-stack; cited: March 29, 2017.
12. J. Houser, A. Pezeshki, J. T. Clement, D. Aaron, and M. M. Mench, *J. Power Sources*, **351**, 96–105 (2017).
13. L. F. Arenas, C. P. de León, and F. C. Walsh, *Electrochimica Acta*, **221**, 154–166 (2016).
14. J. González-García et al., *Ind. Eng. Chem. Res.*, **37**, 4501–4511 (1998).
15. I. V. Zenyuk, D. Y. Parkinson, L. G. Connolly, and A. Z. Weber, *J. Power Sources*, **328**, 364–376 (2016).
16. H. Zhou, H. Zhang, P. Zhao, and B. Yi, *Electrochimica Acta*, **51**, 6304–6312 (2006).
17. X. Li, *Electrochimica Acta*, **170**, 98–109 (2015).
18. Q. Xu and T. S. Zhao, *Phys. Chem. Chem. Phys.*, **15**, 10841–10848 (2013).
19. C. Ponce-de-León, G. W. Reade, I. Whyte, S. E. Male, and F. C. Walsh, *Electrochimica Acta*, **52**, 5815–5823 (2007).
20. C. Ponce-de-León, I. Whyte, G. W. Reade, S. E. Male, and F. C. Walsh, *Aust. J. Chem.*, **61**, 797–804 (2008).
21. Q. Zheng et al., *Appl. Energy*, **132**, 254–266 (2014).
22. K. W. Knehr, E. Agar, C. R. Dennison, A. R. Kalidindi, and E. C. Kumbur, *J. Electrochem. Soc.*, **159**, A1446–A1459 (2012).
23. Q. Zheng, F. Xing, X. Li, G. Ning, and H. Zhang, *J. Power Sources*, **324**, 402–411 (2016).
24. J. S. Newman and C. W. Tobias, *J. Electrochem. Soc.*, **109**, 1183–1191 (1962).
25. J. A. Trainham and J. Newman, *J. Electrochem. Soc.*, **124**, 1528–1540 (1977).
26. W. Tiedemann and J. Newman, *J. Electrochem. Soc.*, **122**, 1482–1485 (1975).
27. C.-N. Sun et al., *J. Electrochem. Soc.*, **161**, A981–A988 (2014).
28. J. D. Milshtein, J. L. Barton, R. M. Darling, and F. R. Brushett, *J. Power Sources*, **327**, 151–159 (2016).
29. R. M. Darling and M. L. Perry, *ECS Trans.*, **53**, 31–38 (2013).
30. J. Newman and W. Tiedemann, *AIChE J.*, **21**, 25–41 (1975).
31. J. Newman and K. E. Thomas-Alyea, *Electrochemical Systems*, 3rd ed., p. 210, John Wiley & Sons, Inc., Hoboken, (2004).
32. W. M. Haynes, *CRC handbook of chemistry and physics: A ready-reference book of chemical and physical data*, 97th ed., CRC Press, Inc., Boca Raton, (2017).
33. Z. Galus and R. N. Adams, *J. Phys. Chem.*, **67**, 866–871 (1963).

34. K. J. Kim et al., *J. Mater. Chem. A*, **3**, 16913–16933 (2015).
35. J. D. Milshtein, S. M. Fisher, T. M. Breault, L. T. Thompson, and F. R. Brushett, *ChemSusChem* (2016). doi: 10.1002/cssc.201700028.
36. A. M. Pezeshki, R. L. Sacci, F. M. Delnick, D. S. Aaron, and M. M. Mench, *Electrochimica Acta*, **229**, 261–270 (2017).
37. E. Knudsen, P. Albertus, K. T. Cho, A. Z. Weber, and A. Kojic, *J. Power Sources*, **299**, 617–628 (2015).
38. X. Wu et al., *J. Solid State Electrochem.* **21**, 429–435 (2017).
39. P. Zhao et al., *J. Power Sources*, **162**, 1416–1420 (2006).
40. R. M. Darling, H.-S. Shiau, A. Z. Weber, and M. L. Perry, *J. Electrochem. Soc.*, **164**, E3081–E3091 (2017).
41. D. Pletcher and F. C. Walsh, *Industrial Electrochemistry*, 2nd ed., p. 81-83, Springer Science+Business Media, LLC, (1993).
42. P. S. Fedkiw, "Mass transfer controlled reactions in packed beds at low Reynolds numbers," thesis, University of California, Berkeley (1978).
43. R. B. Bird, W. E. Stewart, and E. N. Lightfoot, *Transport Phenomena*, 2nd ed., p. 316, John Wiley & Sons, Inc., New York, (2007).
44. M. Bar-llan and W. Resnick, *Ind. Eng. Chem.*, **49**, 313–320 (1957).
45. T. H. Hsiung and G. Thodos, *Int. J. Heat Mass Transf.*, **20**, 331–340 (1977).
46. K. Kato, H. Kubota, and C. Y. Wen, *Chem. Eng. Program Symp. Ser.*, **66**, 87–99 (1970).
47. C. Appel and N. Bonanos, *J. Eur. Ceram. Soc.*, **19**, 847–851 (1999).
48. S. Kumar, S. N. Upadhyay, and V. K. Mathur, *Ind. Eng. Chem. Process Des. Dev.*, **16**, 1–8 (1977).
49. J. E. Williamson, K. E. Bazaire, and C. J. Geankoplis, *Ind. Eng. Chem. Fundam.*, **2**, 126–129 (1963).
50. E. J. Wilson and C. J. Geankoplis, *Ind. Eng. Chem. Fundam.*, **5**, 9–14 (1966).
51. S. N. Upadhyay and G. Tripathi, *J. Chem. Eng. Data*, **20**, 20–26 (1975).
52. D. Schmal, J. Van Erkel, and P. J. Van Duin, *J. Appl. Electrochem.*, **16**, 422–430 (1986).
53. K. Kinoshita and S. C. Leach, *J. Electrochem. Soc.*, **129**, 1993–1997 (1982).
54. B. Delanghe, S. Tellier, and Astruc, *Electrochimica Acta*, **35**, 1369–1376 (1990).
55. M. L. Perry, "Flow battery with interdigitated flow field," US Pat. US 91666243 B2, Filed December 18, 2009.
56. A. Kazim, H. T. Liu, and P. Forges, *J. Appl. Electrochem.*, **29**, 1409–1416 (1999).

10. Performance-based techno-economic analysis for refined materials selection: a case study in aqueous flow battery supporting electrolytes

10.1 Introduction

Investigating new chemistries is one strategy that could lower the electrolyte (energy) cost contribution to the total battery cost via decreased chemical costs or increased electrolyte energy density.[1,2] Key active species characteristics in determining the RFB electrolyte cost are the solubility (M), molar mass (kg mol^{-1}), number of electrons stored per molecule (-), material cost (\$ kg^{-1}), and cell potential (V), and the latter two characteristics have a significant impact on total RFB cost.[1,2] Raising cell potential, by identifying active species with more extreme redox potentials,[2] is a particularly effective approach to reducing RFB costs because increasing cell potential decreases both the electrolyte and reactor (power) cost contributions.[1,2] Battery cost is also sensitive to active material cost,[2] and, as such, many recent studies have sought to identify active species that could serve as cheap replacements for the incumbent RFB chemistries. Abundant inorganic active species (*e.g.*, metal polysulfides[3–5], iodide[4,5]) exhibit very low costs due to large material reserves. Further, redox-active organic molecules (ROMs) are comprised of earth-abundant elements (*i.e.*, hydrogen, carbon, oxygen, nitrogen, sulfur), and their cost is not determined by production rates of raw materials or material reserves.[6] New organometallic active species,[7–13] as well as ROMs, show promise through the addition of functionalizing ligands, enabling rational molecular design. Typically when a new active material is discovered, the supporting electrolyte must simultaneously be tuned to facilitate its implementation. Key technical considerations when designing a supporting electrolyte are the active material solubility, chemical stability, reaction kinetics, and safety.

Supporting electrolyte design, in conjunction with new active species discovery, has targeted improvements in active material solubility, kinetics, and stability, as well as electrolyte safety, and numerous experimental examples of such electrolyte development campaigns exist in literature. As a solubility example, 2,6-dihydroxyanthraquinone is only sufficiently soluble (> 0.5 M) in alkaline electrolytes,[14] and anthraquinone disulfonic acid (AQDS) is more soluble in the protonated state, as opposed to the sodium form.[15,16] Regarding charge transfer kinetics, modifying the supporting electrolyte composition, without adding catalysts or pretreating electrodes, has been shown to dramatically affect the electrochemical reaction rates for both metallic and organic active

species.[17–19] Considering chemical stability, charged methyl viologen[8,20,21] is known to react with molecular hydrogen, making it unsuitable for use in acidic electrolytes where the hydrogen evolution reaction may take place.[22] Finally, as for safety, metal polysulfides[3] or ferrocyanide[3,14] can undergo chemical decompositions in acid to produce toxic hydrogen sulfide or cyanide, respectively. While designing a new electrolyte may be beneficial for enhancing the electrochemical behavior of a new active material, other cell-level performance metrics, such as area specific resistance (ASR) or cell potential, can suffer as a consequence; these cell-level performance metrics are often overlooked while a new electrolyte is developed, clouding the prospect of these new electrolytes as a cost-effective alternative to the state-of-the-art VRFB. For example, neutral and alkaline RFBs tend to exhibit significantly lower power density[3,7,14] than VRFBs[23–25] due less conductive membrane options. Moreover, many new proposed chemistry combinations exhibit theoretical open-circuit potentials (OCP) well below[7,8,15,16,20,26] that of the VRFB (1.4 V).[27]

This study explores how variations in RFB performance due to supporting electrolyte and membrane selection influence system cost. We focus on aqueous electrolytes, as opposed to nonaqueous,[28–30] due to the higher technology-readiness level of AqRFBs and consequently larger amount of associated device information for grid-relevant operation. First, we identify governing physical parameters, namely the membrane ASR, electrolyte conductivity, electrolyte viscosity, and cell potential, which significantly impact RFB cost. Membrane ASR can vary drastically with membrane type, working ion, or electrolyte pH,[31–33] and the latter two can also impact electrolyte conductivity and viscosity. A typically overlooked characteristic, electrolyte viscosity is of critical importance as it directly impacts mass transfer rates in the porous electrodes of a RFB, as well as required pumping power through the entire battery.[34–36] As mentioned before, cell potential is a key parameter that affects the power and energy density of the RFB, both of which define RFB cost.[1,2] Second, to link these materials properties to RFB cost, full-cell ASR is calculated by implementing a one-dimensional porous electrode model that solves for electrode polarization as a function of electrolyte conductivity, charge-transfer kinetics, and convective mass transfer rate. The electrode ASR contribution is combined with ion-exchange membrane (IEM) ASR values in various supporting electrolytes,[3,8,37] as well as newly proposed size selective separators (SSS).[38–42] Third, we then develop a techno-economic model to estimate RFB capital cost as a function of electrolyte composition and cell potential, among other detailed device parameters. The reactor

cost contribution is calculated by leveraging prior literature,[1,2,43] as well as developing new and more detailed descriptions of the electrolyte cost, which enable consideration of cost differences from various supporting salts and specific inclusion of tank costs. We also implement a new estimate of balance of plant (BOP) costs, which accounts for variations in pumping costs with changes in electrolyte flow rate and viscosity, as well as reactor geometry. Combining the reactor, electrolyte, and BOP costs, as well as literature estimates of unit cost less materials,[1,43] permits evaluation of variations in RFB capital cost for different AqRFB supporting electrolytes. Through this dual electrochemical performance and techno-economic analysis, we identify that changes in supporting electrolyte or membrane selection can yield battery cost differences in the \$100's kWh^{-1} and that proton-conducting IEM- or SSS-based RFBs, with high cell potentials (near 1.5 V), are most promising to approach the DOE capital cost target.

10.2 Membrane and Electrolyte Conductivities

Conductivities of IEMs implemented with new RFB electrolytes are rarely reported, and can vary drastically depending on the working ion[31] and the properties of the surrounding supporting electrolyte.[44] As such, we derive membrane (κ_{mem}) and electrolyte ($\kappa_{electrolyte}$) conductivities from a limited amount of available literature data (Table 1). For H^+-IEMs, we assume the conductivity of a membrane employed in a state-of-the-art VRFB,[37] and the associated electrolyte conductivity is taken as an average of VRFB electrolyte conductivities across all states-of-charge (SOC) [27]. For Na^+- and Cl^--IEMs, we estimate membrane conductivity from the high-frequency intercept of full-cell impedance measurements from published flow cells employing these membranes.[3,8] As thick membranes ($\geq$ 120 μm) were employed in the relevant studies, the high-frequency intercept on the experimental Nyquist plot is dominated by the membrane resistance. The conductivity of a NaCl-based RFB electrolyte is taken as an average value from a recent literature study.[8] Although a K^+-IEM has been utilized in two experimental RFB studies,[14,45] the associated conductivity has not been measured, and no impedance data is available to derive an experimental estimate. In the present work, we estimate the conductivity of K^+-IEM by scaling the conductivity of the H^+-IEMs by the ratio of ionic conductivities of the two membranes without active species present.[31] In a similar fashion, we estimate the conductivity of a KOH-based electrolyte by scaling the conductivity of an average VRFB electrolyte by the ratio of the peak ionic conductivities[46] of H_2SO_4 and KOH. From prior systematic studies of Nafion conductivity with various working ions

in supporting electrolyte (no active species), we anticipate that cation-exchange membrane conductivity will decrease in the following order: $H^+ > Na^+ > K^+$. Similarly, from prior data reporting on the conductivity of various acid and salt solutions, we anticipate that the electrolyte conductivity should decrease as: $H_2SO_4 > KOH > NaCl$.[46] The membrane conductivities reported in Table 1 are converted to a membrane area-specific resistance (R_{mem}, Ω cm^2), where Figure 1a denotes the relationship among R_{mem}, the working ion, and the membrane thickness.

Table 1: Membrane conductivities employed in this analysis.

Membrane	**Ion**	**Salt**	κ_{mem} **(mS cm^{-1})**	$\kappa_{electrolyte}$ **(mS cm^{-1})**
Nafion	H^+	H_2SO_4	21 [37]	280 [27]
Nafion	Na^+	NaCl	7.9 [3,†]	150 [8]
Nafion	K^+	KOH	3.2‡	200*
AEM	Cl^-	NaCl	5.3 [8,†]	150 [8]
SSS_{H+}	H^+ / SO_4^{2-}	H_2SO_4	110*	280 [27]
SSS_{Na+}	Na^+ / Cl^-	NaCl	41*	150 [8]

†Estimated from experimental impedance data in the associated reference.
‡Estimated by scaling H^+ / K^+ conductivity without active species.[31,46]
*Estimated from Bruggeman relation (Equation (1)).

Table 1 and Figure 1a also specify example performances for two hypothetical size-selective separators (SSS). Recent reports have recognized that the RFB membrane does not need to be selective to a single ion in the electrolyte, but rather must only reject the active species, permitting any supporting ions to maintain electroneutrality across the cell. From this realization emerged a new approach of pairing SSS with larger active species where the separator allows smaller supporting ions to exchange between the two electrolyte streams while blocking crossover of the larger active species.[38–42,47–49] Since SSS are comprised of non-functionalized polymers, they promise higher conductivities and lower costs as compared to their functionalized IEM counterparts. However, to date, SSS have only been reported in a small number of literature studies,[39,41,42,48–51] limiting the amount of available experimental data. As such, we estimate their effective conductivities (κ_{eff}, mS cm^{-1}) using the Bruggeman relation (Equation (1)), where κ is the electrolyte conductivity (mS cm^{-1}) in the pore phase of the SSS, ε is the SSS porosity (-), and b is the Bruggeman coefficient (b = 1.5).[52] The SSS porosity is assumed to be that of Celgard 2500 (ε = 0.55),[53] a typical nanoporous separator employed in lithium-ion batteries,[38] and the electrolyte conductivities of the pore phase are taken from literature reports (Table 1).[8,27] In the present estimates of SSS conductivities, perfect separator wetting is assumed. For comparison, we estimate

the κ_{mem} for a Na+-IEM to be 41 mS cm^{-1}, and a recent experimental study on SSS, without active species, measured κ_{mem} to be 79 mS cm^{-1}.[48] This discrepancy is attributed to the higher conductivity of a NaCl electrolyte, in the separator pore phase, without any active species present.

$$\kappa_{\text{eff}} = \kappa_{electrolyte}\varepsilon^{b} \quad (1)$$

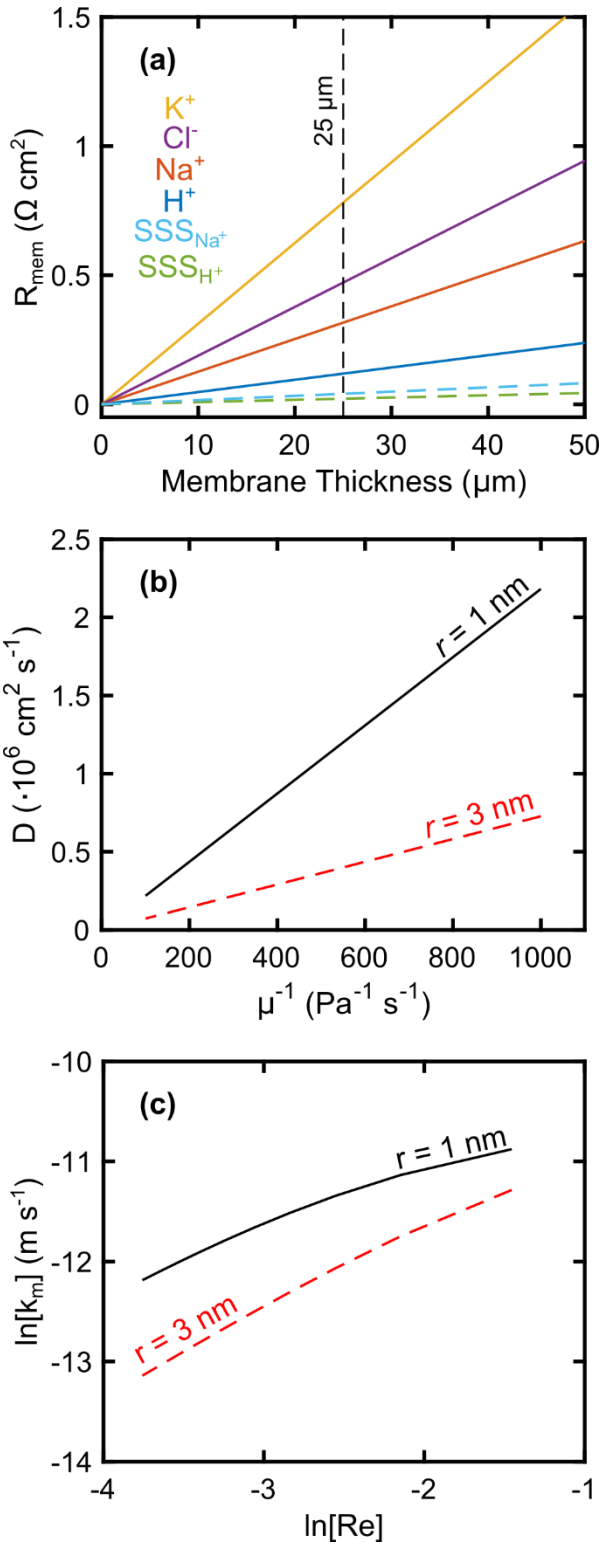

Figure 1: **(a)** Membrane thickness versus membrane ASR (R_{mem}) for various working ion and membrane types. **(b)** Relationship between active species diffusion coefficient and viscosity for a small (r = 1 nm) and large (r = 3 nm) active species. **(c)** Mass transfer coefficient versus electrolyte Re within the porous electrode.

10.3 Transport Properties

To begin estimating transport rates of active materials in RFBs, diffusion coefficients are calculated using the Stokes-Einstein relationship (Equation (2)),[54] where k_B is the Boltzmann constant (1.38×10^{-23} J K^{-1}), T is the electrolyte temperature (298 K), μ is the electrolyte viscosity (Pa·s), and r is the solvated radius of the active species in solution (m). This work will consider electrolyte viscosities in the range of 1 – 10 mPa·s, and given that SSS will likely require larger active species for successful RFB operation, two representative solvated radii are selected. For small active species (*e.g.*, inorganic ions, ROMs) paired with IEMs, r = 1 nm, corresponding to a typical diffusion coefficient of $V^{2+/3+}$ in aqueous media (μ = 1 mPa·s, T = 298 K) of $\approx 2 \times 10^{-6}$ cm^2 s^{-1}.[55] For larger active species (*e.g.*, redox-active oligomers) paired with SSS, we assume a radius 3× that of the small species (r = 3 nm), which is a similar increase as two recent experimental reports on SSS for blocking oligomeric or polymeric active species in RFBs.[39,48] The relationship between diffusion coefficient and electrolyte viscosity is plotted (Figure 1b) for both solvated radii, indicating that larger active species will exhibit slower transport rates. While this analysis does not explicitly consider the case of transport for large redox-active polymers[48] (RAPs) in AqRFBs, the case of a high viscosity electrolyte, with large active species, likely mimics their transport rates, assuming Newtonian flow behavior.

$$D = \frac{k_B T}{6\pi\mu r} \tag{2}$$

The diffusion coefficient of an active material describes transport in the absence of forced convection, which is a key element of electrolyte transport in RFBs. The total effective mass transfer rate (k_m, m s^{-1}) in a porous carbon electrode can be described in two steps (Equation (3)), including the macro-scale mass transfer rate from the flow-field channel to the electrode pores (k_r, m s^{-1}) and the pore-scale mass transfer rate (k_p, m s^{-1})[56]:

$$k_m = \left(k_r^{-1} + k_p^{-1}\right)^{-1} \tag{3}$$

The macro-scale transport rate is provided in Equation (4), where α (-) and β ((m s^{-1})$^{1-\alpha}$) are constants specific to the porous electrode, and v_e is the intra-electrode electrolyte velocity (m s^{-1}) [56,57]. α and β values for transport to a carbon fiber electrode are available in Ref. 58.[58]

$$k_r = \beta v_e^{\alpha} \tag{4}$$

We employ an empirical relationship (Equation (5)) for the pore-scale mass transfer rate (Figure 1c), measured for the case of vanadium transport in a porous carbon-felt electrode,[34] where d_f is the electrode fiber diameter (m) and Re is the Reynolds number (-) for the electrolyte within the porous electrode. For this work, the electrode fiber diameter is assumed to be that of SGL 25AA ($d_f \approx 7$ μm),[59] Note that the diffusion coefficient is not constant in the present analysis and has a dependence on the electrolyte viscosity (Equation (2)).

$$\frac{k_p d_f}{D} = 2 + 1.534\,\mathrm{Re}^{0.912} \tag{5}$$

The Re associated with the porous electrode, sometimes referred to as the Blake number, is similarly defined as in the case of a packed particle bed reactor (Equation (6)). In Equation (6), ρ is the electrolyte density (kg m^{-3}), and ε is the electrode porosity (-). For this work, the electrolyte density is assumed to be that of water (ρ = 1000 kg m^{-3}), and the electrode porosity is that of SGL 25AA carbon paper under ≈ 20% compression (ε = 0.75).[59] The intra-electrode velocity (v_e) is calculated as the mean velocity over the rib of an interdigitated flow field (IDFF) from a typical high performance VRFB experiment (v_e = 0.025 m s^{-1}).[60] All relevant electrode and transport properties are listed in Table 2.

$$\mathrm{Re} = \frac{\rho v_e d_f}{\mu \varepsilon} \tag{6}$$

Table 2: Electrode and transport properties utilized in ASR and pressure drop calculations.

Parameter	Value
a	1.4×10^5 m^{-1}
α	0.4 [58]
b	1.5
β	1.6×10^{-4} m$^{0.6}$ s$^{-0.6}$ [58]
d_f	7×10^{-6} m [59]
ε	0.75 [59]
k	10^{-12} m^2
L_e	0.0003 m
ρ	1000 kg m^{-3}
v_e	0.025 m s^{-1}

10.4 Computing Cell Area Specific Resistance

The full-cell ASR (R_{DC}, Ω cm^2) can broadly be described as the summation of membrane (R_{mem}), contact ($R_{contact}$), and electrode resistances ($R_{electrode}$) in the cell (Equation (7)). Contact resistances assume a fixed experimental value of 35 mΩ cm^2 for SGL 25AA carbon paper under 20% on a

typical carbon composite bipolar plate with an IDFF.[60] The membrane resistances are derived from Figure 1a, assuming an optimistically thin membrane of 25 μm, the dry thickness of Nafion N211.[60]

$$R_{DC} = 2(R_{contact} + R_{electrode}) + R_{mem} \tag{7}$$

10.5 Electrode Resistance Model

The electrode resistance contribution to R_{DC} is computed using a one-dimensional, steady-state porous electrode polarization model that accounts for overpotential losses due to the electrolyte conductivity, Butler-Volmer reaction kinetics, and convective mass transfer rate. Equations (8) through (16) describe how the overpotential distribution in the porous electrode is computed, and subsequently the current distribution, using all dimensionless parameters.

The second derivative of the overpotential distribution $\left(d^2\tilde{\eta}/d\tilde{x}^2\right)$ with respect to the position in thickness of the electrode is proportional to the overall electrochemical reaction rate (Equation (8)), which is a function of several dimensionless parameters. Equation (8) is specifically derived for an electrode at 50% SOC, with transfer coefficients $\alpha_a = \alpha_c = 0.5$, and the solid-phase electrode conductivity (2200 – 2700 mS cm^{-1})[60] is much higher than the electrolyte conductivity (see Table 1). A full derivation of Equation (8) is provided in the Chapter 9.

$$\frac{d^2\tilde{\eta}}{d\tilde{x}^2} = \frac{2\nu^2\tilde{c}\sinh\left(\frac{\tilde{\eta}}{2}\right)}{1+2\theta\tilde{c}\cosh\left(\frac{\tilde{\eta}}{2}\right)} \tag{8}$$

$\tilde{\eta}$ is the dimensionless overpotential, which is defined as the overpotential (η, V) normalized by the thermal potential (RT/F, V), where R is the gas constant (8.314 J mol^{-1} K^{-1}) and F is the Faraday constant (96485 C mol^{-1}):

$$\tilde{\eta} = \frac{F\eta}{RT} \tag{9}$$

$\tilde{x}$ is the dimensionless position in the porous electrode, where x is position (m) and L_e is the electrode thickness (m):

$$\tilde{x} = \frac{x}{L_e} \tag{10}$$

$\tilde{c}$ is the dimensionless concentration, which is defined as the active species concentration (c, mol m^{-3}) normalized by the reference concentration (c^{θ}, typically 1000 mol m^{-3}):

$$\tilde{c} = \frac{c}{c^{\theta}} \tag{11}$$

ν^2 is the dimensionless exchange-current density (Equation (12)), where a is the specific area of the electrode (m^2 m^{-3}), i_0 is the exchange-current density (A m^{-2}) and κ_{eff} is the effective electrolyte conductivity in the porous electrode (S m^{-1}). Physically, ν^2 represents the ratio of charge-transfer and ion-conduction rates in the porous electrode.

$$\nu^2 = \frac{Fai_0 L_e^2}{\kappa_{\text{eff}} RT} \tag{12}$$

θ is the dimensionless limiting current (Equation (13)), defined as the ratio between the exchange and limiting current densities (i_l, A m^{-2}). Physically, θ represents the ratio of charge-transfer and mass transfer rates in the porous electrode.

$$\theta = \frac{i_0}{i_l} \tag{13}$$

The limiting current density relates to the mass transfer coefficient (Equation (14)), where n is the number of electrons transferred per active molecule (-).

$$i_l = nFck_m \tag{14}$$

The dimensionless overpotential distribution in the electrode can be determined by setting a constant overpotential boundary condition at the membrane-electrode interface $\left(\tilde{x}=0\right)$ and a zero ionic current boundary condition at the membrane-current collector interface $\left(\tilde{x}=1\right)$. Once the overpotential distribution has been solved numerically, the dimensionless current density (δ) passing through the membrane can be derived (Equation (15)).

$$\delta = -\frac{1}{2}\frac{d\tilde{\eta}}{d\tilde{x}}\bigg|_{\tilde{x}=0} \tag{15}$$

The geometric cell current density (J, A m^{-2}) is related to δ by Equation (16).

$$J = 2\delta\frac{\kappa_{\text{eff}} RT}{L_e F} \tag{16}$$

Now that current density can be related to the overpotential at the membrane-electrode interface, we can generate polarization curves that describe the current-voltage characteristic of

RFB electrodes at 50% SOC. Relevant values of the θ parameter can be computed by relating θ to k_m (Figure 1c). The effective electrolyte conductivity in the porous electrode (κ_{eff}) is found by using the Bruggeman relation (Equation (1)) and the relevant electrolyte conductivity (Table 1). The electrode area per unit volume (a, $m^2\ m^{-3}$) is estimated using Equation (18) and listed in Table 2.[61] Given these relations, values of θ can be generated as a function of experimentally measured mass transfer coefficients and the dimensionless exchange current density (v^2).

$$\theta = \frac{\kappa_{\text{eff}} RT}{FaL_e^2 nFc} \frac{v^2}{k_m} \tag{17}$$

$$a = \frac{4(1-\varepsilon)}{d_f} \tag{18}$$

Figure 2a illustrates electrode polarization for various Re with optimistically fast reaction kinetics ($v^2 = 2$) and a large active species ($r = 3$ nm), with a H_2SO_4-based electrolyte. Polarization calculations are performed assuming 1.5 M total active species concentration, which is a target value for AqRFBs.[1] The 50% SOC model assumption can represent average performance throughout cell discharge. For all Re, as the current density through the cell increases, the overpotential drop across the electrode increases, but, as Re increases, a smaller overpotential is required to drive the same current through the electrode. This trend occurs because increasing Re correlates with a higher rate of convective mass transfer (i.e., smaller viscosity), yielding lower mass transfer resistances. Re = ∞ represents the case of infinitely fast mass transport, where the electrode experiences losses only due to charge-transfer and electrolyte resistivity. The low overpotential regime ($\leq$ 60 mV) of the polarization curves is linearized to derive a value $R_{electrode}$ for each Re. An overpotential of 60 mV aligns with voltaic efficiency targets (91.6%)[1] during both charge and discharge for AqRFBs, assuming a large cell potential of 1.5 V;[1,38] hence, during typical operation, a RFB electrode at 50% SOC should be polarized by a maximum of $\approx$ 60 mV.

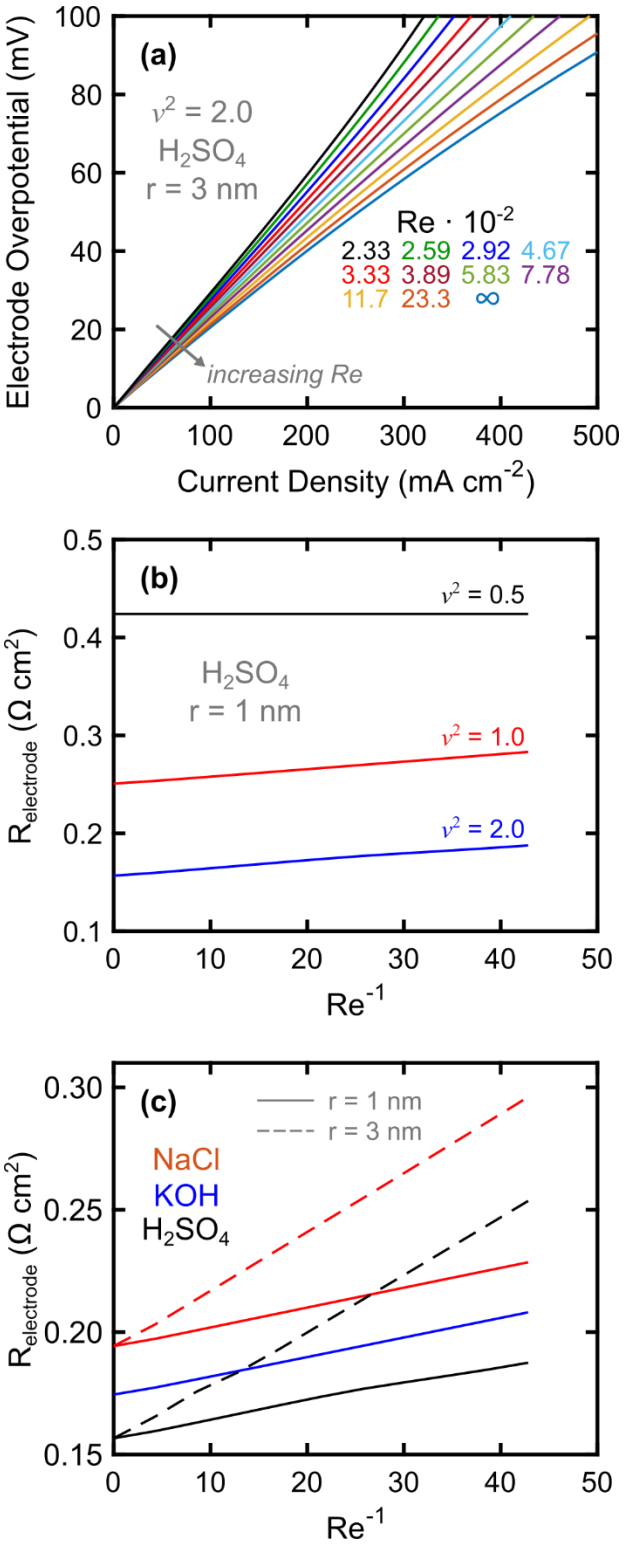

Figure 2: **(a)** Electrode polarization for multiple Re values with v^2 = 2, r = 3 nm, and H_2SO_4-based electrolyte. **(b)** Computed values of $R_{electrode}$ as a function of Re^{-1} for multiple v^2 values, r = 1 nm, and H_2SO_4-based electrolyte. **(c)** Computed values of $R_{electrode}$ as a function of Re^{-1} for the various electrolytes under consideration.

Figure 2b plots $R_{electrode}$ as a function of Re^{-1} for three values of the dimensionless exchange current density (small active species, r = 1 nm, H_2SO_4-based electrolyte), highlighting the critical role of reaction kinetics in defining $R_{electrode}$. Increasing v^2 can deliver significant reductions in $R_{electrode}$ (> 0.25 Ω cm^2), while varying Re changes $R_{electrode}$ by as much as 0.03 Ω cm^2 across the range of Re under consideration for the small active species. As v^2 increases, $R_{electrode}$ becomes more sensitive to Re because the relative contribution of charge-transfer losses shrinks. Since one motivation for implementing a new active material or supporting electrolyte in a RFB is improved reaction rates,[7] all subsequent calculations will incorporate optimistically large exchange current densities. Our value of i_0 is estimated by first assuming that cells with even the highest electrolyte conductivities (*i.e.*, H_2SO_4-based supporting electrolyte) will be ohmic-limited. As such, the H_2SO_4-based electrolyte is assigned v^2 = 2.0, corresponding to i_0 = 7.26 mA cm^{-2}, and this exchange current is fixed in all subsequent analyses. For reference, our estimated value of i_0 is similar to that of AQDS on carbon paper (12.3 mA cm^{-2}),[62] which is known to exhibit rapid kinetics in H_2SO_4-based electrolytes.[16,62]

Figure 2c shows electrode resistances for the three supporting electrolytes under consideration as a function of Re^{-1}, with small and large active species. All resistance curves in Figure 2c employ the high value of exchange current density previously mentioned. As the electrolyte conductivity decreases (*i.e.*, H_2SO_4 to KOH), the electrode resistance increases due to a larger ohmic loss through the porous phase of the electrode. Further, the sensitivity of electrode resistance to changes in Re increases as the active species size increases; the large active species (r = 3 nm) induces a change in $R_{electrode}$ of 0.97 Ω cm^2 across the range of Re considered, while the small active (r = 1 nm) species causes only a 0.03 Ω cm^2 increase. The larger active species exhibits lower diffusion coefficients (Figure 1b), invoking slower mass transport rates (Figure 1c) and subsequently causing greater electrode sensitivity to Re (Figure 2c).

10.6 Full Cell Area Specific Resistance

One can now estimate the full-cell ASR (R_{DC}, Figure 3) of an AqRFB employing various working ions, membranes (IEMs or SSS), or electrolyte viscosities by incorporating the values of $R_{electrode}$ (Figure 2c) into Equation (7). Estimates of R_{DC} for membrane-based RFBs assume transport rates for small active species (r = 1 nm), whereas estimates for SSS-based RFBs assume transport rates for large active species (r = 3 nm). Changing the type of ion passing through a membrane leads to

a linear increase or decrease in R_{DC} due to variations in membrane conductivity, while increasing Re (lower Re^{-1}) decreases R_{DC} due to a higher rate of convective mass transfer. When considering the SSS case, both the NaCl and H_2SO_4 systems offer the lowest R_{DC} at high Re, however, at sufficiently low Re, the H^+-IEM outperforms both SSS options.

Figure 3 ultimately illustrates a critical balance in membrane and supporting electrolyte selection, where the membrane conductivity and electrolyte viscosity must be optimized to deliver the lowest R_{DC} possible. The Na^+-, Cl^--, and K^+-IEMs afford much higher ASR (up to 3.1×) than the H^+-IEM or SSS. Multiple techno-economic analyses have recommended a target $R_{DC} \approx 0.5$ Ω cm^2 for cost-effective AqRFBs,[1,2,38] indicating that only a few of the membrane and working ion combinations presented in Figure 3 could achieve DOE cost targets, in the regime of high Re. The next section uses a techno-economic model to estimate complete RFB capital costs for the different membrane and supporting salt options under consideration here, so that the reader may better appreciate the cumulative cost impact of all the RFB components.

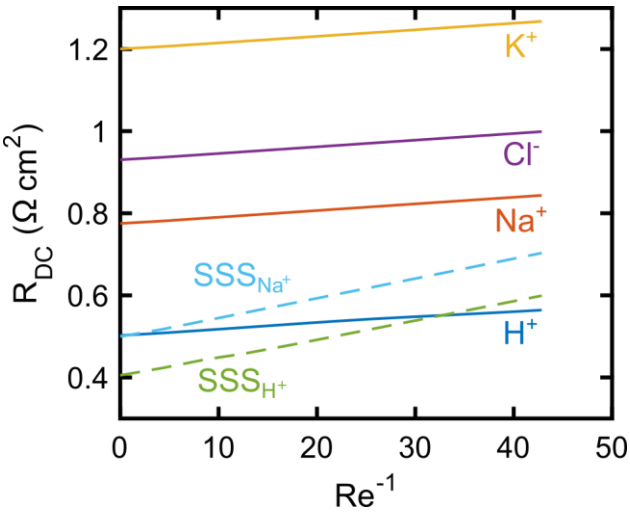

Figure 3: Full-cell ASR (R_{DC}) as a function of Re^{-1} for various working ion types in membranes (solid lines) or size-selective separators (dashed lines). For all data, i_0 = 7.26 mA cm^{-2}, $R_{contact}$ = 35 mΩ cm^2, and all other parameters as provided in Table 2.

10.7 Pressure Drop and Pump Power Requirement

We assume that AqRFBs will employ state-of-the-art IDFFs, which have been shown to balance excellent electrochemical performance with an acceptable pressure drop.[60,63] Darling and Perry described a series of analytical equations to calculate the pressure drop through an IDFF for flow batteries[60] using a formulation originally targeted for polymer-electrolyte fuel cells.[64] The

pressure drop through an IDFF (ΔP, Pa) can be calculated from Equation (19), where ΔP_{ch} is the pressure drop through a channel in the flow field (Pa) and ζ is a dimensionless geometric factor (-).

$$\Delta P = \Delta P_{ch}\left(1+\frac{2+2\cosh\zeta}{\zeta\sinh\zeta}\right) \tag{19}$$

The pressure drop through a channel within the IDFF is computed according to Equation (20), where v_{ch} is the electrolyte velocity in the channel (m s^{-1}), L_{ch} is the channel length (m), and d_h is the channel hydraulic diameter (m).

$$\Delta P_{ch} = \frac{32\mu v_{ch}L_{ch}}{d_h^2} \tag{20}$$

Since a rectangular channel is assumed, the d_h can be calculated in Equation (21), where w_{ch} is the channel width (m), and h is the channel height (m). In this work, w_{ch} and h have fixed dimensions of 0.00117 m and 0.00076 m, respectively, based on a recent experimental RFB study employing IDFFs.[60]

$$d_h = \frac{2w_{ch}h}{w_{ch}+h} \tag{21}$$

The channel velocity is defined in Equation (22), where N is the number of inlet channels in the flow field (-), and Q is the electrolyte flow rate through one side of a single cell (m^3 s^{-1}).

$$v_{ch} = \frac{Q}{Nw_{ch}h} \tag{22}$$

The channel and intra-electrode velocity for the IDFF are related, as shown in Equation (23).

$$\frac{v_e}{v_{ch}} = \frac{w_{ch}h}{L_eL_{ch}} \tag{23}$$

The geometric factor, ζ, in Equation (19) is defined in Equation (24), where k is the electrode permeability (m^2, Table 2) and S is the mean path length of the electrolyte through the electrode and over the rib (m).

$$\zeta^2 = \frac{128L_{ch}^2kL_e}{Sd_h^2w_{ch}h} \tag{24}$$

While S can be numerically computed for the IDFF,[65] such a calculation is beyond the scope of this work. We estimate S as given in Equation (25), where w_{rib} is the width (m) of the rib

in the IDFF. w_{rib} has a fixed dimension of 0.00089 m, based on a recent experimental RFB study employing IDFFs.[60]

$$S \approx w_{ch} + w_{rib} + L_e \tag{25}$$

Later estimates of pump cost will consider cells with a total width (W) of 26 cm and L_{ch} = 31.2 cm (L_{ch}/W = 1.2), which are similar dimensions to kW-scale flow cells,[66–68] resulting in a cell active area of 811 cm^2. For fixed channel and rib widths, W defines the number of inlet channels and ribs in the IDFF (for W = 26 cm, N = 80). To briefly illustrate how pressure drop varies with cell aspect ratio (L_{ch}/W), consider Figure 4a, which plots the pressure drop through a single side of one cell against inverse mass transfer coefficient within the porous electrode, both of which are functions of electrolyte flow rate. Figure 4a illustrates the tradeoff between pressure drop and mass transfer rate for a small (r = 1 nm) active species. As expected, larger convective mass transfer rate (smaller k_m^{-1}) will require higher pressure drops. Further, as the aspect ratio increases (higher L_{ch}/W), a larger pressure drop is required to sustain the same mass transfer rate, due to a larger flow rate requirement to sustain the same intra-electrode velocity.

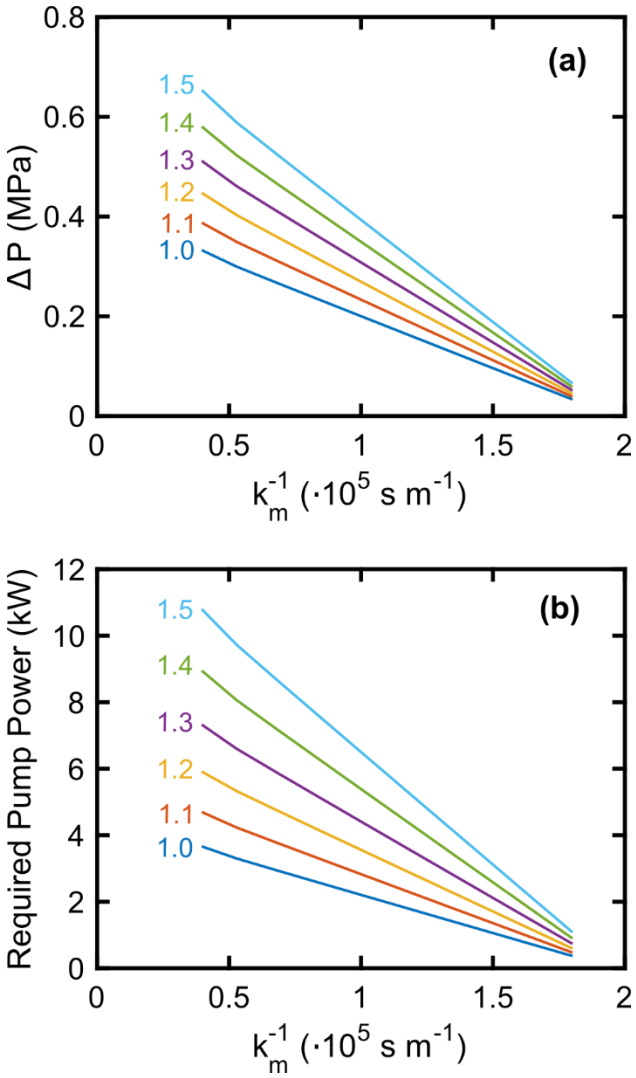

Figure 4: **(a)** Calculated pressure drop through one side of a single RFB cell employing an IDFF, with a channel width of 26 cm. **(b)** Calculated pump power requirement for a single electrolyte stream passing through a RFB stack, where N_{cells} = 60. The legend numbers denote the L_{ch}/W ratio.

The required pump power (P, W) to pass electrolyte through a single side (positive or negative electrolyte) of a RFB can be computed as shown in Equation (26), where ε_{pump} is the pump efficiency (-), and N_{cells} is the number cells in the electrochemical stack (-).[69] We assume that the pump efficiency is ε_{pump} = 0.85[70] and that the RFB stack contains 60 cells, in accordance with a prior RFB cost model.[69] Figure 4b shows how the required pump power varies with mass transfer rate and cell aspect ratio. The trends are similar to the pressure drop calculation in Figure 4a, but the scaling from ΔP to pump power is nonlinear due to a nonlinear dependence of Q on ΔP (Equations (19) and (22)).

$$P = \frac{\Delta P Q N_{cells}}{\varepsilon_{pump}} \tag{26}$$

The primary goal in evaluating pump power requirement is to account for the capital cost of appropriately sized pumps for an aqueous RFB stack, however, the importance of designing a RFB with sufficiently low pump power requirement, relative to the stack output power, should not be overlooked. The pump power requirements plotted in Figure 4b align with state-of-the-art system efficiencies at lower transport rates for our assumed stack geometry. A stack with 1.4 V OCP, 0.4 Ω cm^2 ASR, 91.6% voltage efficiency, aspect ratio of 1.2, and 60 cells delivers a total power of ≈ 18.3 kW, indicating that ≈ 0.92 kW of pump power, for two electrolyte streams, can be afforded to maintain ≤ 5 % system efficiency loss. In subsequent cost calculations, we will assume an optimistic system efficiency of 94 %, which accounts for energy losses due to pumping, power electronics, and thermal management equipment. Critically, when designing a specific, new electrolyte, the pump power requirement must be compared with the nominal battery power output to ensure high system efficiency. For example, a battery with relatively low cell potential and high electrolyte viscosity could engage a RFB design where the pump power actually exceeds the power output from the electrochemical stack. Identifying the viable regions of the efficiency design space is outside the scope of the present analysis, but must be considered when evaluating new, specific RFB chemistries.

10.8 Techno-Economic Analysis

Reactor Cost. To begin bridging membrane and supporting electrolyte selection to RFB cost, the full-cell ASR can be incorporated into a description of RFB reactor cost. In the present analysis, RFB reactor cost ($C_{reactor}$, \$ kW^{-1}) is defined similarly to prior literature (Equation (27)),[1,2] where U is the cell potential (V), ε_{sys} is the system efficiency (-), and ε_v is the voltaic efficiency (-). Additionally, c_{stack} is the areal cost of the electrochemical stack materials (\$ m^{-2}), including bipolar plates, gaskets, electrodes, and current collectors, and c_{mem} is the areal membrane (or separator) cost (\$ m^{-2}).

$$C_{reactor} = \frac{(c_{stack} + c_{mem}) R_{DC}}{\varepsilon_{sys} \varepsilon_v (1 - \varepsilon_v) U^2} \tag{27}$$

The separation of stack hardware and membrane costs contrasts prior studies that combine these two entities into one term;[1,2] this distinction offers a more flexible framework for

incorporating various membranes. We also consider present and future-state areal reactor and membrane costs, since these materials costs are anticipated to decrease with bulk purchasing required for future large-scale manufacturing, which will be described later (Section 5.4). Estimates of the electrochemical stack costs and IEMs are adapted from prior literature for present and future-state (Table 3).[1,69] Estimates for present and future-state costs of SSS are assumed to be that of reverse-osmosis membranes (≈ \$30 m^{-2})[71] and lithium-ion battery separators (≈ \$1 m^{-2})[1], respectively. The voltaic efficiency is assumed to be 91.6 %.[1] R_{DC} values are extracted from Figure 3. Hence, the reactor cost is described as a function of the full-cell ASR. As R_{DC} increases, a larger area electrochemical stack is required to drive the same total current at the same voltaic efficiency, yielding a more expensive reactor overall.

Table 3: Benchmark reactor and electrolyte cost parameters assumed in the analysis for present and future states.

Modeling Parameter	**IEM + Small Active Species**		**SSS + Large Active Species**	
	Present	*Future State*	*Present*	*Future State*
Stack cost per unit area, c_{stack}	\$200 m^{-2}	\$72.5 m^{-2}	\$200 m^{-2}	\$72.5 m^{-2}
Membrane cost, c_{mem}	\$500 m^{-2}	\$50 m^{-2}	\$30 m^{-2}	\$1 m^{-2}
Open-Circuit Cell Voltage, U	1.4 V	1.5 V	1.4 V	1.5 V
Discharge time, t_d	5 h			
System discharge efficiency, $\varepsilon_{sys,d}$	0.94			
Voltage discharge efficiency, $\varepsilon_{v,d}$	0.916			
Round-trip coulombic efficiency, $\varepsilon_{q,rt}$	0.97			
Stoichiometric coefficient, s	1			
Allowable state-of-charge range, χ	0.80			
Equivalent weight, M/n	100 g $mol_{e^-}^{-1}$		125 g $mol_{e^-}^{-1}$	
Actives cost per unit mass, c_m	\$5 kg^{-1} [1]			
Mean molar salt ratio, r_{avg}	1.0			
Active Species Molarity, b	1.5 M			
Tank Cost, c_t	\$0.15 L^{-1}			

Figure 5a shows reactor cost as a function of cell potential for the various working ion / membrane combinations for present-day costs of the electrochemical stack and membrane. The extreme values of Re can be interpreted as electrolytes at fixed flow rate with viscosities of 1.0 and 10 mPa·s, respectively, which are the assumed upper and lower bounds on AqRFB electrolyte viscosity. As indicated by Equation (27), reactor cost decreases as U^{-2} and thus the reactor cost sensitivity to variations in cell performance, caused by the working ion type or electrolyte viscosity, decreases as cell potential increases. For the IEM cases, changing working ion type or

electrolyte viscosity can vary reactor cost by over \$900 kW^{-1} at lower cell potentials (< 1.0 V). The SSS offer the lowest reactor costs, across all cell potentials, for present day due to implementation of the relatively inexpensive separator, as compared to the IEM.

Again considering Equation (27), as the combined stack and membrane cost ($c_{stack} + c_{mem}$) per unit area decreases, the total reactor cost ($C_{reactor}$) becomes less sensitive to differences in R_{DC}. Figure 5b explicitly illustrates how the total reactor cost grows as a function of $c_{stack} + c_{mem}$ for the different membrane / working ion configurations, where larger values of R_{DC} necessitate that the reactor cost grows more quickly with larger $c_{stack} + c_{mem}$. This sensitivity to the stack and membrane costs indicates that RFBs with more expensive cell components must offer lower cell ASR to keep reactor costs down. Considering that present-day stack and membrane costs are much higher than their anticipated future-state costs at mass-scale production, engineering low ASR cells today via rational selection of membranes and supporting salts is of the upmost importance in facilitating early adoption of RFBs. Given that SSS are anticipated to be more than an order-of-magnitude less expensive than IEMs, assuming present estimates, the SSS is an extremely attractive option to pursue immediately, offering substantial cost savings across all cell potentials.

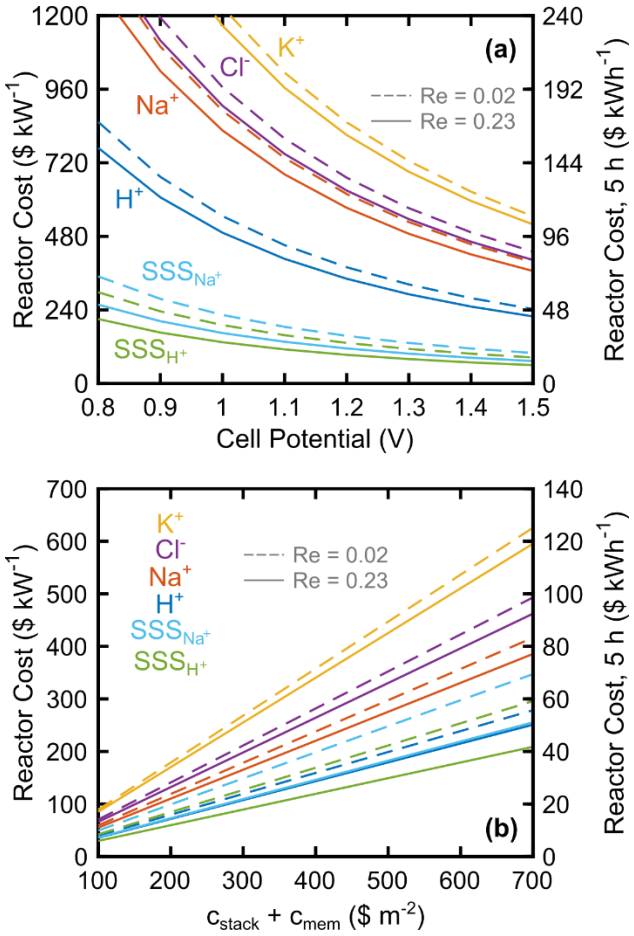

Figure 5: Present-day reactor cost as a function of **(a)** cell potential or **(b)** areal reactor cost for various working ion / membrane types and two extreme values of Re. For \$ kWh^{-1} cost estimates, a 5 h discharge time is assumed.

Equation (28) describes the total electrolyte cost normalized by the energy delivered upon discharge ($C_{electrolyte}$, \$ kWh^{-1}) with the following parameters: ε_q is the coulombic efficiency (-), F is the Faraday constant (0.0268 kAh), M is the molar mass of the active material (kg mol^{-1}), s is the stoichiometric coefficient of the discharge reaction (-), χ is the depth-of-discharge (-), n_e is the number of electrons stored per mole of active material (-), c_m is the active species cost per unit mass (\$ kg^{-1}), r_{salt} is the arithmetic mean ratio of moles of salt per mole of active species across both electrolytes (-) [2], M_{salt} is the molar mass of the supporting salt (kg mol^{-1}), c_{salt} is the salt cost per unit mass (\$ kg^{-1}), c_t is the tank cost per unit volume (\$ L^{-1}), and $\bar{c}$ is the mean active species molarity across both sides of the cell (M). Note that the present model explicitly accounts for the salt and tank cost contributions to the electrolyte cost, in contrast with prior reports [1,2]. The + / - subscripts denote the positive / negative sides of the battery, respectively. The cost of water as a solvent is neglected in this estimate as the cost contribution of deionized water (≈ \$0.001 kg^{-1})[72] is

at least one order-of-magnitude lower than all other electrolyte components. Tank cost is fixed at \$0.15 L^{-1} for all electrolytes under consideration since inexpensive polypropylene or polyethylene tanks should be chemically compatible across all pH.[1] Additionally, the coulombic efficiency and allowable SOC range are set to 97 % and 80 %, respectively.[1].

$$C_{electrolyte} = \left(\frac{1}{\varepsilon_{sys}\varepsilon_q\varepsilon_v FU} \right) \cdot \left[\frac{s_+ M_+ c_{m,+}}{n_{e,+}\chi_+} + \frac{s_- M_- c_{m,-}}{n_{e,-}\chi_-} + 2\left(r_{salt} M_{salt} c_{salt} + \frac{c_t}{\bar{c}} \right) \right] \quad (28)$$

Since one motivation for designing a new AqRFB electrolyte is to leverage inexpensive active materials, we assume an optimistically low cost for the active material of \$5 kg^{-1}.[1] Precursors to some proposed ROMs come close to this value today.[2] For example, anthraquinone is a precursor to multiple proposed ROMs[14,16] and costs ≈ \$4.40 kg^{-1}.[16] For comparison, vanadium sulfate costs ≈ \$22 kg^{-1} [1] and sulfur (S_8) costs ≈ \$0.20 kg^{-1}.[73] The active species molecular weight is another key parameter that defines electrolyte cost because the molecular weight normalized by the number of electrons transferred (equivalent weight (g $mol_{e^-}^{-1}$)) specifies the mass of active material that must be purchased to store a certain amount of charge. In the present analysis, we assume a moderate equivalent weight of 100 g $mol_{e^-}^{-1}$ for small active species.[2] For comparison, the equivalent weight of vanadium is 51 g $mol_{e^-}^{-1}$, whereas AQDS has an equivalent weight of 184 g $mol_{e^-}^{-1}$, assuming that AQDS has $2e^-$ transfer capability.[16] In the case of RFBs with SSS, we estimate that the active species equivalent weight must be ≈ 1.25× that of a small active species, paired with an IEM, to successfully implement size exclusion; this equivalent weight increase is similar to that of the added molecular weight imposed by linkers between redox-active centers on oligomerized ROMs.[39] Finally, the active-species concentration is set to 1.5 M, for consistency with previous cell polarization calculations, which defines the total tank size required to store a particular amount of energy. Other electrolyte cost parameters are listed in Table 3.

We choose to acknowledge the cost contribution of the supporting electrolyte, which is typically overlooked,[2] to evaluate its relative magnitude in determining RFB cost. The molar masses and costs for H_2SO_4, NaCl, and KOH are listed in Table 4. Figure 6 shows how electrolyte cost varies as a function of r_{salt} for the salt types listed in Table 4 and two active species equivalent weights. r_{salt} represents the number of moles of salt per mole of active species on one side of the RFB, and typical r_{salt} values for VRFB electrolytes can vary between 0.7 – 2.[60,74] For comparison, recent studies on new AqRFB active species experimentally illustrated that by employing multifunctional, ionic active species, the need for a supporting salt can be completely

eliminated.[7,75] The slopes of the electrolyte cost curves in Figure 6 are defined by the salt costs ($ kg^{-1}), and the y-intercepts (Figure 6) represent the cost contributions from the tanks and active species. As such, the higher equivalent weight active species yield a larger electrolyte cost in the limit of zero salt. Overall, variations in electrolyte cost with supporting electrolyte type and amount are relatively small in comparison to other cost contributions for AqRFBs.

Table 4: Supporting electrolyte cost parameters used in electrolyte cost calculations.

Working Ion	Salt	Molar Mass (g mol^{-1})	c_{salt} ($ kg^{-1})
H^+	H_2SO_4	98.1	0.075 [73]
Na^+ / Cl^-	NaCl	42.4	0.055 [76]
K^+	KOH	56.1	0.30 [77]

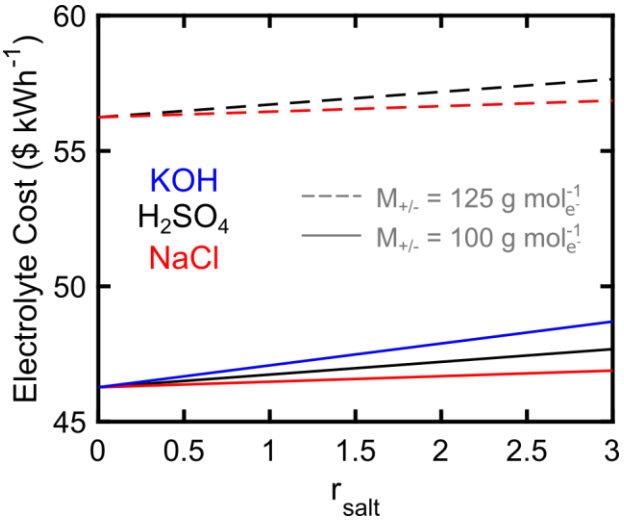

Figure 6: Electrolyte cost as a function of r_{salt} (the number of moles of salt per mole of active species on one side of the RFB) for different salt types and active species equivalent weights. U = 1.4 V and c_m = $5 kg^{-1}.

Balance-of-Plant. The balance-of-plant (BOP) costs (C_{BOP}, $ kW^{-1}) for RFBs typically comprise costs associated with ancillary equipment, normalized by the power output of the RFB stack. In the present work, the BOP cost accounts for thermal-management systems (*e.g.*, heat exchangers), controls, and pumps. Note that this work does not consider power-conditioning equipment (*e.g.*, inverters) or installation costs.[2] Since we do not anticipate the cost of thermal management or controls to vary significantly with supporting electrolyte composition, we assume that their cost ($C_{control}$) is $60 kW^{-1}, as estimated in a recent RFB techno-economic analysis.[1] The total C_{BOP} is calculated as shown in Equation (29),[1] where N_{pump} is the number of pumps required

to operate the RFB and C_{pump} is the pump cost per power (\$ kW^{-1}). Since the BOP cost is normalized by the RFB stack power, N_{pump} = 2 because each electrolyte stream will require one pump.

$$C_{BOP} = C_{controls} + N_{pump} C_{pump} \tag{29}$$

Pump cost $\left(c_{pump}^{\$}, \$\right)$ is estimated using the cost correlation in Equation (30),[70] where P is the required pump power (kW). The pump cost (\$) as a function of required pump power is depicted in Figure 7a.

$$c_{pump}^{\$} = -1100 + 2100 \cdot P^{0.6} \tag{30}$$

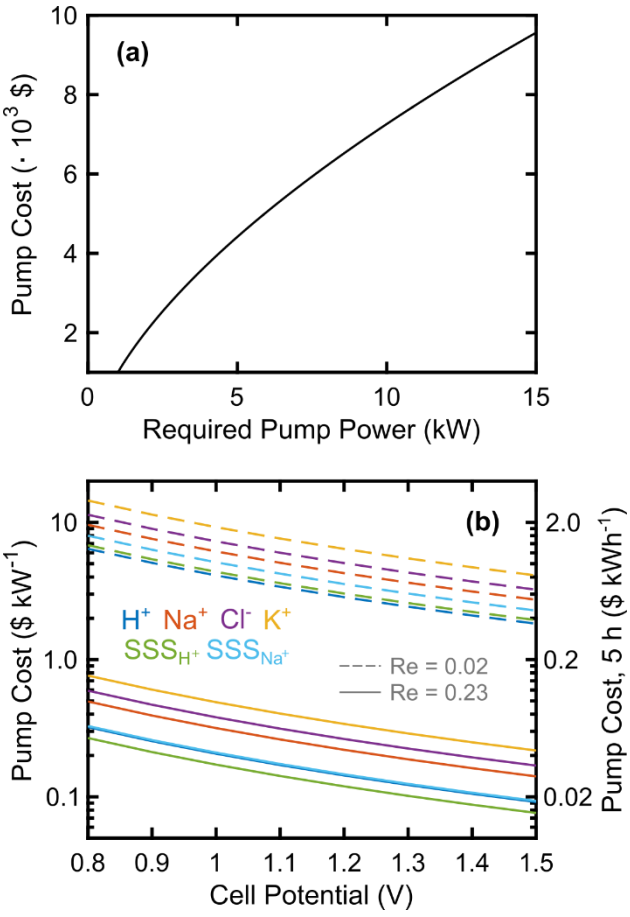

Figure 7: **(a)** Pump cost (thousands of \$) as a function of required pump power. **(b)** Pump cost (\$ kW^{-1}) normalized by nominal stack power output. For \$ kWh^{-1} cost estimates, a 5-h discharge time is assumed.

We normalize the pump cost by the power capability of the electrochemical stack (Equation (31)). The variations in battery energy efficiency with changes in pumping energy requirements are typically small[35,36] and would also require details of the battery's thermal management system.

Thus, for simplicity, we choose to hold ε_{sys} constant at 94 %.[1] Figure 7b shows how pump costs (\$ kW^{-1}, left axis) vary as a function of cell potential for the upper and lower Re values considered in this work. As the reactor performance improves via increased cell potential, the effective pump cost decreases because less total pumping power is required to deliver a certain power upon discharging the battery. Additionally, the high Re case (*e.g.*, low viscosity) has a much weaker dependence of pump cost on cell potential because of a small pressure drop and improved mass transfer rates. Note that when normalizing the pump cost by discharge time (\$ kWh^{-1}, Figure 7b right axis), the pump cost is < \$2 kWh^{-1} for nearly all design conditions, indicating that pump costs are small as compared to reactor (Figure 5) and materials costs (Figure 6) in the target discharge duration time. Thus, although varying electrolyte viscosity will impact pumping costs, the overall contribution to battery cost will be relatively small; viscosity has a significantly larger impact on cell ASR, which affects the reactor cost contribution.

$$C_{pump} = \frac{c_{pump}^{\$} R_{DC}}{\varepsilon_{sys}\varepsilon_v(1-\varepsilon_v)U^2 L_{ch} W} \tag{31}$$

Unit Cost Less Materials. The final cost contributions to consider for estimating RFB capital cost are termed *unit cost less materials* (C_{UCLM}),[43] which is also sometimes referred to as *additional costs*.[1,2,78] The unit cost less materials accounts for all RFB costs excluding purchased goods. *Purchased goods* refers to all RFB parts manufactured by specialty firms and implemented in the electrochemical stack, electrolyte, or BOP.[43] For instance, carbon-paper electrodes are an example of a purchased good that will be used in the electrochemical stack, but the manufacturing cost of implementing the carbon paper in the stack falls under the unit cost less materials. The unit cost less materials in this work specifically accounts for depreciation, research and development, sales, administration, variable overhead, direct labor, and warranty costs.[43] Note that the present analysis excludes an estimate of profit margin, which has been incorporated in prior analyses.[1,2,43,78] As such, this work considers *battery cost*, as opposed to *battery price*.

The unit cost less materials depends on the production volume of RFB components. As production volume increases, the unit cost less materials will decrease due to increased utilization of capital-intensive manufacturing infrastructure. As before, we first consider a present-day estimate of unit cost less materials at the low RFB production volumes at the time of publication. We also consider a future-state estimate of unit cost less materials, assuming that RFB annual production achieves the volume to store 1% of the world's energy consumption for 5 h (2 GW, 10

GWh).[43] The present day estimate of unit cost less materials is taken to be \$1550 kW^{-1}, which was originally computed by engaging a gap analysis between present-day costs of RFB materials and costs of energy storage systems in the field.[1] For the future-state estimate, we assume values calculated by Ha and Gallagher, which are listed in Table 5 for convenience.[43]

Table 5: Cost contributions used in the estimate of future-state unit cost less materials.[43]

Contribution	Cost (\$ kW^{-1})
Warranty	50.6
Sales & Administration	30.0
Research & Development	23.7
Depreciation	7.9
Direct Labor	4.7
Variable Overhead	3.2
C_{UCLM}	120

Battery Cost. Now that the reactor, electrolyte, BOP costs, as well as the unit cost less materials, have been computed for all membranes and supporting electrolytes under investigation, these cost contributions can be combined in Equation (32) to describe the battery cost. The total RFB cost ($C_{battery}$, \$ kWh^{-1}) is defined as the total cost of the battery normalized by the energy delivered upon discharge. Since the reactor, BOP, and additional costs are all defined in units of \$ kW^{-1}, their costs are normalized by a total discharge time (t_d) of 5 h. Note that the DOE target capital cost of \$150 kWh^{-1} includes the costs of power conditioning equipment and installation, which has been estimated to be ≈ \$250 kW^{-1} [1], so the \$150 kWh^{-1} DOE target translates to a battery cost of ≈ \$100 kWh^{-1} in the present analysis.[2]

$$C_{battery} = \frac{\left(C_{reactor} + C_{BOP} + C_{UCLM}\right)}{t_d} + C_{electrolyte} \tag{32}$$

Figure 8 shows battery costs as a function of cell potential for the membrane and supporting salt combinations under consideration, along with a low and high value of Re number, corresponding to a 10× viscosity change. Present day (Figure 8a) and future-state estimates (Figure 8b) illustrate how changes in stack and membrane cost with production volume impact battery cost. For present day, differences in the RFB performance and electrolyte costs can manifest as cost differences > \$300 kWh^{-1}, in the limit of low cell potentials (< 1 V). At high cell potentials (1.5 V), the difference is smaller, but still reaches ≈ \$100 kWh^{-1} between the SSS and K^+-IEM designs. Viscosity changes can induce a difference in battery cost as high as \$30 kWh^{-1} for designs

with higher R_{DC} and low cell potential. Surprisingly, however, a 10-fold variation in electrolyte viscosity has a relatively small impact on RFB cost.

For present-day costs, RFBs implementing SSS have a significant advantage over the IEM options. The separator cost is so much lower than that of an IEM, the SSS options are cheapest across all cell potential regardless of reactor performance. The use of the higher conductivity electrolyte (H_2SO_4) with the SSS offers marginally better cost performance due to reduced ASR. Hence, the SSS concept is an excellent technological choice when RFB production quantities are small, as they are at the time of publication. When the stack and IEM costs decrease, as assumed for future state, SSS options with high electrolyte viscosity perform worse than IEMs with H^+ or Na^+ charge carriers due to the slower transport and higher materials cost associated with large active species. The combination of SSS with a low electrolyte viscosity remains as the least expensive combination, even with future-state reactor or membrane costs.

The future-state cost estimates (Figure 8b) only show the high Re case, and all cost curves are much closer together as compared to present-day estimates. The smaller differences (\$10 – 30 kWh^{-1}) in future-state battery cost stem from the lower anticipated stack and membrane costs, which makes the battery cost less sensitive to variations in reactor performance (Figure 5b). Despite substantial cost reduction, battery costs only surpass the \$100 kWh^{-1} guideline for cell potentials > 1.2 V, and the H^+-IEM offers the best opportunity to exceed the benchmark cost, whereas the K^+-IEM only reaches the benchmark cost with precisely a 1.5 V cell.

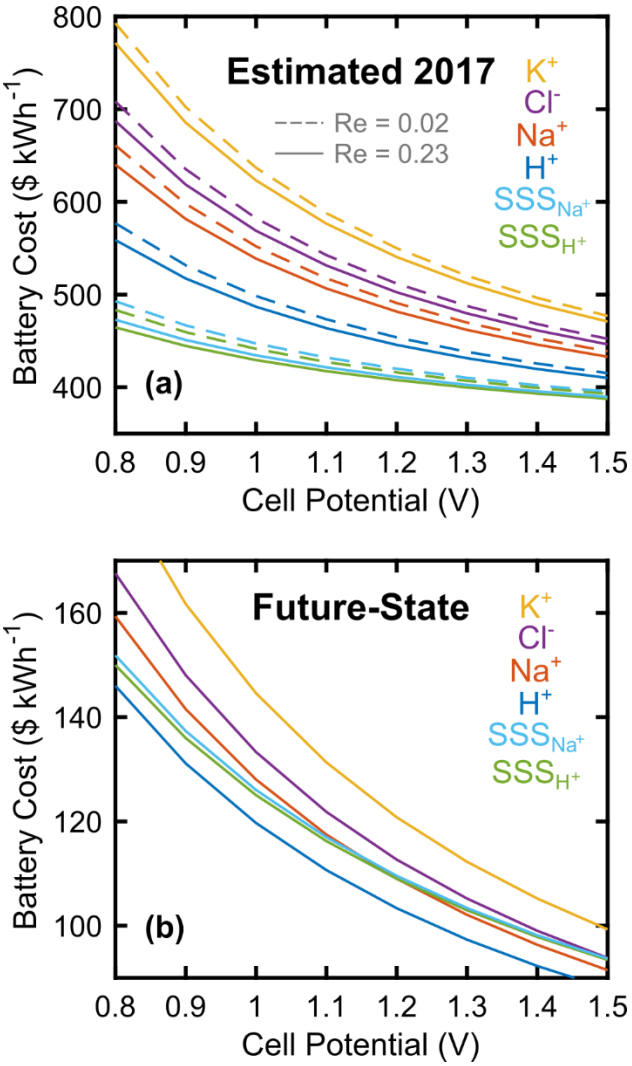

Figure 8: Battery cost as a function of cell potential with **(a)** present- and **(b)** future-state costs, for various working ion / membrane types and two extreme values of Re. This analysis assumes 5-h discharge time.

10.9 Conclusions

RFBs are promising electrochemical devices for grid-scale energy storage, but their capital costs must be reduced for ubiquitous adoption. As such, recent reports have investigated new active species for RFBs geared towards lower cost or improved performance, and identification of a promising active material typically involves engineering the supporting electrolyte to optimize stability, solubility, and reaction kinetics. When engineering a new supporting electrolyte, however, changes to the charge-carrier ion or the viscosity can negatively impact cell performance. Selection of supporting salts with large cations or anions, which have relatively low mobilities in IEMs, can result in much larger membrane resistances than what is observed in state-of-the-art H^+-

conducting IEMs. In addition, increased electrolyte viscosity leads to larger mass transfer losses, further increasing cell ASR.

This work quantifies changes in RFB cost performance for different supporting electrolytes paired with IEMs. Membrane ASR is derived from RFB reports employing cation or anion exchange membranes with various charge-carriers (H^+, Na^+, Cl^-, and K^+) in concentrated electrolytes. The ASR contribution of the RFB electrodes is quantified by implementing a steady-state, one-dimensional porous-electrode model that describes cell overpotential as a function of current density, incorporating losses from the electrolyte resistivity, Butler-Volmer reaction kinetics, and convective mass transfer. The consideration of mass transfer losses allows us to link the description of electrode resistance to the electrolyte viscosity through a mass transfer coefficient power law correlation. The physical description of cell ASR is then integrated into a techno-economic model that estimates RFB cost for the different membrane and supporting electrolyte options under consideration, accounting for the reactor, electrolyte, BOP, and additional costs. Variations in cell performance due to the working ion selection and electrolyte viscosity can yield battery cost differences in the \$100's kWh^{-1}, and this analysis allows for quantification of cost performance changes by selecting certain electrolyte characteristics. The battery cost curves in Figure 8 can also be used to quantify how much extra cell potential is required to overcome a performance loss due to selecting a less mobile ion or more viscous electrolyte.

Beyond the conventional RFB design incorporating small active species and an IEM, this work also considers size-selective separators as a cost-effective alternative to IEMs. The SSS concept utilizes nanoporous separators with no functionalization for ion selectivity, and the active species are large enough that they cannot pass through the separator pores. Supporting electrolyte ions, however, can pass freely through the SSS, imparting higher ionic conductivities that their IEM counterparts. Drawbacks of the SSS concept is that the larger active species will exhibit slower transport rates and will have higher active material costs, but these performance setbacks are offset by the markedly lower cost associated with the SSS. For present day materials costs, SSS separators offer the lowest RFB costs. With the benchmark performance and cost values assumed in this analysis, the H^+-IEM option offers the best opportunity to achieve the DOE target capital cost at cell potentials > 1.2 V. For present costs, however, SSS combined with low cost

active materials and electrolytes, appear the most attractive pathway forward in RFB development, offering significantly lower capital cost.

10.10 References

1. R. M. Darling, K. G. Gallagher, J. A. Kowalski, S. Ha, and F. R. Brushett, *Energy Environ. Sci.*, **7**, 3459–3477 (2014).
2. R. Dmello, J. D. Milshtein, F. R. Brushett, and K. C. Smith, *J. Power Sources*, **330**, 261–272 (2016).
3. X. Wei et al., *J. Electrochem. Soc.*, **163**, A5150–A5153 (2016).
4. Z. Li, G. Weng, Q. Zou, G. Cong, and Y.-C. Lu, *Nano Energy*, **30**, 283–292 (2016).
5. G.-M. Weng, Z. Li, G. Cong, Y. Zhou, and Y.-C. Lu, *Energy Environ. Sci.*, **10**, 735–741 (2017).
6. J. Winsberg, T. Hagemann, T. Janoschka, M. D. Hager, and U. S. Schubert, *Angew. Chem. Int. Ed.*, **56**, 686–711 (2016).
7. E. S. Beh et al., *ACS Energy Lett.*, **2**, 639–644 (2017).
8. B. Hu, C. DeBruler, Z. Rhodes, and T. L. Liu, *J. Am. Chem. Soc.*, **139**, 1207–1214 (2017).
9. C. Bae, E. P. L. Roberts, M. H. Chakrabarti, and M. Saleem, *Int. J. Green Energy*, **8**, 248–264 (2011).
10. K. Gong et al., *ACS Energy Lett.*, **1**, 89–93 (2016).
11. Y. H. Wen et al., *J. Electrochem. Soc.*, **153**, A929–A934 (2006).
12. J. Goeltz et al., "Aqueous redox flow batteries comprising metal ligand coordination compounds," US Pat. US 20160276693 A1, Filed May 27, 2016.
13. N. Arroyo-Currás, J. W. Hall, J. E. Dick, R. A. Jones, and A. J. Bard, *J. Electrochem. Soc.*, **162**, A378–A383 (2015).
14. K. Lin et al., *Science*, **349**, 1529–1532 (2015).
15. B. Yang, L. Hoober-Burkhardt, F. Wang, G. S. Prakash, and S. R. Narayanan, *J. Electrochem. Soc.*, **161**, A1371–A1380 (2014).
16. B. Huskinson et al., *Nature*, **505**, 195–198 (2014).
17. M. Privman and T. Hepel, *J. Electroanal. Chem.*, **382**, 137–144 (1995).
18. J. D. Milshtein, L. Su, C. Liou, A. F. Badel, and F. R. Brushett, *Electrochimica Acta*, **180**, 695–704 (2015).
19. T. J. Carney, S. J. Collins, J. S. Moore, and F. R. Brushett, *Chem. Mater.* (2017). In press.
20. T. Liu, X. Wei, Z. Nie, V. Sprenkle, and W. Wang, *Adv. Energy Mater.*, **6**, 1501449 (2015).
21. T. Janoschka, N. Martin, M. D. Hager, and U. S. Schubert, *Angew. Chem. Int. Ed.*, **382**, 14427–14430 (2016).
22. C. L. Bird and A. T. Kuhn, *Chem Soc Rev*, **10**, 49–82 (1981).
23. M. L. Perry, R. M. Darling, and R. Zaffou, *ECS Trans.*, **53**, 7–16 (2013).
24. D. S. Aaron et al., *J. Power Sources*, **206**, 450–453 (2012).
25. Q. H. Liu et al., *J. Electrochem. Soc.*, **159**, A1246–A1252 (2012).
26. L. Hoober-Burkhardt et al., *J. Electrochem. Soc.*, **164**, A600–A607 (2017).
27. M. Skyllas-Kazacos, L. Cao, M. Kazacos, N. Kausar, and A. Mousa, *ChemSusChem*, **9**, 1521–1543 (2016).
28. Y. Huang, S. Gu, Y. Yan, and S. F. Y. Li, *Curr. Opin. Chem. Eng.*, **8**, 105–113 (2015).
29. J. A. Kowalski, L. Su, J. D. Milshtein, and F. R. Brushett, *Curr. Opin. Chem. Eng.*, **13**, 45–52 (2016).

30. W. Wang and V. Sprenkle, *Nat. Chem.*, **8**, 204–206 (2016).
31. M. Doyle, M. E. Lewittes, M. G. Roelofs, S. A. Perusich, and R. E. Lowrey, *J. Membr. Sci.*, **184**, 257–273 (2001).
32. C. G. Arges, J. Parrondo, G. Johnson, A. Nadhan, and V. Ramani, *J. Mater. Chem.*, **22**, 3733–3744 (2012).
33. B. Pivovar, *Contract*, **303**, 275–3000 (2012).
34. Q. Xu and T. S. Zhao, *Phys. Chem. Chem. Phys.*, **15**, 10841–10848 (2013).
35. J. Houser, J. Clement, A. Pezeshki, and M. M. Mench, *J. Power Sources*, **302**, 369–377 (2016).
36. J. Houser, A. Pezeshki, J. T. Clement, D. Aaron, and M. M. Mench, *J. Power Sources*, **351**, 96–105 (2017).
37. C.-N. Sun, M. M. Mench, and T. A. Zawodzinski, *Electrochimica Acta*, **237**, 199–206 (2017).
38. R. Darling, K. Gallagher, W. Xie, L. Su, and F. Brushett, *J. Electrochem. Soc.*, **163**, A5029–A5040 (2016).
39. S. E. Doris et al., *Angew. Chem. Int. Ed.*, **55**, 1595–1599 (2016).
40. Online: "ARPA-E | Smart-FBS," https://arpa-e.energy.gov/?q=slick-sheet-project/smart-fbs; cited: May 9, 2017.
41. H. Zhang, H. Zhang, X. Li, Z. Mai, and J. Zhang, *Energy Environ. Sci.*, **4**, 1676–1679 (2011).
42. B. Li et al., *ChemSusChem*, **7**, 577–584 (2014).
43. S. Ha and K. G. Gallagher, *J. Power Sources*, **296**, 122–132 (2015).
44. Z. Tang et al., *J. Electrochem. Soc.*, **160**, F1040–F1047 (2013).
45. K. Lin et al., *Nat. Energy*, **1**, 16102 (2016).
46. Rosemount Analytical, "Conductance data for commonly used chemicals," *44-6039/rev.B* (2010).
47. W. Lu et al., *Chem Soc Rev*, **46**, 2199–2236 (2017).
48. T. Janoschka et al., *Nature*, **527**, 78–81 (2015).
49. G. Nagarjuna et al., *J. Am. Chem. Soc.*, **136**, 16309–16316 (2014).
50. J. Winsberg et al., *Polym Chem*, **7**, 1711–1718 (2016).
51. J. Winsberg et al., *Adv. Mater.*, **28**, 2238–2243 (2016).
52. J. A. Trainham and J. Newman, *J. Electrochem. Soc.*, **124**, 1528–1540 (1977).
53. Online: "2500_Data_Sheet_2008-12_20004," http://www.ldcgm.com/Celgard/CELGARD-4550.pdf; cited: May 9, 2017.
54. R. B. Bird, W. E. Stewart, and E. N. Lightfoot, *Transport Phenomena*, 2nd ed., p. 316, John Wiley & Sons, Inc., New York, (2007).
55. T. Yamamura, N. Watanabe, T. Yano, and Y. Shiokawa, *J. Electrochem. Soc.*, **152**, A830–A836 (2005).
56. X. L. Zhou, T. S. Zhao, L. An, Y. K. Zeng, and L. Wei, *J. Power Sources*, **339**, 1–12 (2017).
57. B. Delanghe, S. Tellier, and Astruc, *Electrochimica Acta*, **35**, 1369–1376 (1990).
58. D. Schmal, J. Van Erkel, and P. J. Van Duin, *J. Appl. Electrochem.*, **16**, 422–430 (1986).
59. I. V. Zenyuk, D. Y. Parkinson, L. G. Connolly, and A. Z. Weber, *J. Power Sources*, **328**, 364–376 (2016).
60. R. M. Darling and M. L. Perry, *J. Electrochem. Soc.*, **161**, A1381–A1387 (2014).
61. R. Carta, S. Palmas, A. M. Polcaro, and G. Tola, *J. Appl. Electrochem.*, **21**, 793–798 (1991).
62. Q. Chen, L. Eisenach, and M. J. Aziz, *J. Electrochem. Soc.*, **163**, A5057–A5063 (2016).
63. C. R. Dennison, E. Agar, B. Akuzum, and E. C. Kumbur, *J. Electrochem. Soc.*, **163**, A5163–A5169 (2016).
64. J. P. Owejan et al., *Int. J. Heat Mass Transf.*, **49**, 4721–4731 (2006).

65. A. Kazim, H. T. Liu, and P. Forges, *J. Appl. Electrochem.*, **29**, 1409–1416 (1999).
66. E. Knudsen, P. Albertus, K. T. Cho, A. Z. Weber, and A. Kojic, *J. Power Sources*, **299**, 617–628 (2015).
67. X. Wu et al., *J. Solid State Electrochem.* **21**, 429–435 (2017).
68. P. Zhao et al., *J. Power Sources*, **162**, 1416–1420 (2006).
69. V. Viswanathan et al., *J. Power Sources*, **247**, 1040–1051 (2014).
70. G. Towler and R. K. Sinnott, *Chemical engineering design: principles, practice, and economics of plant process design*, 2nd ed., Elsevier, (2012).
71. A. Zhu, P. D. Christofides, and Y. Cohen, *J. Membr. Sci.*, **344**, 1–5 (2009).
72. R. Turton, R. Bailie, W. Whiting, and J. Shaeiwitz, *Analysis, synthesis and design of chemical processes*, 3rd ed., p. 231, Pearson Education, (2008).
73. Online: "Chemicals A-Z," http://www.icis.com/chemicals/channel-info-chemicals-a-z/; cited: May 9, 2017.
74. A. M. Pezeshki, R. L. Sacci, F. M. Delnick, D. S. Aaron, and M. M. Mench, *Electrochimica Acta*, **229**, 261–270 (2017).
75. Y. Liu et al., *Adv. Energy Mater.*, 1601224 (2016).
76. S. Schlag, J. Glauser, and K. Yokose, *Chemical Economics Handbook: Sodium Chloride*, (2008).
77. B. Suresh, C. Funada, and Y. Ping, *Chemical Economics Handbook: Potassium Chemicals*, (2010).
78. J. D. Milshtein, S. M. Fisher, T. M. Breault, L. T. Thompson, and F. R. Brushett, *ChemSusChem* (2016). doi: 10.1002/cssc.201700028.

11. Conclusions and Outlook

11.1 Summary

In this thesis, we have first engaged a techno-economic analysis to quantify key technical hurdles impeding further price reductions for RFBs. This approach focused on defining materials selection guidelines and flow cell performance metrics for a RFB with future-state production scale. Note that significant cost reductions are possible simply by taking advantage of economies of scale or identifying cheaper suppliers for balance-of-plant equipment.[1,2] Broadly, NAqRFBs are a much more infant technology in comparison to their aqueous counterparts; hence, NAqRFBs require technological advancement in nearly every technological area. AqRFBs, as the more mature technology format, could benefit from lower cost active materials and membranes. The guidelines set in Chapter 1 serve as a launching point for the experimental and modeling studies in the subsequent chapters.

Experimental studies relating to the RFB electrolyte have addressed technological attributes that are under-addressed in the literature. A new class of organic molecule has been explored for implementation as an active species in aqueous electrolytes (Chapter 3), since prior literature had been limited to the quinone family of molecules. This thesis also reports on the first attempt of a multi-electron transfer prototype flow cell (Chapter 4), highlighting convoluted charge-discharge plateaus and materials compatibility challenges. Simultaneously, Chapters 4 and 5 identify pathways to reduce the amount of supporting salt in NAqRFBs, as the salt has been identified as the most expensive electrolyte component on a per mass basis. Reducing the salt cost contribution to the total electrolyte cost is a price reduction pathway that has been completely ignored in recent literature.

After some experimental investigations of electrolytes for RFBs, this thesis transitions to understanding limitations in flow cell design. An initial diagnostic study (Chapter 6), employing the single-electrolyte flow cell technique, considers how properties of a model electrolyte impact flow cell performance. From this study, the general conclusion is that ohmic and mass transfer losses are a major concern for NAqRFBs, while charge transfer losses appear negligible. Using this foundational knowledge, along with engineering intuition, this thesis investigates a highly soluble active species in conjunction with a state-of-the-art VRFB architecture to deliver the lowest non-aqueous flow cell ASR published to date (Chapter 7). A subsequent refined study (Chapter 8)

reverts to the single-electrolyte flow cell technique to systematically evaluate the impacts of electrolyte selection, separator type, electrode thickness, flow rate, and active species concentration on the ASR of non-aqueous flow cells. This study is the first of its kind for NAqRFBs and highlights contrasting conclusions as compared to the critical design criteria for AqRFBs.

Throughout the various experimental investigations of flow cell ASR, a lack of quantitative mass transfer descriptions for RFBs became evident through literature review. Thus, this thesis embarks on a mixed experimental and modeling study (Chapter 9) to quantify rates of mass transfer for four flow field designs. Using a one-dimensional porous electrode polarization model, of concise mathematical relationship, the relationship between mass transfer coefficient and flow rate was quantified for each of the flow field designs under consideration. The cell performance model was then coupled with the original, guiding techno-economic model (Chapter 10) to create a performance and cost based model for refining RFB materials selection. This multimodal modeling effort was applied to a case study investigating the price performance of AqRFBs as a function of membrane type, supporting salt, and electrolyte viscosity, illustrating that detailed materials choices can have drastic impacts on RFB price.

11.2 Outlook on Active Species Development

The materials design space for RFBs has recently moved beyond metal-based active species (i.e., vanadium) into the realm of non-metallic inorganics, organometallics, and organics. Non-metallic inorganics active species, such as metal polysulfides or iodine, offer impressively low costs,[3] but these inorganics are only as diverse as the periodic table allows. Considering the future-state active species cost target of \$5 kg^{-1},[1] most redox active elements are cost-prohibitive for implementation in a grid energy storage device.[4] Some engineered inorganic species deliver impressively extreme redox potentials, such as lithium borate cluster salts,[5] but these species have gained little to no attention in RFBs. Inorganic active species may have success in a limited number of chemistries simply due to low cost, but the lack of opportunity for rational materials design imparts a low ceiling for their technological growth.

Organometallics break through the limitations of the periodic table by combining stable, metallic redox active centers with functionalizing ligands. Given the wide array of ligand choices and methods for their molecular modifications, organometallics can be rationally engineered to

improve properties for enhanced RFB performance. A simple example is the addition of an ionic amine group to ferrocene, raising the solubility of that compound 10-fold,[6] but ligand modification has also been shown to shift redox potential, increase reaction rates, and improve stability.[7,8] Many recent reports, however, investigate active species with unrealistically expensive metal active centers, employing elements such as cobalt, ruthenium, or uranium, among others.[9] Considering the cost of all reagents for synthesizing a new organometallic can be an easy way to screen out cost-prohibitive options at the early stages of material discovery. Additionally, considering the number of synthetic steps required to produce a new organometallic, along with the yields of each step, can be an additional indicator of cost. Materials that require many synthetic steps or have low yields will be too expensive to produce, even if the precursors are low cost. Successful organometallic development campaigns will likely employ low-cost and abundant metal active centers, such as iron, manganese, or chrome, with easy to synthesize ligands.

ROMs present the most unexplored of the active material spaces for future RFBs. Organic molecules are typically comprised of earth abundant elements, indicating that their cost is not determined by the cost of raw materials or materials reserves; ROM cost will be linked entirely to the complexity of the synthetic route to produce them.[8] These species also offer the same attractive feature as organometallics: the opportunity for rational materials engineering.[7] The field of organic chemistry spans an enormous number of molecules, ranging from major differences in their core structure to minor differences in functionalizing side groups. As such, the ROM design space is ripe for picking, but also presents a daunting materials search task. Presently, no ROMs exhibit sufficiently desirable properties for implementation in a grid-scale device.[7] Efficiently down-selecting ROMs will require improved communication among electrochemical engineers, who are designing battery systems to achieve cost and performance targets, and organic chemists, who have a deep understanding of structure-property relationships for organic molecules. Bridging this communication gap is a non-trivial task in that these two groups of scientists often have different foundational education and different strategies for scientific success. As bountiful as the ROM space may be, their development lags behind inorganics and organometallics, but could one day offer the state-of-the-art RFB functionality.

11.3 Challenges of Multi-electron Transfer

One attractive feature being investigated for next generation RFB active species in the capability of multiple electron transfer events on a single active species. Multi-electron transfer is desirable for two reasons. First, active species that exhibit two or more electron transfer events that are separated by a large potential gap could be utilized on both sides of a RFB in a symmetric configuration. In fact, the state-of-the-art VRFB functions in this fashion.[10] Both ROMs and organometallics have been studied for use in symmetric RFBs.[9,11–14] Second, active species that exhibit multiple electron events that exhibit very similar redox potentials could be implemented on the same side of a RFB to increase capacity and energy density. Using multi-electron transfer to increase battery capacity appears a simple concept, but the spacing between the redox events is critical in defining cell performance. Ideally, the multiple electron transfer events will occur simultaneously, as is the apparent case for quinones in aqueous media.[15–17] As the redox events separate in potential space, the RFB will exhibit distinct charging plateaus associated with the various electron transfer events, and the relative duration of each plateau will depend upon the overpotential applied to each electrode. Thus, the duration of each charge plateau will depend on cycling rate, and thereby the voltaic efficiency will be drastically affected. Maintaining high efficiencies will be increasingly challenging as the redox events separate, and rating devices for guaranteed power and energy delivery will be ever more complicated. Thresholds on potential separations for multi-electron transfer on a single side of a RFB need to be instituted, along with a quantitative understanding of how key performance metrics will degrade.

11.4 Thermodynamics of Concentrated Organic Electrolytes

To date, electrolytes for NAqRFBs have been poorly characterized. The electrolyte, during operation, will contain a reduced active species, oxidized active species, supporting cation, supporting anion, and solvent, indicating that, at a minimum, the electrolyte is 5-component melt. Recent literature, however, treats the active species as if the solution contains only the active species and solvent.[12,18] The "solubility" of the active material depends upon the electrolyte state-of-charge (SOC), as well as the supporting salt identity and concentration. This thesis has shown that the solubility of ROMs can decrease dramatically from the charged to discharged state,[19] in pure solvent, and has also shown that the presence of supporting salt can decrease active material concentration,[19,20] among other studies.[21,22] The non-aqueous electrolyte should be treated as a

complex melt, and warrants thermodynamic analysis similar to that of molten alloys or salts. One recent study has produced a phase diagram describing the phases of a concentrated TEMPO-based melt, but only considers the one chemical system and does not address SOC.[23] Differential scanning calorimetry (DSC)[23] can be used to generate phase diagrams of organic-based RFB electrolytes as a function of temperature and SOC, as well as concentration of active material and supporting salt. Practically, electrolyte phase diagrams can identify stable regions where the electrolyte remains as a liquid, permitting specification of RFB operating conditions that ensure precipitation of active material or salt will not occur during battery cycling. Additionally, such phase diagrams will improve our thermodynamic understanding of NAqRFB electrolytes, which can inform future electrolyte development. Finally, DSC studies can measure heat capacities of the electrolyte, and this critical thermodynamic information can then be implemented to optimize thermal management for RFBs.

11.5 Thermal Management and Temperature Effects

State-of-the-art VRFBs must operate within a tight thermal stability window (10 – 40 ºC)[24] to avoid precipitation of the VO_2^+ cation. As such, VRFB deployments require thermal management equipment to keep the electrolyte temperature within the narrow stability window, but, despite this critical operational element, VRFB thermal balance calculations have only been performed in a limited number of literature reports.[25,26] These calculations should be rigorously performed, especially in relationship to the cost of heat exchangers and temperature controls systems required to maintain stable operation of any RFB. Further, the possibility of larger thermal stability windows associated with emerging electrolytes should be investigated; a wider temperature operating range could lead to decreased costs associated with thermal management or improved battery lifetime. Non-aqueous electrolytes may be particularly interesting for increasing the thermal stability window of RFBs. While non-aqueous electrolytes in lithium-ion batteries are regarded as a safety hazard due to possible thermal runaway,[27] such electrolytes may offer greater operational flexibility in RFBs due to the lower vapor pressure associated with many non-aqueous solvents (e.g., propylene carbonate), as compared to water. Further, RFB cycling at above-ambient temperatures should be investigated to improve operational current density by reducing ohmic losses, as well as increasing mass or charge transfer rates.

11.6 Future of Flow Field Design

The past decade has seen drastic improvements in RFB cell design through the implementation of the zero-gap architecture[28] and fuel cell-like flow fields.[29] Four primary designs for flow fields have surfaced, including the flow-through, parallel, serpentine, and interdigitated options,[29] among other niche design such as the pin-type[30] or spiral flow fields[31] have been investigated. The flow-through design and parallel flow field are on the brink of being discarded due to unreasonably high pressure drop or poor mass transport, respectively.

At present, the interdigitated flow field (IDFF) appears to be the most suitable option for RFB cell design due as that flow field best balances electrochemical performance and pressure drop.[32] The IDFF employs a complicated flow geometry, combining transport through open channels and nonlinear segments of porous media in series. Due to the complexity of the IDFF design, no geometric design rules exist for how to best optimize transport and pressure drop. While iterative optimization is an acceptable solution for boosting cell performance when only one electrolyte composition is being considered, the outburst of newly proposed electrolytes, with variable properties, make the guess-and-check optimization approach infeasible. Chemistry-agnostic design rules that dictate the channel and electrode dimensions for an IDFF as a function of the electrolyte properties (i.e., viscosity, rate constant), would be extremely valuable by enabling near-optimized design of flow fields for implementation with new electrolytes.

The current manifestation of the serpentine flow field (SFF), employing a single, snaking path through the cell's active area, develops an unacceptably large pressure drop; this version of the serpentine design does not allow for linear scaling of pressure drop with cell active area. An unexplored concept would be to implement multiple snaking sections throughout the flow field. The number of turns for each channel could be optimized to balance pressure drop and electrolyte penetration into the porous electrode.

11.7 Electrodes: Beyond Surface Science

Electrodes have been studied extensively for VRFBs, specifically for identifying supplier, catalysts, or pretreatments that can enhance reaction rates of the vanadium electron transfer events. Aside from serving as a heterogeneous catalytic surface, the electrode morphology plays a significant role in dictating mass transfer rates of active species to the fiber surface. Certain experimental studies have investigated how different commercially available porous carbon

electrodes impact cell performance,[31,32] but little effort has been put forth to understand transport within these media. The mass transport rates afforded in porous, fibrous electrodes are quite different than traditional predictions in packed bed reactors. Building experimental correlations or modeling transport within the actual electrode structure could offer new insight as to which electrodes can be best paired with which electrolyte properties. A natural extension would be to then define design rules for electrode morphology to yield the best electrochemical performance with a new electrolyte. Finally, developing structure property relationships that describe the electrode conductivity, surface area, and transport characteristic under compression and as a function of morphology would be beneficial for RFB cell optimization.

11.8 Scalability

In general, early-stage researchers assume that RFB power (reactor area) and capacity (tank size) can scale completely independently.[33] As has been illustrated in numerous flow battery studies, however, this independent scaling is not always the case since the accessed capacity during cycling varies with current density.[34] As current density increases, mass transfer limitations lead to large cell polarizations, leaving the remaining capacity inaccessible under normal operating voltage limits. Thus, changing the power-to-energy (P/E) ratio should affect the range of accessible SOCs and cell efficiencies. These effects remain unreported in the contemporary literature but are critically important when considering the battery as a gird storage asset.

Regarding cell size, all experimental RFB studies presented in thesis are performed with cells that have active areas $\leq$ 25 cm^2. Small-scale cells offer key benefits and limitations for quantitating mass transfer in a RFB. Practically, these cells only require a small quantity of electrolyte materials to perform cycling, polarization, or impedance experiments. Further, shrinking the active area of the flow cell permits investigations of cell performance under controlled flow conditions, where even electrolyte and active material concentration are anticipated. Under such conditions, mass and charge transfer effects, as they relate to the porous electrode and flow field design, can be directly investigated without concern for other mass transfer limitations that arise in large-scale cells (400 – 900 cm^2),[35–37] such as uneven flow distribution, manifold transport losses, and shunt currents. For example, filter-press style electrochemical reactors for use in polysulfide-bromine RFBs have illustrated that non-uniform flow dispersion can yield non-negligible differences in transport resistance, and pressure drop will scale non-

linearly with increasing active area for IDFF or SFF designs.[32,37] Shunt currents[38] represent a stack-level phenomena that cannot be accurately probed in single-cell devices. While Chapter 8 briefly discusses scaling of pressure drop through an IDFF, such an analysis only begins to touch upon the nontrivial scaling challenges associated with RFBs. Dedicated scaling laws for each promising flow field type should be developed to indicate how channel dimensions and cell aspect ratio should vary with increasing active area to maintain balance between stack power and pressure drop at large-scale.

11.9 Cycling Protocols

The focus of lab-scale cycling is to prove that new chemistries can store and release energy or a new component can improve cycling performance (e.g., efficiency, capacity accessed). In contrast, as grid-storage devices, RFBs will undergo charge-discharge profiles unique to the services they provide (either single services or, more likely, stack services to improve the value of storage). For example, the same system used for load-leveling that requires long charge times (8–12 h) and intermediate discharge times (3–5 h) may also serve to enable power quality assurance that requires fast charge and discharge times of $\leq$ 1 h.[39,40] Variable electricity inputs and outputs (Figure 1) can affect battery lifetime and performance because the battery will often be held at extreme states-of-charge (SOCs) and will undergo intermittent cycling to meet service demands. Such conditions are not typically tested during early stage research. Only after significant time and monetary investment will the system be scaled-up for field-testing, at which point the new RFB design could prove inadequate for desired grid applications.

Research-scale RFB prototypes typically operate under constant-current density charge and discharge, but variable ratios of charge-to-discharge current densities, corresponding to different charge and discharge times, are anticipated in grid-connected cycling.[36] Variable charge-to-discharge current densities combined with periodic potential holds, associated with lulls in electricity input/output, can cause the battery energy efficiency, SOC, and accessible capacity to vary substantially. Of particular interest is the battery behavior at extreme SOCs as, in addition to concentration- and thermodynamically-driven changes in the cell resistance; RFBs may exhibit increased rates of deleterious side reactions which lead to self-charge and / or capacity fade. Examples of such side reactions include hydrogen evolution in the negative electrolyte of aqueous RFBs,[41] oxygen driven self-discharge of active species,[42] radical decay of organic active species,[43]

or active species crossover.[44] Such processes would not manifest under rapid and repetitive constant-current cycling.

In addition to informing optimal RFB cycling strategies, such cycle protocols would enable researchers to predict better the promise of a new chemistry, membrane, electrode, or cell design. This knowledge, in turn, will aid in down selecting from the plethora of newly proposed RFB designs before making necessary investments for field-testing. Such efforts will complement emerging battery testing centers[45,46] by providing the necessary baseline data to motivate scale-up. Ultimately, reformed cycling protocols could increase the speed at which promising new chemistries transition from a laboratory prototype to commercial realization.

11.10 References

1. R. M. Darling, K. G. Gallagher, J. A. Kowalski, S. Ha, and F. R. Brushett, *Energy Environ. Sci.*, **7**, 3459–3477 (2014).
2. S. Ha and K. G. Gallagher, *J. Power Sources*, **296**, 122–132 (2015).
3. R. Dmello, J. D. Milshtein, F. R. Brushett, and K. C. Smith, *J. Power Sources*, **330**, 261–272 (2016).
4. B. L. Spatocco and D. R. Sadoway, *Electrochem. Eng. Scales Vol. 15 Mol. Process.*, **7**, 1 (2015).
5. Z. Chen et al., *Electrochem. Solid-State Lett.*, **13**, A39 (2010).
6. X. Wei et al., *Adv. Energy Mater.*, **5**, 1400678 (2015).
7. J. A. Kowalski, L. Su, J. D. Milshtein, and F. R. Brushett, *Curr. Opin. Chem. Eng.*, **13**, 45–52 (2016).
8. J. Winsberg, T. Hagemann, T. Janoschka, M. D. Hager, and U. S. Schubert, *Angew. Chem. Int. Ed.*, **56**, 686–711 (2016).
9. Y. Huang, S. Gu, Y. Yan, and S. F. Y. Li, *Curr. Opin. Chem. Eng.*, **8**, 105–113 (2015).
10. G. Kear, A. A. Shah, and F. C. Walsh, *Int. J. Energy Res.*, **36**, 1105–1120 (2012).
11. M. H. Chakrabarti, R. A. W. Dryfe, and E. P. L. Roberts, *Electrochimica Acta*, **52**, 2189–2195 (2007).
12. W. Duan et al., *J Mater Chem A*, **4**, 5448–5456 (2016).
13. T. Janoschka, C. Friebe, M. D. Hager, N. Martin, and U. S. Schubert, *ChemistryOpen*, **6**, 216–220 (2017).
14. R. A. Potash, J. R. McKone, S. Conte, and H. D. Abruna, *J. Electrochem. Soc.*, **163**, A338–A344 (2016).
15. B. Huskinson et al., *Nature*, **505**, 195–198 (2014).
16. B. Yang, L. Hoober-Burkhardt, F. Wang, G. S. Prakash, and S. R. Narayanan, *J. Electrochem. Soc.*, **161**, A1371–A1380 (2014).
17. M. Quan, D. Sanchez, M. F. Wasylkiw, and D. K. Smith, *J. Am. Chem. Soc.*, **129**, 12847–12856 (2007).
18. W. Duan et al., *ACS Energy Lett.*, 1156–1161 (2017).
19. J. D. Milshtein et al., *Energy Env. Sci*, **9**, 3531–3543 (2016).
20. S. M. Laramie, J. D. Milshtein, T. M. Breault, F. R. Brushett, and L. T. Thompson, *J. Power Sources*, **327**, 681–692 (2016).

21. A. A. Shinkle, T. J. Pomaville, A. E. S. Sleightholme, L. T. Thompson, and C. W. Monroe, *J. Power Sources*, **248**, 1299–1305 (2014).
22. J. R. Dahn et al., *J. Electrochem. Soc.*, **152**, A1283–A1289 (2005).
23. K. Takechi, Y. Kato, and Y. Hase, *Adv. Mater.*, 2501–2506 (2015).
24. A. Parasuraman, T. M. Lim, C. Menictas, and M. Skyllas-Kazacos, *Electrochimica Acta*, **101**, 27–40 (2013).
25. H. Al-Fetlawi, A. A. Shah, and F. C. Walsh, *Electrochimica Acta*, **55**, 78–89 (2009).
26. A. Tang, J. Bao, and M. Skyllas-Kazacos, *J. Power Sources*, **216**, 489–501 (2012).
27. T. M. Bandhauer, S. Garimella, and T. F. Fuller, *J. Electrochem. Soc.*, **158**, R1–R25 (2011).
28. D. S. Aaron et al., *J. Power Sources*, **206**, 450–453 (2012).
29. X. L. Zhou, T. S. Zhao, L. An, Y. K. Zeng, and L. Wei, *J. Power Sources*, **339**, 1–12 (2017).
30. X. Li and I. Sabir, *Int. J. Hydrog. Energy*, **30**, 359–371 (2005).
31. C. R. Dennison, E. Agar, B. Akuzum, and E. C. Kumbur, *J. Electrochem. Soc.*, **163**, A5163–A5169 (2016).
32. R. M. Darling and M. L. Perry, *J. Electrochem. Soc.*, **161**, A1381–A1387 (2014).
33. A. Z. Weber et al., *J. Appl. Electrochem.*, **41**, 1137–1164 (2011).
34. Y. K. Zeng, T. S. Zhao, L. An, X. L. Zhou, and L. Wei, *J. Power Sources*, **300**, 438–443 (2015).
35. X. Wu et al., *J. Solid State Electrochem.* **21**, 429–435 (2017).
36. P. Zhao et al., *J. Power Sources*, **162**, 1416–1420 (2006).
37. E. Knudsen, P. Albertus, K. T. Cho, A. Z. Weber, and A. Kojic, *J. Power Sources*, **299**, 617–628 (2015).
38. R. M. Darling, H.-S. Shiau, A. Z. Weber, and M. L. Perry, *J. Electrochem. Soc.*, **164**, E3081–E3091 (2017).
39. U . S . Department of Energy - Headquarters Advanced Research Projects Agency – Energy (ARPA-E), *Grid-Scale Rampable Intermittent Dispatchable Storage Funding Opportunity Announcement*, p. 10, (2010).
40. G. Fitzgerald, J. Mandel, J. Morris, and H. Touati, *The economics of battery energy storage: How multi-use, customer-sited batteries deliver the most services and value to customers and the grid*, Rockey Mountain Institute, (2015).
41. Y. K. Zeng, X. L. Zhou, L. Zeng, X. H. Yan, and T. S. Zhao, *J. Power Sources*, **327**, 258–264 (2016).
42. K. Ngamsai and A. Arpornwichanop, *J. Power Sources*, **295**, 292–298 (2015).
43. X. Wei et al., *Angew. Chem. Int. Ed.*, **54**, 8684–8687 (2015).
44. K. W. Knehr, E. Agar, C. R. Dennison, A. R. Kalidindi, and E. C. Kumbur, *J. Electrochem. Soc.*, **159**, A1446–A1459 (2012).
45. Online: "BEST Test & Commercialization Center – Energy – DNV GL," https://www.dnvgl.com/services/best-test-commercialization-center-5587; cited May 9, 2017.
46. Online: "Home | Sustainable Power and Energy Center," http://jacobsschool.ucsd.edu/sustainablepower/; cited May 9, 2017.

A. GEN1 Flow Cell Standard Operating Procedure

This appendix is adapted from a standard operating procedure manual developed for and distributed across the Joint Center for Emery Storage Research (JCESR) in 2015. The original purpose of this material was to provide JCESR researchers with a standard experimental procedure for engaging flow cell studies with an easy-to-use set-up.

A.1 Bill of Materials

Description	Supplier	Part #	Qty	Price	Extended Price
RAW MATERIALS FOR MACHINING					
316 Stainless Steel Tight Tolerance Blank with Certificate, 5/8" Thick, 6" x 6"	McMaster-Carr	8896K184	1	$ 243.16	$ 243.16
Film Made with Teflon PTFE 0.010" Thick, 12" Width, 1' Length	McMaster-Carr	8569K41	1	$ 11.69	$ 11.69
Easy-to-Machine Polypropylene Sheet, 1/8" Thick, 12" x 12" Opaque White (White or Black)	McMaster-Carr	2898K11	1	$ 4.20	$ 4.20
Optically Clear Cast Acrylic Sheet, 1/8" Thick, 12" x 12"	McMaster-Carr	8560K239	1	$ 8.63	$ 8.63
OFF-SHELF HARDWARE FOR FLOW CELL					
Metric Nylon Unthreaded Spacer, 4.5mm OD, 14mm Length	McMaster-Carr	93657A720	16	$ 1.01	$ 16.16
Chemical-Resistant Polypropylene Barbed Fitting, High-Temperature, Straight, 1/16" Tube ID x 1/8 Male Pipe (10 Pack)	McMaster-Carr	5121K351	1	$ 4.41	$ 4.41
Black-Oxide Coated Type 18-8 Stainless Steel Hex Nut, M3x0.5 Thread Size, 5.5mm Wide, 2.4mm High (Pkg of 100)	McMaster-Carr	98676A100	1	$ 5.39	$ 5.39
Black-Oxide Steel Oversized Flat Washer, M3 Screw Size, 3.2mm ID, 8.0mm OD (Pkg of 25)	McMaster-Carr	98035A101	1	$ 11.11	$ 11.11
Black-Oxide Class 12.9 Socket Head Cap Screw, Alloy Steel, M3 Thread, 40mm Length, 0.50mm Pitch (Pkg of 25)	McMaster-Carr	91290A136	1	$ 2.29	$ 2.29
Banana Plug Male to #6-32 Threaded Stud	Mouser Electronics	565-3263	2	$ 2.11	$ 4.22

TOOLS FOR FLOW CELL ASSEMBLY					
Commercial Grade Pipe Thread Sealant Tape, 16 Yard L x 1/4" Wide, .0028" Thick, 0.5 G/CC Density	McMaster-Carr	4591K11	1	$ 1.86	$ 1.86
Adjustable Slip-Release Torque Screwdriver, 2 to 12 in.-lbs. Torque Range, with Certificate	McMaster-Carr	5871A52	1	$ 477.12	$ 477.12
Premium Combination Wrench, 6 Point, 7/16" Size, 7-1/4" Length, Polished, Long	McMaster-Carr	5772A34	1	$ 12.70	$ 12.70
Metric Hex Insert Bit, 7-Piece Set, 1/4" Shank, Size 2mm-8mm, in Vinyl Holder	McMaster-Carr	7389A41	1	$ 13.29	$ 13.29
30 Degree Angle Miniature Open-End Wrench, 5.5 mm, Black Blade with Chrome Plated Handle	McMaster-Carr	7793A36	1	$ 7.69	$ 7.69
PUMP & PUMP HEAD					
Masterflex L/S Digital Drive Pump, 100 RPM, 115/230 VAC	Cole-Parmer	07522-30	1	$ 1,898.00	$ 1,898.00
Masterflex L/S two-channel Easy Load II pump head, SS rotor	Cole-Parmer	77202-60	1	$ 372.00	$ 372.00
TUBING FOR PUMP HEADS					
Long-Life Clear Tygon PVC Tubing, 1/16" ID, 3/16" OD, 1/16" Wall Thickness (25 feet)	McMaster	55485K71	1	$ 108.25	$ 108.25
Long-Life Clear Tygon PVC Tubing, 1/8" ID, 1/4" OD, 1/16" Wall Thickness (25 feet)	McMaster	55485K72	1	$ 124.75	$ 124.75
Masterflex Norprene Tubing (A60 G), L/S 14, 50 Feet	Cole-Parmer	06404-14	1	$ 49.25	$ 49.25
TUBING (CHEAP, NOT FOR PUMP HEADS)					
Laboratory Clear Tygon PVC Tubing, 1/8" ID, 1/4" OD, 1/16" Wall Thickness (25 feet)	McMaster	5155T17	1	$ 22.50	$ 22.50
Norprene Tubing, 1/16" ID x 3/16" OD, 50 ft/pack	Cole-Parmer	06410-01	1	$ 39.00	$ 39.00
TUBING CONNECTORS					
Chemical-Resistant Polypropylene Barbed Fitting, Straight for 1/16" Tube ID (10 Pack)	McMaster	53415K101	1	$ 5.00	$ 5.00
Chemical-Resistant Polypropylene Barbed Fitting, Straight for 1/8" Tube ID (10 Pack)	McMaster	53415K103	1	$ 6.32	$ 6.32

A.2 Suggested Electrochemical Equipment

1. CH Instruments, Inc. 760E Bipotentiostat
    - Cheap and functional bipotentiostat with galvanostatic cycling capabilities
    - No impedance capability
    - Easiest way to get started with electrochemical measurements

2. Biologic VMP3 Potentiostat
    - High quality potentiostat
    - 1 nA current resolution
    - Up to 16 channels for data acquisition
    - Optional impedance capabilities
    - Maximum current: 450 mA
    - Good option for both electroanalytical experiments and battery testing

3. Arbin Battery Tester
    - Customizable battery tester
    - Can handle 5 A current or higher
    - Contact Arbin to design a system for your needs
    - No impedance capability
    - Best used for battery testing

A.3 How to Assemble the GEN1 Flow Cell

An accompanying instructional video has been posted to YouTube:

https://www.youtube.com/watch?v=pHgToSUUuZ8

Required parts and tools:

a) Tube fittings (4)
b) Teflon gaskets (2)
c) Banana plugs (2)
d) Screws (8)
e) Flow fields (2)
f) Plastic insulating sheet
g) Washers (16)
h) Nuts (8)
i) Torque wrench
j) 7/16” wrench
k) 5.5 mm wrench
l) Separator template
m) Daramic separator
n) Razor blade
o) GFA6 carbon felt
p) Teflon tape

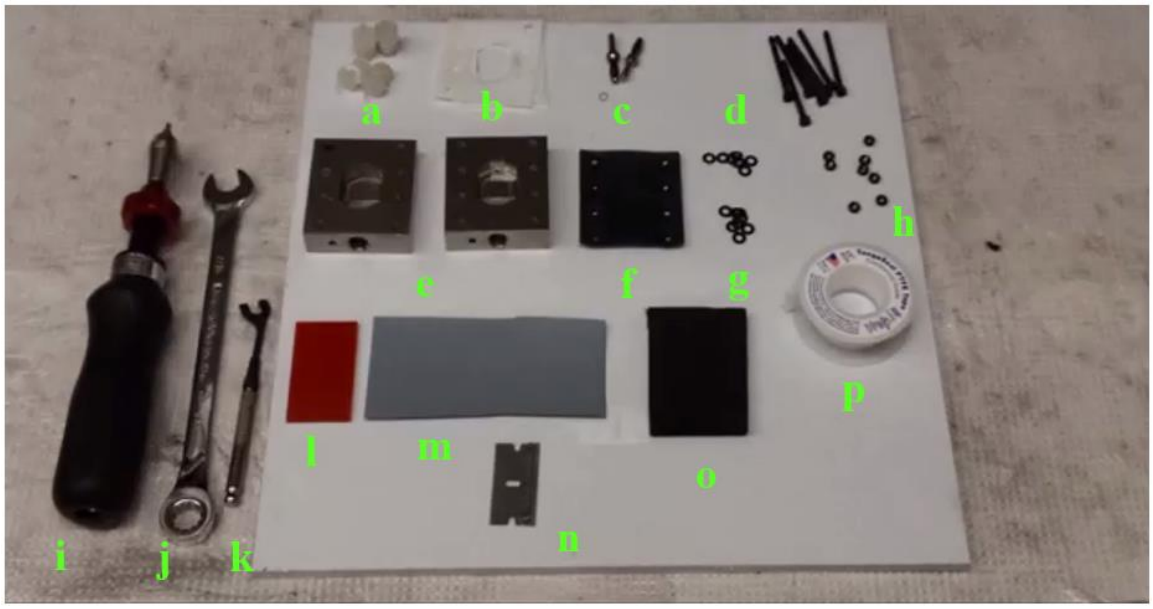

Cell Preparation and Assembly:

1. Insert 4 tube fittings into the flow field:
    a. Use scissors to cut Teflon tape into small pieces and wrap the Teflon tape around the tube fitting threads *opposite the direction* of the threads
    b. Repeat for remaining 3 tube connections.

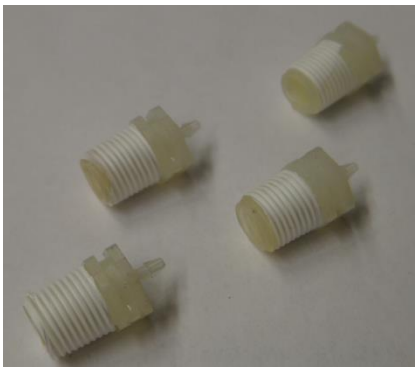

    c. Screw the 4 Teflon wrapped tube fittings into the flow field (finger tighten).
    d. Use 7/16" wrench to tighten fittings. **CAUTION:** Don't over-tighten or the plastic threads may rip.

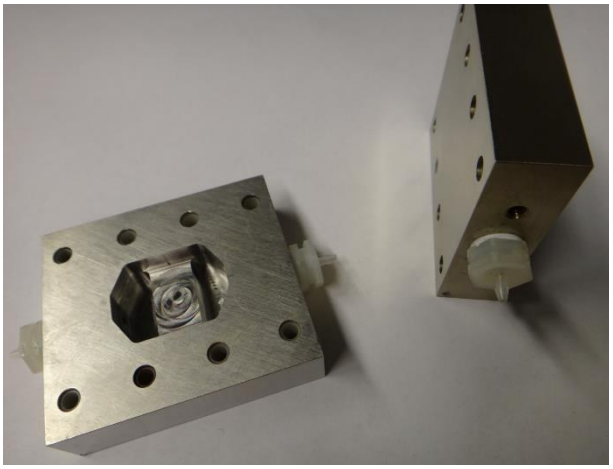

2. Cut the Daramic separator to size (2 layers) by using a razor blade to trace around the supplied template. Multiple layers help to minimize cross over during operation.

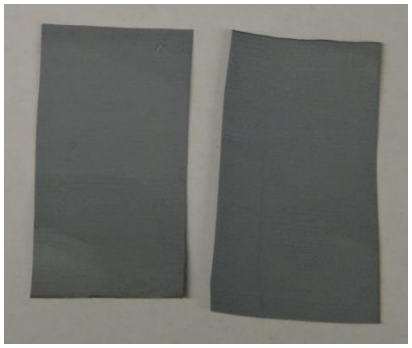

3. Cut the carbon felt into electrodes (2) using a razor blade to match the octagonal shape of the flow field. Use one of the Teflon gaskets as a template. The carbon felt is GFA6 (see bill of materials) and should completely fill the cavity of the flow cell.

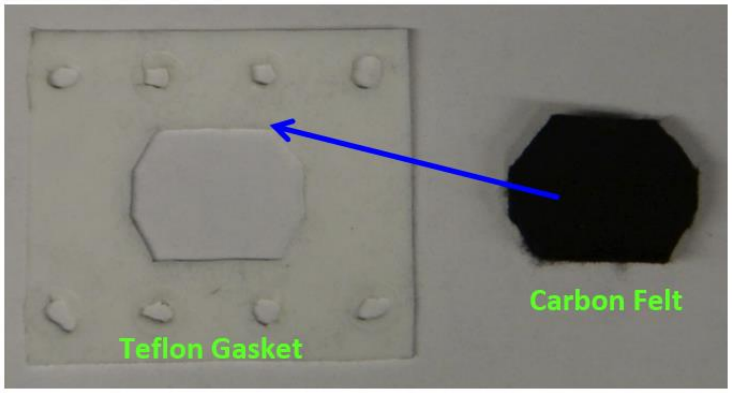

4. Prepare the first flow field:
    a. Set one of the flow fields on its side. Place a washer on each screw (8) and then feed the screws with washers through the back of the cell. **NOTE:** The Nylon inserts electrically insulate the screws from the stainless steel cell. Check that they are in place before beginning assembly.

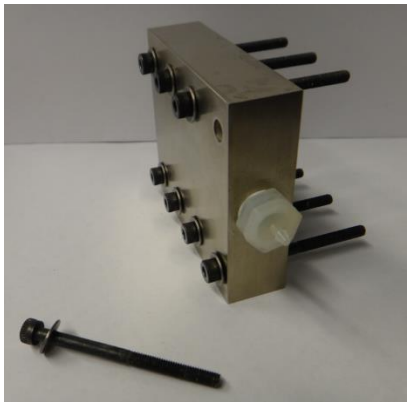

    b. Flip flow field to back so that the screws are held in place by the table.

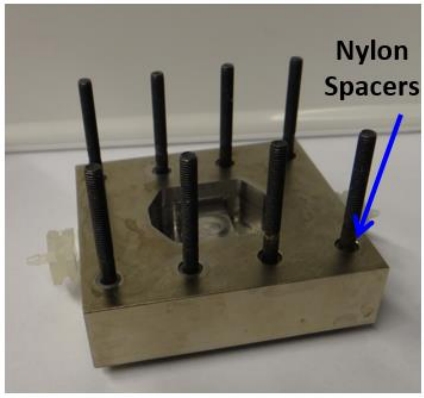

c. Place one Teflon gasket over the flow field, using the screws for alignment. It should completely cover the stainless steel and there should be no gap between the stainless steel and the Teflon gasket.
d. Take one carbon felt electrode and place in the flow field.

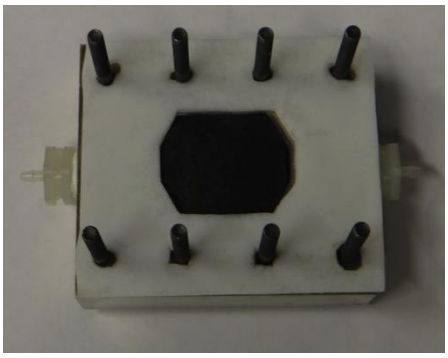

e. Add the two layers of Daramic so they are completely covering the felt. **Caution:** Don't allow the separator to touch the holes on the gasket or the screws. Additionally, the separator should not extend beyond the flow field.

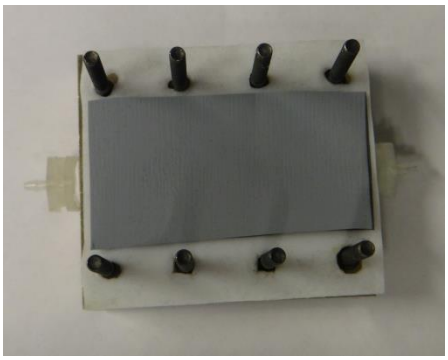

f. Place the second Teflon gasket on top of the cell. The octagonal hole in the Teflon separator should be completely filled by the Daramic separator.

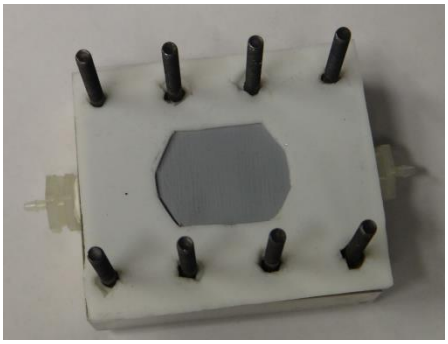

5. Prepare the second flow field by placing the remaining piece of carbon felt in the flow channel. Then flip the second flow field onto the exposed gasket of the first flow field assembly. **NOTE:** The connections for the banana plugs should be on the same side of the cell. Place the plastic insulating sheet on top of the assembled cell.

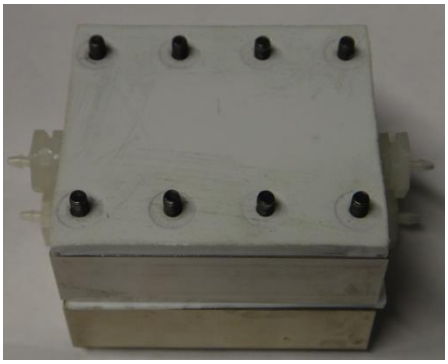

6. Place the remaining washers (8) on the exposed screws. Then, take the nuts (8) and tighten them by hand onto the screws. **Note:** At this point make sure everything is well connected by checking that the cell assembly does not move when jostled.

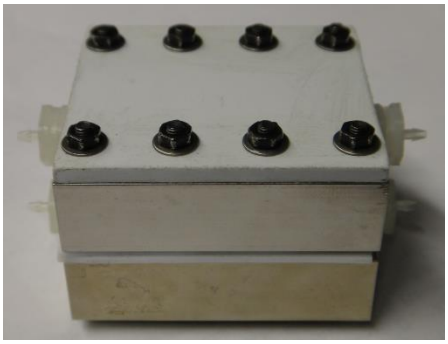

7. Final cell preparation (**NOTE:** Final compression: 7 lb-in):
    a. Use a torque wrench to tighten each bolt to 3 lb-in. A star pattern should be used while tightening (ex. 4, 5, 1, 8, 2, 7, 3, 6) to ensure equal compression across the cell and minimize leaking.

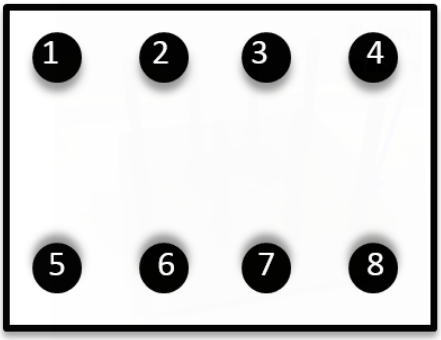

    b. Incrementally increase the torque by tightening each bolt to 5 lb-in and then to 7 lb-in, using the same star pattern for each step. **NOTE:** After this step is complete, double-check each screw to ensure the correct torque

8. Screw the banana plugs (2) into the holes on the front faces of the flow fields. You now have an assembled GEN1 flow cell.

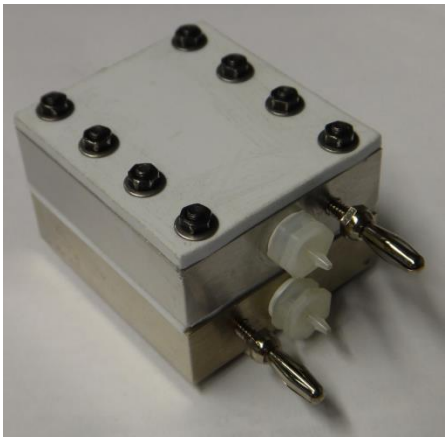

A.4 How to Operate the GEN1 Flow Cell

An accompanying instructional video has been posted to YouTube:

https://www.youtube.com/watch?v=vv1-rTBS3-s

1. Attach the pump head to pump according to the pump head manual.

2. Feed long lifetime tubing (see bill of materials) through the pump heads. Connect long lifetime tubing to cheaper tubing using hose couplings. Please refer to the pump head manual for instruction on how to insert tubing correctly.

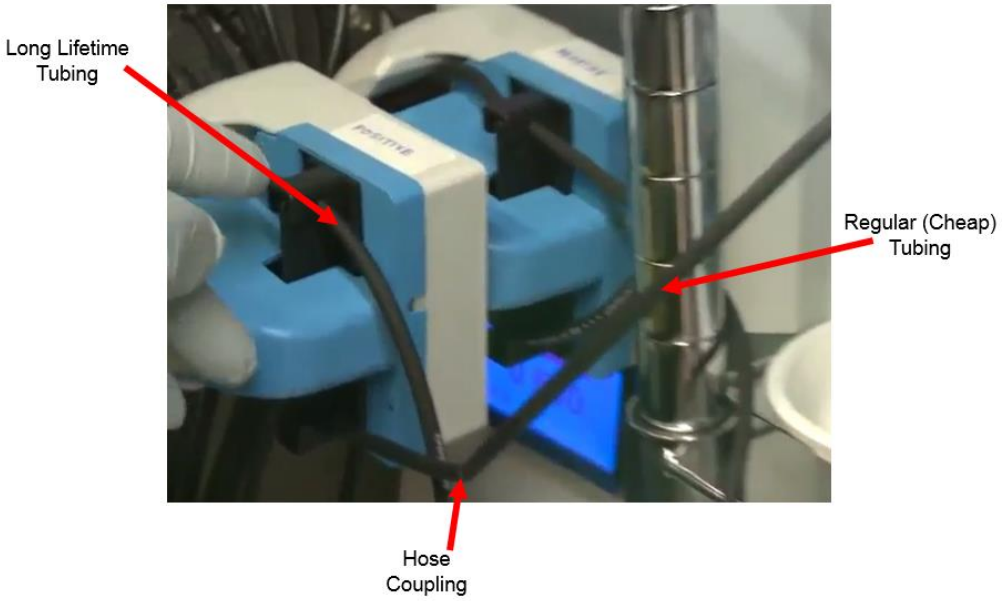

3. Add electrolyte (with dissolved active species) to the reservoirs. Use <u>AT LEAST 10 mL</u> of solution per side of the flow battery. If you are running the $V(acac)_3$ validation, the prepared solution should be brown. If the solution is not brown, then the $V(acac)_3$ supply has been contaminated and will yield poor results.

4. Seal the tops of the reservoirs with Parafilm or a sealed cap in order to minimize evaporation of the solvent.

5. Connecting the positive electrolyte tubing to the flow cell:
    a. Take the section of tubing coming from the pump head and seal it around the inlet for the positive electrolyte in the flow cell.

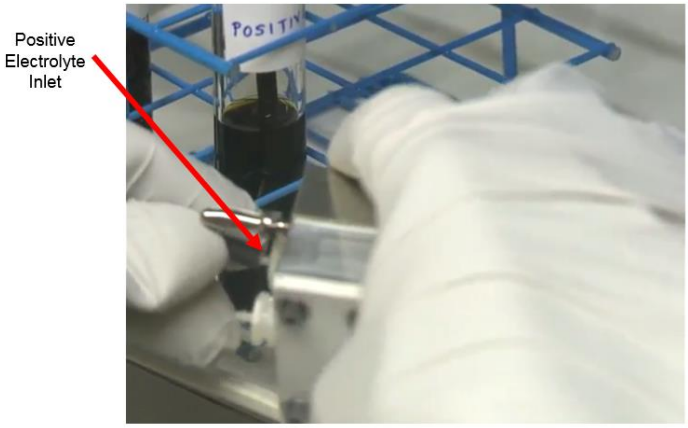

    b. Connect a section of tubing for the outlet of the positive electrolyte in the flow cell.

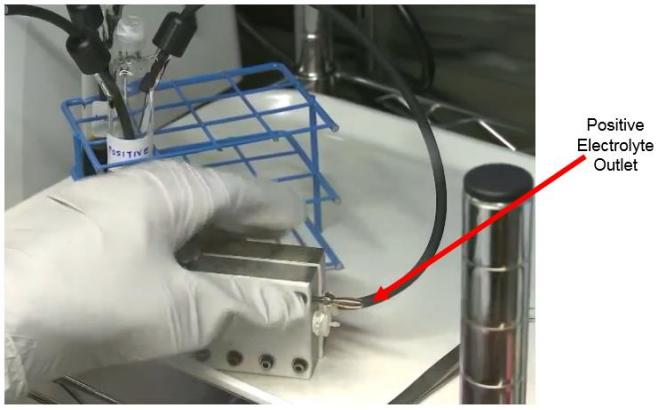

6. Connect the positive electrolyte tubing to the positive electrolyte reservoir. The section of tubing which exits the flow cell should be suspended above the surface of the electrolyte. The section of tubing which enters the pump head should be submerged at the bottom of the electrolyte. Flow direction is shown in yellow.

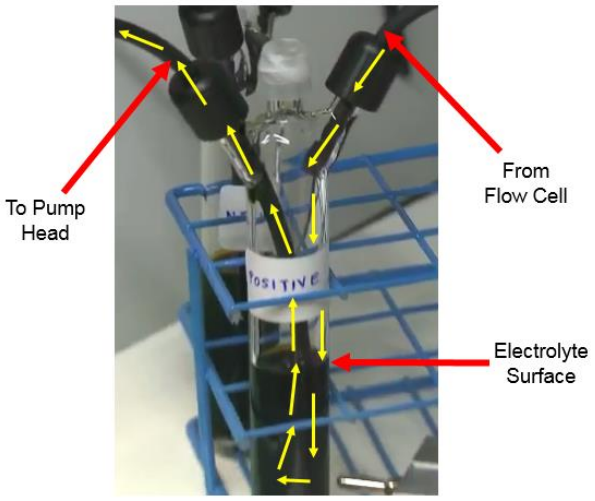

7. Connect the tubing for the negative electrolyte in the same manner as the positive electrolyte. Ensure that the tubing inlets for both reservoirs are connected to the same side of the flow cell.

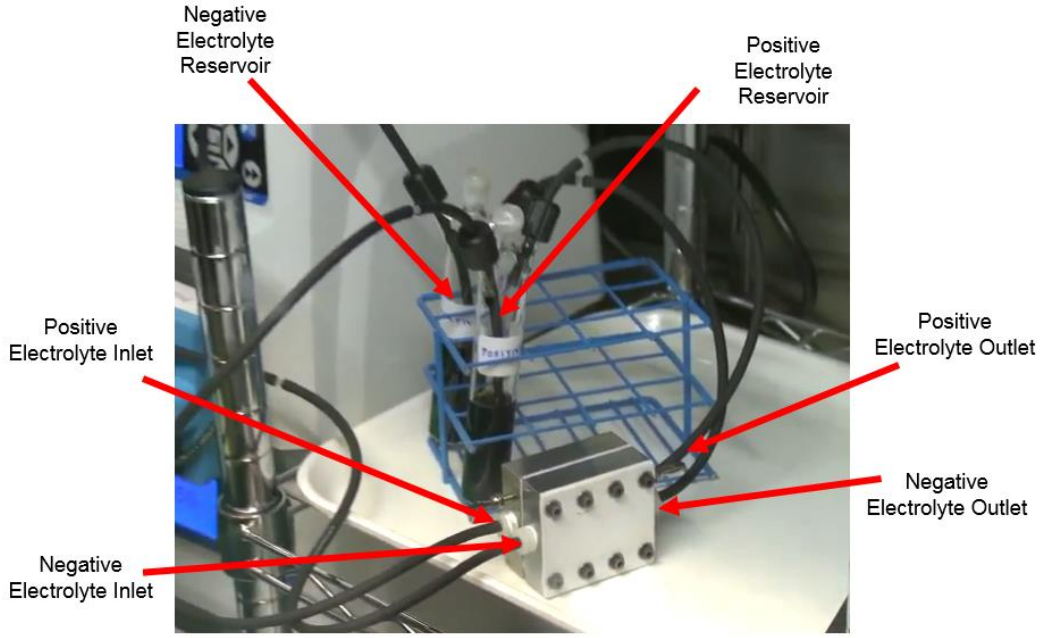

8. Begin flowing electrolyte by pressing the “Play” button on the pump. If you are running a $V(acac)_3$ validation, use a flow rate of 20 mL min^{-1}. Observe the liquid level in the reservoir begin to decrease as the electrolyte fills the tubing and the flow cell.

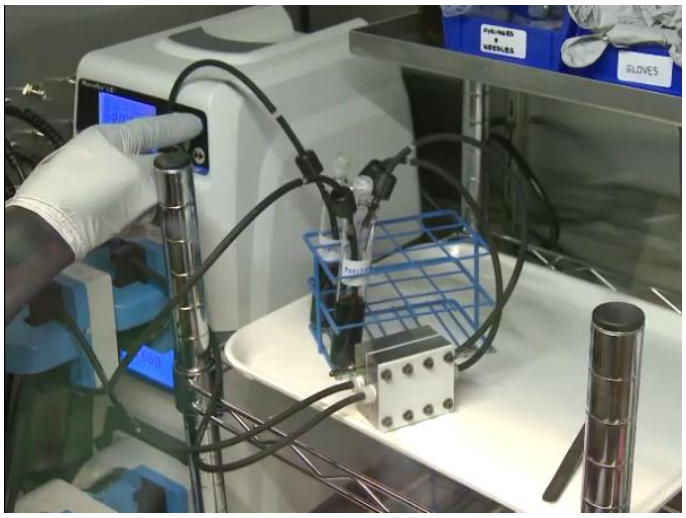

9. Once the tubing and flow cell have been filled with electrolyte, you will observe electrolyte dripping down into the reservoir from the tubing which exits the flow cell. If you do not observe dripping check the tubes for clogging.

10. Remove air bubbles which may be sitting inside the cell by holding the cell vertically and tapping it for approximately 30 seconds.

11. Before beginning any electrochemical measurements, ensure that the flow cell is sitting on an insulating surface to ensure that electrical shorting will not occur during operation.

12. Place the flow cell on top of a kim-wipe. This will make identifying leaks easier, if any do appear.

13. Prop the outlet of the flow cell so that it is at a higher elevation than the inlet. This will help to remove any air bubbles which may form during operation.

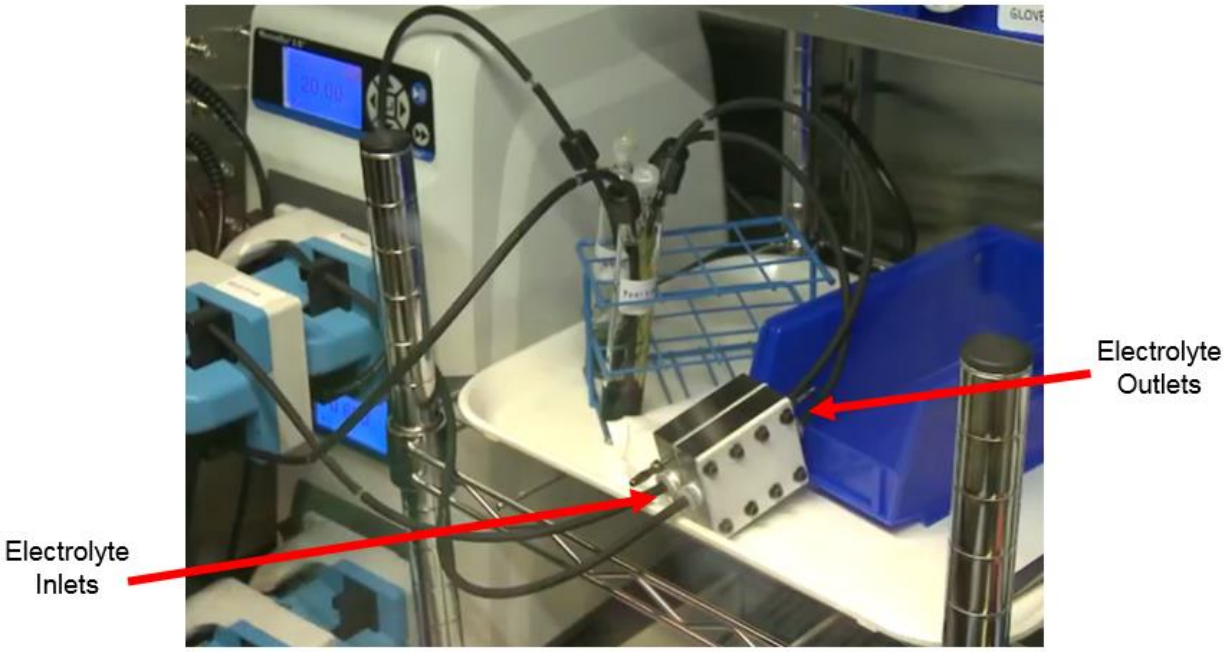

14. Connect the potentiostat or battery tester leads to the flow cell using alligator clips or banana plugs. For asymmetric cells, ensure that the positive and negative electrical leads are appropriately connected to the positive and negative flow channels. Do not allow the electrical leads to short circuit the cell. All stainless steel parts are electrically active.

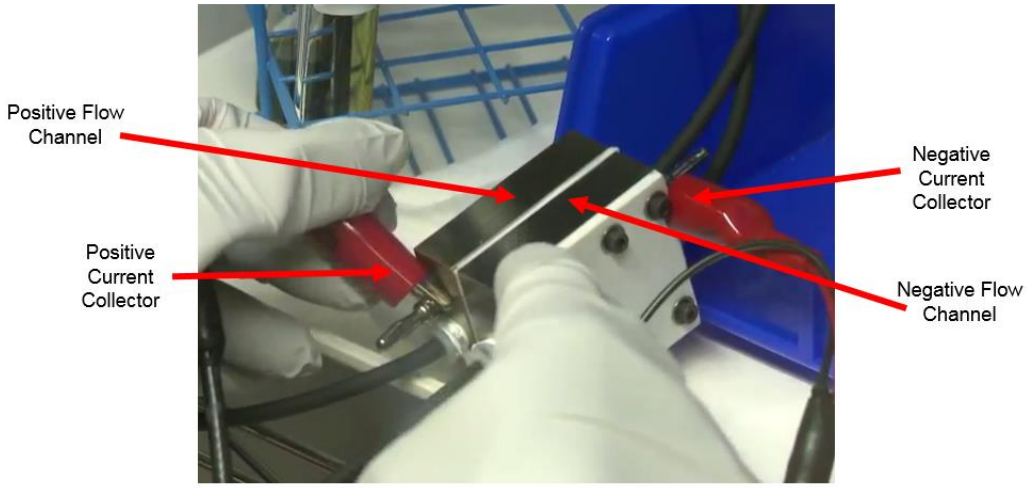

15. Measure the impedance of the cell to ensure all electrical connections are well-made. The high frequency intercept for the $V(acac)_3$ validation should be ~2 Ω.

16. Begin flow cell cycling experiment.

17. Once flow cell cycling begins, color changes in the solution can be used to indicate whether or not the electrolytes are charging or discharging. In the case of the $V(acac)_3$ validation, the negative electrolyte should turn green at 100% SOC, and the positive electrolyte should turn blue at 100% SOC.

18. Once the cell is done cycling, take another impedance measurement.

19. Now that the cell cycling is complete, it is time to dismantle the cell. First, stop the pumping.

20. Next, reverse the flow direction, and begin pumping again. This will drain the flow cell, filling it with argon. You will observe a rise in the electrolyte surface levels in the reservoirs. You can hold the cell vertically (so that the fluid falls with gravity) to ensure that all of the electrolyte exits the cell. Hold the cell vertically until you observe bubbling in your reservoirs, which will indicate that only gas is being pumped through the cell.

21. Turn off the pump and dismantle your cell. While the cell is not connected, rinse the tubing with the solvent until the solvent runs clear in order to clean the inside of the tubing. Otherwise, solid deposits can build up and clog the tubing and/or contamination between experiments will occur.

A.5 Validation Data from the GEN1 Flow Cell with Vanadium Acetylacetonate

1. Chemical Structure of Vanadium Acetylacetonate ($V(acac)_3$)

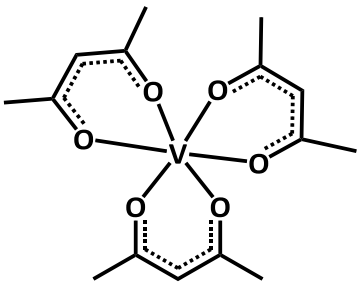

2. Detailed test conditions

   a. GEN1 flow cell assembly
   b. 0.1 M $V(acac)_3$ / 0.5 M $TBAPF_6$ / MeCN
   c. Electrolyte Volume: 10 mL
   d. 2 Layers of Daramic 175 separator
   e. Current Density: 5 mA cm^{-2}
   f. Voltage cutoffs: 0.9 – 2.27 V
   g. Electrode material: GFA6 (hexagonal, 4.63 cm^2)
   h. PTFE gasket
   i. Flow rate: 20 mL min^{-1}

3. Example efficiency data collected from **(a)** Massachusetts Intitute of Technology, **(b)** the University of Michigan, and **(c)** Pacific Northwest National Lab. Mean efficiencies in the table below are average values from 10 cycles.

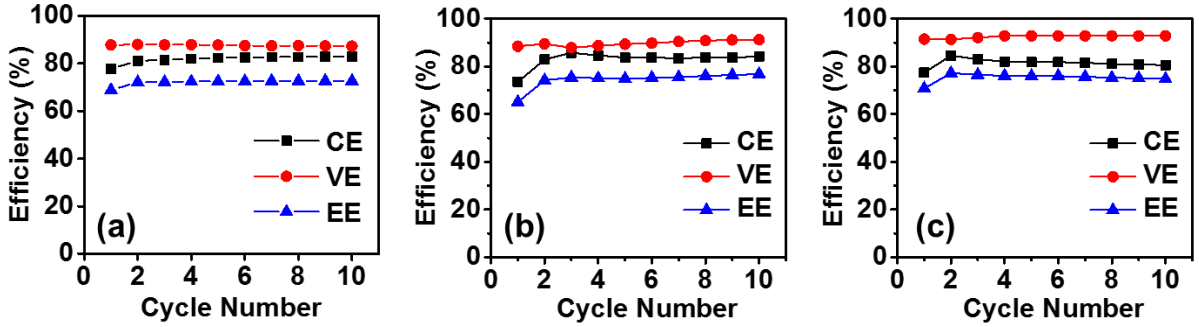

Efficiency	Coulombic (%)	Voltaic (%)	Energy (%)
MIT	84	88	73
UMich	84	90	76
PNNL	82	92	75

4. Example capacity retention data collected from **(a)** Massachusetts Intitute of Technology, **(b)** the University of Michigan, and **(c)** Pacific Northwest National Lab.

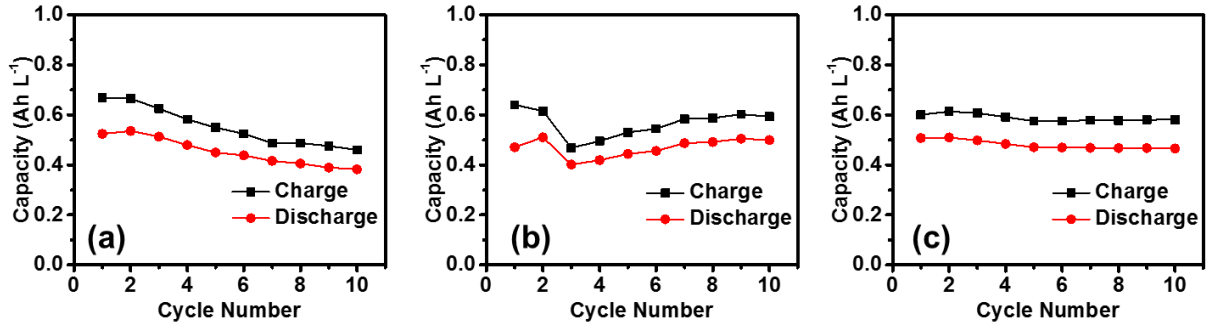

5. Example time vs. potential data collected from **(a)** Massachusetts Intitute of Technology, **(b)** the University of Michigan, and **(c)** Pacific Northwest National Lab.

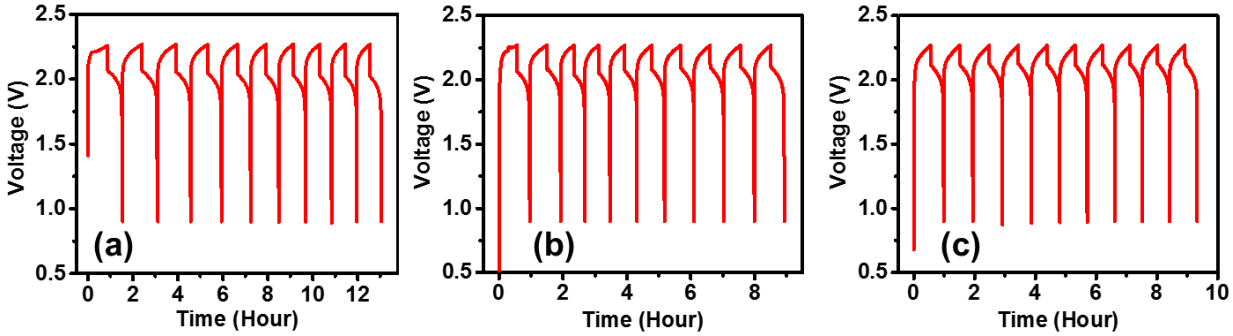

A.6 2D Engineering Drawings of the GEN1 Cell

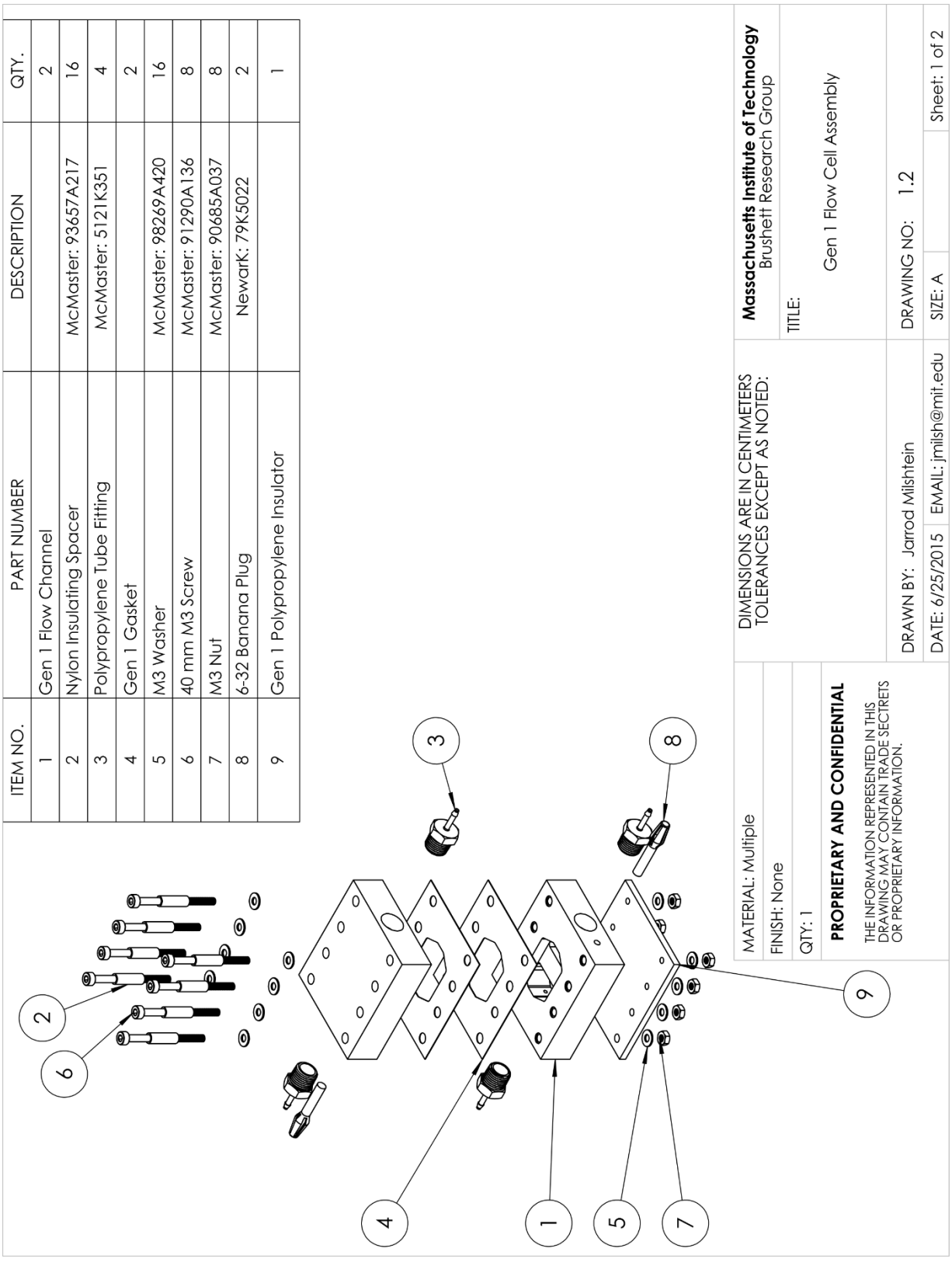

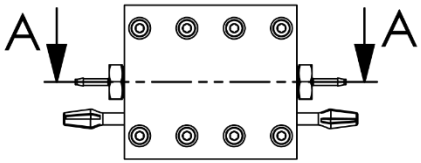

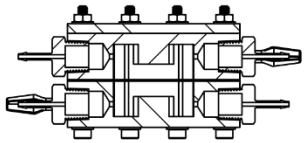

SECTION A-A

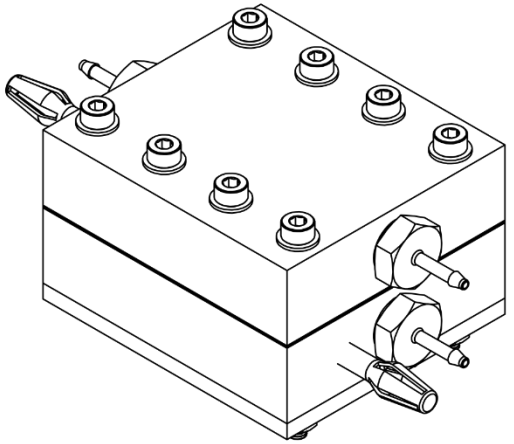

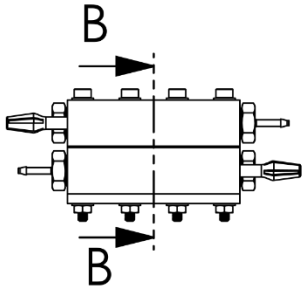

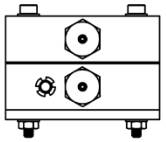

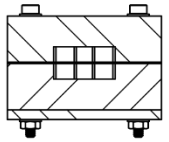

SECTION B-B

MATERIAL: Multiple	DIMENSIONS ARE IN CENTIMETERS TOLERANCES EXCEPT AS NOTED:	**Massachusetts Institute of Technology** Brushett Research Group
FINISH: None		TITLE: Gen 1 Flow Cell Assembly
QTY: 1		
PROPRIETARY AND CONFIDENTIAL THE INFORMATION REPRESENTED IN THIS DRAWING MAY CONTAIN TRADE SECTRETS OR PROPRIETARY INFORMATION.	DRAWN BY: Jarrod Milshtein	DRAWING NO: 1.2
	DATE: 6/25/2015 EMAIL: jmilsh@mit.edu	SIZE: A Sheet: 2 of 2

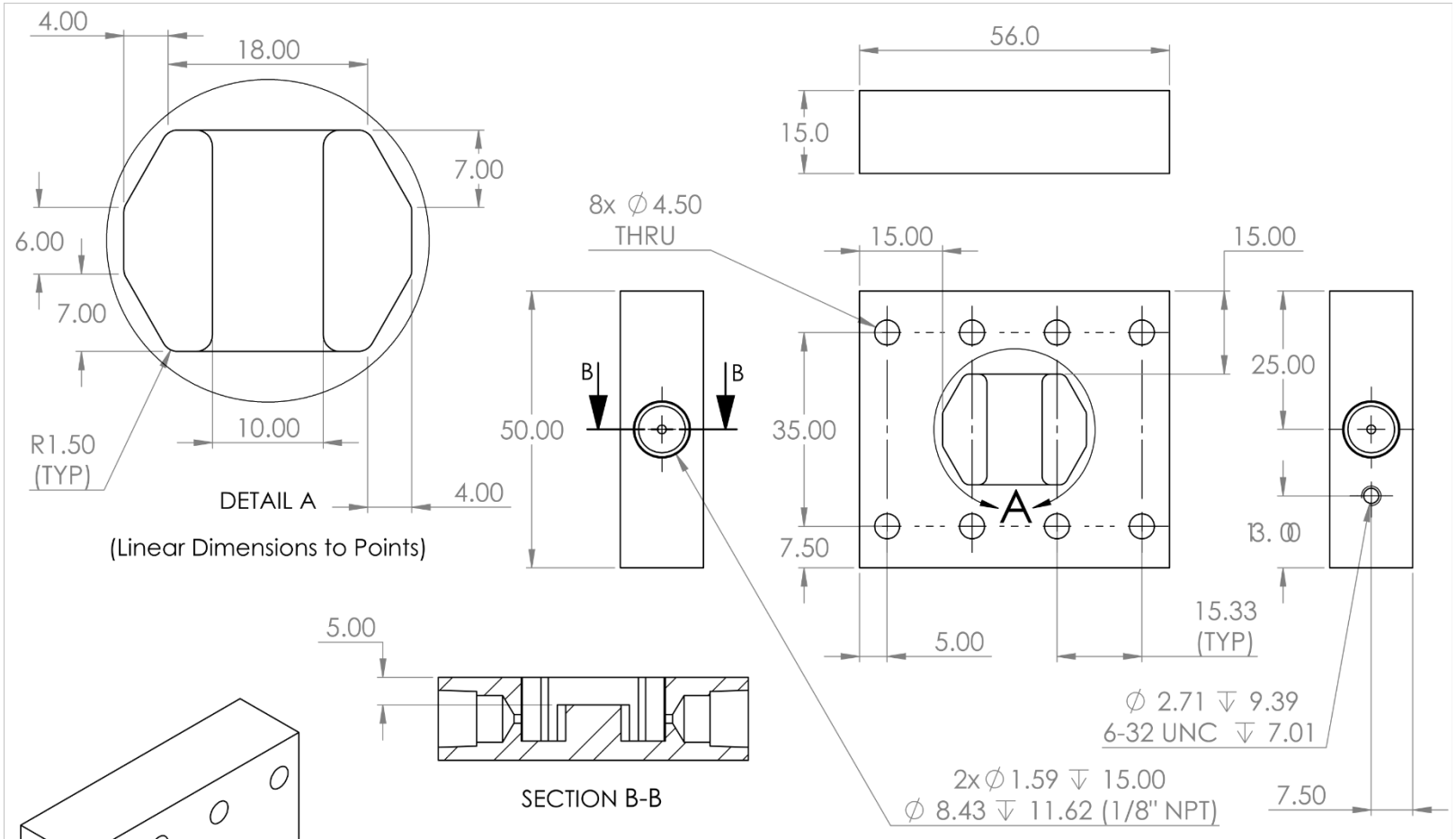

MATERIAL: 316 Stainless Steel	DIMENSIONS ARE IN MILLIMETERS TOLERANCES EXCEPT AS NOTED: ANGULAR: (MACH ±1/2°) (BEND ± 1°) TWO PLACE DECIMAL ± .38 THREE PLACE DECIMAL ± .13 SURFACE FINISH: 63 CONCENTRICITY: ±.08	**Massachusetts Institute of Technology** Brushett Research Group
FINISH: None		TITLE: Flow Channel
QTY: 2		
PROPRIETARY AND CONFIDENTIAL THE INFORMATION REPRESENTED IN THIS DRAWING MAY CONTAIN TRADE SECRECTS OR PROPRIETARY INFORMATION.	DRAWN BY: Jarrod Milshtein	DRAWING NO: 1.2
	DATE: 6/25/2015 EMAIL: jmilsh@mit.edu	SIZE: A Sheet: 1 of 1

2 1

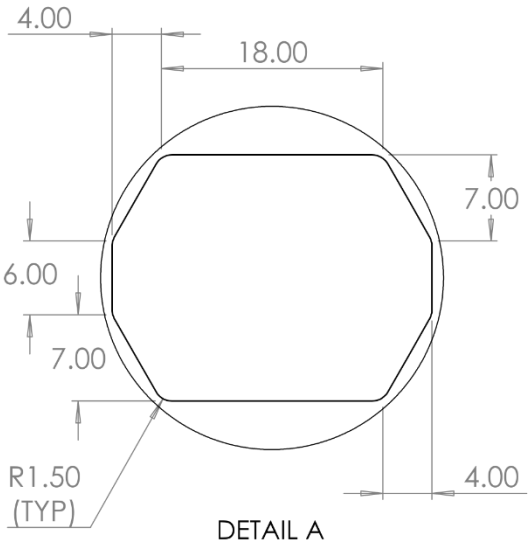

DETAIL A

(Linear Dimensions to Points)

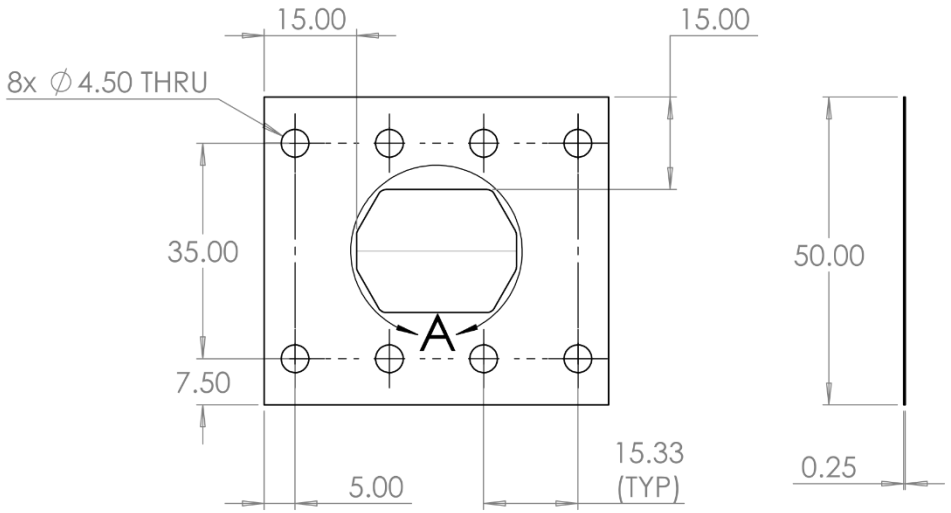

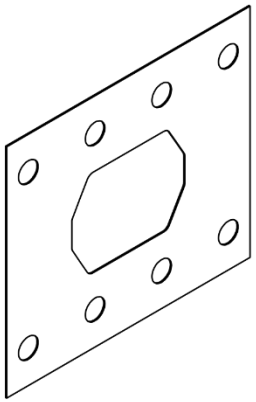

MATERIAL: PTFE	DIMENSIONS ARE IN MILLIMETERS TOLERANCES EXCEPT AS NOTED: ANGULAR: (MACH ±1/2°) (BEND ± 1°) TWO PLACE DECIMAL ± .38 THREE PLACE DECIMAL ± .13	**Massachusetts Institute of Technology** Brushett Research Group
FINISH: None		TITLE: Gasket
QTY: 2		
PROPRIETARY AND CONFIDENTIAL THE INFORMATION CONTAINED IN THIS DRAWING MAY CONTAIN TRADE SECRETS OR PROPRIETARY INFORMATION.	DRAWN BY: Jarrod Milshtein	DRAWING NO: 1.2
	DATE: 6/25/2015 EMAIL: jmilsh@mit.edu	SIZE: A Sheet: 1 of 1

2 1

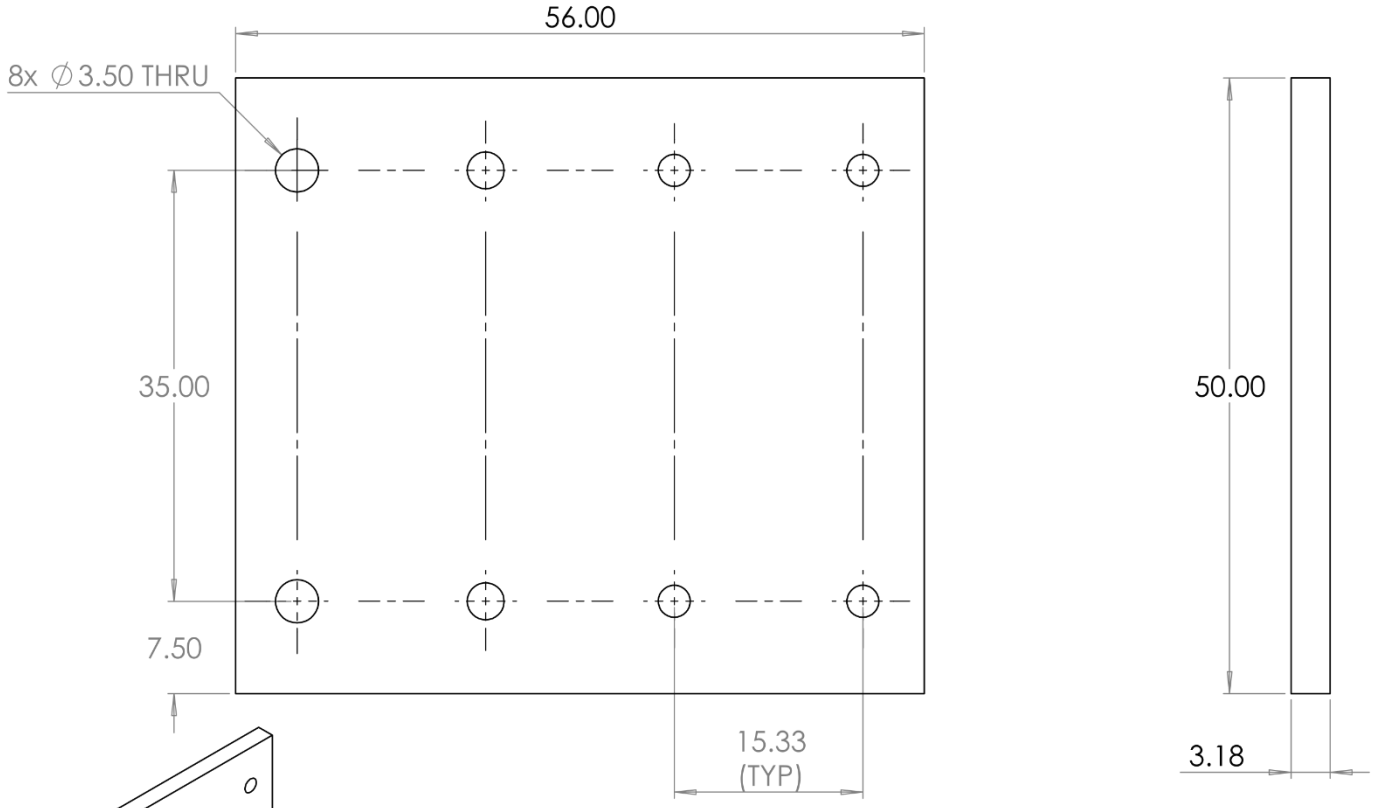

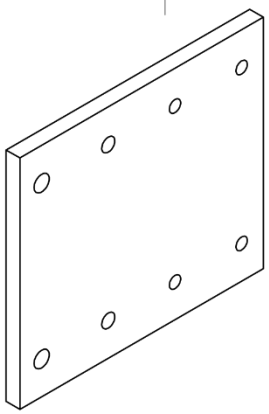

MATERIAL: Polypropylene	DIMENSIONS ARE IN MILLIMETERS TOLERANCES EXCEPT AS NOTED: ANGULAR: (MACH ±1/2°) (BEND ± 1°) TWO PLACE DECIMAL ± .38 THREE PLACE DECIMAL ± .13	**Massachusetts Institute of Technology** Brushett Research Group
FINISH: None		TITLE: Polypropylene Insulator
QTY: 1		
PROPRIETARY AND CONFIDENTIAL THE INFORMATION REPRESENTED IN THIS DRAWING MAY CONTAIN TRADE SECRETS OR PROPRIETARY INFORMATION.	DRAWN BY: Jarrod Milshtein	DRAWING NO: 1.2
	DATE: 6/25/2015 EMAIL: jmilsh@mit.edu	SIZE: A Sheet: 1 of 1

2 1

B. GEN2 Flow Cell Standard Operating Procedure

This appendix is adapted from a standard operating procedure manual developed for and distributed across the Joint Center for Emery Storage Research (JCESR) in 2016. The original purpose of this material was to provide JCESR researchers with a standard experimental procedure for engaging high-performance flow cell studies with inexpensive, chemically compatible, and adaptable hardware.

B.1 Bill of Materials

Part	Description	Supplier	Part Number
Basic GEN2 Materials Set			
Polypropylene Flow In/Out Plate*	Custom Design Gen 2.4 Cell Flow Distributor & Backing Plate, Request Quote	Adaptive Engineering	N/A
1/8" Thick Graphite Sheet Stock (1 ft^2)*	0.125" X 12" X 12" Custom G347B Plate, Ground 1 Dimmension, Request Quote	MWI Inc.	G347B-311-1CC
Graphite Flow Field*	Custom Design Gen 2.4 Flow Field, Request Quote	Adaptive Engineering	N/A
Bolts (Pkg. of 25)	18-8 Stainless Steel Socket Head Cap Screw, 1/4"-28 Thread, 2-1/4" Length, pkg 25	McMaster-Carr	92196A340
Nuts (Pkg. of 100)	Type 18-8 Stainless Steel Hex Nut, 1/4"-28 Thread Size, 7/16" Wide, 7/32" High	McMaster-Carr	91845A105
Kal-Rez O-rings for Organics	Extreme-Chemical Kalrez 4079 O-Ring, Dash Number 014	McMaster-Carr	9568K19
.005 Teflon Gasket Material (1 ft^2)	Film Made with Teflon® PTFE, 0.005" Thick, 12" Width, price per ft	McMaster-Carr	8569K38
.010 Teflon Gasket Material (1 ft^2)	Film Made with Teflon® PTFE, 0.010" Thick, 12" Width, price per ft	McMaster-Carr	8569K41
.003 Teflon Gasket Material (1 ft^2)	Film Made with Teflon® PTFE, 0.003" Thick, 12" Width, price per ft	McMaster-Carr	8569K36
.002 Teflon Gasket Material (1 ft^2)	Film Made with Teflon® PTFE, 0.002" Thick, 12" Width, price per ft	McMaster-Carr	8569K34
.001 Teflon Gasket Material (0.7 ft^2)	PTFE Shim Stock, Sheet, 0.001" Thick, 8" x 12"	McMaster-Carr	1192N11
Banana Plugs	Pomona Electronics 3263 Test Plugs & Test Jacks 6/32 STUD UNINS PLUG BU-00241	Mouser Electronics	565-3263
Barbed Tube Fittings	Chemical-Resistant Polypropylene Barbed Fitting, High-Temperature, Straight, 1/16" Tube ID x 1/8 Male Pipe, pkg 10	McMaster-Carr	5121K351
Recommended Supplements for Better Sealing with Organics			
Swagelok PFA Tube Fittings‡	PFA Male Connector, 1/8" tube to 1/8" NPT	Swagelok	PFA-220-1-2
Swagelok PFA Notcher‡	PFA 1/8" Groove Notcher	Swagelok	MS-GC-2
3/16" Tube - 1/18" Tube adapter, SS	Type 316 Stainless Steel Yor-Lok Tube Fitting, Straight Connector for 3/16" x 1/8" Tube OD	McMaster-Carr	5182K701
Swagelok PFA Tubing‡	1/8" PFA Swagelok Tubing, 100ft	Swagelok	PFA-T2-030-100
PFA Reservoirs	10 mL Sealed Jar, (2) 1/8" Ports	Savillex	102-0010-01

Carbon Paper - GDL 25AA	GDL 25 AA Diffusion Media, DIN A4 21 x 29 cm	NafionStore	GDL-25-AA-EU-US
1/2" Teflon Tape	Commercial Grade Pipe Thread Sealant Tape, 16 Yard L x 1/2" Wide, .0028" Thick, 0.5 G/CC Density	McMaster-Carr	4591K12
Norprene Tubing L/S-14	Masterflex Norprene tubing (A60 G), L/S 14, 50 ft, HV-06404-14	Cole-Parmer	06404-14
Compressible PTFE Gasket Tape*†	GORE® gasket tape without adhesive 2" x 0.010" x 50', Request Quote	Johnson Packings	0050102.00NA
Recommended Supplements for Better Sealing with Aqueous Systems			
3/16" Tube - 1/8" Tube adapter, PTFE*	Swagelok 3/16" tube to 1/8" tube reducer, PTFE, Custom, Request Quote	Swagelok	T-300-1-2
Swagelok PFA Tube Fittings‡	PFA Male Connector, 1/8" tube to 1/8" NPT	Swagelok	PFA-220-1-2
Swagelok PFA Notcher‡	PFA 1/8" Groove Notcher	Swagelok	MS-GC-2
Swagelok PFA Tubing‡	1/8" PFA Swagelok Tubing, 100ft	Swagelok	PFA-T2-030-100
Nafion Membrane	Nafion™ Membrane N115, 30cm x 30cm	Nafion Store	N115-US-0.30x0.30
Viton O-rings for Acid	Chemical-Resistant Multipurpose O-Ring, Viton®, 1/16 Fractional Width, Dash Number 014	McMaster-Carr	9464K19
Recommended Assembly Tools			
Micro-torque driver	Adjustable Slip-Release Torque Screwdriver, 2 to 12 in.-lbs. Torque Range, with Certificate	McMaster-Carr	5871A52
3/16" Hex bit	3/16" Hex Bit, 1/4" Hex Shank	McMaster-Carr	8526A67
Gasket Punch, 2up*	Custom Die for Gen 2.4 Gasket Cutting, Request Quote	Millenium Die	N/A - Custom
Static Eliminator	Staticmaster Ionizing Cartridge, NRD LLC 2U500	Thomas Scientific	3620A30
Thickness Gauge	Mitutoyo Loop Handle Dial Thickness Gauge, 0-0.05" Range, 1-1/8" Throat Depth, Number 7326S	McMaster-Carr	2102A3
Recommended Pump			
Pump Drive	Masterflex L/S Digital Drive, 100 RPM, 115/230 VAC 07522-30	Cole-Parmer	FF-07522-30
Pump Head	Masterflex L/S two-channel Easy-Load II pump head, SS rotor.	Cole-Parmer	FF-77202-60

Common Assembly Tools: 7/16" Wrench, 7/16" Socket Wrench, 1/2" Socket Wrench, 1/2" Wrench, 1/4" Wrench (2x), Tweezers, Razor Blade, Electrode Template, Membrane Template, Scissors

B.2 How to Cut Gaskets for the GEN2 Flow Cell

An accompanying instructional video has been posted to YouTube:

https://www.youtube.com/watch?v=RFqcaIDrlA8&feature=youtu.be

Gasket Cutting Procedure:

1. Lay your gasket punch (or die) on a flat surface with the blades pointing upward.

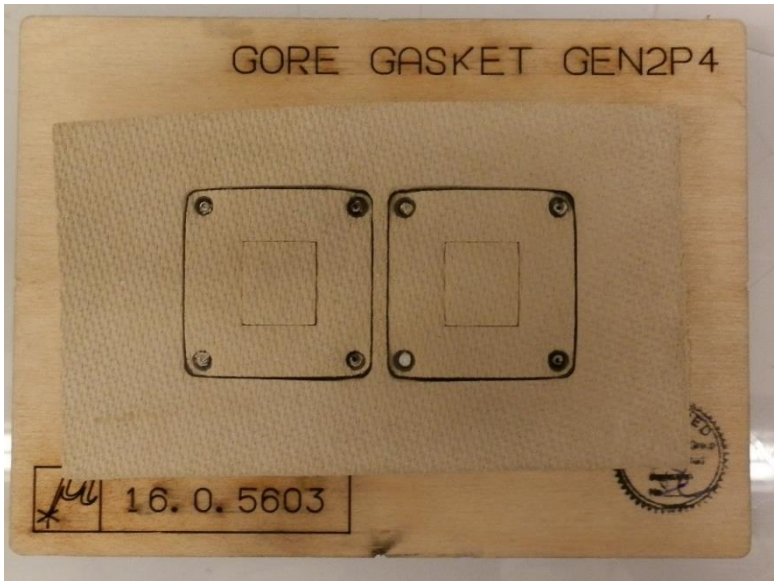

2. Cut a small rectangle of PTFE (Teflon) sheeting to lay flat over the blades of the gasket die.

3. Place a flat piece of acrylic over the Teflon sheet. This acrylic is meant to prevent the blades from dulling quickly against the platens of the carver press.

4. Slide a flat sheet of steel under the gasket die. This is meant to protect the platens from the dull edge of the blades, which can be seen from the back of the gasket die.

5. Open the Carver press enough to insert your layered assembly.

6. Insert your layered assembly carefully, so as not to disturb the alignment of the PTFE sheeting over the blades.

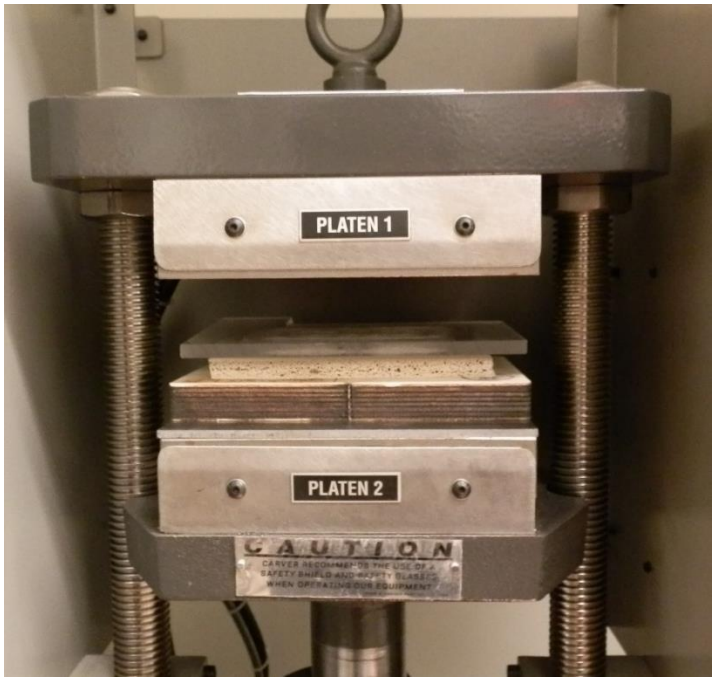

7. Raise the lower platen until your assembly just touches the upper platen.

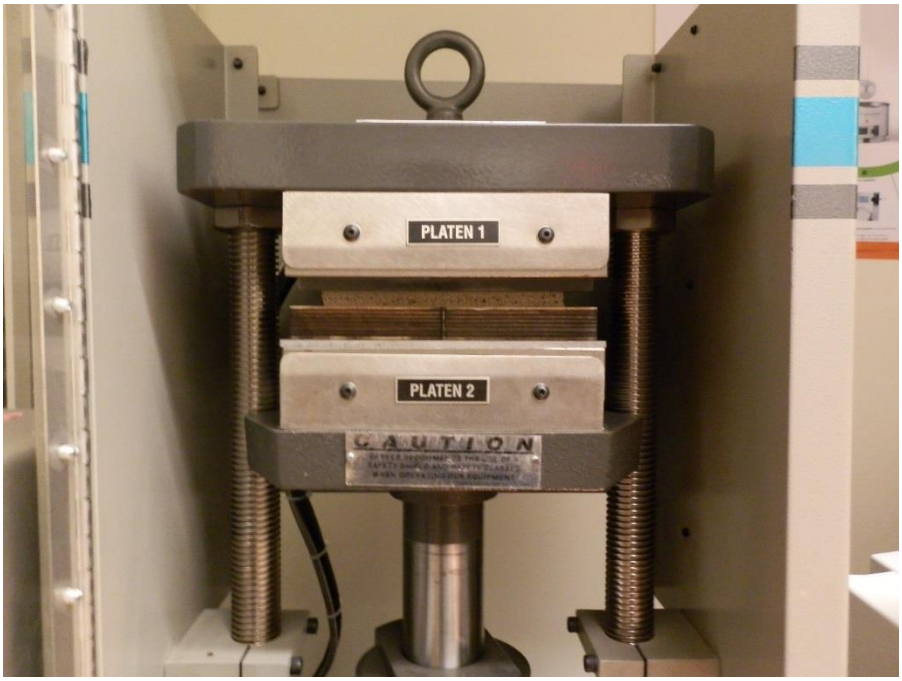

8. Crank the lever to raise the applied force. We typically press to 3000lbf on our 6in. x 6in. press.

9. Release the hydraulic force, and remove your assembly from the press. Pull the acrylic off.

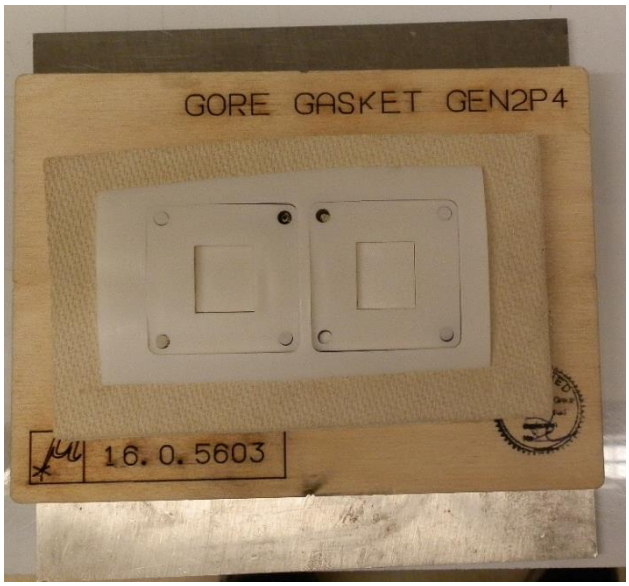

10. Separate the PTFE pieces to obtain your gaskets.

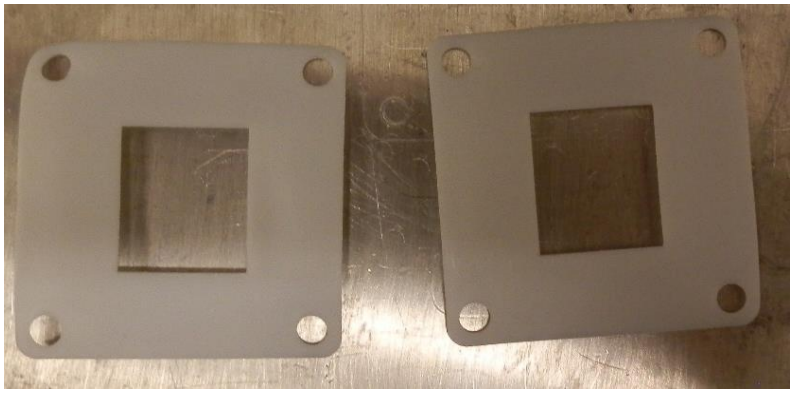

B.3 How to Assemble the GEN2 Flow Cell

An accompanying instructional video has been posted to YouTube:

https://www.youtube.com/watch?v=eEPBM8QQw3U

<u>Required Parts and Tools:</u>

A) Bolts (4x)
B) Nuts (4x)
C) O-rings (4x)
D) Tube Fittings (4x)
E) Banana plugs (2x)
F) Alignment pins (4x)
G) Carbon paper electrodes
H) Separator
I) Graphite flow fields (2x)
J) Electrolyte diffusers (2x)
K) Teflon gaskets
L) Teflon tape
M) Static wand
N) 7/16” wrench
O) 1/4" wrench (2x)
P) 1/2” socket wrench
Q) Torque screwdriver
R) Scissors
S) Spring-loaded micrometer

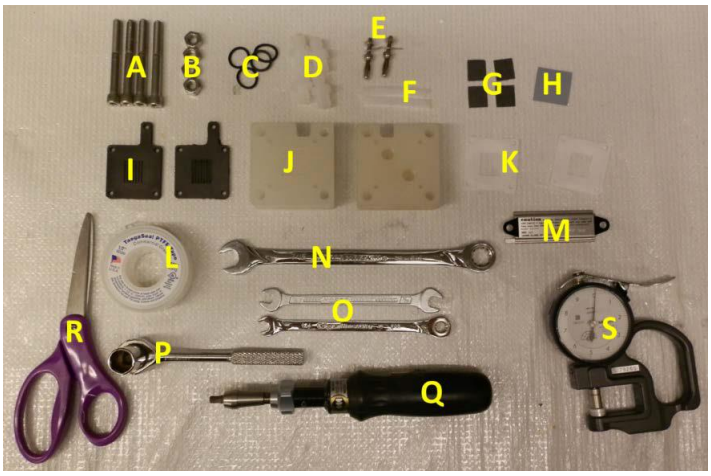

Procedure:

1. Measure and select the electrodes and gaskets

    a. Using a spring-loaded micrometer, measure the thickness of the electrodes for each side of the flow cell. The spring-loaded mechanism will ensure that the same force will be applied during every electrode measurement.

    b. Calculate the required gasket thickness using the Excel calculator spreadsheet. You will need to input the electrode thickness and desired compression. 20% compression is typically a good compression to begin.

    c. Using a spring-loaded micrometer, measure the effective thickness of the Teflon gaskets. Apply pressure with your fingers to the spring mechanism to ensure the Teflon is "compressed." You can layer together multiple pieces of Teflon gaskets to achieve your target gasket thickness.

2. Wrap (4x) PFA compression tube fittings (Swagelok, PFA-220-1-2) with Teflon tape.

3. Lay the polypropylene electrolyte diffusers with the slotted face pointing upward (2x).

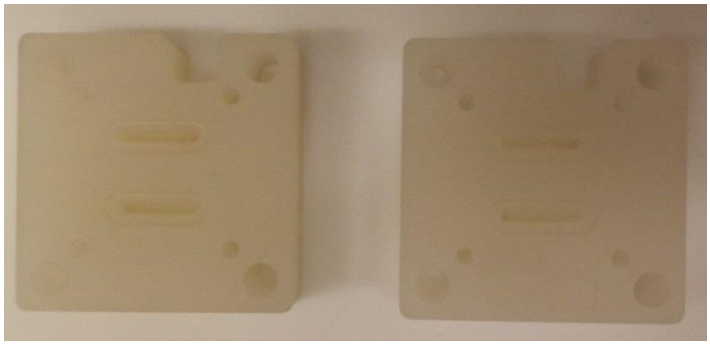

4. Push O-rings (4x) into the rounded groove surrounding the slots.
   a. For non-aqueous electrolytes experiments, use Kalrez O-rings.
   b. For acid electrolyte experiments, use Viton O-rings.

c. For alkaline electrolytes, use EPDM O-rings.

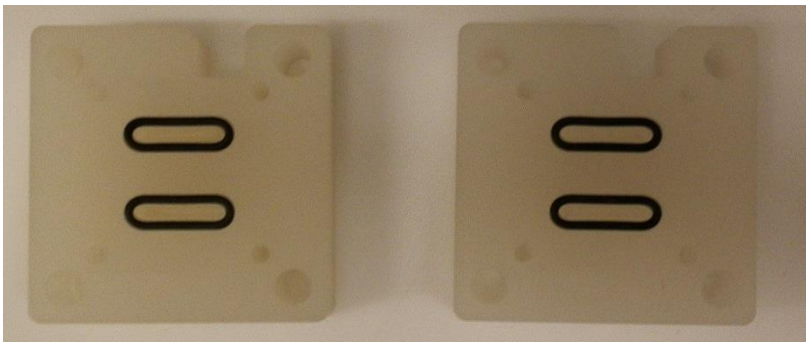

5. Lay 1x of the electrolyte diffusers (with O-rings) down with bolts (4x) inserted from the bottom side:

6. Place 4 PFA or Teflon alignment pins into the electrolyte diffuser:

7. Slide the first graphite flow field over the alignment pins. The tab should be on the RIGHT side of the cell. The tab should align with the notch in the electrolyte diffuser.

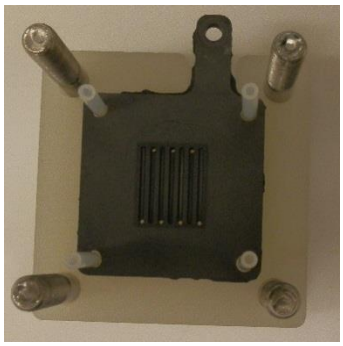

8. Slide the first set of Teflon gaskets over the alignment pins. The grooves in the flow field will be visible through the center of the gasket.

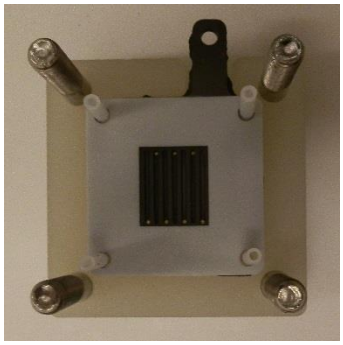

9. Align the first carbon paper electrode inside the square hole in the Teflon gasket. There should be a small gap between the carbon paper electrode and Teflon gasket on all sides. The carbon paper electrode will cover the flow field grooves.

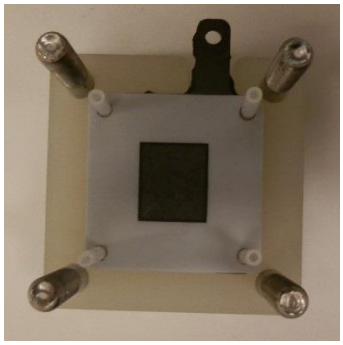

10. Place the separator over the carbon paper electrode and Teflon gasket. There should be approximately equal distance between the separator and Teflon gasket edges. The separator will cover the carbon paper electrode.

11. Slide the second set of Teflon gaskets over the alignment pins.

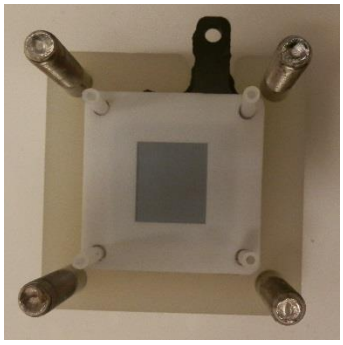

12. Align the second carbon paper electrode inside the square hole in the Teflon gasket. There should be a small gap between the carbon paper electrode and Teflon gasket on all sides. The second carbon paper electrode will cover the center of the exposed separator.

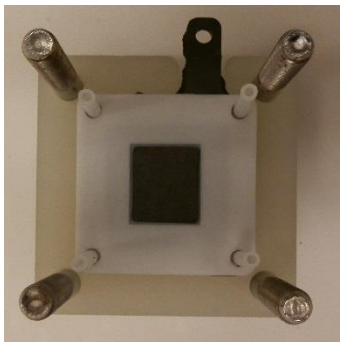

13. Slide the second flow field plate over the alignment pins. The grooves in the flow field should be facing DOWN. The tab should be on the LEFT side of the cell.

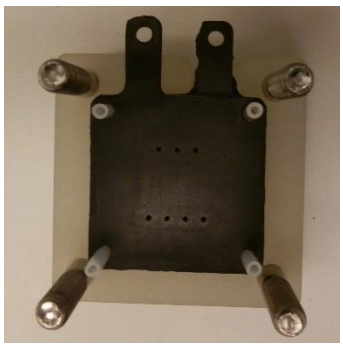

14. Slide the second electrolyte diffuser (with O-rings inserted) over the Teflon alignment pins and bolts. The open slots and O-rings should be facing DOWN. The notch in the electrolyte diffuser should be aligned with the graphite tab on the LEFT.

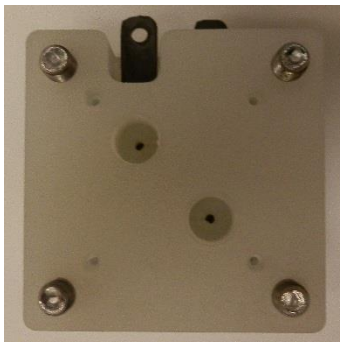

15. Thread the #1/4-28 nuts (4x) over the bolts until they are finger tight.

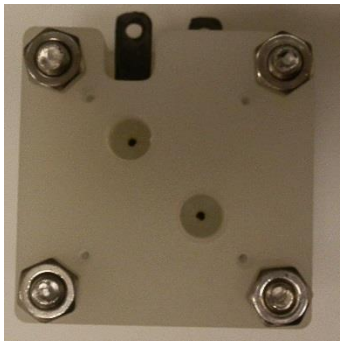

16. Push the banana plugs (2x) through the holes in the graphite tabs. The banana connection sides should point through the notch in the electrolyte diffusers. On the threaded side of the banana plug, place a metal spacer and thread on the nut. Secure the banana plug using two 1/4" wrenches. Tighten the nut as much as possible without deforming the banana plug or breaking the graphite tab. The graphite tab breaks easily under lateral force. This is a key connection to ensure that the contact resistances of the cell are sufficiently low.

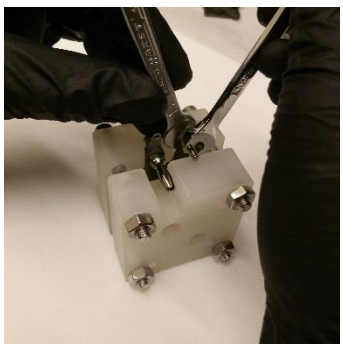

17. Use a torque screwdriver (or wrench) and 7/16” wrench to tighten each bolt to 3 lb-in. Follow a star pattern around the cell (e.g. 1, 4, 2, 3) to ensure equal compression across the cell and minimize leaking.

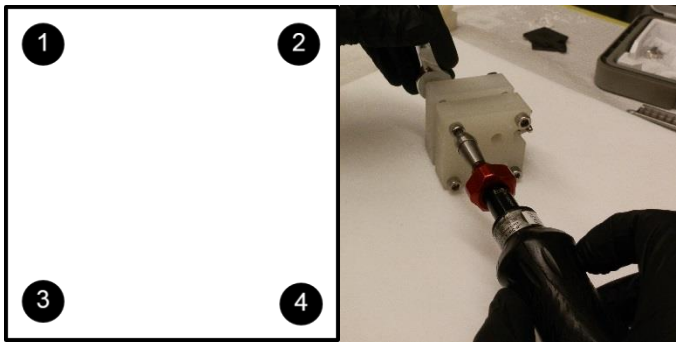

18. Incrementally increase the torque by tightening each bolt to 5 lb-in, 7 lb-in, and then to 10 lb-in using the same star pattern for each step.

19. Double check each screw to ensure the correct torque has been applied.

20. Screw in the PFA compression fittings so that they are finger tight.

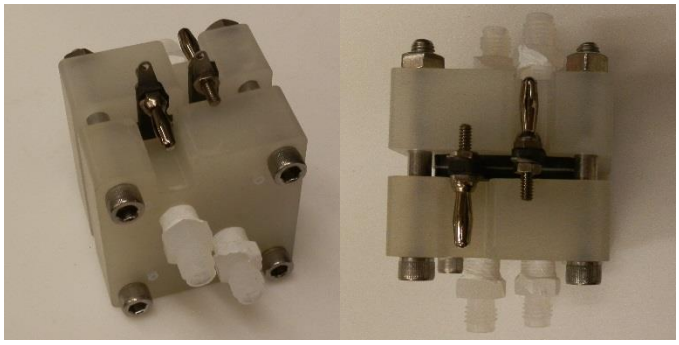

21. Tighten the PFA compression fittings using a 1/2” socket wrench. Leave approximately a 1/8 in gap between the hex nut and the surface of the electrolyte diffuser. Over-tightening the PFA fittings can actually increase the likelihood of leaks.

22. The final assembled flow cell:

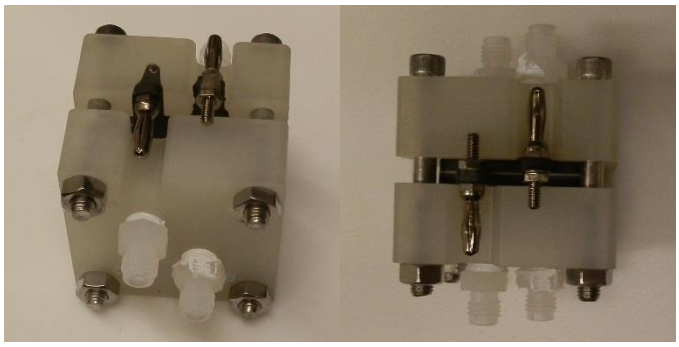

B.4 How to Operate the GEN 2 Flow Cell

An accompanying instructional video has been posted to YouTube:

https://www.youtube.com/watch?v=ne8Khp2bUVw

Procedure:

22. Attach the pump head to pump according to the pump head manual.

23. Bring an assembled GEN 2 flow cell into the glove box.

24. Screw down the blue PFA compression caps that attach to the pumping that loops through the pump head. Tubing through the pump head should attach to the two TOP tube fittings. Do this until finger tight.

25. Finish tightening the blue caps with a 1/2" wrench. Do not overtighten. See Swagelok manual for proper connection practices.

26. Tighten down two more tubes with compression fittings on one end. These tubes will connect to the reservoir. These tubes should connect to the BOTTOM tube fittings.

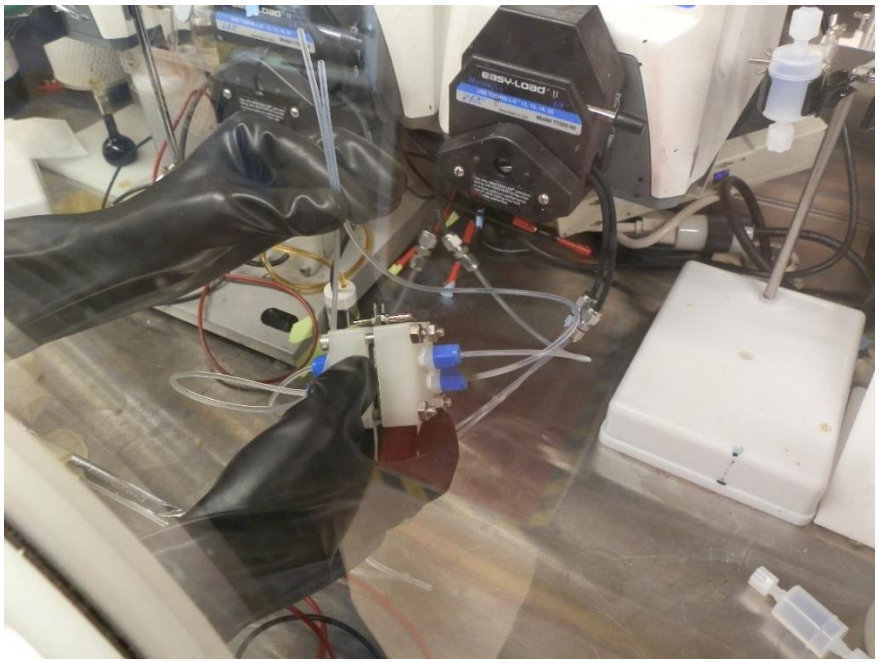

27. Secure the PFA reservoirs in place.

28. Connect the tubes coming from the BOTTOM fitting on the flow cell to the bottom ports on the reservoirs.

29. Tighten the PFA threaded fitting with your fingers.

30. Ensure that the pump is in “volume dispense” mode. Use the disconnected tubing ends to pull 10 mL of electrolyte through the flow cell and into the reservoirs.

31. Stop pumping. Connect the remaining tubes (don’t cross the lines!). Switch the direction of the pump and turn back to continuous mode.

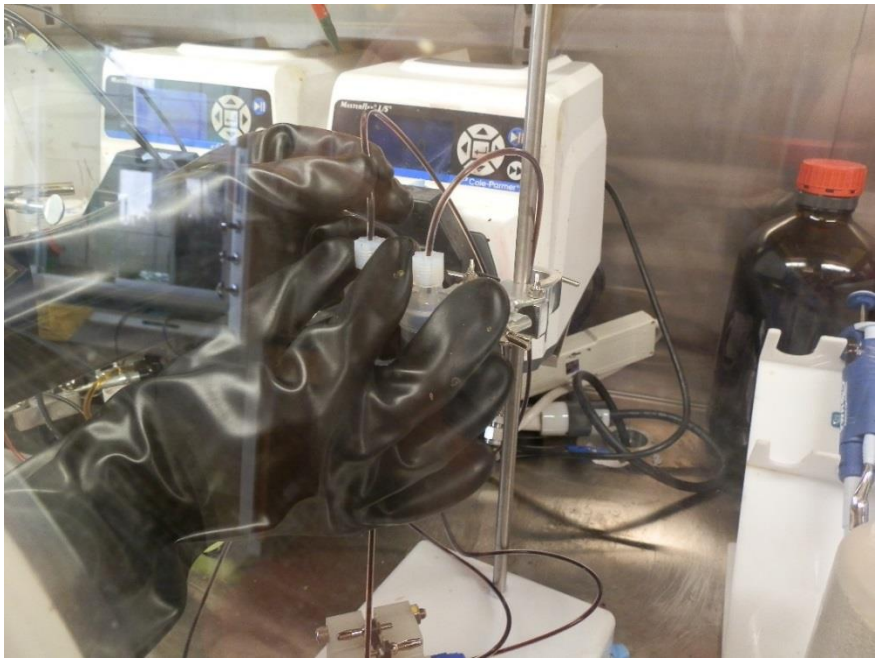

32. Turn on the pump in continuous mode. The electrolyte should be pulled from the bottom of the reservoir and through the bottom tube fittings in the flow cell. Pumping from bottom to top in the flow cell helps to remove air bubbles.

33. Check for rapid leaks and turn the flow cell side to side several times to purge air bubbles trapped in the cell.

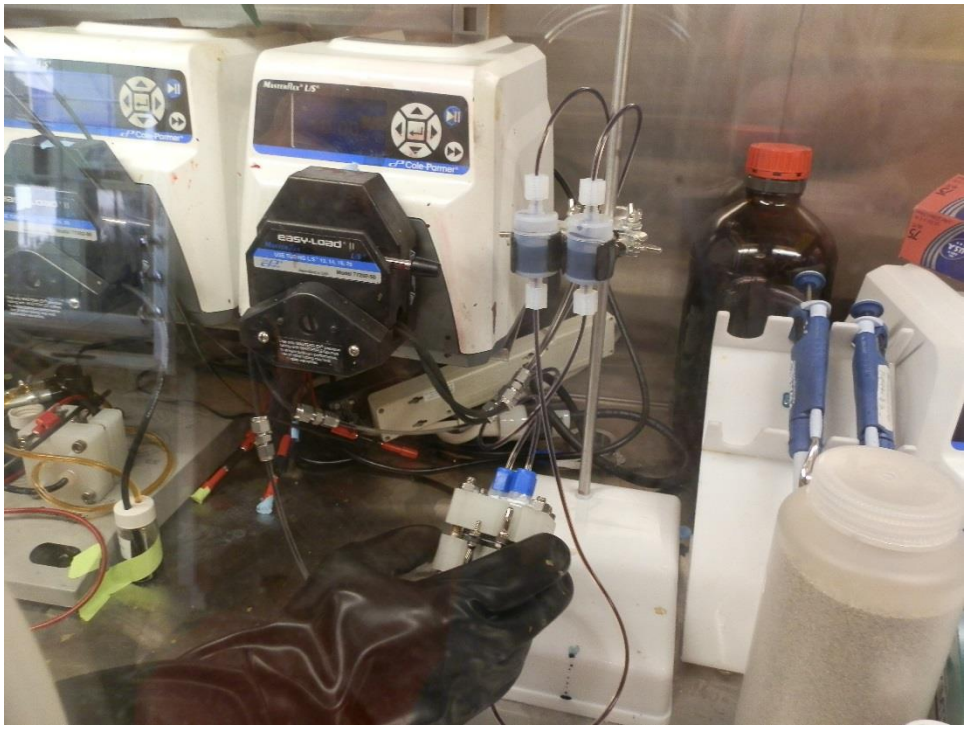

34. Connect the potentiostat or battery tester leads to the flow cell using alligator clips or banana plugs. Banana plugs should be oriented so that they are inside the notch in the electrolyte diffuser. When putting on the banana plugs, press with even pressure on both sides of the graphite tab to make sure that the tab does not break.

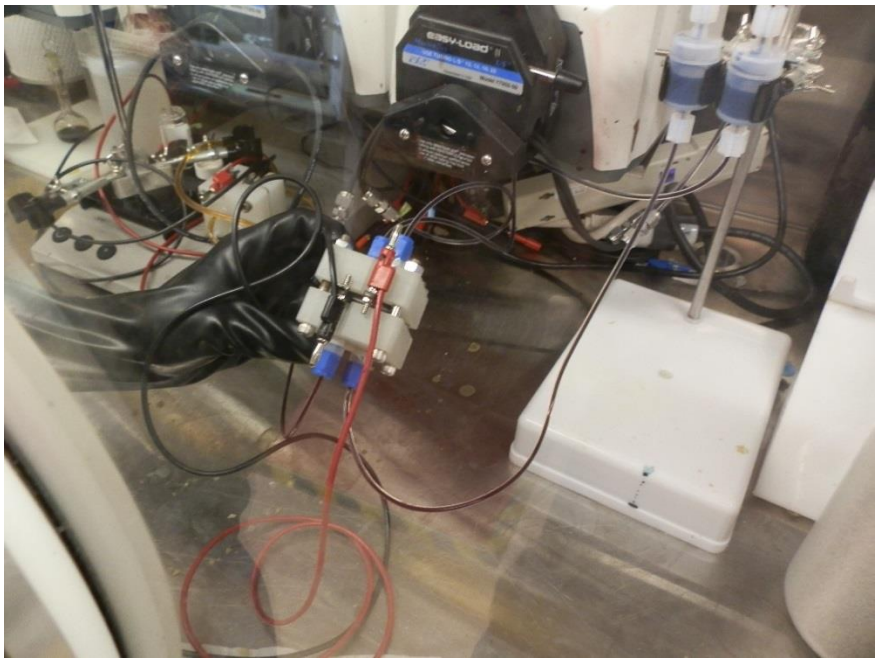

35. Now you are ready to begin cycling experiments. The final experimental set-up should look like:

B.5 How to Clean the GEN2 Flow Cell

Procedure:

1. Carefully disconnect the potentiostat leads from the Gen 2 cell banana plugs.

2. Use the pump to return all of the electrolyte to the reservoir(s). This often involves switching the pump direction, but the exact method to do this may depend on the setup that you've used.

3. Empty the reservoir(s) into the appropriate waste container, and rinse with an appropriate solvent. A safe choice is to use the solvent in your electrolyte. We've found acetone to be fairly effective for cleaning up organic electrolytes.

4. Refill the reservoir(s) with about 10mL of solvent and circulate this through your flow cell system for about 5 minutes. We'll typically use a flowrate of 10mL/min.

5. Once again, use the pump to return all of the fluid to the reservoir(s).

6. Empty the reservoir(s) into the appropriate waste container.

7. Disconnect the tubing from the flow cell fittings.

8. Move the flow cell and reservoirs to a ventilated hood for further cleaning.

9. Carefully remove the banana plugs and set them aside for your next experiment.

10. Disassemble the rest of the flow cell piece by piece in the hood and rinse each part with an acetone squirt bottle over the organics waste container or a beaker to catch the discharge.

11. The fittings, polypropylene backing, and alignment pins may be submerged in a beaker of acetone and placed in a bath sonicator for a half hour to remove residue.

12. The bolts, nuts, and banana plugs should be cleaned on a need-to-clean basis as they don't contact the electrolyte and their corrosion will impact your ohmic resistance and assembly.

13. Thoroughly rinse the PTFE gaskets and the graphite plates with acetone. Don't sonicate the PTFE gaskets in acetone as this will wrinkle them and reduce their sealing effectiveness. Don't sonicate the graphite plates at all as this degrades them.

14. After you finish rinsing and sonicating in acetone, dispose of the acetone in an organic waste stream, place the polypropylene plates, the fittings, and the gaskets in a beaker of water. Sonicate this for 30 minutes.

15. Rinse the graphite plates, polypropylene plates, fittings, and gaskets with DI or RO water, and place them in a drying oven at 60-80oC overnight in preparation for your next use.

B.6 GEN2 Flow Cell Validation Conditions and Results

An accompanying instructional video has been posted to YouTube:

https://www.youtube.com/watch?v=ne8Khp2bUVw

Electrolyte Composition and Volume:

- 0.25 M vanadium acetylacetonate (STREM chemicals)
- 0.5 M tetrabutylammonium tetrafluoroborate (BASF)
- Acetonitrile (Acros Organics, Extra Dry)
- 10 mL per side

Cell Configuration:

- Daramic 175 separator (1 layer)
- SGL 25AA Carbon Paper Electrodes (2 layers, as received)
    - 20% compression, 1.6 cm x 1.4 cm
- PTFE gaskets
- Kalrez O-rings
- PFA compression fittings
- Savillex reservoirs
- 10 mL min^{-1} flow rate

Cell Cycling Conditions:

- 20 mA cm^{-2} (55 mA)
- Upper Potential Cutoff: 2.27 V
- Lower Potential Cutoff: 1.0 V

Impedance Measurement of As-Assembled Cell: $R_\Omega = 2.14\ \Omega\ cm^2$

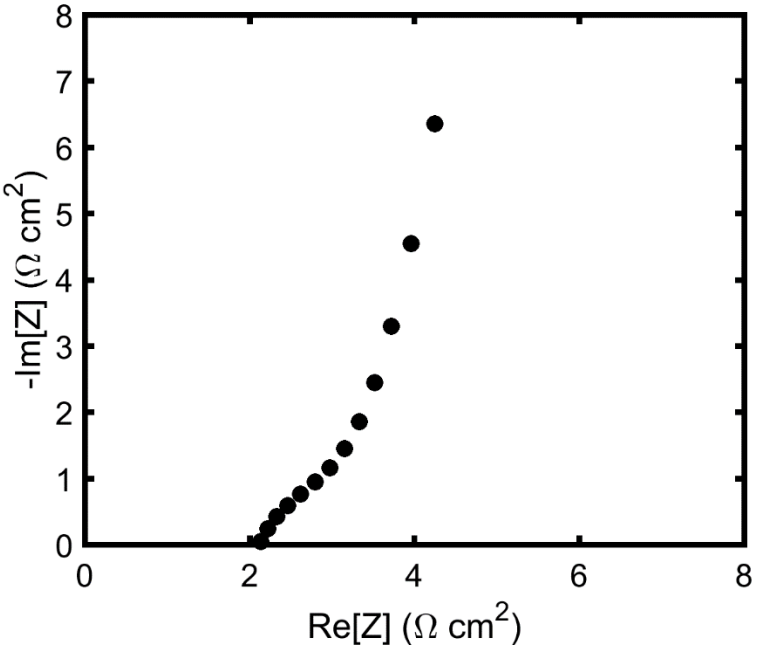

Polarization Curve at 50% SOC:

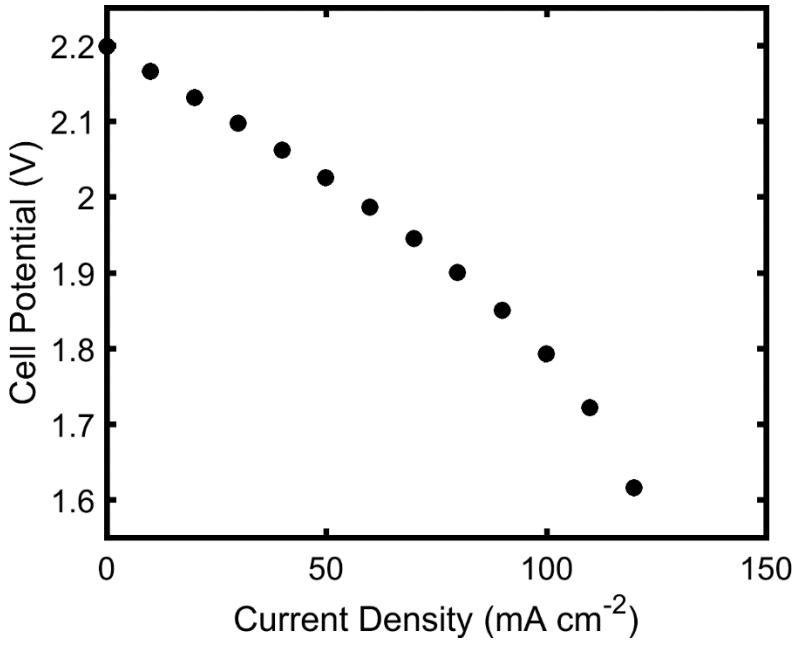

Power Density Curve at 50% SOC:

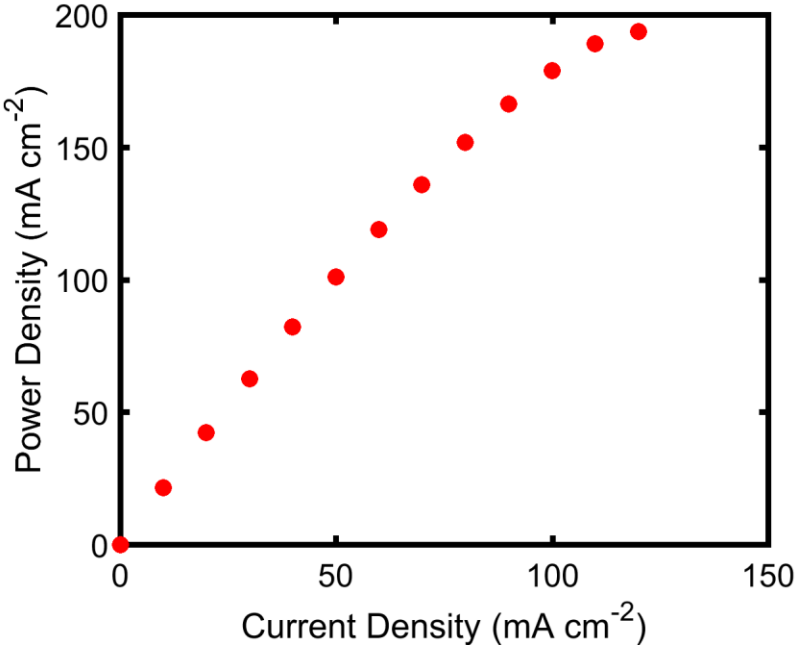

Impedance Spectra at 50% SOC: R_{Ω} = 1.80 Ω cm^2, R_{DC} = 3.09 Ω cm^2

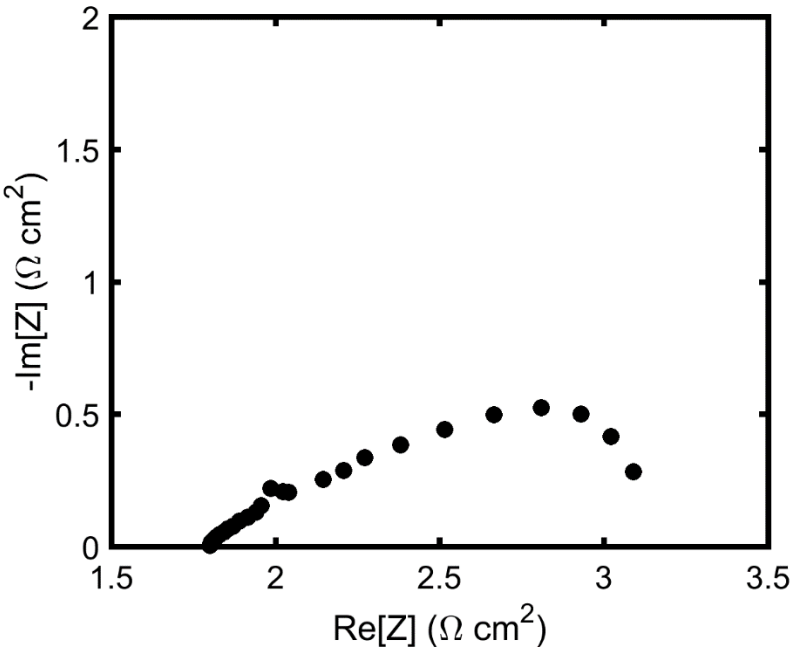

Cycling Performance for 20 Cycles:

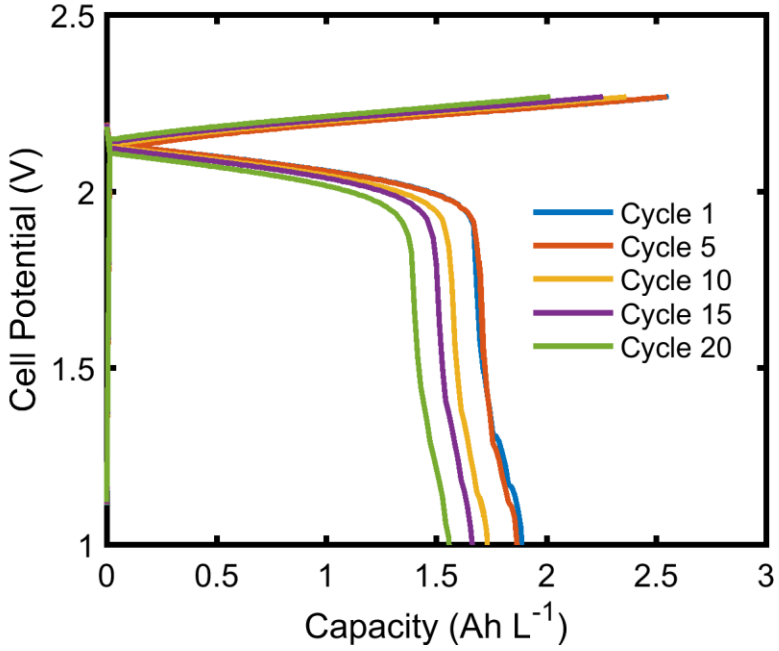

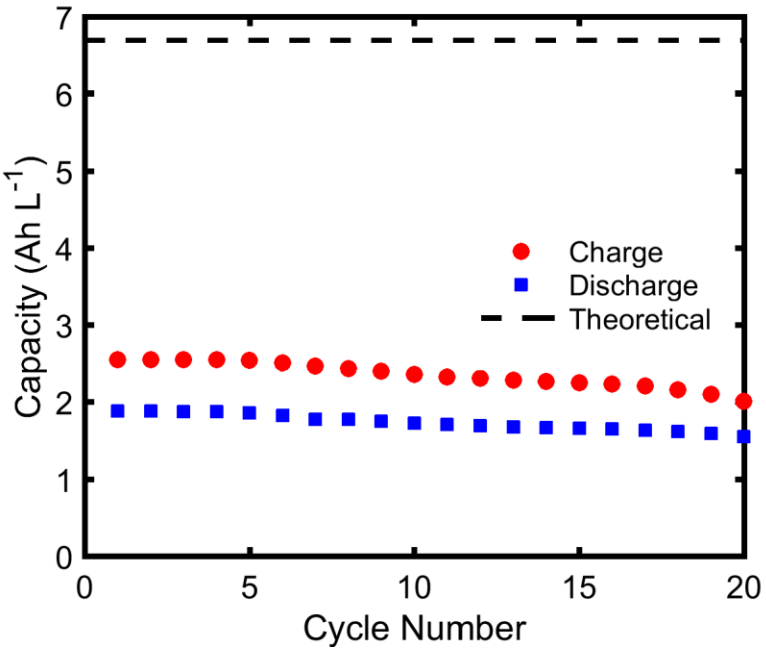

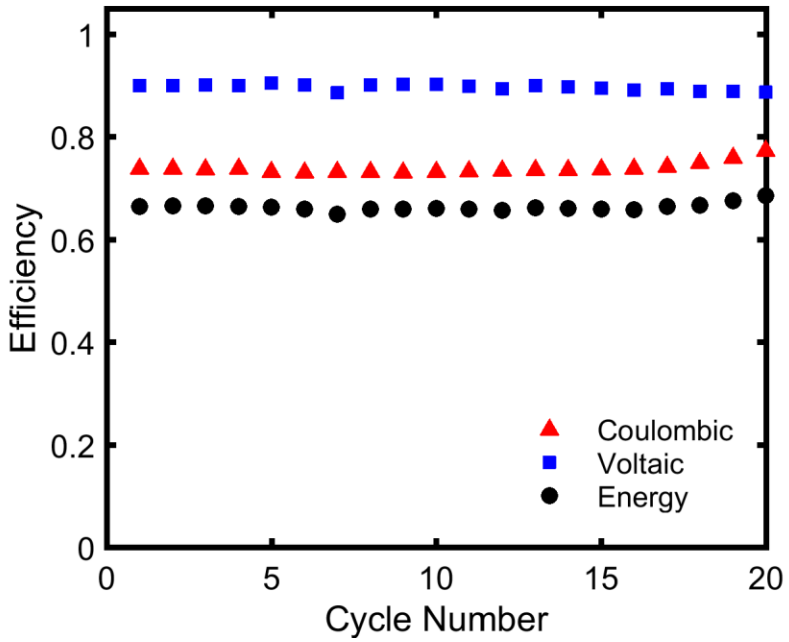

	Coulombic Efficiency (%)	*Voltaic Efficiency (%)*	*Energy Efficiency (%)*	*Charge Capacity (Ah L^{-1})*	*Discharge Capacity (Ah L^{-1})*	*Discharge Capacity Fade (%)*
Mean Value, 20 cycles	**74**	**90**	**66**	**2.36**	**1.74**	**17.4**

B.7 Flow Cell Configurations

Single Electrolyte Flow Cell (Figure 1):

How it works: The flow cell is connected to a single reservoir containing a model active material[1] (e.g., TEMPO, Fc1N112-TFSI, viologen) at 50% state-of-charge (SOC).[2,3] The electrolyte flows through the positive electrode side of the cell, oxidizing some fraction of the active material. Upon leaving the cell, the active species is recirculated through the negative electrode, reducing the active species, after which the electrolyte returns to the reservoir. Thus, the reservoir SOC should be unchanging with time.

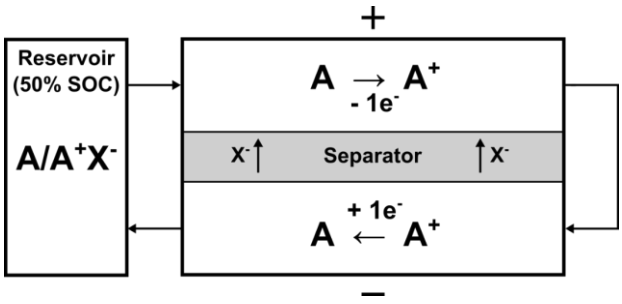

Figure 1: Schematic of the single electrolyte flow cell, where A is the neutral active species, A^+ is the charged active species, and X^- is a monovalent anion.

What can we learn?: This technique is best suited for determining flow cell area-specific resistance (ASR) via polarization or impedance measurements. In this configuration, the cell operates at steady-state over a wide range of flow rates and current densities.[2] Further, crossover effects do not degrade performance, and this technique offers simple cell-level analysis without the need for reference electrodes, since nearly identical processes occur on either side of the cell.[3] Polarization measures the overall cell performance, while impedance can help breakdown the ASR into its various components: ohmic, charge transfer, and mass transfer. This technique indicates reactor performance as a function of flow field design, electrode morphology, electrode thickness, flow rate, separator type, active species concentration, electrolyte conductivity, and electrolyte viscosity. .

Typical Operating Conditions: Active species concentration ≥ 0.5 M. Solution viscosity < 50 mPa·s. Scan ± 0.6 V during polarization measurements. Scan from 5 mHz to 1 MHz during impedance measurements.

Symmetric Flow Cell (Figure 2):

How it works: The symmetric flow cell allows for cycling of both the reduced and oxidized states of an active material without the presence of additional compounds. The reduced form of the active species (A) serves as the starting positive electrolyte material, while the oxidized active species (A^+) is the initial negative electrolyte material. In this configuration, the active species on either side of the cell oscillates between A and A^+, shuttling a charge-balancing counter-anion across the cell [1].

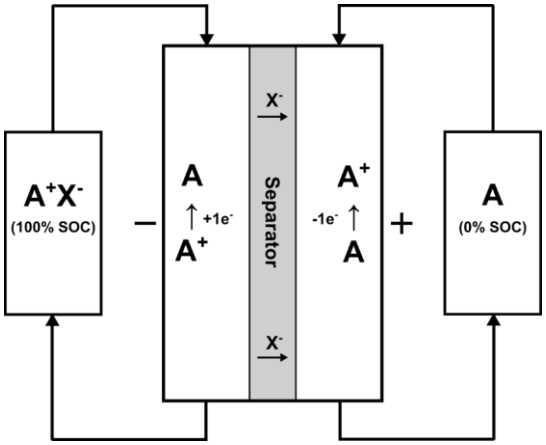

Figure 2: Schematic of charging in a symmetric flow cell, where A is the neutral active species, A^+ is the charged active species, and X^- is a monovalent anion.

What can be learned?: This technique is essentially an alternative to bulk electrolysis with several advantages and is best used for determining the capacity retention and coulombic efficiency of a single active species. Bulk electrolysis employs a dilute ($\leq$ 5 mM) active species, which is cycled against a sacrificial counter electrode, isolated from the reaction of interest by a porous glass frit.[4] The symmetric flow cell technique offers a more controlled electrolyte environment by removing the need for a counter electrode of dissimilar material, eliminating the possibility of side-product species crossing from the counter electrode chamber and contaminating the working electrolyte. The flowing electrolyte also improves mass transfer, enabling higher concentration cycling studies, and investigates active material stability on porous carbon electrodes relevant to flow battery applications (e.g., carbon paper, carbon felt), as opposed to reticulated vitreous- or glassy-carbon.[1] This technique can also monitor changes in ASR as a function of SOC with polarization or impedance measurements.

Typical Operating Conditions: Active species concentration $\geq$ 50 mM. Current density will depend on active species concentration and separator selection, but should be between 5 – 150 mA

cm^{-2}. Should access 70% – 85% of total theoretical capacity during charging. Pick current density to allow for optimal capacity access. Solution viscosity < 50 mPa·s.

Full Flow Cell (Figure 3):

How it works: The full flow battery contains active species that charge to different oxidation states on either side of the battery, storing energy upon charging and delivering energy upon discharging. The cell can be asymmetric, with different parent active species on either side (e.g., Refs.[4,5]), or symmetric, with the same parent active species on both sides (e.g., Refs.[6,7]).

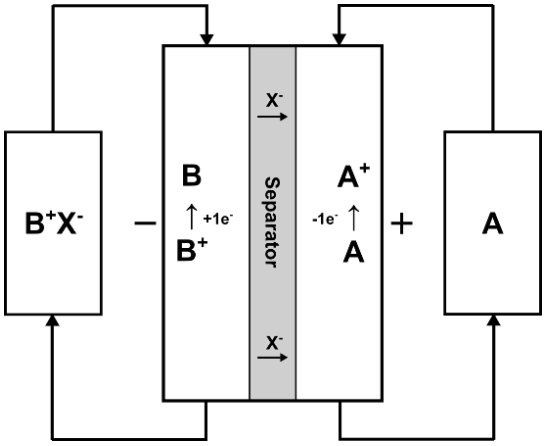

Figure 3: Schematic of charging in a full flow cell, where A and B are the positive and negative electrolyte active materials, respectively. X^- is a monovalent anion.

What can be learned?: This experiment evaluates the performance of a full flow cell, including coulombic, voltaic, and energy efficiencies, as well as capacity retention. Monitoring the reservoirs electrochemically[8,9] or spectroscopically[6,10] can determine SOC and / or crossover rates.

Typical Operating Conditions: Active species concentration ≥ 0.1 M. Current density will depend on active species concentration and separator selection, but should be between 5 – 150 mA cm^{-2}. Should access 70% – 85% of total theoretical capacity during charging. Pick current density to allow for optimal capacity access. Solution viscosity < 50 mPa·s.

1. J. D. Milshtein, J. L. Barton, R. M. Darling, and F. R. Brushett, *J. Power Sources*, **327**, 151–159 (2016).
2. R. M. Darling and M. L. Perry, *ECS Trans.*, **53**, 31–38 (2013).
3. R. M. Darling and M. L. Perry, *J. Electrochem. Soc.*, **161**, A1381–A1387 (2014).
4. S. M. Laramie, J. D. Milshtein, T. M. Breault, F. R. Brushett, and L. T. Thompson, *J. Power Sources*, **327**, 681–692 (2016).

5. I. L. Escalante-García, J. S. Wainright, L. T. Thompson, and R. F. Savinell, *J. Electrochem. Soc.*, **162**, A363–A372 (2015).
6. W. Duan et al., *J Mater Chem A*, **4**, 5448–5456 (2016).
7. R. A. Potash, J. R. McKone, S. Conte, and H. D. Abruna, *J. Electrochem. Soc.*, **163**, A338–A344 (2016).
8. L. Su et al., *J. Electrochem. Soc.*, **163**, A5253–A5262 (2016).
9. G. Nagarjuna et al., *J. Am. Chem. Soc.*, **136**, 16309–16316 (2014).
10. M. Skyllas-Kazacos and M. Kazacos, *J. Power Sources*, **196**, 8822–8827 (2011).

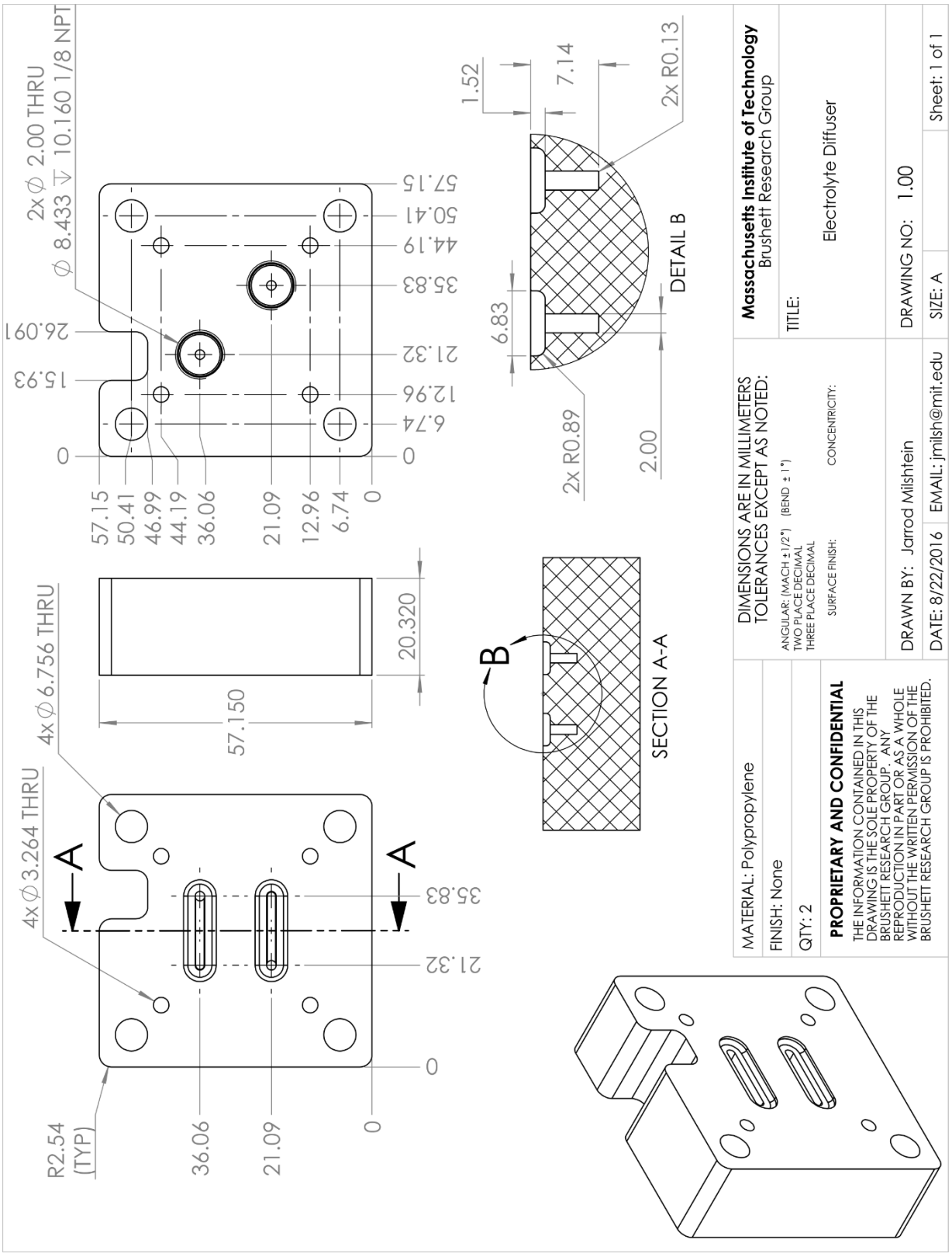
2x ⌀ 2.00 THRU
⌀ 8.433 ↧ 10.160 1/8 NPT
4x ⌀ 3.264 THRU
4x ⌀ 6.756 THRU
R2.54 (TYP)
A
A
B
SECTION A-A
DETAIL B
2x R0.89
2x R0.13
1.52
7.14
6.83
2.00
57.150
20.320
57.15
50.41
46.99
44.19
36.06
21.09
12.96
6.74
0
35.83
21.32
15.93
26.091
MATERIAL: Polypropylene
FINISH: None
QTY: 2
PROPRIETARY AND CONFIDENTIAL
THE INFORMATION CONTAINED IN THIS DRAWING IS THE SOLE PROPERTY OF THE BRUSHETT RESEARCH GROUP. ANY REPRODUCTION IN PART OR AS A WHOLE WITHOUT THE WRITTEN PERMISSION OF THE BRUSHETT RESEARCH GROUP IS PROHIBITED.
DIMENSIONS ARE IN MILLIMETERS
TOLERANCES EXCEPT AS NOTED:
ANGULAR: (MACH ±1/2°) (BEND ± 1°)
TWO PLACE DECIMAL
THREE PLACE DECIMAL
SURFACE FINISH:
CONCENTRICITY:
DRAWN BY: Jarrod Milshtein
DATE: 8/22/2016
EMAIL: jmilsh@mit.edu
Massachusetts Institute of Technology
Brushett Research Group
TITLE:
Electrolyte Diffuser
DRAWING NO: 1.00
SIZE: A
Sheet: 1 of 1
1
2

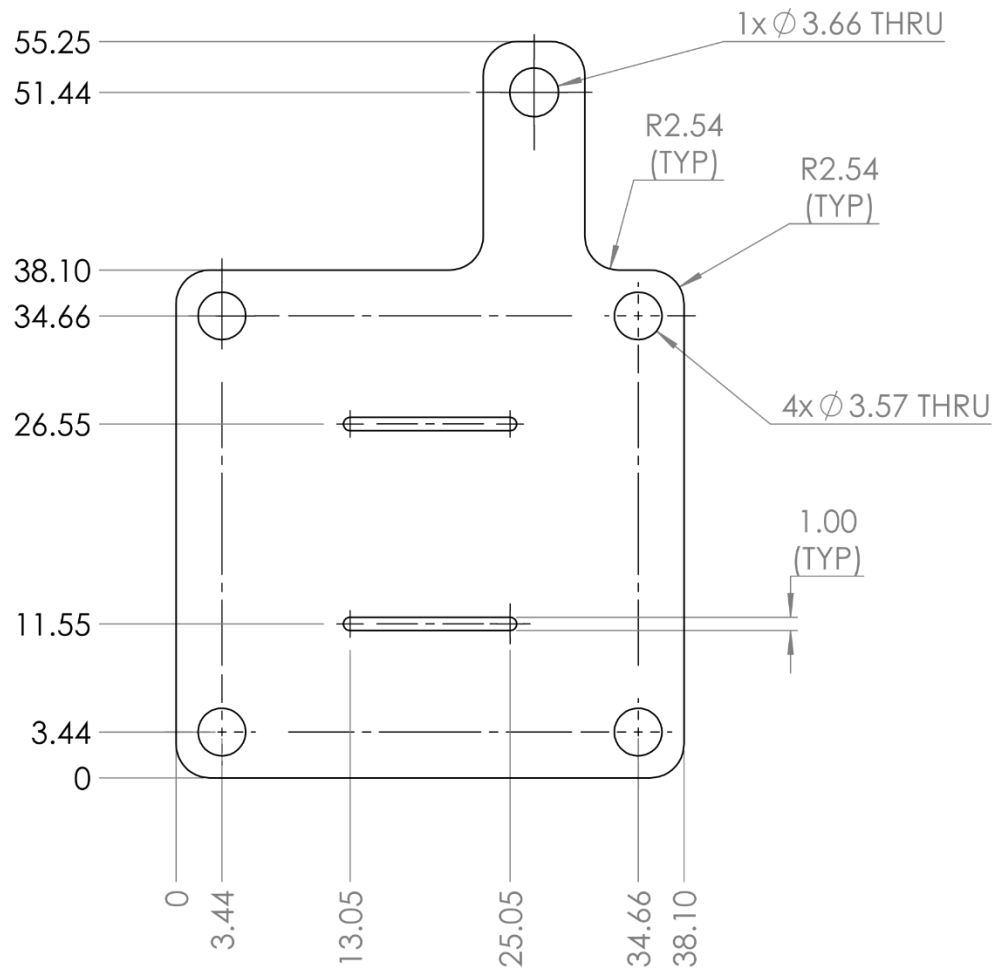
55.25
51.44
38.10
34.66
26.55
11.55
3.44
0
1x ∅ 3.66 THRU
R2.54
(TYP)
R2.54
(TYP)
4x ∅ 3.57 THRU
1.00
(TYP)
0
3.44
13.05
25.05
34.66
38.10
3.18

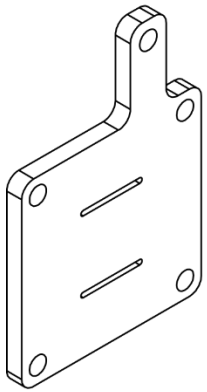

Isometric

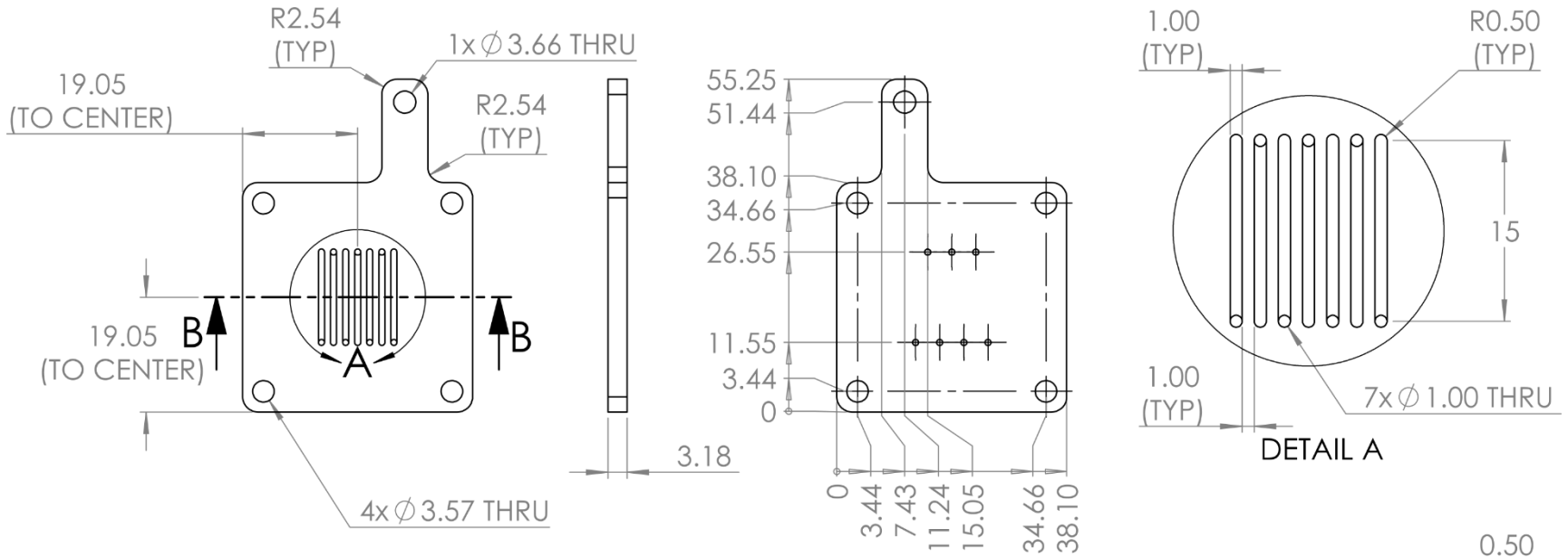

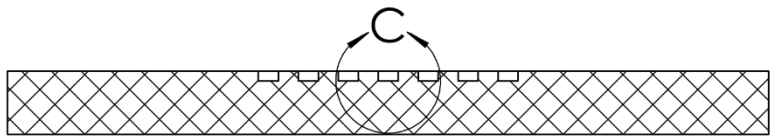

SECTION B-B

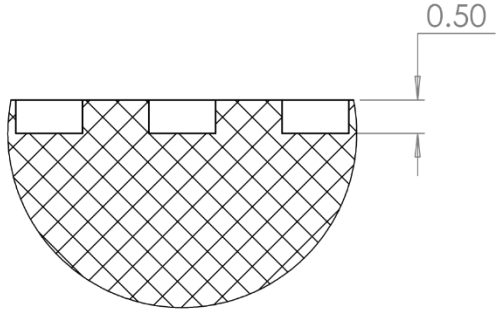

DETAIL C

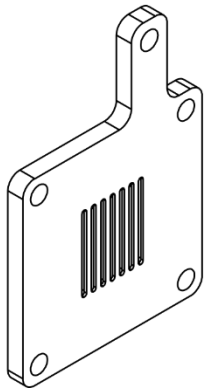

360

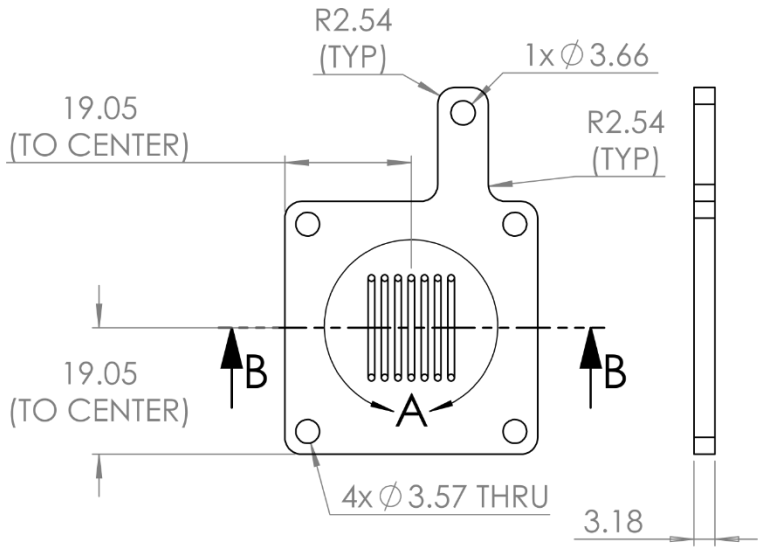

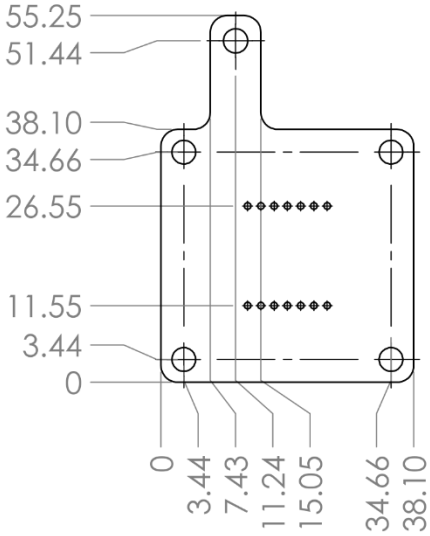

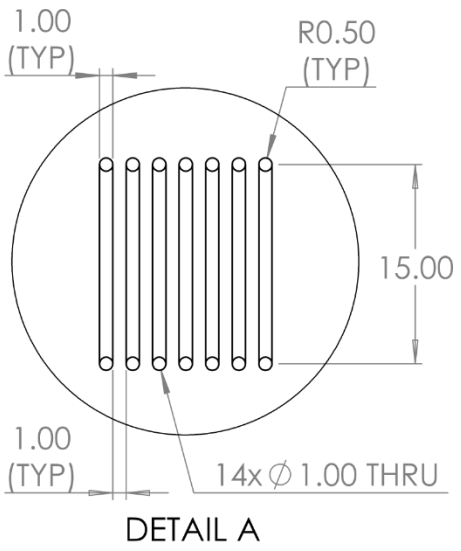

DETAIL A

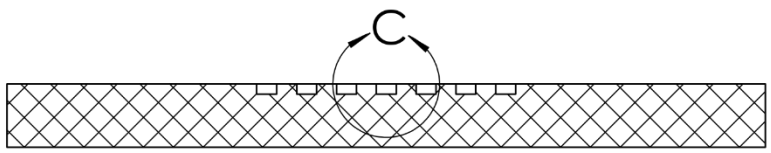

SECTION B-B

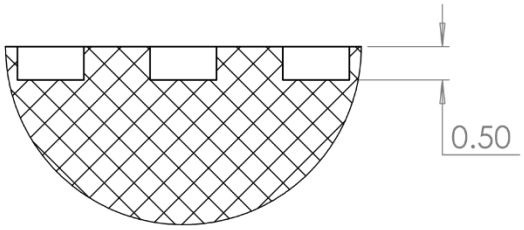

DETAIL C

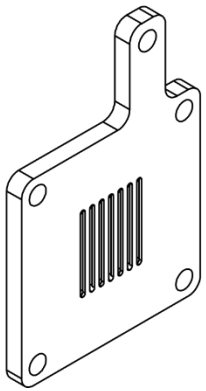

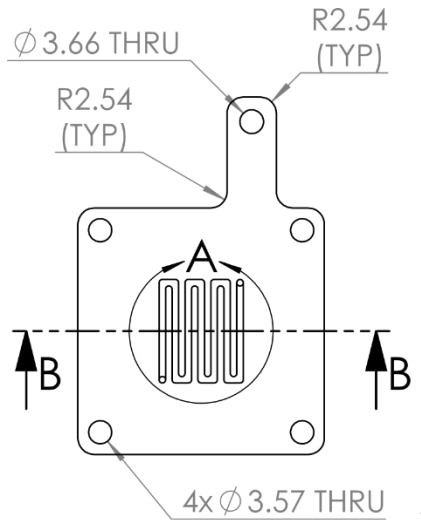

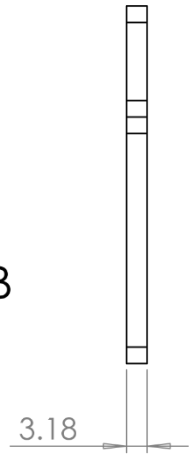

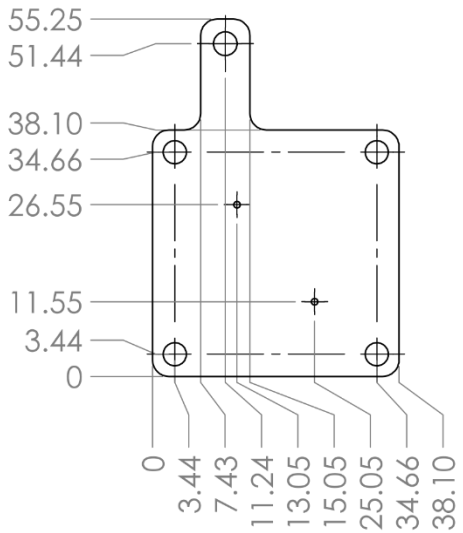

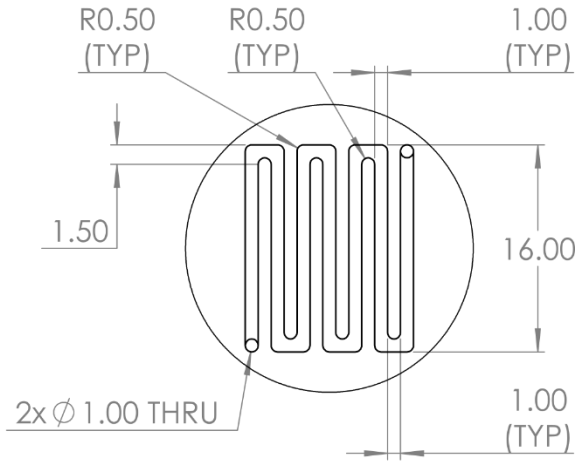

DETAIL A

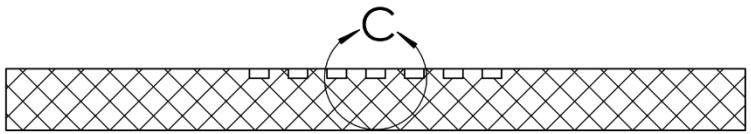

SECTION B-B

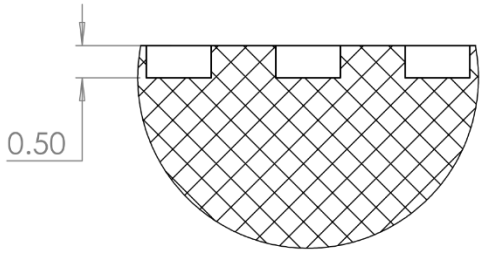

DETAIL C

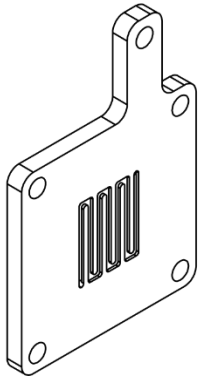

B.9 GEN2 Flow Cell Chemical Compatibility Chart

		Non-Aqueous Solvents					
Part	**Material**	*Carbonates*	*Acetonitrile*	*Dimethoxyethane*	*Dimethylformamide*	*Dichloromethane*	*Acetone*
Flow Field	Impregnated Graphite	A	A	A	A	A	A
End Plates	Polypropylene	A	A	A	A	D	A
Barbed Tube Fittings	Polypropylene	A	A	A	A	D	A
Compression Tube Fittings (Type 1)	Perfluoroalkoxy alkane (PFA)	A	A	A	A	A	A
Compression Tube Fittings (Type 2)	Stainless Steel	A	A	A	A	A	A
Gasket	PTFE	A	A	A	A	A	A
O-rings (Type 1)	Kalrez	A	A	A	A	A	A
O-rings (Type 2)	Viton	C	D	C	C	A	D
O-rings (Type 3)	EPDM	U	U	U	B	D	A
Pump Head Tubing	Norprene	A	C	B	B	B	C
Other Tubing	Perfluoroalkoxy alkane (PFA)	A	A	A	A	A	A

		Aqueous Solvents				
Part	**Material**	*Ethanol*	*Isopropyl Alcohol*	*Sulfuric Acid (0 - 75%)*	*Hydrochloric Acid*	*Alkaline Solutions*
Flow Field	Impregnated Graphite	A	A	A	A	A
End Plates	Polypropylene	A	A	A	B	A
Barbed Tube Fittings	Polypropylene	A	A	A	B	A
Compression Tube Fittings (Type 1)	Perfluoroalkoxy alkane (PFA)	A	A	A	A	A
Compression Tube Fittings (Type 2)	Stainless Steel	A	A	D	D	C
Gasket	PTFE	A	A	A	A	A
O-rings (Type 1)	Kalrez	A	A	A	A	A
O-rings (Type 2)	Viton	A	A	A	A	D
O-rings (Type 3)	EPDM	A	A	B	C	A
Pump Head Tubing	Norprene	B	B	A	A	A
Other Tubing	Perfluoroalkoxy alkane (PFA)	A	A	A	A	A

A	Excellent
B	Good
C	Fair
D	Severe Attack
U	Unknown